AN INVESTIGATION OF COLORADO FRONT RANGE WINTER STORMS USING A NONHYDROSTATIC MESOSCALE NUMERICAL MODEL DESIGNED FOR OPERATIONAL USE

John S. Snook

Roger A. Pielke, Adviser

Colorado State University

DEPARTMENT OF ATMOSPHERIC SCIENCE

PAPER NO. 541

AN INVESTIGATION OF COLORADO FRONT RANGE WINTER STORMS USING A NONHYDROSTATIC MESOSCALE NUMERICAL MODEL DESIGNED FOR OPERATIONAL USE

John S. Snook

Department of Atmospheric Science
Colorado State University
Fort Collins, Colorado
Fall 1993

Atmospheric Science Paper No. 541

ABSTRACT

AN INVESTIGATION OF COLORADO FRONT RANGE WINTER STORMS USING A NONHYDROSTATIC MESOSCALE NUMERICAL MODEL DESIGNED FOR OPERATIONAL USE

State-of-the-art data sources such as Doppler radar, automated surface observations, wind profiler, digital satellite, and aircraft reports are for the first time providing the capability to generate real-time, operational three-dimensional gridded data sets with sufficient spatial and temporal resolutions to diagnose the structure and evolution of mesoscale systems. A prototype data assimilation system of this type, called the Local Analysis and Prediction System (LAPS), is being developed at the National Oceanic and Atmospheric System's Forecast Systems Laboratory (FSL). The investigation utilizes the three-dimensional LAPS analyses for initialization of the full physics, nonhydrostatic Regional Atmospheric Modeling System (RAMS) model developed at the Colorado State University to create a system capable of generating operational mesoscale predictions.

The LAPS/RAMS system structured for operational use can add significant value to existing operational model output and can provide an improved scientific understanding of mesoscale weather events. The results are presented through two case study analyses, the 7 January 1992 Colorado Front Range blizzard and the 8-9 March 1992 eastern Colorado snow storm. Both cases are ideal for this investigation due to the significant mesoscale variation observed in the precipitation and flow structure. The case study results demonstrate the ability to successfully detect and predict mesoscale features using a mesoscale numerical model initialized with high resolution (10 km horizontal grid interval), non-homogeneous data. Conceptual models of the two snow storms are developed by utilizing

the RAMS model output in combination with observations and other larger domain model simulations.

The strong influence of the Colorado topography on the resultant flow is suggested by the generation of a lee vortex that frequently develops east of the Front Range and south of the Cheyenne Ridge in stable, northwest synoptic flow. The lee vortex, often called the "Longmont anticyclone", exhibits surface flow characteristics that are similar to results from low Froude number flow around an isolated obstacle. A series of numerical experiments using RAMS with idealized topography and horizontally homogeneous initial conditions are presented to investigate typical low Froude number flow characteristics in the vicinity of barriers representative of the Colorado topography. The results are compared to the findings of previous investigations and to the case study observations and numerical predictions. The findings suggest that the Colorado orography significantly altered the low-level flow in both case studies resulting in mesoscale variation of observed precipitation. Improved representation of the topography by the model led to the majority of the forecast improvement.

John S. Snook
Department of Atmospheric Science
Colorado State University
Fort Collins, Colorado 80523
Fall 1993

ACKNOWLEDGEMENTS

I would like to thank my committee members, Drs. Roger Pielke, John McGinley, David Randall, Richard Johnson, and Paul Mielke, for their help and guidance throughout this study. Thanks to Dr. William Cotton for his last minute assistance during the final defense. Special thanks to my advisor, Dr. Roger Pielke, whose encouragement and optimism always kept me on track. Also to Dr. John McGinley, whose support and encouragement, as not only a committee member but as a friend, made all this possible.

Thanks to Drs. Craig Tremback and Robert Walko for their advice and expertise pertaining to the model. The support of Dallas McDonald and her cohorts, Bryan Critchfield and Tony Smith, towards the many miscellaneous details is appreciated. The financial support of the Forecast Systems Laboratory is acknowledged.

Finally, on a more personal note, the many hours sitting in a G-car with Paul Schultz will not be forgotten. Despite being a Tiger fan, the advice, support, and humor of Jerry Schmidt helped immensely. Thanks to my parents, who have always encouraged and supported my education. Last, and most importantly, my deepest appreciation to my wife, Jackie, who was always there, even on that last all nighter of pasting figures.

TABLE OF CONTENTS

LIST OF FIGURES

LIST OF TABLES

Chapter 1

INTRODUCTION

State-of-the-art data sources such as Doppler radar, automated surface observations, wind profiler, digital satellite and aircraft reports are providing a vastly improved view of the atmosphere to the operational meteorological community. Using these data sources, three-dimensional gridded data sets can be assembled in real-time with sufficient spatial and temporal resolutions to diagnose the structure and evolution of mesoscale systems.

A data assimilation system of this type, called the Local Analysis and Prediction System (LAPS) (McGinley 1989, McGinley et al. 1991), is being developed at the National Oceanic and Atmospheric System's Forecast Systems Laboratory (FSL). FSL ingests real-time meteorological data that will be representative of data sets available to the operational community by the mid-1990s. LAPS integrates all available data to generate real-time, high-resolution (10 km horizontal grid interval), three-dimensional analyses of meteorological state variables, which can then be used in computer workstation product format or as input to appropriate algorithms and numerical forecast models.

Three-dimensional LAPS analyses afford the opportunity to initialize a full-physics, nonhydrostatic mesoscale numerical model with operational (non-homogeneous) data at resolutions ($\sim$10 km horizontal grid interval) greater than previously feasible. Potentially, the mesoscale model forecasts can provide improved operational forecasts and an improved scientific understanding of mesoscale weather events.

The objectives of this dissertation are to 1) evaluate the accuracy of forecasts from a mesoscale numerical model initialized with high-resolution, non-homogeneous data, 2) determine if the model forecasts can detect mesoscale features, hence adding value to currently available regional scale model forecasts and 3) demonstrate the ability to utilize

the model output to provide an improved scientific understanding of mesoscale weather events. Wesley (1991) notes that the Colorado Front Range is an excellent laboratory for winter storm studies due to the wide variety of meteorological phenomena. Since these phenomena often exhibit significant mesoscale variation, the Colorado Front Range is an ideal location to evaluate mesoscale model forecasts. The objectives will be addressed by initializing the Regional Atmospheric Modeling System (RAMS) developed at Colorado State University with LAPS analyses from two significant Colorado Front Range snowstorms; 7 January and 8-9 March 1992. Strong winds, heavy snowfall, and significant mesoscale precipitation variation were observed in both cases. In addition, pertinent idealized simulations will be performed to isolate particular atmospheric phenomena that can enhance the scientific understanding of the case studies.

This investigation is unique in that it is one of the first attempts to use operational analyses to initialize a numerical forecast model at horizontal grid intervals of 10 km. This is now possible because of the state-of-the-art, high-resolution data sources available to the operational community. Also, advances in desk top computer workstation and data storage technology are enabling the capability to produce mesoscale numerical forecasts in real-time at a reasonable cost (Cotton et al. 1993). Three-dimensional visualization techniques, available with the advanced desk top computer workstations, enable the forecaster to display and interpret the enormous amounts of data generated by the mesoscale forecast model in a reasonable amount of time. Results from this study demonstrate, for the first time, a real time analysis and prediction system with the capability to forecast and display mesoscale systems.

A review of previous research related to this investigation is discussed in Chapter 2. The experiment design is presented in Chapter 3. Two Colorado Front Range winter storm case studies and RAMS simulations are described in Chapters 4 and 5. Pertinent idealized simulations of flow over complex terrain and results are presented in Chapter 6. Finally, Chapter 7 provides a summary and conclusions.

Chapter 2

BACKGROUND

Various approaches have been attempted to further the understanding of meteorological phenomena in the vicinity of complex terrain. Case study analyses of significant weather events have provided pertinent conceptual models. Since a wide variety of terrain influenced weather phenomena effects the Colorado Front Range, numerous field projects and case study analyses have been conducted over this region. More recently, numerical simulations of Front Range winter storms have provided further insight into the processes important to describing meterological phenomena over mountainous terrain. Numerical modeling using operational data has been progressing towards higher spatial resolutions and is just now entering the mesoscale resolutions necessary to have any chance of forecasting the mesoscale variation often observed in Front Range winter storms. Other investigations have focused on using idealized terrain to provide a basis for understanding the complexities of flow around three-dimensional obstacles. Results from these studies have provided further physical insight towards interpreting and understanding actual weather phenomena in the vicinity of complex terrain. A review of the literature using four research approaches and how it is pertinent to this investigation is presented in the following sections.

2.1 Observational Studies of Front Range Winter Storms

Significant winter precipitation along the Colorado Front Range is typically associated with synoptically driven easterly "upslope" flow, opposite in direction from the climatologically prevailing westerlies (Reinking and Boatman 1986). These upslope events are normally categorized into two types: 1) systems with fully developed, deep cyclonic circulations and 2) shallow anticyclonic systems. Wesley (1991) also cites cases where both

circulations are important at different atmospheric levels. Most observational studies of Colorado Front Range winter storms have concentrated on the effects of the upslope circulations interacting with the complex terrain. For some winter storm cases, the juxtaposition of prevailing westerlies and easterly upslope circulations further complicates an already intricate situation. These cases present difficult forecast problems with sharp gradients in precipitation typically observed. Recognizing the implications of the various flow interactions and how to better forecast them is an important aspect of this investigation.

An early observational investigation of the weather normally associated with eastern Colorado cyclones was presented by Fawcett and Saylor (1965). Results were derived from a composite of 21 typical Colorado spring storms occurring during February, March, and April of 1959 through 1963. The average eastern Colorado heavy snow scenario begins with a western United States 500 mb trough and associated vorticity center that travels eastward along the Utah-Arizona and Colorado-New Mexico borders before propagating northeastward towards the Midwest. A surface low pressure center is located approximately 650 km downstream from the 500 mb vorticity maxima. Heavy snow occurs about 500 km to the north-northwest of the surface low center and is enhanced by terrain-induced upward vertical motion.

Howard and Tollerud (1988) and Tollerud et al. (1991) generated a storm-relative composite structure of the heaviest snow-producing Colorado Front Range winter storms that occurred between 1952 and 1987. The results depict a typical scenario of a fully developed, deep cyclonic event. The composite storm evolution shows the cyclone to emanate from the Eastern Pacific developmental trough and begin to deepen over the northwest portion of the United States. The storm track for the middle and late cyclone stages moves eastward across the Four Corners region and then northeastward into the Midwest, consistent with the results of Fawcett and Saylor (1965).

Reinking and Boatman (1986) provided a comprehensive description of upslope precipitation events. The deep cyclonic storms are more likely to produce heavy snow than the shallow anticyclonic systems that sometimes only generate stratus and no precipitation. Of course, these scenarios represent the extremes and either circulation type can

produce a wide spectrum of precipitation, both spatially and between cases, that is often attributed to the Front Range topography (e.g. Schlatter et al. 1983, Wesley 1991). Observational case studies have provided insight into the numerous mesoscale variations that can occur with Front Range winter storms.

Lilly (1981) used Doppler radar and automated surface observations to investigate a Colorado Front Range anticyclonic upslope precipitation event occurring on 9-10 February 1981. Doppler radar was instrumental in defining several dynamically significant features including the evolving wind profile in the upslope region, the ascent of cold, post-frontal air, and the entrainment of the cold air into the upper level westerlies. Due to the excessive amount of precipitation combined with very cold surface temperatures, Lilly concluded that over half of the snow observed near the foothills fell out of the overriding westerlies. Lilly's investigation is an early example of the need to have high resolution observations to study the mesoscale details of Front Range winter storms.

Schlatter et al. (1983) presented a detailed analysis of the northeast Colorado 1982 Christmas eve blizzard that dropped 0.5 to 1.0 m of snow including 0.6 m at Denver, a 24 h record. The synoptic scale features of the storm were very similar to the composite analyses determined by Fawcett and Saylor (1965). Yet, tremendous mesoscale variability in snowfall amounts was observed with a gradient of 1.0 m across a distance of only 90 km. Automated surface observations and wind profiler data enabled a more complete picture of the snowfall variations. However, Schlatter et al. noted that the variations are difficult to explain quantitatively and that there is much to learn before the details of these storms can be forecasted accurately.

Boatman and Reinking (1984) studied the circulations and precipitation associated with shallow anticyclonic upslope storms. Schematic models of anticyclonic upslope storms illustrated the possible interactions of prevailing westerly flow with the shallow arctic air mass situated over the Plains. For these cases, the cold dome acts as the primary lifting source. Due to their shallow nature, only about 50% of these systems precipitate. Complex microphysical processes are important in determining the precipitation structure in anticyclonic events (Reinking and Boatman 1986). Convective processes typically do not

affect the precipitation except in a few spring season cases when surface heating is greater (e.g. Papineau 1992). Characteristic cloud temperatures imply supercooled conditions through the entire cloud depth. Ice crystals are generated through the heterogeneous nucleation process and crystal growth is predominantly by vapor deposition. The "seeder-feeder" process (e.g. Cotton and Anthes 1989) can have a significant effect on the amount and intensity of precipitation.

Young and Johnson (1984) investigated the meso- and microscale structure of a Front Range cold front with anticyclonic upslope behind the front. Using automated surface observations, the chronology of the surface front was described. As the front approached Colorado from the north, the western end of the front was held back by the Cheyenne Ridge located on the Colorado-Wyoming border. The portion of the front east of the Cheyenne Ridge continued southward unimpeded. An anticyclonic eddy formed in the lee of the Cheyenne Ridge such that frontal passage at stations in the lee of the Ridge occurred from the southeast. This author and others (Brown, personal communication) have frequently observed similar anticyclonic eddies when the synoptic flow ranges from the northwest to north. Since the center of the gyre is frequently located near the city of Longmont, the eddy is often referred to as "the Longmont anticyclone." The Longmont anticyclone can enhance upslope flow and precipitation along the Front Range. The relationship of the anticyclone with the lee-side eddies observed in the idealized simulations is a focus of this investigation.

Occasionally, heavy snowfall does occur in association with anticyclonic upslope flow (Dunn 1987). Dunn investigated a case from 8-9 December 1985 where a large High Plains anticyclone pushed a synoptic scale cold front south through all of eastern Colorado. Behind the cold front, locally heavy snow developed east of the Front Range. Dunn suggested that the post-frontal upslope flow produced a narrow band of cold air damming and a mesofront similar to coastal fronts observed during cold air damming events east of the Appalachian mountains (Bosart 1975). Heaviest snowfall was observed immediately west of the mesofront and was likely attributed to mid-level, synoptically driven southeasterly flow overrunning the mesofront, suggesting a connection between synoptic-scale

and mesoscale features. The extreme variability in observed precipitation with these cases makes the forecast very difficult. Dunn provided a conceptual model which, combined with high resolution automated observations, has improved public forecasting of anticyclonic heavy snow events.

Although orographic influences are typically significant in Front Range winter storms, dynamical effects can not be neglected. Dunn (1988) studied a Front Range snow storm from September 1985 where dynamics provided the primary forcing and orographic influences were minimal. Furthermore, standard pattern recognition and quasi-geostrophic forecasting techniques provided little insight into the dynamical forcing of the observed vertical motion and precipitation. A more detailed investigation using high resolution observations was necessary to show the correlation between ageostrophic forcing, caused by jet-streak dynamics and frontogenetical circulations, and the heavy snowfall. Dunn also noted the atmosphere had the potential to respond to the forcing through the release of conditional symmetric instability (CSI; Bennetts and Hoskins 1979).

Two case studies where convergence zones developed along the Colorado Front Range due to blocking of upslope flow were investigated by Wesley and Pielke (1990). Both cases exhibited distinctly layered temperature and wind structures with enhanced precipitation east of the mountains. However, the blocking induced convergence developed differently for the two cases. In the first case (30-31 March 1988), the convergence resulted from the damming of cold air against the mountain barrier. A band of heavy snow was observed west of the convergence line and resulted from moist easterly flow overriding the low-level cold pool, similar to the process reported by Dunn (1987). A moist westerly flow above the two lower layers created a potential seeder process similar to that reported by Lilly (1981) and Reinking and Boatman (1986).

The second case study (9-10 February 1988) indicated a less distinct region of convergence resulting from topographical blocking of easterly flow. No evidence of cold air damming was observed. The precipitation pattern appeared to be more closely correlated with the topography. An important difference between the two cases was the first situation contained a shallow, low-level cold pool beneath relatively weak mid-level easterlies, while

the second case had a weak cold pool beneath deep, relatively warm easterlies. Bands of heavy snow oriented parallel to the thermal wind vector were observed in both cases indicating that the release of CSI likely enhanced the precipitation. Wesley and Pielke noted that these low-level convergence zones occur frequently along the Colorado Front Range in association with winter upslope events. As stated in previous investigations, more research is required to fully understand the extreme precipitation variability on scales of less than 50 km that is typical of Front Range winter storms.

Wesley et al. (1990) investigated the extreme arctic outbreak along the Colorado Front Range of 1-5 February 1989. Unusually heavy snow occurred when considering the very cold surface temperatures of -25°C. The precipitation gradient along the Front Range was similar to the cold air damming case of 30-31 March 1988 (Wesley and Pielke 1990). However, Wesley et al. proposed that moist, mid-level westerly flow overrunning the deep cold pool produced a significant portion of the precipitation as opposed to overrunning mid-level easterly flow in the traditional cold air damming scenario. This process is consistent with observations from the arctic outbreak case of 9-10 February 1981 (Lilly 1981). The unusually deep cold pool protruded into the moist southwesterly flow creating enhanced ascent and a seeder-feeder situation. Observations of aggregated and heavily-rimed snow crystals and two-dimensional model simulations helped confirm the overrunning westerly flow scenario.

Colorado Front Range winter storms often contain bands of heavier snow that are embedded within the precipitation shield and are oriented parallel to the thermal wind (Lilly 1981, Dunn 1988, Wesley and Pielke 1990). These observations indicate that the release of CSI is often significant in enhancing the snowfall. Snook (1992) demonstrated the utility of high resolution observation systems (e.g. Doppler radar, wind profiler) combined with mesoscale analysis techniques to evaluate CSI within a Front Range snow event. The composite studies of Howard and Tollerud (1988) and Tollerud et al. (1991) also illustrate that the atmospheric conditions typical of a Front Range winter storm are conducive to the release of CSI. The heaviest observed snowfall showed a high correlation with the quantitative amount of available CSI.

Low-level barrier jets are sometimes observed with winter storms in the vicinity of mountains (e.g. Parish 1982). Along the Front Range, the northerly barrier jet is typically linked to the damming of cold air up against the mountain barrier and may be enhanced by cyclogenesis to the south and east (Wesley 1991). Moist easterly flow forced over the dammed cold air creates areas of enhanced precipitation (Dunn 1987, Colman 1989). A low-level barrier jet was observed along the Colorado Front Range using Doppler radar and wind profiler data during the heavy snow event of 26 December 1987 (Dunn 1992). Embedded within a large area of light to moderate snow was a narrow band of heavy snow located beneath the barrier jet. In contrast to mesofrontal overrunning, Dunn suggested that the heavy snow band resulted from along barrier ascent of air within the sloped barrier jet and the precipitation was further enhanced by the release of CSI. The frequent observation of narrow heavy snow bands along the Colorado Front Range led Dunn to propose that further investigation of this mesoscale phenomenon is warranted. Using an analysis scheme, such as LAPS, that incorporates Doppler velocity data and other mesoscale observations could lead to an improved understanding of these Front Range winter storm events.

Observations of Front Range winter storms exhibit a wide variety of atmospheric structures. Orographic, dynamic, and microphysical processes must be all considered together when appraising these systems. One common feature is the potential to generate extreme variations in precipitation amounts over small spatial scales. Case study results using state-of-the-art observations (e.g. automated surface observations, wind profiler, and Doppler radar) have provided more detailed conceptual models of these systems. These findings have furthered the understanding and improved the forecasting of Front Range winter storms.

2.2 Numerical Simulations of Front Range Winter Storms

Only a few numerical simulations of Colorado Front Range winter storms appear in the literature. This may be attributed to the complexity and significant scale interaction present in these systems (Wesley 1991). Operational models with spatial resolutions too

coarse to resolve the mesoscale details often provide inadequate predictions of Front Range snowstorms. Advances in mesoscale modeling during the past decade (e.g. Ross 1986) have presented the opportunity to investigate and forecast Front Range winter storms in greater detail. Increased model grid resolution allows an improved representation of the complex orography. Hence, the investigations published thus far have primarily concentrated on the effects of topography on Front Range weather.

Several three-dimensional model simulations were performed by Abbs and Pielke (1987) to investigate orographic effects on northeast Colorado snowstorms. Case study observations from two northeast Colorado snowstorms, 24 December 1982 and 9 December 1985, showed northeasterly and southeasterly synoptic flow, respectively. Two numerical simulations were performed using the RAMS mesoscale model. A 15 km horizontal grid resolution was employed and the model was initialized with horizontally uniform fields. Model output from the first simulation, initialized with northeasterly flow, indicated a good qualitative agreement between predicted surface winds and observations. Regions of predicted upward vertical velocity correlated well with areas of observed snowfall. The second model simulation was initialized with low-level southeasterlies and upper-level southwesterlies. Model predicted surface winds did not compare favorably with observations. Automated surface observations from 9 December 1985 indicated the passage of a cold front from the north. The introduction of a cold pool into the northeast portion of the model domain was attempted in a third simulation. The model predicted surface winds compared much better with the observations. Abbs and Pielke concluded that the model could successfully demonstrate the relationship between the prevailing wind direction and observed snowfall distribution. The snowfall distribution correlated closely with terrain forcing.

Wesley et al. (1990) performed several two-dimensional experiments using RAMS to corroborate their observational results. They analyzed the influence of an existing deep pool of cold air positioned immediately east of the mountain barrier on the mid-level westerlies. They concluded that the cold pool retarded the downward penetration of the downslope flow, similar to Lee et al. (1989). Also, the cold pool appeared to force a deep region of ascent over the western portion of the cold pool.

The first attempt to simulate a Front Range winter storm using a mesoscale model initialized with non-homogeneous data was accomplished by Wesley (1991). RAMS was initialized with the National Meteorological Center (NMC) objective analyses for the deep cyclonic storm of 30-31 March 1988. The inner grid horizontal increment was 22 km and a full microphysics version of the model was employed. The simulation successfully depicted the development of strong upslope flow and heavy precipitation. When compared to operational model forecasts from NMC, the RAMS forecast of orographic enhancement of precipitation was much more accurate. Increased spatial grid resolution and improved topographical representation were significant contributors to this improvement. The forecasts of synoptic scale fields were less accurate than the operational model predictions however, which led to an underestimate of the observed blocked dynamic structure along the mountain barrier. This result underscores the importance of synoptic scale and mesoscale interactions in Front Range winter storms and the resulting weather. An enlargement of the outer grid domain was suggested as a possible solution to this problem. Further experimentation with improved model initialization was suggested for future research.

Model results from Wesley (1991) demonstrate the ability to obtain improved forecasts of orographic effects on vertical motion and precipitation using a mesoscale model initialized with non-homogeneous data. The results also indicate the importance of quality model initialization. Recent additions to the observational network along the Front Range, including Doppler radar, wind profiler, automated surface observations, and digital satellite data, are enabling improved atmospheric analyses suitable for mesoscale model initialization. The improved observational network combined with the advances in mesoscale numerical modeling offers the opportunity to investigate Front Range winter storms in detail much greater than previously possible.

2.3 Numerical Modeling using Operational Data

Historically, as data resolution and quality improve, as model numerics become more sophisticated, as communication capabilities increase, and as computers become faster, operational numerical model prediction uses smaller grid resolutions. Ross (1986) provides

a brief history of operational numerical weather prediction in the United States. The NMC is the central facility to implement operational numerical models in the United States. NMC has progressed from the limited-area fine-mesh model (LFM), introduced in 1976 with 190.5 km horizontal grid increments at 60°N (Gerrity 1977), to the nested grid model (NGM), introduced in 1985 with about 84 km grid spacing at 45°N on the finest mesh (Hoke et al. 1989), and plans to implement the step-mountain eta coordinate model (Mesinger et al. 1988) at a finer (30 km grid interval) resolution (Black and Mesinger 1991). Despite steady improvement in operational numerical forecasts, the operational models still have problems with wintertime systems containing low-level arctic air masses over the High Plains (Junker et al. 1989, Wesley 1991) and orographically influenced features (Rasmussen et al. 1992). Increased resolution of observations and improved model grid resolutions are necessary to provide better forecasts of winter storms in the vicinity of mountains. Research applications using mesoscale models with improved initialization are beginning to achieve this goal.

Warner and Seaman (1990) describe a real-time experimental mesoscale modeling system at The Pennsylvania State University (PSU). A hydrostatic version of the PSU/NCAR Mesoscale Model is used to generate numerical weather forecasts for the northeastern United States. The system employs a nested grid approach with a 30 km horizontal grid increment on the fine mesh. Operational data obtained from NMC are automatically combined with local observations to provide analyses for model initialization. 24 to 36 h forecasts are typically generated. Real-time model output for two case studies demonstrates the capability to provide greater detail in forecast fields of pressure, wind, and precipitation when compared to the NMC operational model output. In addition to improved forecasts, the real-time system has led to enhanced conceptual models and improvements in model physics.

A similar configuration of the PSU/NCAR Mesoscale Model, version 4 (MM4) was implemented during the Winter Icing and Storms Project 1991 (WISP91) to aid in operational planning (Rasmussen et al. 1992). Two parallel forecasts were performed, one using an MM4 initialization scheme and another using a MAPS initialization scheme (see

next paragraph). Model performance results are pending. A hydrostatic version of the PSU/NCAR Mesoscale Model, version 5 (MM5) with warm water microphysics and a 20 km fine grid was implemented to support the STorm scale Operational and Research Meteorology-Fronts Experiment and Systems Test (STORM-FEST) during the winter of 1992 and a nonhydrostatic version of MM5 was configured to support the WISP Instrumentation Test (WISPIT) during the winter of 1993 (Grell, personal communication). A nonhydrostatic version of MM5 has been recently developed and successfully tested on idealized and real-data simulations (Dudhia 1993).

FSL has been tasked with demonstrating the feasibility of operating real-time analysis and prediction systems at even smaller grid resolutions. The Mesoscale Analysis and Prediction System (MAPS) has been developed on a 60-km national scale grid using 25 sigma/isentropic hybrid levels (Benjamin et al. 1991) to provide updated model analyses and forecasts every 3 h. MAPS has been implemented at NMC as the Rapid Update Cycle (RUC) in 1993.

The first attempts to use MAPS as an initialization to a full physics, nonhydrostatic numerical model (i.e., RAMS) is discussed by Schmidt and Snook (1992) and Thompson (1993). Thompson provided daily real-time forecasts using RAMS with a 25 km inner grid and initialized with MAPS for the winters of 1991-92 and 1992-93. One objective was to investigate any improvement in the prediction of orographically-forced precipitation in the Colorado region. An important component of the investigation was the development of an objective statistical verification scheme to compare the mesoscale model forecasts with the operational model output. The scheme relies on the multivariate randomized block permutation (MRBP) technique developed by Mielke (1991). MRBP results indicated improvements over current operational models in forecasts of temperature, geopotential height, and wind. Improvements in precipitation amounts were obtained only when using a full microphysics version of the model.

The FSL LAPS generates regional scale analyses of atmospheric variables every hour using a 10 km grid with 21 isobaric levels. Snook and Schmidt (1992) describe the initial attempt to use LAPS as an initialization to RAMS. Since LAPS incorporates mesoscale

data not available to national scale analyses, a LAPS model initialization should improve mesoscale model forecasts. This investigation will use LAPS analyses as RAMS initialization to investigate the possibilities of generating real-time mesoscale predictions. Model output will be compared to other operational forecasts to verify if real-time mesoscale models can enhance the local short-range (0-12 h) forecast.

2.4 Idealized Simulations

Intuition tells us that complex terrain should have a significant effect on the ambient air flow. Early observers who lived in mountainous regions of the world provided crude evidence that this is indeed the case. For example, Abe (1932) used time-lapse photography of mountain clouds to infer vertical motions initiated by topographical features. Glider pilots also confirmed the existence of mountain induced atmospheric waves (e.g. Horsley 1945).

Corby (1954) provided a survey of the state-of-the-art knowledge of airflow over mountains. Investigations had primarily concentrated on either theoretical studies or physical model experiments. Corby noted the early theoretical works of Kelvin, Lamb and Queney that led to a general theory of adiabatic perturbations in a stratified rotating atmosphere of which flow over a mountain is a particular application. Scorer (1949) expanded the theory by considering variations on lapse rate and vertical wind shear. Physical model experiments up to that time had only limited success (Corby 1954) because of difficulties (or lack of knowledge) in achieving dynamic similarity between the model and the full scale problem.

Sheppard (1956), in a short correspondence, asked the question, 'Under what conditions will an airstream rise over a mountain range?' In other words, what criteria determine whether an air parcel travels over a mountain or simply around it. Using simple energy arguments, Sheppard hypothesized that an upstream parcel must have enough kinetic energy to overcome the potential energy based on the height of the barrier above the parcel elevation to pass over the mountain; otherwise, the parcel would pass around the mountain. The hypothesis allows for a combination of the two conditions where low

level parcels would go around the barrier and higher level parcels would go over the barrier. From these arguments, flow will be diverted around an obstacle when the incoming flow (U) is weak, the stability (N) is strong, and the obstacle height (h) is high. Hence, the resulting flow impinging on an obstacle will be primarily in an x-y cross section for low Froude number (defined as Fr = U/Nh) cases and will be primarily in an x-z cross section for high Froude number cases. Thus, for high Froude numbers, the weather on the lee of the barrier will be primarily affected by mountain wave activity and will in general be dry. For low Froude numbers, the lee side weather will be primarily affected by flow coming around the barrier. This flow may create areas of low level convergence and divergence that can have significant implications on the mesoscale variation of lee side precipitation. It is these low Froude number situations that are of interest in this investigation.

Drazin (1961) noted that Sheppard's query had not been answered since previous investigations fell into two categories: 1) experiments that used mountains with low aspect ratios allowing one to linearize the equations but neglected flow around the mountain and 2) two-dimensional flow experiments where the mountain had no sides for the flow to go around. In both cases, only flow over the top of the barrier was considered. Drazin presented the first theoretical attempt to describe the flow *around* a three-dimensional obstacle. Since linear theory is not applicable to low Froude number (i.e. Fr $<$ 1) situations, Drazin utilized potential flow theory that becomes valid as the Froude number approaches zero. The primary flow is the potential flow of a uniform stream around the obstacle. The analytical equations described flow fields that were consistent with Sheppard's hypotheses, but Drazin had no actual data from either observations or physical experiments to confirm the results. Although Sheppard's kinetic energy arguments have been recently refuted (Smith 1989a, Smith 1989b, Smith 1990), the works of Sheppard and Drazin provided the basis for future investigations of low Froude number flow.

Even today, the bulk of the literature pertaining to airflow over complex terrain does not consider flow around the barrier (i.e. Fr $<$ 1). For example, only one section by Durran (1990) and a short appendix by Smith (1990) consider flow around the barrier in the American Meteorological Society's meteorological monograph, 'Atmospheric Processes

over Complex Terrain.' Durran (1990) notes that significant progress has been made in understanding the flow around relatively simple three-dimensional objects, but our current understanding of flow around three-dimensional mountains is far from complete. The progress achieved thus far in understanding low Froude number flow in the vicinity of complex terrain has primarily occurred through conclusions drawn from four types of investigations: 1) physical model experiments, 2) observational, 3) theoretical, and 4) numerical model experiments.

2.4.1 Physical Model Experiments

Physical model experiments have successfully simulated flow patterns in the vicinity of complex terrain for over 50 years (Meroney 1990). These experiments typically utilized wind tunnels or towing tanks where an object was pulled through a stratified fluid. Advantages of physical modeling include near-infinitesimal resolution allowing a realistic simulation of subgrid scale interactions. The use of real fluids automatically provides the correct form of the conservation equations including nonhydrostatic, non-Boussinesq, compressible flow without truncation or differencing errors. Physical model experiments provided the first visual evidence of stably stratified (low Froude number) flow in the vicinity of complex terrain. Early investigations were designed to confirm the analytical results of Drazin. The experiments verified the general consensus that air parcels travel around an obstacle for low Froude number cases and the parcels travel over the obstacle for high Froude number cases. The experiments also helped define the limits of applicability for the linear and potential flow theories. Although some of the presented conclusions relied on Sheppard's flawed kinetic energy arguments, the observations from the physical experiments played a significant role in confirming future theoretical approaches.

Brighton (1978) reviewed Drazin's theory and extended it to rotating flow. He showed that the theory breaks down at an elevation of U/N below the top of the obstacle. Results from water channel experiments using low Froude numbers varying from 0.03 to 0.3 corroborated most of Drazin's analytic solutions. However, a feature not predicted by the theory was the generation of lee side vortices and vortex shedding. Brighton suggested

that the eddies resulted from the separation of viscous shear layers generated at the obstacle boundaries and that the flow is constrained to a horizontal plane due to the strong stratification.

Baines (1979) designed a towing tank experiment to compare fluid flow past a two-dimensional barrier with and without a gap on one side. For the no-gap cases, blocked flow was observed with Fr $<$ 0.5 and all the fluid flowed over the barrier with Fr $>$ 0.5. When a gap was introduced, all the fluid below a critical level flowed around the barrier through the gap for Fr $<$ 0.5. The flow above the critical level traveled over the barrier in a vertical two-dimensional plane. With a gap and Fr $>$ 0.5, all the flow traveled over the barrier similar to the no-gap simulation. The blocking criterion of Fr $<$ 0.5 found by Baines was significantly less than Sheppard's criterion of Fr $<$ 1.0 which led Baines to speculate that Sheppard's "naive" energy argument may not apply to the two-dimensional case.

Using both towing tank and wind tunnel experiments, Hunt and Snyder (1980) conducted a systematic investigation of flow over a bell shaped hill with Froude numbers varying from 0.1 to 1.7. They determined that for Froude numbers less than approximately 0.4, the flow was nearly horizontal verifying Drazin's theory and establishing a limit of applicability. Downstream from the barrier, a symmetric pair of vortices were observed creating an upstream flow along the center line. The vortices were smaller and closer to the base of the hill as the Froude number approached one. Hunt and Snyder attributed the vortices to surface shear stress, similar to Brighton (1978). For Froude numbers between 0.4 and 1.0, a combination of lee wave flow above the around-the-barrier flow was observed, with the lee wave patterns more dominant as the Froude number approached one. The height of the upstream dividing streamline (H_s) is defined as the elevation between the two flow regimes. The physical experiments showed H_s to be roughly equal to h(1-Fr), which is consistent with Brighton's conclusion of Drazin's theory breaking down at a height of U/N below the top of the obstacle. Flow around the barrier was not observed for Froude numbers greater than one.

Castro et al. (1983) conducted towing tank experiments similar to those of Hunt and Snyder (1980) but used barriers shaped as triangular ridges with various aspect ratios.

Their results confirmed the general conclusions of previous theoretical and experimental studies of flow over surface obstacles. In addition, they showed that the change in obstacle shape did not affect H_s. Further towing experiments were conducted by Snyder et al. (1985) using barriers with a variety of shapes and orientations. They also used flow containing vertical speed shear and wind directions not perpendicular to the barrier. Results showed H_s to be approximately the same for a given stability profile and a variety of roughly axisymmetric barrier shapes. The rule of H_s=h(1-Fr) was found to be a lower limit for cases with significant wind shear and for situations with triangular wedges having steep slopes. In these cases, an upwind vortex developed that led Snyder et al. to speculate that the flow rolled up in the vortex and passed around the barrier despite initially having sufficient kinetic energy to pass over the barrier. They suggested an extension to the conceptual model of Sheppard such that a parcel may have sufficient kinetic energy to pass over the barrier but does not necessarily do so. Insignificant changes in H_s were observed for cases with the wind angle less than 45° from perpendicular to the barrier. However, H_s increased as the wind direction deviated by angles of greater than 45°, apparently due to the parcel following a path around the barrier that requires less potential energy to overcome than for the path over the top.

Castro (1987) used towing tank experiments to investigate the criteria necessary to obtain wave breaking over three-dimensional obstacles. Observations showed wave breaking conditions to be dependent on the Froude number and the barrier aspect ratio. When flow splitting occurred for the small to moderate aspect ratio cases, the wave breaking was retarded.

The physical model experiments have provided valuable observations of flow in a densely stratified fluid over three-dimensional obstacles. They provided visual evidence of when flow travels around an obstacle rather than over it. The observations are most valuable when compared to results derived from observational, theoretical, and numerical investigations.

2.4.2 Observational Investigations

Actual observations of terrain induced flow patterns described by the physical model experiments are difficult to obtain. The mesoscale size of these features are typically too small to be observed by the standard weather network and are too large to be seen by an observer (Chopra 1973). Furthermore, actual topography is often far more complex than the idealized terrain used in the physical model experiments. Therefore, most observational experiments must rely on data obtained from field projects using an extensive observational network in the vicinity of an isolated topographical feature, such as a mid-oceanic island.

The TIROS weather satellites and photographs from the Gemini space missions provided the first visual evidence of mesoscale vortex patterns in the lee of islands (Chopra 1973). Chopra described this phenomenon as the atmospheric analog of von Kármán vortex streets that can develop downstream in a liquid flowing past a cylindrical obstacle (e.g. Tritton 1977). Chopra noted that the island of Hawaii acts as a barrier in the easterly trade winds that generates a cyclonic eddy to the north and an anticyclonic eddy to the south. The west (Kona) coast of Hawaii receives more rainfall than any other leeward area in the Hawaiian islands chain due to its location in the convergence zone between the lee vortices. Although there is no evidence that the Hawaiian vortices evolve into vortex streets, they appear similar to the symmetric eddies observed in physical model experiments by Brighton (1978) and Hunt and Snyder (1980).

Spangler (1987) used data collected during a field program that released tracer gases upwind of an isolated 100 m hill and observed the plume behavior. Spangler used seven nighttime cases where the tracer gases were released below or at H_s to evaluate several methods that used the Froude number to predict H_s. The "release height" Froude number was found to be the best predictor of whether the air at a particular level would travel around or over the hill. The release height Froude number is computed using the wind at tracer gas release height, the atmospheric density between the release height and hilltop, and the height equal to the difference in elevation between release height and hilltop.

Rasmussen et al. (1989) used observational data collected during the Joint Hawaii Warm Rain Project of 1985 to initialize and validate model simulations of the atmosphere around the island of Hawaii. They determined that the interaction of the easterly trade wind flow with the island obstacle controls the basic climatic regions on Hawaii. Several features that were observed in the physical model experiments were also observed and numerically predicted by Rasmussen et al., including strong blocking in the oncoming flow, upstream flow reversal with low-level convergence, and strong deflection and acceleration of the flow around the island. The results led Smolarkiewicz and Rotunno to conduct an interesting series of numerical experiments using idealized terrain that are described in the following sections.

2.4.3 Theoretical Investigations

Two distinct theories for flow past an isolated mountain had been established; potential flow theory (Drazin 1961) for low Froude number situations and linear theory (e.g. Wurtele 1957) for high Froude number cases. Questions that remained included determining the applicable ranges for the two theories and which theory, if either, best described the actual flow for Froude numbers representative of the typical atmosphere.

Smith (1980) used the linear theory approach of Wurtele to investigate hydrostatic flow past an isolated, circular, bell-shaped mountain. The analytic results showed the low level flow to split to avoid the mountain and the lateral deflections persisted downstream of the mountain. The low level divergence is compensated by the descent of warm air aloft, hence the predictions are closely associated with the generation of mountain waves. Smith was the first to suggest that the linear results were not consistent with the conceptual model of Sheppard (1956).

Smith compared the high Froude number (linear) theory with the low Froude number (potential flow) theory (Drazin 1961). A key difference is the forecast structure of pressure and vertical parcel displacements. The low Froude number theory predicts symmetric fore-aft structure with no mountain waves and temporary horizontal parcel displacements while the high Froude number theory predicts asymmetric structure associated with the generation of mountain waves and permanent horizontal parcel displacements downstream

of the the mountain. Smith's interpretation shows the two theories to be distinct and unconnectable yet qualitatively complimentary since low Froude number theory can predict vertical motions and high Froude number theory can predict horizontal parcel displacements.

The physical model results for low Froude number cases indicated horizontal parcel displacements to persist downstream. Also, for Froude numbers just high enough to allow vertical parcel displacements, the displacements are strongly asymmetric. This implies that the linear theory may better describe the observed flow around an obstacle. Smith suggested that a well designed laboratory experiment or numerical experiment could determine the ranges of validity for the two theories and the transition between the two theories.

Smith (1982) extended the linear theory of Queney (1948) by using a modified expansion valid for large Rossby numbers allowing one to investigate the flow past larger mountain barriers. The theoretical results showed the pressure and vertical motion fields to be unaffected by the Coriolis force, however significant asymmetries are predicted for the horizontal displacements. For a north-south oriented mountain range in the Northern Hemisphere, more flow is deflected to the north of the barrier than to the south. As an air parcel approaches the mountain, the orographic pressure disturbance (i.e. blocking) slows the parcel resulting in a decreased Coriolis force. The parcel accelerates northward under the influence of the background pressure gradient. Smith suggests that the resulting formulas can provide a simplistic check on output from more complete numerical models.

Phillips (1984) applied the linear theory (Smith 1980) to derive analytical solutions for mountains with elliptical horizontal cross sections. By varying the eccentricity of the mountain, Phillips investigated the transition between the circular barrier case (Smith 1980) and the two-dimensional limit of an infinitely long ridge. The effects of wind direction were studied by rotating the barrier. Surface pressure perturbation patterns are presented for several elliptical orientations. Phillips compared the maximum pressure perturbation of the circular barrier case to other elliptical shapes and determined that the maximum is about 10% greater for an elliptical barrier three to four times longer than wide and about 30% greater for the two-dimensional infinite ridge.

Pierrehumbert (1984) applied an alternative expansion method to the linear theory (Smith 1982) to investigate the factors that affect the strength of a barrier effect on an impinging flow. The results indicated that for wide mountain barriers, the slope determines the strength of the barrier effect. For narrow mountains, the barrier effect is determined by the maximum mountain height. Hence, it is more important to preserve maximum terrain height rather than mountain volume when it is necessary to smooth orography for use in numerical models.

Smith lamented in 1988 that the complete answer to Sheppard's (1956) question of whether low level air parcels will travel around or over the barrier had still not been found. Smith noted that despite the predicted result of horizontal flow around the barrier by potential flow theory (Drazin 1961, Brighton 1978), further predictions are dubious since the method is not capable of capturing gravity wave dynamics. The physical model experiments successfully illustrated the tendency for low Froude number flow to travel around rather than over the barrier, but they did not provide the answer to Sheppard's question. Inconsistencies between the linear theory and the widely accepted conceptual model of Sheppard with extensions by Snyder et al. (1985) needed to be resolved.

Smith (1988) rederived the linear theory (Smith 1980) in isoteric (constant specific volume) coordinates. In geometric coordinates, the linearized lower boundary condition is a constant density surface applied at the terrain elevation (Smith 1980) and is only an approximation. The linearized lower boundary condition is exactly satisfied in isoteric coordinates where the constant density surface is applied at an elevation independent of the terrain. The resulting flow solution contains no Bernoulli height term, which is the basis of the Sheppard energy argument. The flow solution showed a collapse of density surfaces on the leeward slope and the development of two stagnation points (similar to the singular points observed by Hunt and Snyder) located on the windward slope and at a point aloft directly over the hill. The flow predictions compared favorably with the physical model results of Hunt and Snyder (1980) and with relevant numerical experiments.

These results led Smith to suggest that the kinetic energy argument of Sheppard does not play any role in airflow blocking and splitting. Smith (1990) later presented

these arguments in a concise manner where he stated that the diagnostic equation used by Sheppard (1956) is physically incorrect due to the emphasis on potential energy rather than pressure variation controlling the wind speed. Also, the early agreement between the conceptual model and results from physical and numerical model experiments was fortuitous and other predictions were more obviously incorrect.

Smith (1989a, 1989b) expounded the predictions of the isoteric linear theory and discussed the importance of the stagnation points. The discussion is organized through the development of a regime diagram for hydrostatic flow over a mountain. Smith notes that two phenomena can alter the kinematic or geometric nature of the mountain wave, flow splitting (i.e. flow around the mountain) and wave breaking. Hence, each regime will be bounded by a curve representing the onset of either (or both) phenomena. Common features of the two critical phenomena are that each begins with the formation of a stagnation point and each is associated with a recirculation region. Smith notes that other phenomena (e.g. boundary layer separation) may also alter mountain wave phenomena, but is is unclear if these phenomena are independent of flow splitting and wave breaking.

The two stagnation points predicted by the linear theory (Smith 1988) are related to the two critical phenomena. Flow splitting begins to occur when the windward slope stagnation point forms while wave breaking is initiated when the stagnation point aloft forms. Once a stagnation point forms, the linearization theory breaks down and the flow field can be significantly changed everywhere. Thus, it is important to determine which stagnation point forms first to predict which regime will develop. Using these concepts, Smith constructed a regime diagram for an atmosphere with constant stability and no vertical wind shear. The diagram axes represent the barrier shape (i.e. horizontal aspect ratio) and the barrier size (i.e. nondimensional barrier height or inverse Froude number). For regions with low aspect ratio and small barrier size (i.e. high Froude number), the mountain wave only regime is predicted. Flow splitting is expected in a region containing large barrier size (i.e. small Froude number) and small aspect ratio. Wave breaking occurs for an area containing large barrier size and high aspect ratio. A fourth region representing a combination of flow splitting and wave breaking is estimated. This region can not be

determined exactly from linear theory since the theory becomes invalid once one regime develops.

Modifications to the regime boundaries are presented for a range of Richardson numbers to account for differences created by vertical wind shear in the mean flow. Forward shear decreases the effective stability of the flow and the faster flow aloft requires a larger pressure rise for stagnation to occur. The result is a delay in the development of the stagnation point aloft. The length of the delay is a function of decreasing Richardson number (i.e. increasing wind shear). Hence, as the Richardson number decreases, a lower Froude number is required for wave breaking to occur. Smith comments that severe wind events are rare in the mid-latitudes since it is difficult to achieve the wave breaking criteria for typical tropospheric values of the Richardson number.

Smith suggests that future efforts towards the understanding of airflow over mountains should be guided by the regime diagram. A more accurate representation of the flow regime boundaries and definitions for the subregions are needed. The effects of viscosity, diffusion, and turbulence on flow splitting and wave breaking and their influence on the surrounding flow needs to be investigated. Smith notes that numerical models should be used to fill out the regime diagram.

2.4.4 Numerical Model Experiments

The rapid advancement in computer power during the past two decades has made numerical model experiments a viable method for studying the atmosphere. Numerical models provide an alternative method to the physical model experiments for obtaining simulations of airflow over complex terrain. Model output can be used to confirm results from the theoretical and physical model investigations. Since the model can simulate non-linear effects, one can more thoroughly investigate phenomena where the analytic theory becomes invalid. The ability to conduct multiple sensitivity studies is a very powerful tool to validate and extend the hypotheses of linear theory. Model simulations are also quite useful for investigating the effects of airflow over actual (i.e. not idealized) terrain and for providing insight into observed barrier related atmospheric phenomena.

Prior to utilizing the model for these investigations, model credibility must be established (Pielke 1984) by satisfying several criteria such as demonstrating that the model can reproduce results described by the linear theory. Early numerical simulations of airflow over complex terrain primarily concentrated on two-dimensional, high Froude number mountain wave phenomena (e.g. Clark and Peltier 1977, Klemp and Lilly 1978, Peltier and Clark 1979). Although these investigations are not directly applicable to this study, they did establish model credibility for future work. Numerical model applications are particularly useful for the low Froude number situations where non-linear effects can be significant. More recently, through the use of numerical models, significant progress has been achieved in understanding low Froude number flow over simple and complex three-dimensional terrain.

Warner et al. (1978) used a mesoscale primitive equation model to demonstrate the ability to simulate a wide variety of mesoscale phenomena. Of the four numerical experiments conducted, one was initialized with high static stability uniform flow over idealized terrain. Model forecasts showed the flow to travel around an isolated circular mountain rather than over it. The realistic results led Warner et al. to suggest that the model could probably be used with complex terrain and arbitrary conditions of stability.

Somieski (1981) applied several simplifications to a numerical model in an effort to understand some basic atmospheric mechanisms in the vicinity of isolated terrain. A three-dimensional hydrostatic primitive equation model was linearized to allow the comparison of model results to quasigeostrophic analytic solutions (e.g. Smith 1979). An isolated circular mountain with constant height, but varying diameter representing different aspect ratios and Rossby numbers, was located in the model domain center. The model was initialized with uniform flow and a thermal sounding more stable than the standard atmosphere. Results for the wide diameter mountain show significantly more flow deflected to the left of the barrier than to the right, but very little asymmetry in the vertical motion field. This is consistent with the analytic results (Smith 1982) that include the effects of the Coriolis force. Much less flow field asymmetry was noted for the narrow width mountain where the effects of the Coriolis force are considerably less. The U-shaped upward vertical motion

field appears similar to the field predicted by the linear theory (Smith 1980) with no earth rotation. Somieski applied the model using actual terrain from the German Bavarian Hills. Although the model predictions appeared reasonable, the available observations were not of fine enough resolution to verify any mesoscale detail.

Thorsteinsson (1988) used a non-linear isentropic model to investigate the hydrostatic flow of stably stratified air passing by an isolated bell-shaped mountain. Sensitivity experiments were designed to examine the effects of a changing Rossby number (0.4–1.0) and a changing Froude number (0.25–1.0). Two features were evident in all the experiments: an upward propagating hydrostatic gravity-inertia wave located above and to the lee of the mountain and low level splitting around the mountain. As the Froude number decreased, more low level flow was diverted around the mountain and lee-side downslope flow originated from potentially warmer upwind strata. As the Rossby number decreased, increased asymmetry in the low level flow was observed with more flow passing on the left side of the mountain in the Northern Hemisphere.

Smolarkiewicz et al. (1988) studied the convergence zone and associated cloud band often observed upwind of the island of Hawaii. Previous investigations suggested that the convergence zone formed along the boundary between the prevailing trade winds and an island density current. The density current resulting from a combination of nocturnal valley outflow and a coastal land breeze circulation, hence relating the observed cloud band to the diurnal cycle. However, detailed observations from a field experiment were not completely consistent with the diurnal cycle hypotheses. In fact, the observations were more consistent with the water tank experiments of Hunt and Snyder (1980) which led Smolarkiewicz et al. to consider the problem from the fluid dynamics framework of strongly stratified flow past a three-dimensional obstacle.

The potential flow theory (Drazin 1961) applied to the Hawaiian problem predicted vertical velocities three orders of magnitude smaller than the observed values, leading the authors to conclude that existing theory is inadequate to describe the observations. A series of numerical model experiments was designed to investigate the formation and evolution of the convergence zone. Four experiments varied the mean wind speed to

evaluate the sensitivity of changing Froude number from 0.0 to 0.4 (typical Froude number values for Hawaii are ~0.1-0.4). Model predictions compared well with the observations and with the results of Hunt and Snyder (1980). The upwind separation line correlated well with the observed cloud band and doubling the Froude number to 0.4 indicated deeper vertical motion at the upwind stagnation point. For a higher Froude number of 0.8, the upwind convergence zone and associated stagnation point did not form and the cloud field developed into an orographic regime. Smolarkiewicz et al. concluded that the observed upwind convergence zone and associated cloud band are dynamically forced by strongly stratified flow past a three-dimensional obstacle and is not primarily related to the diurnal cycle.

An interesting sidelight resulting from the numerical experiments was the prediction of a pair of vortices on the lee of the island. The lee vortices were also observed in the physical model experiments (e.g. Brighton 1978, Hunt and Snyder 1980) and were generally attributed to surface friction effects. However, Smolarkiewicz et al. used a free slip boundary condition (i.e. no surface friction) by design and the lee vortices still formed in the numerical predictions. These results led the authors to suggest that the only possible source of the lee vortices is vortex tilting.

Smolarkiewicz and Rotunno (1989a) focused on the mechanics of the lee vortices in low Froude number flow through idealized numerical experiments and analytic theory. They emphasized the need to study these features using a numerical model since existing theories did not cover stratified flow past an obstacle for Froude numbers ~0.1-0.5. Nine parallel simulations were initialized using an isolated bell shaped mountain with Froude numbers from 0.055 to 2.2. No viscous boundary layer (i.e. free slip) was employed to eliminate the effects of surface friction. Model predictions with Froude number greater than 0.5 closely resembled the linear theory solutions (Smith 1980). As the Froude number passed below 0.5, the formation of the two lee vortices and a small area of upwind flow reversal became apparent. These processes appeared together and occurred without the viscous boundary layer effects. Qualitatively, the low Froude number model predictions agreed with the physical model results of Hunt and Snyder (1980).

Smolarkiewicz and Rotunno reiterated that the only possible source for the lee vortices development is the tilting of horizontal vorticity in the lee of the obstacle. Since the ambient wind flow contains no horizontal vorticity, baroclinic processes associated with the deformation of isentropic surfaces near the obstacle must be responsible for the generation of horizontal vorticity. A linear analysis with first and second order terms included was presented as an explanation of the vorticity tilting and lee vortex development. The analysis shows that first order vertical velocities generated near the obstacle create a first order baroclinic field. The first order baroclinicity allows the development of first order horizontal vorticity. By including second order terms, it is possible to generate second order vertical vorticity from the tilting of first order horizontal vorticity. Hence, the shape of the isentropic surfaces near the obstacle describes the vorticity distribution of the lee vortices. This argument suggests that the lee vortices are closely associated with the dynamics of gravity waves. No lee vortices were predicted for the cases with very small Froude number and with Froude number greater than 0.5 indicating that the boundary layer separation mechanism is important for these ranges of Froude number where lee eddies were observed in the laboratory experiments. However, for Froude number between 0.1 and 0.5, Smolarkiewicz and Rotunno concluded that the inviscid mechanism coexists and likely dominates the boundary layer separation mechanism.

Smolarkiewicz and Rotunno (1990) continued their examination of low Froude number flow past an isolated three-dimensional obstacle. This investigation focused on the upwind flow reversal zone that was predicted together with the lee vortices (Smolarkiewicz and Rotunno 1989a). Although the upwind effects are not a primary concern of this dissertation, several relevant issues were noted. A set of sensitivity experiments were conducted to investigate the effects near obstacles of varying aspect ratio, β = across stream length / along stream length. For $\beta = 0.5$, the lee vortices developed without the upwind flow reversal indicating the two phenomena are independent. For increasing β, the lee vortices grew larger and developed further downstream. The vortices also showed a tendency to develop closer to the lateral edges of the obstacle leaving a region of shallow lee side downslope flow for $\beta = 8$. Smolarkiewicz and Rotunno concluded that the linear

theory properly captured the important features for $\beta \leq 1$, but the utility of linear theory is less clear for $\beta > 1$.

Smith (1989c), in a reply to Smolarkiewicz and Rotunno (1989a), claimed that the lee vortices form suddenly with the onset of upwind stagnation rather than progressively in association with the developing mountain waves. This argument is supported by the numerical calculations showing no lee eddy development without a stagnation point (Thorsteinsson 1988) and a near discontinuity in the eddy strength as the Froude number decreases (Smolarkiewicz and Rotunno 1989a). Smith associated the coincidental development of the stagnation point and the lee eddies to a bifurcation in the mountain airflow problem where the steady state flow field changes abruptly as the Froude number decreases passed a critical value. For the two-dimensional problem, wave breaking is correlated to a similar bifurcation process. For the three-dimensional case, both bifurcation processes (i.e. wave breaking and lee eddies) must be considered as the Froude number decreases.

Smolarkiewicz and Rotunno (1989b) and Rotunno and Smolarkiewicz (1991) stated that the results presented in Smolarkiewicz and Rotunno (1989a) were steady state and did not imply any conclusions on the generation and relationship of wave breaking and lee vortices. An analysis on the formation of lee vortices was performed through an initial value approach where an initially stationary obstacle is accelerated to a constant speed in a stratified fluid. Numerical results suggested that lee vortex formation and lee wave breaking are distinct phenomena. Also, when the flow is accelerated from rest, the lee flow reversal occurs first at the ground and deepens with time (Crook et al. 1990). Since the experiments showed the lee vortex to form before the lee wave breaks, Rotunno and Smolarkiewicz concluded that lee vortex generation is not the result of wave breaking and that wave breaking and lee vortices should be considered separate physical entities even though they can both occur simultaneously.

Stein (1992) presented a numerical investigation of the regime diagram (e.g. Smith 1989b) for two dimensional flow over a mountain. A primary goal of the work is to validate the French Weather Service limited area model PERIDOT. The hydrostatic model adequately reproduced the expected two dimensional flow over a mountain with a sufficiently large

half-width. Stein intends to present an exploration of the three dimensional regime diagram in Part II of his investigation.

Mayr (1993) investigated the evolution of orogenic blocking. Several model simulations initialized with homogeneous data using realistic topography over the Rocky Mountain region indicated that the Froude and Rossby numbers controlled the development of blocking consistent with previous investigations. However, actual observations using remotely sensed wind and temperature data indicated situations where changes in the cross-barrier wind speed and stability did not trigger a transition from one state to another as the theory would suggest. Mayr looked at other mechanisms that might affect blocking. Results indicated that synoptic and radiative forcings play a significant role in the blocking evolution. The approach of a synoptic scale trough can negate the effects of the mountain induced meso-high, creating a non-blocked situation. A synoptic scale ridge following the passage of a trough can reestablish or strengthen the block. Significant daytime heating can create a well-mixed boundary layer that may connect with the overriding synoptic scale flow and destroy a blocked state. The blocking state may reappear after sunset when radiative cooling aids in reestablishing the upwind meso-high. These results underscore the necessity to account for all physical mechanisms when attempting to describe observed atmospheric phenomena.

2.4.5 Summary

Idealized simulations of flow in the vicinity of complex terrain have provided a wealth of information. Observational and physical model investigations have provided insight into when air flows around versus over a barrier. They have also aided in determining the application limits of theoretical investigations. Numerical models, which can incorporate actual topography, diurnal effects, and synoptic scale forcings, have extended the results beyond the limits of physical and theoretical models and closer to reality. A primary focus of this investigation will be to draw upon the knowledge gained from these idealized simulations and to apply this knowledge to provide an enhanced understanding of real-time mesoscale observations and numerical model predictions along the Colorado Front Range.

Chapter 3

EXPERIMENT DESIGN

A unique aspect of this dissertation is to utilize the MAPS and LAPS operational analyses that have incorporated all conventional and state-of-the-art data sources to initialize a mesoscale numerical model (RAMS). RAMS is a full microphysics, non-hydrostatic primitive equation model developed as a merger of several previous models (Wesley 1991, Pielke et al. 1992, Nicholls et al. 1993). The complexity of the model physics is controllable through a menu driven selection list. A discussion of the operational data sources, the model initialization procedures, and the model configuration for the case study simulations follows.

3.1 The Mesoscale Analysis and Prediction System – MAPS

MAPS provides the capability to investigate mesoscale phenomena in detail greater than previously possible with operational NMC analysis products. The inclusion of numerous aircraft reports and wind profiler data in addition to other conventional observations allows MAPS to generate upper air analyses of the atmospheric state variables every three hours on a national 60 km grid increment domain (Benjamin et al. 1991, Smith and Benjamin 1993, Fig. 3.1). The system utilizes a 25 sigma/isentropic level hybrid coordinate system that provides increased resolution in the vicinity of highly baroclinic features. MAPS generates 12 h forecasts every 3 h using a hydrostatic numerical scheme with the primary intent of providing background fields for future analyses. MAPS is run operationally at FSL and routinely interpolates the analyses and forecasts to a standard isobaric coordinate system for display on the prototype National Weather Service meteorological computer workstation. In addition to the upper air analysis system, MAPS generates separate surface analyses every hour on a regional 30 km grid increment domain (Miller

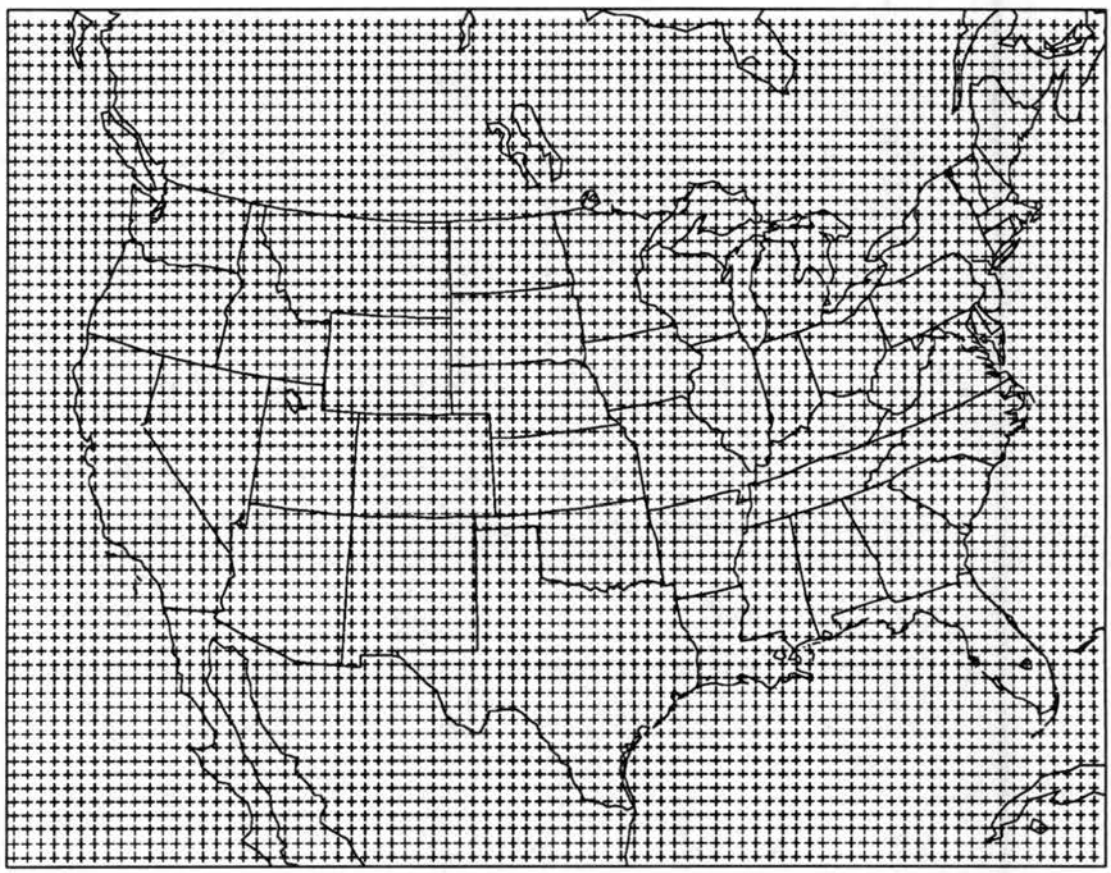

Figure 3.1: MAPS domain and horizontal grid configuration ($\Delta x = \Delta y = 60$ km).

and Benjamin 1992). The surface analysis system incorporates all available automated surface observations plus the standard surface aviation observations (SAO).

3.2 The Local Analysis and Prediction System – LAPS

LAPS provides even greater mesoscale detail on a local Colorado forecast domain by enhancing the MAPS analyses with the addition of all available local data sources. Local data sets include five minute surface observations from FSL's 22 station automated mesonet, the prototype WSR-88D Doppler radar located about 10 km northeast of Denver, the wind profiler data located at Platteville, Colorado, and digital infrared satellite data ingested at FSL directly from the Geostationary Operational Environmental Satellite (GOES, Fig. 3.2). LAPS uses a regional 10 km grid increment domain covering most of Colorado and small portions of adjacent states (Fig. 3.3) to provide surface and three-dimensional analyses of atmospheric state variables every hour (McGinley 1989, McGinley et al. 1991). The LAPS grid is nested exactly within the national 60 km grid interval MAPS domain. The LAPS domain covers a 600 x 600 km area in the horizontal and uses 21 isobaric levels from 1100 to 100 mb with a constant 50 mb increment. LAPS terrain (Fig. 3.4) is derived from the Defense Mapping Agency (DMA) 30 s spatial interval elevation data by averaging all DMA elevations within each LAPS 10 km^2 grid box area.

The LAPS three-dimensional univariate wind analyses incorporate Doppler radar, wind profiler, aircraft reports, automated surface observations, MAPS, and other conventional data sources (Albers 1989). Height and temperature information are obtained solely from the 60 km MAPS analyses and forecasts. The LAPS moisture analyses use digital satellite and microwave radiometer data to add mesoscale detail to the MAPS moisture fields (Birkenheuer 1991). LAPS also generates separate surface analyses of atmospheric state variables (McGinley et al. 1991) in addition to the three-dimensional analyses. Digital satellite data and automated surface observations provide mesoscale detail to the other available surface data sources.

The LAPS balance package is an attempt to provide consistency between the univariate mass and wind analyses. A variational technique using the equations of motion as

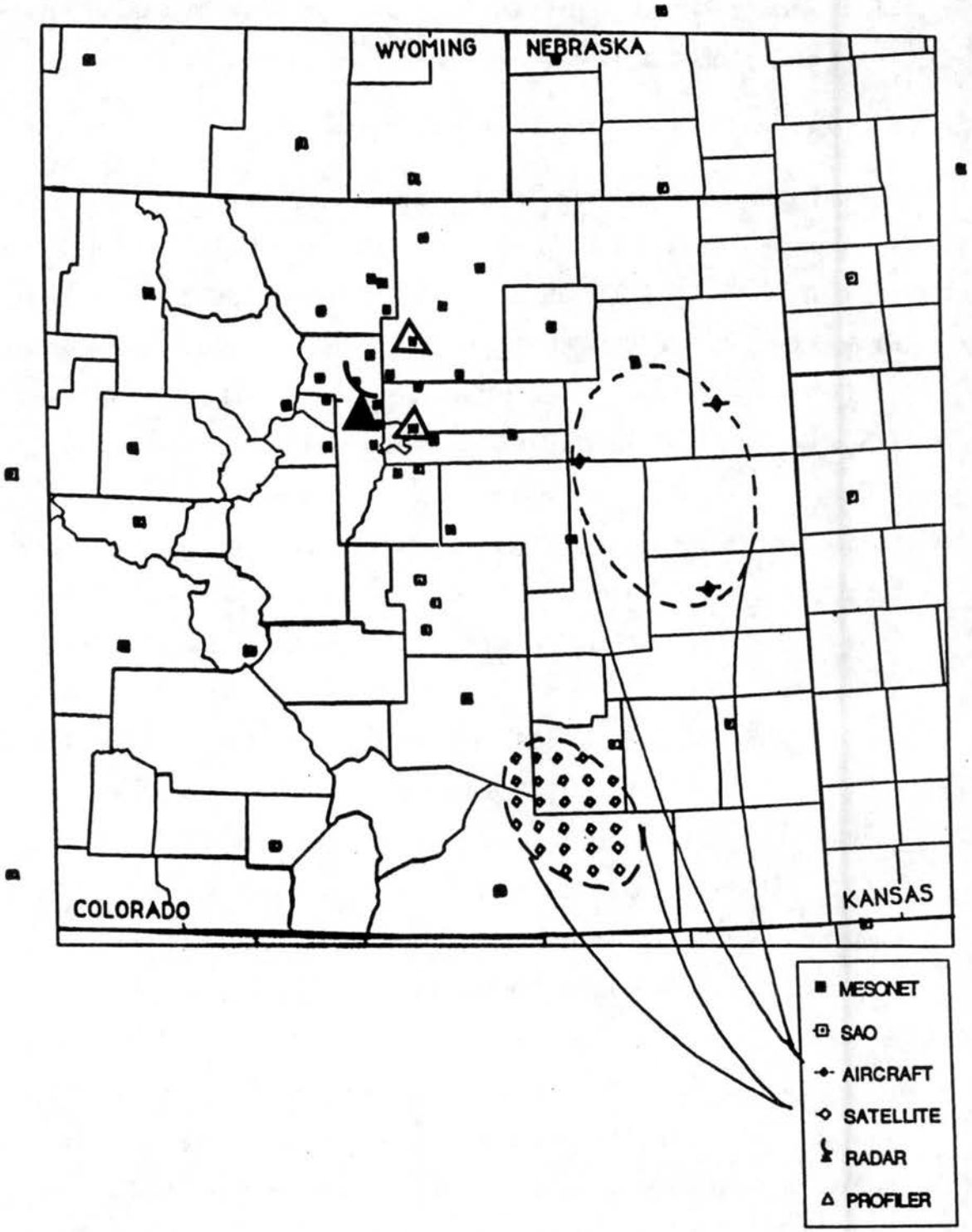

Figure 3.2: Weather data available in northeast Colorado. Insets show typical data densities extended over the domain for aircraft and GOES satellite data during an average 90-min period. From McGinley et al. 1991.

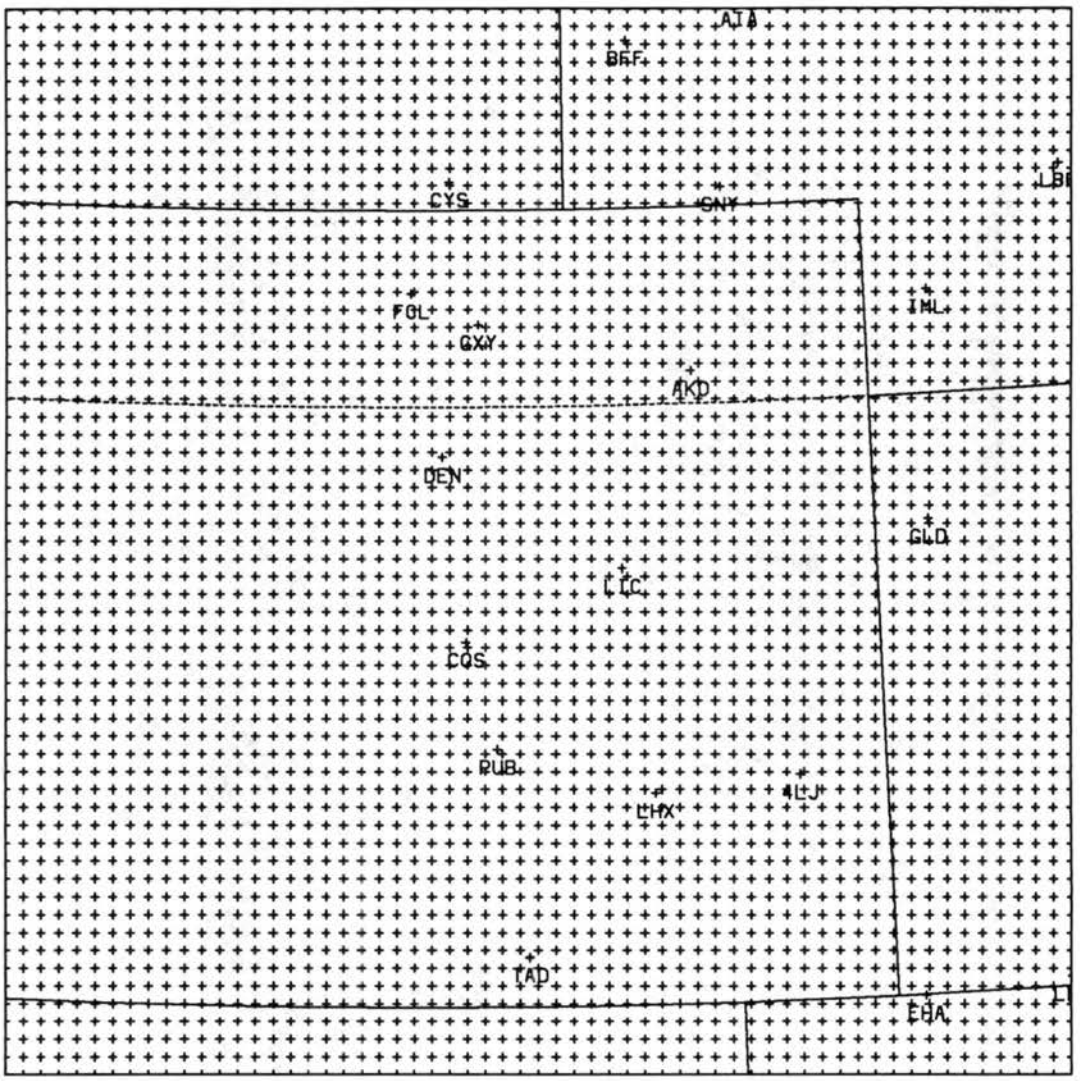

Figure 3.3: LAPS domain and horizontal grid configuration ($\Delta x = \Delta y = 10$ km). SAO locations east of the Continental Divide are indicated by standard 3-letter abbreviations.

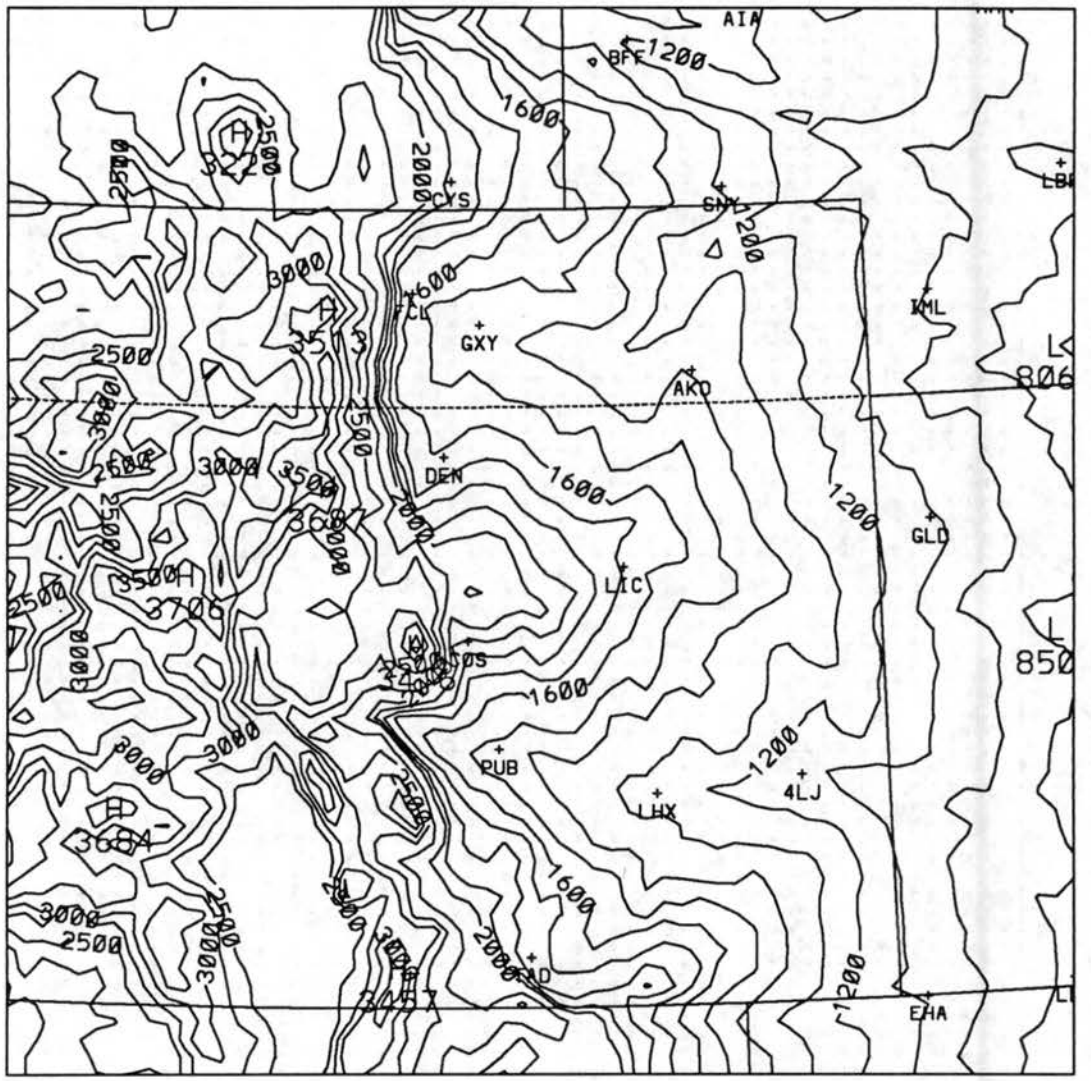

Figure 3.4: LAPS topography (m). Contour interval is 100 m below 2000 m and 250 m above 2000 m.

weak constraints and the continuity equation as an absolute constraint (McGinley 1987, Snook and McGinley 1990) combines the mass and momentum fields to produce dynamically consistent analyses. The balance package is tuned to introduce mesoscale detail to the LAPS mass field from the LAPS wind field that has incorporated high resolution data sources not available to the mass field analyses. The dynamically consistent analyses provide an alternative model initialization that will be tested in this investigation.

3.3 Model Initialization and Grid Configuration

RAMS is initialized with operational non-homogeneous data from LAPS and MAPS for two case studies to evaluate the accuracy of mesoscale numerical forecasts and to demonstrate the ability to utilize the model output to provide an improved scientific understanding of mesoscale weather events. The RAMS mesoscale numerical model is configured such that the LAPS analyses can be used as model initialization with as little manipulation to the initial fields as possible. Table 3.1 summarizes the model configuration for the case study simulations.

Table 3.1: Model grid configuration for case study simulations.

Model Category	Option
grid dimensions	61 x 61 x 25
horizontal grid increment	10 km
vertical grid increment	300 m stretched to 750 m
model top height	15.3 km
topography	1) LAPS 2) MAPS

The horizontal model domain is equivalent to LAPS (i.e. 61 x 61 grid points with a 10 km grid increment). The vertical grid is a stretched sigma-z coordinate system with a 300 m

grid spacing nearest the ground, a stretch factor of 1.1, and a maximum grid spacing of 750 m. Hence, the model top is approximately 15.3 km above the surface. The vertical grid spacing is designed to maintain all the available resolution in the LAPS analyses while foregoing any greater resolution to allow implementation in real-time. Model topography is set equal to the LAPS terrain and is not smoothed to facilitate the inclusion of LAPS surface data without interpolation.

A time-dependent lateral boundary condition is implemented that uses a Davies (1976) nudging scheme to force the model variables toward analyzed values derived from either future LAPS analyses (i.e. a model simulation) or MAPS real-time forecasts (i.e. a true forecast). The 600 x 600 km domain may be small for the type of mesoscale forecasts that will be attempted. Adverse effects from the lateral boundaries may contaminate the results especially after several hours of prediction. For instance, a parcel traveling at 20 m s^{-1} would traverse the entire domain in less than nine hours. The domain was selected to match the available operational data analyses (i.e. LAPS). If the proposed model grid is insufficient in size, a larger, possibly nested, grid system may be required. The downside to a larger grid system is that it may not be feasible to run operationally given the current computer capabilities at FSL.

The LAPS isobaric analyses are linearly interpolated in the vertical to the RAMS sigma-z coordinate system. Horizontal interpolation is not required because the model points correspond exactly with the LAPS analysis points. When the separate LAPS surface analyses are included, they are blended into the three-dimensional analyses up to 500 m AGL using a height-weighted average of the two analyses such that the surface data receives full weight at the model ground level while the three-dimensional analysis receives full weight at 500 m AGL. Initializing the model with three-dimensional, 60 km MAPS analyses provides the basis to evaluate the value added by initializing with higher resolution LAPS data. For these experiments, bilinear interpolation is used to horizontally interpolate the MAPS data to the LAPS grid. Either LAPS or MAPS topography is used. The MAPS 60 km topography is interpolated to the 10 km LAPS grid using an overlapping quadratics scheme (Fig. 3.5).

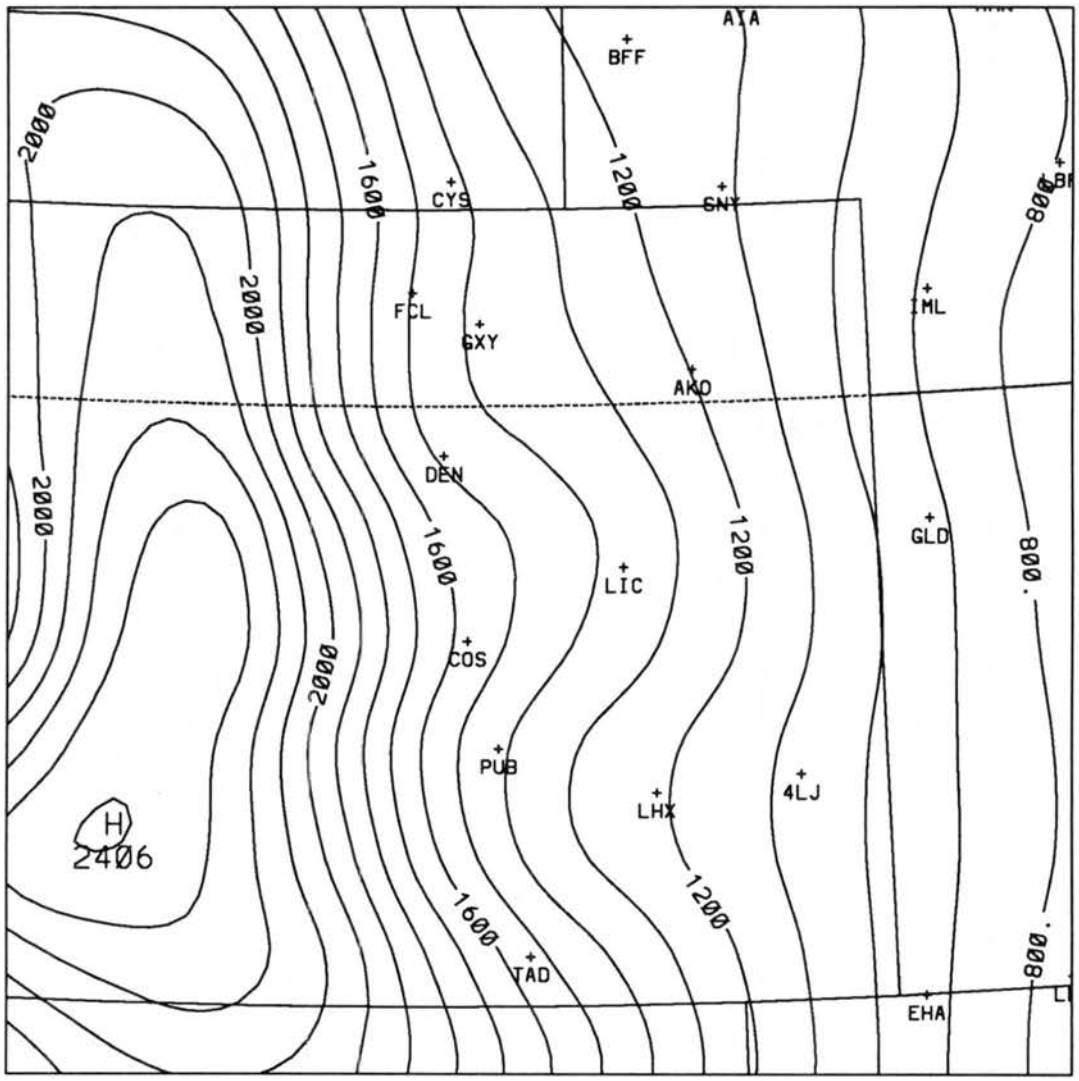

Figure 3.5: MAPS topography (m). Contour interval is 100 m.

Sensitivity experiments (Table 3.2) are conducted using seven model configuration variations (with abbreviations for future reference): 1) 10 km three-dimensional LAPS analyses (LAPS), 2) 10 km three-dimensional LAPS dynamically consistent analyses (LBAL), 3) 10 km three-dimensional LAPS analyses with LAPS surface data blended in (LSFC), 4) 10 km three-dimensional LAPS analyses with blended LAPS surface data and full microphysics employed (LMIC), 5) 10 km three-dimensional LAPS analyses with blended surface data (no microphysics) and MAPS real-time forecasts available to the Davies lateral boundary condition (LFCS), 6) 60 km MAPS analyses interpolated to the 10 km LAPS grid using LAPS topography (MAPS), and 7) 60 km MAPS analyses interpolated to the 10 km LAPS grid using MAPS topography (MTOP).

Table 3.2: Sensitivity experiments for case study simulations.

Data Analyses	Abbreviation
1) 10 km LAPS 3-D analyses	LAPS
2) 10 km LAPS dynamically consistent	LBAL
3) #1 with blended LAPS surface data	LSFC
4) #3 with full microphysics	LMIC
5) #3 with MAPS forecast boundary	LFCS
6) 60 km MAPS interpolated to 10 km	MAPS
7) #6 with MAPS topography	MTOP

Comparing results from the LAPS and LBAL initializations will determine the value of the LAPS dynamically consistent fields as model initialization. Evaluating the effects of including the separate LAPS surface analyses will be accomplished with the LSFC initialization. The effects of full microphysics and precipitation will be evaluated through the LMIC simulations. True model forecasts will be generated with the LFCS simulations

which will help evaluate the importance of accurate lateral boundary conditions. The MAPS initialization will help define the value added by using higher resolution LAPS data while the MTOP initialization will determine the value added by using higher resolution topography.

3.4 Model Physics

RAMS model physics are selected to complement the grid scale resolution and the winter season meteorology. The model physics are summarized in Table 3.3.

Table 3.3: Model physics for case study simulations.

Model Category	Option
initialization	1) LAPS real-time analyses 2) MAPS real-time analyses
thermodynamics	nonhydrostatic 1) water vapor and cloud water 2) full microphysics
radiation	radiative effects of water vapor and clouds
cumulus parameterization	none
lateral boundary condition	Davies relaxation to 1) future LAPS analyses 2) MAPS forecasts
top boundary condition	rigid lid with modified Rayleigh friction-absorbing layer
surface boundary condition	0.5 m, 11-level soil model
turbulence	deformation K closure
time-step	30 s

A nonhydrostatic version of the model is employed with two levels of moisture complexity. First, condensation of water vapor to cloud water occurs wherever supersaturation is

attained. However, other forms of liquid or ice water are not considered. The second level of moisture complexity is to fully implement the microphysical parameterizations of liquid and ice. Five microphysical species, rain water, pristine ice, snow, aggregates, and graupel, are included (Flatau et al. 1989). A radiation parameterization scheme that includes the radiative effects of liquid and ice water (Chen and Cotton 1983) is utilized. The cumulus parameterization options are not employed. A rigid lid with a modified Rayleigh friction-absorbing layer (Cram 1990) five grid points deep is used for the top boundary condition. At the surface, a 0.5 m, 11-level soil model (Tremback and Kessler 1985) is utilized. Soil temperatures at all levels are initially set equal to the analyzed surface temperature. Soil moisture initialization is based on the analyzed surface relative humidity. Turbulence closure is accomplished using a deformation K scheme (Smagorinsky 1963, Tremback 1990).

3.5 Model Validation

Model validation is necessary to address two objectives of this dissertation: 1) evaluating the accuracy of a mesoscale numerical model initialized with operational non-homogeneous data and 2) comparing the forecast accuracy with the performance of other operational model predictions. One of the more difficult tasks in mesoscale numerical model research is quantifying the accuracy of the model predictions. The difficulties are primarily due to the lack of observational data on the scale of this investigation (Thompson 1993). Model validation will be attempted through two approaches: qualitative and quantitative.

The qualitative evaluation applies the meteorologists analysis skills and experience with mesoscale weather phenomena to subjectively compare model predictions with the physical observations and other visual accounts (e.g. human observations, media reports) of the case studies. Although not as rigid as a quantitative approach, the qualitative evaluation can ascertain the existence of particular features (e.g. the mesoscale Longmont anticyclone) within the model predictions and is useful for subjective comparison with other model output. The qualitative investigation also aids in accomplishing another

objective of this dissertation, demonstrating the ability to utilize the model output to provide an improved scientific understanding of mesoscale weather events.

The quantitative approach applies statistical verification methods that compare model output with observational data. However, uncertainties arise from the fact that the observations are not coincident with the model grid points. This requires either interpolating the model gridded data to the observation locations or analyzing the observations onto the model grid. The former process introduces uncertainties through the interpolation procedure and only provides results where observations exist. Likewise, uncertainties arise with the latter process which also utilizes an interpolation procedure where the observations may not be representative of the model grid volume. Furthermore, the spatial availability of the observations dictates the scales resolvable within the analyzed field which may be different from the resolvable scales of the model. Despite the uncertainties, the statistical evaluation used in this dissertation will employ both forms of interpolation to present quantitative results using traditional and non-traditional schemes.

The quantitative comparison schemes are bias, root-mean-square (RMS), and multivariate randomized block permutation (MRBP, Mielke 1991) procedures. Thompson (1993) describes the shortcomings of using verification methods (such as RMS) that are based on a *squared* Euclidean distance function. Nonetheless, these schemes have been widely used and are in many cases the only statistics available for comparison to other model results. Mielke (1984, 1986) claims that to properly compare atmospheric models and observations, the comparison scheme should be based on an *ordinary* Euclidean distance function, since meteorological data exist in this space. The MRBP scheme described by Mielke (1991) adheres to this criteria and has been successfully applied by Tucker et al. (1989), Lee (1992), and Thompson (1993) for statistically analyzing numerical model output.

Bias and RMS statistics are computed by subtracting the model forecast from the observation or analysis (OBS - RAMS). Bias differences are calculated by:

$$\text{Bias} = \frac{1}{n}\sum_{n=1}^{r}(x_O - x_R),$$

where r is the number of available observations or analysis grid points, x_O is the observation or analysis value, and x_R is the model predicted value. RMS differences are computed by:

$$\text{RMS} = \left[\frac{1}{n}\sum_{n=1}^{r}(x_O - x_R)^2\right]^{\frac{1}{2}}.$$

The MRBP statistic is determined for a particular meteorological variable by comparing a gridded analysis, derived from observations, with the model prediction that occupies the same grid. The gridded analysis and model prediction are partitioned into blocks (b), the first containing the analysis field and the second containing the model prediction (Thompson 1993). If more than one model prediction is to be considered, each prediction occupies another block (Tucker et al. 1989). Hence, the total number of blocks is equal to the number of model predictions plus one for the analysis. There are g treatments within each block that represent the number of case applications (e.g. a 12 and 24 h forecast) for each model prediction and the analysis. Within each treatment, there are r responses that represent the number of measurements (i.e. the number of grid points). The MRBP statistic is determined from:

$$\delta = \left[g\binom{b}{2}\right]^{-1}\sum_{i=1}^{g}\sum_{j<k}\Delta(x_{ij}, x_{ik}),$$

where $\sum_{j<k}$ is the sum over all j and k such that $1 \leq j < k \leq b$ and $\Delta(x, y)$ is the symmetric distance function value of the two points in ordinary Euclidean space. The symmetric distance function is given by:

$$\Delta(x, y) = \left[\sum_{i=1}^{r}(x_i - y_i)^2\right]^{\frac{1}{2}}.$$

A test statistic, termed the P-value, determines the probability that the model prediction patterns could be generated by chance alone and is computed by:

$$T = (\delta - \mu_\delta)/\sigma_\delta,$$

where μ_δ is the exact mean and σ_δ^2 is the exact variance of the distribution δ under the null hypothesis. Finally, a chance corrected agreement measure, ρ, is defined as:

$$\rho = 1 - (\delta/\mu_\delta).$$

The agreement measure estimates the composite measurement agreement between blocks for all treatments. A ρ of 1.0 indicates perfect agreement between data sets while values of 0.0 or less indicate no agreement. In addition, very small P-values suggest a low probability that the model prediction agreement is by chance. Hence, it is desirable to obtain a high ρ with a low P-value. For this investigation, MRBP statistics are computed using only one prediction model and one forecast time period at a time, thus, $b = 2$ and $g = 1$. Since the model predictions are nudged towards analyses at the lateral boundaries, the four outermost grid points on all sides are not included in the statistical computations. Hence, 2809 (53 x 53) grid points (r) are considered.

Model validation is computed separately for surface observations and upper air observations. At the surface, temperature, moisture, and wind observations are available from the 22 station FSL mesonet and from up to 51 SAO locations. Model output are interpolated to the surface observation locations using an overlapping quadratics scheme. Since differences exist between the model and surface observation elevations, several adjustments are made to the interpolated model output. Model temperatures are adjusted by the difference in elevation multiplied by a standard lapse rate of –6.5 K km^{-1}. Model wind speeds are reduced by a factor of 0.66. The factor is derived from a logarithmic wind profile (Louis 1979) assuming a near zero Richardson number and using a surface wind observation level of 10 m and the model surface roughness value of 0.05 m. No adjustments are made to the model moisture variable. Bias and RMS statistics are computed using every location where surface data is available. Spatial and temporal quality control of the observations is completed by the LAPS operational system.

Gridded analysis statistics at the surface are accomplished by comparing the LAPS surface analysis with predictions from the lowest model sigma level. Horizontal interpolation is not necessary because the LAPS and RAMS horizontal grids are coincident.

However, some vertical extrapolation is implemented as discussed previously to account for the difference between the surface and lowest model sigma level elevations. In addition to the bias and RMS statistics, the MRBP agreement measure (ρ) is calculated.

Model validation with upper air observations is difficult due to the sparsity of data. The only available upper air data sources within the model domain are the Denver rawinsonde and the Platteville, Colorado wind profiler. A qualitative comparison of upper air model predictions to the observations is accomplished by generating time series of upper air model wind forecasts for direct comparison to the wind profiler data.

Upper air gridded analysis statistics are accomplished by comparing the LAPS three-dimensional univariate analyses with the model predictions. Since LAPS (isobaric) and RAMS (sigma-z) use different vertical coordinate systems, vertical interpolation is necessary on one of the data sets. First, LAPS analyses are interpolated to the RAMS sigma-z surfaces as discussed previously for model initialization. Bias, RMS, and MRBP statistics are then computed on each sigma-z surface. Second, the RAMS predictions are interpolated back to the LAPS isobaric levels and the statistics are generated on more traditional pressure surfaces.

Chapter 4

CASE STUDY – 7 JANUARY 1992

A severe blizzard developed east of the Colorado Front Range on 7 January 1992 (Snook and Schmidt 1992, Schmidt and Snook 1992). The storm is of interest because of 1) the sustained band of heavy snow that produced 20-40 cm (8-16 inches) of snowfall along a north-south line approximately 40 km east of the Front Range mountain barrier, while the barrier itself received less than 5 cm (2 inches) of snowfall and 2) the strong gusty surface winds in excess of 20 m s^{-1} that generated blizzard conditions across eastern Colorado for most of the day. Denver received a new 24-h record January snowfall of 34.8 cm (13.7 inches) and a storm total of 37.6 cm (14.8 inches, Fig. 4.1). The band of heaviest observed snowfall is coincident with Colorado's primary north-south thoroughfare (I-25) causing major transportation problems that stranded hundreds of motorists (Storm Data 1992). The combination of strong surface winds and heavy snow forced numerous road closures and Stapleton International Airport ceased operations for several hours. The considerable spatial variability within the observed wind and snowfall distributions makes this storm an excellent case to address the mesoscale numerical forecast objectives of this dissertation.

4.1 Synoptic-Mesoscale Overview

The 7 January 1992 storm exhibited many characteristics of a typical Colorado Rocky Mountain heavy snow event with one significant exception, the development of strong surface westerly winds east of the Continental Divide. The development of the westerlies and their impact on the observed snowfall and other surface characteristics is traced in a presentation of the storm overview.

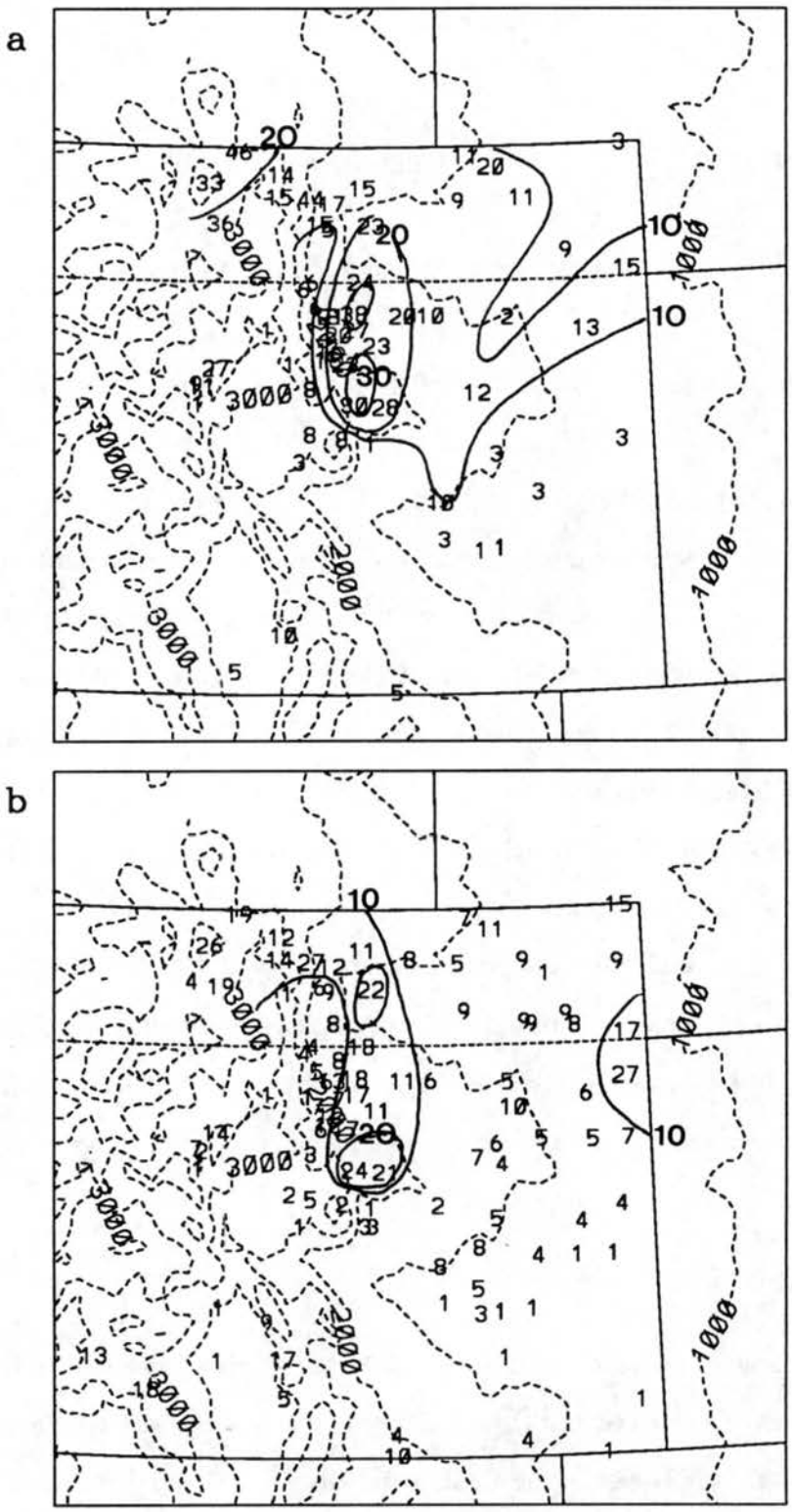

Figure 4.1: Observed precipitation during the 7 January 1992 snow storm, (a) snowfall (cm) and (b) melted water equivalent (mm).

4.1.1 Synoptic-scale observations

NMC analyses of the 500 mb height and isotachs (Fig. 4.2) show a significant open short wave located over the western United States at 1200 UTC 6 January 1992. A 35 m s^{-1} jet maximum is analyzed curling around the base of the trough. The 500 mb wave traveled eastward across Utah and closed off with a central height of 5406 m over southcentral Colorado by 1200 UTC 7 January. The 35 m s^{-1} jet streak continued to occupy the base of the trough at 0000 UTC 7 January and moved through the trough axis by 1200 UTC 7 January. The evolution of the 500 mb height field closely resembles the composite analyses of a typical Colorado *spring* storm (Fawcett and Saylor 1965) and is unusual for an early January cyclone. The system is clearly categorized as a deep cyclonic circulation type as defined by Reinking and Boatman (1986). The period of moderate to heavy snow at Denver occurred primarily between 1400 and 2000 UTC 7 January (Fig. 4.3) during which time the 500 mb low deepened to 5372 m and progressed slowly northeastward to the western Kansas-Nebraska border. The jet streak strengthened to greater than 40 m s^{-1} during this time as it exited northeast from the trough axis. A similar evolution is observed at 700 mb (Fig. 4.4) with the low closing off at 2870 m over east-central Colorado at 1200 UTC 7 January and the system becomes vertically stacked by 0000 UTC 8 January.

The 700 mb NGM dew point analysis at 1200 UTC 7 January (Fig. 4.5a) indicates a fetch of moist air ahead of the trough position extending from south Texas northward through western Oklahoma, Kansas, and Nebraska and curling westward into northeast Colorado and southeast Wyoming. The formation of a dry slot is indicated by the low dew points extending from the Mexican Baja Peninsula into central New Mexico. Significant warm advection is indicated across the Nebraska Panhandle and southeast Wyoming (Fig. 4.5b). By 0000 UTC 8 January, the fetch of moist air has moved eastward extending from east Texas through Arkansas and Missouri into Iowa and westward into Nebraska and South Dakota (Fig. 4.6a). The dry slot is colocated with the left rear quadrant of the 700 and 500 mb jet streaks and is positioned across the Texas Panhandle and western Oklahoma. The area of strongest 700 mb warm advection is suggested over western Nebraska

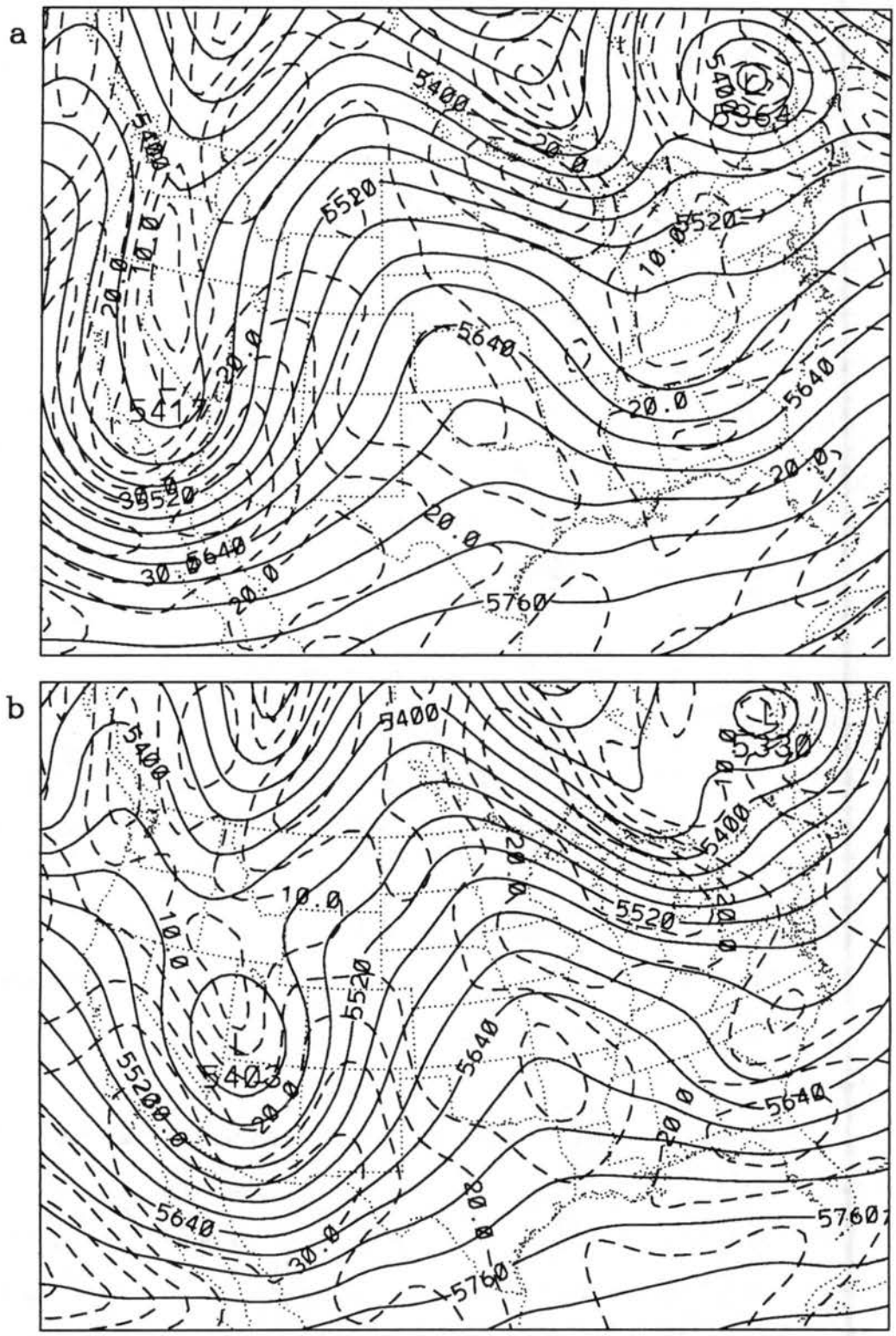

Figure 4.2: NGM 500 mb height (m, solid contours) and isotach (m s^{-1}, dashed contours) analyses from (a) 1200 UTC 6 January and (b) 0000 UTC 7 January 1992.

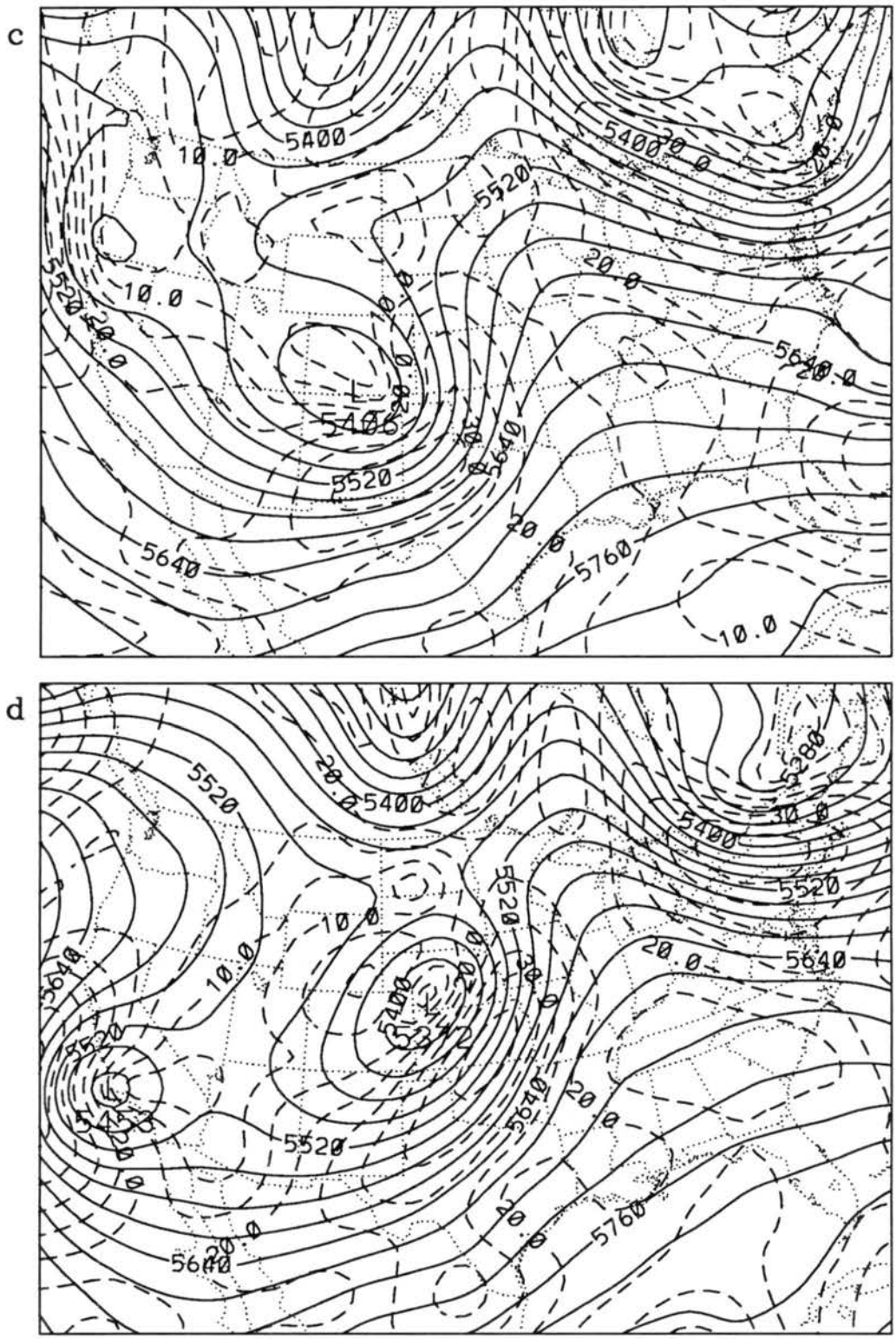

Figure 4.2: Continued: (c) 1200 UTC 7 January and (d) 0000 UTC 8 January 1992.

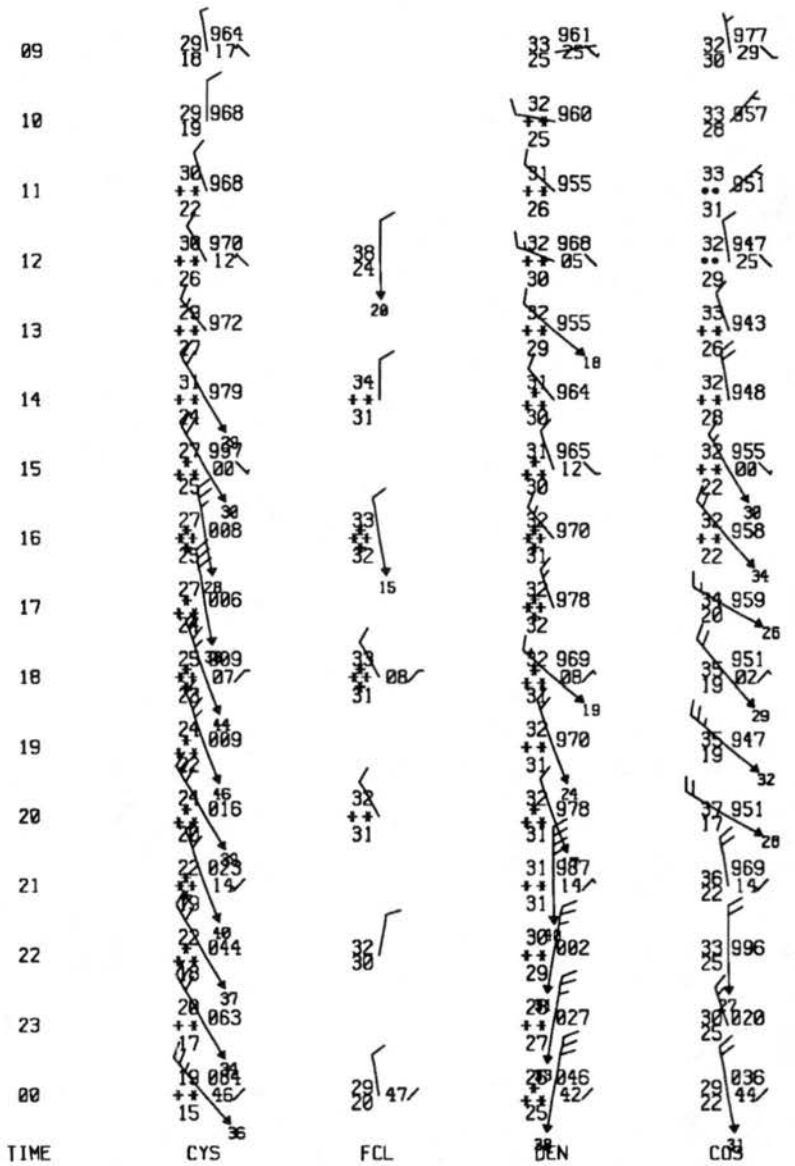

Figure 4.3: Surface aviation observations from 0900 UTC 7 January through 0000 UTC 8 January 1992 for Cheyenne (CYS), WY, Ft. Collins (FCL), Denver (DEN), and Colorado Springs (COS), CO.

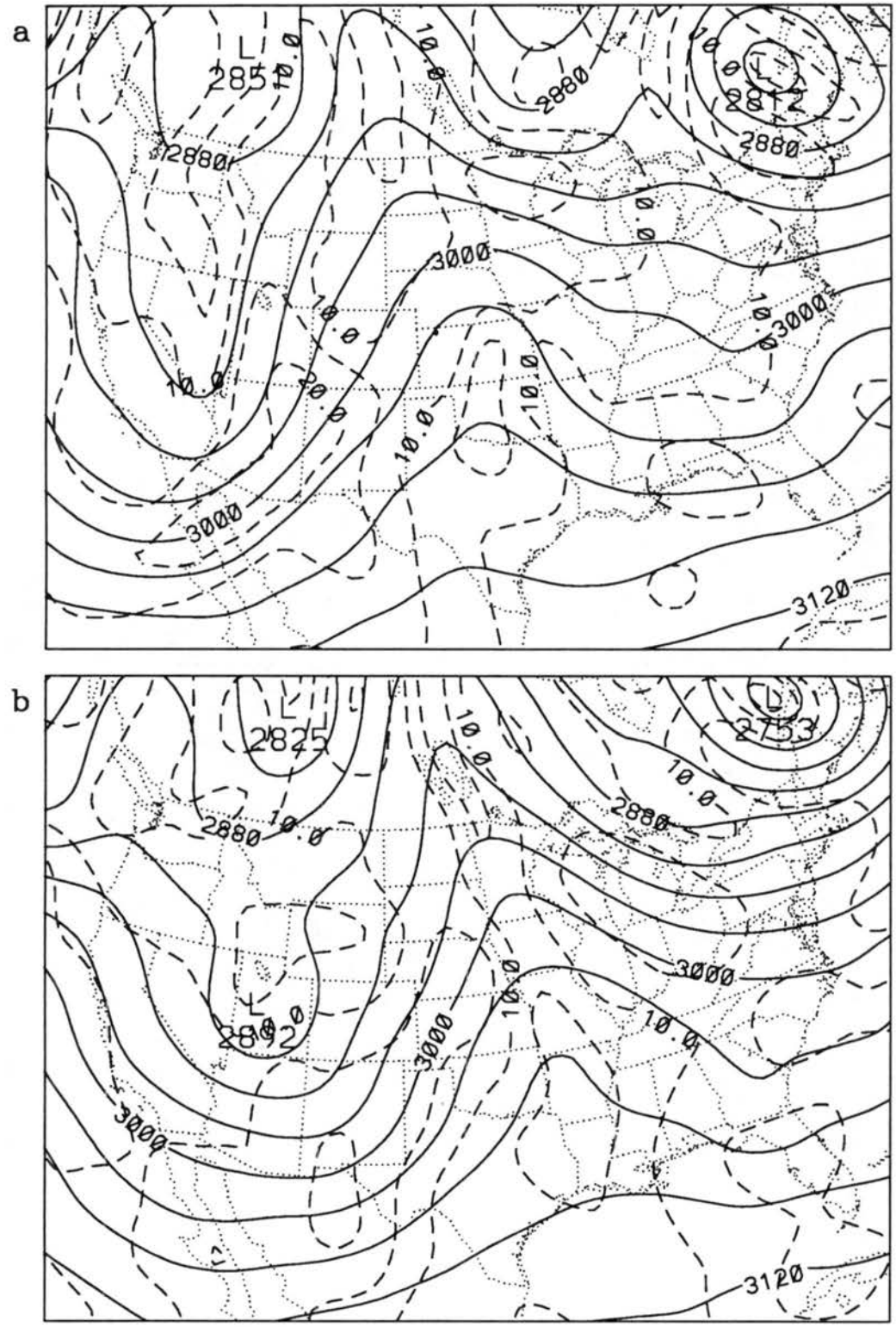

Figure 4.4: NGM 700 mb height (m, solid contours) and isotach (m s^{-1}, dashed contours) analyses from (a) 1200 UTC 6 January and (b) 0000 UTC 7 January 1992.

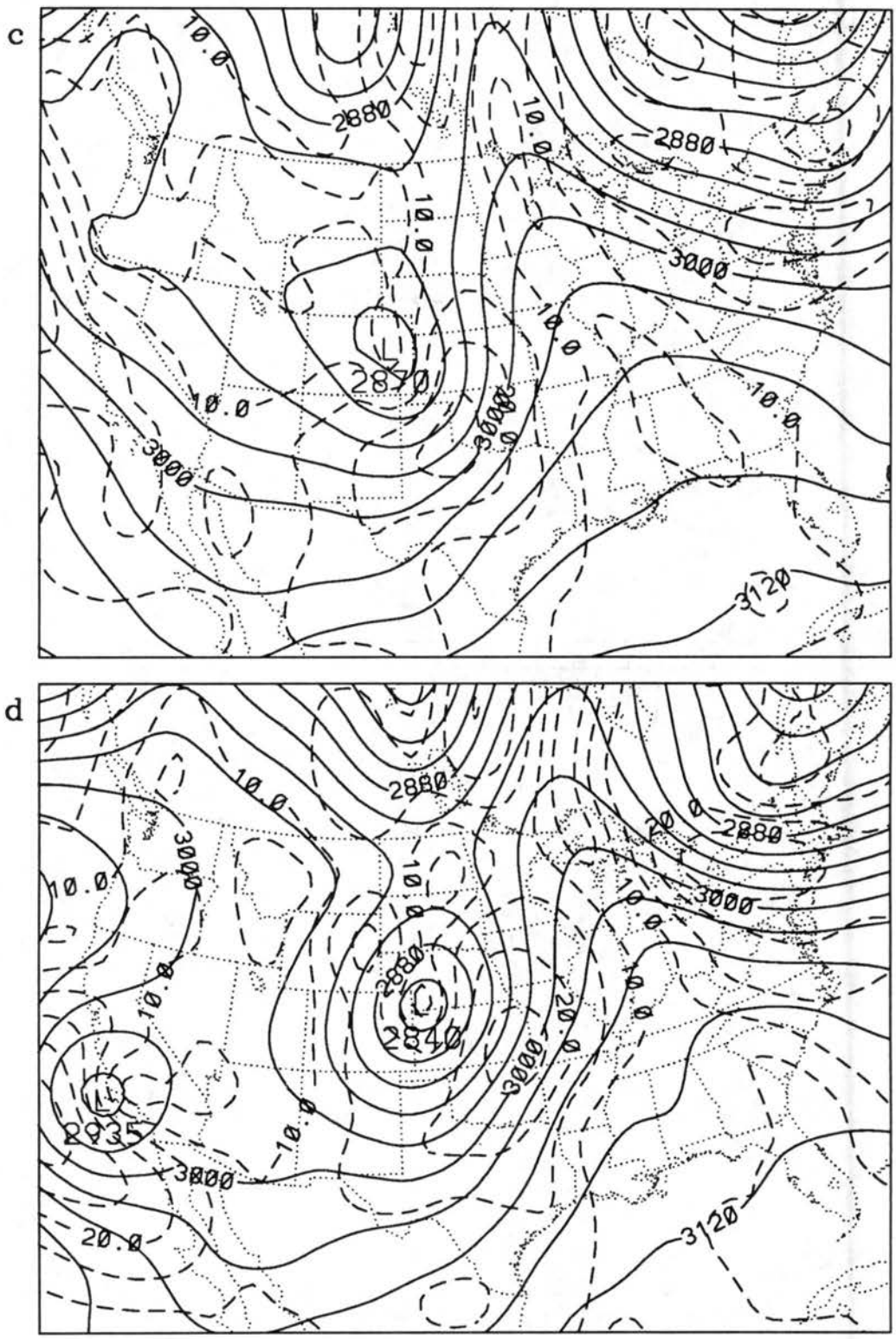

Figure 4.4: Continued: (c) 1200 UTC 7 January and (d) 0000 UTC 8 January 1992.

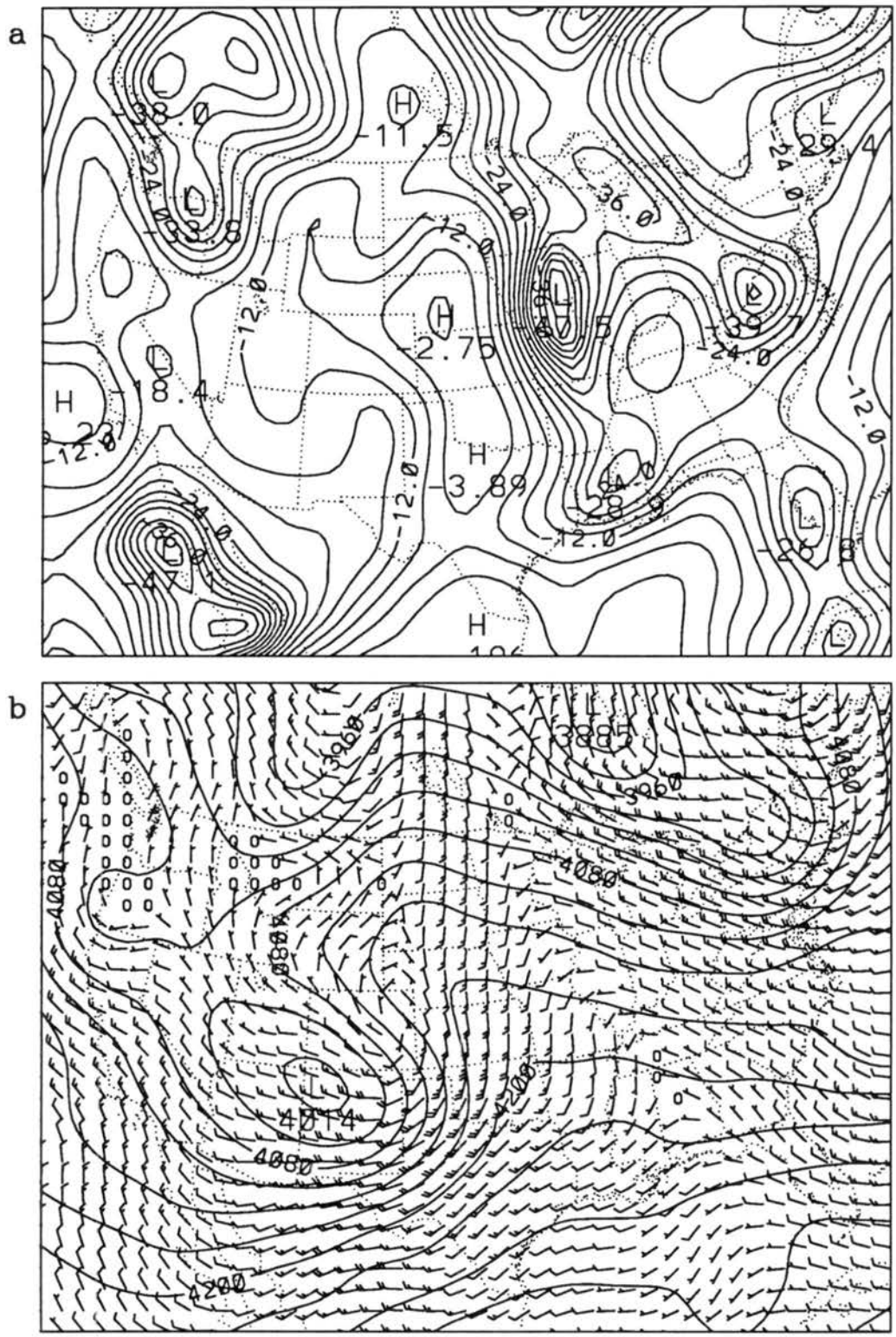

Figure 4.5: NGM analyses from 1200 UTC 7 January 1992 of (a) 700 mb dew point (°C), and (b) 850-500 mb thickness (m) and 700 mb wind barb (m s^{-1}).

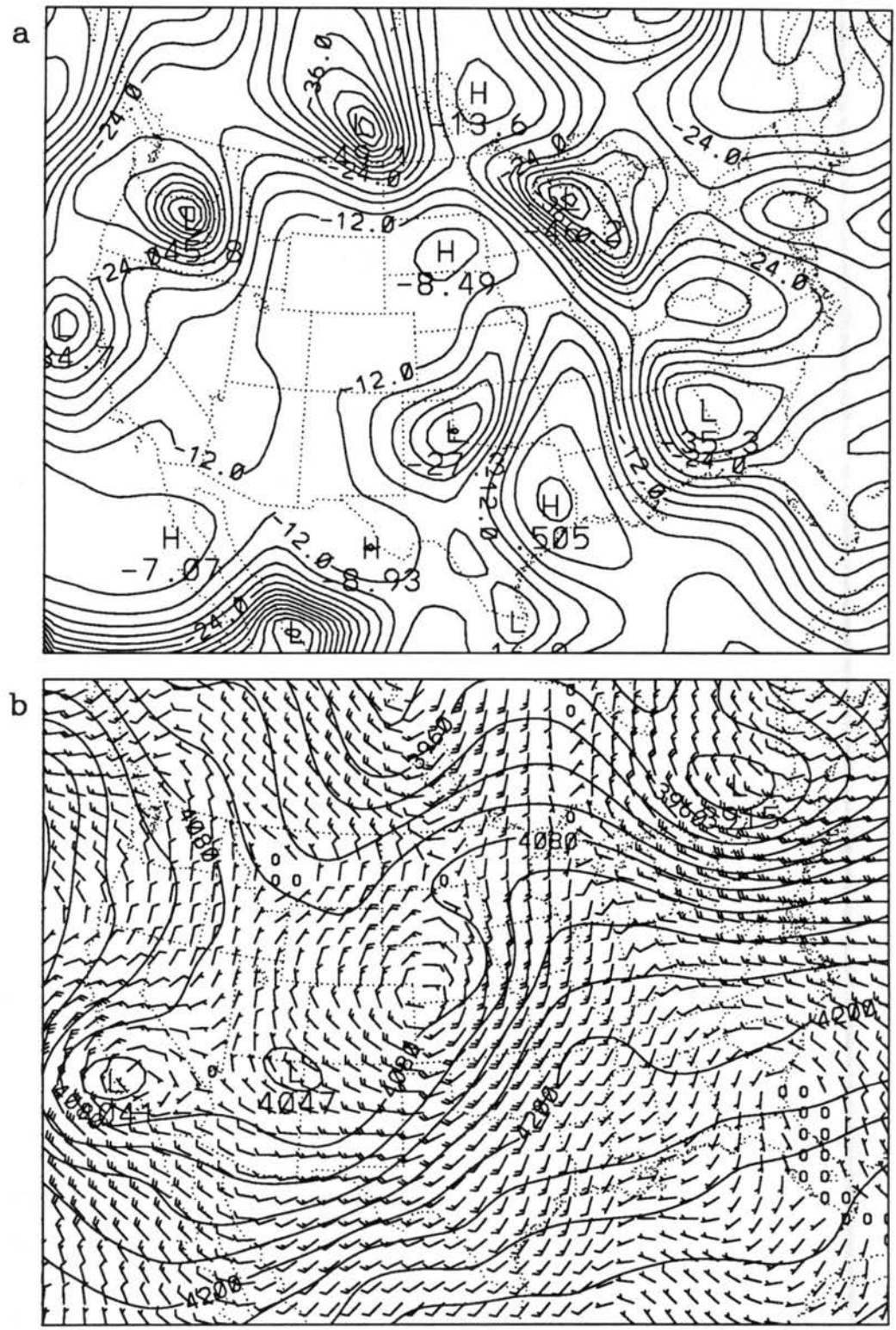

Figure 4.6: NGM analyses from 0000 UTC 8 January 1992 of (a) 700 mb dew point (°C), and (b) 850-500 mb thickness (m) and 700 mb wind barb (m s^{-1}).

and western South Dakota (Fig. 4.6b). A band of higher cloud tops associated with the warm advection is observed in the 1230 UTC infrared satellite image (Fig. 4.7). An east-west swath of heavy snow fell across the Nebraska Panhandle into southeast Wyoming, while in Colorado, the heaviest snow fell beneath the band of higher cloud tops along a north-south band extending from Greeley to the Palmer Lake Divide south of Denver.

4.1.2 Mesoscale observations

The focus of this dissertation is to investigate the north-south band of heavy snow that fell in Colorado where terrain influences are typically important. One might expect from the deep easterly upslope circulation observed with this system that either orographic uplift (e.g. Schlatter 1983) or cold air damming (e.g. Dunn 1987) would position the region of greatest snowfall along the Front Range and into the Foothills. However, south of Fort Collins, the band of greatest snowfall was observed well east (~40 km) of the mountain barrier while Front Range communities received snow depths of less than 5 cm (2 inches).

Examination of the MAPS upper air and surface analyses begins to provide insight into the possible reasons for the eastward displacement of the observed snowfall. The higher resolution MAPS analyses show that the upper level low did not progress smoothly over the Rocky Mountains, but rather redeveloped in the left front quadrant of a secondary, but stronger, jet streak. Fig. 4.8 depicts MAPS 500 mb analyses of height, wind barbs, and isotachs at three hour intervals from 0600 to 1500 UTC 7 January. At 0600 UTC, the 500 mb low is located over central Utah with a small 18 m s^{-1} (35 knot) jet streak positioned to the northeast. Another more significant jet streak of 28 m s^{-1} (55 knots) is located within the southeast portion of the long wave trough over eastern New Mexico and southeastern Colorado. By 0900 UTC, the primary low has moved into northeast Utah and the associated jet streak has weakened to 10 m s^{-1} (20 knots) over southwest Wyoming. Meanwhile, the stronger jet streak has strengthened to 30 m s^{-1} (60 knots) over southeastern Colorado with indications of a secondary low and associated circulation developing in the left front quadrant over central Colorado. A double low structure with two distinct cyclonic circulations are apparent at 1200 UTC. The primary jet streak has continued to strengthen to greater than 35 m s^{-1} (70 knots) over the Oklahoma and Texas

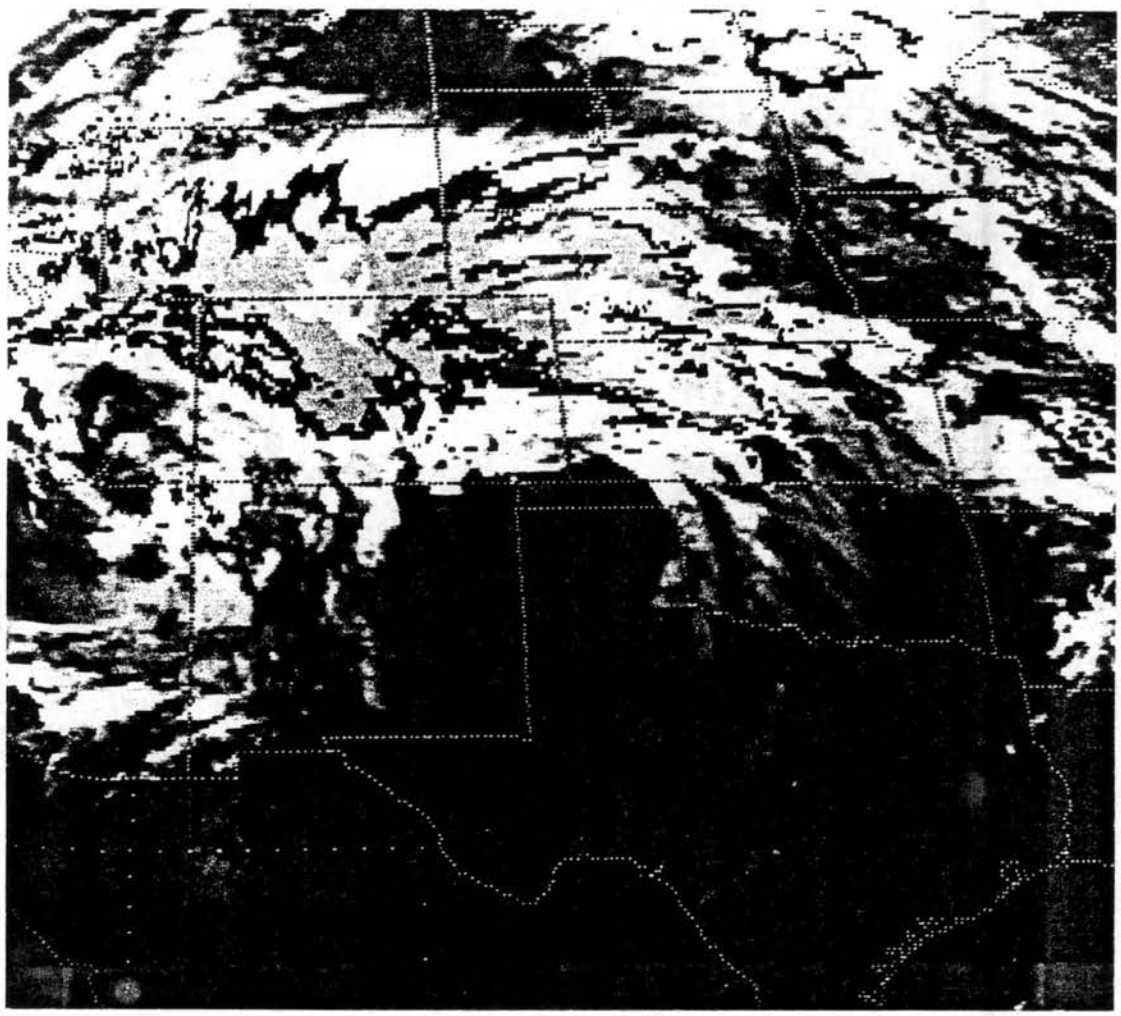

Figure 4.7: Infrared (11.2 μm) satellite image from 1230 UTC 7 January 1992.

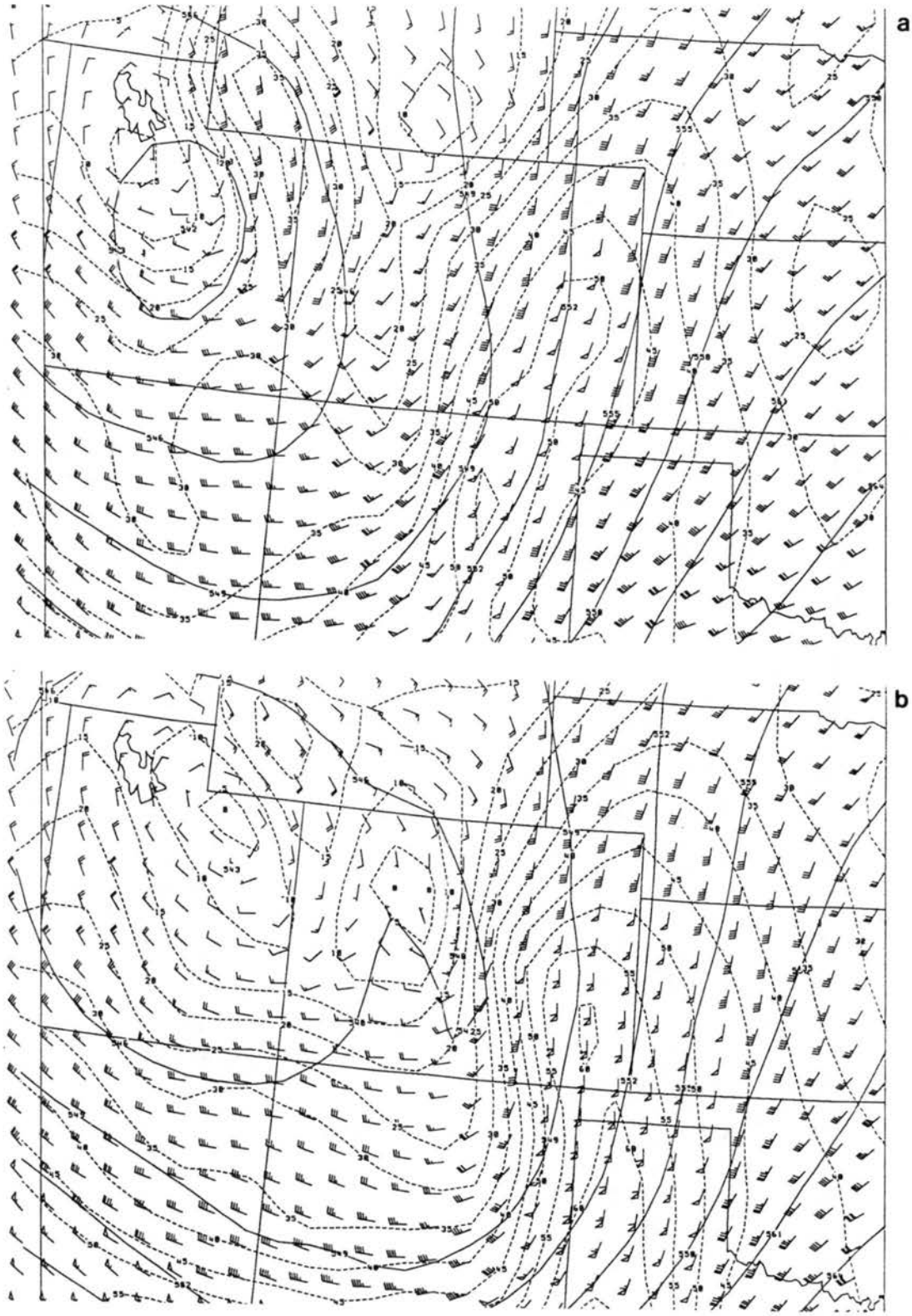

Figure 4.8: MAPS 500 mb height (dm), wind barb (knots), and isotach (knots) analyses from (a) 0600 UTC and (b) 0900 UTC 7 January 1992.

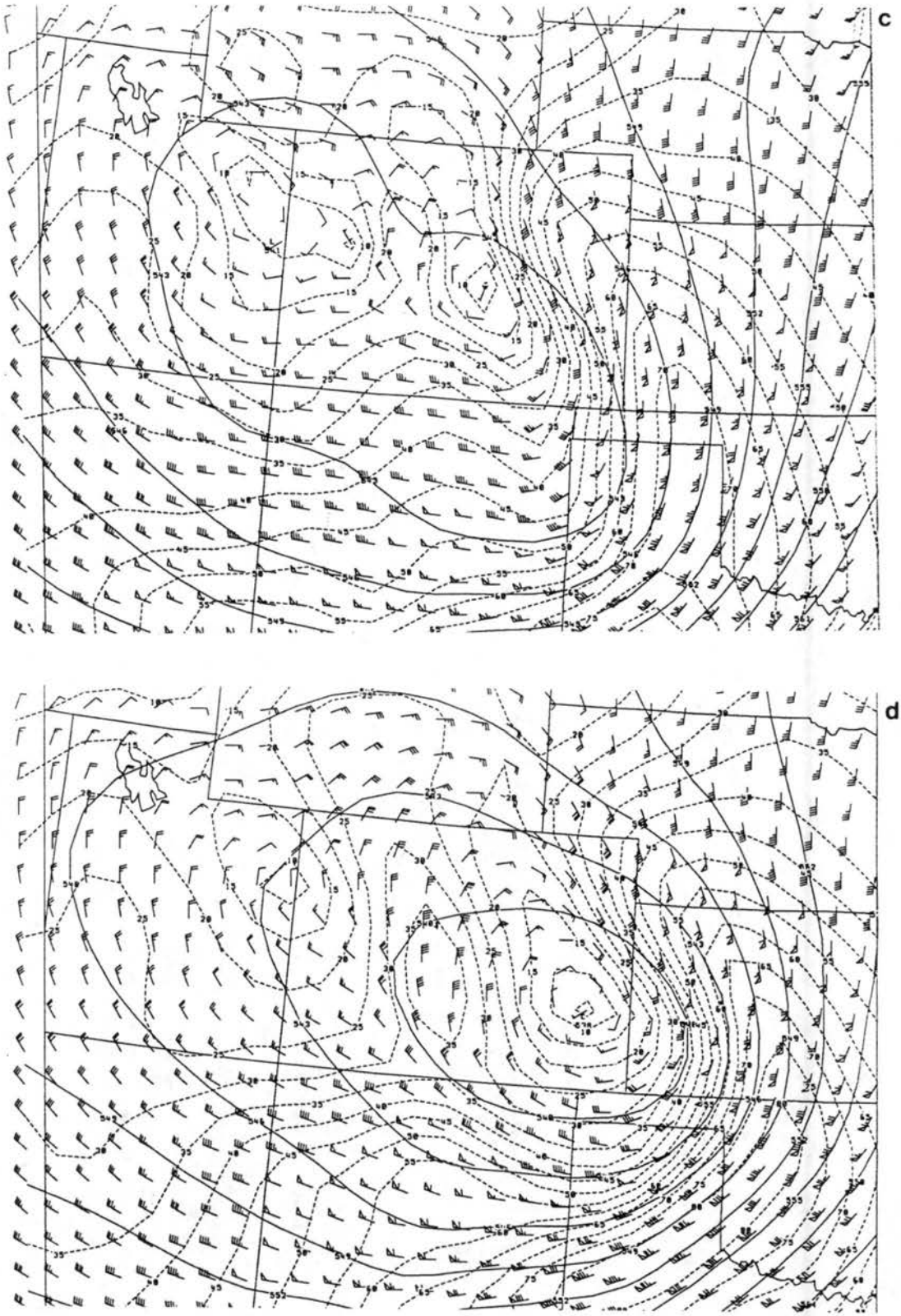

Figure 4.8: Continued: (c) 1200 UTC and (d) 1500 UTC 7 January 1992.

Panhandles. By 1500 UTC, only the new low is apparent over east-central Colorado with the associated jet streak exceeding 40 m s^{-1} (80 knots) over the Texas Panhandle and western Oklahoma.

The rapid redevelopment of the low east of the mountain barrier is well correlated with the significant pressure falls and rapid development of the eastern Colorado cyclone observed during this time period in the surface observations (Fig. 4.3) and analyses. MAPS 30 km analyses of surface pressure reduced to 1500 m elevation and 3-h pressure change at three hour intervals from 0600 to 1500 UTC 7 January are presented in Fig. 4.9. MAPS has demonstrated that reducing the surface pressure to a height near the mean elevation of the Colorado Eastern Plains provides an improved representation of the surface pressure field when compared to a mean sea level pressure analysis. The analysis at 0600 UTC shows an elongated region of low pressure positioned east of the Rocky Mountain barrier that is likely associated with lee side troughing. A pressure fall center is positioned over south-central Colorado and is beneath the left front quadrant of the 500 mb jet. A 3.5 mb pressure fall center is positioned in eastern Colorado at 0900 UTC. A more consolidated low center is evident in the lee of the Colorado mountain barrier. At 1200 UTC, significant pressure falls continue beneath the 500 mb jet left front quadrant as the 1500 m low strengthens in southeast Colorado. The region of greatest pressure falls moved into western Kansas by 1500 UTC while the 1500 m low is located in east-central Colorado. The MAPS surface analyses show significant surface pressure falls to occur beneath the left front quadrant of the 500 mb jet streak during this period. In association, a significant surface cyclone develops in eastern Colorado. It is important to note that the geostrophic upslope is located primarily in the Nebraska Panhandle and eastern Wyoming while strong geostrophic northerlies are suggested along the lee of the Colorado mountains.

Actual surface winds show the development of a significant ageostrophic wind component directed into the intensifying cyclone. MAPS 30 km analyses of surface wind and SAO reports (Fig. 4.10) at 0600 UTC 7 January suggest a double low structure, one east of Ft. Collins and the other near Trinidad. Significant southeasterly flow over the High Plains has transported low level moisture northward with the 0°C dew point isopleth into

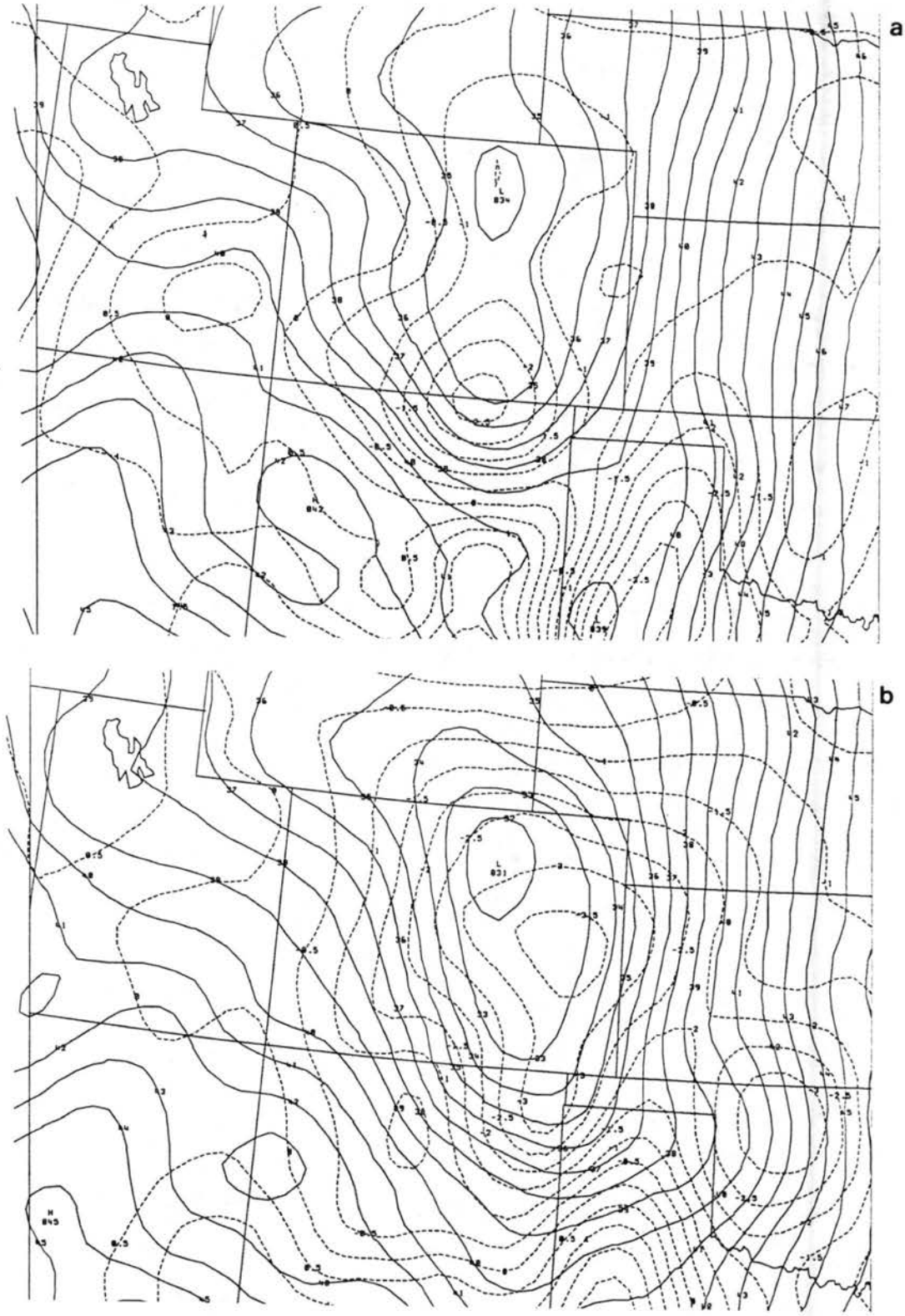

Figure 4.9: MAPS 1500 m pressure (mb) and 3 h pressure change (mb) analyses from (a) 0600 UTC and (b) 0900 UTC 7 January 1992.

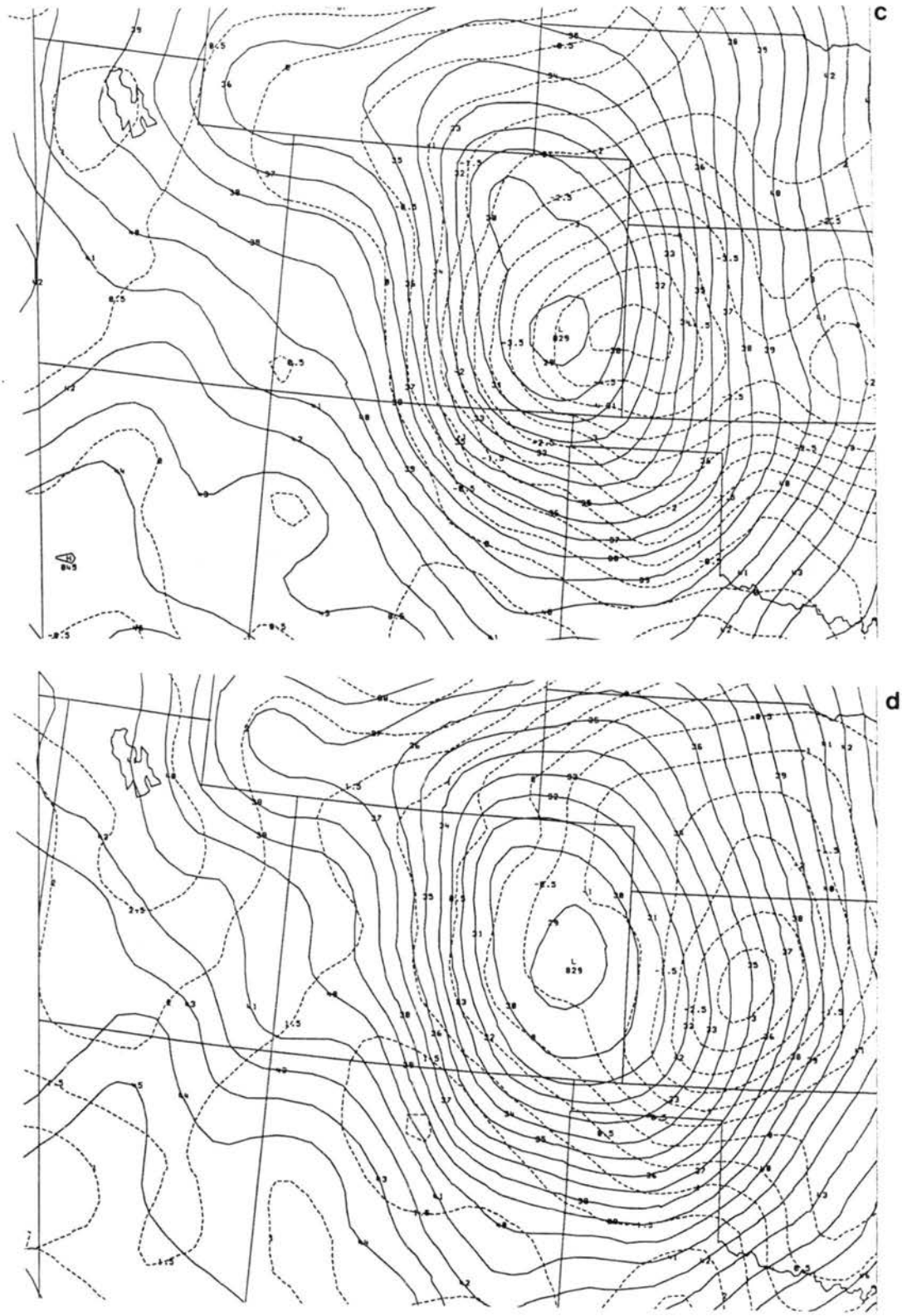

Figure 4.9: Continued: (c) 1200 UTC and (d) 1500 UTC 7 January 1992.

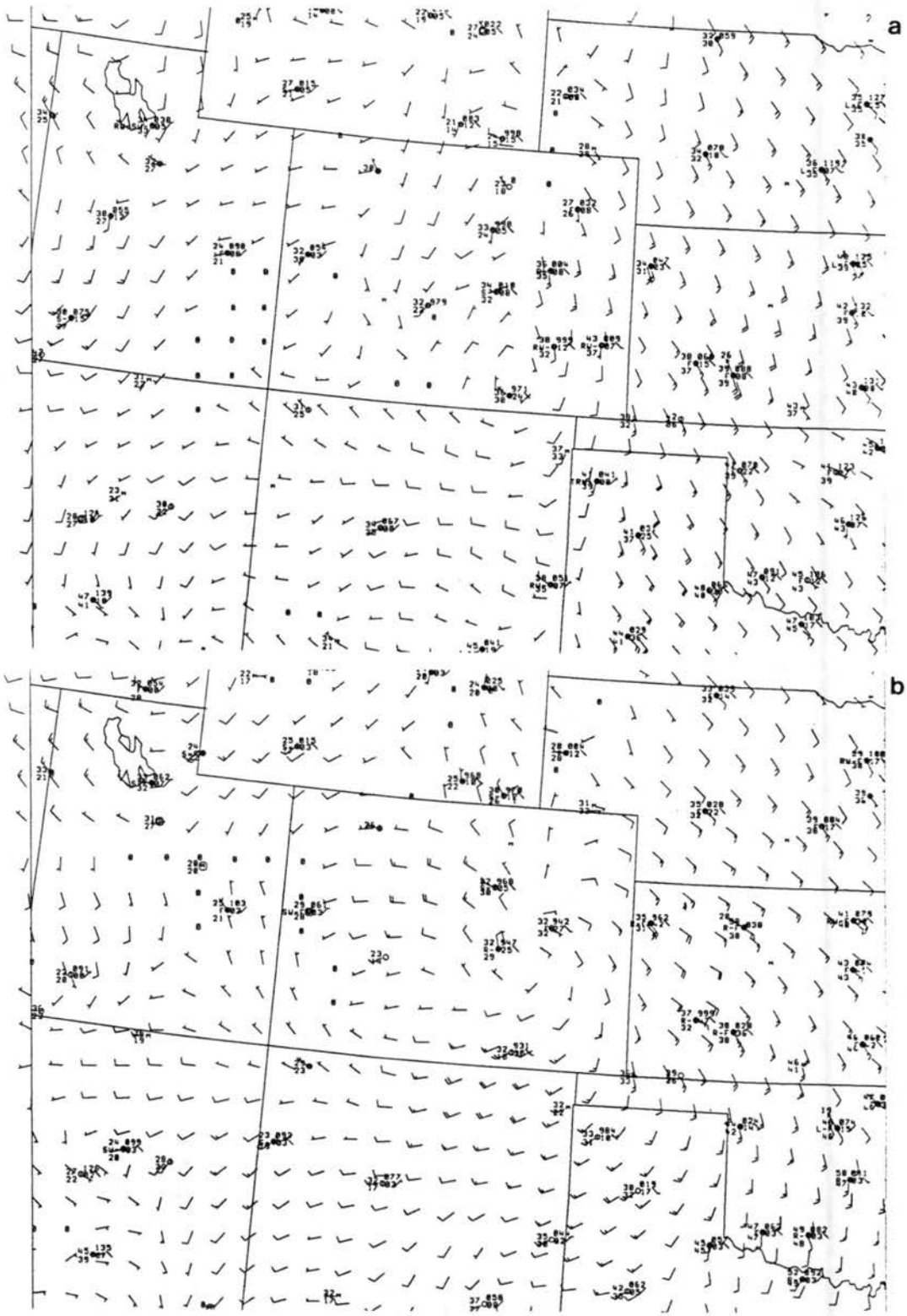

Figure 4.10: MAPS surface wind barb (knots) analyses and SAO reports from (a) 0600 UTC and (b) 1200 UTC 7 January 1992.

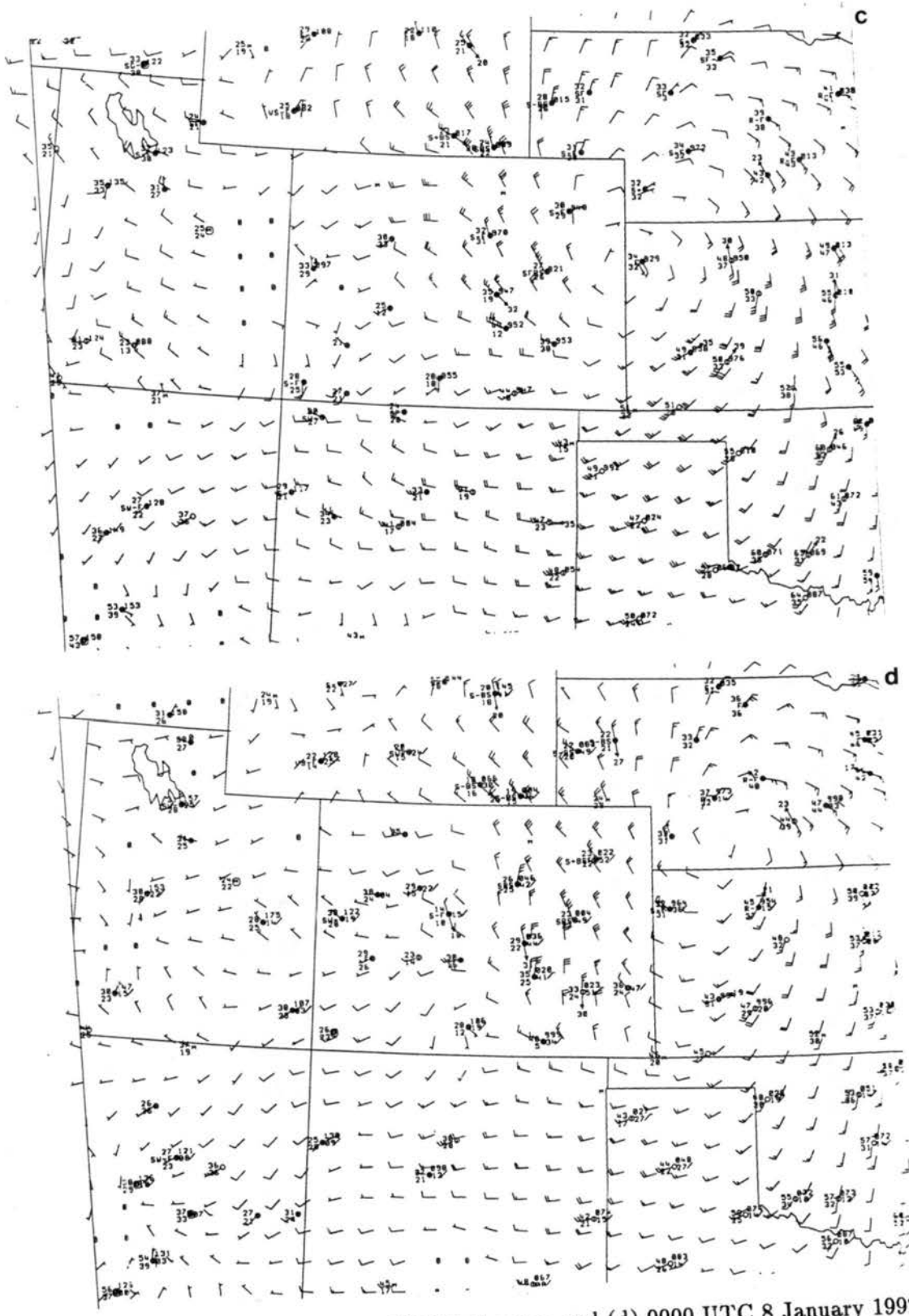

Figure 4.10: Continued: (c) 1900 UTC 7 January and (d) 0000 UTC 8 January 1992.

southern Nebraska. By 1200 UTC, MAPS analyzed wind speeds along the Colorado Front Range exceeded 10 m s^{-1} (20 knots) from the west. The surface low is positioned west of Limon and a significant turning of the wind into the cyclone is indicated. Relatively moist air has wrapped into southeast Wyoming where dew points rose 5°C in the six hour period. Light snow began at 1100 UTC in Cheyenne and at 1000 UTC in Denver with light rain beginning at 1100 UTC in Colorado Springs (Fig. 4.3).

A well developed surface cyclone is located just southwest of Goodland, Kansas at 1900 UTC (Fig. 4.10, the 1800 UTC MAPS surface wind analysis was not available). Strong westerly flow (15 m s^{-1}, 30 knots) continued over the Continental Divide west of Denver and the development of strong northwesterly flow was evident from southeast Wyoming into northeast Colorado. Relatively high dew points continue to wrap into the cyclone from the northeast and low dew points in northeast New Mexico and extreme southern Colorado suggest the location of the dry slot and downward mixing. The surface cyclone progressed to the western Nebraska-Kansas border by 0000 UTC with strong northwesterly flow continuing over southeast Wyoming and eastern Colorado except at Denver and Pueblo where the wind direction is northeast. Winds at Cheyenne remained northwesterly throughout the event and were quite strong during the afternoon with gusts exceeding 20 m s^{-1} (40 knots). Winds were also northwesterly at Denver through 2000 UTC, an unusual direction for heavy snow due to the downslope component near the surface. After 2000 UTC, the winds shifted to north and northeast with the velocity increasing to greater than 15 m s^{-1} (30 knots) and gusts reaching 20 m s^{-1} (40 knots).

Rawinsonde observations from Denver, North Platte, NE, and Lander, WY (Fig. 4.11) indicate a near saturated environment up to at least 500 mb. A stable layer is observed between the surface and 700 mb. The combination of the stable layer (i.e. low Froude number), strong northwesterly flow over the Cheyenne Ridge, and a northeast wind at Denver suggests favorable conditions for the development of a Longmont anticyclone (Young and Johnson 1984).

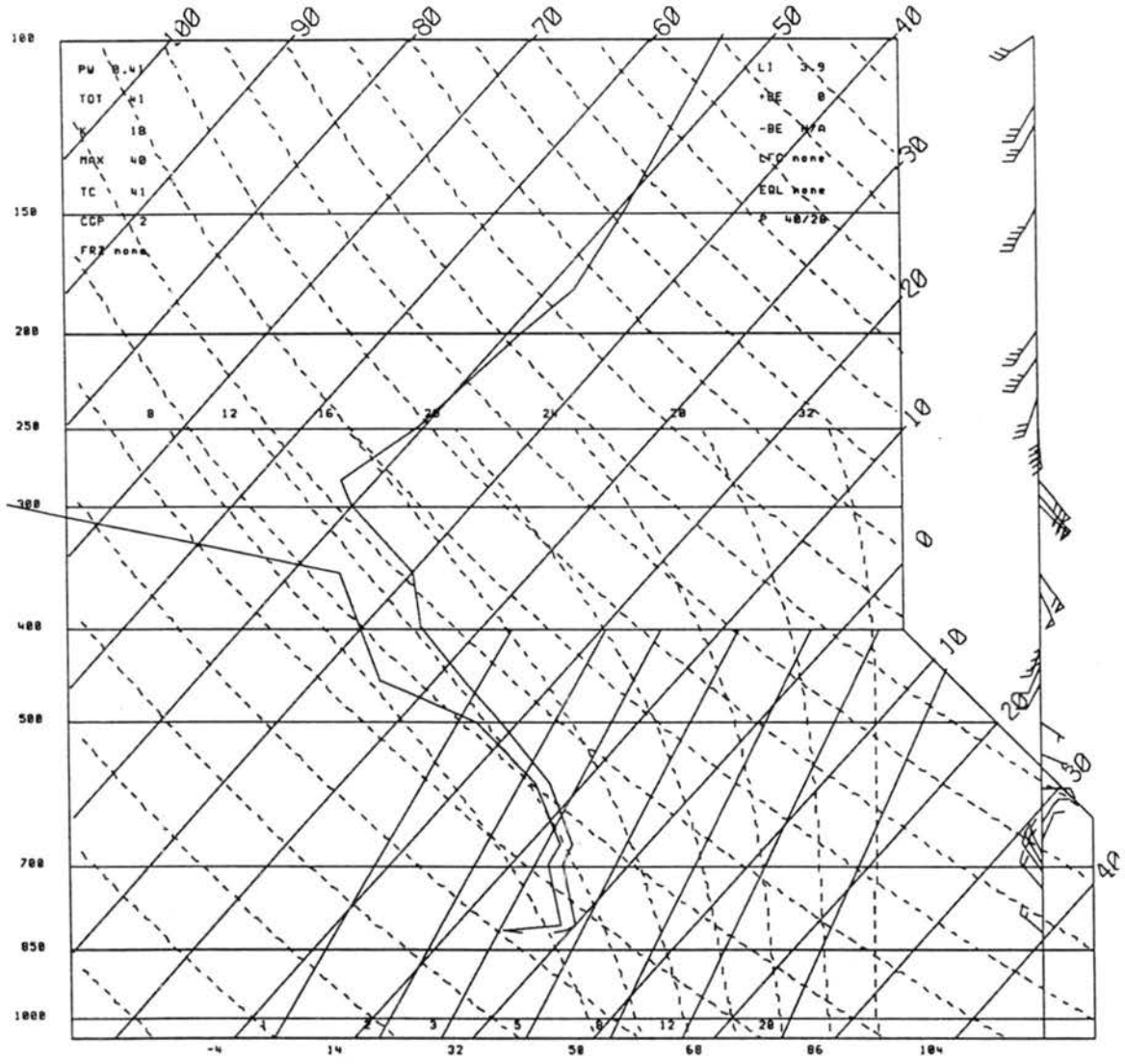

Figure 4.11: Rawinsonde observations from 1200 UTC 7 January 1992 at (a) Denver, CO.

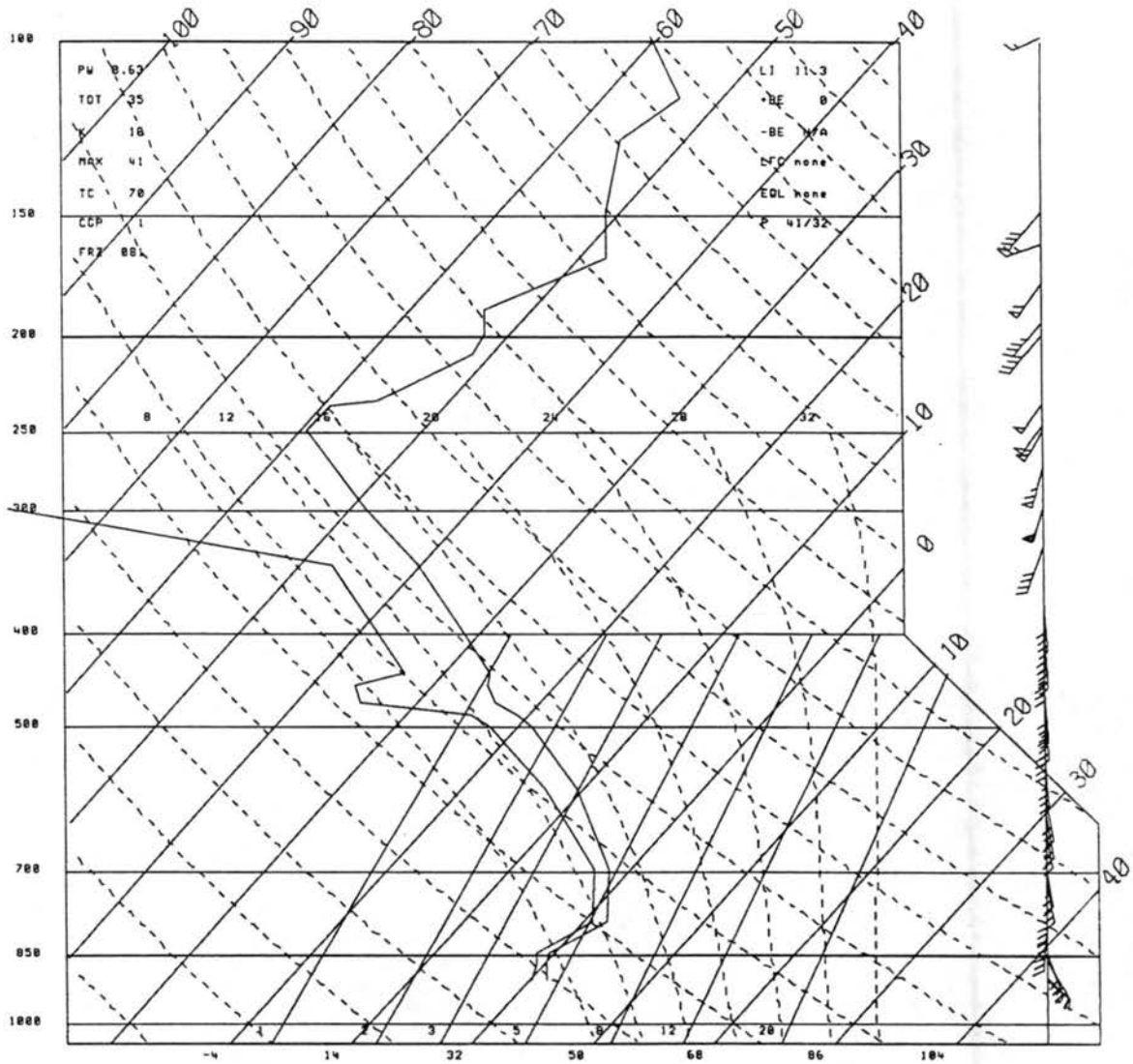

Figure 4.11: Continued: (b) North Platte, NE.

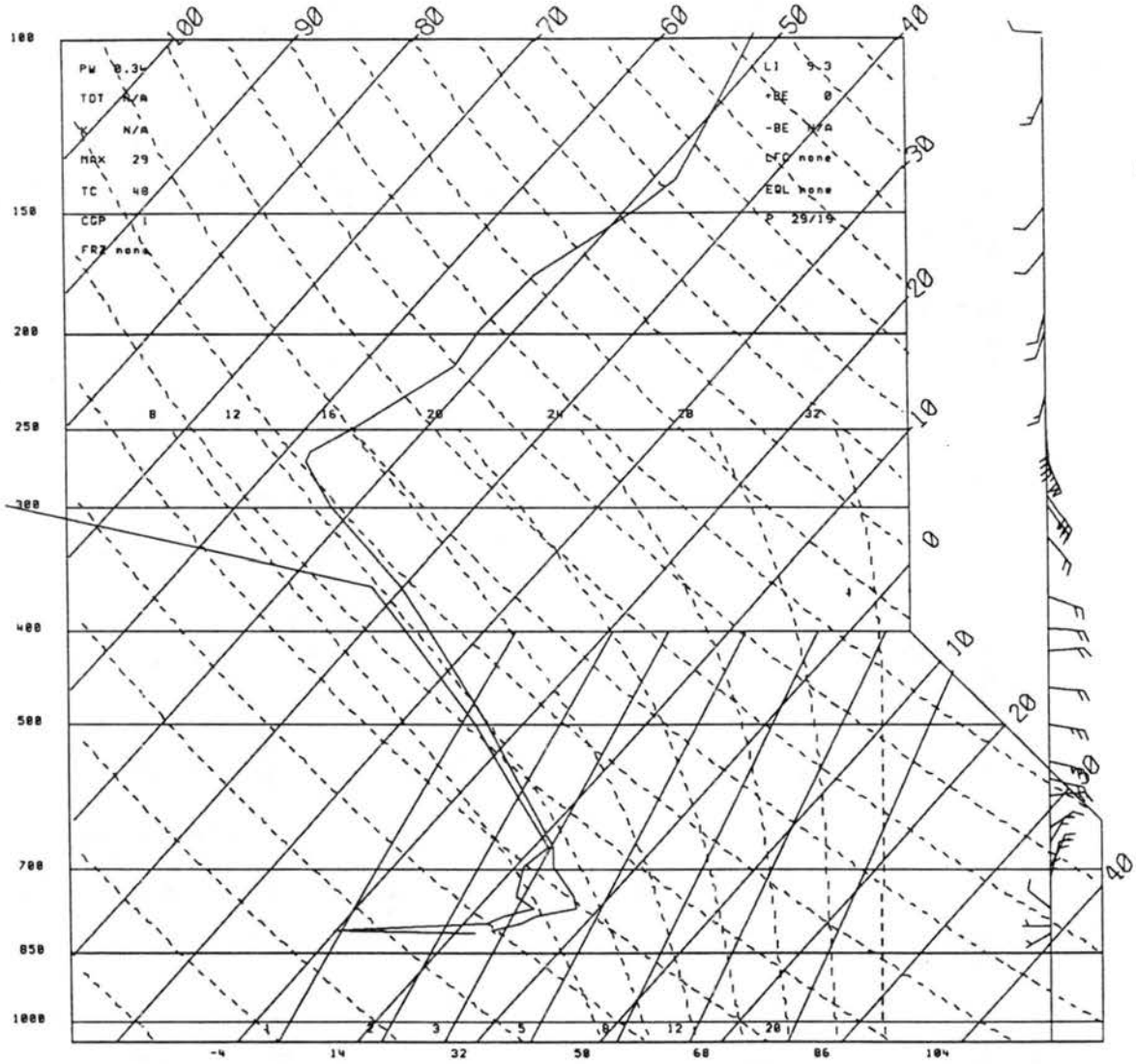

Figure 4.11: Continued: (c) Cheyenne, WY.

4.1.3 Local scale observations

Examination of Doppler radar, wind profiler data, and automated surface observations provides an even closer view of the cyclone development and associated wind flow. Reflectivity data from a Doppler radar (Fig. 4.12) located approximately 10 km northeast of Denver provides an indication of the areal extent, intensity, and evolution of the snowfall. The north-south band of heavy snow is indicated by the region of reflectivity exceeding 25 dBZ centered along a line stretching from east of Ft. Collins, across Denver, and southeast to the Palmer Lake Divide. A band of low reflectivity is observed between the mountain barrier and the heavy snow band. This basic pattern continued through 0000 UTC 8 January with a decrease in areal coverage near the end of the period.

The Platteville, CO wind profiler, located along the western edge of the heavy snow band, depicts three distinct flow regimes in the vertical (Fig. 4.13). Between 0700 and 0800 UTC the low-level winds shifted from south to north-northwest. The layer of low-level north-northwest winds expanded up to 4 km by 1800 UTC. A middle layer of mostly east winds developed after 0700 UTC and increased in depth with time. At 1800 UTC, the easterlies were observed between 4 and 11 km. Upper layer winds were mostly from the south and veered with time in response to the eastward movement of the long wave trough. After 1800 UTC, the mid-layer easterlies shifted to near northerly by 0000 UTC resulting in a deep layer of northerlies up to 10.5 km. Prior to 1800 UTC, the ascent of the easterly flow over the low-level northerlies was a likely contributor to the heavy band of observed snowfall. However, areas of moderate to heavy snow continued after 1800 UTC with winds strong from the north.

Mid-level easterlies above low-level northerlies often indicates a cold air damming situation (e.g. Dunn 1987). However, observations from the FSL mesonet (Fig. 4.14) indicate that strong west winds persisted through the entire event in the mountain (western) stations, warmer temperatures occurred adjacent to the Front Range, and there was no easterly flow in the eastern portion of the domain, all indicators that this is not a cold air damming case. Another interesting aspect of the mesonet observations is the development of light northeasterlies adjacent to the Front Range. With strong northwest flow

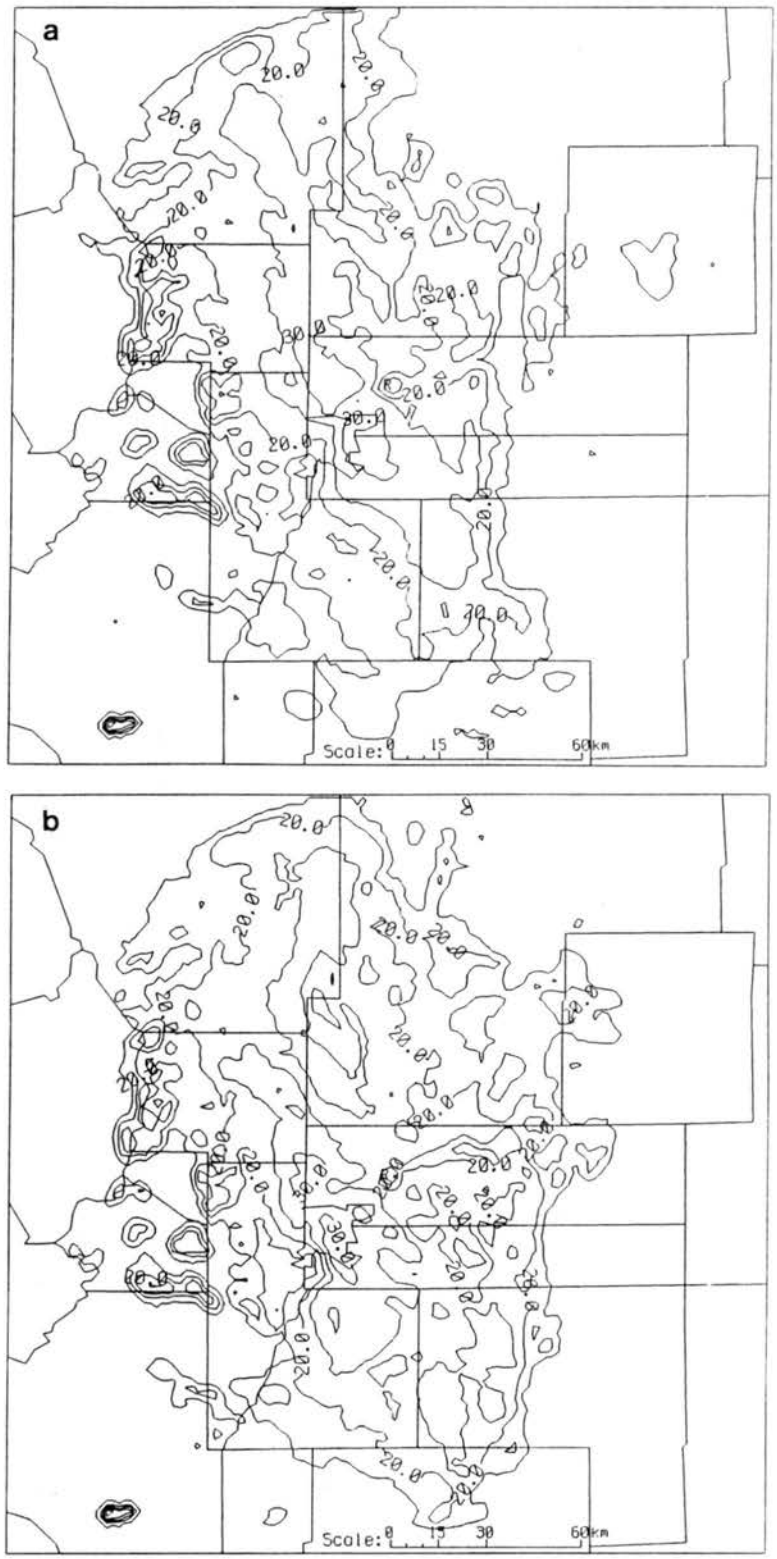

Figure 4.12: Prototype WSR-88D radar reflectivity (dBZ) from just northeast of Denver (denoted by the "R"). Ground clutter is not removed. (a) 1200 UTC and (b) 1500 UTC 7 January 1992.

Figure 4.12: Continued: (c) 1800 UTC and (d) 2100 UTC 7 January 1992.

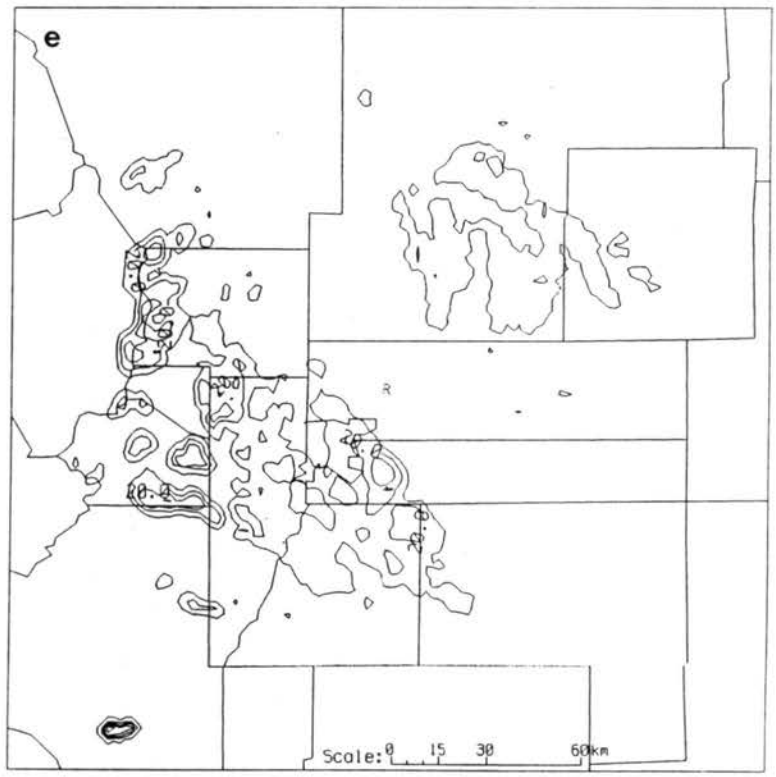

Figure 4.12: Continued: (e) 0000 UTC 8 January 1992.

observed by the northern stations, the mesonet indicates a Longmont anticyclone regime (Young and Johnson 1984). However, unlike other cases where precipitation develops along the Front Range on the convergence line between the northwesterlies and the northeasterlies (e.g. Wesley 1991), the heavy snow fell further east. The heavy snow actually fell within a region of observed strong northwesterly flow that increased significantly with time. Doppler radar velocity data (not shown) also indicated the development of strong (25 m s^{-1}) north-northwest flow colocated with the band of heavy snow.

4.1.4 Summary

The synoptic scale observations indicate that the 7 January 1992 blizzard was more typical of a Colorado spring storm (Fawcett and Saylor 1965). The cyclone had many characteristics of a deep cyclonic, upslope circulation storm (Boatman and Reinking 1986). However, two aspects of the storm were unusual: 1) the development of strong westerly lower tropospheric flow east of the Continental Divide and 2) the eastward displacement of greatest snowfall away from the mountain barrier. Significant pressure falls observed over

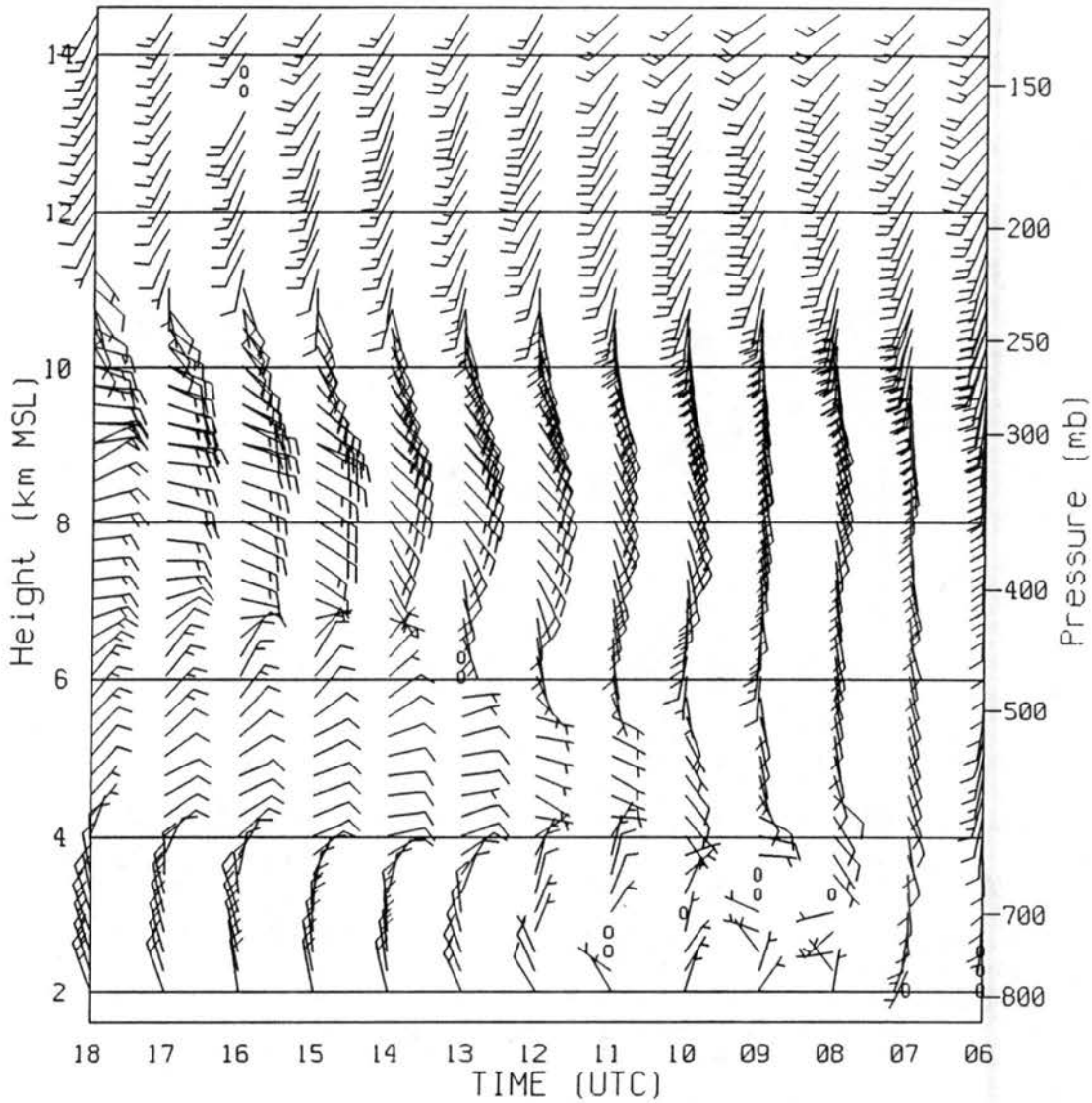

Figure 4.13: Time-height series of wind (m s^{-1}) from the Platteville, CO wind profiler from (a) 0600 to 1800 UTC 7 January 1992.

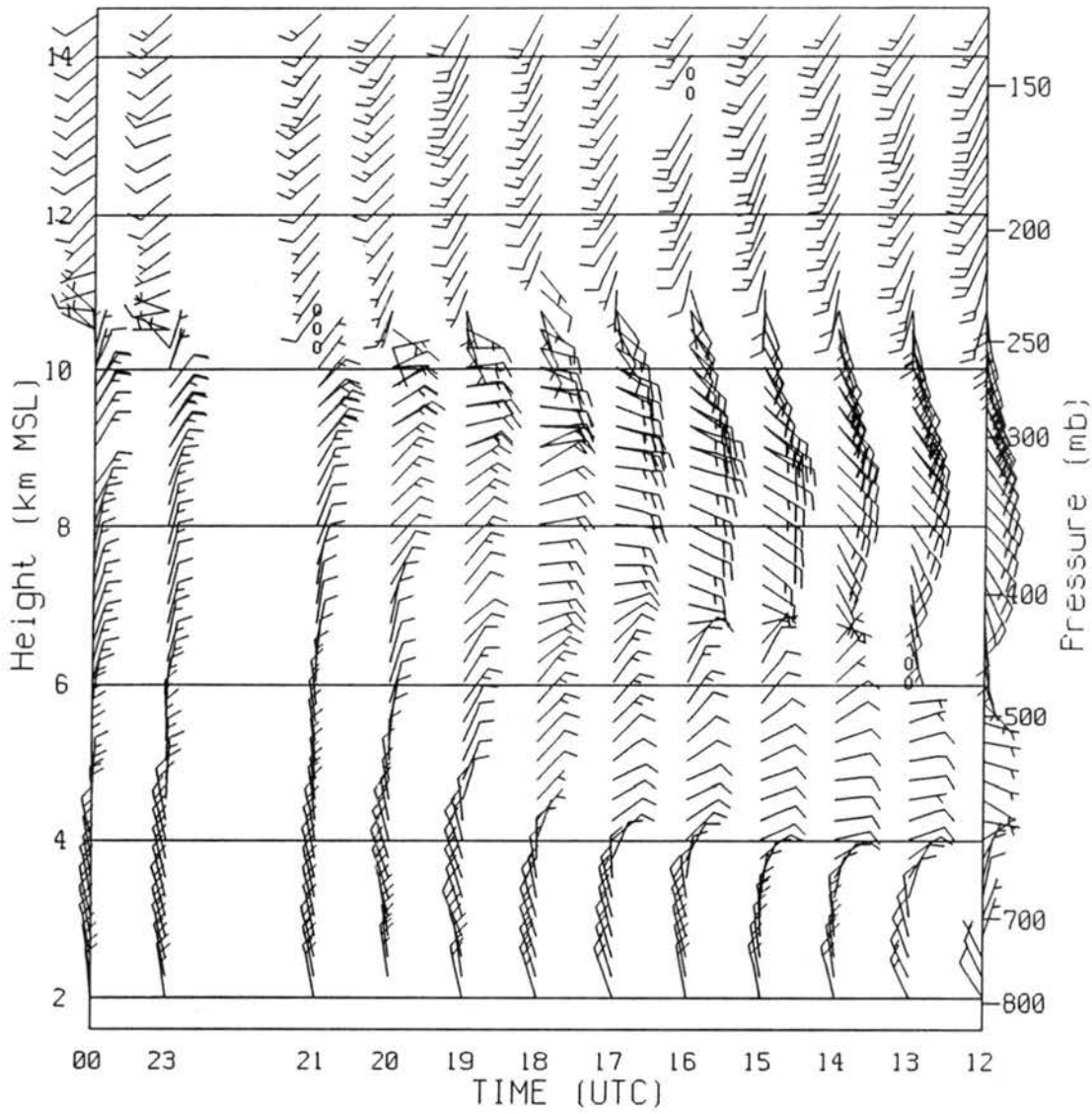

Figure 4.13: Continued: (b) 1200 UTC 7 January to 0000 UTC 8 January 1992.

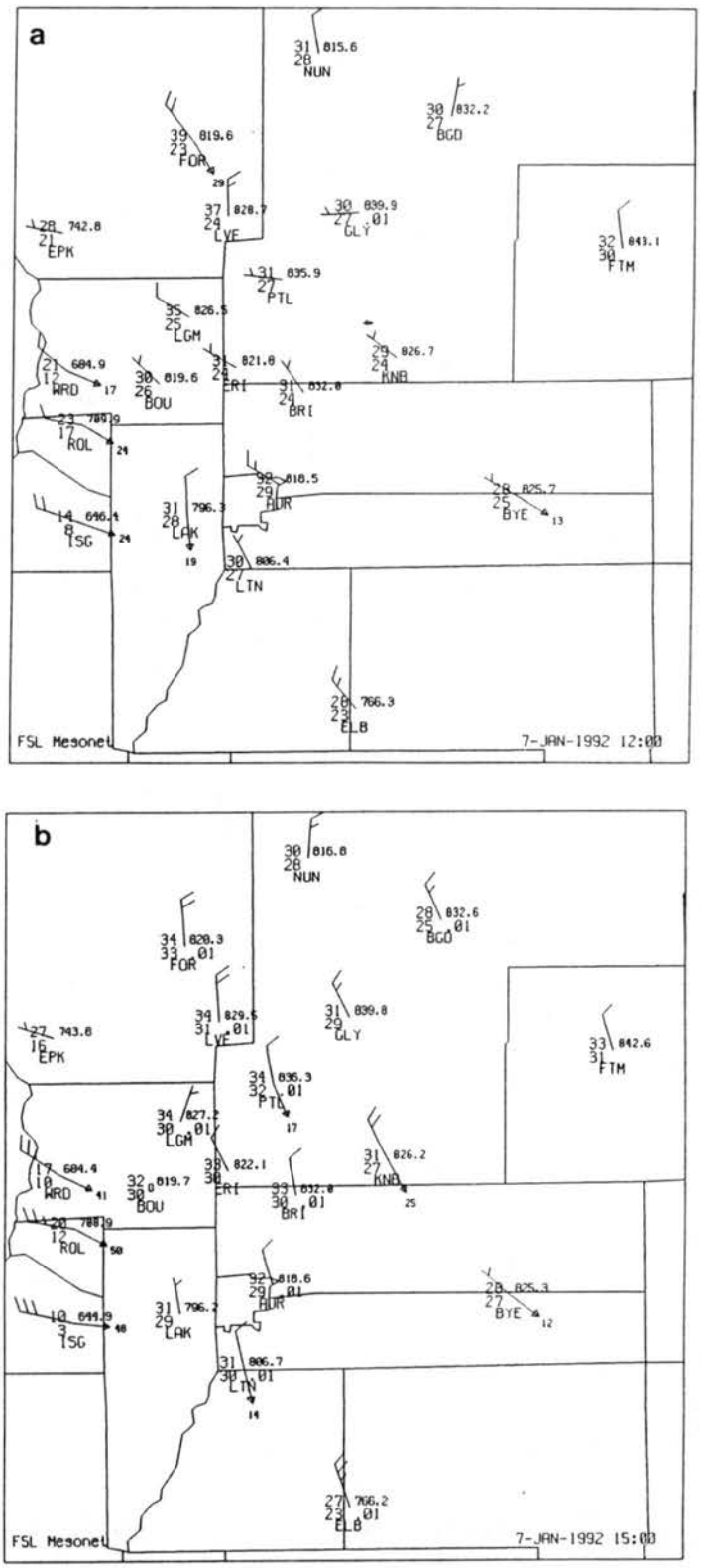

Figure 4.14: Automated surface observations from the FSL mesonet for (a) 1200 UTC and (b) 1500 UTC 7 January 1992 (winds are in knots).

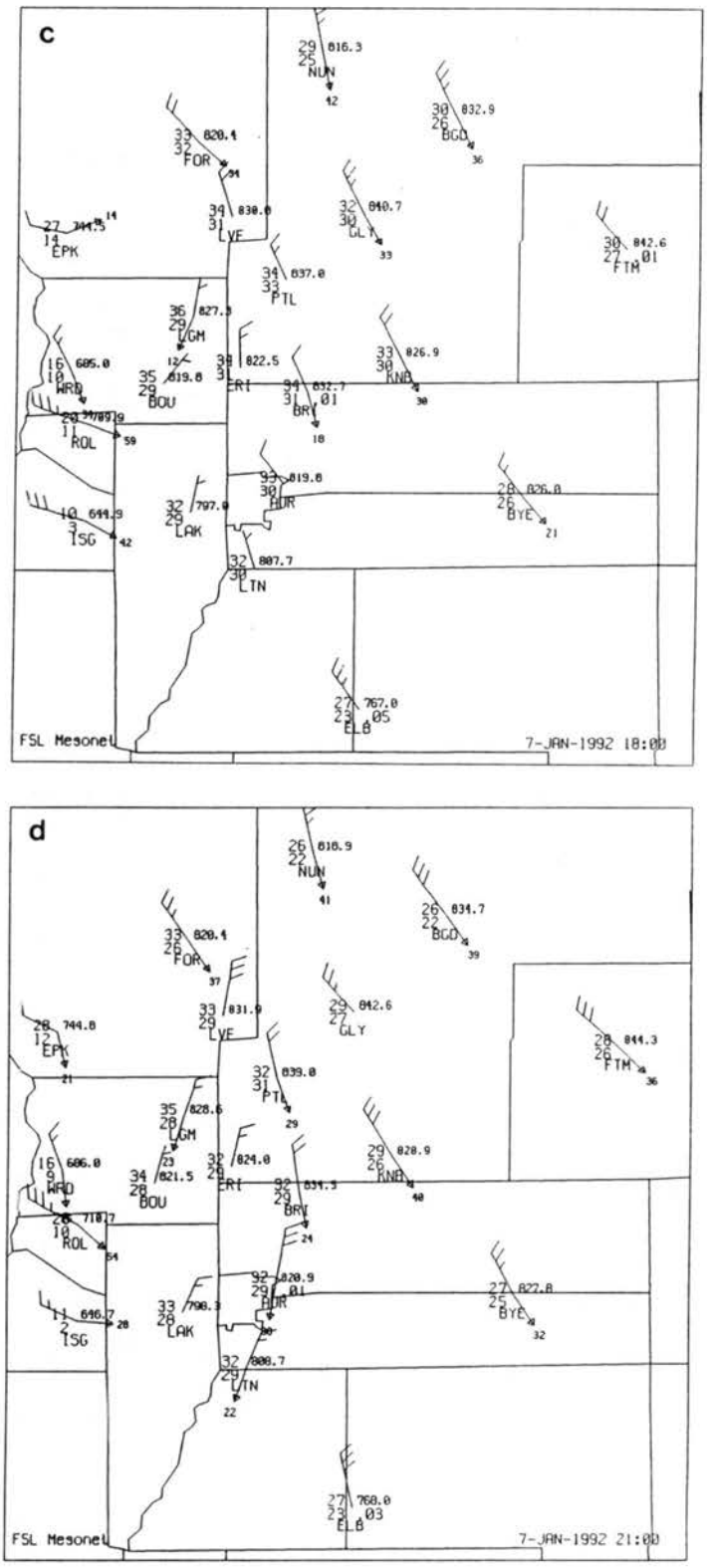

Figure 4.14: Continued: (c) 1800 UTC 7 January and (d) 2100 UTC 7 January 1992

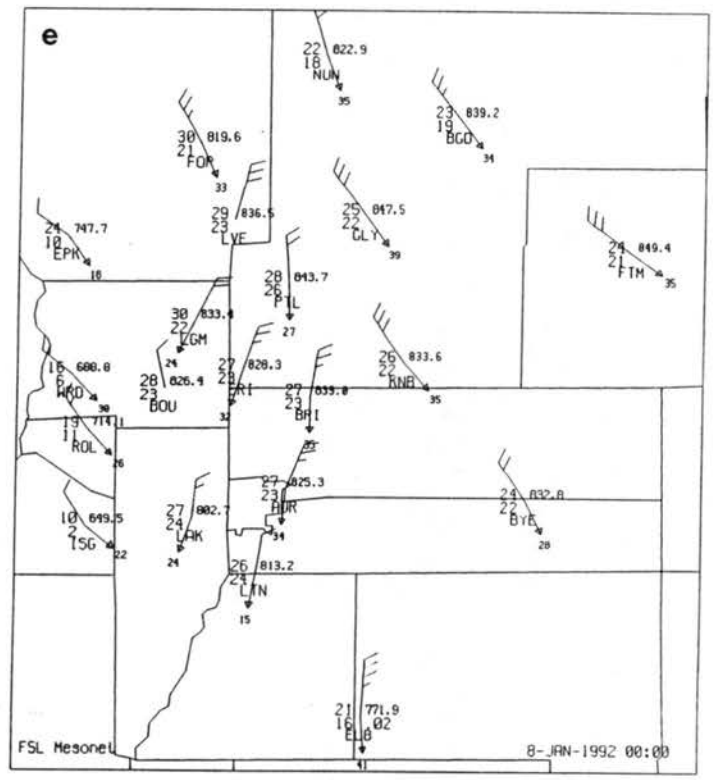

Figure 4.14: Continued: (e) 0000 UTC 8 January 1992

the Eastern Plains are well correlated with the redevelopment of the upper level low east of the mountain barrier. The isallobaric effect of the pressure falls likely contributed to the development of an ageostrophic wind component directed into the developing cyclone and to the formation of the strong westerly surface flow observed east of the Continental Divide. Since westerly downslope flow is typically warmer and drier, this feature likely contributed to the warmer temperatures and low amounts of snowfall observed along the Front Range. The observations of strong northwesterly flow over the Cheyenne Ridge and weak northeasterlies adjacent to the Front Range combined with a stable (i.e. low Froude number) boundary layer indicates the development of a Longmont anticyclone regime (Young and Johnson 1984). Although the Longmont anticyclone has been correlated in other storms with bands of enhanced snowfall, the band of heavy snow fell further east in a region of strong northwesterly flow.

4.2 Model Simulations

The observations of 7 January 1992 indicate several interesting mesoscale features including: 1) persistent strong downslope flow east of the mountain barrier crest, 2) the development of weak northeasterlies adjacent to the Front Range, 3) the generation of strong northwesterlies at the surface and low-levels over the Eastern Plains, and 4) the eastward displacement of greatest snowfall away from the mountain barrier. To determine if the mesoscale model forecasts can resolve these features and provide further meteorological insight as to their existence, the RAMS mesoscale model is initialized with real-time 10 km grid increment LAPS analyses from 7 January 1992.

All seven RAMS simulations were initialized with analyses from 1200 UTC 7 January. Twelve hour forecasts were completed using identical model physics, except for the LMIC simulation which uses the full microphysics option. The LSFC and LMIC simulations are presented first to investigate the meteorology of the case study. Four other sensitivity simulations are presented next followed by results from a true operational forecast experiment.

4.2.1 LSFC simulation - RAMS initialized with LAPS

The LSFC simulation is initialized with the 10 km grid interval LAPS mass, wind, and moisture analyses. The separate LAPS surface analysis is also blended into the model initialization. A comparison of the low-level (146 m AGL) RAMS forecast winds with surface aviation observations (SAO, Fig. 4.15), FSL mesonet reports (Fig. 4.14), and LAPS surface analyses (Fig. 4.16) indicates that the model simulation developed the important mesoscale surface features. At 1500 UTC, the 3 h forecast shows westerly ridge top winds west of Denver have strengthened to 25 m s^{-1} while weak northeasterlies have developed along the Front Range, both of which compare favorably with the SAOs, mesonet observations, and LAPS objective analysis. Some minor differences are noted in the location and structure of the cyclonic surface circulation. The model indicates a stronger surge of westerly flow in southern Colorado than is indicated by the LAPS analysis. The discrepancies may be partially accounted for by the difference in elevation

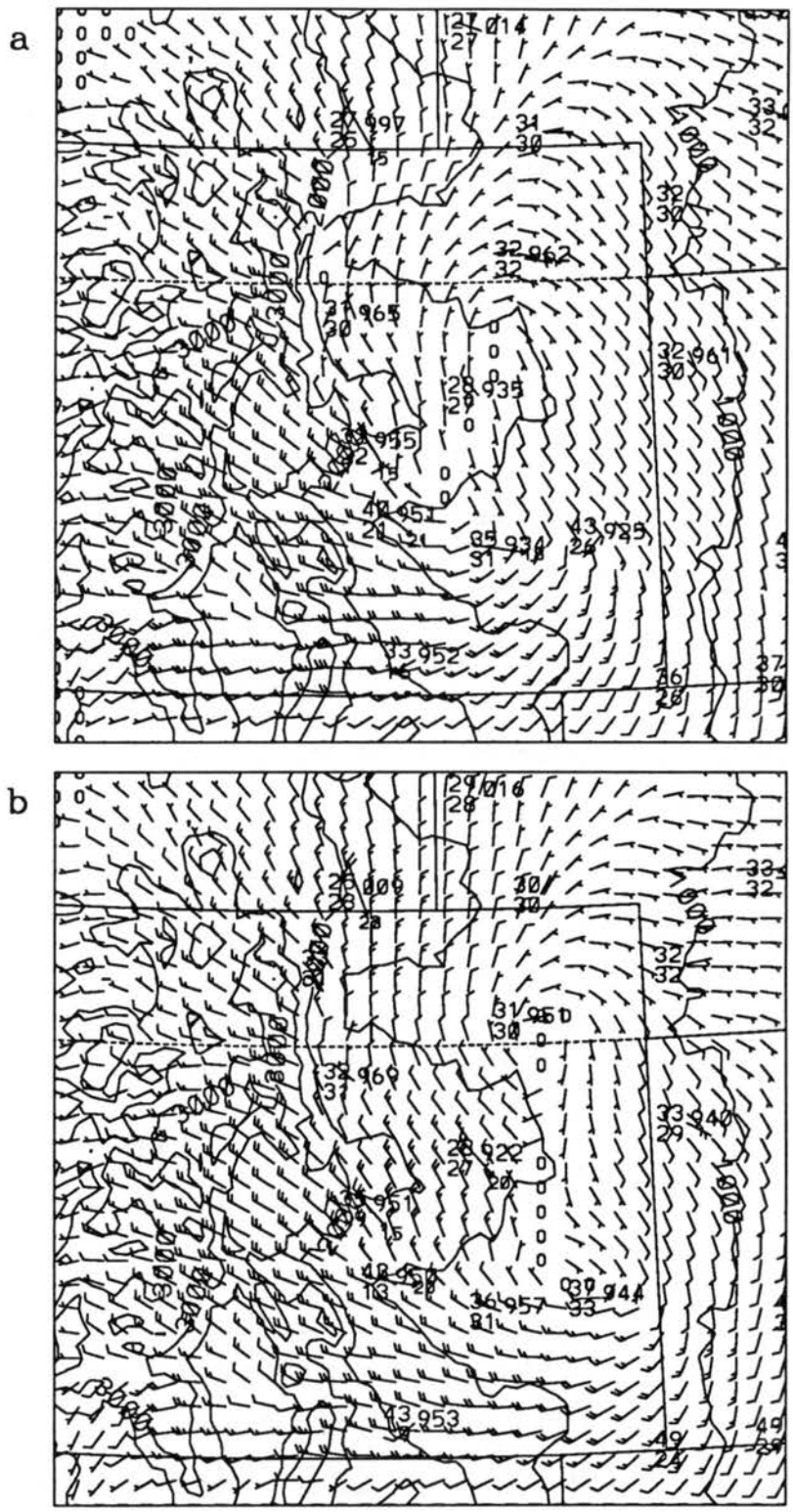

Figure 4.15: RAMS (LSFC) low-level (146 m AGL) wind (m s^{-1}) predictions and actual SAO reports at model validation time from (a) the 3 h forecast valid at 1500 UTC and (b) the 6 h forecast valid at 1800 UTC 7 January 1992. Solid contours represent model topography. Wind barbs are displayed at every other grid point.

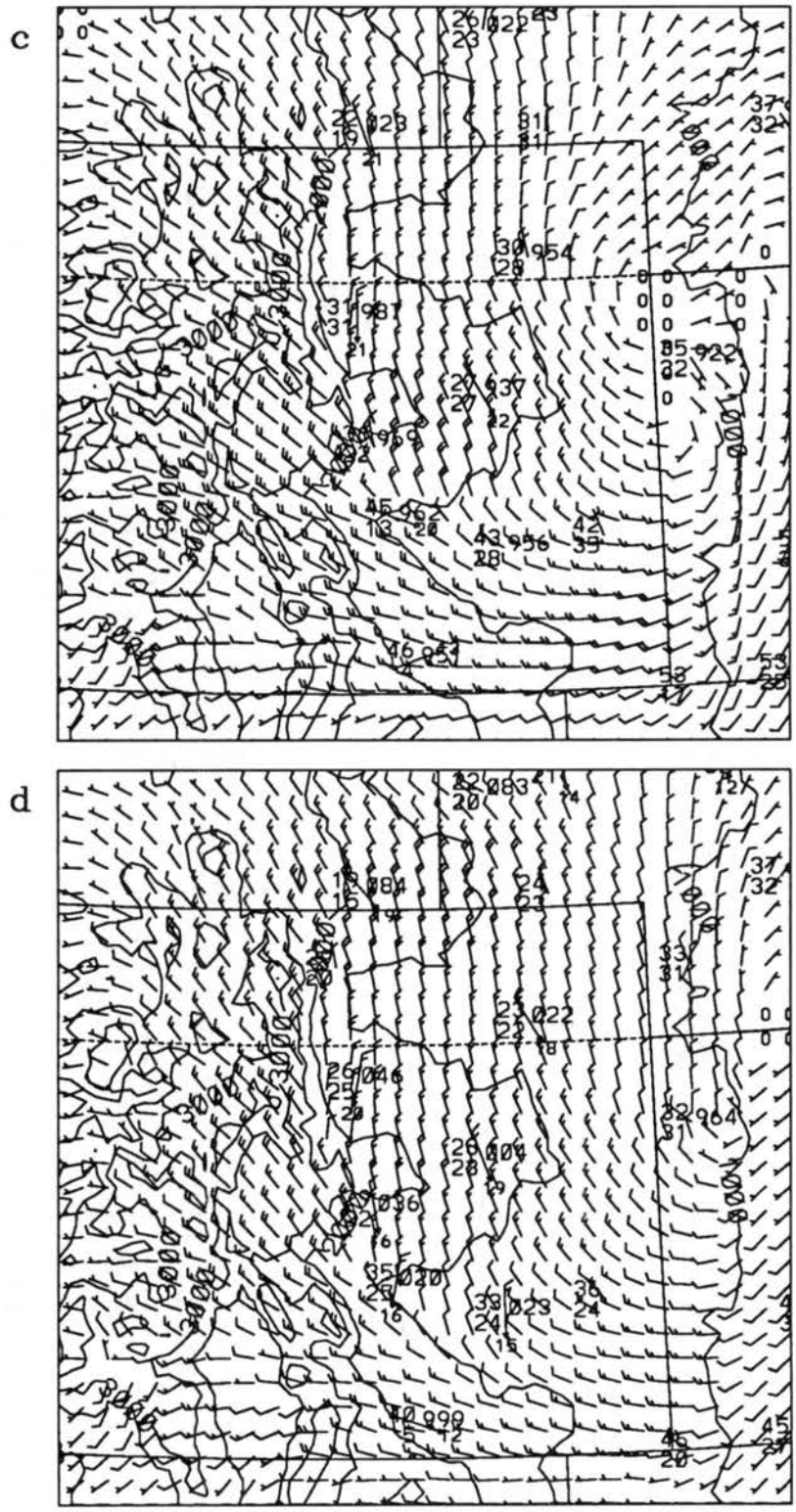

Figure 4.15: Continued: (c) the 9 h forecast valid at 2100 UTC 7 January and (d) the 12 h forecast valid at 0000 UTC 8 January 1992.

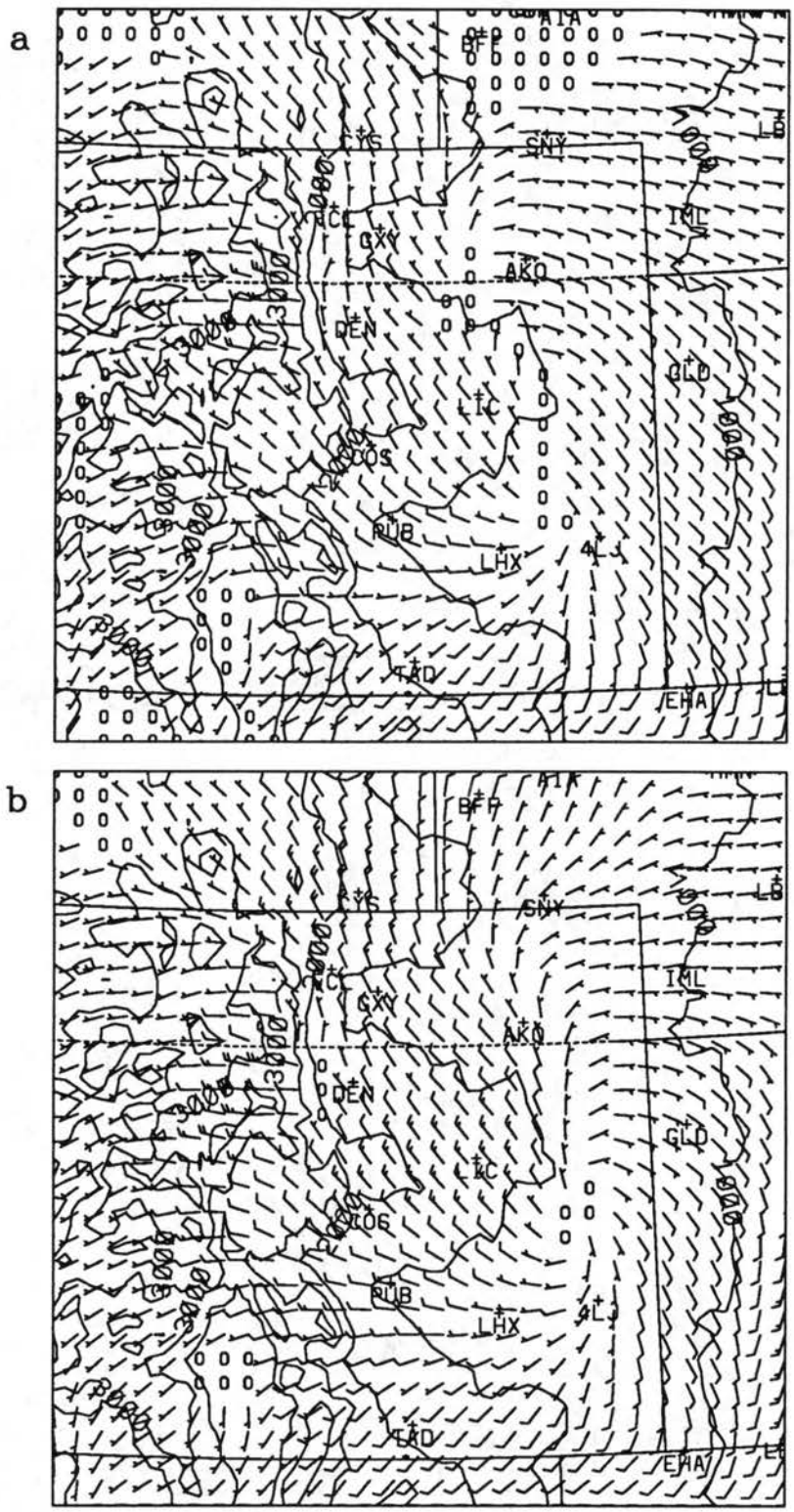

Figure 4.16: LAPS surface wind (m s^{-1}) analyses from (a) 1500 UTC and (b) 1800 UTC 7 January 1992. SAO locations east of the Continental Divide are indicated by standard 3-letter abbreviations. Wind barbs are displayed at every other model grid point.

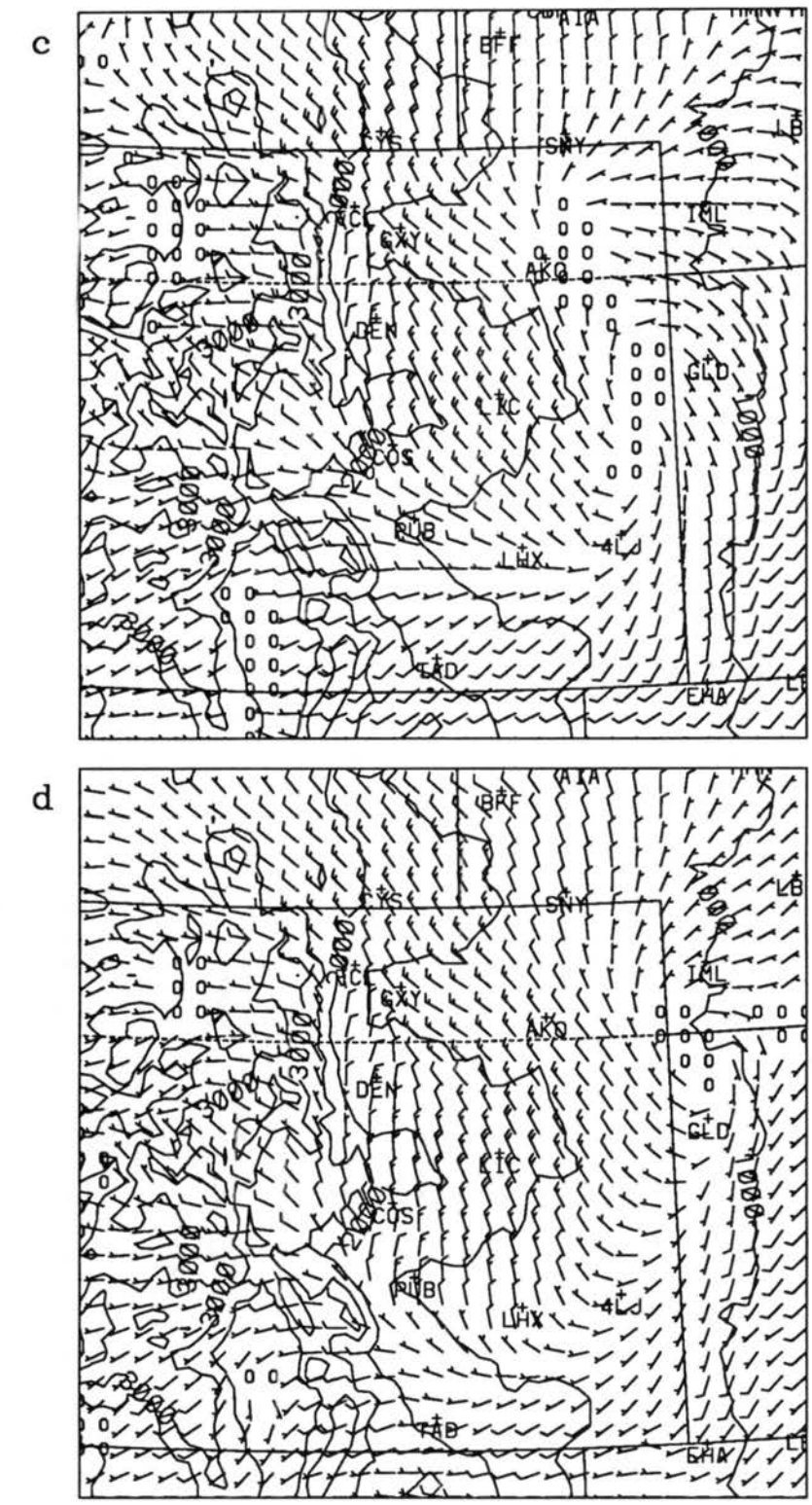

Figure 4.16: Continued: (c) 2100 UTC 7 January and (d) 0000 UTC 8 January 1992.

between the LAPS surface analysis (10 m AGL) and the RAMS forecast (146 m AGL) which can be expected to be greater in the morning prior to full mixing of the boundary layer.

The 6 h RAMS forecast (1800 UTC) shows continued strengthening of the westerly ridge top winds to 30 m s^{-1} and an area of weak northeasterly flow north and west of Denver, consistent with observations. Over the Eastern Plains, the LAPS analysis depicts the surface cyclone as a north-south elongated shear line extending from east of Akron (AKO) southward to west of Lamar (4LJ). A similar looking shear line is predicted by RAMS and is located approximately 10 km west of the LAPS analyzed shear line. It is difficult to ascertain the exact location and structure of the shear line due to the sparsity of data in this region. However, both the RAMS forecast and LAPS analysis show close agreement to the available observations. Two regions of strong winds are observed in LAPS and forecasted by RAMS, northerlies over the Cheyenne Ridge and northwesterlies over the Palmer Lake Divide west of Limon (LIC). The model continues to predict strong westerly flow south of the surface cyclone.

RAMS continues to forecast strong westerly ridge top winds at 2100 UTC with a slight decrease in magnitude to 25 m s^{-1}. RAMS winds adjacent to the Front Range are northerly and do not indicate as much of an eastward component as observed at several of the mesonet stations. High winds ($\sim$20 m s^{-1}) in RAMS continue over the Cheyenne Ridge and the Palmer Lake Divide that compare favorably with LAPS analyses and observations. The structure of the surface cyclone, located near the Colorado-Kansas border, is similar in both RAMS and LAPS, however, the RAMS forecast position is about 20 to 30 km east of the LAPS position. Again, the exact location of the low is difficult to ascertain due to the sparsity of data in this region.

RAMS 12 h forecast winds at 0000 UTC indicate a backing and weakening of the winds over ridge top while north-northeast winds are predicted in the Denver area. Strong north-northwest flow is forecast west of the surface cyclone. The center of the RAMS cyclonic circulation is located near the model boundary along the Nebraska-Kansas border and is located approximately 50 km east of the LAPS position.

The RAMS forecasts have developed the essential surface mesoscale features of this system. Persistent strong downslope flow east of the barrier crest is predicted. The development of northwesterly flow over the Cheyenne Ridge and northeasterly flow adjacent to the Front Range is consistent with observations and appears to have the general characteristics of a Longmont anticyclone (Young and Johnson 1984). The model successfully forecast the development of strong north-northwest flow over the Eastern Plains that created the severe blizzard conditions in this region.

Upper air features of the cyclone also appear to be well predicted by the model simulation. The RAMS upper air forecasts are interpolated from the model σ_z surfaces to isobaric surfaces for comparison to MAPS upper air analyses. Wind and moisture fields are interpolated linearly with height while the mass field is interpolated linearly with ln p. Since a single isobaric surface may transect several σ_z surfaces, especially over the mountains, the resulting isobaric analyses contain some noise. Hence, a 13 point smoother is applied to the height fields primarily for aesthetic reasons.

The 500 mb RAMS height and wind forecasts (Fig. 4.17) show reasonably close agreement with the respective 500 mb MAPS analyses (Fig. 4.18). The 3 h RAMS forecast valid at 1500 UTC shows a 5406 m closed low located east of Pueblo (PUB) which is about 30 m higher and 100 km west of the MAPS low located west of Lamar (4LJ). As expected from a prediction using a 10 km grid increment, significantly more mesoscale information is offered by RAMS. However, it is very difficult to validate this information given the sparsity of upper air observations and the coarser 60 km grid increment MAPS analyses. This difficulty is present for all upper air comparisons and the ramifications will be discussed further in the objective model validation section.

The magnitudes of the 500 mb low in the RAMS prediction and MAPS analysis are equal at 1800 UTC with the forecast position located about 100 km southwest of the MAPS analyzed location. A similar progression of the 500 mb low to the Nebraska-Kansas border by 0000 UTC is observed in the RAMS predictions and the MAPS analyses. The RAMS forecasts appear to have correctly predicted the general characteristics of the 500 mb flow, however, it is difficult to ascertain if RAMS has correctly provided any additional mesoscale information.

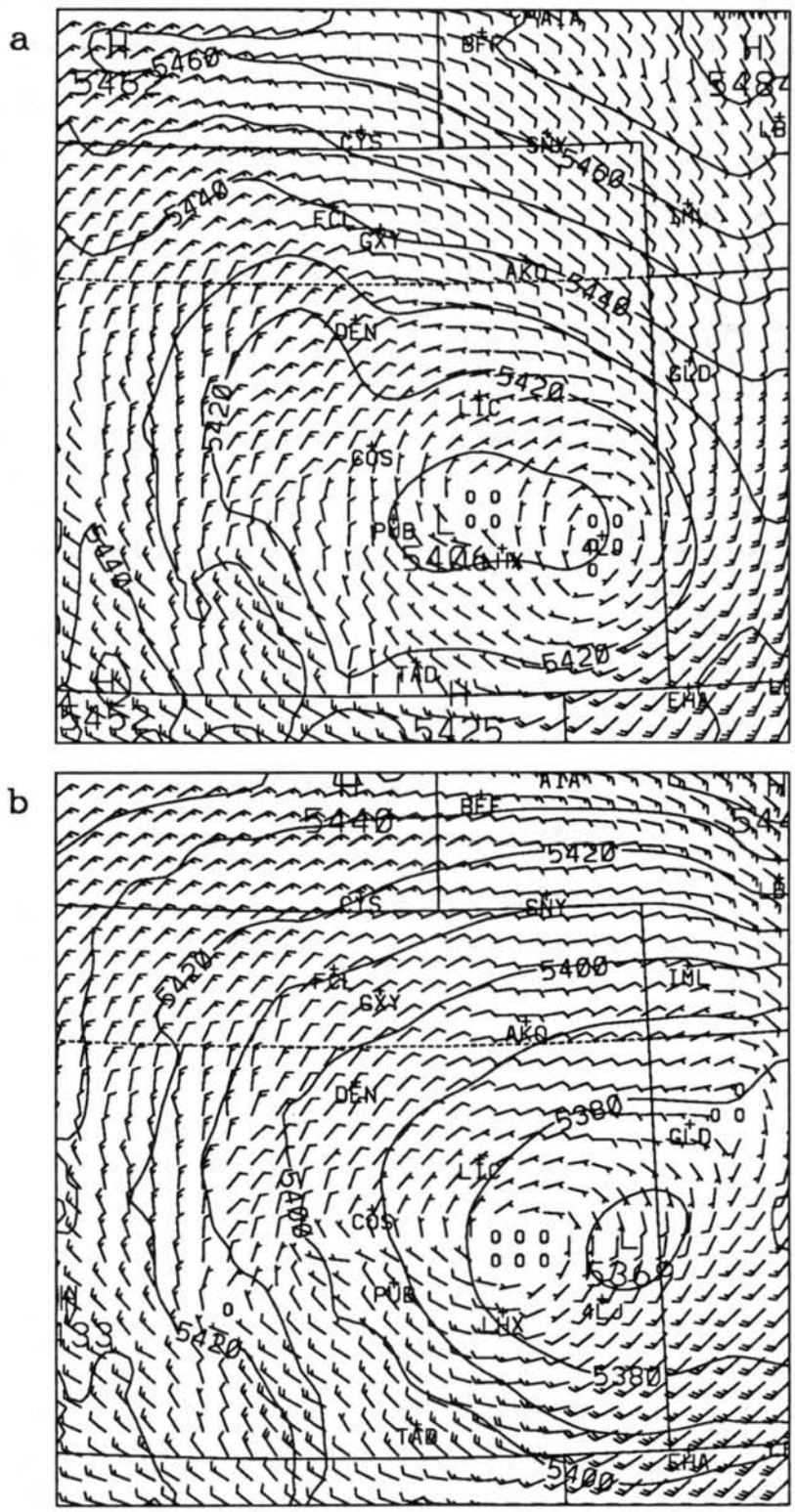

Figure 4.17: RAMS (LSFC) 500 mb height (m) and wind (m s^{-1}) predictions from (a) the 3 h forecast valid at 1500 UTC and (b) the 6 h forecast valid at 1800 UTC 7 January 1992.

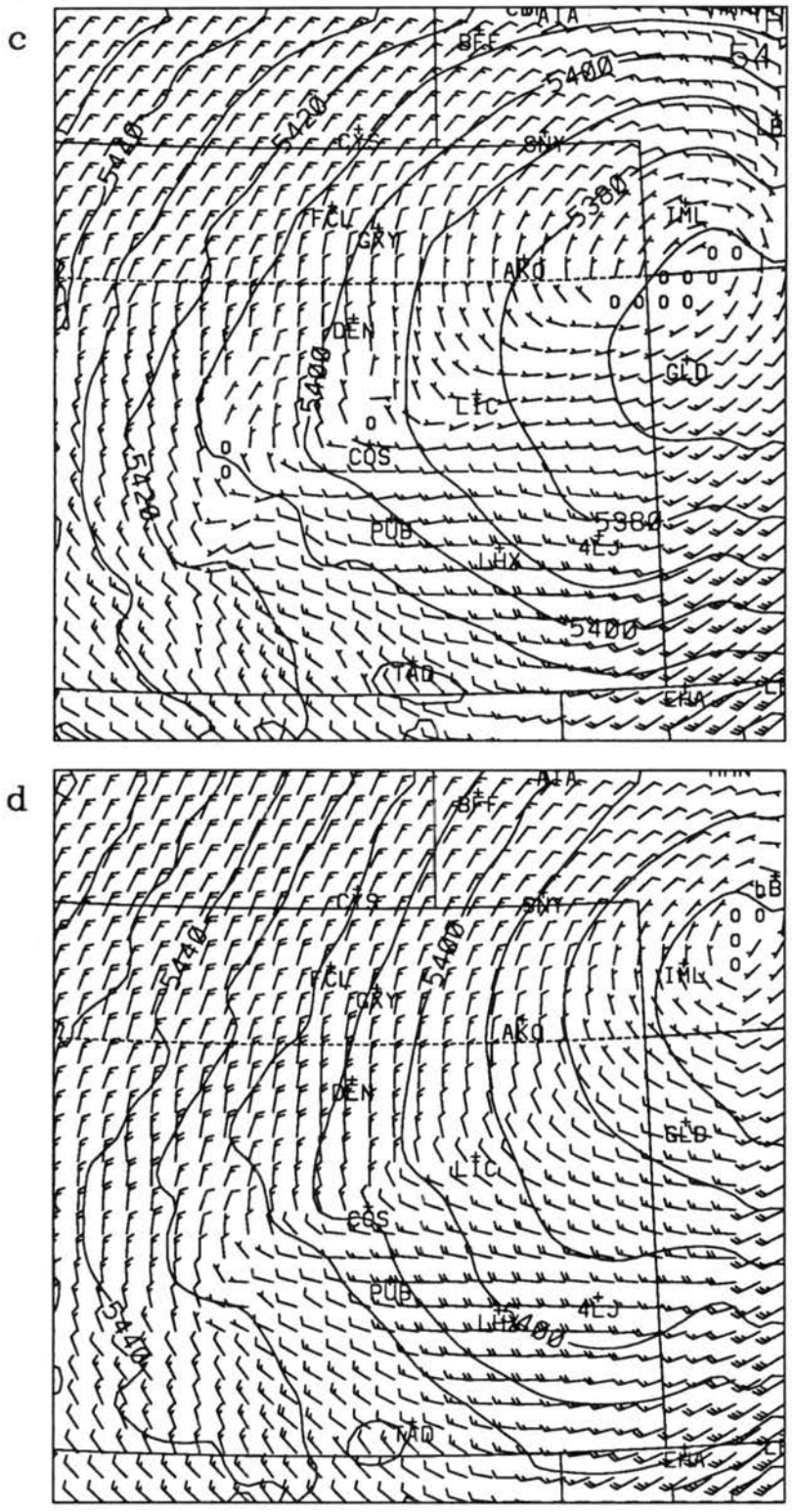

Figure 4.17: Continued: (c) the 9 h forecast valid at 2100 UTC 7 January and (d) the 12 h forecast valid at 0000 UTC 8 January 1992.

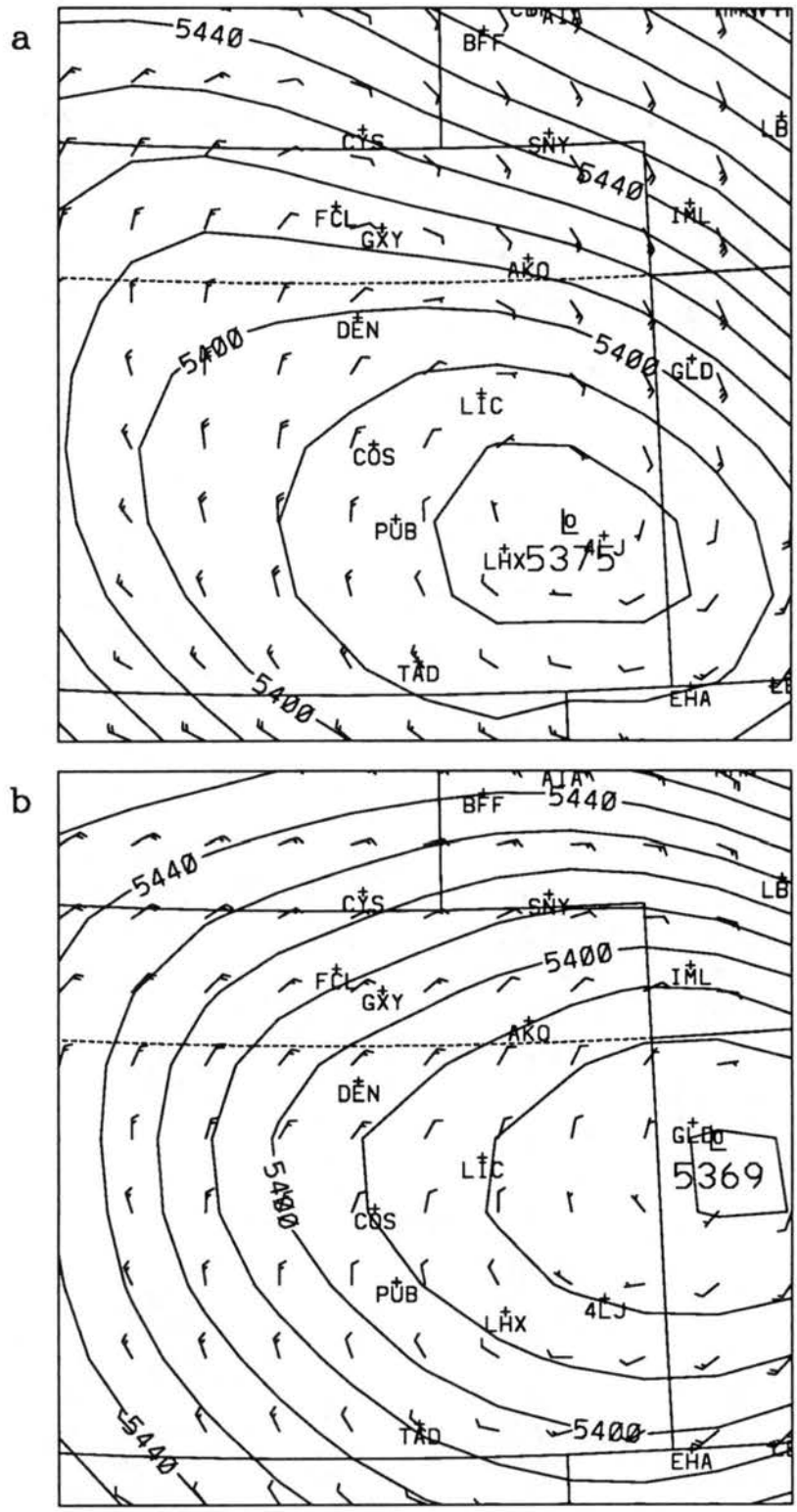

Figure 4.18: MAPS 500 mb height (m) and wind (m s^{-1}) analyses from (a) 1500 UTC and (b) 1800 UTC 7 January 1992.

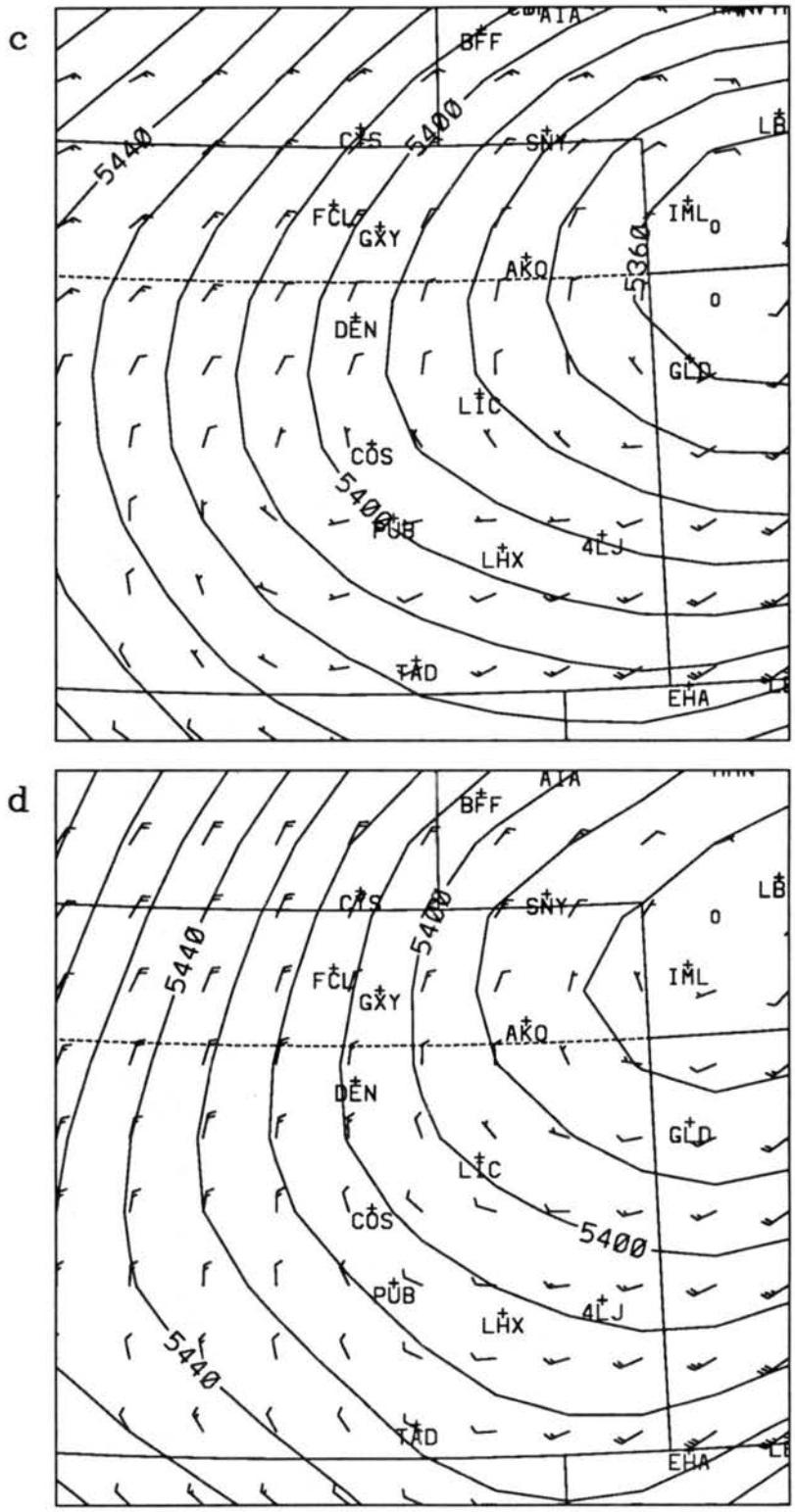

Figure 4.18: Continued: (c) 2100 UTC 7 January and (d) 0000 UTC 8 January 1992.

The Platteville wind profiler was the sole instrument available during this case that provided high temporal resolution upper air observations (Fig. 4.13). Comparing a time series of RAMS upper air wind forecasts from the nearest model grid point to Platteville (Fig. 4.19) with the wind profiler observations provides a glimpse of the mesoscale accuracy of the RAMS upper air predictions. The RAMS predictions clearly define the three

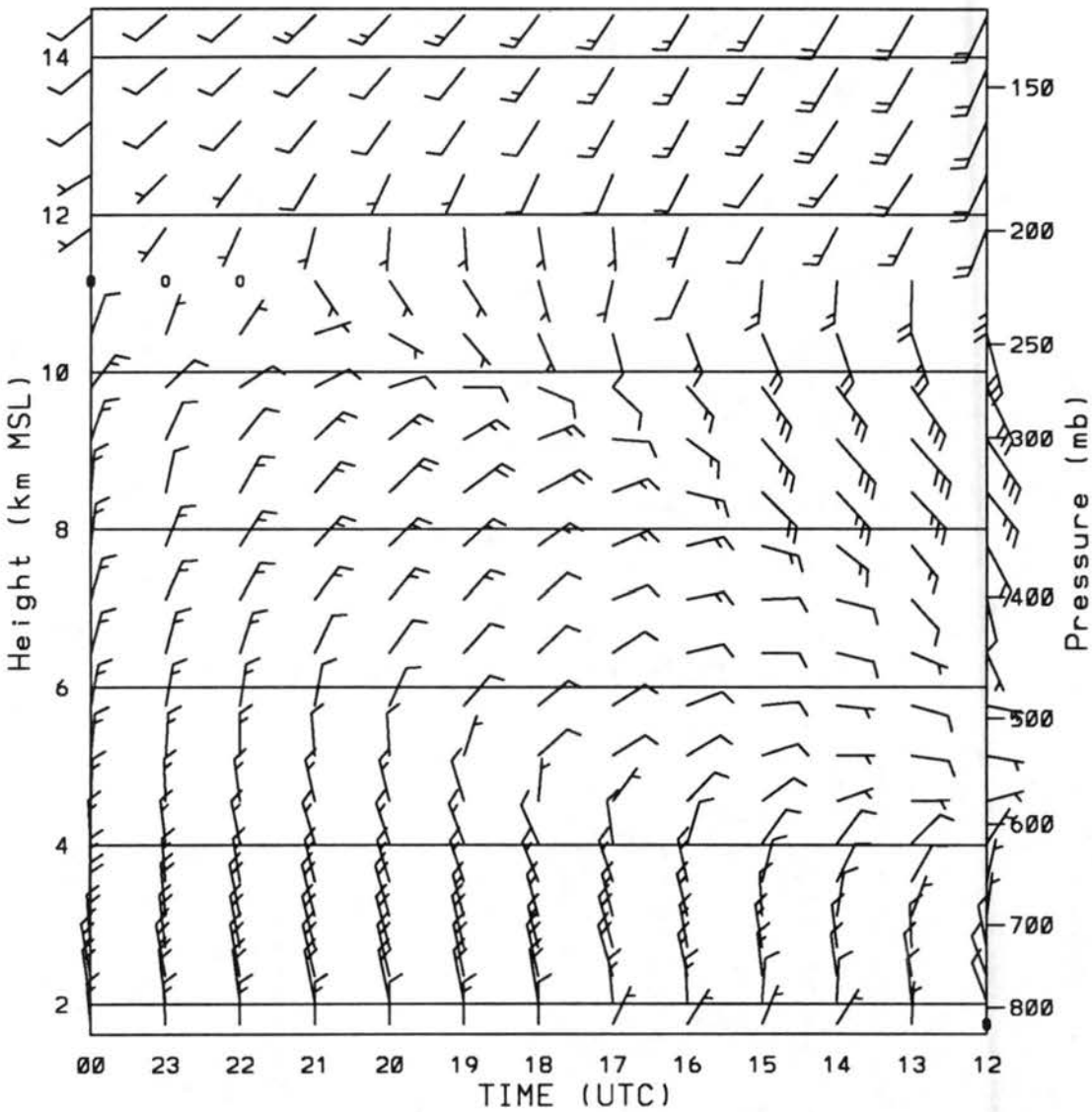

Figure 4.19: Time-height series of RAMS (LSFC) forecast wind (m s^{-1}) for the model grid point closest to Platteville, CO from the 0 to 12 h prediction valid at 1200 UTC 7 January through 0000 UTC 8 January 1992.

distinct flow regimes in the vertical observed by the Platteville wind profiler. The temporal evolution of the low layer northerlies as they expand upward and of the mid-layer

easterlies backing to northerly is well forecast by RAMS. The depth of the flow regimes and the interfaces between each regime (e.g. the weaker winds near 11 km from 2100 to 0000 UTC) is very realistic. The lowest level winds (below the first available gate in the wind profiler) from 1300 to 1700 UTC depict the northeasterly flow associated with the Longmont anticyclone regime which suggests the shallowness of this feature. FSL mesonet observations (Fig. 4.14) and a RAMS forecast wind time series from Denver (Fig. 4.20) suggest that the low-level northeasterlies progressed southward with time which may be correlated to the strengthening of the northwest flow over the Cheyenne Ridge. The Denver time series also indicates the development of a low-level north-northwest jet with a maximum speed of 25 m s^{-1} at 2000 UTC near 650 mb which is observed in the Doppler velocity data (not shown).

A band of moisture wrapping around the cyclone and moving into the Front Range from the northeast is indicated by the RAMS forecasts. Fig. 4.21 shows RAMS predictions of the highest total (vapor and liquid) mixing ratio in the model column. The 3 h forecast (valid at 1500 UTC) shows a mixing ratio maximum of 6 g kg^{-1} over northeast Colorado. The maxima progresses westward to northcentral Colorado by 6 h (1800 UTC), southward across Greeley (GXY) and Denver (DEN) at 9 h (2100 UTC) and further south to near Colorado Springs (COS) by 12 h (0000 UTC). The band of moisture appears to be well correlated with the observed snowfall over the Eastern Plains. However, much of the heavy snow observed from Ft. Collins to Denver fell prior to the arrival of greatest moisture.

Although the moisture adjacent to the Front Range may have been initially limited, the observed heavy snow band appears to be well correlated with a region of significant upward vertical motion. RAMS forecasts of maximum vertical motion (Fig. 4.22) indicate a persistent north-south band of upward vertical motion to exist from Ft. Collins (FCL) to south of Denver (DEN). The 3 h forecast (1500 UTC) shows the band to exceed 0.5 m s^{-1} and strengthens to greater than 0.75 m s^{-1} by 6 h (1800 UTC). The maximum upward vertical motion band moves southward by 9 h (2100 UTC) and is primarily south of Denver at 12 h (0000 UTC). The location and movement of the predicted band of upward vertical motion is well correlated with the Doppler radar reflectivity (Fig. 4.12).

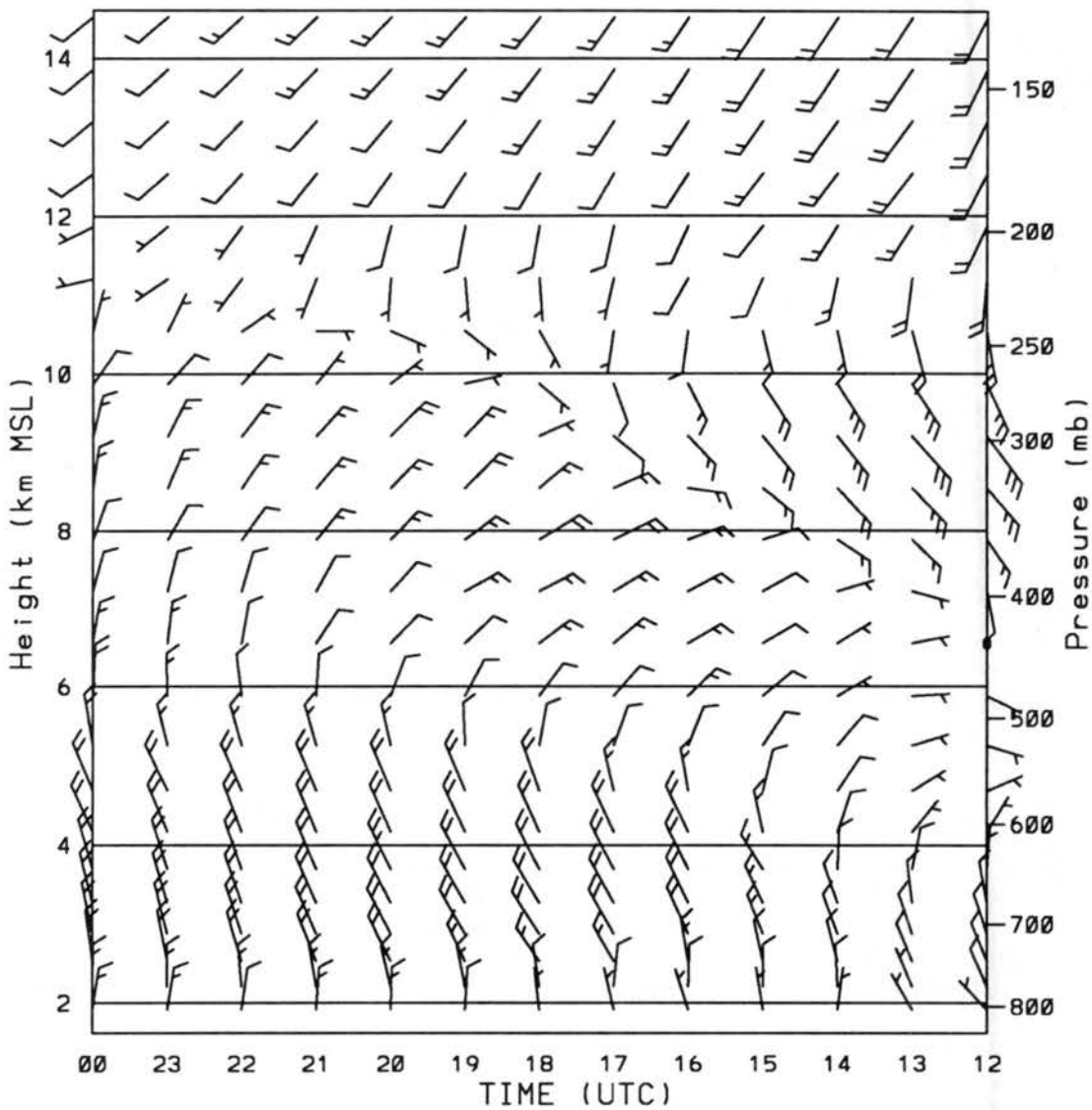

Figure 4.20: Time-height series of RAMS (LSFC) forecast wind (m s^{-1}) for the model grid point closest to Denver, CO from the 0 to 12 h prediction valid at 1200 UTC 7 January through 0000 UTC 8 January 1992.

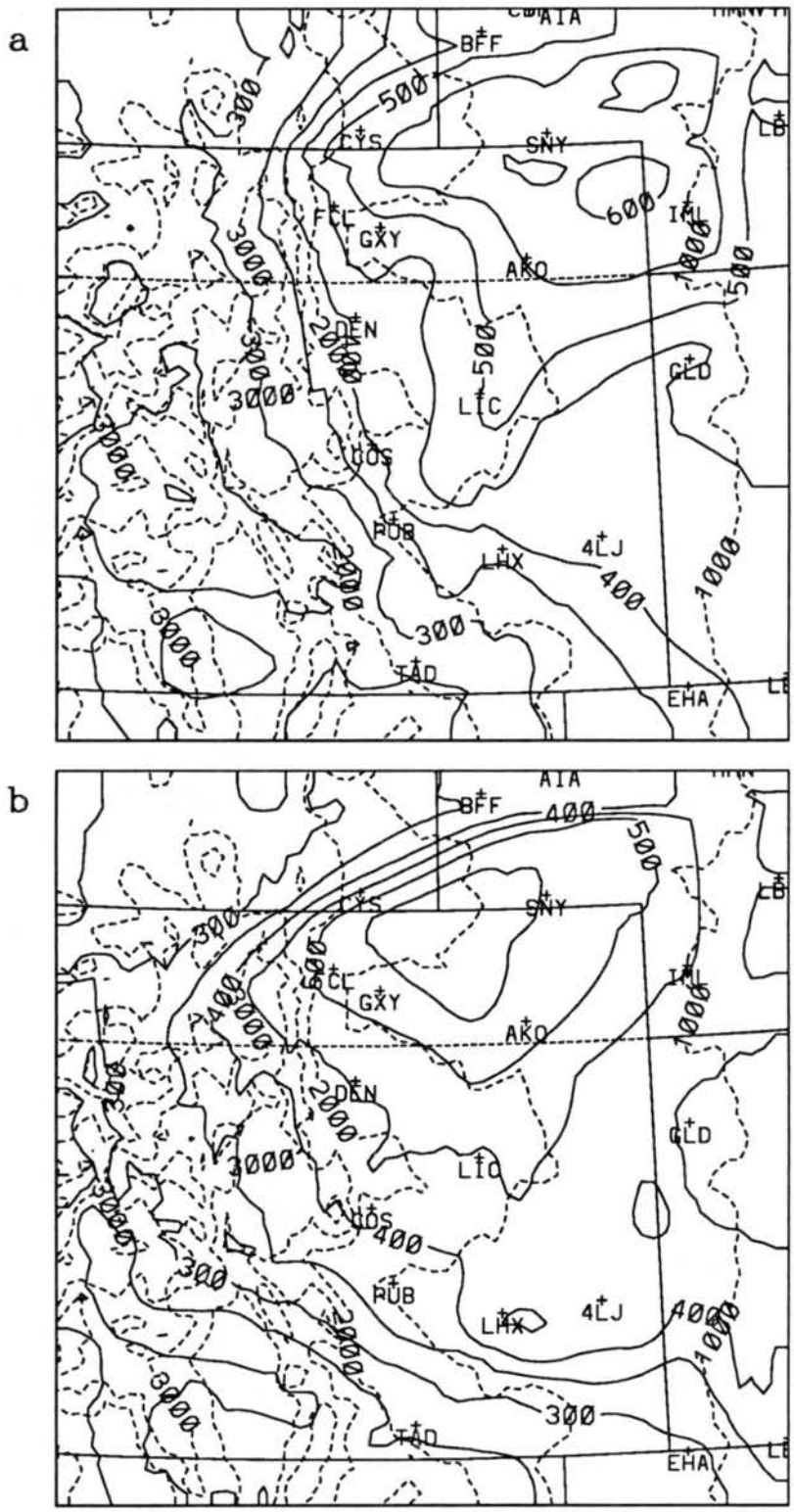

Figure 4.21: RAMS (LSFC) maximum total (vapor and liquid) mixing ratio (g kg^{-1}) predictions from (a) the 3 h forecast valid at 1500 UTC and (b) the 6 h forecast valid at 1800 UTC 7 January 1992. Contour interval is 0.5 g kg^{-1} and 100 units = 1.0 g kg^{-1}.

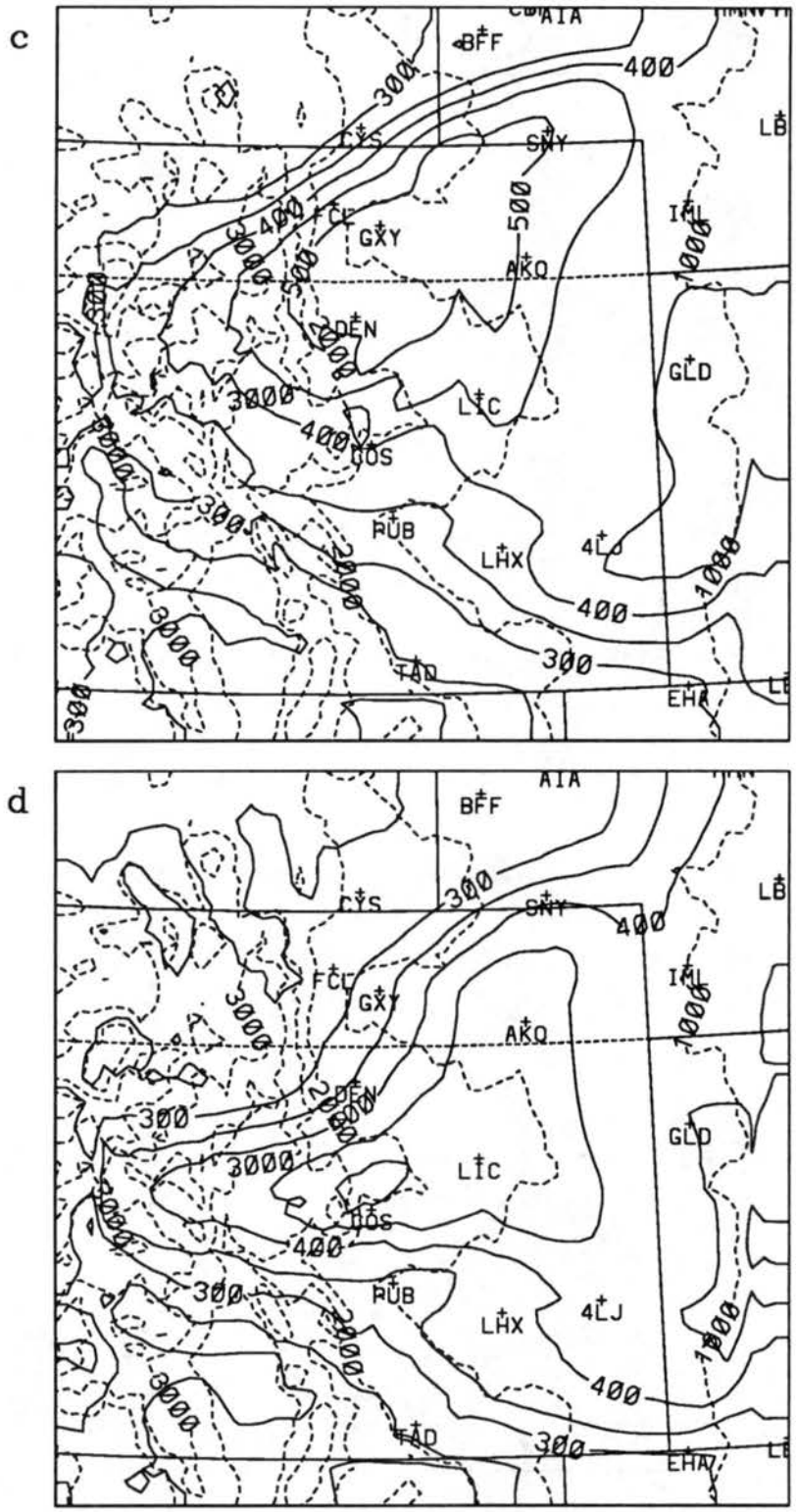

Figure 4.21: Continued: (c) 2100 UTC 7 January and (d) 0000 UTC 8 January 1992.

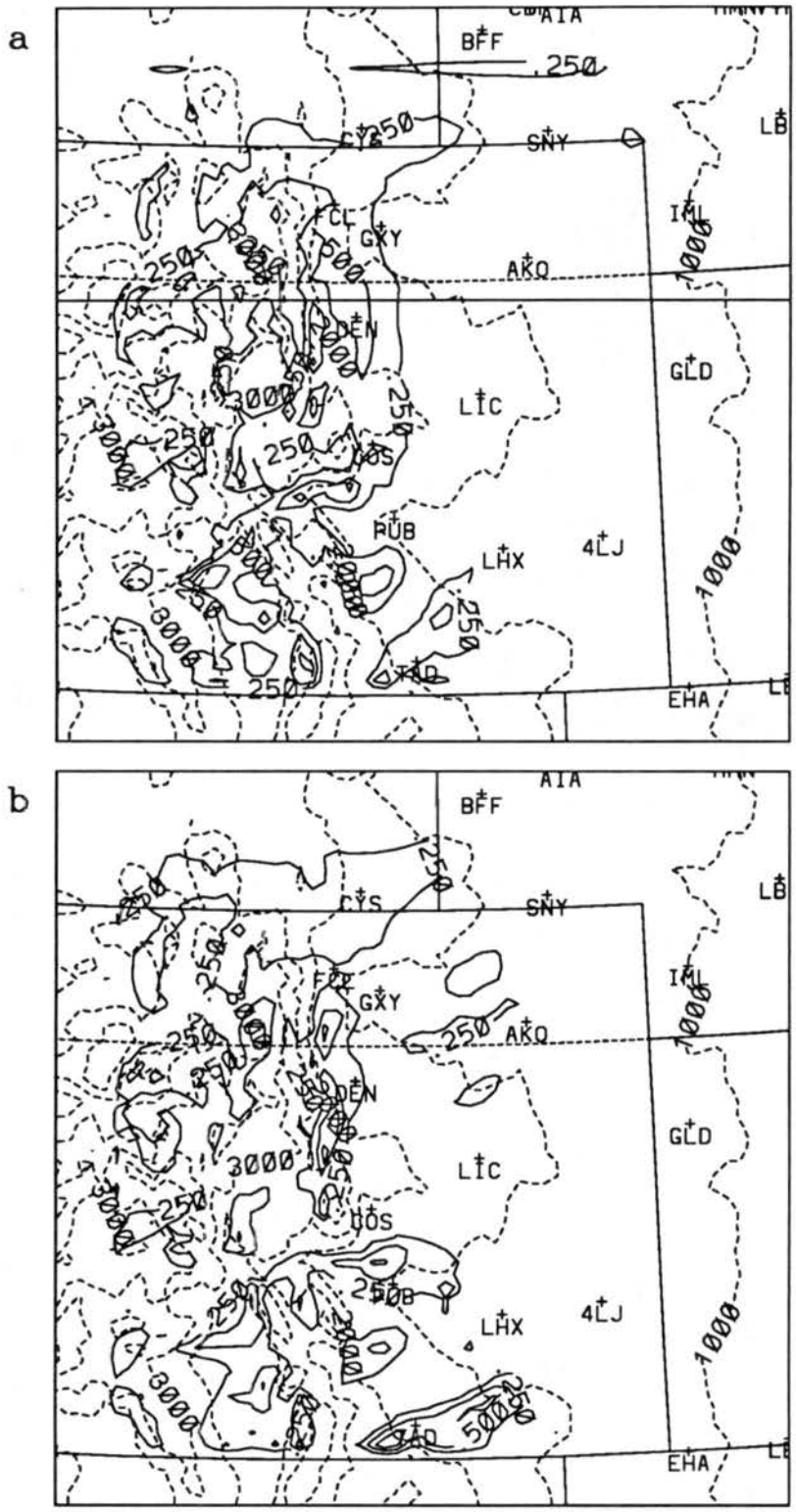

Figure 4.22: RAMS (LSFC) maximum upward vertical motion (m s^{-1}) predictions from (a) the 3 h forecast valid at 1500 UTC and (b) the 6 h forecast valid at 1800 UTC 7 January 1992. Contour interval is 0.25 m s^{-1}.

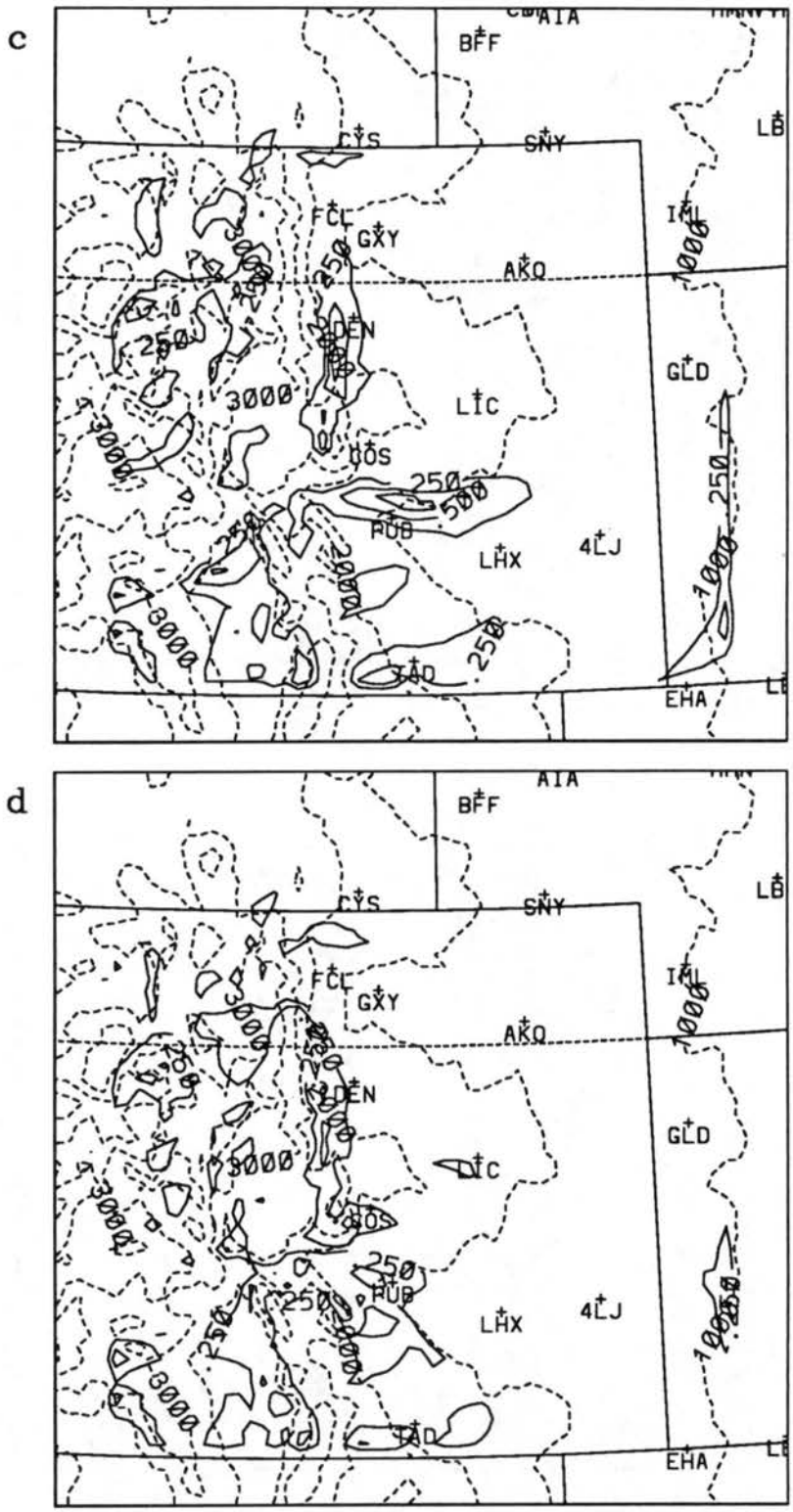

Figure 4.22: Continued: (c) 2100 UTC 7 January and (d) 0000 UTC 8 January 1992.

A three-dimensional view of the moisture and vertical velocity shows the band of moisture to be a low to mid-tropospheric feature ($\sim$ 700-600 mb) that is sloped from northeast to southwest while the band of upward vertical motion appears to be closely associated with the development of a lee mountain wave east of the Continental Divide. A representative sample of vertical cross sections illustrates these features. A west-east vertical cross section (located just north of Denver, see Fig. 4.22a) of RAMS forecast potential temperature at 3 h (Fig. 4.23a) indicates a weakly developed lee mountain wave east of the barrier. The mountain wave appears to be confined to the lower troposphere, within in a layer of relatively stable air below 6 km. A layer of less stable air is indicated above 6 km, resulting in a static stability profile that decreases with height. This type of two layer atmospheric configuration supports the generation of a trapped lee wave system (Scorer 1949). Hence, the development and maintenance of the mountain wave is likely due to the trapped lee wave process.

Downward vertical motion exceeding 1.0 m s^{-1} is indicated in the western portion of the lee wave (Fig. 4.23b). A double maximum of upward vertical motion is predicted with a 0.5 m s^{-1} center located at 4 km in the eastern portion of the lee wave. The second maxima (0.6 m s^{-1}) is located higher at 5 km and appears to be the result of easterly flow (Fig. 4.23c) rising up and over the lee wave. This is consistent with the mid-layer easterly flow observed at 1500 UTC by the Platteville wind profiler (Fig. 4.13). Total mixing ratio suggests a band of moisture rising from east to west in association with the easterly flow (Fig. 4.23d).

The 6 h RAMS predictions indicate amplification of the lee mountain wave with potentially warmer air progressing down the barrier creating a baroclinic zone adjacent to the Front Range (Fig. 4.24a), consistent with temperature observations by the FSL mesonet (Fig. 4.14). Downward vertical motion associated with the mountain wave has progressed down to the base of the barrier (Fig. 4.24b). A double upward vertical motion maximum continues to be predicted, but the lower maxima near 3 km (0.45 m s^{-1}) is now stronger than the upper maxima near 5 km (0.2 m s^{-1}). Model predicted u-component flow (Fig. 4.24c) shows the westerly component wind to extend further out onto the Plains

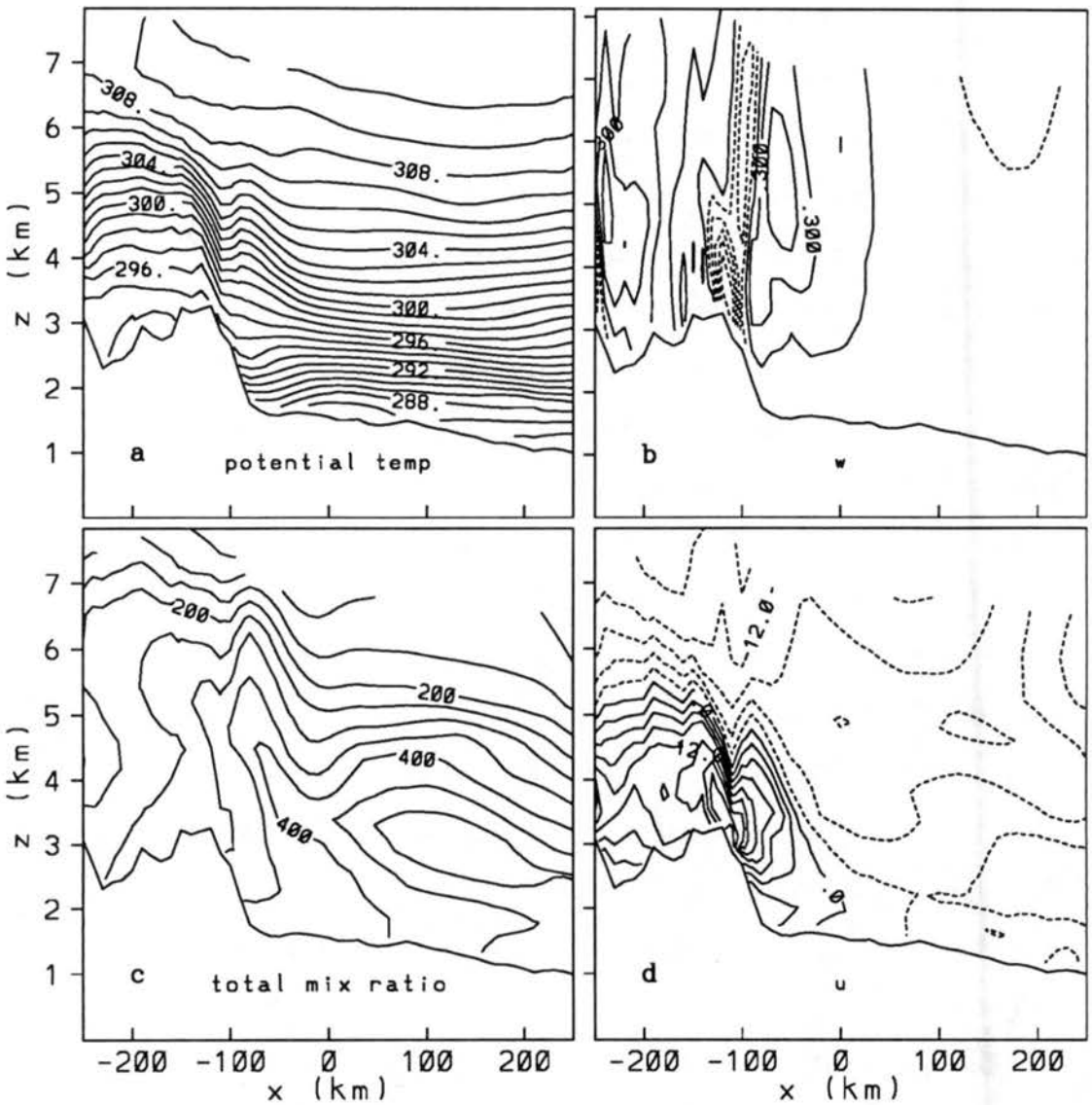

Figure 4.23: West-east vertical cross sections from RAMS (LSFC) 3 h forecast valid at 1500 UTC 7 January 1992 of (a) potential temperature (K), (b) upward vertical motion (m s^{-1}, contour interval = 0.2 m s^{-1}), (c) total mixing ratio (g kg^{-1}, contour interval = 0.5 g kg^{-1}, 100 units = 1.0 g kg^{-1}), and (d) u-component wind (m s^{-1}, contour interval = 3.0 m s^{-1}). Cross section location is represented by the solid line in Fig. 4.22a.

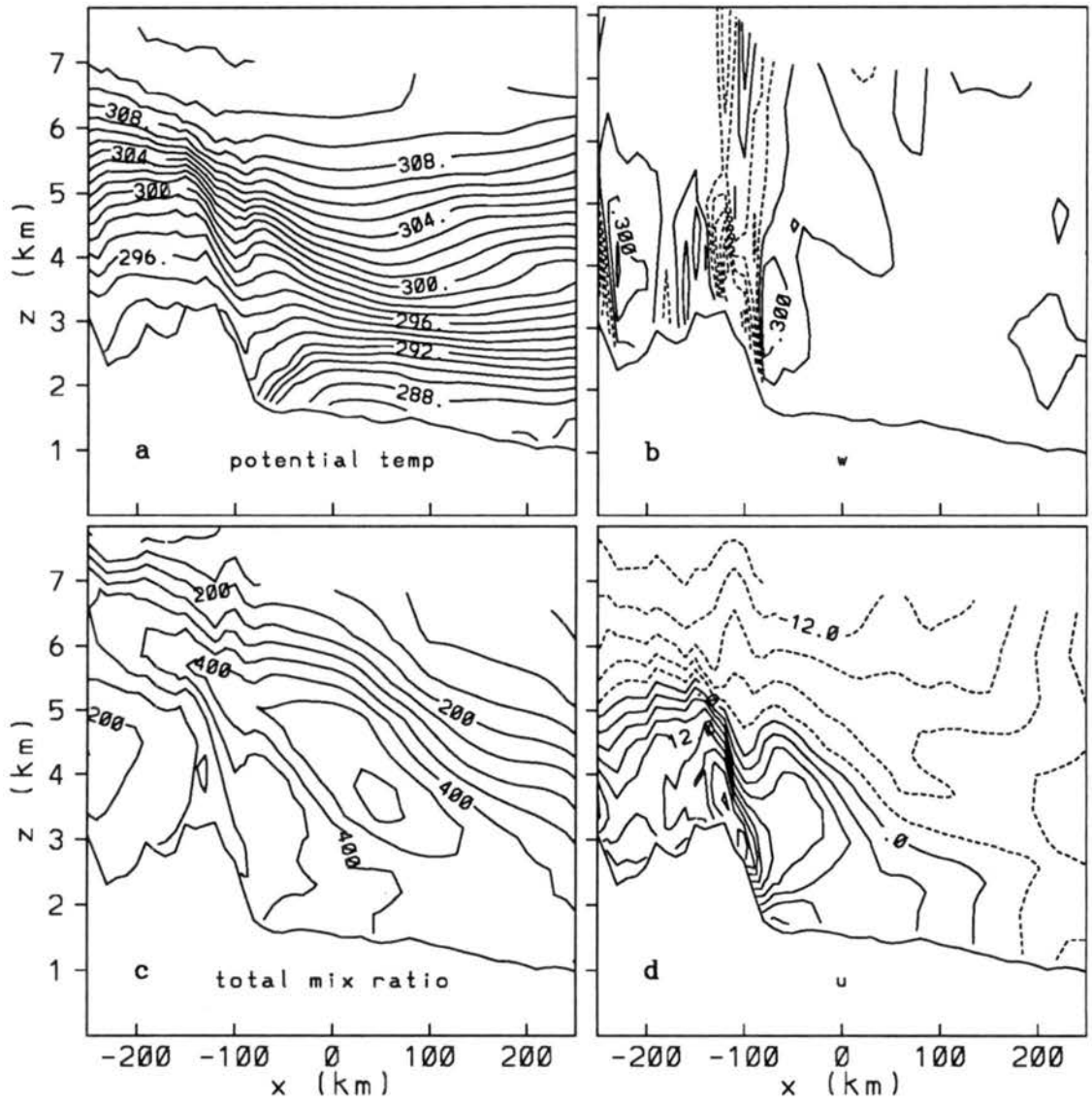

Figure 4.24: As in Fig. 4.23 except for 6 h forecast valid at 1800 UTC 7 January 1992.

at this time and to be greater in depth adjacent to the Front Range. The result is weaker easterly component flow rising over the mountain wave and hence weaker upward vertical motion at 5 km. These predictions are consistent with the observed Platteville profiler winds between 4 and 6 km that backed from east to northeast between 1500 and 1800 UTC (Fig. 4.13). The predicted total mixing ratio (Fig. 4.24d) continues to show relatively moist air rising above the mountain wave from the east and low-level drying is suggested east of the barrier in conjunction with the downward motion.

The lee mountain wave continues to be evident in the 9 h predicted potential temperature field with a further enhancement of the baroclinic zone adjacent to the Front Range (Fig. 4.25a). Downward vertical motion remains in the western portion of the lee wave while upward vertical motion (0.45 m s^{-1} near 3 km) is only depicted within the eastern region of the wave (Fig. 4.23b). A westerly component to the flow occupies nearly the entire cross section below 5 km (Fig. 4.25c), consistent with the Platteville profiler observations (Fig. 4.13). Easterly component flow forecast above 5 km appears to be too high to be forced upward by the mountain wave, hence, the second, higher upward vertical motion maxima is no longer evident. The development of a significant northerly component jet core (20 m s^{-1}) is depicted adjacent to the Front Range (Fig. 4.25d) in association with the baroclinic zone observed in the potential temperature field.

The lee wave amplitude appears to have decreased in the 12 h forecast of potential temperature, while the baroclinic zone adjacent to the Front Range remains in place (Fig. 4.26a). The downward/upward vertical motion couplet is depicted within the lee wave (Fig. 4.26b). Strong westerly component flow continues in the lee of the barrier except for a small area of easterly component adjacent to the barrier (Fig. 4.26c), consistent with the northeasterly surface observations in the FSL mesonet. The combination of surface northeasterly and northwesterly component flow surrounding a cold dome and strong northerly low-level flow impinging on the Palmer Divide (Fig. 4.24d) suggests that blocking by the Palmer Divide is occurring. Divergence of the surface flow observed by the southern stations in the FSL mesonet at 2100 and 0000 UTC (Fig. 4.14) and a wind shift from northwesterly to northerly at Colorado Springs (COS) between 2000 and 2100 UTC

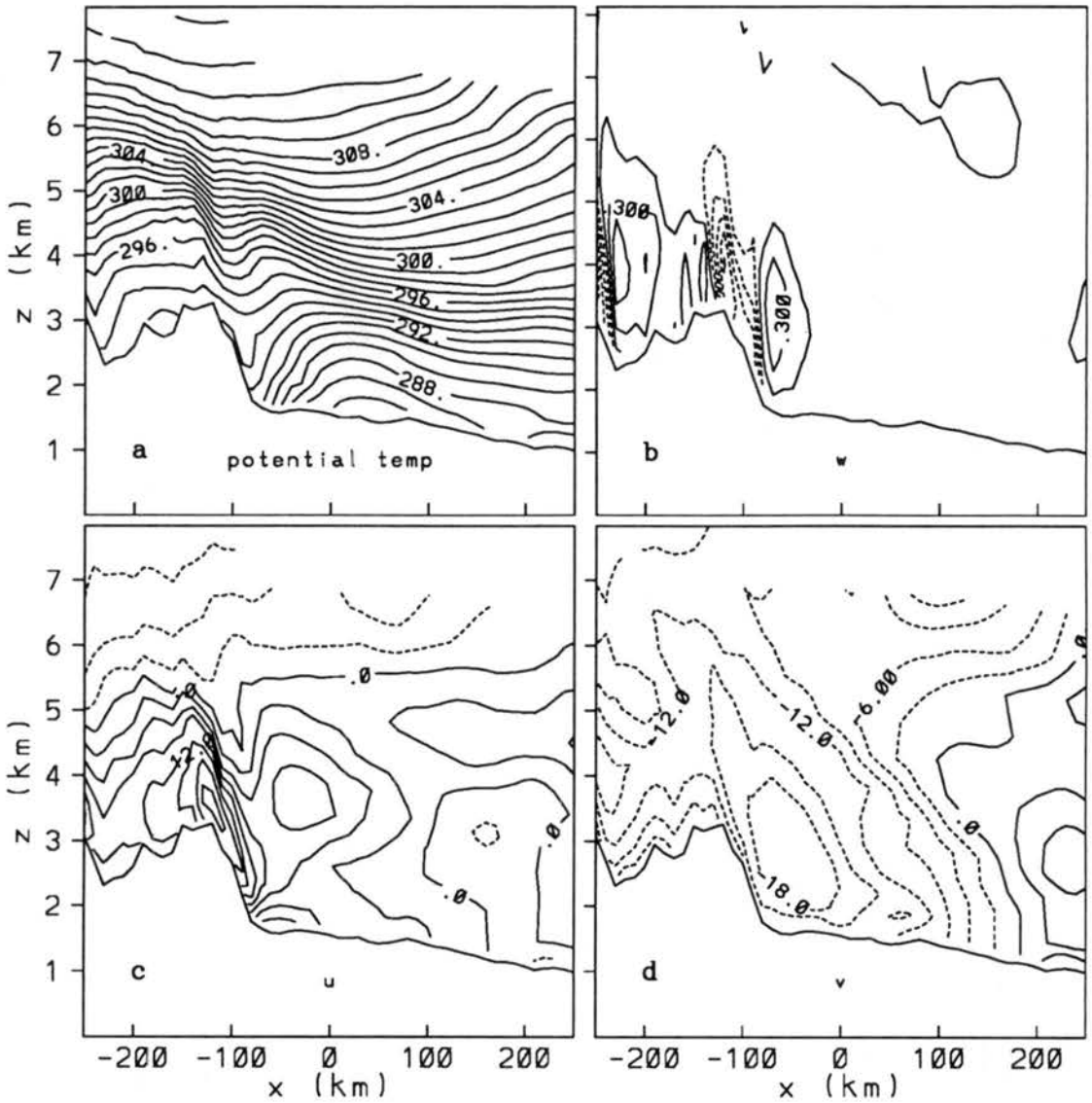

Figure 4.25: West-east vertical cross sections from RAMS (LSFC) 9 h forecast valid at 2100 UTC 7 January 1992 of (a) potential temperature (K), (b) upward vertical motion (m s^{-1}, contour interval = 0.2 m s^{-1}), (c) u-component wind (m s^{-1}, contour interval = 3.0 m s^{-1}), and (d) v-component wind (m s^{-1}, contour interval = 3.0 m s^{-1}). Cross section location is represented by the solid line in Fig. 4.22a.

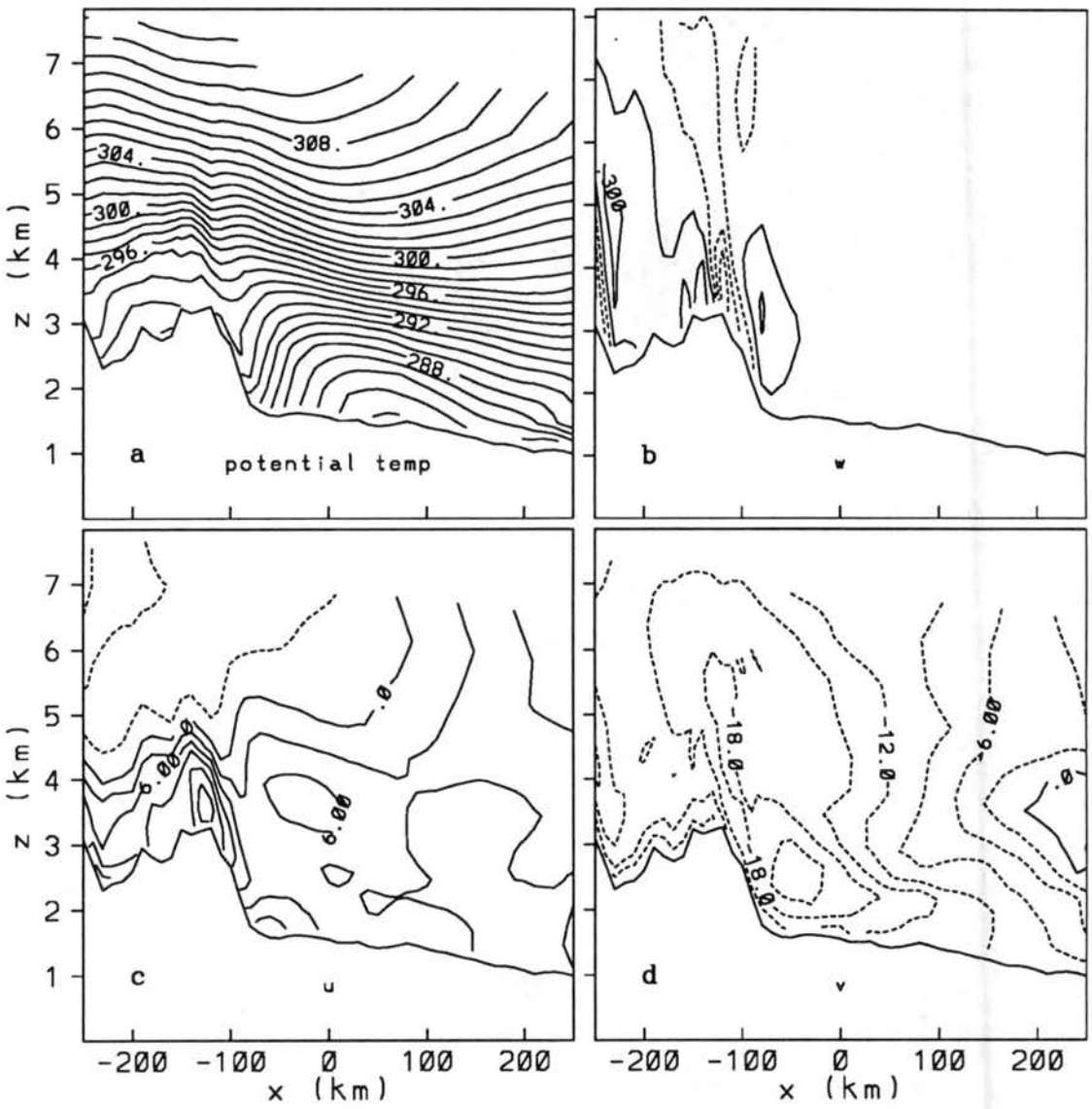

Figure 4.26: As in Fig. 4.25 except for 12 h forecast valid at 0000 UTC 8 January 1992.

(Fig. 4.3) are further indications that blocking may be occurring north of the Palmer Divide.

4.2.2 LMIC simulation - a full microphysics prediction

The LSFC simulation provides a mesoscale representation of the mass, wind, and moisture structure of the 7 January 1992 blizzard. With the addition of liquid and ice phase microphysics to the LSFC simulation, precipitation processes and their effects on other processes can be investigated.

Significant differences are not evident between the mass and wind fields of the LSFC and LMIC simulations. Low-level (146 m AGL) wind forecasts from the LMIC simulation (Fig. 4.27) indicate a similar structure and evolution of the surface cyclone. The LMIC simulation develops significant westerly flow over the mountains west of Denver and strong northwesterly flow west of the surface cyclone, similar to the LSFC simulation. Minor differences are noted in the structure of the northeasterly flow adjacent to the Front Range. The northeasterlies at 1500 UTC are slightly more pronounced in the LSFC case, especially south of Colorado Springs (COS). At 1800 UTC, the northeasterlies are not forecast north and west of Denver (DEN) as they were in LSFC and observed by the FSL mesonet (Fig. 4.14c). The LMIC prediction at 2100 UTC indicates more significant northeasterlies southwest of Denver that were observed by the FSL mesonet (Fig. 4.14d). But at 0000 UTC, the opposite is evident with more northeasterlies around the Denver area noted in the LSFC forecast. The LMIC prediction indicates the development of northeasterlies near Pueblo (PUB) which is observed by the SAO and is not forecast by LSFC.

LMIC upper air analyses of height and wind (not shown) show only insignificant differences from the corresponding LSFC fields. Comparing the LSFC and LMIC time series of RAMS upper air wind forecasts near Platteville (Figs. 4.19a and 4.28) indicates close agreement except near the surface where the LSFC predictions show more pronounced northeasterly flow between 1400 and 1900 UTC.

The LMIC predictions of maximum upward vertical motion (Fig. 4.29) are similar to the LSFC forecasts (Fig. 4.22) for the Ft. Collins to Denver band, but differences are noted

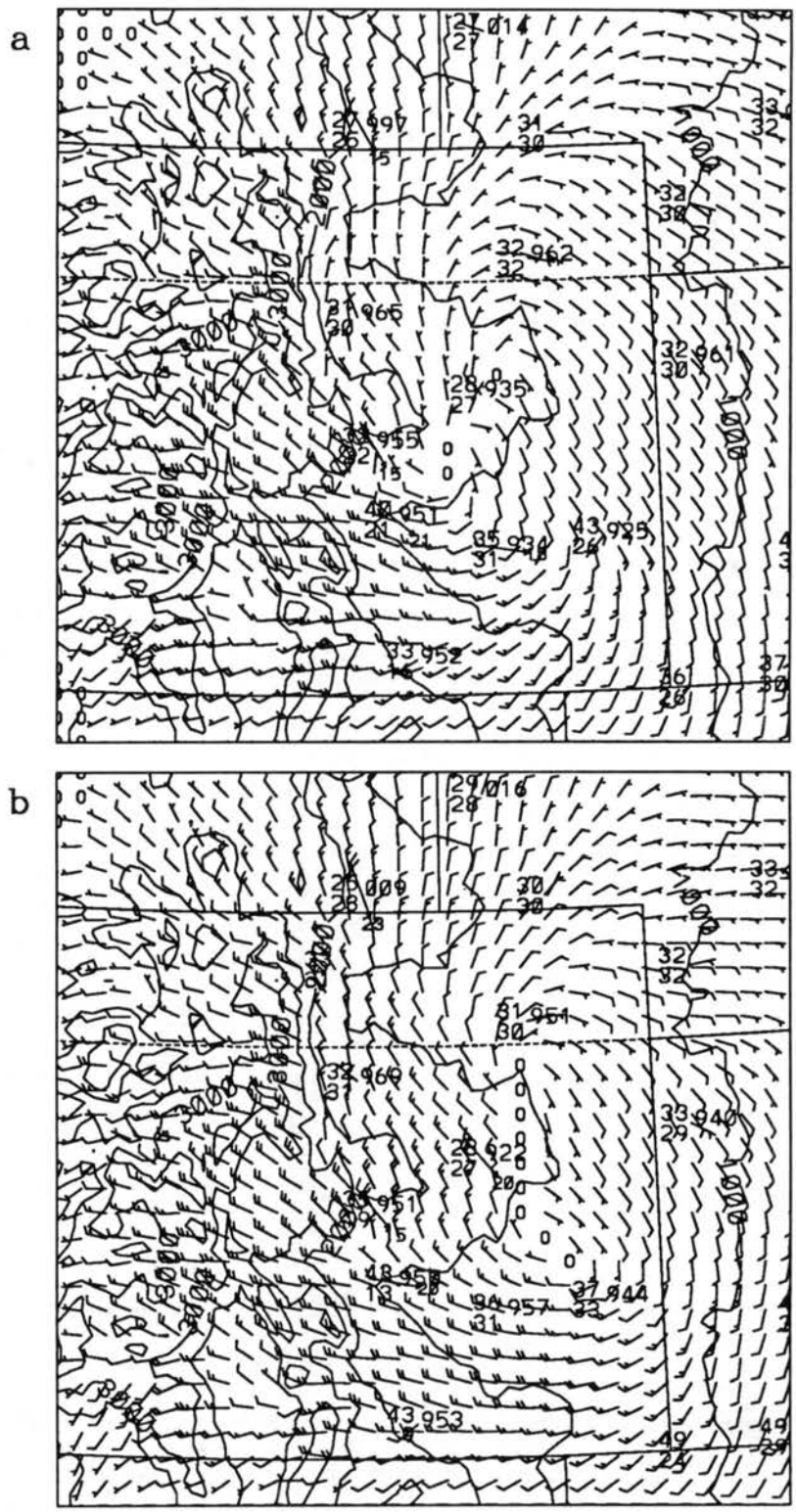

Figure 4.27: RAMS (LMIC) low-level (146 m AGL) wind (m s^{-1}) predictions and actual SAO reports at model validation time from (a) the 3 h forecast valid at 1500 UTC and (b) the 6 h forecast valid at 1800 UTC 7 January 1992.

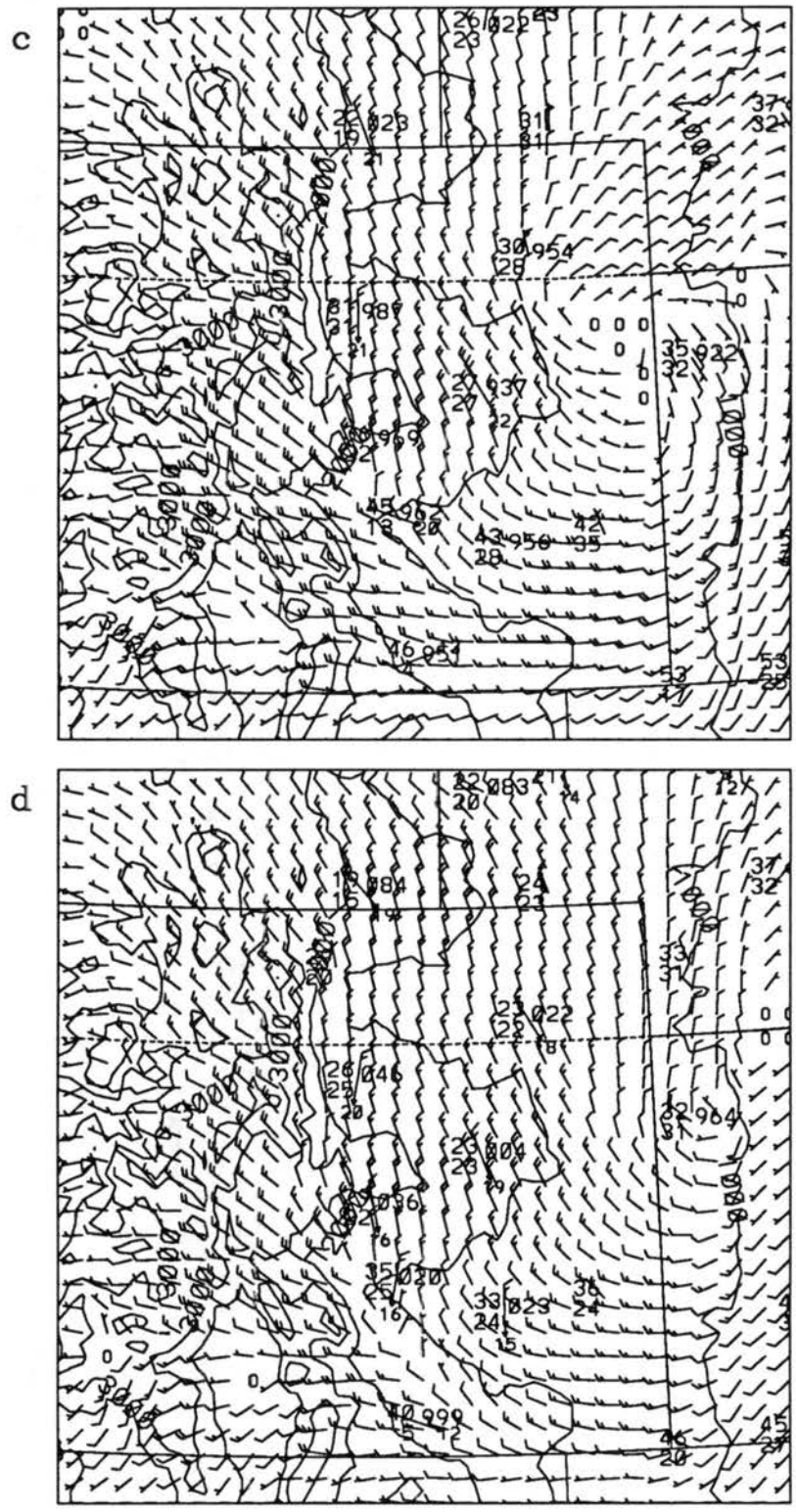

Figure 4.27: Continued: (c) the 9 h forecast valid at 2100 UTC 7 January and (d) the 12 h forecast valid at 8 January 1992.

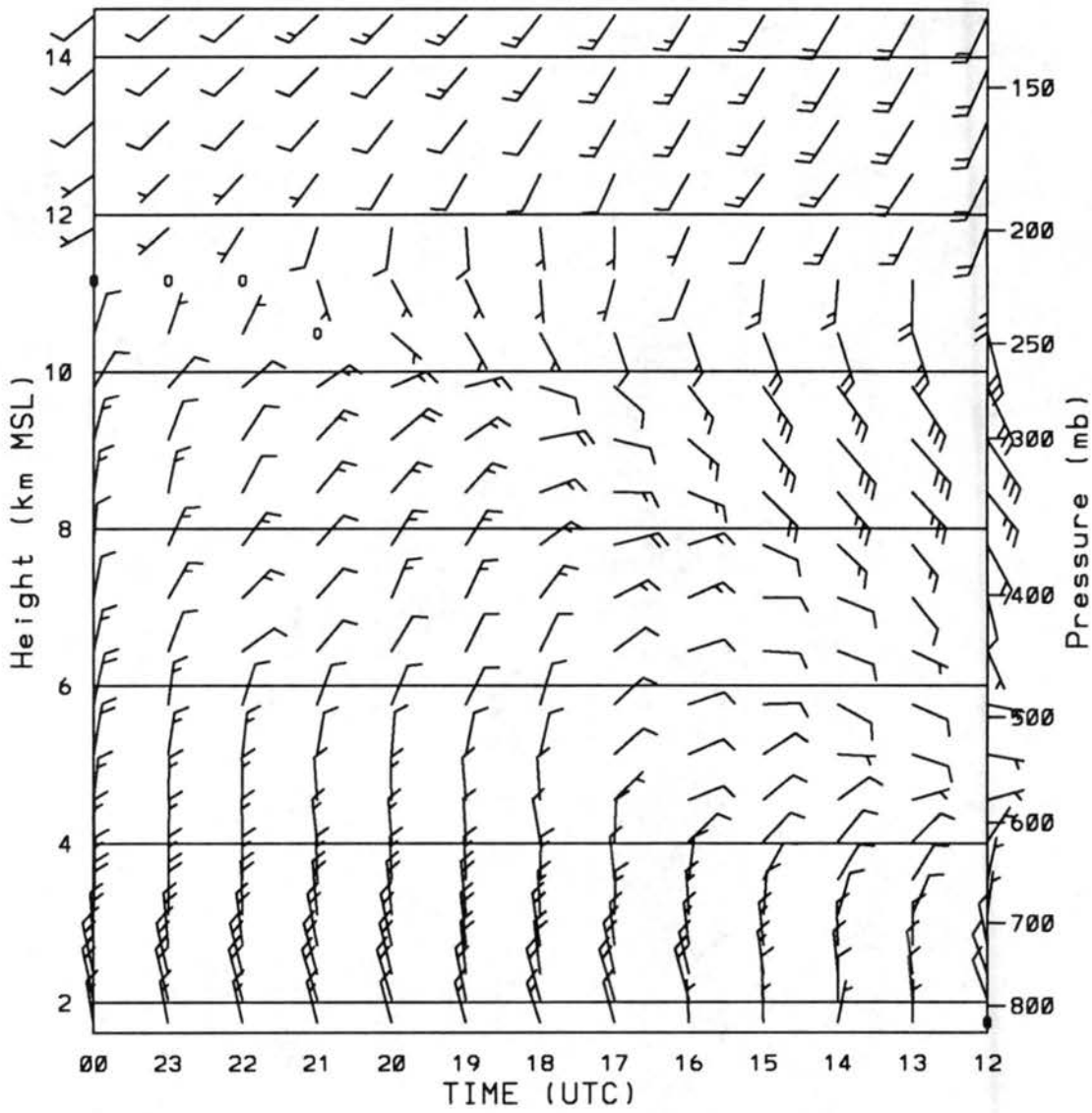

Figure 4.28: Time-height series of RAMS (LMIC) forecast wind (m s^{-1}) for the model grid point closest to Platteville, CO from the 0 to 12 h prediction valid at 1200 UTC 7 January through 0000 UTC 8 January 1992.

over the northeast Plains of Colorado. The 3 h forecasts of vertical motion indicate that the magnitude and shape of the upward vertical motion band adjacent to the Front Range are very close. However, two significant southwest-northeast oriented bands (>0.75 m s^{-1}), one east of Cheyenne (CYS) and the other northeast of Akron (AKO), are evident in the LMIC simulation that are not predicted in the LSFC simulation. The LSFC simulation includes the effects of diabatic heating resulting from vapor condensation to liquid, but conversion to ice is not accounted for. Hence, the additional diabatic heating effects of liquid to ice must be contributors to the stronger predicted upward vertical motion in the LMIC simulation. A similar comparison is observed in the 6 h forecasts with the region of greater than 0.25 m s^{-1} upward vertical motion extending from Denver northeastward into the Nebraska Panhandle. At 9 and 12 h, the two simulations are quite close again with the LMIC prediction showing the dissipation of significant ascent over the Northeast Plains.

Representative west-east vertical cross sections provide an indication of the precipitation processes occurring. Three hour predictions (Fig. 4.30) of potential temperature and vertical motion indicate a mountain lee wave and a downward/upward vertical motion couplet, similar to the LSFC simulation (Fig. 4.23). Recall that the upward vertical motion appears to be the result of rising motion in the lee wave near 3 km and lifting of easterly flow over the lee wave near 5 km. A tall (5 km) vertical column of snow is colocated with the region of upward vertical motion and a maximum of aggregates is positioned in the lower half of the column. The regions of greatest snow and aggregates at the surface are displaced slightly east of the mountain barrier with the total quantity decreasing westward up the Front Range. Two factors are likely contributors to the decreased Front Range snow: 1) snow that might fall into the region of downward vertical motion over the Front Range will quickly evaporate (and probably act to accentuate the downward motion) and 2) the strong low-level westerly flow tends to blow the snow eastward over the Plains.

Amplification of the lee wave is evident at 6 h (Fig. 4.31) with potentially warmer air east of the barrier crest that enhances the baroclinic zone noted in the LSFC simulation. The downward/upward vertical motion couplet continues with the region of primary ascent

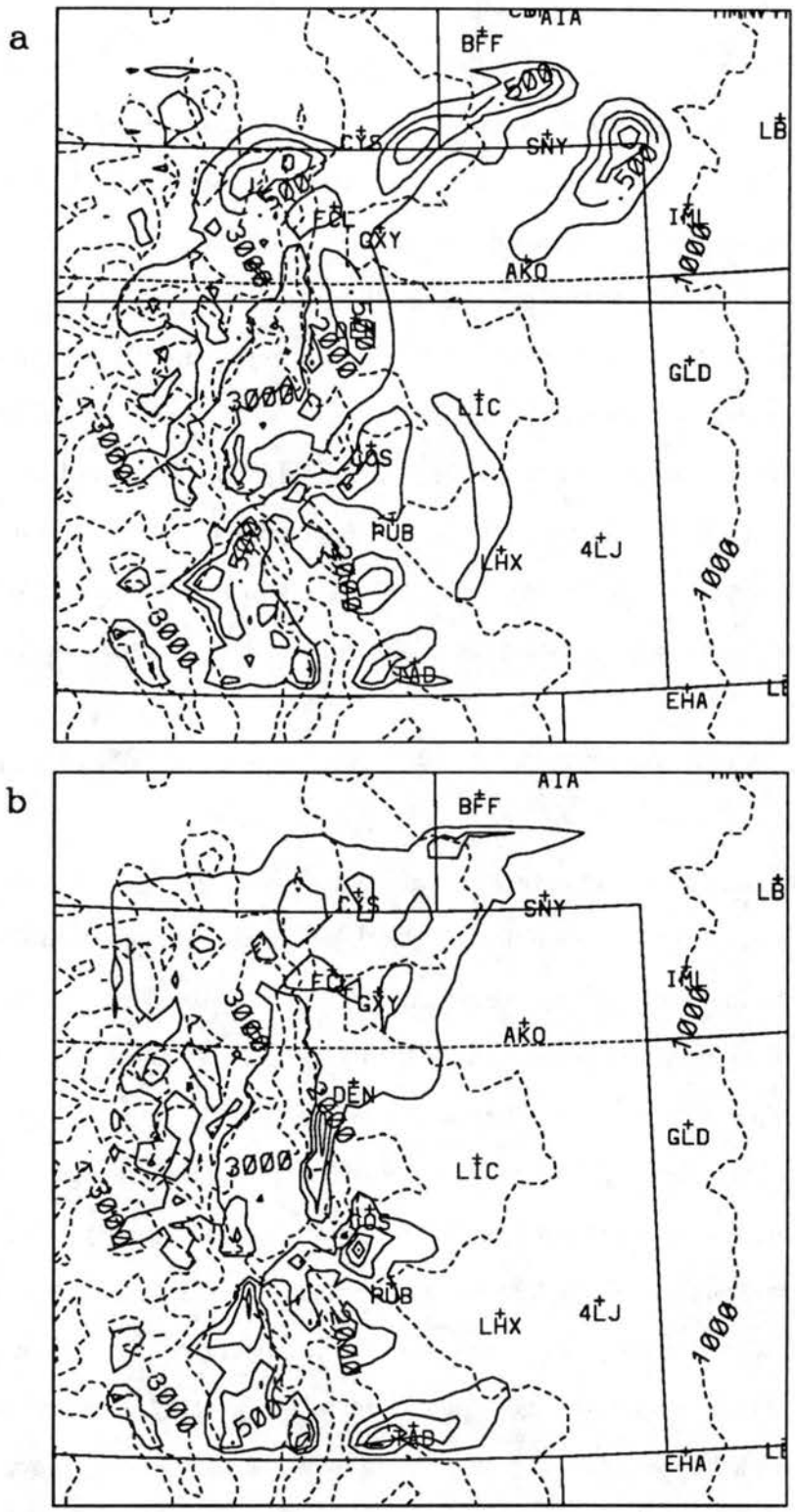

Figure 4.29: RAMS (LMIC) maximum upward vertical motion (m s^{-1}) predictions from (a) the 3 h forecast valid at 1500 UTC and (b) the 6 h forecast valid at 1800 UTC 7 January 1992. Contour interval is 0.25 m s^{-1}.

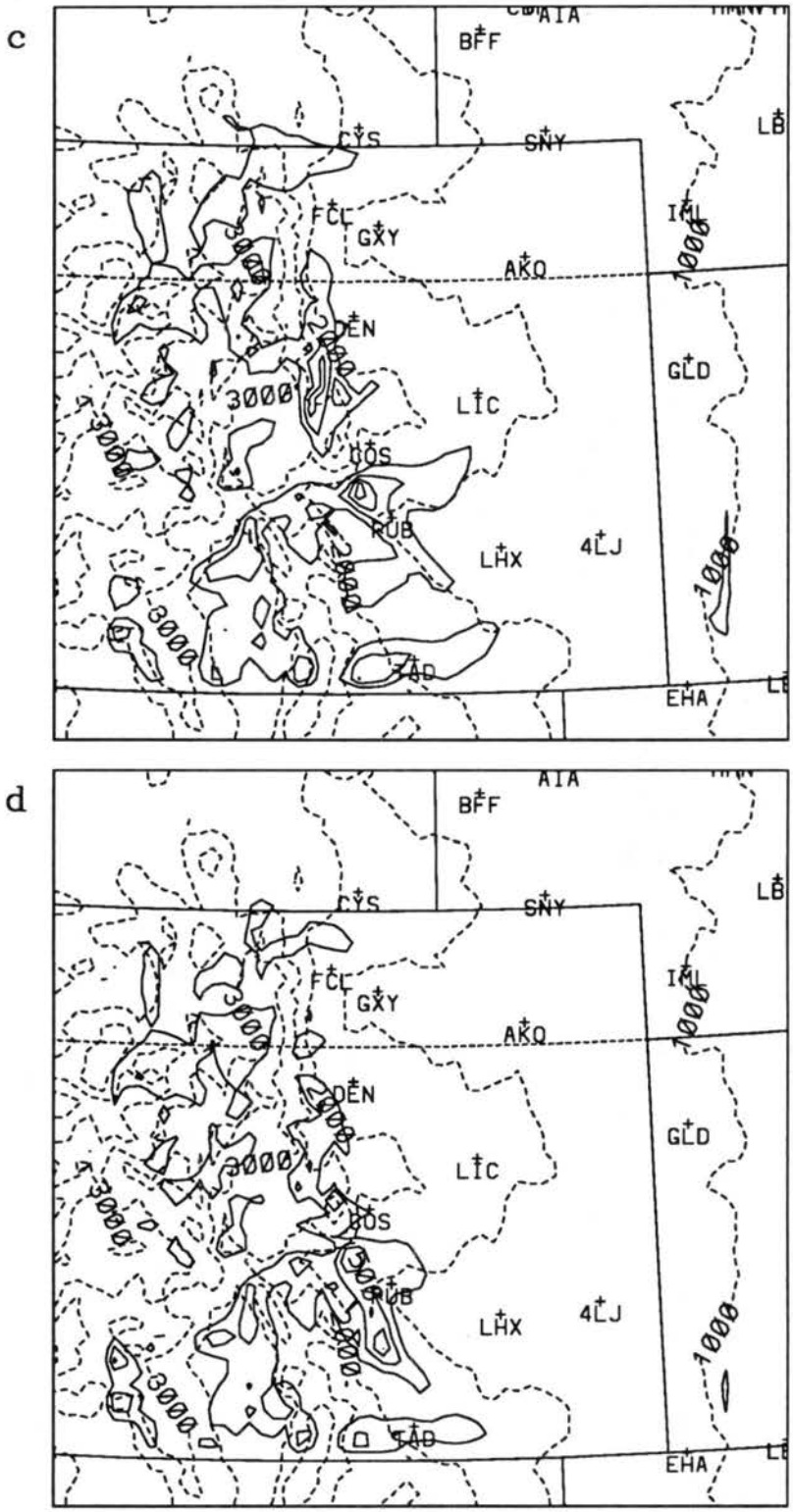

Figure 4.29: Continued: (c) the 9 h forecast valid at 2100 UTC 7 January and (d) the 12 h forecast valid at 8 January 1992.

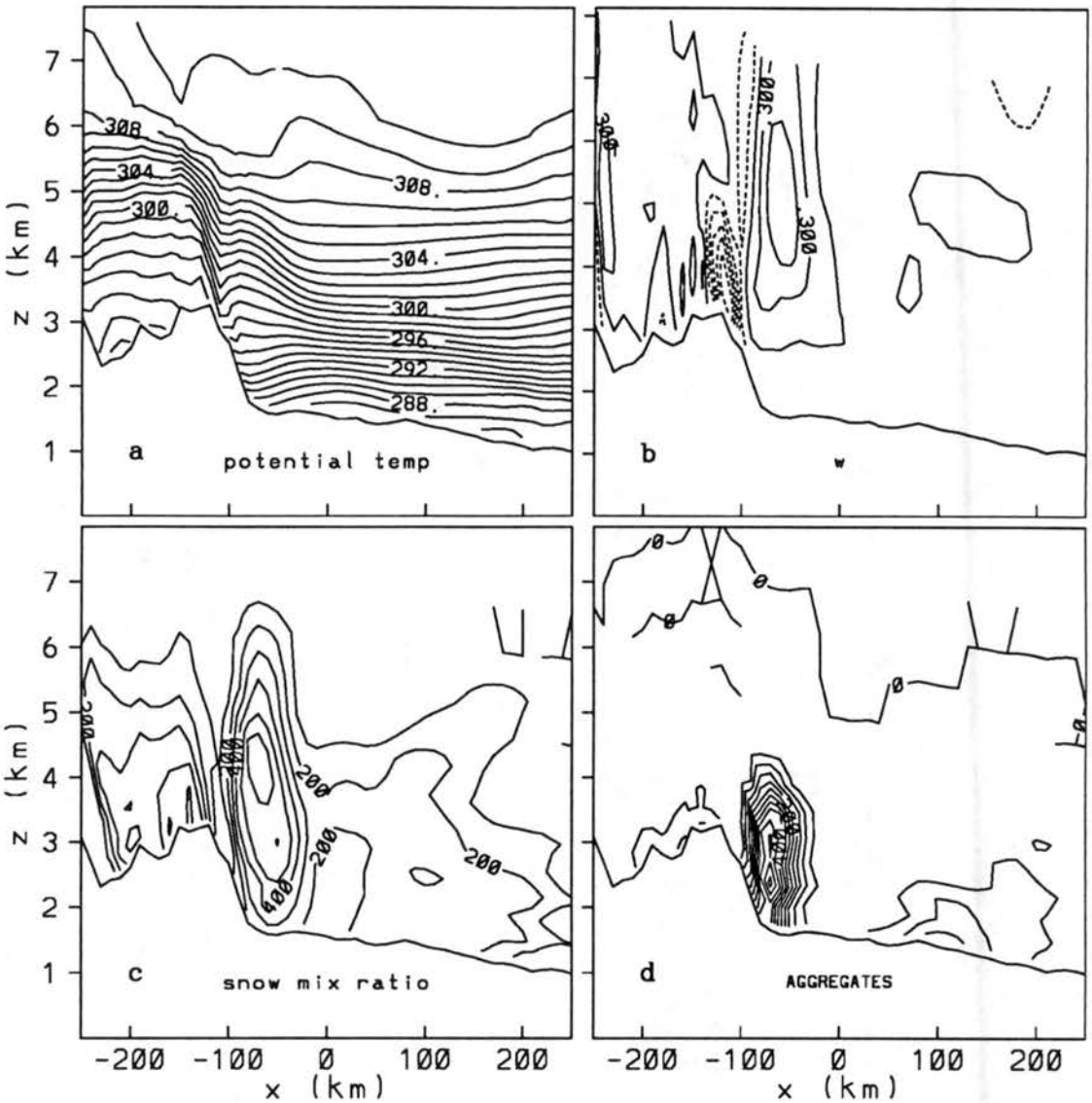

Figure 4.30: West-east vertical cross sections from RAMS (LMIC) 3 h forecast valid at 1500 UTC 7 January 1992 of (a) potential temperature (K), (b) upward vertical motion (m s^{-1}, contour interval = 0.2 m s^{-1}), (c) snow mixing ratio (g kg^{-1}, contour interval = 0.1 g kg^{-1}, 100 units = 0.1 g kg^{-1}), and (d) aggregate mixing ratio (g kg^{-1}, contour interval = 0.05 g kg^{-1}, 100 units = 0.1 g kg^{-1}). Cross section location is represented by the solid line in Fig. 4.29a.

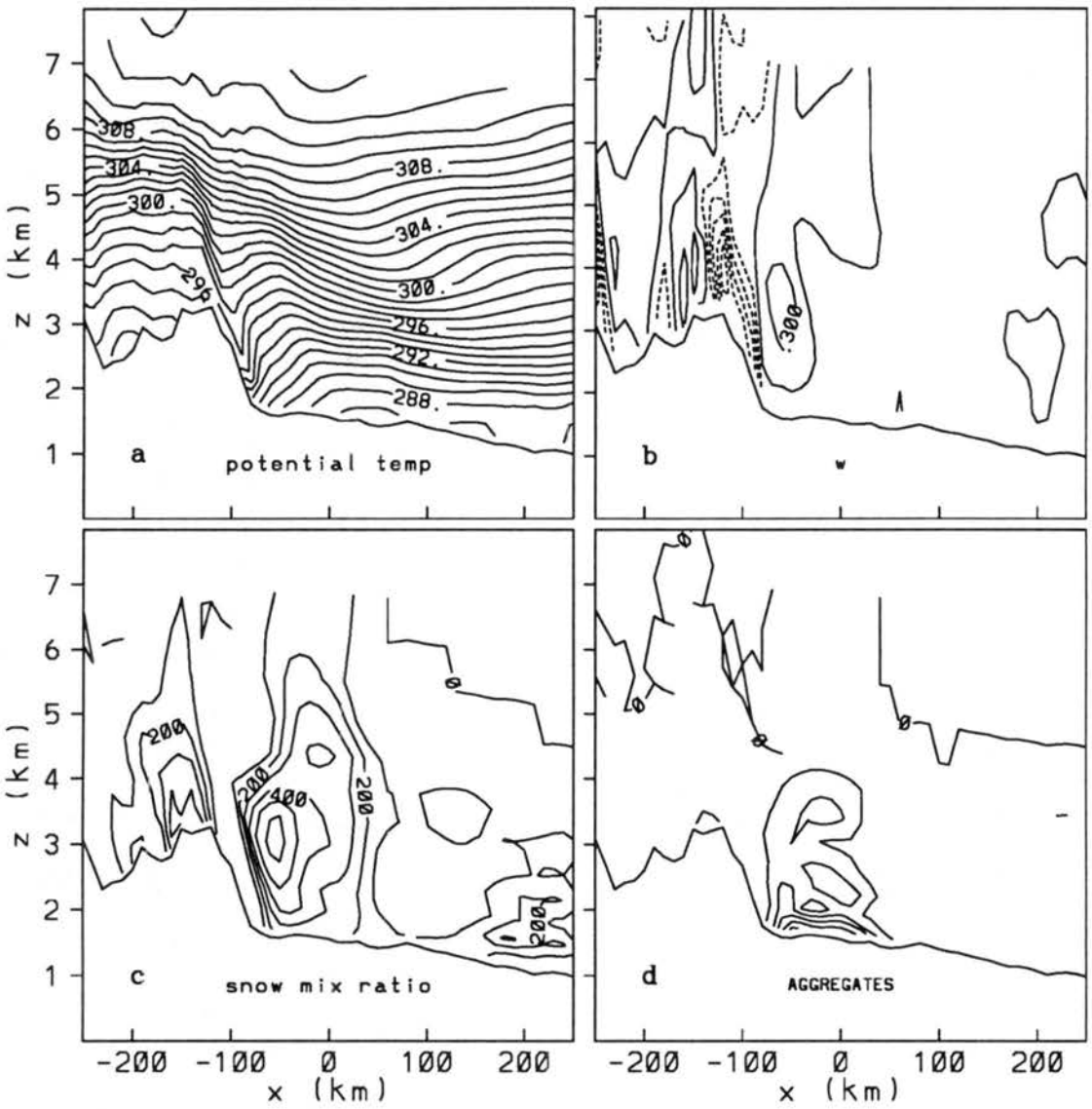

Figure 4.31: As in Fig. 4.30 except for 6 h forecast valid at 1800 UTC 7 January 1992.

located in the eastern portion of the lee wave and a secondary ascent region positioned in the easterly component flow rising over the lee wave. Snow mixing ratio is again correlated with the regions of ascent and aggregates are maximized below the areas of greatest snow mixing ratio. A narrow dry zone with no snow or aggregates is depicted over the Front Range in association with the dry region of descent in the western portion of the lee wave. The extension of the westerly component flow over the Plains suggests that snow and aggregates are carried eastward and hence the predicted broadening in the vertical columns of snow and aggregates. The regions of greatest surface snow and aggregates are now displaced approximately 40 km east of the barrier.

The lee mountain wave and associated surface baroclinic zone are evident in the 9 h predicted potential temperature field (Fig. 4.32). The forecast vertical motion continues to show the downward/upward couplet with no evidence of easterly component flow rising over the wave, similar to the LSFC simulation. The columns of greatest snow and aggregates east of the Front Range are now confined below 4 km with a significant vertical tilt. The dry slot continues over the Front Range and significant westerly component flow likely creates the predicted tilt in precipitation. Surface snow and aggregates continue to be greatest at about 40 km east of the mountain barrier with some decrease in magnitude.

The 12 h predicted potential temperature indicates a decrease in the amplitude of the mountain wave and the continued presence of the baroclinic zone over and east of the Front Range (Fig. 4.33). The downward/upward couplet is evident with a decrease in the magnitude of ascent adjacent to the Front Range. Snow and aggregates east of the Front Range are primarily confined to the lowest 1 km AGL. Greatest surface amounts of snow and aggregates are located about 30 km east of the barrier.

The full microphysics version of RAMS generates a quantitative precipitation forecast. The 12 h forecast of melted precipitation (Fig. 4.34) indicates that the model is capable of resolving the mesoscale variation that was observed (Fig. 4.1). The north-south band of model predicted precipitation from Greeley to south of Denver agrees well with the observed band in location and magnitude. Other features predicted by RAMS that correspond well with the observations include the dry zones along the Front Range

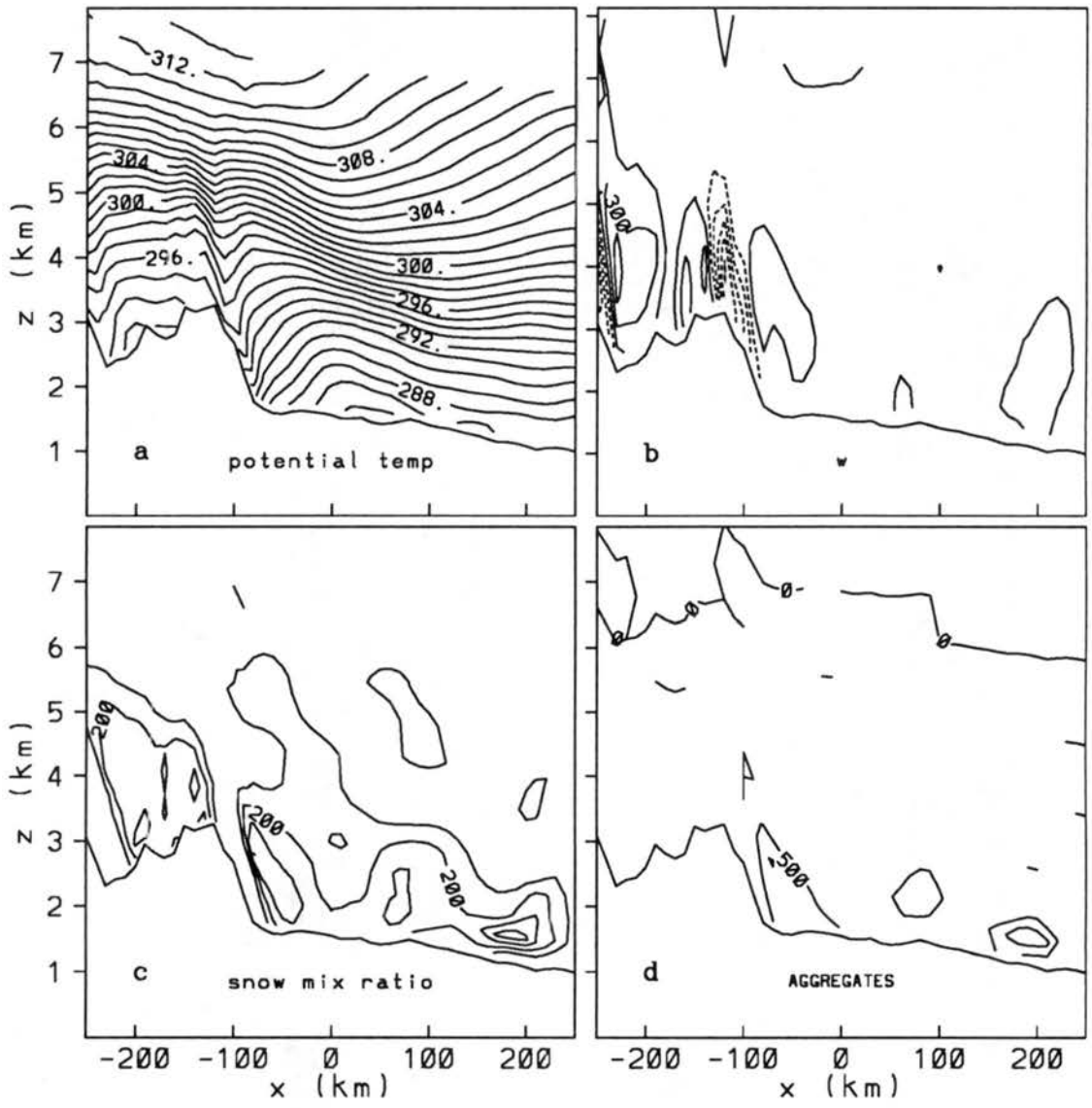

Figure 4.32: As in Fig. 4.30 except for 9 h forecast valid at 2100 UTC 7 January 1992.

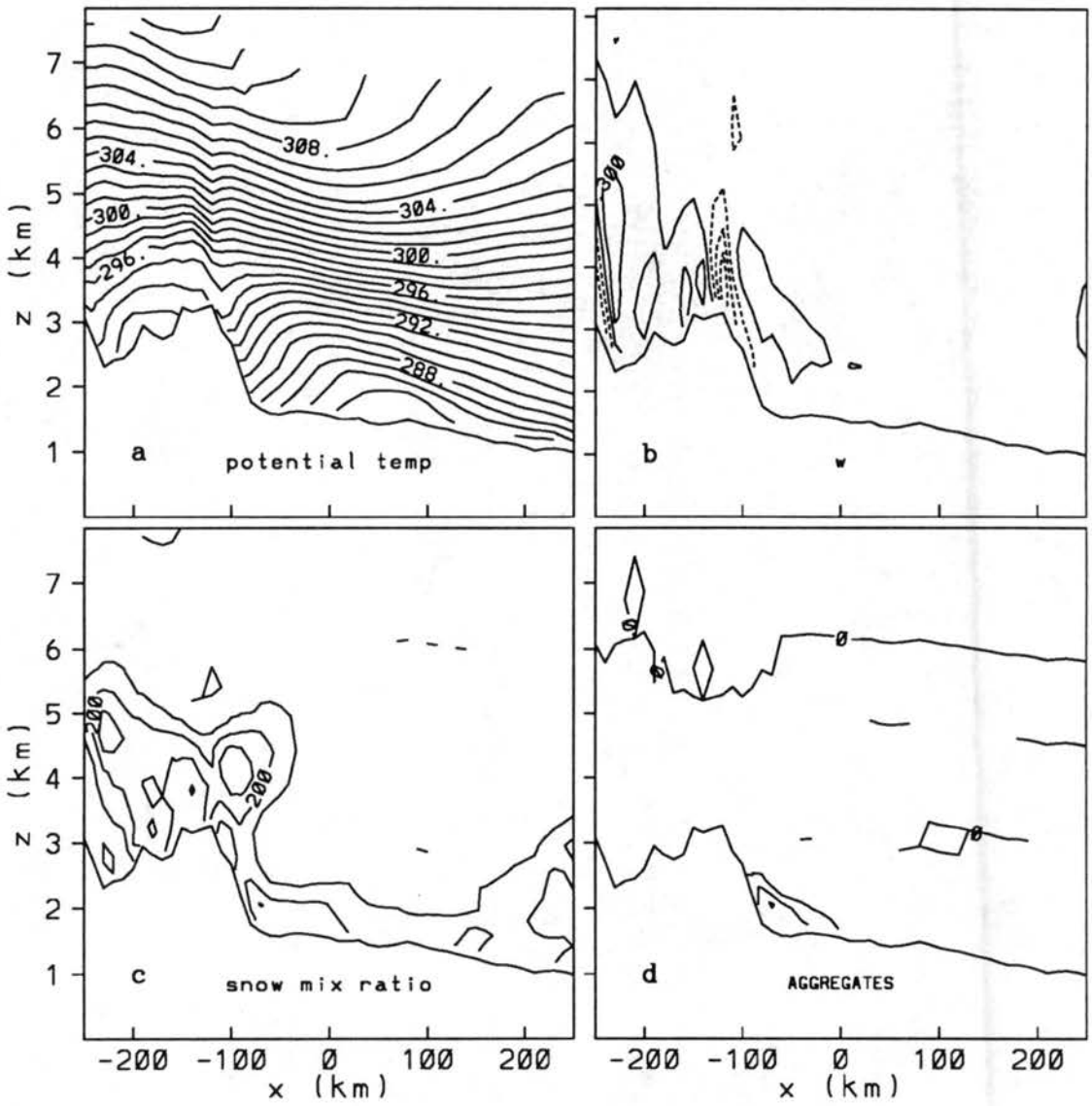

Figure 4.33: As in Fig. 4.30 except for 12 h forecast valid at 0000 UTC 8 January 1992.

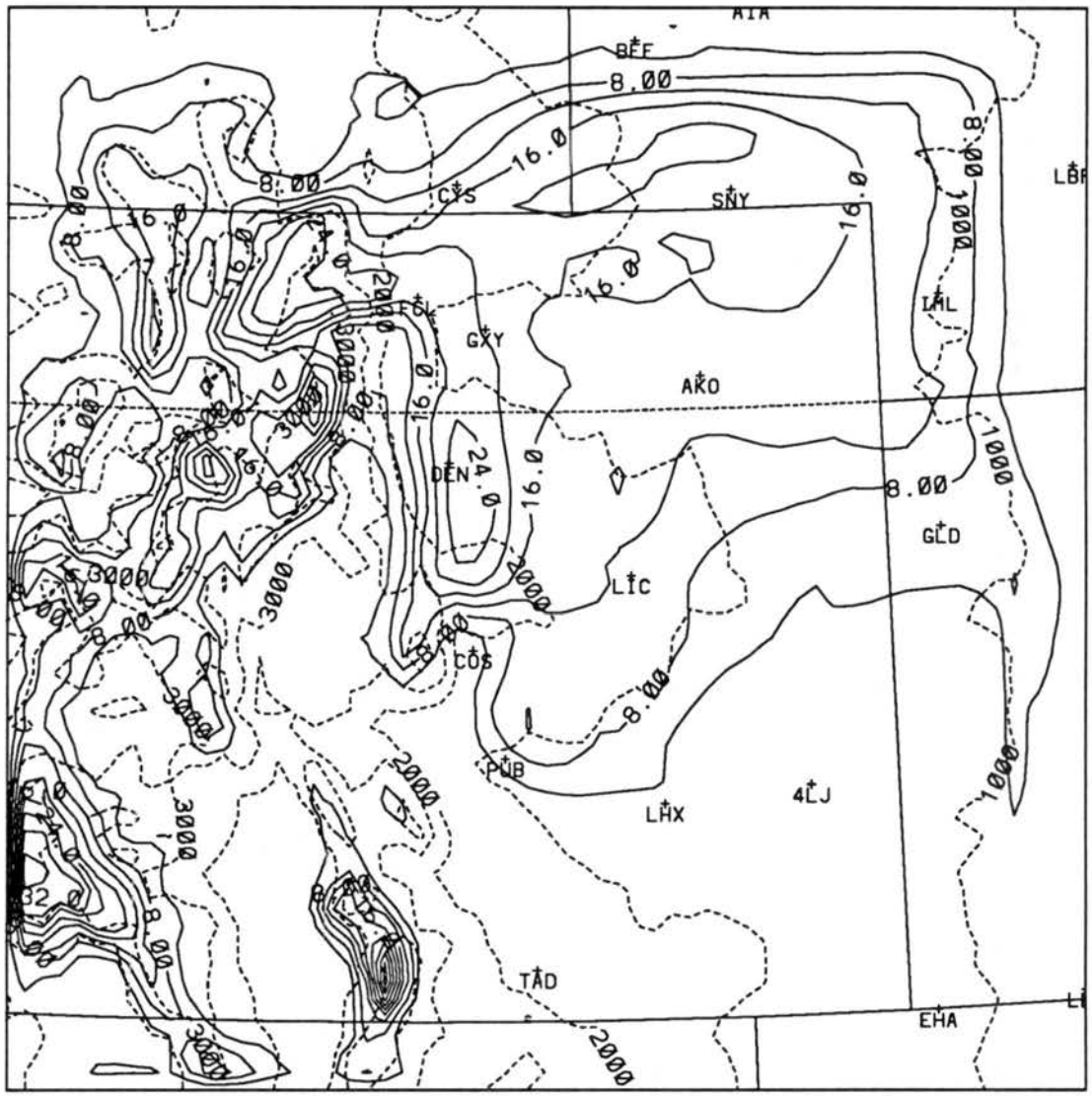

Figure 4.34: RAMS (LMIC) 12 h melted precipitation (mm) forecast.

and around Colorado Springs (COS), the westward extension of maximum precipitation from Ft. Collins to the Continental Divide, the east-west band of precipitation from southeast Wyoming to the Nebraska Panhandle, and the overall coverage of the greater than 4 mm precipitation area.

4.2.3 Other sensitivity simulations

Comparisons of predictions from the four sensitivity simulations (LAPS-initialized with LAPS data except separate LAPS surface analyses are not included, LBAL-initialized with the LAPS variationally adjusted mass and wind analyses, MAPS-initialized with MAPS data and LAPS topography, MTOP-initialized with MAPS data and MAPS topography) to the LSFC forecasts show the majority of significant differences to exist in MTOP suggesting that improved forecasts using LAPS initialization is primarily due to better representation of the actual terrain rather than enhancements to the initialization of atmospheric state variables. Six hour forecasts of low-level (146 AGL) winds (Fig. 4.35) from LAPS, LBAL, and MAPS agree closely with the LSFC predicted winds except for some differences in wind speeds near the Continental Divide west of Denver. Forecast mountain wind speeds are strongest in LSFC with progressively weaker speeds in LBAL, LAPS, and MAPS. MTOP predicted wind speeds over the mountains are about half of those forecast by LSFC. Since the coarser terrain representation of MTOP positions the highest topography further west than reality, the highest wind speeds are considerably further west of Denver. Also, only a hint of northeasterly flow adjacent to the Front Range is evident and the transition from westerlies over the mountains to northerlies over the Plains is much more gradual. Similar results are evident in the 12 h forecast low-level winds (Fig. 4.36) with the primary differences existing in MTOP where high mountain wind speeds are displaced westward and northeasterly flow in the Denver area is nonexistent.

Upper air comparisons away from terrain-influenced regions are all very similar. Time series of forecast winds near Platteville (Fig. 4.37) indicate that all four sensitivity simulations resolved the structure and evolution of the three distinct wind regime layers observed by the Platteville wind profiler (Fig. 4.13). Three hour predictions of maximum up-

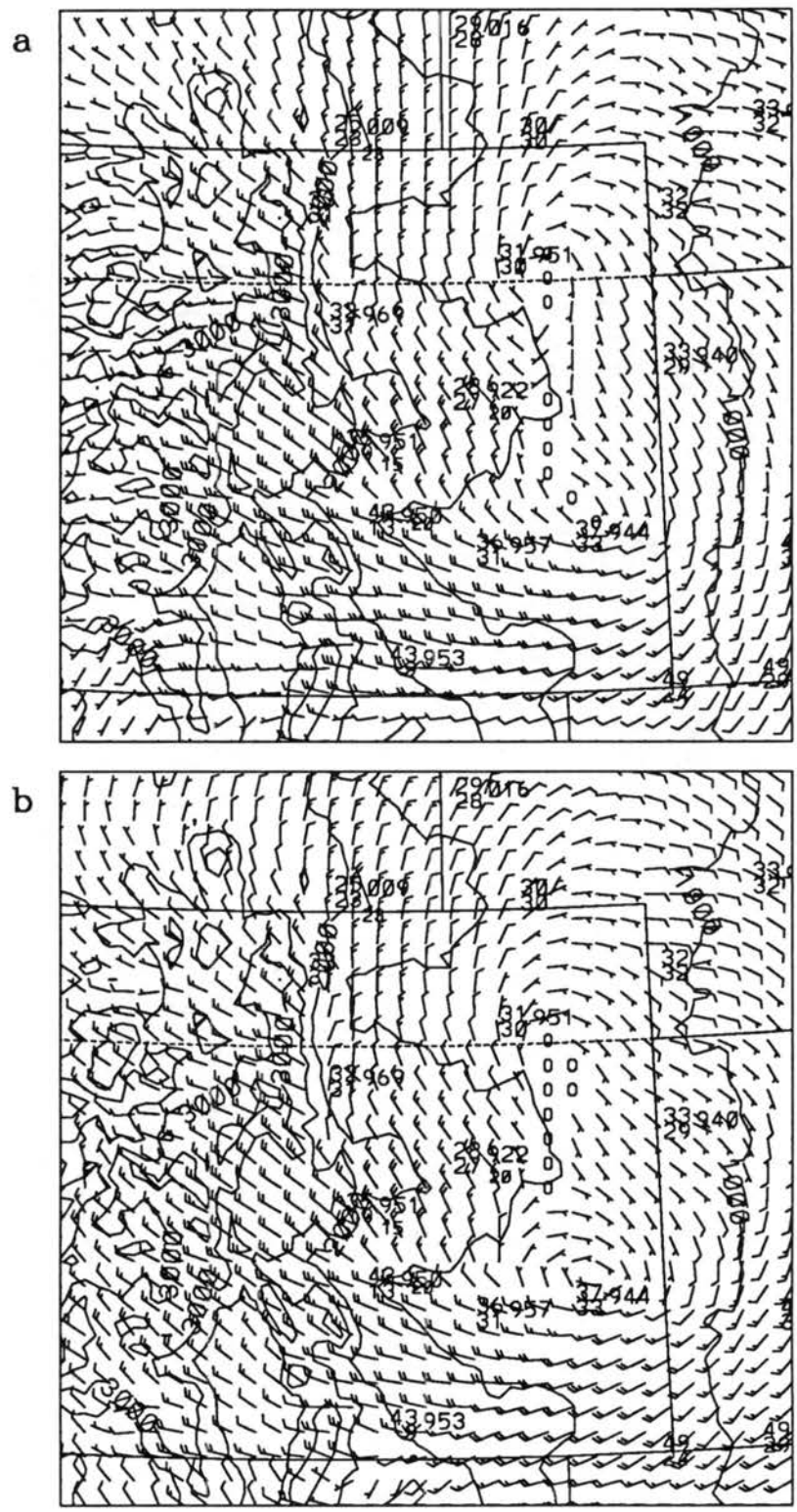

Figure 4.35: RAMS low-level (146 m AGL) wind (m s^{-1}) predictions and actual SAO reports at model validation time from 1800 UTC 7 January 1992 for (a) the LAPS simulation and (b) the LBAL simulation.

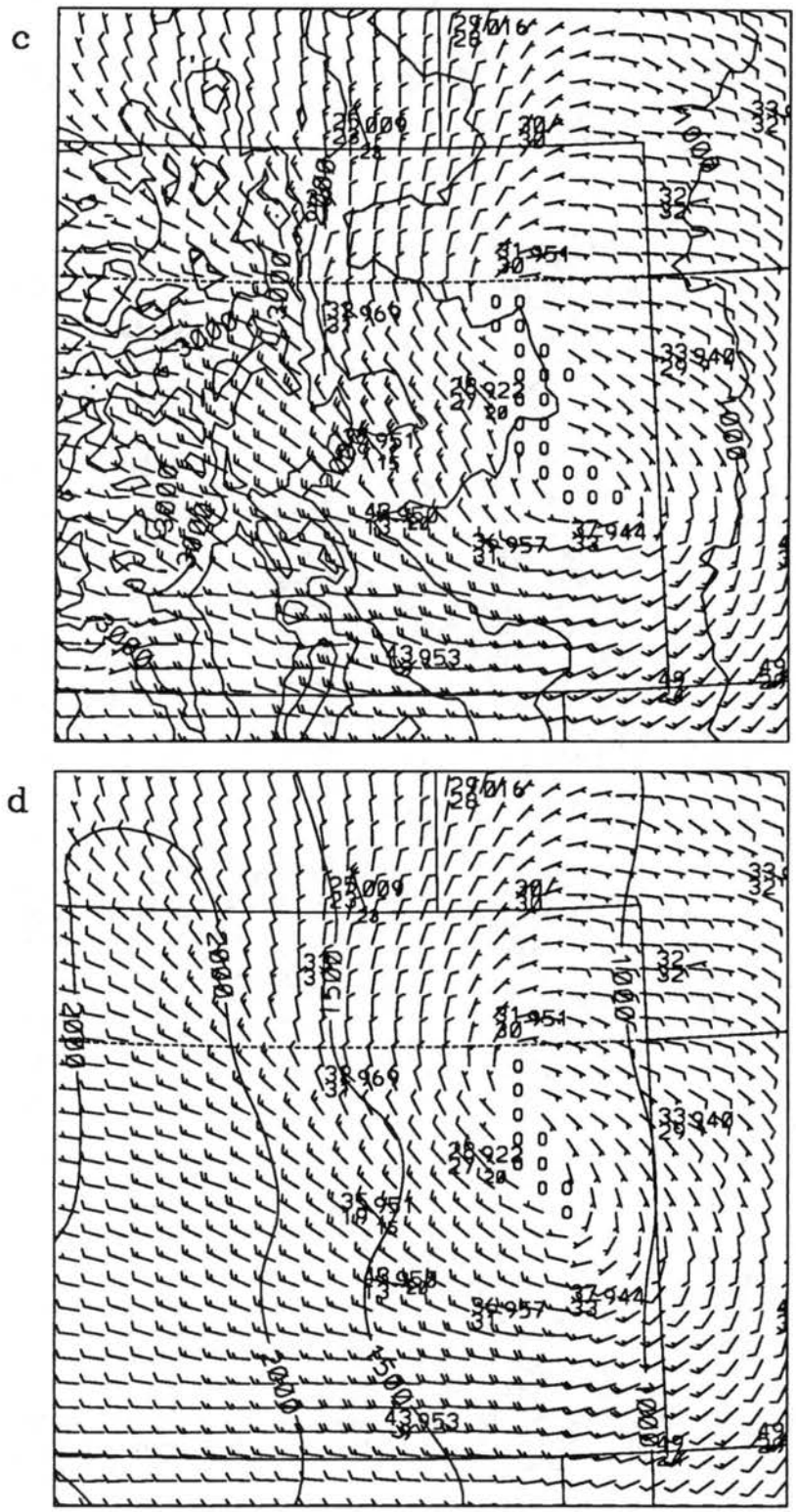

Figure 4.35: Continued: (c) the MAPS simulation and (d) the MTOP simulation.

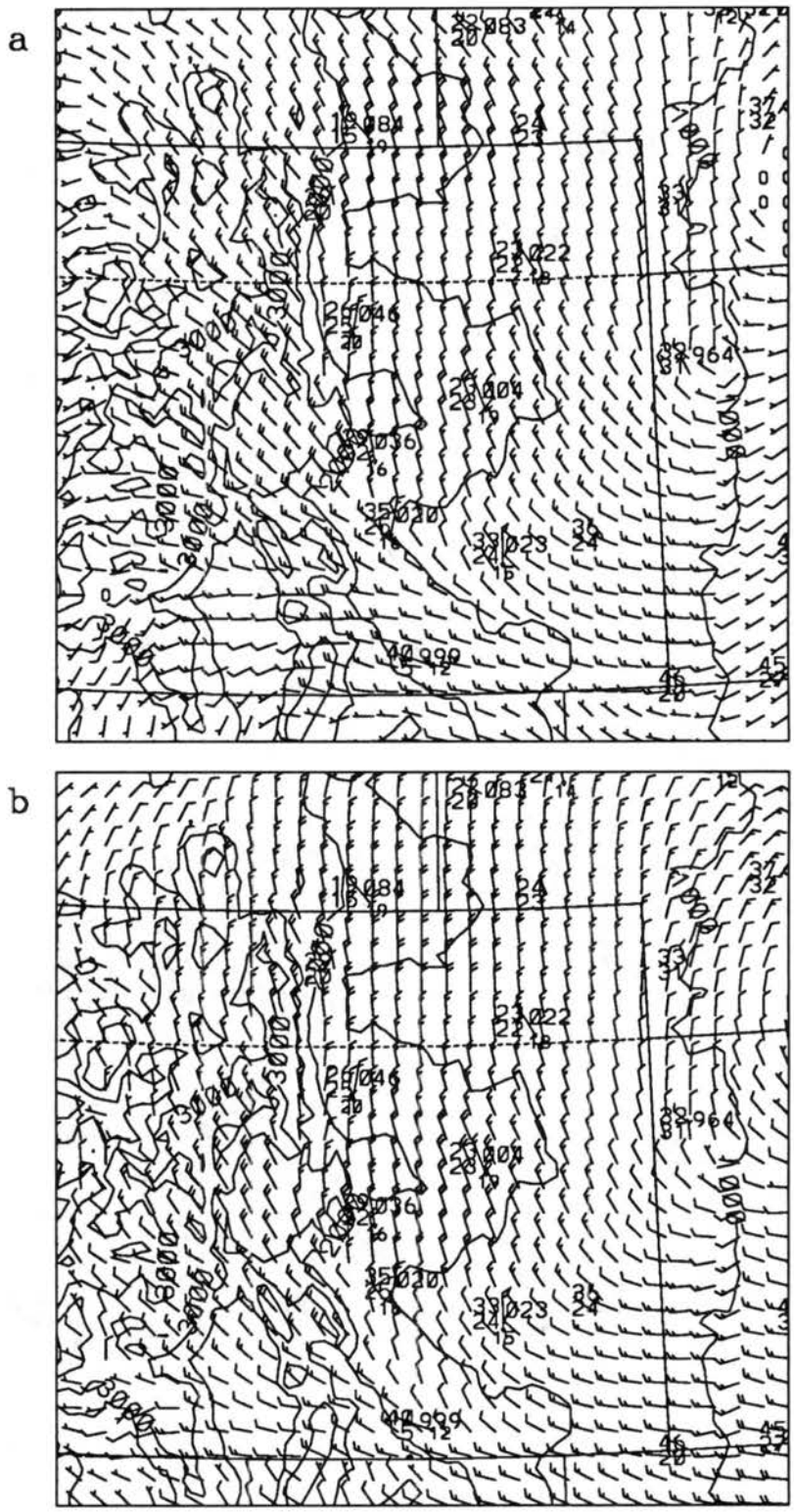

Figure 4.36: As in Fig. 4.35 except for 12 h forecast valid at 0000 UTC 8 January 1992.

c

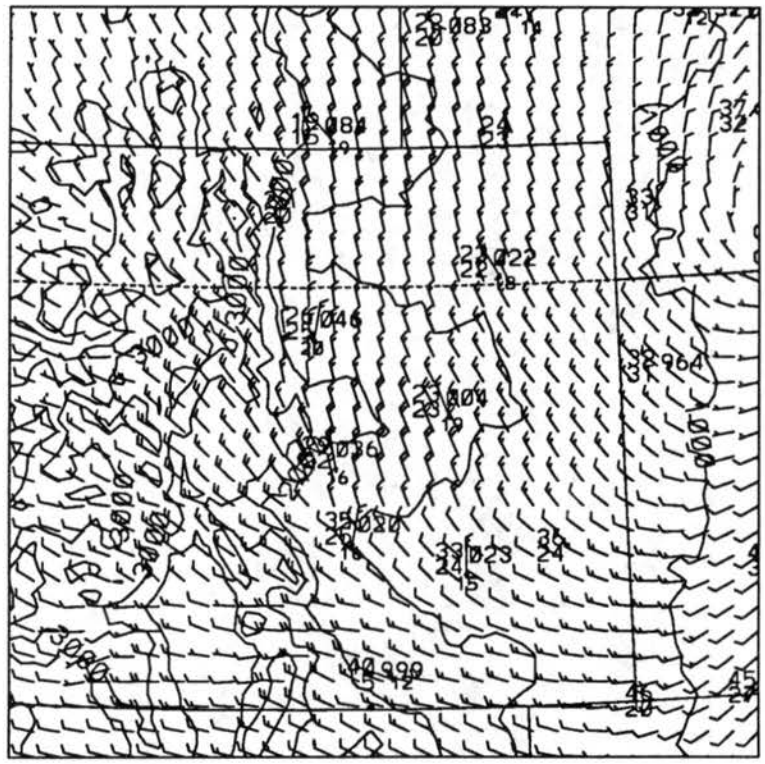

d

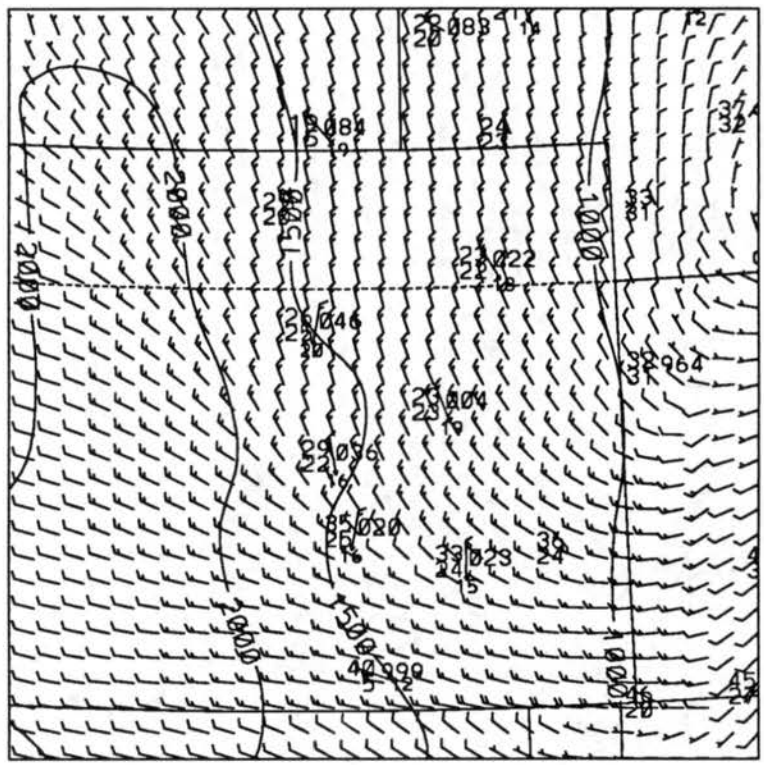

Figure 4.36: Continued:

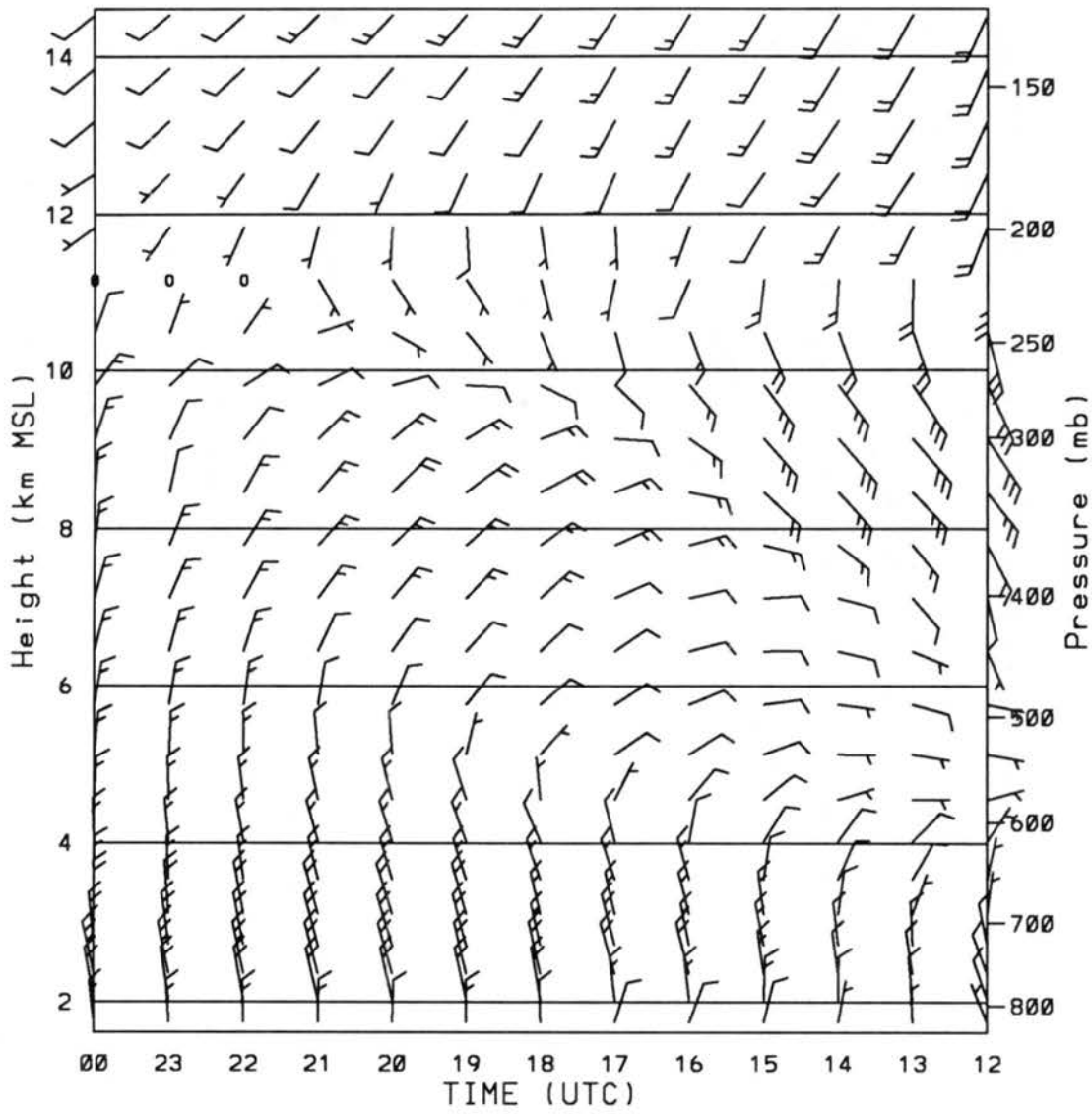

Figure 4.37: Time-height series of RAMS forecast wind (m s^{-1}) for the model grid point closest to Platteville, CO from the 0 to 12 h prediction valid at 1200 UTC 7 January through 0000 UTC 8 January 1992 for (a) the LAPS simulation.

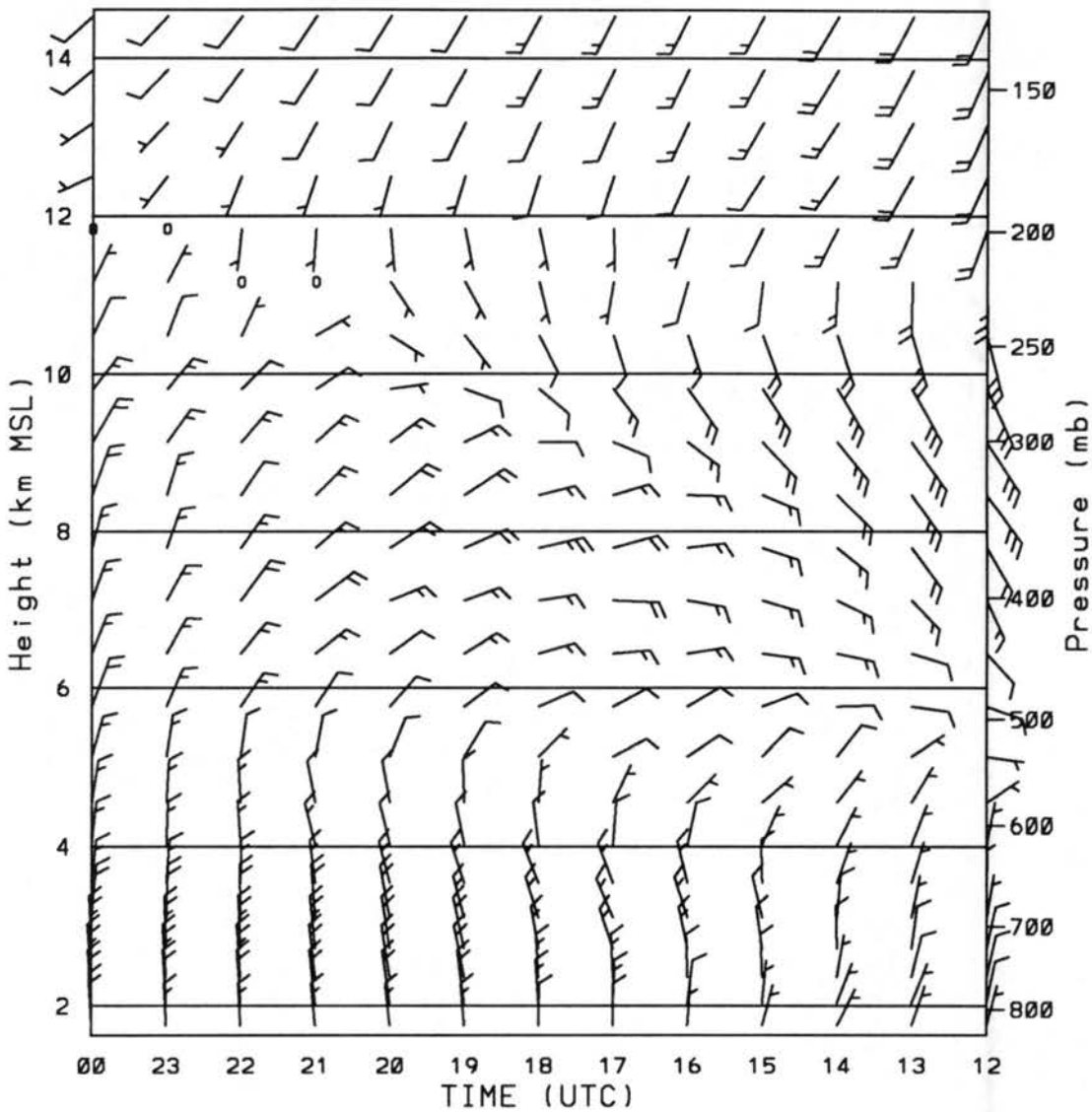

Figure 4.37: Continued: (b) the LBAL simulation.

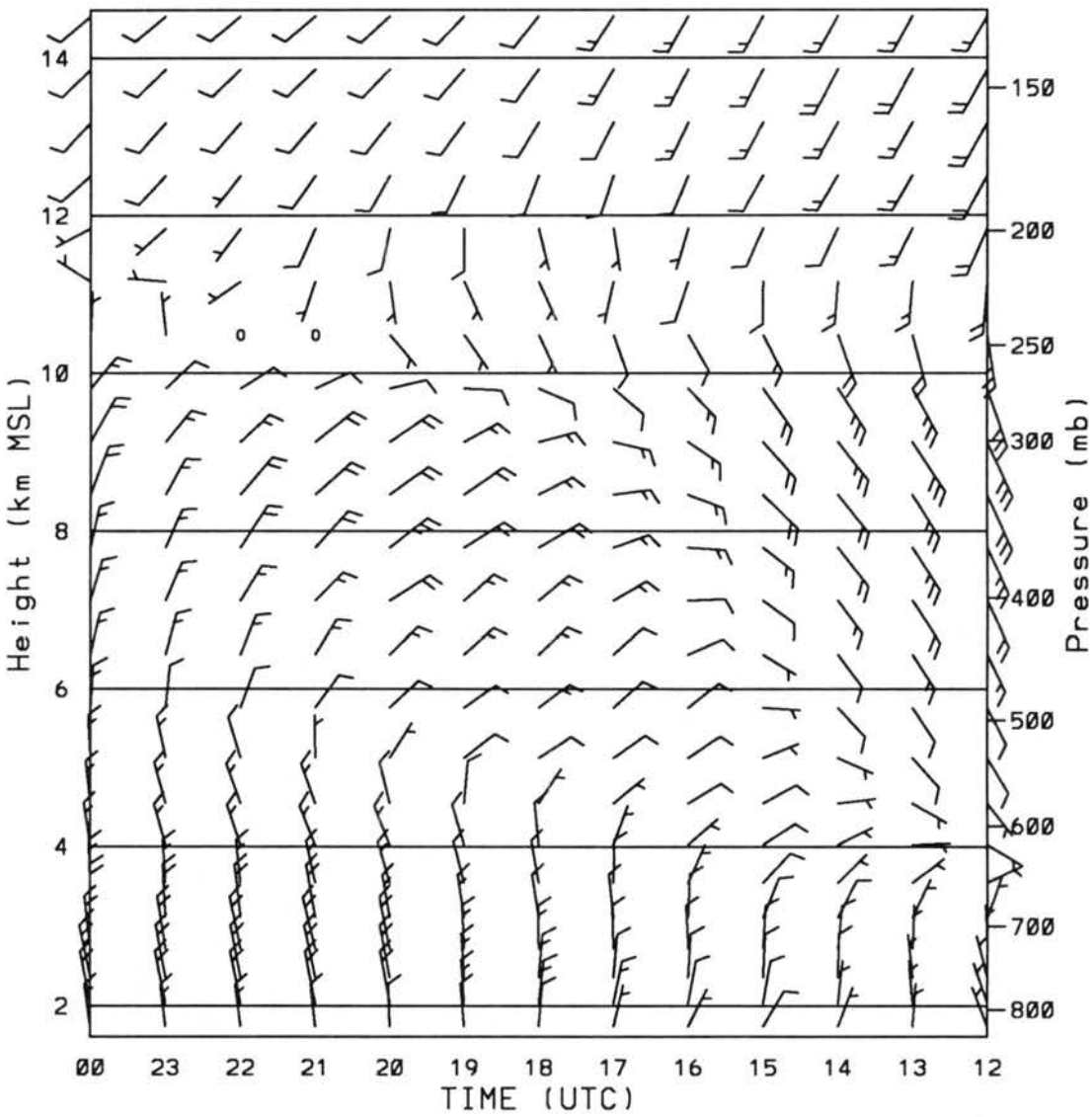

Figure 4.37: Continued: (c) the MAPS simulation.

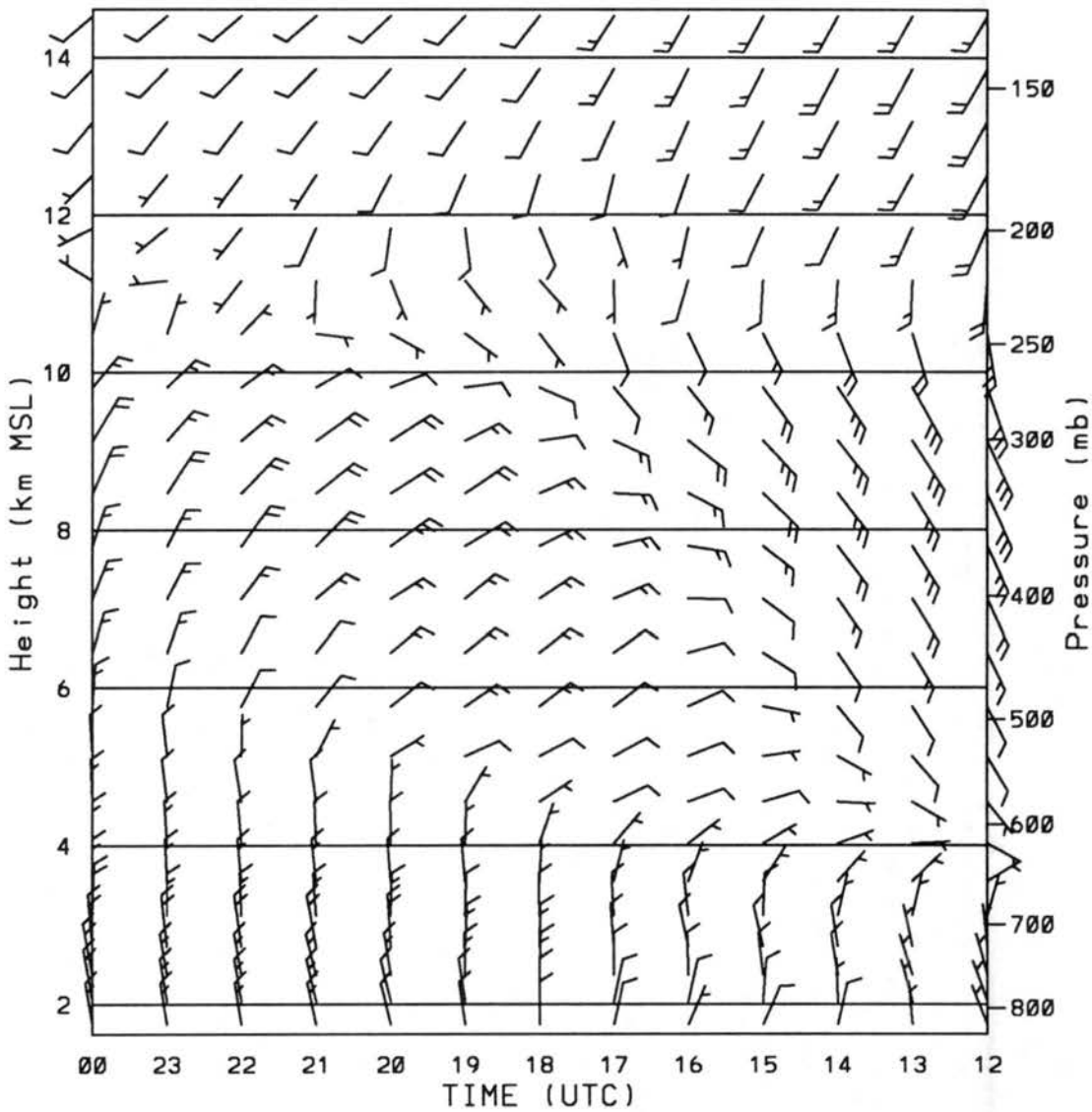

Figure 4.37: Continued: (d) the MTOP simulation.

ward vertical motion (Fig. 4.38) all depict a north-south band of ascent from Ft. Collins to south of Denver. Compared to LSFC, the magnitude of ascent is somewhat less for LAPS, LBAL, and MAPS while the MTOP ascent region is broader and about 50% weaker. Another significant difference is the lack of forecast ascent from Greeley (GXY) northeastward to the Nebraska Panhandle by the MAPS initialized runs (i.e. MAPS and MTOP).

While significant differences between simulations initialized with LAPS and MAPS are not evident in the mass and horizontal wind fields, representative vertical cross sections reveal that predictions initialized with LAPS contain more structure and greater amounts of moisture in several regions. West-east vertical cross sections located just north of Denver for the four sensitivity simulations are illustrated in Figures 4.39 – 4.42. Potential temperature predictions indicate the development of a lee mountain wave in all four simulations with the MTOP wave significantly broader and less amplified. The upward vertical motion is weakest in MTOP and LBAL and strongest in LAPS. The lower maximum within the the eastern portion of the lee wave is evident in the LAPS initialized runs (LAPS and LBAL) but not in the MAPS initialized simulations (MAPS and MTOP). The most significant differences are in the predicted moisture. The MAPS initialized runs indicate greatest moisture near the surface with lesser amounts rising in the easterly flow over the lee wave. Less moisture in the regions of ascent suggests less diabatic heating leading to weaker lifting in the MAPS initialized simulations. This trend continues through the entire 12 h forecast cycle resulting in maximum upward vertical motion for LSFC to be at least 50% greater than MAPS in the north-south band adjacent to the Front Range.

4.2.4 LFCS simulation - an operational forecast

Results from the above simulations have demonstrated the ability to realistically represent mesoscale features using a numerical model initialized with 10 km grid interval, non-homogeneous data. All of the experiments attempted thus far, however, have utilized future 0 h analyses as nudging targets for the lateral boundary conditions; an unrealistic configuration for operational forecasting. To simulate a true real-time, operational

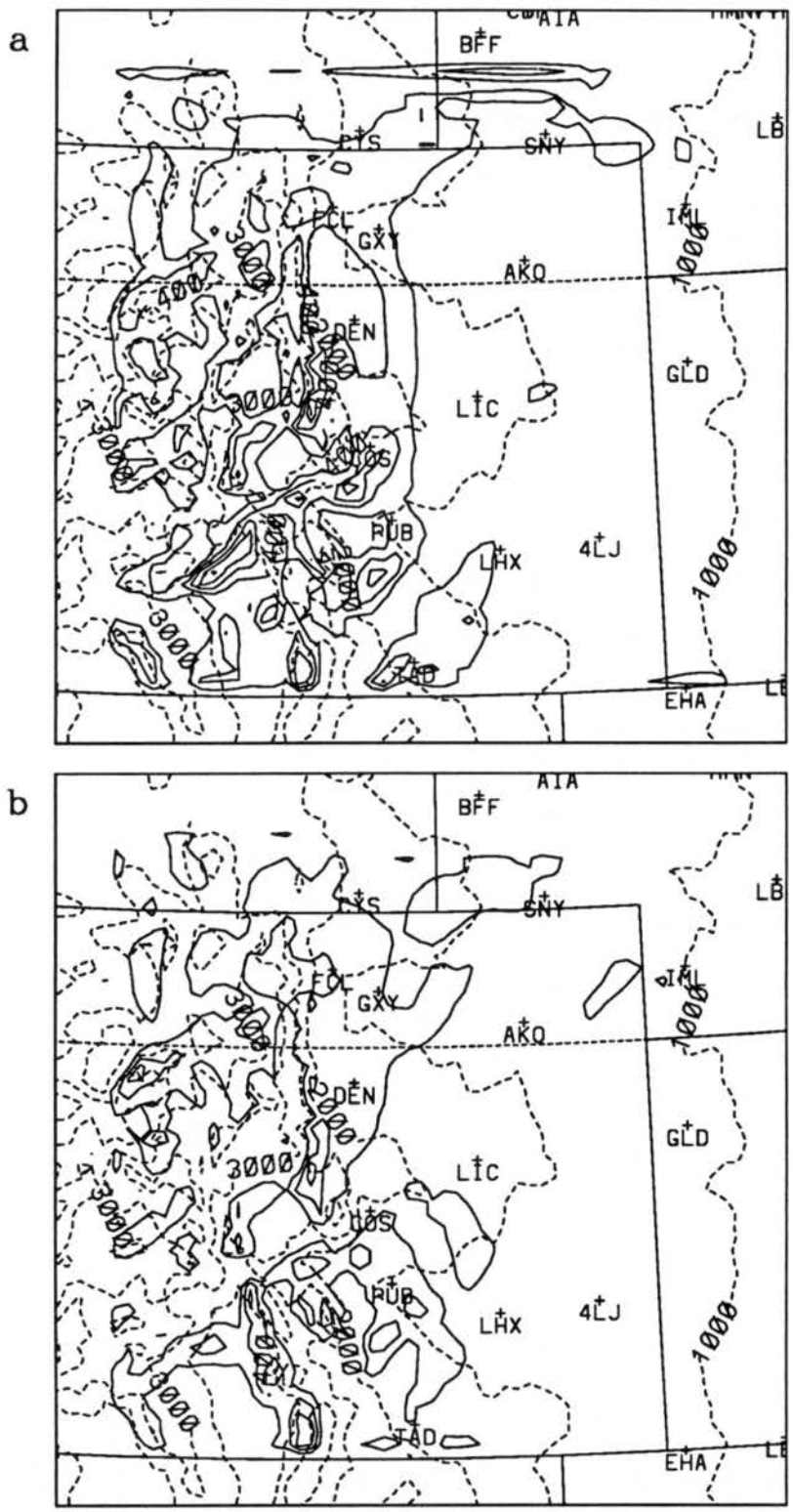

Figure 4.38: RAMS maximum upward vertical motion (m s^{-1}) predictions from the 3 h forecast valid at 1500 UTC 7 January 1992 for (a) the LAPS simulation and (b) the LBAL simulation. Contour interval is 0.2 m s^{-1}.

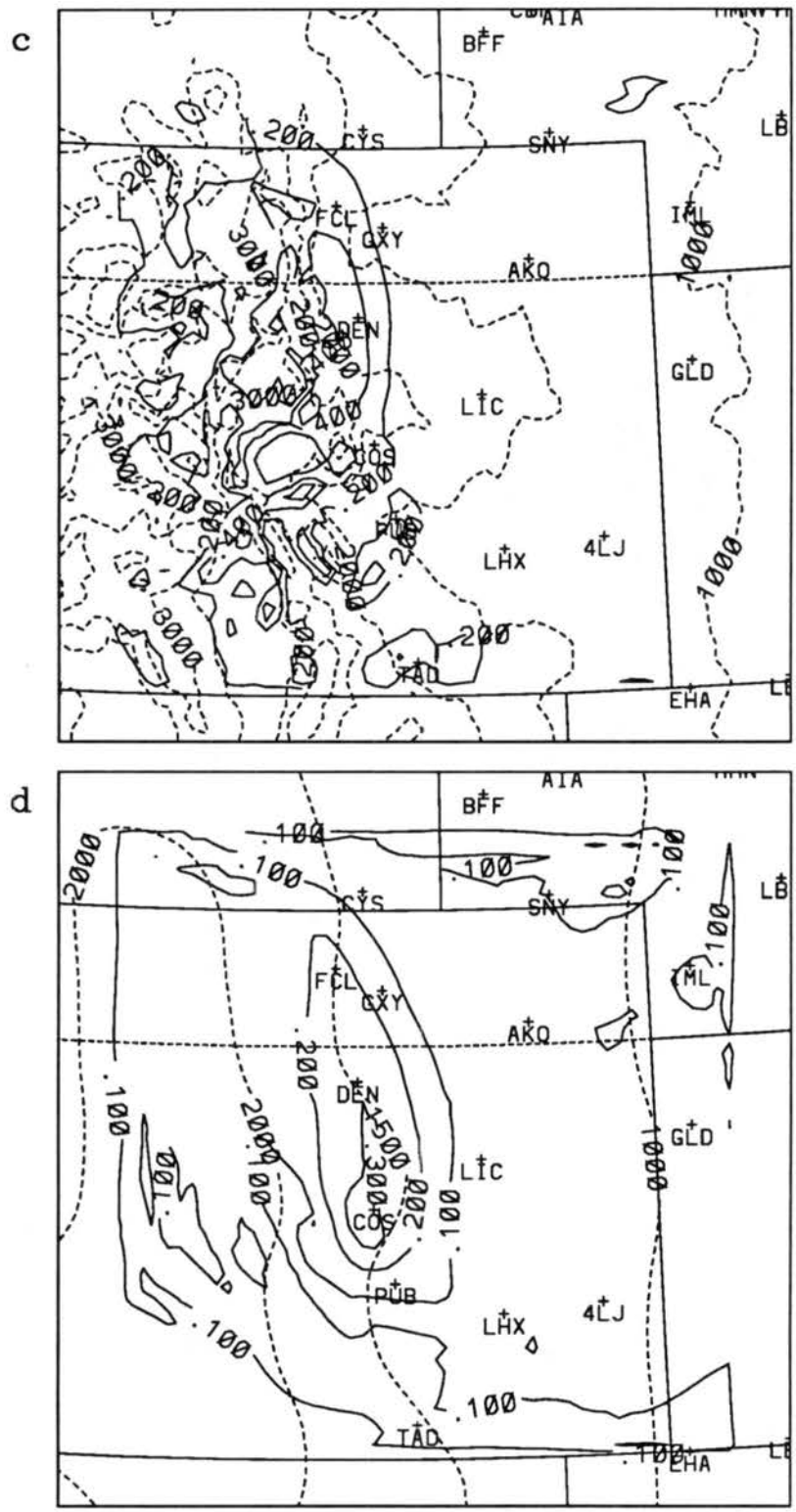

Figure 4.38: Continued: (c) the MAPS simulation (contour interval = 0.2 m s^{-1}) and (d) the MTOP simulation (contour interval = 0.1 m s^{-1}).

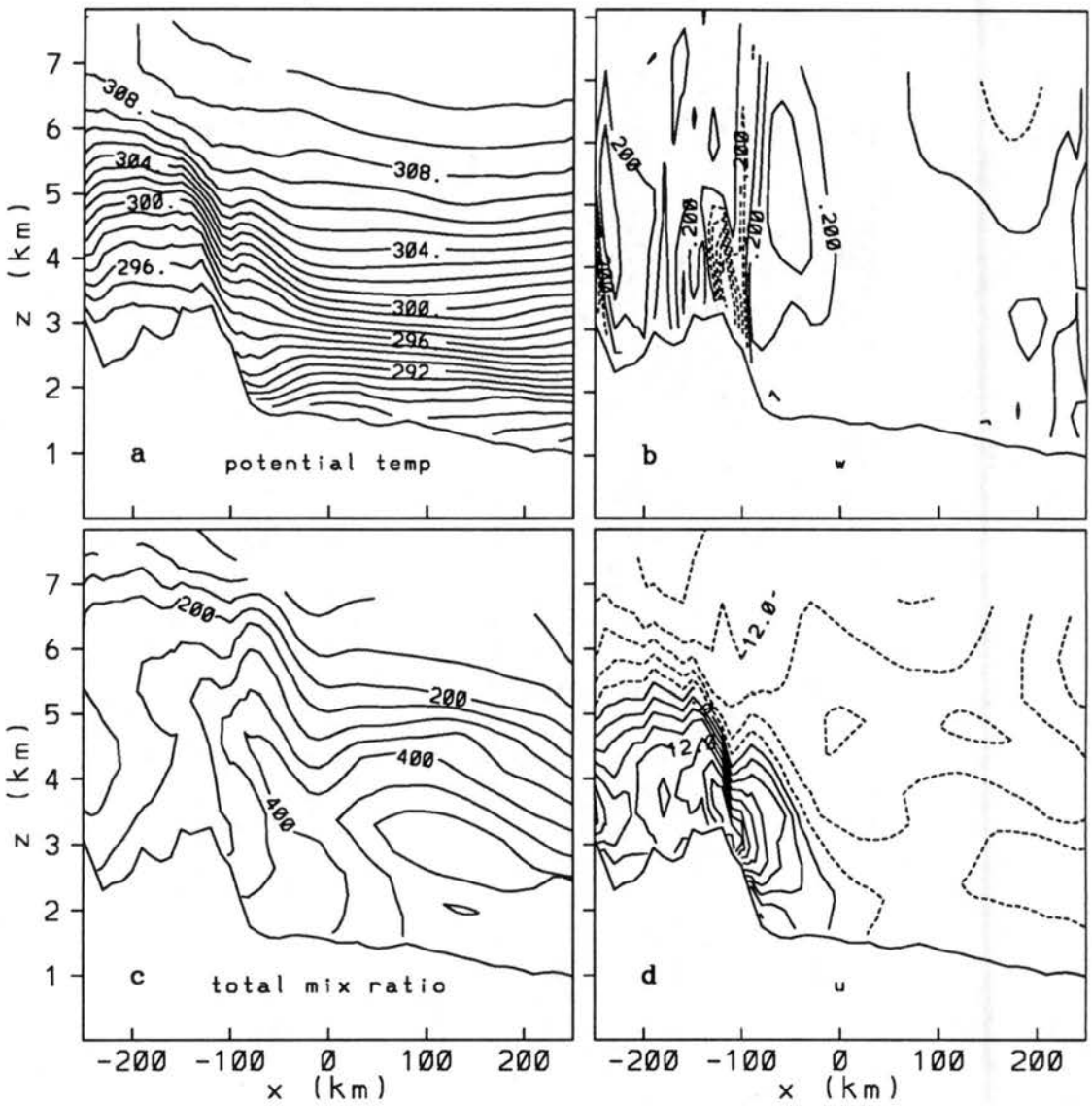

Figure 4.39: West-east vertical cross sections from RAMS (LAPS) 3 h forecast valid at 1500 UTC 7 January 1992 of (a) potential temperature (K), (b) upward vertical motion (m s^{-1}, contour interval = 0.2 m s^{-1}), (c) total mixing ratio (g kg^{-1}, contour interval = 0.5 g kg^{-1}, 100 units = 1.0 g kg^{-1}), and (d) u-component wind (m s^{-1}, contour interval = 3.0 m s^{-1}). Cross section location is represented by the solid line in Fig. 4.22a.

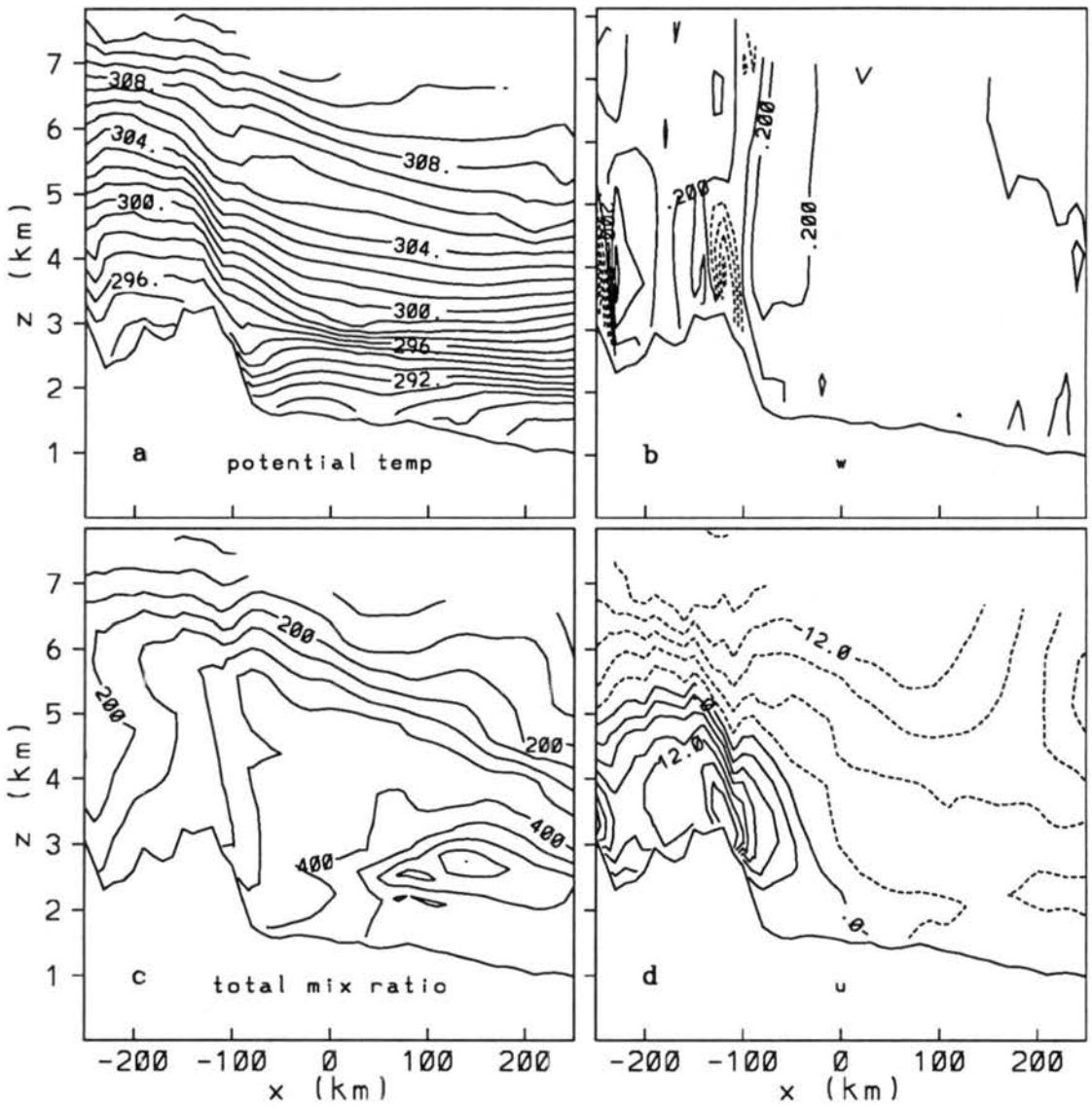

Figure 4.40: As in Fig. 4.39 except for the LBAL simulation.

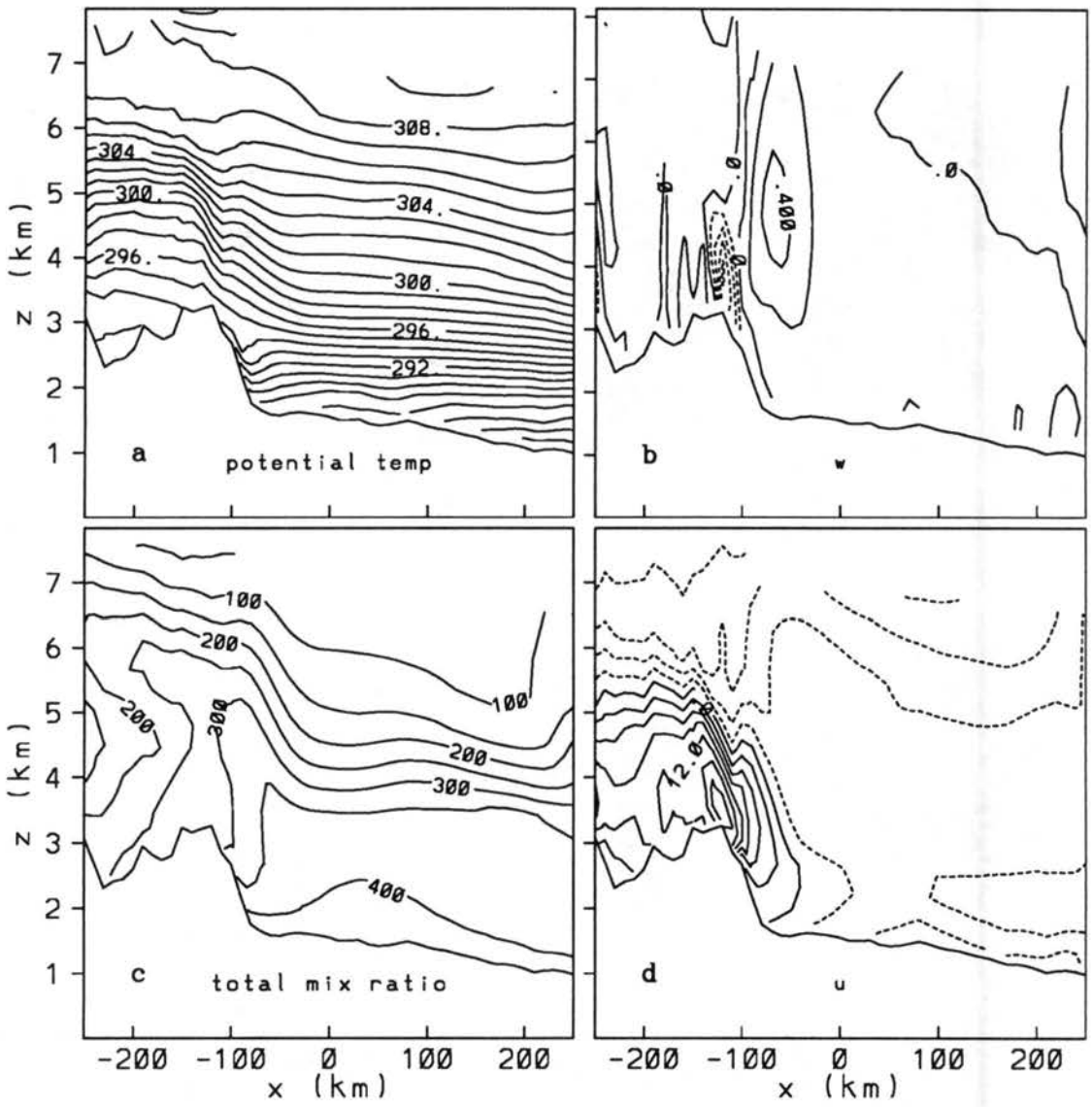

Figure 4.41: As in Fig. 4.39 except for the MAPS simulation.

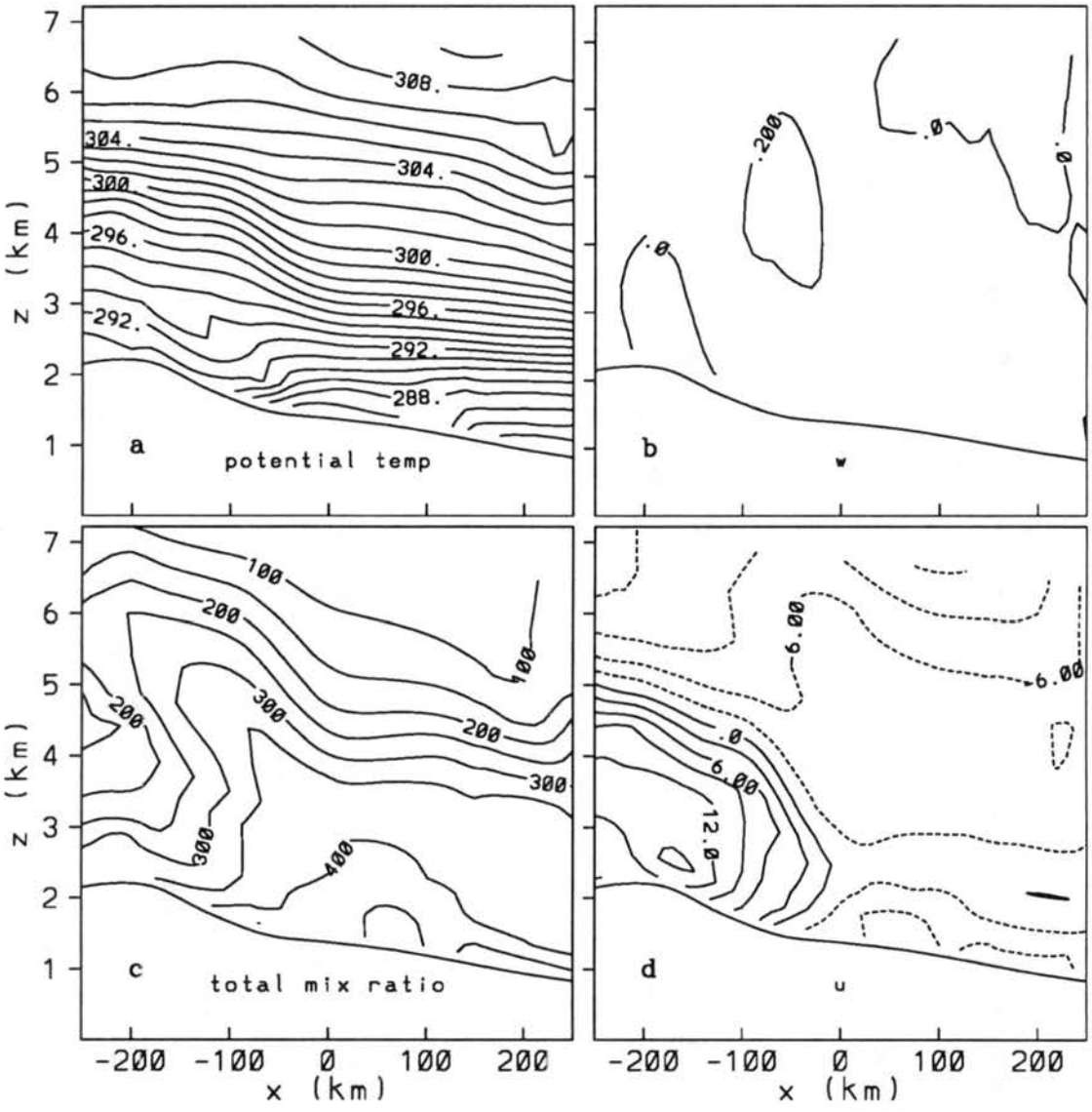

Figure 4.42: As in Fig. 4.39 except for the MTOP simulation.

forecast, the LFCS experiment uses lateral boundary conditions derived from the larger domain MAPS prediction. The primary objective of the LFCS experiment is to determine if the model prediction quality can be maintained using a real-time, operational configuration.

Examination of the LFCS model output suggests that prediction quality is maintained away from the lateral boundaries. The LFCS predictions of low-level winds (Fig. 4.43) indicate excellent agreement with the LSFC simulation in the vicinity of the Front Range while the evolution of the surface cyclone position degrades slowly with time. No detectable differences exist between the LFCS and LSFC forecast low-level winds at 3 h. The position and structure of the surface cyclone, the strong westerly flow over the mountains west of Denver, and the northeasterlies adjacent to the Front Range are all nearly identical. By 6 h, the structure of the LFCS surface cyclone is similar to the LSFC cyclone, but the position is displaced about 20 km west. Northeasterly flow continues adjacent to the Front Range while forecast wind speeds over the Continental Divide have increased to 30 m s^{-1}. The progression of the LFCS surface cyclone continues to evolve a little slower than the LSFC cyclone with a 9 h forecast position approximately 50 km west of the LSFC position, but actually closer to the LAPS 2100 UTC analyzed position (Fig. 4.16c). LFCS forecasts of strong westerly flow over the mountains, northeasterly flow adjacent to the Front Range, and the development of 20 m s^{-1} northwesterly flow in the Limon (LIC) vicinity all compare favorably with the LAPS analysis and surface observations. The LFCS surface cyclone position at 12 h is located approximately 30 km southwest of Goodland, KS (GLD) and is about 100 km south of the LAPS analyzed position (Fig. 4.16d). The operational forecast continues to realistically represent the northeasterly flow adjacent to the Front Range, the decrease in wind speed intensity over the mountains, and the significant northwesterly flow over the Plains.

LFCS forecasts of 500 mb height and wind (Fig. 4.44) appear similar in structure and evolution when compared to the LSFC predictions (Fig. 4.17). However, the magnitudes of the LFCS heights are too high with differences of 10-15 m at 3 h, increasing to 20-40 m by 12 h. The time series of LFCS winds near Platteville (Fig. 4.45) indicates close

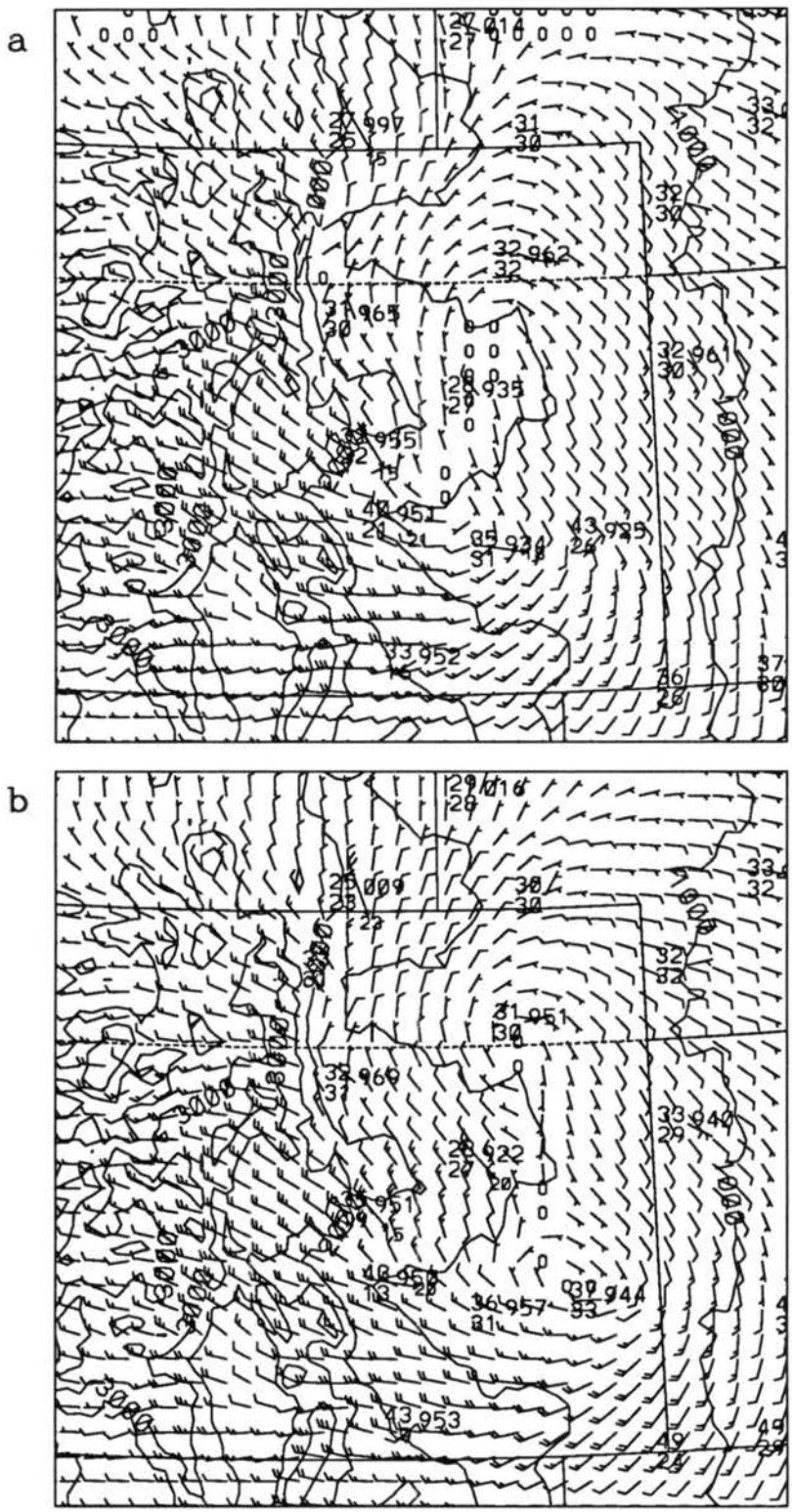

Figure 4.43: RAMS (LFCS) low-level (146 m AGL) wind (m s^{-1}) predictions and actual SAO reports at model validation time from (a) the 3 h forecast valid at 1500 UTC and (b) the 6 h forecast valid at 1800 UTC 7 January 1992.

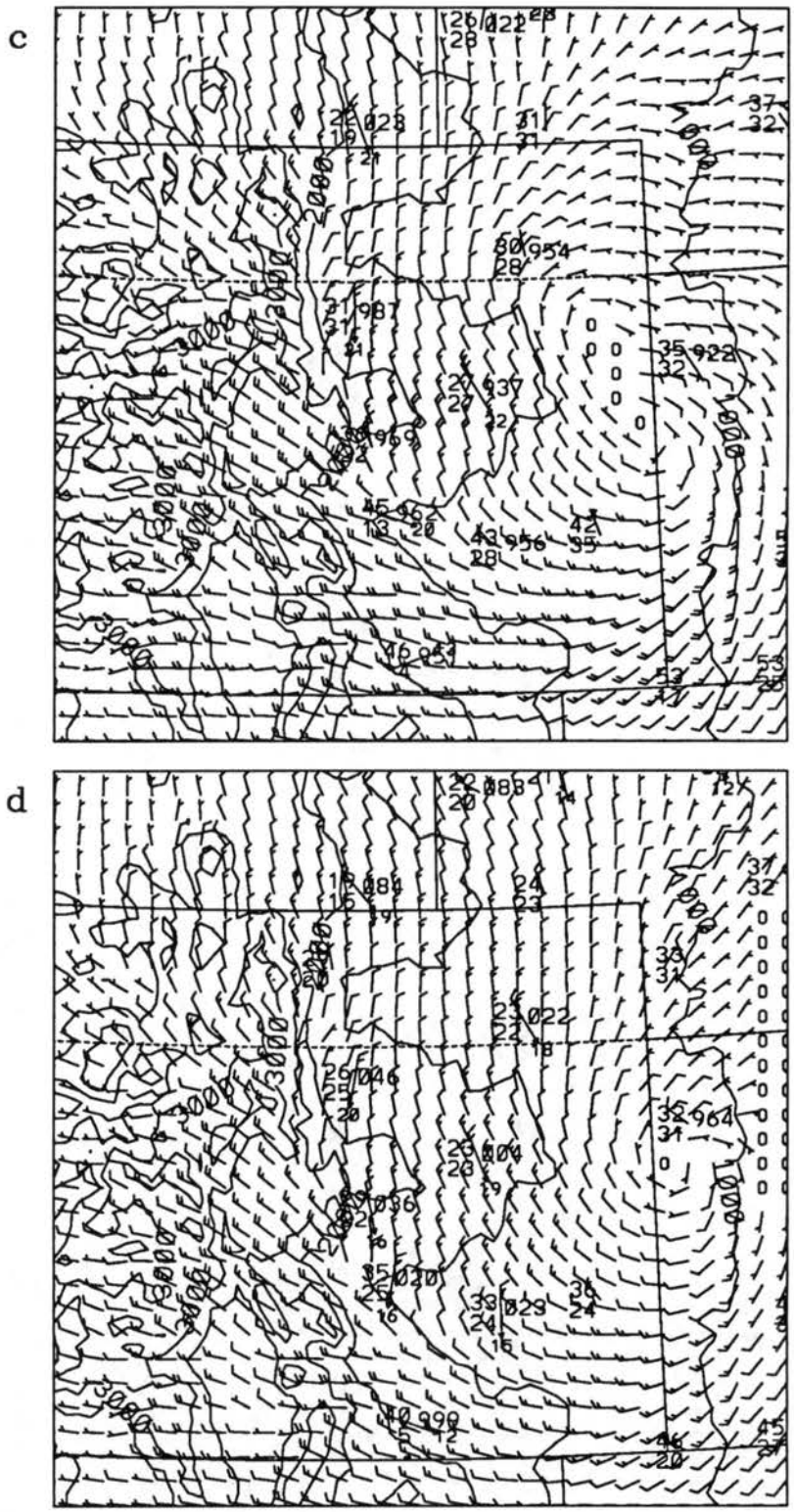

Figure 4.43: Continued: (c) the 9 h forecast valid at 2100 UTC 7 January and (d) the 12 h forecast valid at 0000 UTC 8 January 1992.

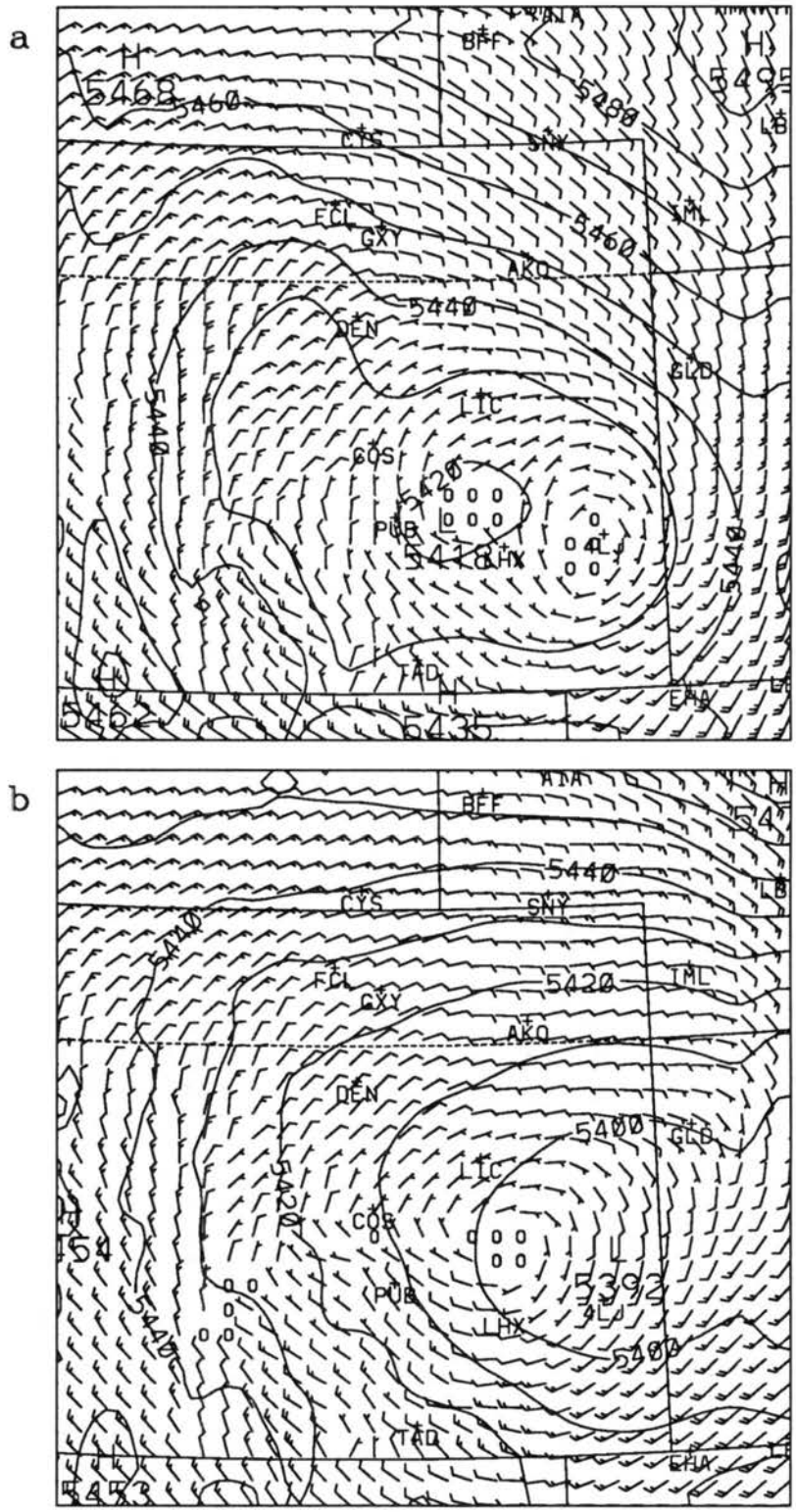

Figure 4.44: RAMS (LFCS) 500 mb height (m) and wind (m s^{-1}) predictions from (a) the 3 h forecast valid at 1500 UTC and (b) the 6 h forecast valid at 1800 UTC 7 January 1992.

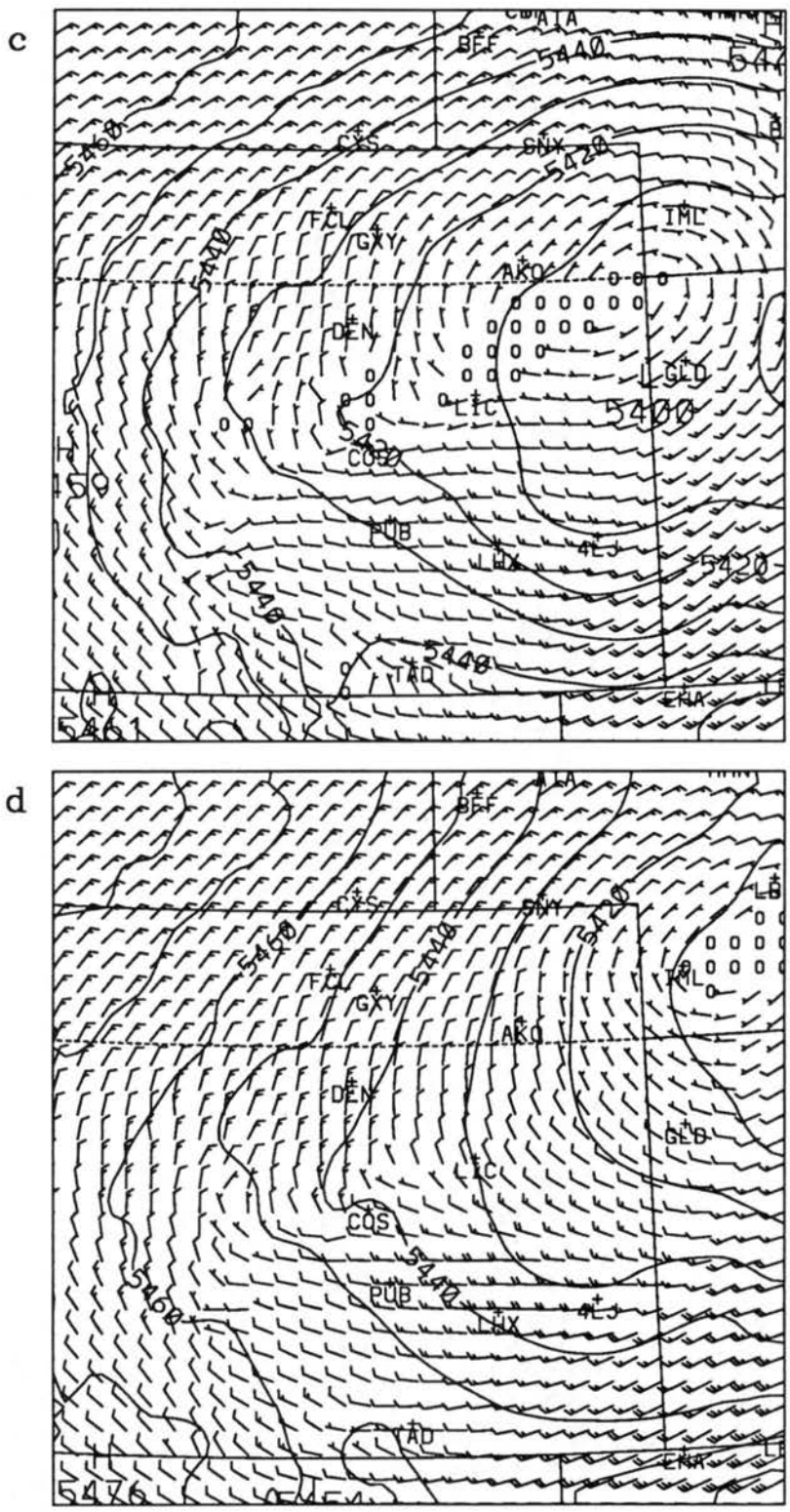

Figure 4.44: Continued: (c) the 9 h forecast valid at 2100 UTC 7 January and (d) the 12 h forecast valid at 0000 UTC 8 January 1992.

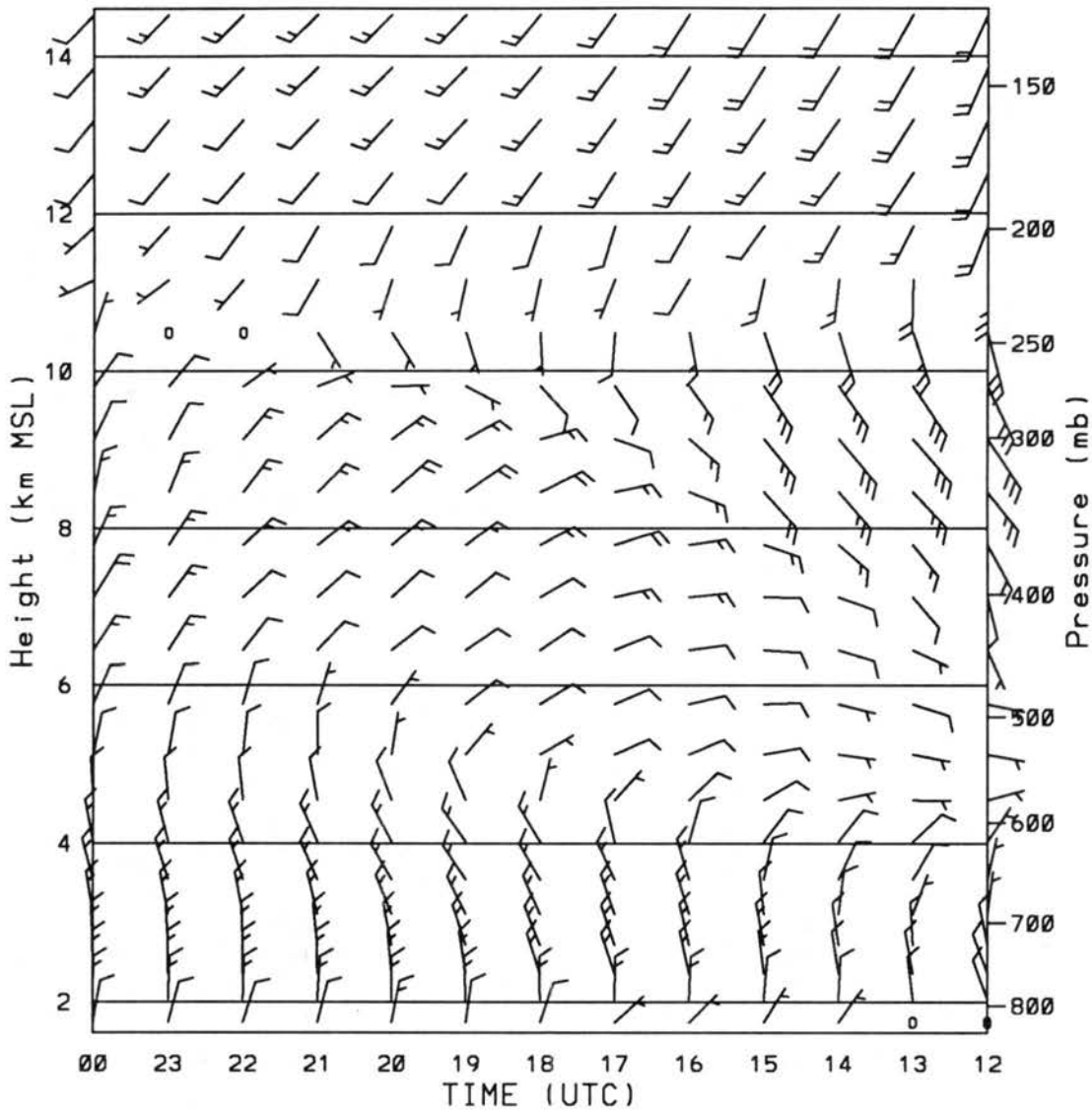

Figure 4.45: Time-height series of RAMS (LFCS) forecast wind (m s^{-1}) for the model grid point closest to Platteville, CO from the 0 to 12 h prediction valid at 1200 UTC 7 January through 0000 UTC 8 January 1992.

agreement to the LSFC time series (Fig. 4.19) with the prediction of the three layer wind regime as observed by the Platteville wind profiler (Fig. 4.13). LFCS predictions of maximum upward vertical motion (Fig. 4.46) agree closely with the forecasts from LSFC (Fig. 4.22) especially in the Ft. Collins to Denver region where the band of maximum ascent occurred. A comparison of vertical cross sections from LFCS (not shown) and LSFC also indicate a similar evolution of mass, wind, and moisture away from the lateral boundaries.

4.3 Model Validation

Quantitative RAMS model validation is composed of analyzing bias, RMS, and MRBP statistics generated from a comparison of LAPS analyses and model predictions. Since more observations are available at the surface than in the upper air, separate surface LAPS analyses are generated. The validation is completed for two categories: surface and upper air.

4.3.1 Surface

Hourly bias and RMS differences are computed for the seven RAMS simulations using all available surface observations compared to model predicted variables (Fig. 4.47). Statistics are generated for temperature, mixing ratio, dew point, wind speed, and wind direction. Note that about half of the observation locations are within the FSL mesonet area (Fig. 3.2). Hence, when evaluating the statistics, the results will be weighted towards the model performance in this region. Also, since the surface pressure data are not available for the SAO locations, mixing ratio measurements are only available from the FSL mesonet so the results for this variable are only valid for the mesonet area.

The temperature bias statistics show a diurnal trend that is probably attributed to the adjustment of model temperature to account for the differences in elevation between the surface observations and the lowest model sigma level. The winter morning boundary layer is typically very stable with isothermal or greater lapse rates. Hence, the warming of the model temperature by the standard lapse rate tends to create the warm model bias suggested in the morning forecasts. Conversely, the afternoon lapse rates are typically

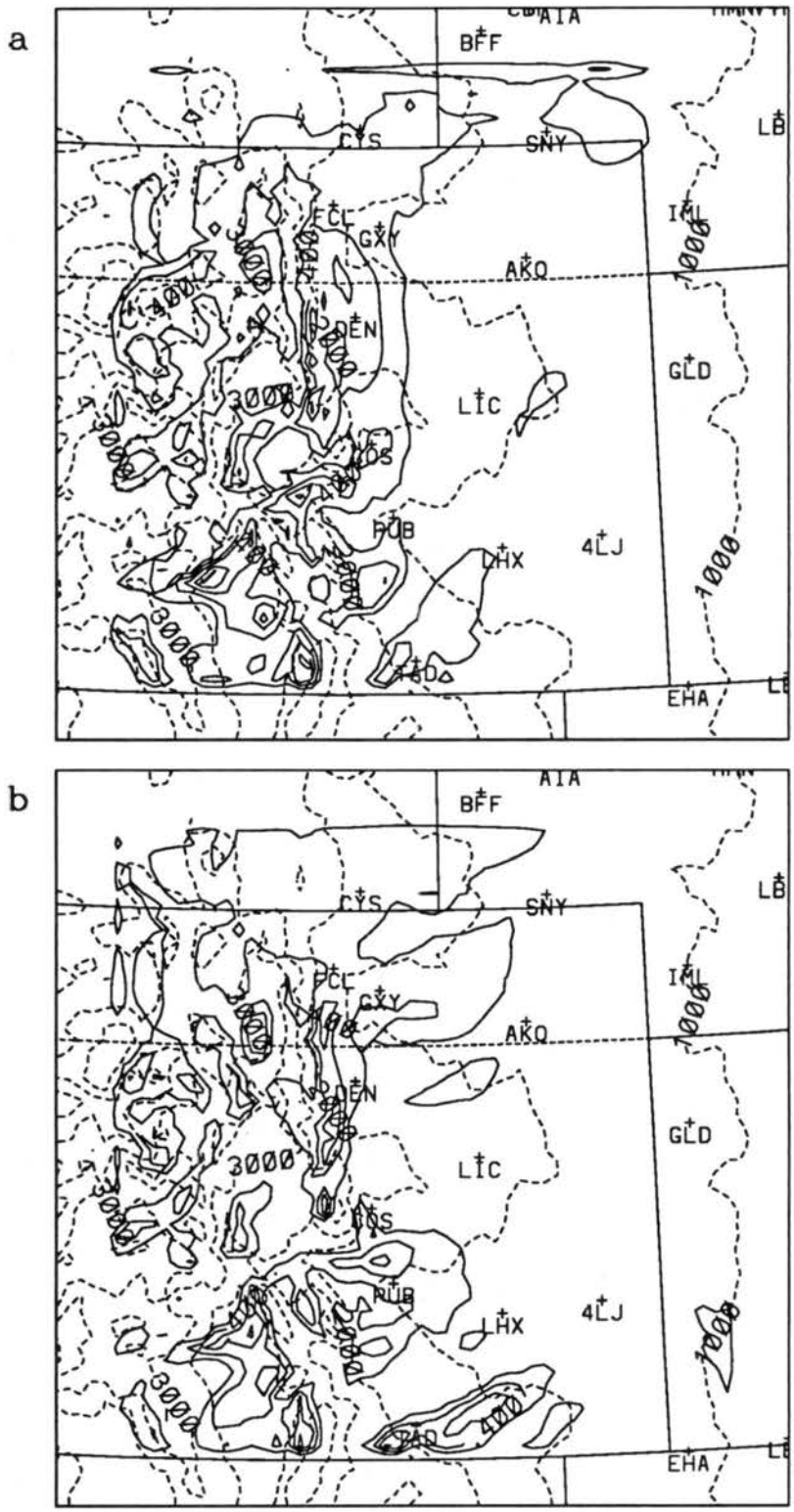

Figure 4.46: RAMS (LFCS) maximum upward vertical motion (m s^{-1}) predictions from (a) the 3 h forecast valid at 1500 UTC and (b) the 6 h forecast valid at 1800 UTC 7 January 1992. Contour interval is 0.2 m s^{-1}.

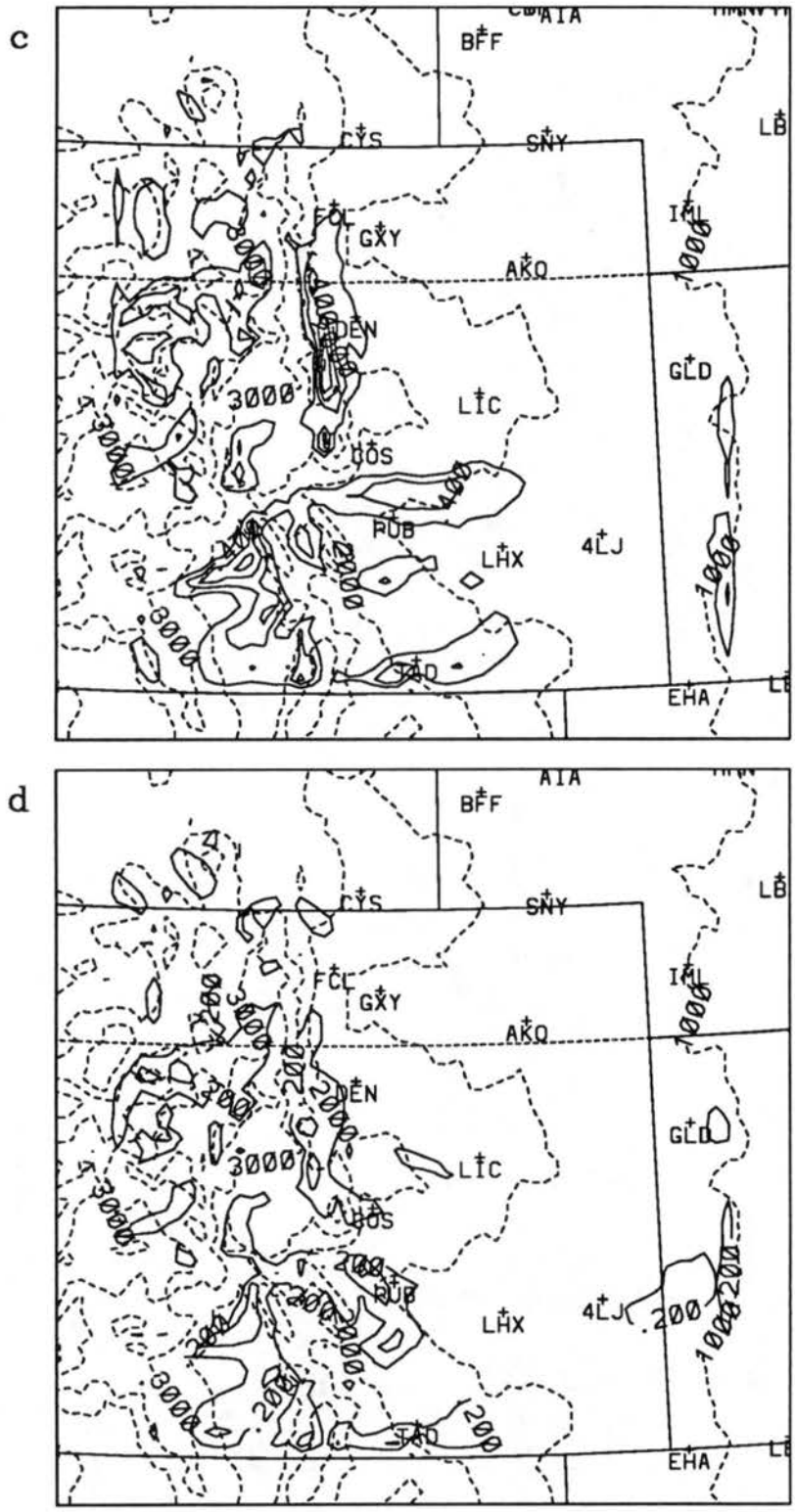

Figure 4.46: Continued: (c) 2100 UTC 7 January and (d) 0000 UTC 8 January 1992.

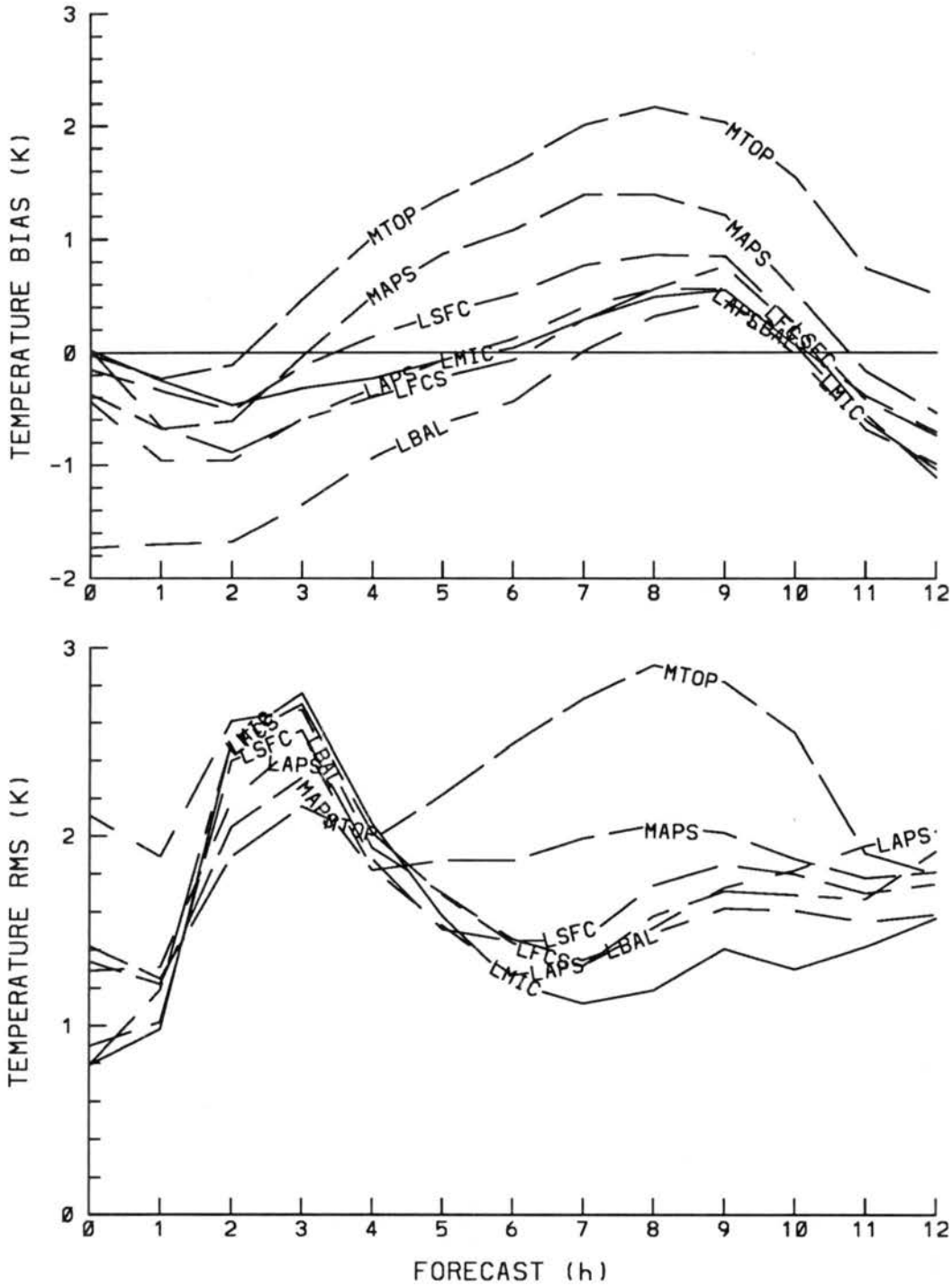

Figure 4.47: Hourly bias and RMS differences for the seven RAMS simulations compared to surface observations. Differences are computed by subtracting RAMS from the observations for (a) temperature (K).

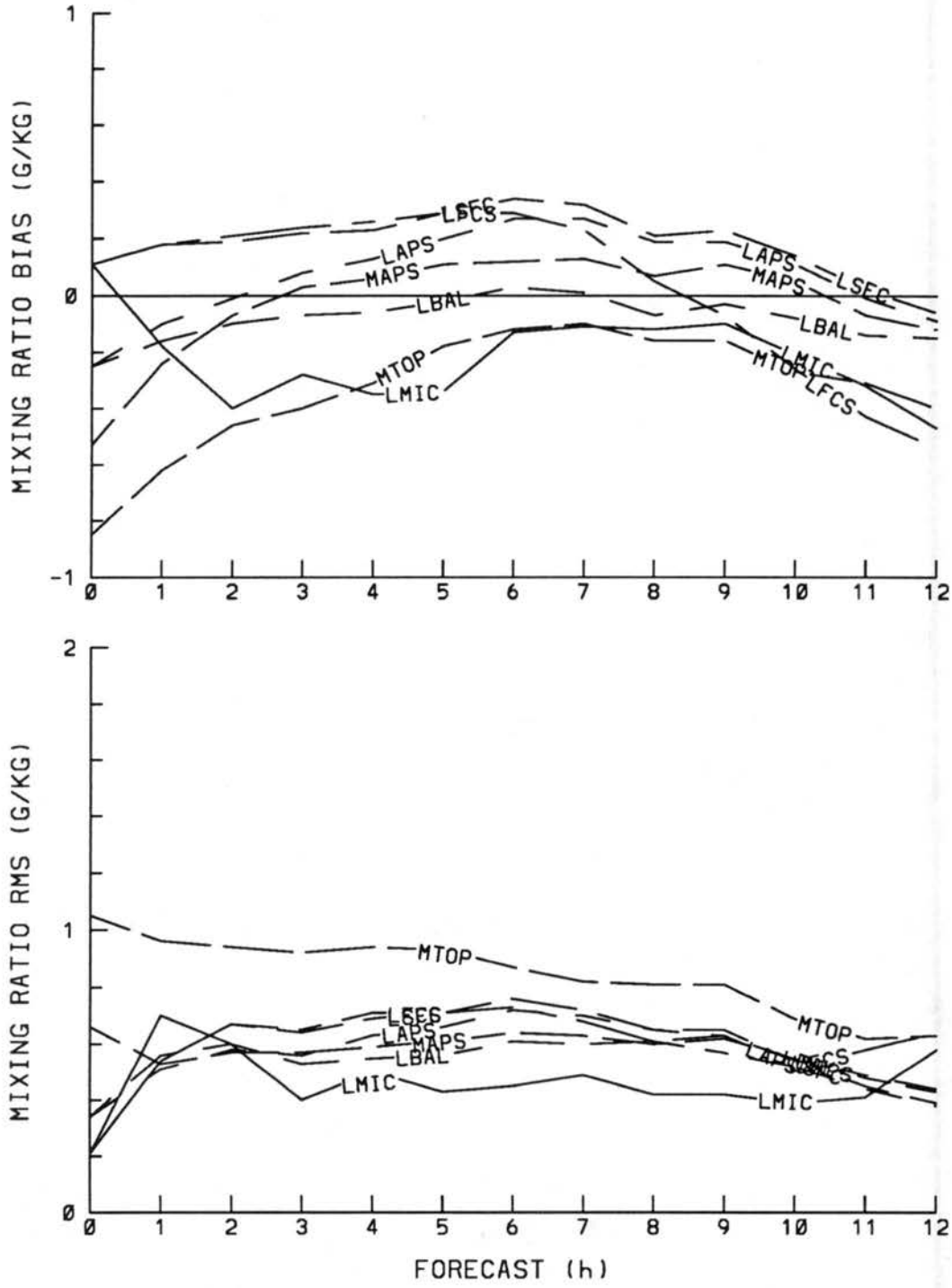

Figure 4.47: Continued: (b) mixing ratio (g kg^{-1}).

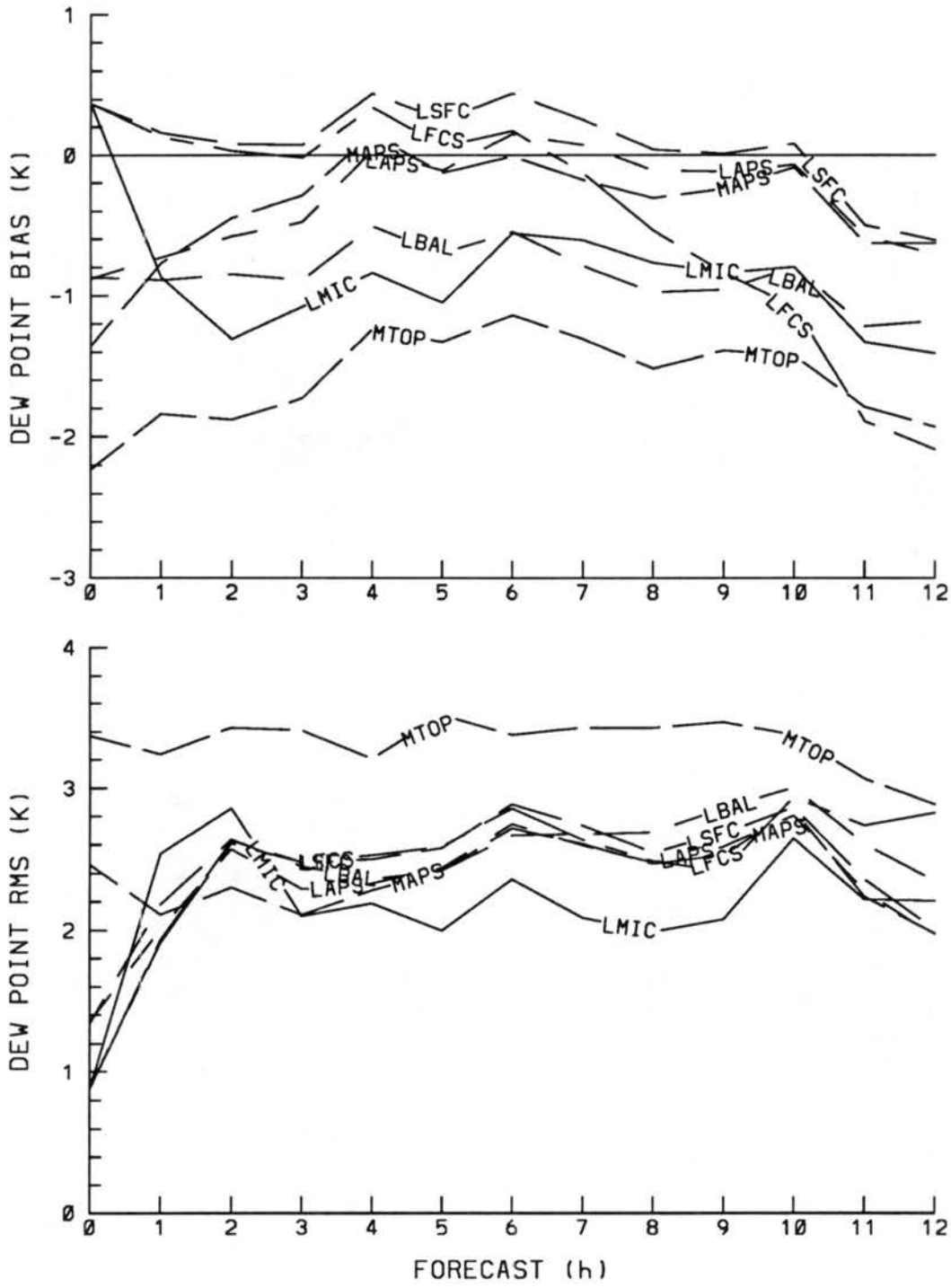

Figure 4.47: Continued: (c) dew point (K).

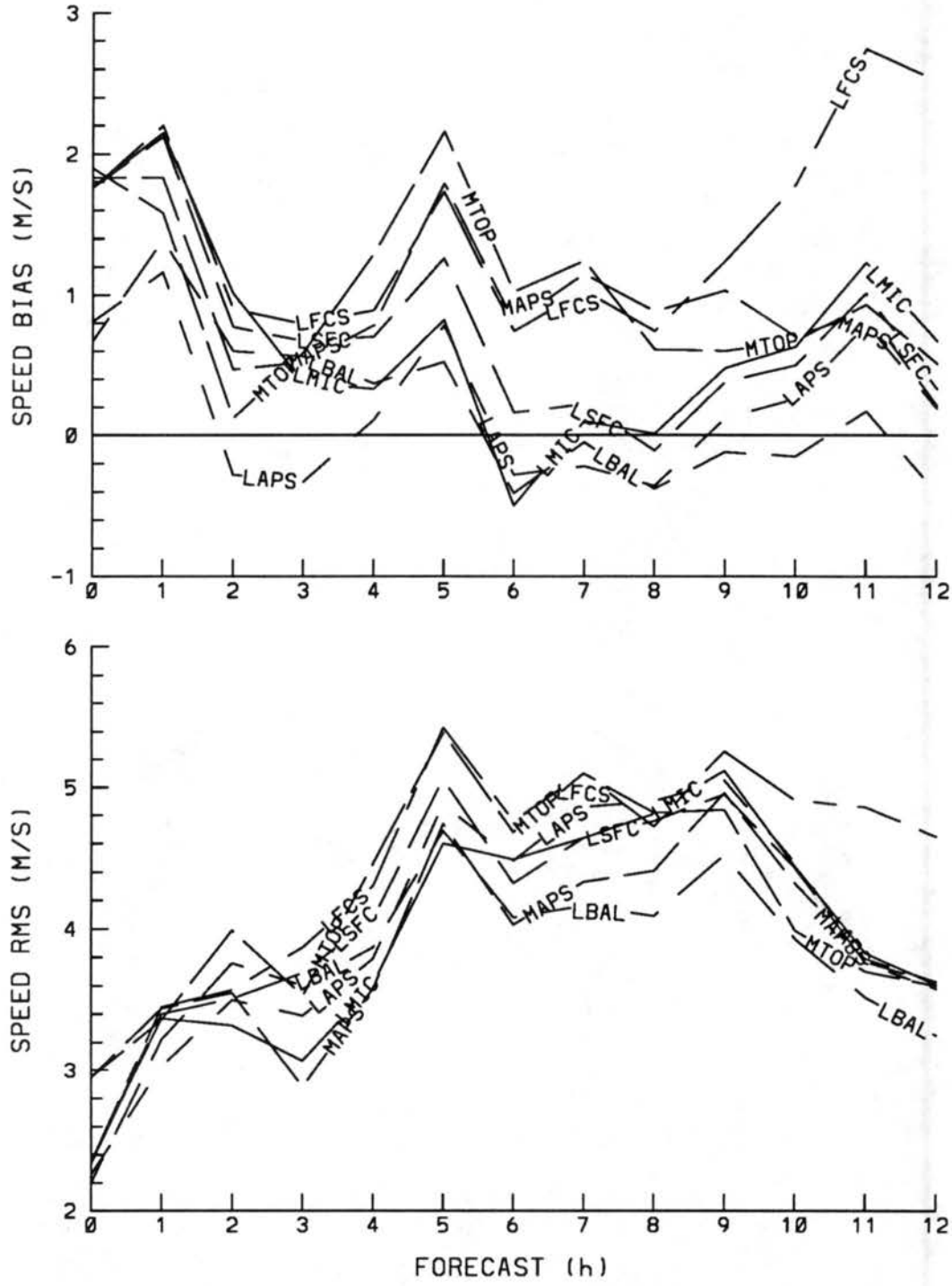

Figure 4.47: Continued: (d) wind speed (m s^{-1}).

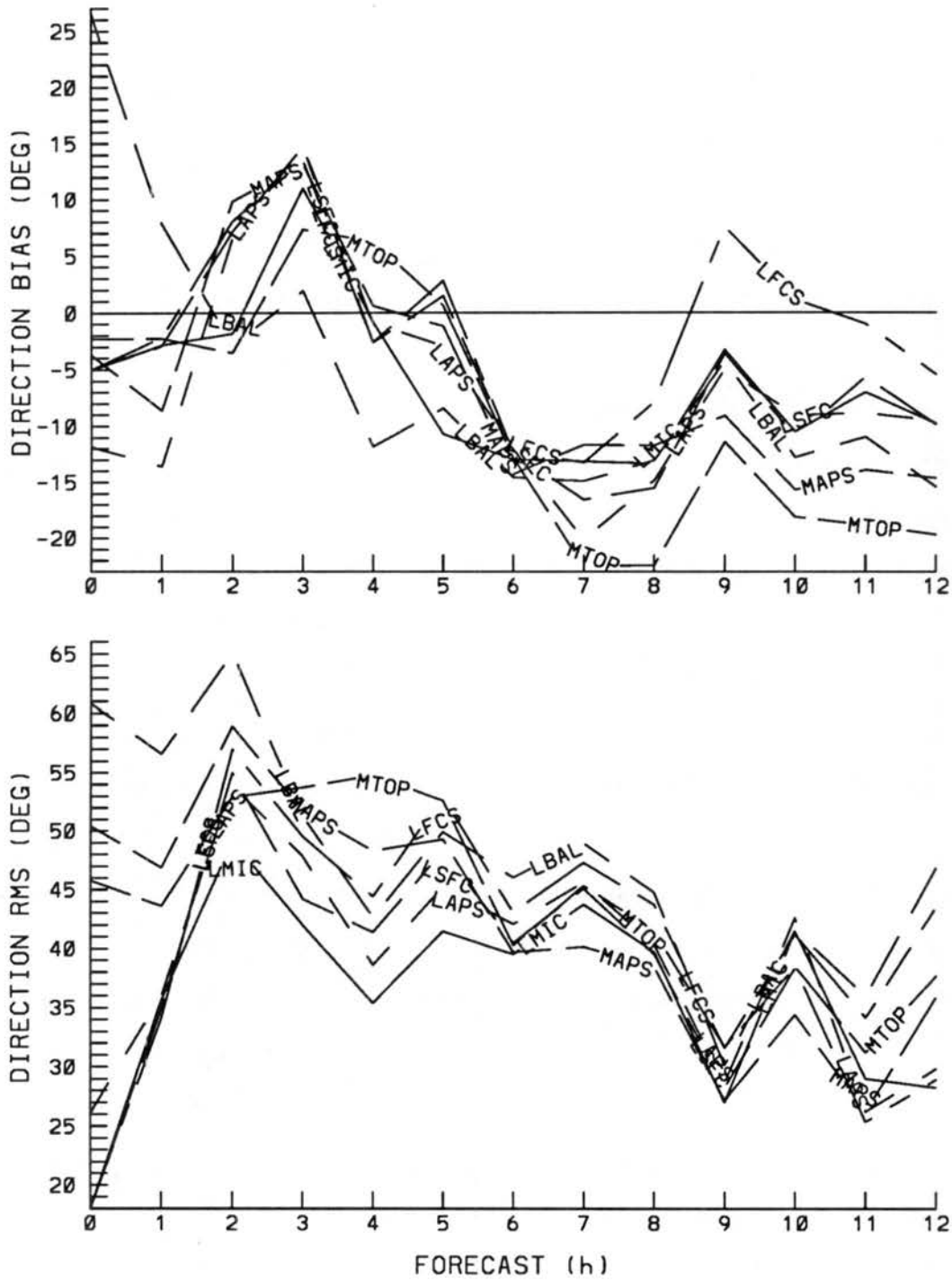

Figure 4.47: Continued: (e) wind direction (degrees).

smaller than the standard lapse rate which creates a cold model bias during the afternoon. With the exception of LBAL prior to 4 h, the temperature bias for the LAPS initialized simulations (LAPS, LBAL, LSFC, LMIC, and LFCS) remains less than 1 degree for the entire 12 h forecast. The MAPS initialized simulations (MAPS and MTOP) have greater temperature biases of up to 2 degrees and tend to be warmer than the LAPS initialized simulations. Both bias and RMS temperature results indicate little difference in performance between the LAPS initialized runs, slight improvement by the LAPS initialized runs over MAPS, and more significant improvement compared to MTOP.

LAPS, LBAL, LSFC, LFCS, and MAPS all appear relatively close in mixing ratio bias and RMS except after 10 h when LFCS starts to degrade. An improvement at most time periods is indicated by LMIC while MTOP is in less agreement with the observations. Similar results are indicated in the dew point statistics where RMS differences are between 2 and 3 degrees, except for MTOP which is about 0.5 degrees larger.

The wind speed bias indicates that the model predictions are generally weaker than the observations by around 1 m s^{-1}. Bias and RMS results show no run to be particularly better than another except for LFCS which degrades after 8 h and some small improvements by LBAL. Since the lowest model level is higher than the actual surface observation elevation, the model level winds experience less surface friction effects than the surface level winds. Hence, a negative bias in wind direction can be expected when comparing winds from these two levels. A correction to the model predicted wind direction is not applied to compensate for this effect. The wind direction bias statistics indicate a negative bias for all the simulations at most time periods. All the simulations performed nearly equivalently in the wind direction RMS results.

Hourly bias, RMS, and MRBP statistics are calculated for all seven RAMS simulations using LAPS gridded surface analyses compared to RAMS predictions of temperature, mixing ratio, wind speed, and wind direction (Fig. 4.48). The advantage of the gridded analysis comparison is that the statistical results are representative of the whole domain. However, the method assumes that the LAPS gridded analyses represent the actual surface conditions which is not a good assumption in data sparse areas.

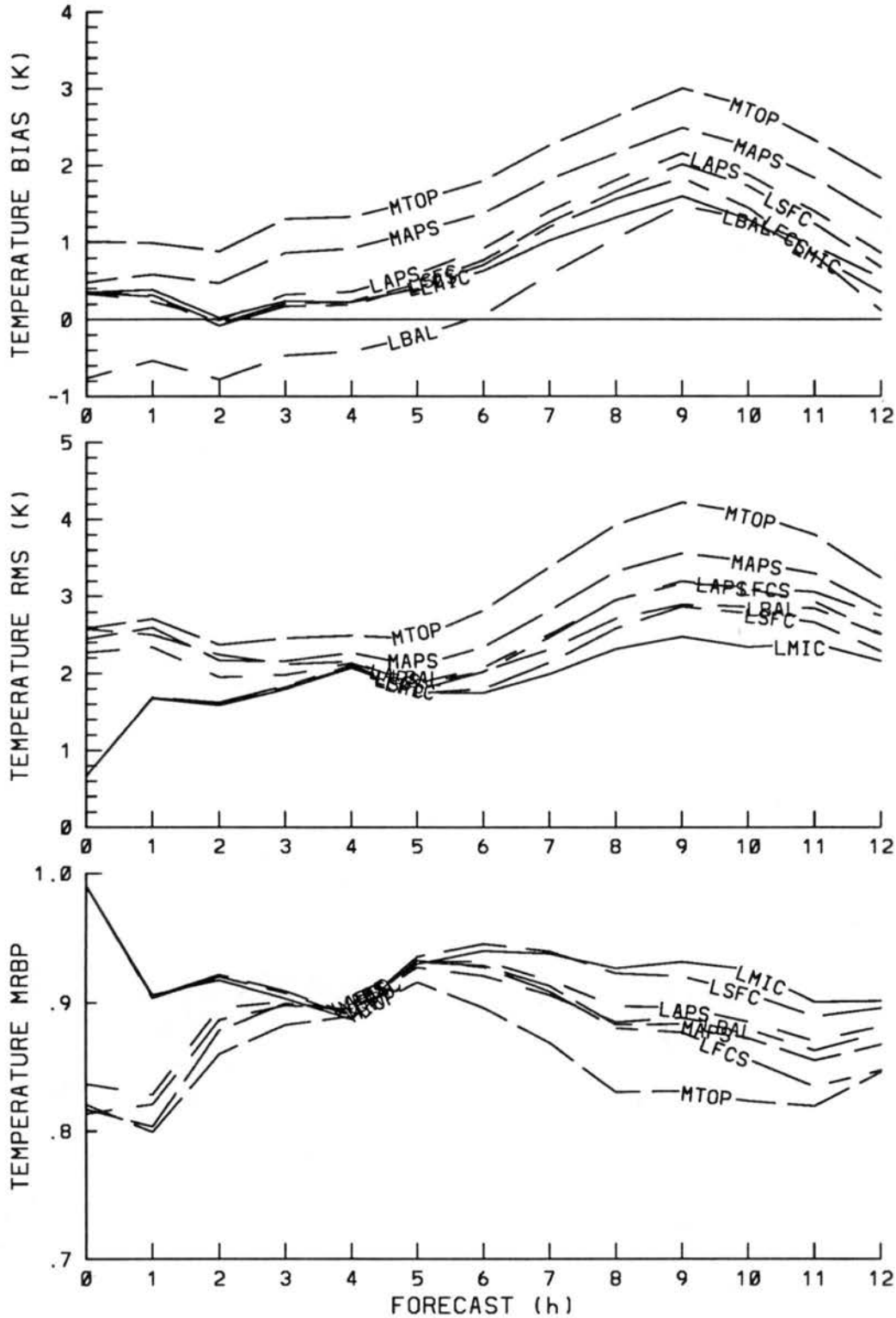

Figure 4.48: Hourly bias, RMS, and MRBP statistics for the seven RAMS simulations compared to LAPS gridded surface analyses. Differences are computed by subtracting RAMS from LAPS for (a) temperature (K).

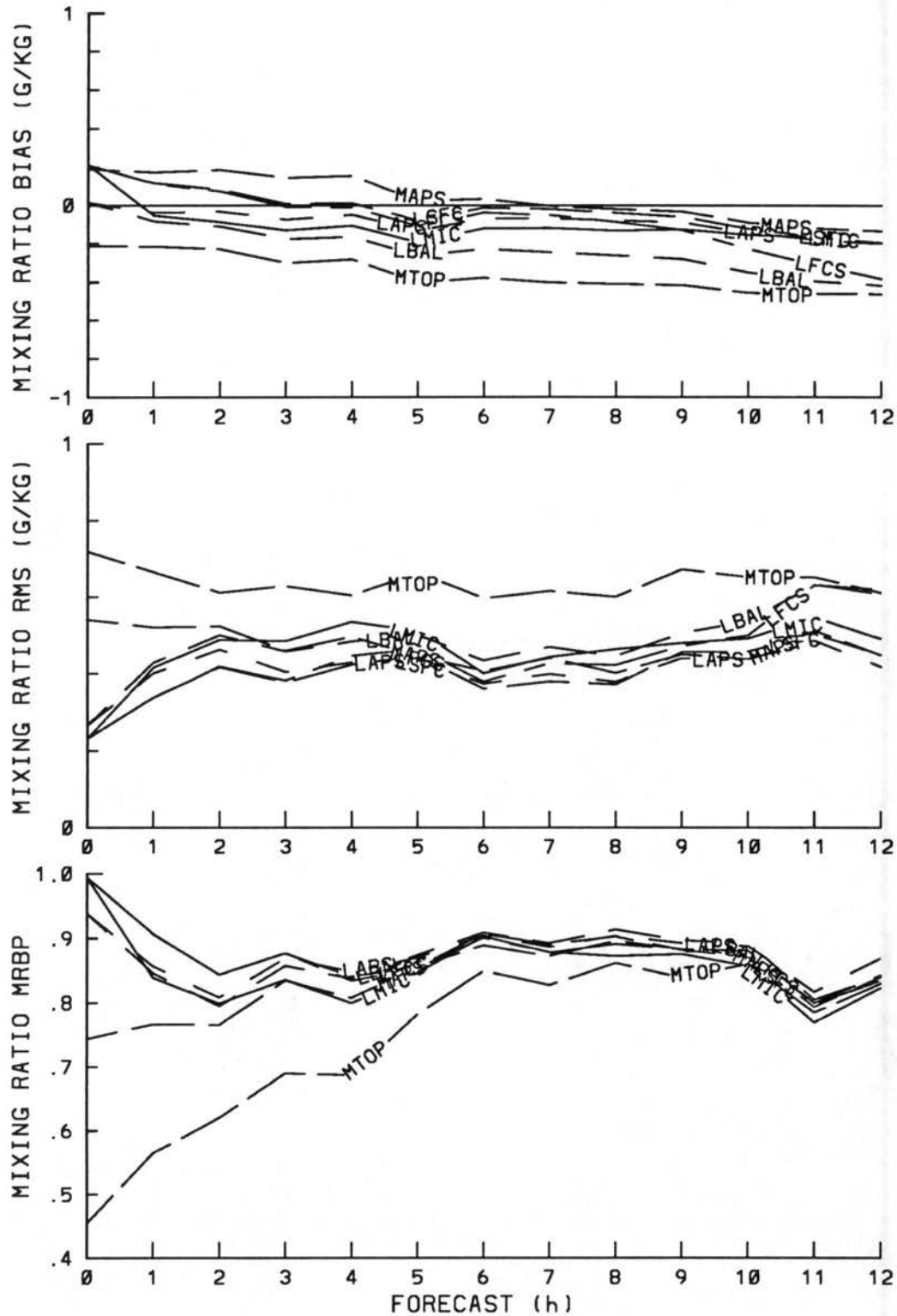

Figure 4.48: Continued: (b) mixing ratio (g kg^{-1}).

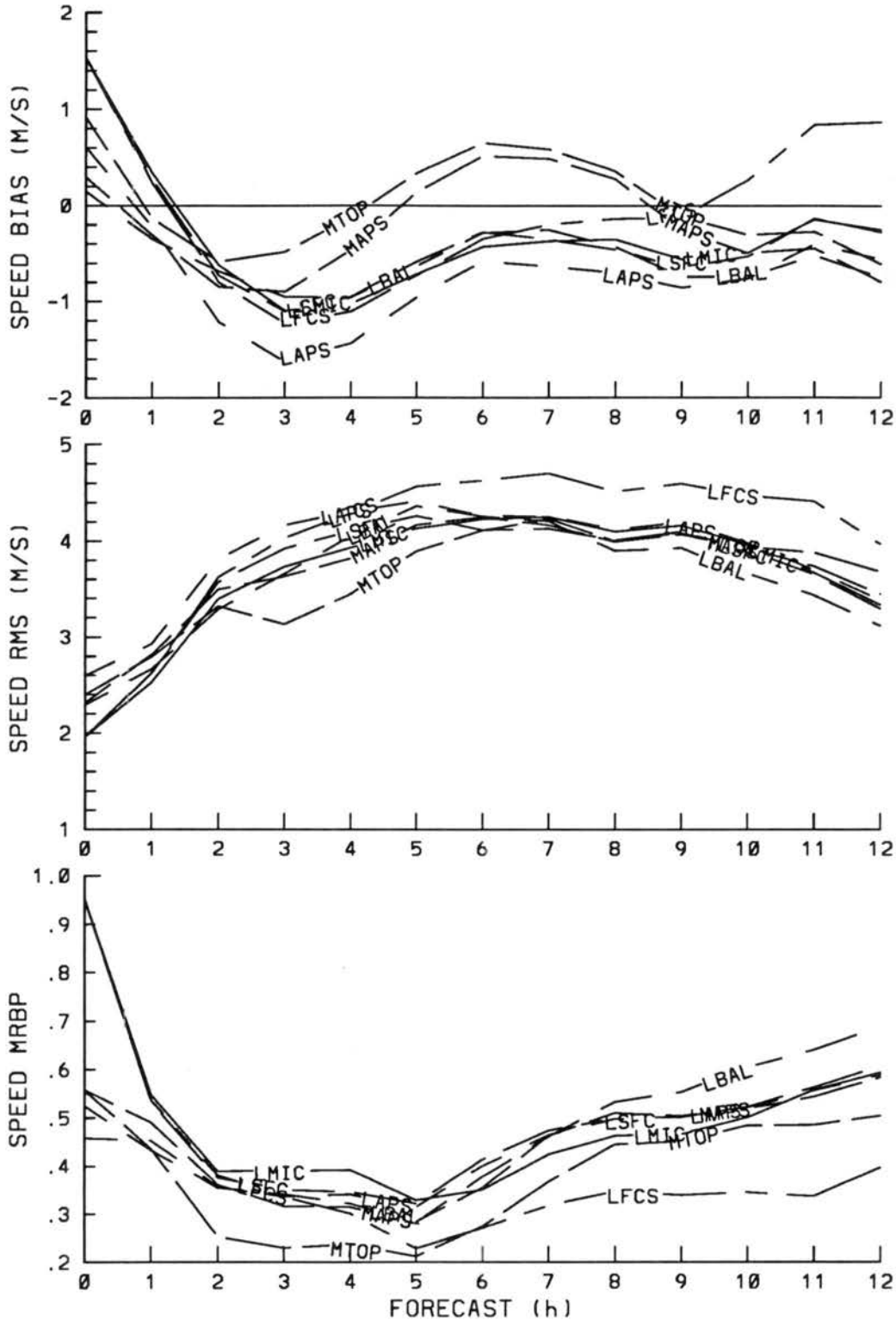

Figure 4.48: Continued: (c) wind speed (m s^{-1}).

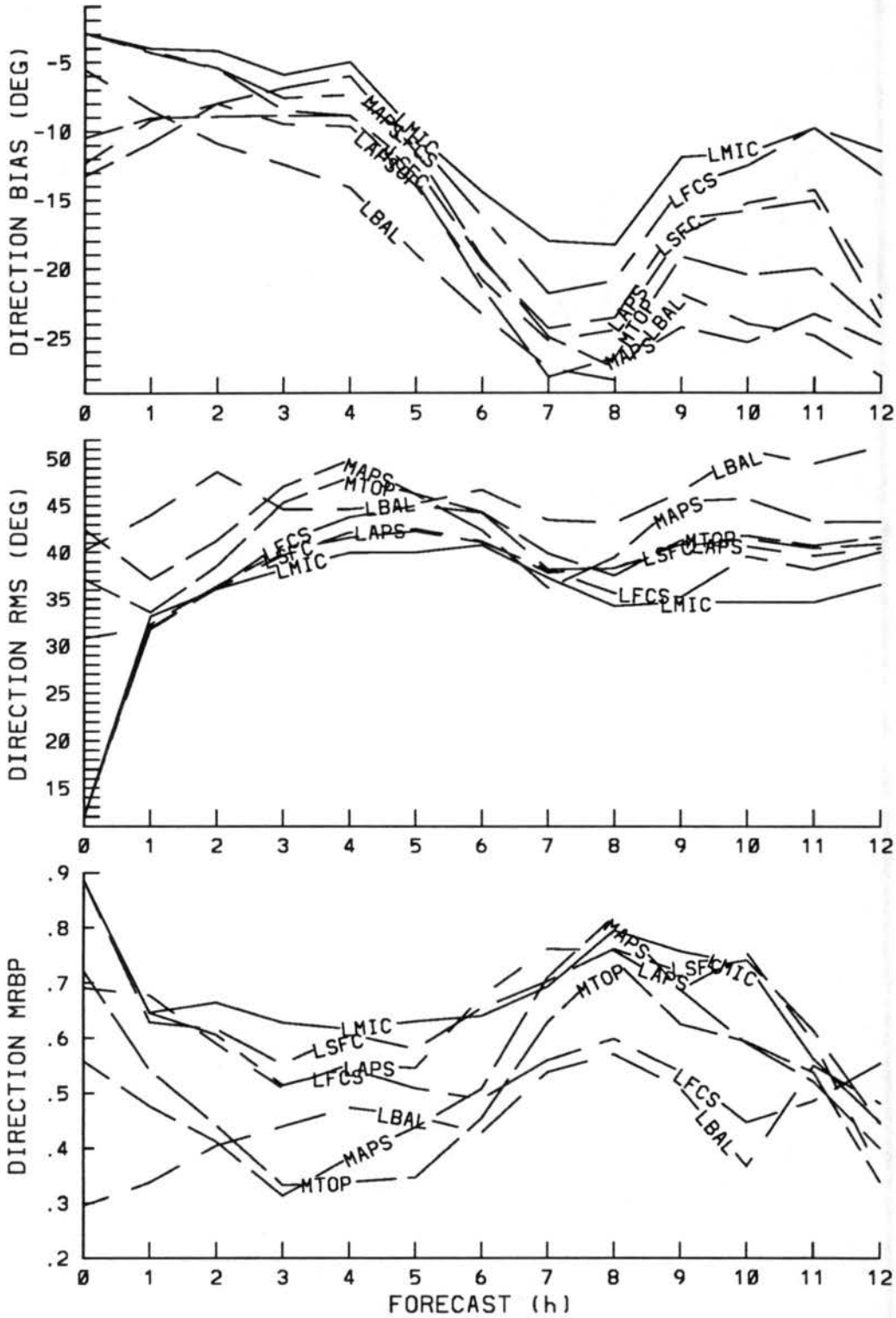

Figure 4.48: Continued: (d) wind direction (degrees).

The temperature bias results are similar to the observations with the same diurnal trend, except the predictions are nearly 1 degree cooler. RMS results are mostly between 2 and 3 degrees, somewhat larger than the observational results, and they suggest better performance by the LAPS initialized runs over MAPS and MTOP. The MRBP temperature agreement measure is very good with values around 90%. Again, the LAPS initialized runs have outperformed MAPS and MTOP except for LFCS which degrades after 8 h. The model predictions show a slight moist bias of around 0.1 g kg^{-1} when compared to the LAPS analyses. RMS and MRBP statistics are close for all the simulations with an agreement measure in the range of 80 to 90%, except for MTOP which shows lower agreement.

In contrast to the observational comparison, the gridded comparison indicates the model predicted wind speeds to be mostly stronger than the LAPS analyses. RMS wind speed differences are between 2 and 3 m s^{-1} in the early forecasts and rise to about 4 m s^{-1} after 5 h. The wind speed agreement measure is lower than the temperature and moisture agreement with values mostly in the 20 to 60% range. The results show LFCS agreement to fall below the other runs after 4 h. The wind direction bias is negative as expected when considering the differences in elevation between the lowest model level and the surface. RMS wind direction differences are larger (~40 degrees) with LMIC showing slightly better agreement and LBAL showing slightly worse performance than the other simulations.

4.3.2 Upper air

Upper air model validation statistics are computed by comparing the model forecast with the corresponding LAPS three-dimensional analysis on each model sigma level and at 500 mb. The LAPS system incorporates all available local data sources with conventional data sources in an attempt to resolve mesoscale (down to 40 km) features using a 10 km horizontal grid interval. However, even with the additional local data sources, the resolution of the upper air observations is not nearly sufficient to fully support the 40 km grid resolution used by LAPS and RAMS. Hence, the model predicted fields will contain higher resolution information than the LAPS gridded analyses resulting in an unfair statistical

comparison (Thompson 1993). If the model predicts a mesoscale feature that is not resolvable by the analysis, it may appear that the model performed poorly, when in fact the model may have correctly predicted the feature. In other words, the model is penalized for generating any features with resolution greater than the observations, irregardless of the accuracy.

MRBP agreement measure statistics of temperature, perturbation Exner function (π^*), relative humidity, u, v, and total wind speeds, and absolute vorticity are illustrated in Figs. 4.49 and 4.50 for the 6 and 12 h RAMS forecasts. The mass variables (temperature and π^*) performed best, followed by wind, and then moisture, similar to results found by Thompson (1993) using RAMS initialized with MAPS data. Since moisture typically exhibits the greatest amount of atmospheric spatial variability, the problem of insufficient observations affects this comparison the most. Only minor variations in agreement measure are observed in the four LAPS initialized simulations (LAPS, LSFC, LBAL, LMIC). Temperature and perturbation Exner function agreement measures are mostly greater than 90%. Relative humidity statistics indicate good agreement (~90%) near the surface, less agreement around sigma levels 6-8 (~600 mb), increased agreement up to the tropopause, and no agreement in the vicinity of the tropopause (sigma levels 18-20). U- and v-component wind speeds show mostly greater than 80% agreement except around sigma level 13 (~400 mb) where the v-component shows less agreement. Total wind speed agreement reflects the combined performance of u and v. The agreement measures at 500 mb are all close to their respective values on sigma surfaces except for temperature which is consistently lower, probably due to interpolation from sigma to isobaric levels.

The true forecast (LFCS) shows close agreement with the four LAPS simulations indicating that the forecast lateral boundary conditions have had only minimal adverse affects at 6 h. The MAPS simulation indicates relatively close performance to the four LAPS runs in wind and moisture, however, MAPS perturbation Exner function shows less agreement than LAPS. The qualitative results from the sensitivity simulations suggested that LAPS moisture predictions contained more mesoscale detail than the MAPS forecasts. Evidently, the number of upper air observations is insufficient to verify this. More

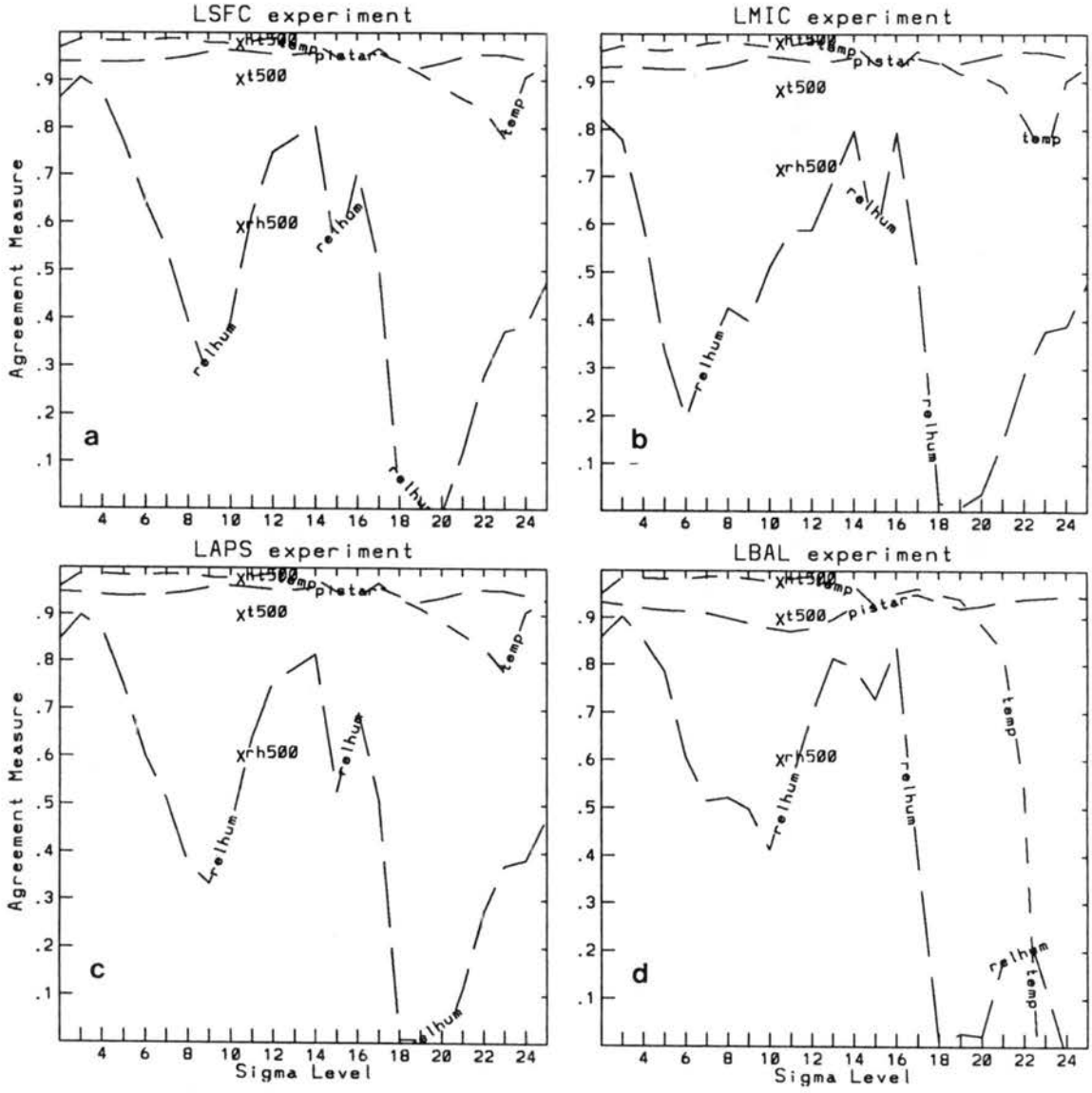

Figure 4.49: Upper air MRBP statistics for the seven RAMS simulations and the MAPS forecast compared to LAPS gridded upper air analyses. Thermodynamic variables from the 6 h forecasts valid at 1800 UTC 7 January 1992 are presented for (a) LSFC, (b) LMIC, (c) LAPS, and (d) LBAL simulations.

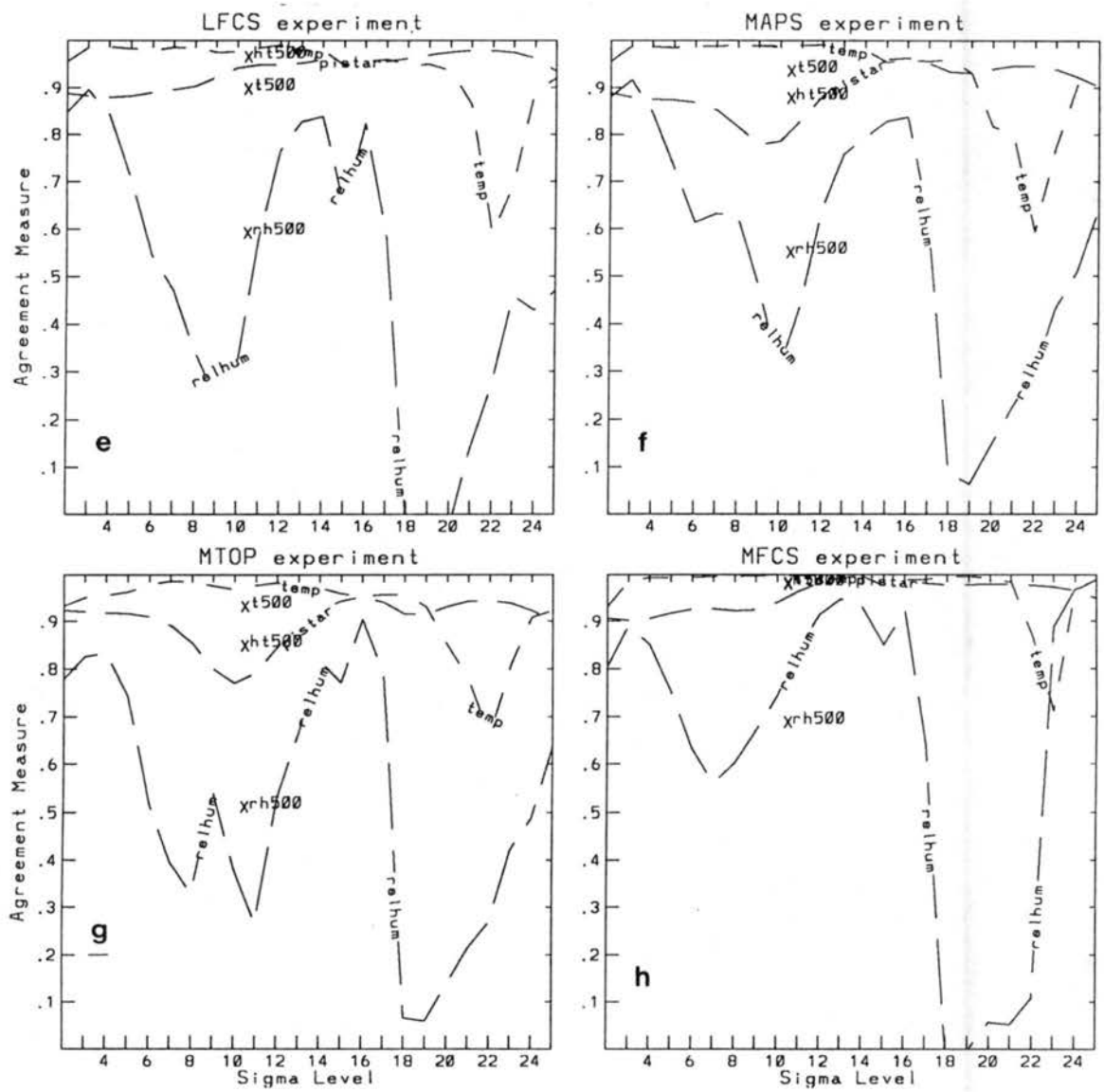

Figure 4.49: Continued: (e) LFCS, (f) MAPS, (g) MTOP, and (h) MFCS simulations.

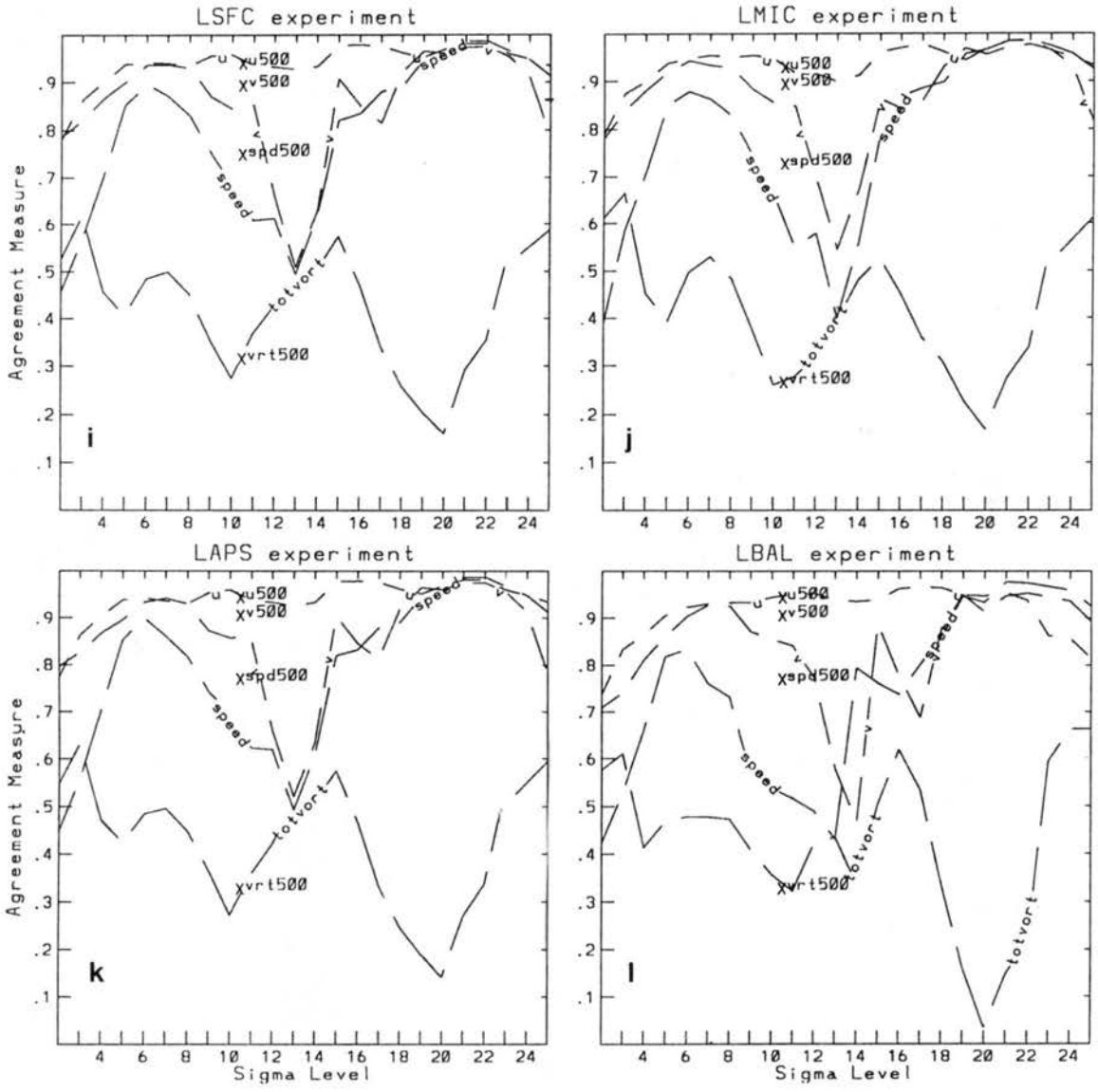

Figure 4.49: Continued: Wind variables presented for (i) LSFC, (j) LMIC, (k) LAPS, and (l) LBAL simulations.

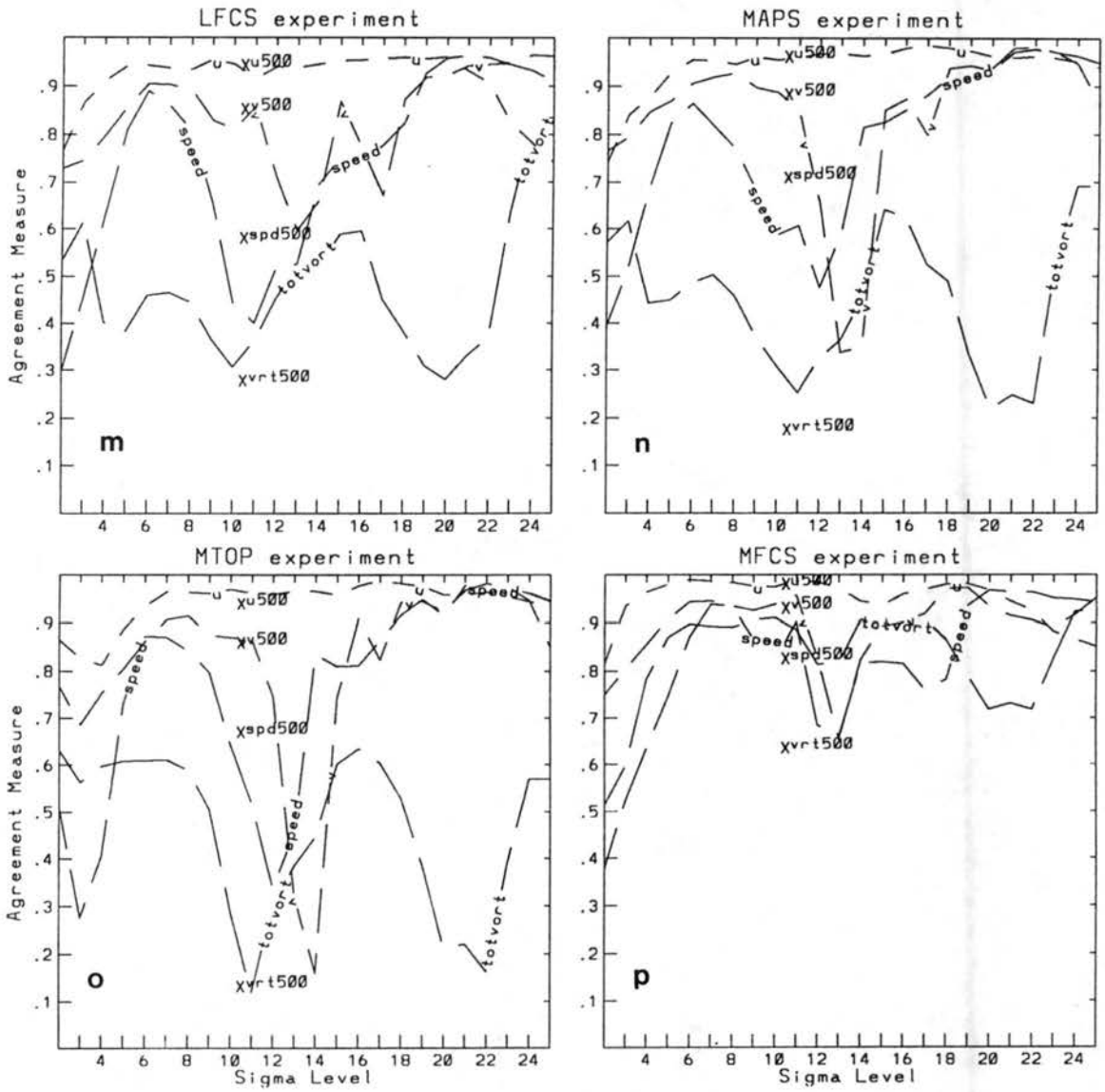

Figure 4.49: Continued: (m) LFCS, (n) MAPS, (o) MTOP, and (p) MFCS simulations.

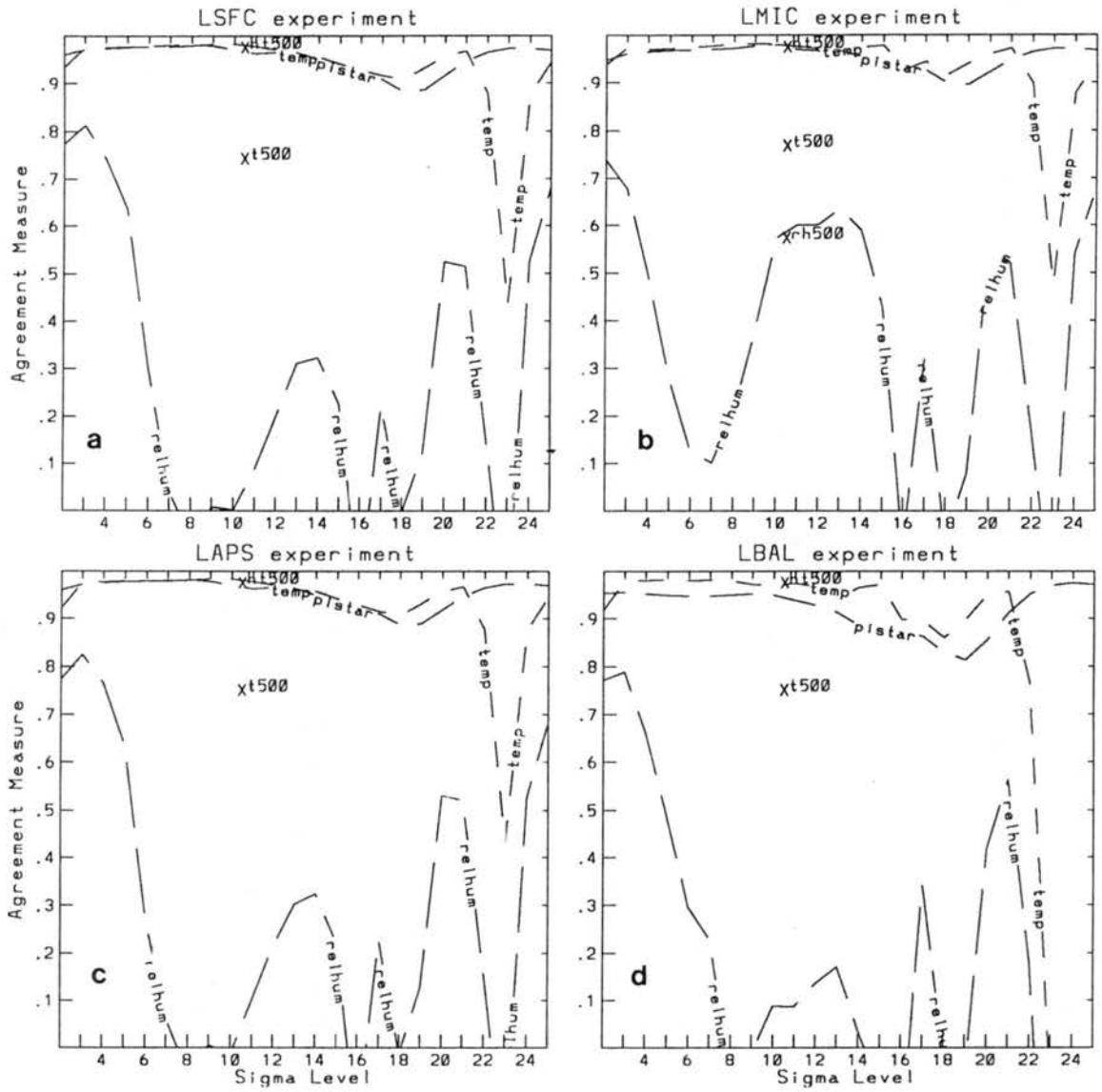

Figure 4.50: As in Fig. 4.49 except for 12 h forecast valid at 0000 UTC 8 January 1992.

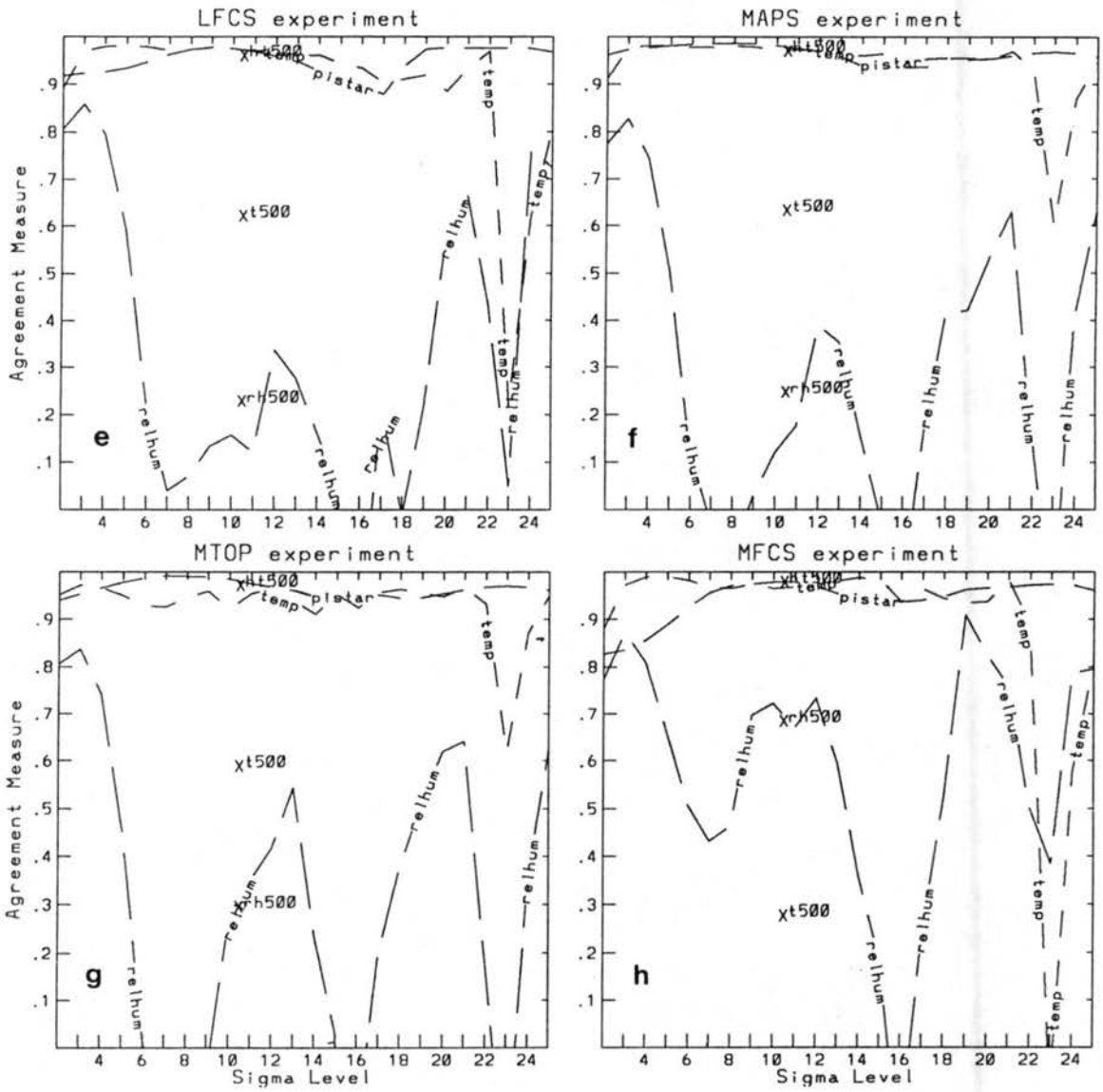

Figure 4.50: Continued:

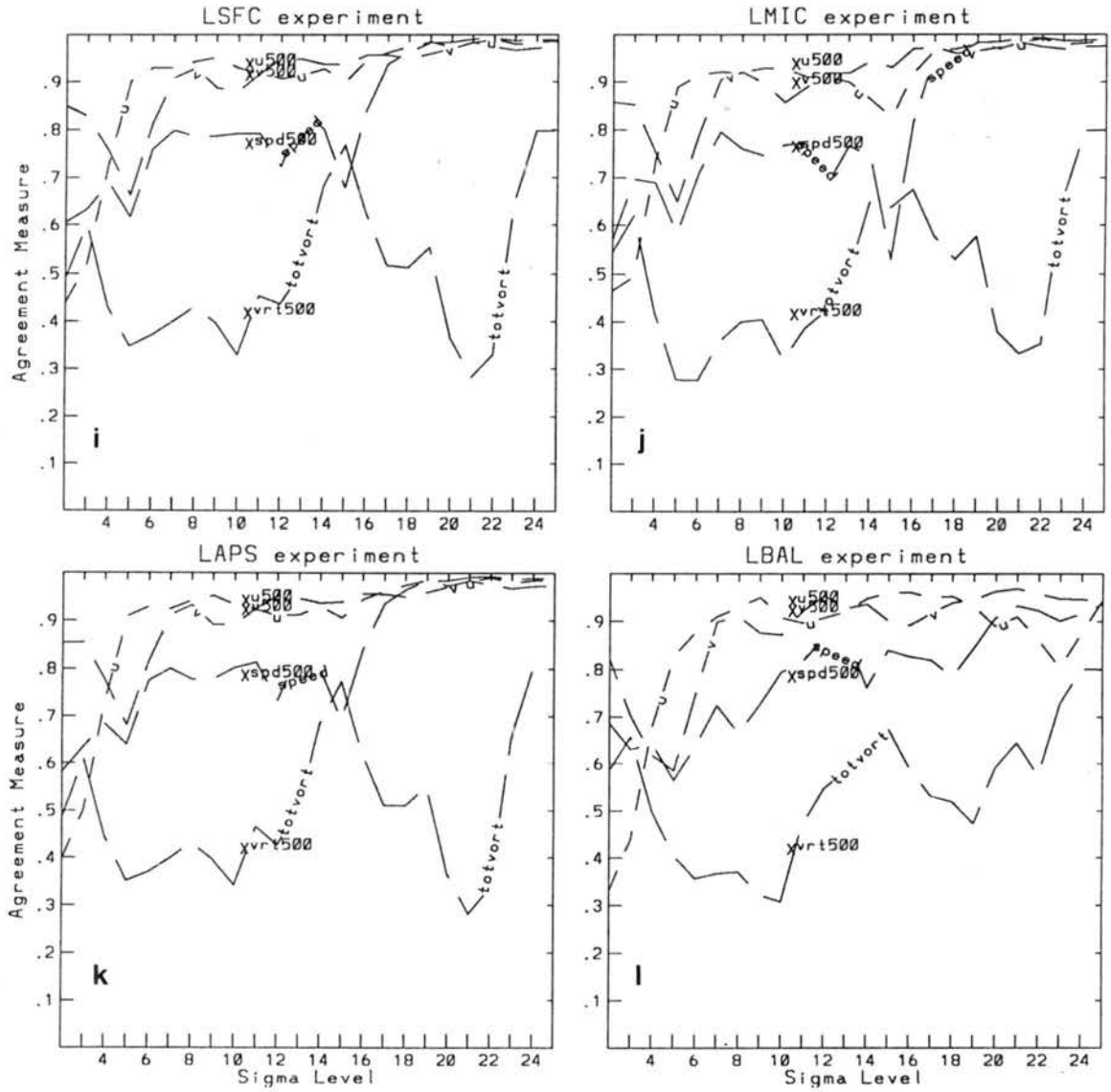

Figure 4.50: Continued:

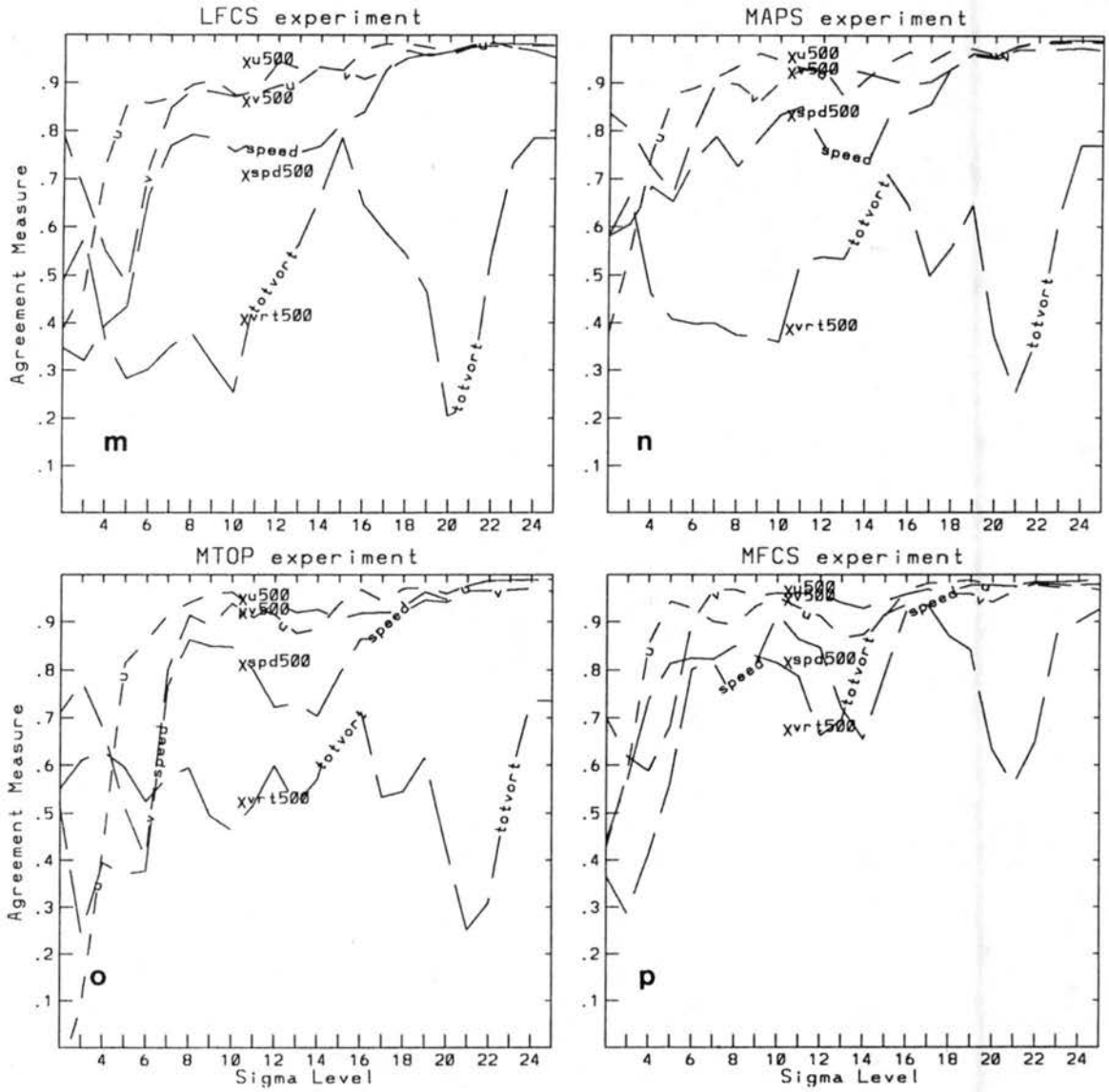

Figure 4.50: Continued:

significant decreases in agreement are indicated by MTOP compared to LAPS suggesting that the majority of the improvement by LAPS over MAPS is due to the increased topography resolution rather than improvements to the data initialization. Finally, a comparison of the operational MAPS forecast from the MAPS 60 km grid increment prediction model (MFCS) with LAPS shows improved agreement by MFCS with the analyses everywhere except near the surface. This result is probably due to the insufficient upper air observation resolution problem discussed above. Near the surface, where more plentiful observations exist, the higher resolution RAMS predictions outperform the coarser resolution MAPS predictions.

The 12 h agreement measures are similar for the four LAPS simulations (LAPS, LSFC, LBAL, LMIC), except for LMIC which shows better moisture agreement than the other LAPS runs. Compared to the 6 h results, only the predictions of relative humidity show a significant drop in agreement. The true forecast (LFCS) continues to perform closely to the LAPS simulations except for some decrease with agreement in the low-level winds. Similar to the 6 h results, the MAPS agreement is comparable to LAPS, while the MTOP agreement is somewhat less than LAPS. The MAPS 60 km grid increment operational forecast model (MFCS) agreement with the analyses is again closer than the RAMS agreement except in the lowest sigma levels; again an indication of the problem with insufficient upper air observations.

Thompson (1993) computed similar MRBP statistics for a whole winter season of RAMS forecasts initialized with data derived from the 60 km grid increment MAPS analyses. Thompson used a two nested grid configuration with a 25 km grid increment inner mesh covering most of Colorado. MRBP agreement measures were computed by comparing the 25 km grid interval RAMS predictions with 100 km grid increment analyses, which, as Thompson noted, is an unfair statistical comparison as discussed above. A comparison of results for this one case (7 January 1992) to Thompson's whole season results indicates significant improvement in all variables except upper level moisture. Of particular interest is the significant improvement near the surface in mass (from 50 to 90%), moisture (from 30 to 80%), and wind speed (from 25 to 55%). Thompson noted that numerical models

typically show poor agreement at the surface for temperature and relative humidity. The results from the 7 January 1992 case study suggest that the additional mesoscale surface observations have improved the predictions of surface temperature and moisture and have improved the surface analyses used for comparison resulting in much better statistical agreement. While the surface forecast improvements are encouraging, a much larger comparison sample is necessary to provide statistically significant results.

4.4 Comparison to Operational Forecasts

A qualitative comparison of the LFCS simulation with other operational models helps to answer one of the dissertation objectives: can a mesoscale numerical model initialized with high-resolution, non-homogeneous data detect mesoscale features and add value to currently available regional scale model forecasts? The LFCS simulation is compared to operational predictions from NMC's NGM and FSL's MAPS models.

The 6 h MAPS forecast of surface winds (Fig. 4.51) shows the cyclone position to be in east-central Colorado, close to the RAMS predicted position (Fig. 4.43) and the LAPS analyzed location (Fig. 4.16), while the NGM 6 h forecast (Fig. 4.52) positions the low a little further east near the Kansas border. The RAMS forecast provides greater mesoscale detail especially over the mountains with 30 m s^{-1} predicted wind speeds compared to 15 m s^{-1} in the MAPS forecast, and adjacent to the Front Range where RAMS predicts northeasterlies as observed in the FSL mesonet. The RAMS forecast suggests stronger northwest flow than MAPS west of the surface cyclone which appears to be in closer agreement to the Limon (LIC) SAO.

Both the 12 h MAPS and NGM forecasts position the surface cyclone in west-central Kansas, a little south of the LAPS and MAPS analyzed location on the western Kansas-Nebraska border. The RAMS forecast position is also south of the analyzed location, but closer than the MAPS and NGM forecasts. Recall that the MAPS forecast is the nudging target for the RAMS lateral boundary condition which probably influenced the RAMS forecast position. The RAMS 12 h forecast surface winds provide a closer agreement to observations than either MAPS or NGM with the strong, but weakening, northwest flow

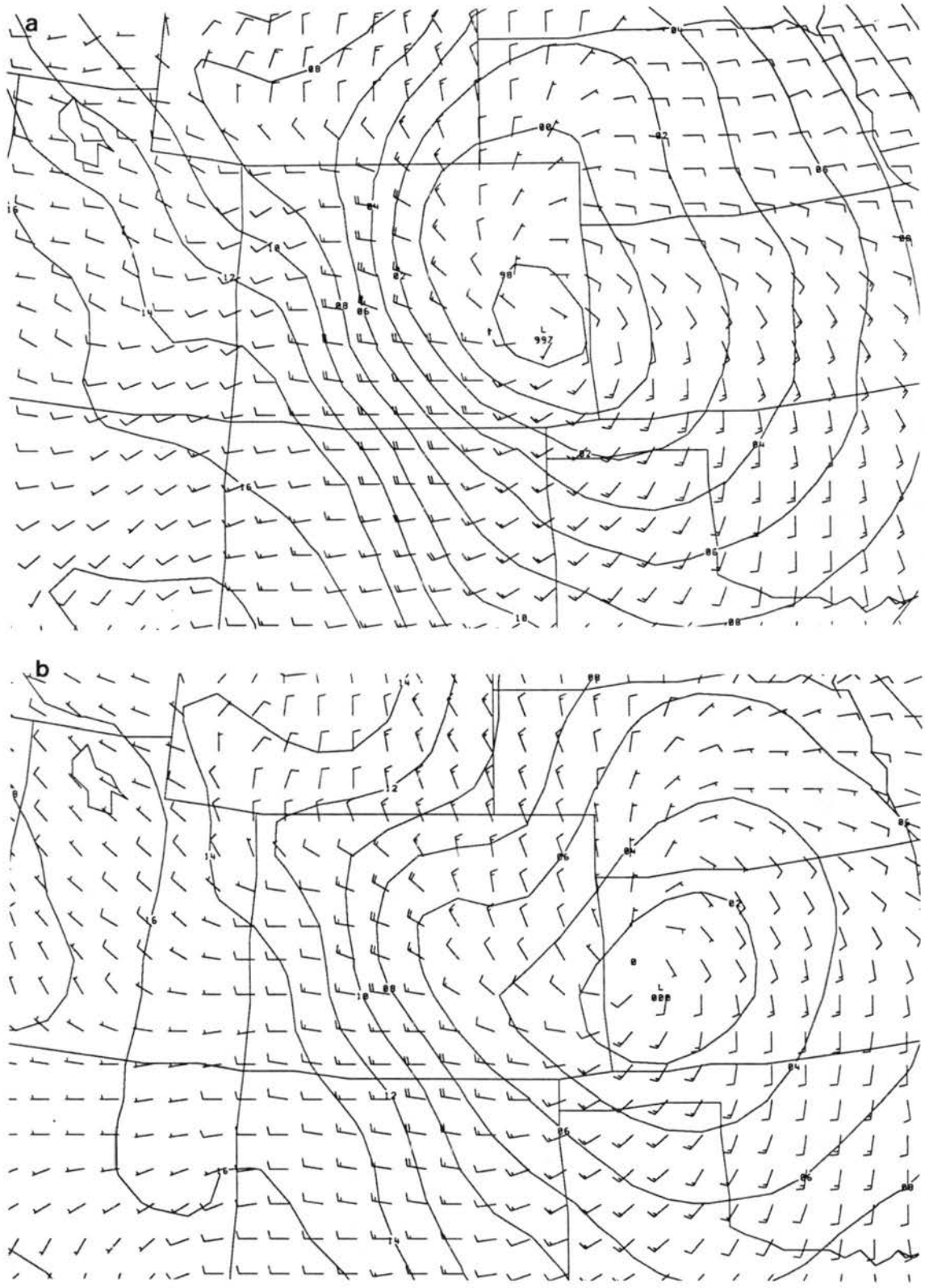

Figure 4.51: MAPS mean sea-level pressure (mb) and surface wind (knots) predictions from (a) the 6 h forecast valid at 1800 UTC 7 January and (b) the 12 h forecast valid at 0000 UTC 8 January 1992.

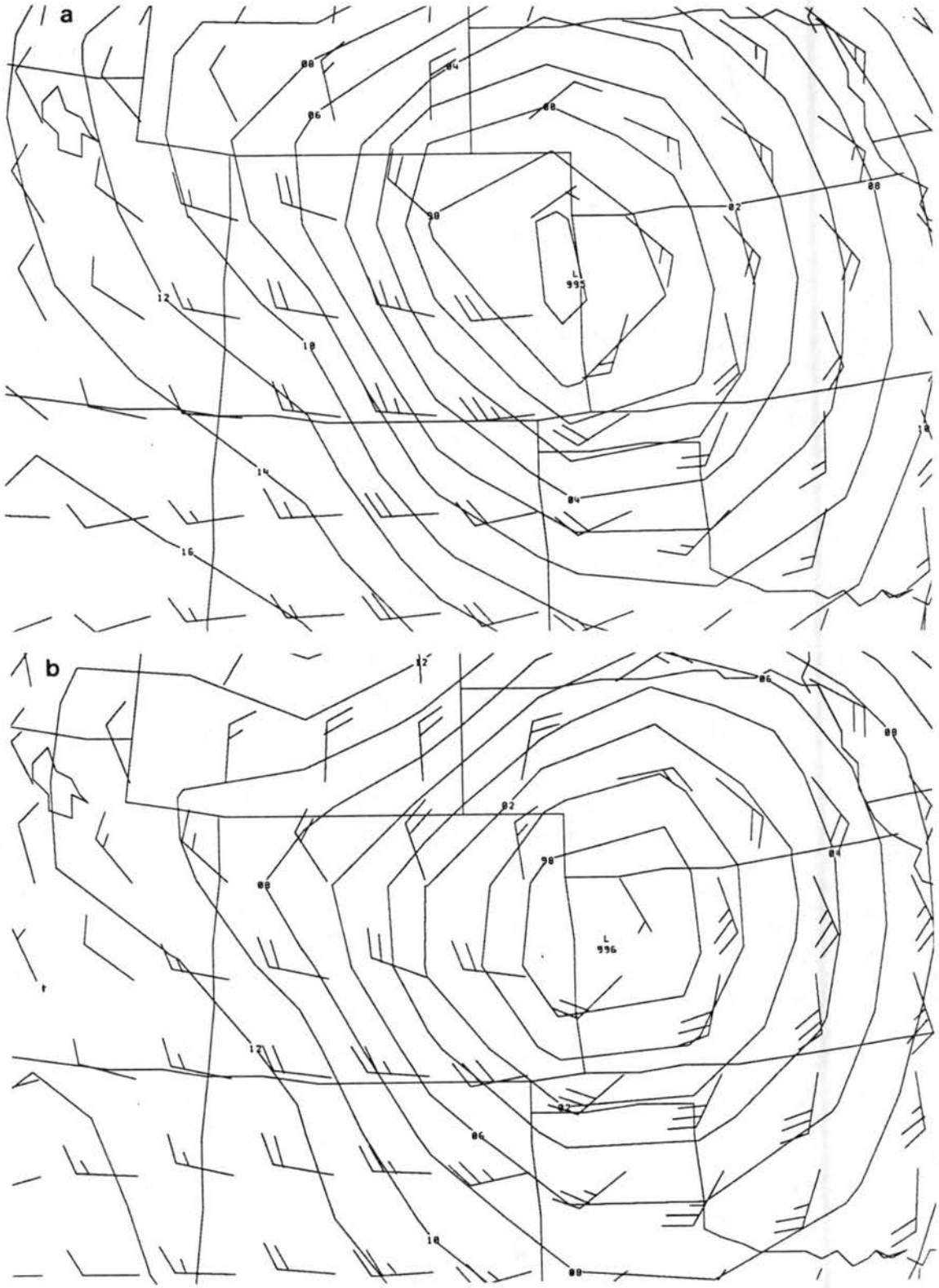

Figure 4.52: NGM mean sea-level pressure (mb) and surface wind (knots) predictions from (a) the 6 h forecast valid at 1800 UTC 7 January and (b) the 12 h forecast valid at 0000 UTC 8 January 1992.

over the mountains, the northeasterly flow adjacent to the Front Range, and the strength of the northwesterly flow west of the surface cyclone.

The 6 h 500 mb MAPS (Fig. 4.53), NGM (Fig. 4.54), and RAMS (Fig. 4.44) height forecasts indicate that all are slow in moving the upper-level low when compared to the MAPS analyzed position, but MAPS and NGM predicted closer agreement to the analyzed magnitude than RAMS. At 12 h, all three forecasts of the 500 mb low are close to the MAPS analyzed position in southwest Nebraska, with MAPS and NGM again in better agreement with the analyzed magnitude.

The 12 h NGM precipitation forecast (Fig. 4.55) indicates a large swath of greater than 0.64 cm (0.25 inches) melted water from northeast Colorado, across western Nebraska, and into southcentral South Dakota. The model appears to have predicted a quasi-geostrophically forced area of precipitation typically observed north-northwest of the surface low center (Fawcett and Saylor 1965) which was observed across southeast Wyoming and the Nebraska Panhandle. There is, however, no suggestion of any mesoscale structure within the forecast precipitation swath. The MAPS 3 and 6 h precipitation forecasts (Fig. 4.56) valid at 1500 and 1800 UTC indicate a northwest-southeast band of heavy precipitation over and east of the northern and central Colorado mountains. Compared to the NGM, MAPS appears to have provided an improved prediction of the observed heavy snow east of the Colorado Front Range, but MAPS was still unable to resolve the mesoscale structure of the dry band observed along the Front Range. Although the RAMS microphysics simulation (LMIC) is not a true forecast, there are indications that the higher resolution RAMS precipitation forecast is capable of resolving the dry band (Fig. 4.34). This capability combined with the enhanced forecasts of surface winds suggests that the RAMS predictions are capable of adding significant value to the currently available short-range (0-12 h) operational forecasts.

4.5 Discussion

The case study presentation from 7 January 1992 demonstrates the ability to successfully detect and predict mesoscale features using a mesoscale numerical model initialized

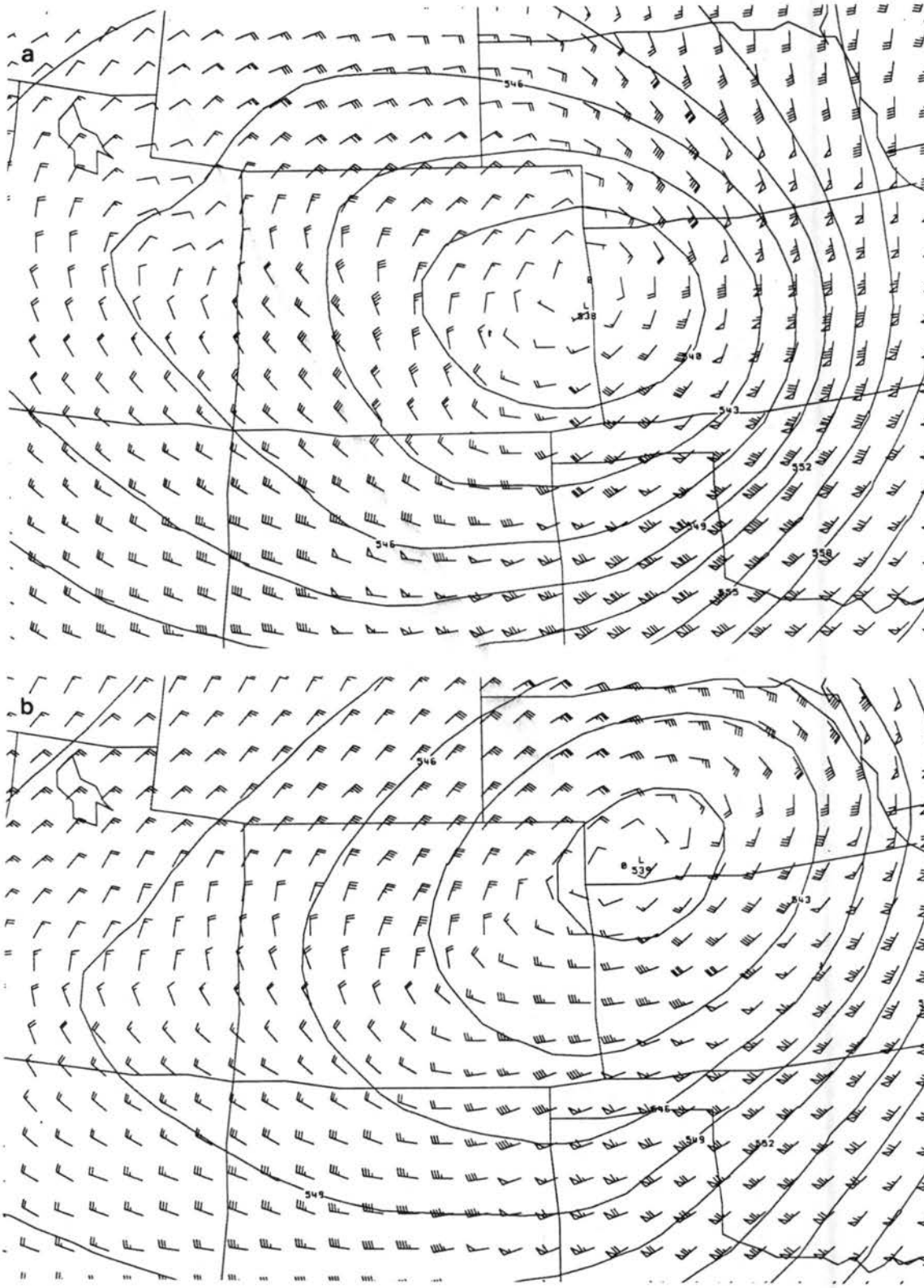

Figure 4.53: MAPS 500 mb height (dm) and wind (knots) predictions from (a) the 6 h forecast valid at 1800 UTC 7 January and (b) the 12 h forecast valid at 0000 UTC 8 January 1992.

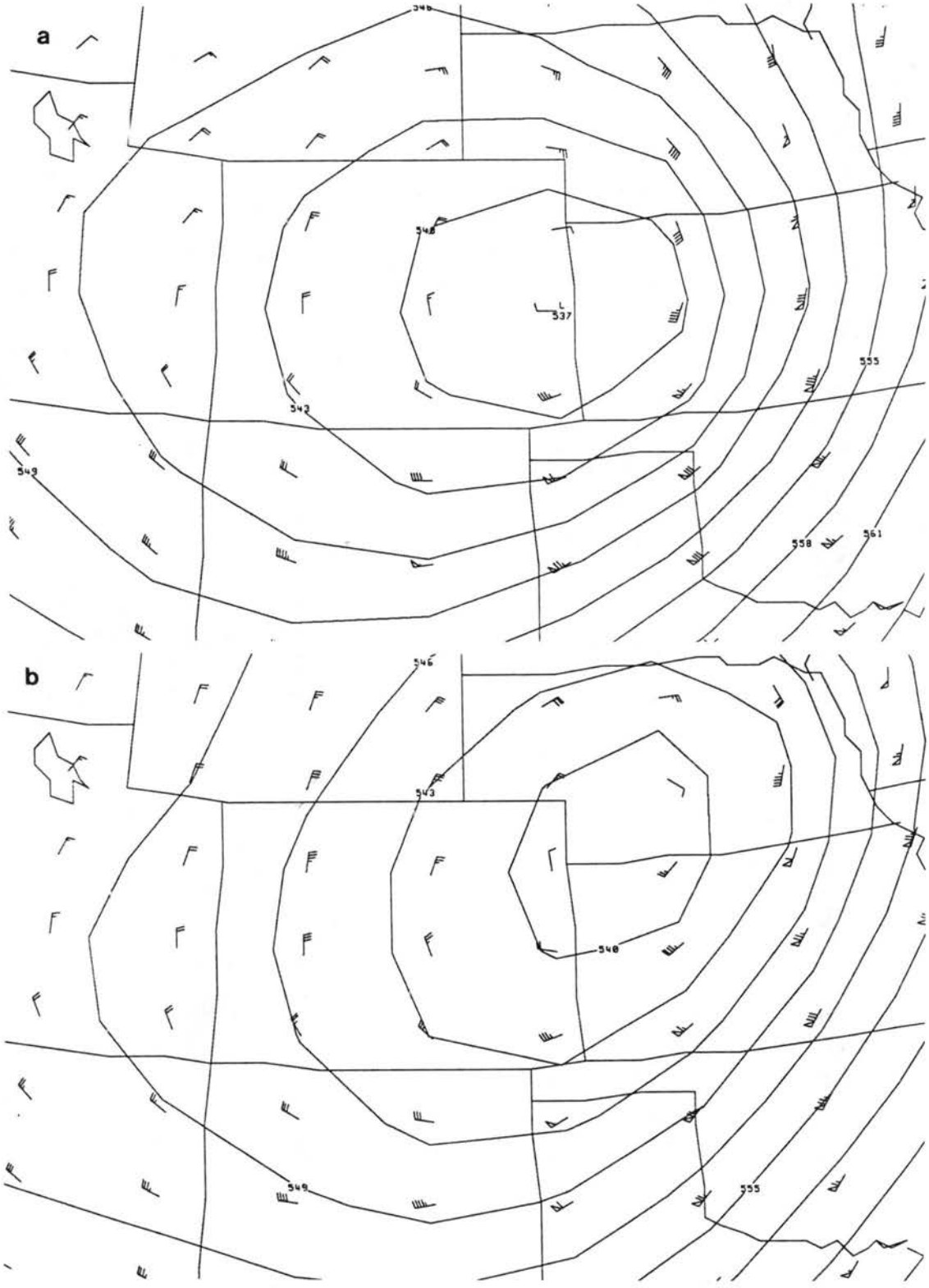

Figure 4.54: NGM 500 mb height (dm) and wind (knots) predictions from (a) the 6 h forecast valid at 1800 UTC 7 January and (b) the 12 h forecast valid at 0000 UTC 8 January 1992.

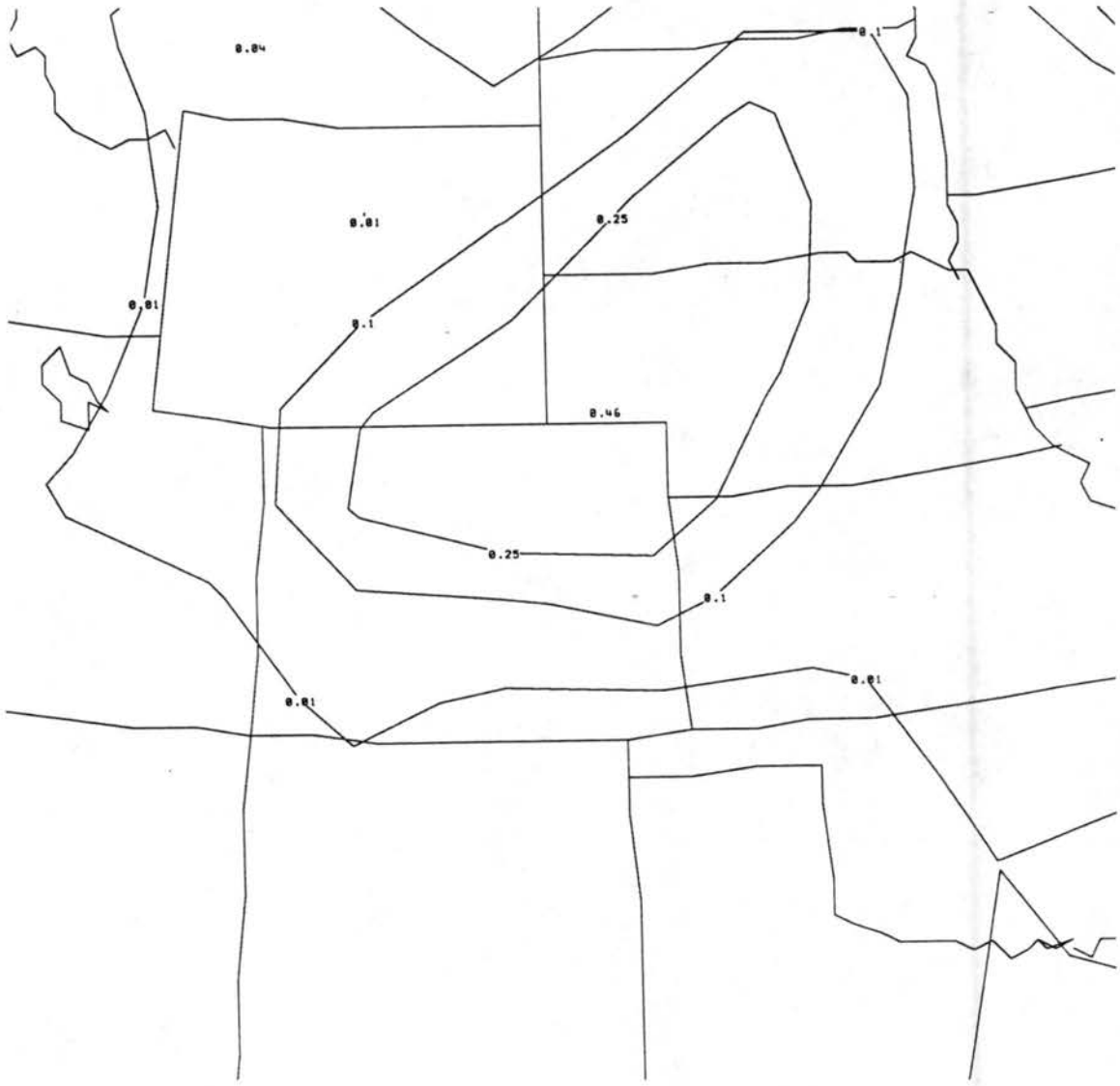

Figure 4.55: NGM 12 h melted precipitation (inches) forecast valid at 0000 UTC 8 January 1992.

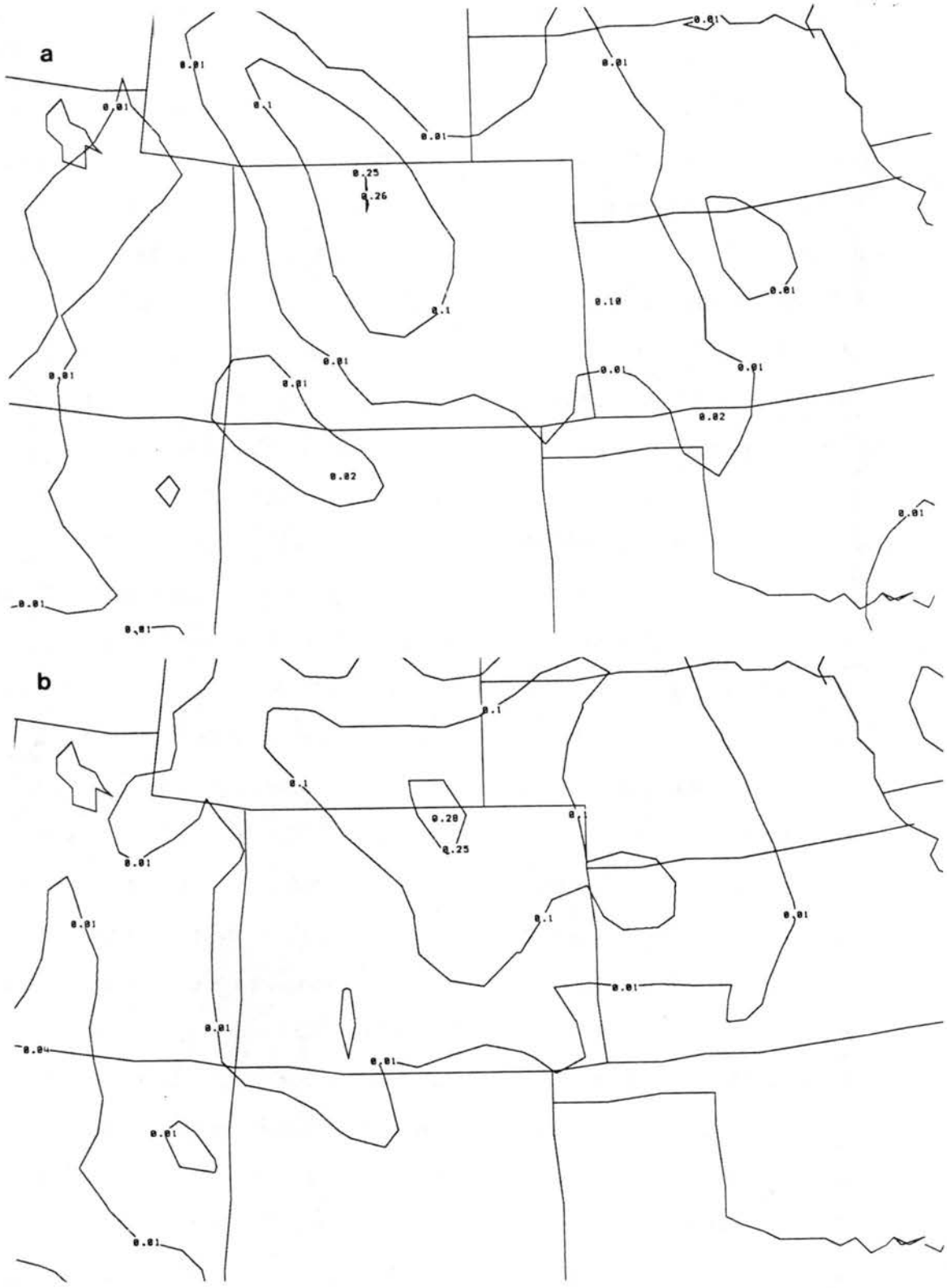

Figure 4.56: MAPS 3 h melted precipitation (inches) forecasts from (a) the 3 h prediction valid at 1500 UTC and (b) the 6 h prediction valid at 1800 UTC 7 January 1992.

with high-resolution (10 km horizontal grid interval), non-homogeneous data. Observations from 7 January indicate several interesting mesoscale features including 1) persistent strong downslope flow east of the mountain barrier crest, 2) the development of weak northeasterlies adjacent to the Front Range, 3) the generation of strong northwesterlies at the surface and low-levels over the Eastern Plains, and 4) the eastward displacement of greatest snowfall away from the mountain barrier. RAMS model predictions initialized with LAPS analyses were able to resolve all four of these mesoscale features. The true RAMS forecast (LFCS) indicated the development of 30 m s^{-1} westerly flow over the Continental Divide that persisted through most of the forecast period, the generation of weak northeasterly flow adjacent to the Front Range, and the development of 20 m s^{-1} northwesterly surface flow over the Palmer Divide. The LMIC simulation shows the eastward displacement of greatest precipitation away from the mountain barrier with a dry zone along the Front Range. A qualitative comparison to other operational forecast models and a quantitative statistical model validation indicate that the RAMS predictions are capable of adding local scale, short-range (0-12 h) forecast value to the currently available regional scale model forecasts. Results from the sensitivity simulations suggest that the majority of the forecast improvements are due to the improved representation of the topography rather than better initialization by LAPS compared to MAPS, except near the surface where additional local data sources add significant mesoscale detail to the LAPS analyses.

A discussion of the mesoscale aspects of the 7 January blizzard demonstrates the ability to utilize the model output in combination with observations and other larger domain model simulations to provide an improved scientific understanding of mesoscale weather events. A significant difference between this storm and other eastern Colorado heavy snow events is the development of the strong westerly flow over and east of the Continental Divide. Surface observations and RAMS predictions also indicate a stable boundary layer with strong northwest flow over the Cheyenne Ridge and weak northeasterlies adjacent to the Front Range, suggesting the development of a Longmont anticyclone. Based on the surface flow alone, one might expect a band of heavy snow to develop on the convergence zone located between the strong westerlies and the weak northeasterlies. However,

the heavy snow band actually developed further east along a zone of difluence positioned between the northeasterlies and a region of strong northwesterlies over the Eastern Plains.

Three-dimensional views of the RAMS simulations provide insight into why the heavy snow fell further east. The vertical profiles of wind and static stability were favorable for the generation of trapped lee waves. The development of a trapped lee wave created a region of dry downslope flow with little or no precipitation over the Front Range. East of the downslope region, an area of ascent is indicated within the eastern half of the mountain wave. Between 1200 and 1800 UTC, mid-level easterly component flow rises over the mountain wave creating an additional region of ascent and advects relatively moist air into the area. The two regions of ascent combined with the moisture to generate a column of precipitation consisting of snow and aggregates that fall in a north-south band approximately 40 km east of the mountain barrier. The lee wave continues after 1800 UTC but the mid-level easterly component flow backs to a northerly direction that no longer ascends over the mountain wave. Low-level ascent continues in the eastern half of the mountain wave which sustains a shallow column of snow and aggregates along the north-south band east of the barrier. Observations and RAMS predictions indicate a reduction in snowfall intensity after 1800 UTC.

The RAMS simulations have provided insight into the impacts of the westerly flow on the observed snowfall and other surface characteristics. Determining the factors that created and sustained the westerly flow, however, requires an earlier view of the system beyond the scope of this investigation. A likely contributor to the development of the westerlies is the redevelopment of the cyclone over southeast Colorado as indicated by the MAPS analyses.

Two aspects remain to complete this dissertation. First, the results presented thus far are based primarily on one case study. To add further credence to the results, another case study will be analyzed. Second, the case study results have shown several interesting surface flow characteristics, including evidence of a Longmont anticyclone. The investigation of several idealized simulations designed to isolate these characteristics will provide further understanding into their implications on this and other case studies and their relationship to the general theory of flow around an obstacle.

Chapter 5

CASE STUDY – 8-9 MARCH 1992

A variety of severe weather affected the eastern half of Colorado on 8 and 9 March 1992. A strong, fast moving arctic cold front pushed across the region ushering in heavy snow and high winds. Ahead of the front, strong thunderstorms developed in relatively warm, unstable air. Numerous reports of hail, up to one inch in diameter, and two tornadoes were observed (Storm Data 1992). The rapid approach and the severity of the arctic front caught many weekend travelers by surprise. Heavy snow fell along the Front Range with total amounts reaching nearly 60 cm (2 feet, Fig. 5.1). Strong winds of 15 to 20 m s^{-1} (30 to 40 knots) with gusts to 25 m s^{-1} (50 knots) produced blizzard conditions and 1 to 2 m snow drifts that closed highways and created numerous power outages. The heavy snow, high winds, convection, and strong arctic cold front make this case a suitable complement to the 7 January 1992 case study for investigating the mesoscale numerical forecast objectives of this dissertation.

5.1 Synoptic-Mesoscale Overview

The case study investigation will focus on the arctic cold front because of its mesoscale character and its significant impact on the general public. A storm overview traces the development of the arctic front and its impact on the observed snowfall and other surface characteristics.

5.1.1 Synoptic-scale observations

NMC 500 mb analyses of heights and isotachs (Fig. 5.2) at 1200 UTC 8 March 1992 indicate a broad trough located over the western United States with an embedded 5461 m closed low analyzed over west-central Arizona. An associated 30 m s^{-1} (60 knot) jet

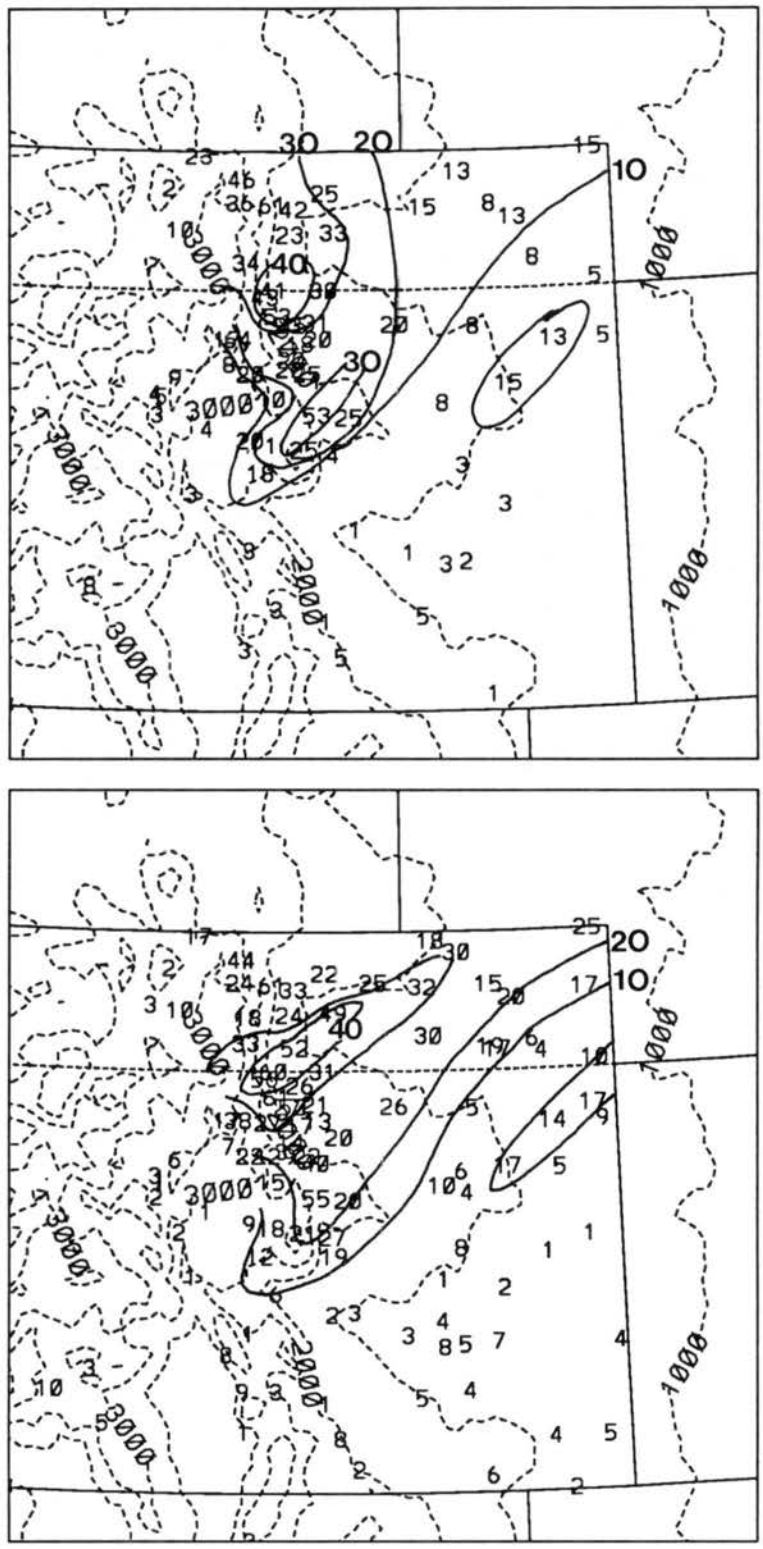

Figure 5.1: Observed precipitation during the 8-9 March 1992 snow storm, (a) snowfall (cm) and (b) melted water equivalent (mm).

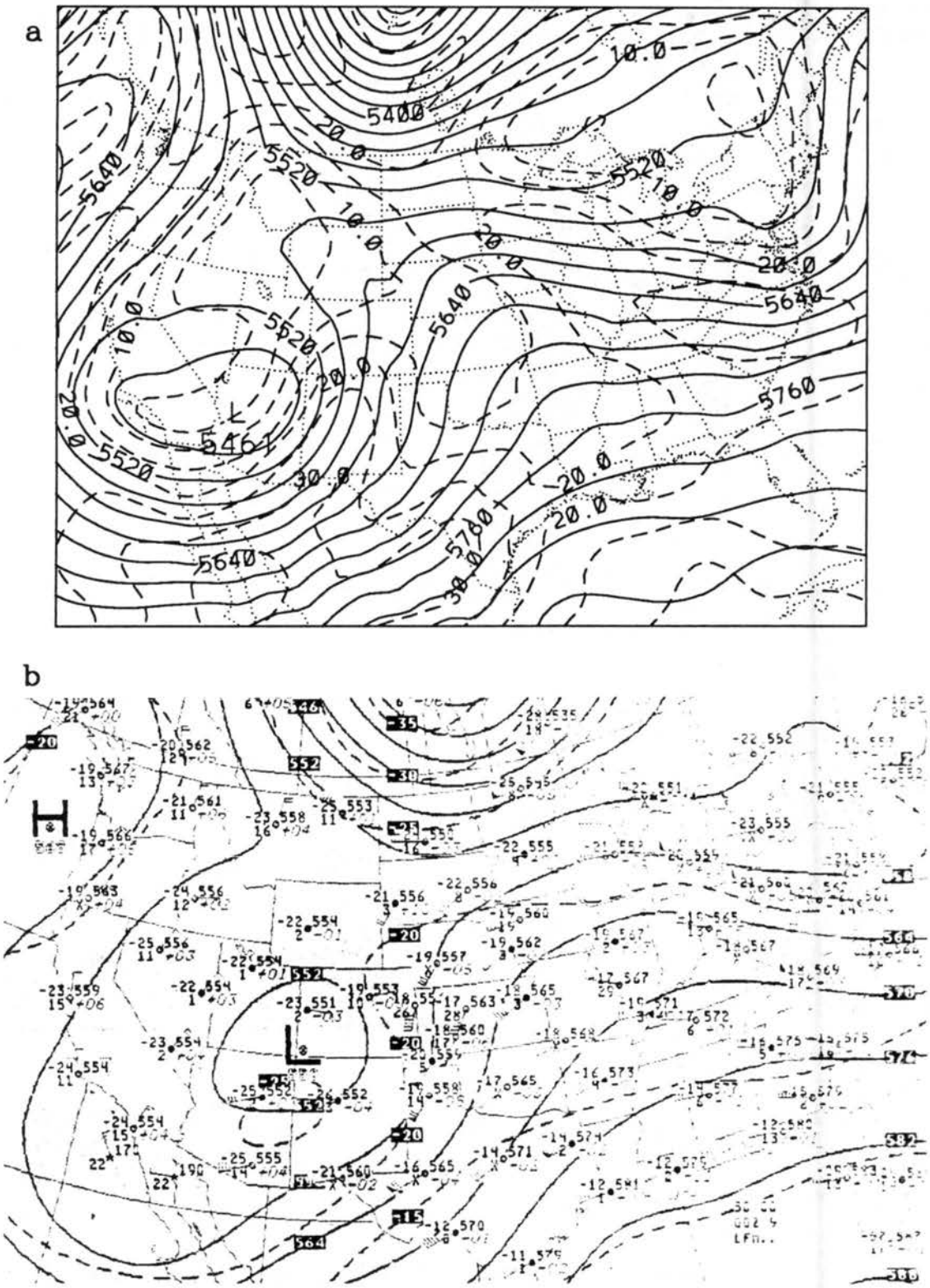

Figure 5.2: NGM 500 mb height (m, solid contours) and isotach (m s^{-1}, dashed contours) analyses from (a) 1200 UTC 8 March and (b) 0000 UTC 9 March 1992.

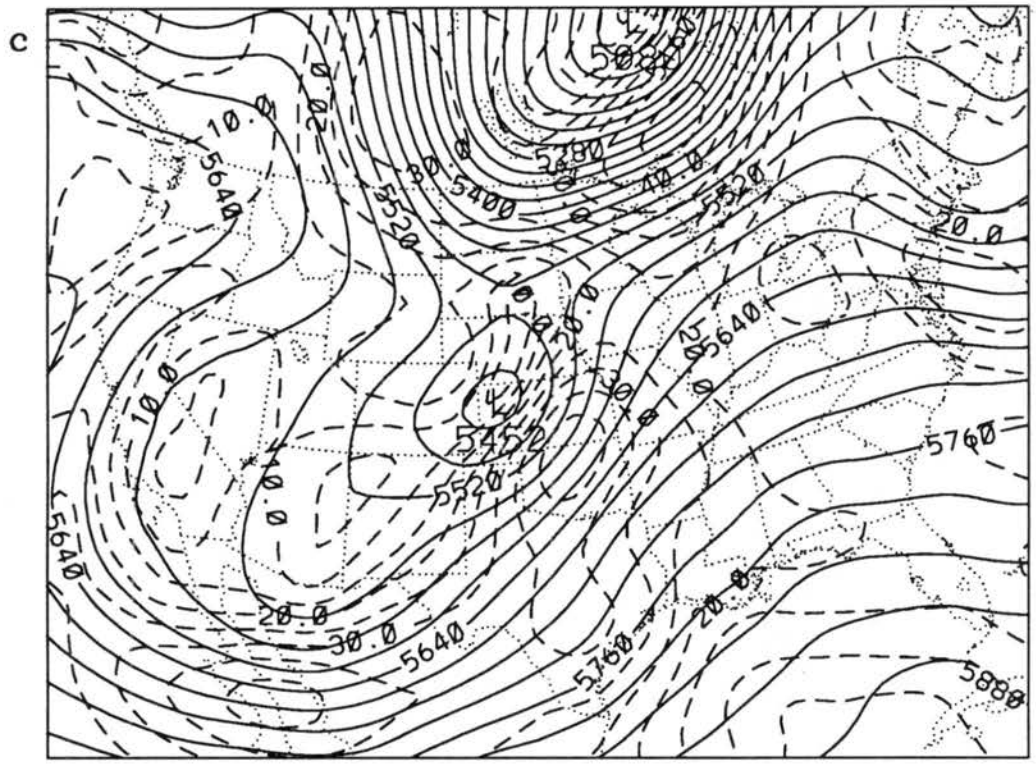

Figure 5.2: Continued: (c) 1200 UTC 9 March 1992.

streak is positioned to the southeast of the low. The closed low travels to the Four Corners area and weakens somewhat to 5500 m by 0000 UTC 9 March. The jet streak remains southeast of the low with analyzed wind speeds exceeding 35 m s^{-1} (70 knots). During the next 12 hours, the 500 mb low travels across Colorado to an analyzed position over northwest Kansas while the jet streak strengthens to 40 m s^{-1} (80 knots) and is centered across north-central Oklahoma and southeast Kansas.

A closed 700 mb low is also indicated for the entire 24 h period (Fig. 5.3). The 700 mb low is analyzed north-northeast of the 500 mb low and travels from the western Utah-Arizona border at 1200 UTC 8 March, to central Colorado at 0000 UTC 9 March, and to southern Nebraska by 1200 UTC 9 March. The 700 mb low strengthens considerably during the last 12 hours from 2950 to 2899 m. The system can be described as a deep cyclonic circulation type (Reinking and Boatman 1986) and exhibits many characteristics of a typical Colorado spring storm (Fawcett and Saylor 1965).

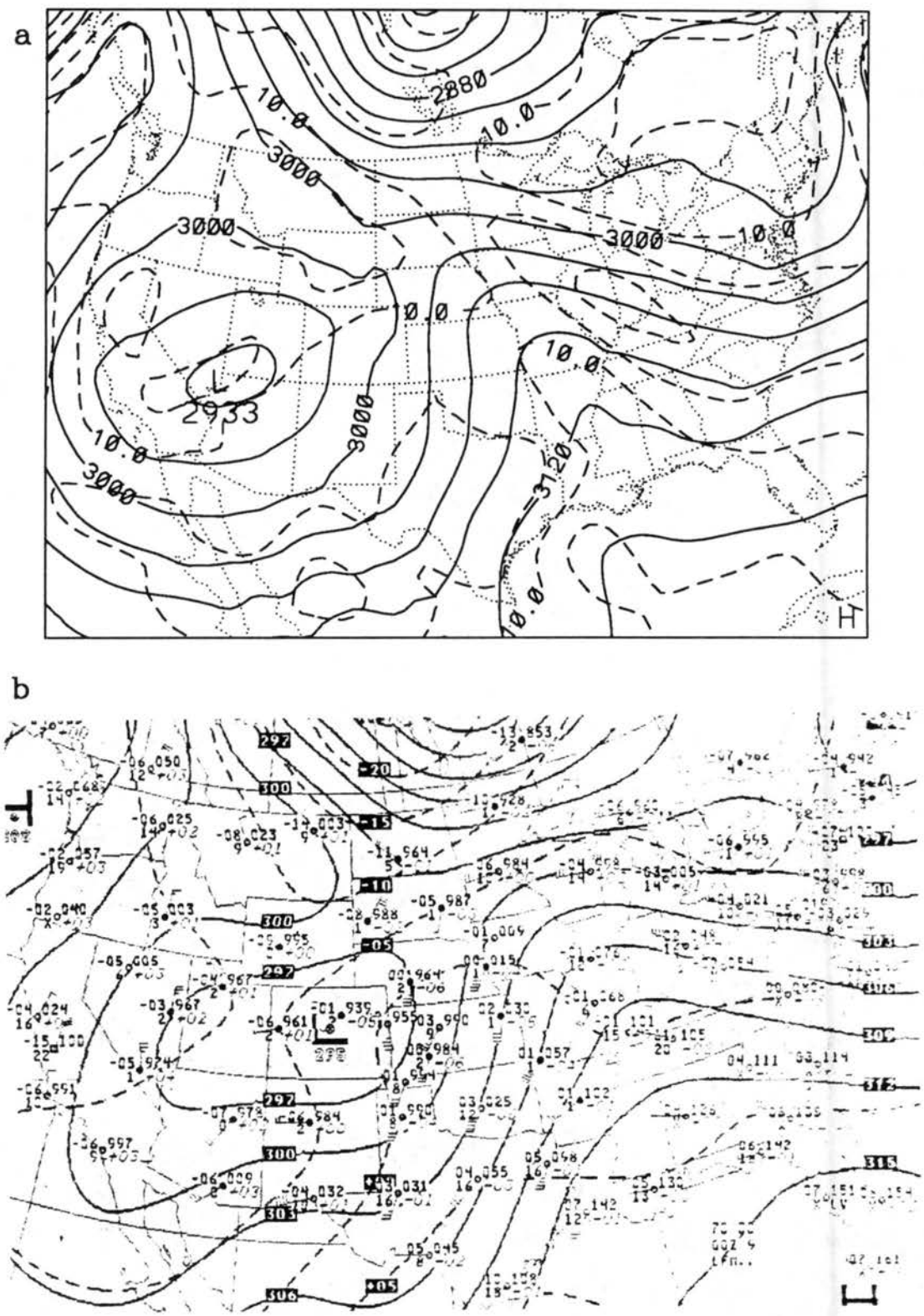

Figure 5.3: NGM 700 mb height (m, solid contours) and isotach (m s^{-1}, dashed contours) analyses from (a) 1200 UTC 8 March and (b) 0000 UTC 9 March 1992.

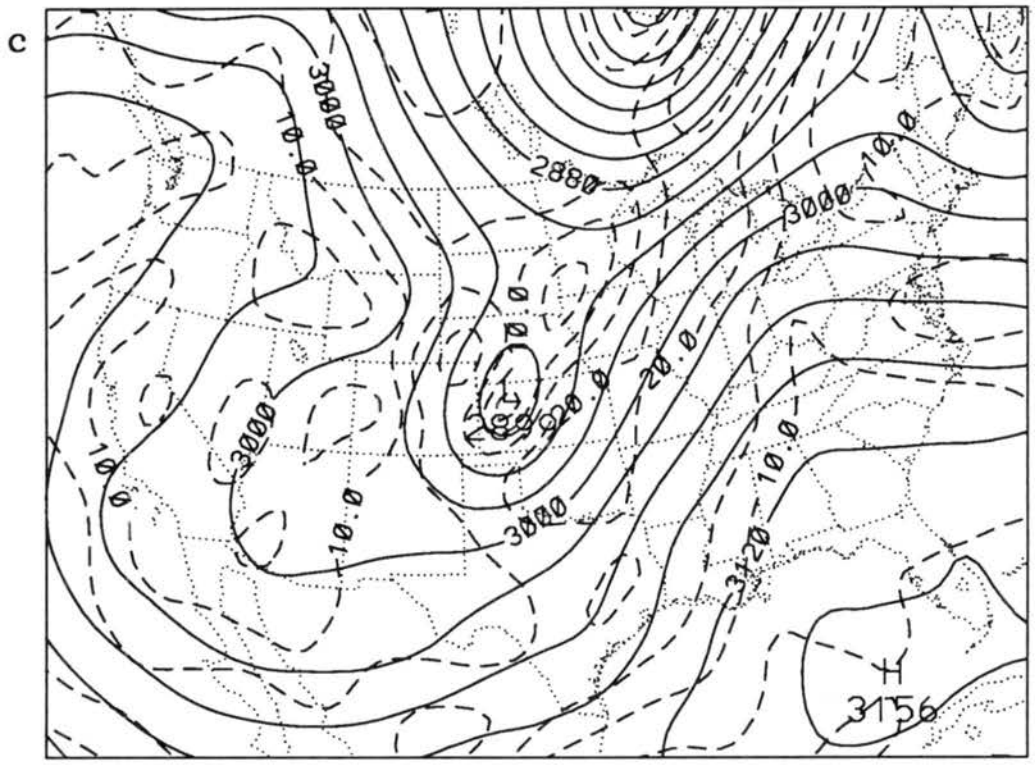

Figure 5.3: Continued: (c) 1200 UTC 9 March 1992.

5.1.2 Mesoscale observations

The 8-9 March 1992 system contained a large surface anticyclone to the north of the cyclone, unlike the 7 January 1992 case study. This feature is often observed (e.g. Wesley 1991) and the coupled eastward movement of the 500 mb low and the dense surface high can create a lee-side cold surge that leads to persistent upslope flow (Reinking and Boatman 1986). High spatial and temporal analyses of the boundary layer are necessary to illustrate the evolution of the arctic front. Surface frontal propagation is evident in a SAO time series (Fig. 5.4) where frontal passage occurs between 1900 and 2000 UTC at Cheyenne, between 2300 and 0000 UTC at Denver, and between 0200 and 0300 UTC at Colorado Springs. High winds, rising surface pressures, and heavy precipitation, except at Colorado Springs, are all observed following frontal passage.

MAPS 1500 m pressure and 3-h pressure change (Fig. 5.5) indicates an arctic high well north of Colorado, a developing surface low over southeast Colorado, and an associated rise/fall pressure change couplet. The arctic high is analyzed in southeast Montana

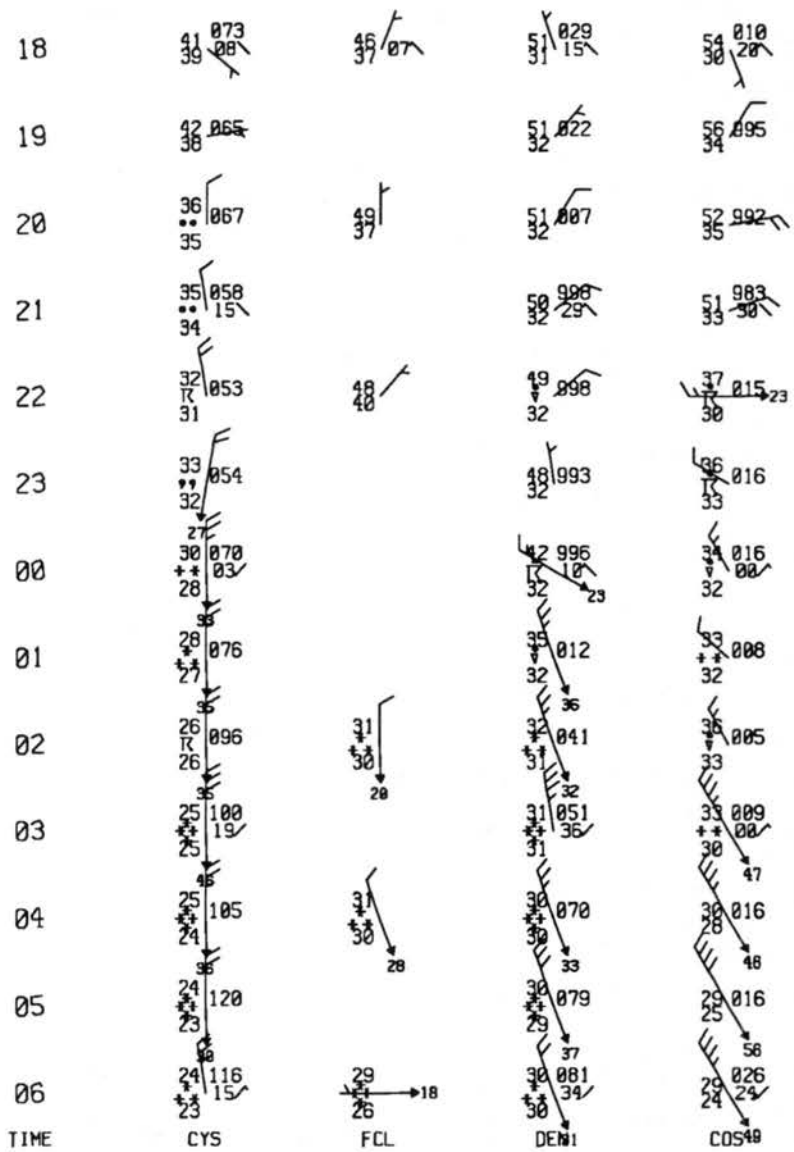

Figure 5.4: Surface aviation observations from 1800 UTC 8 March through 0600 UTC 9 March 1992 for Cheyenne (CYS), WY, Ft. Collins (FCL), Denver (DEN), and Colorado Springs (COS), CO.

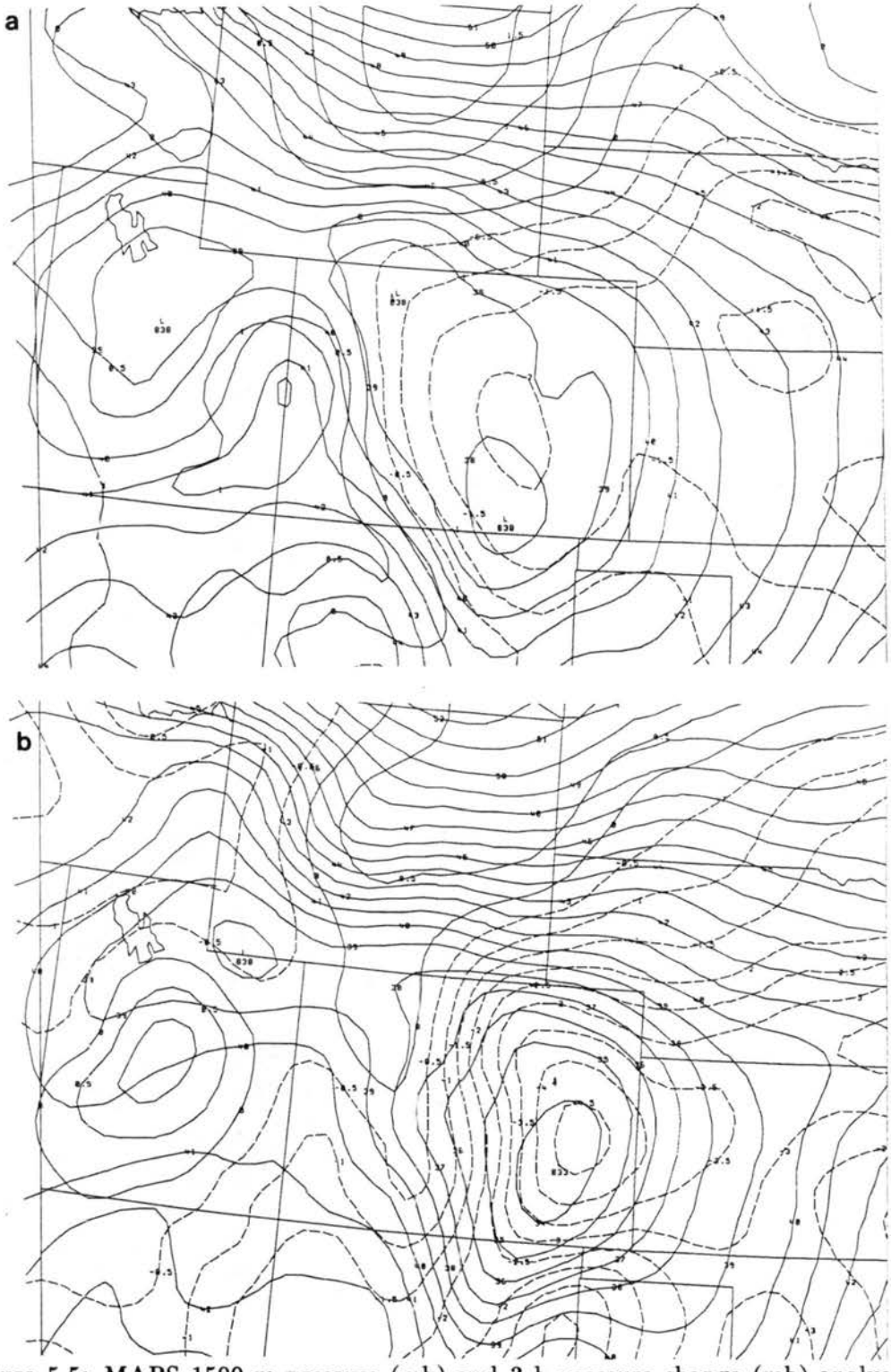

Figure 5.5: MAPS 1500 m pressure (mb) and 3 h pressure change (mb) analyses from (a) 1800 UTC and (b) 2200 UTC 8 March 1992.

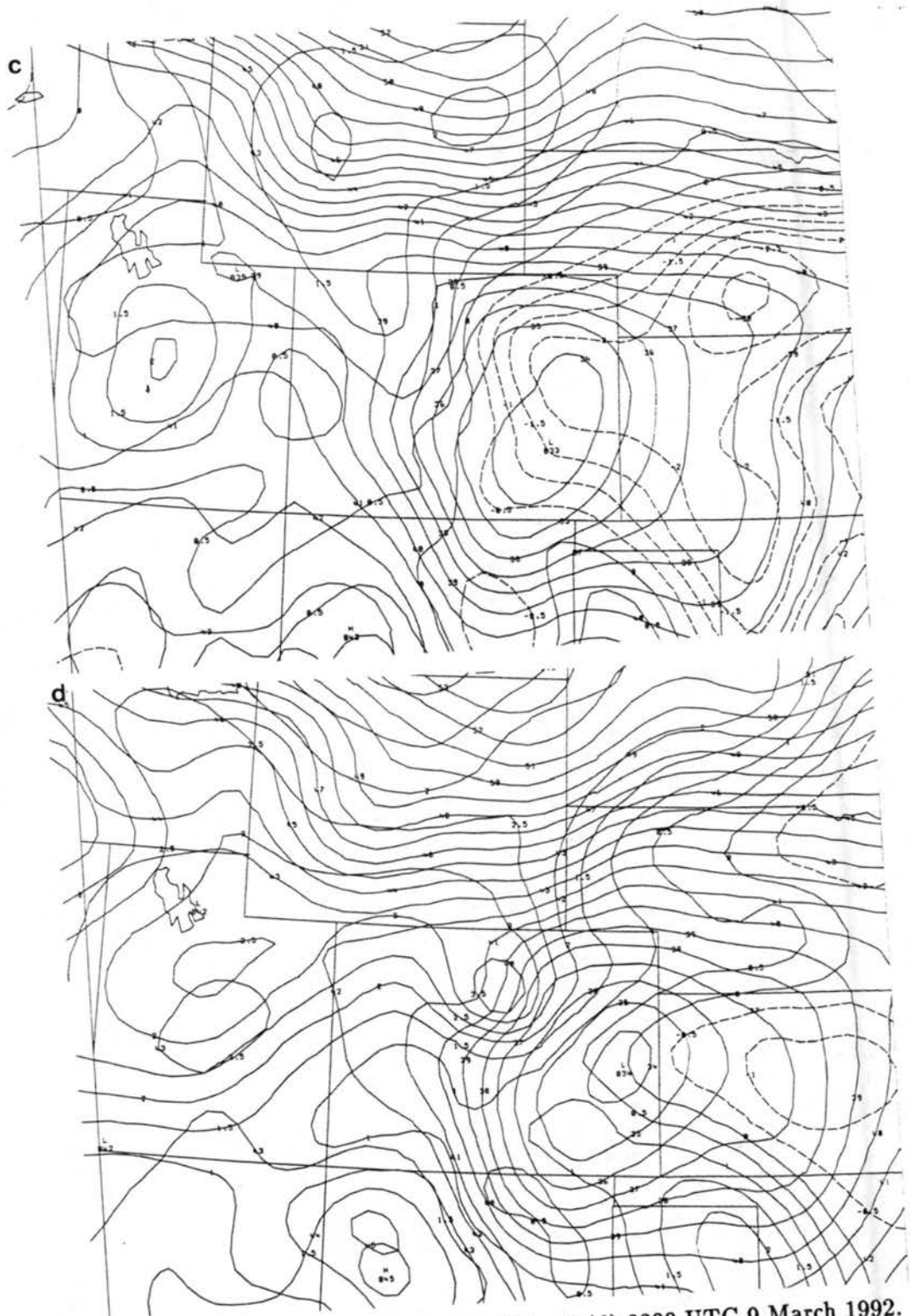

Figure 5.5: Continued: (c) 0000 UTC and (d) 0300 UTC 9 March 1992.

at 1800 UTC with the surface low positioned in south-central Colorado. By 2200 UTC (MAPS surface analyses were not available at 2100 UTC), a 3-h pressure fall of 4.5 mb in east-central Colorado has caused a significant increase in the pressure gradient between the surface high and low. The 1500 m pressure field suggests strengthening geostrophic upslope flow over northeast Colorado and eastern Wyoming. The arctic high remains in Montana at 0000 UTC but the pressure rise area now extends into northern Colorado indicating the movement of the arctic air mass into this region. Pressure falls continue in eastern Colorado and extend into western Kansas and southern Nebraska. The 1500 m pressure field continues to suggest strong geostrophic upslope flow over northeast Colorado and eastern Wyoming. At 0300 UTC, a pressure rise center is located along the northern Colorado Front Range indicating the arctic front has passed through most of northeastern Colorado. The 1500 m surface low has propagated to east-central Colorado and the pressure falls are occurring mostly in Kansas.

Actual surface winds indicate the development of strong northerly flow behind the cold front. North-northeast MAPS analyzed surface winds (Fig. 5.6) are confined primarily to northern Wyoming at 1800 UTC. A cyclonic surface circulation is evident in southcentral Colorado. By 2200 UTC, the surface northerlies have spread across southern Wyoming into extreme northern Colorado. Convective activity is indicated by SAO reports in Cheyenne, southwest Nebraska, and central Colorado. The surface northerly flow has spread southward through Denver by 0000 UTC with convective activity continuing ahead of the arctic front. Very strong surface northerlies (>15 m s^{-1}, >30 knots) are analyzed along the Front Range from Cheyenne to Colorado Springs at 0300 UTC. A well defined cyclonic circulation is indicated over east-central Colorado.

Heavy snow events along the Front Range typically contain strong easterly component upslope flow. Although the actual surface winds do not indicate this flow regime, a deep layer of upslope flow above the boundary layer is evident in the MAPS upper air analyses. The 700 mb MAPS analyses of height and wind (Fig. 5.7) at 1800 UTC indicate a cyclonic circulation positioned over central Utah with southerly flow evident over most of Colorado. Strong easterly flow is located over central Wyoming, coincident with the arctic front. At

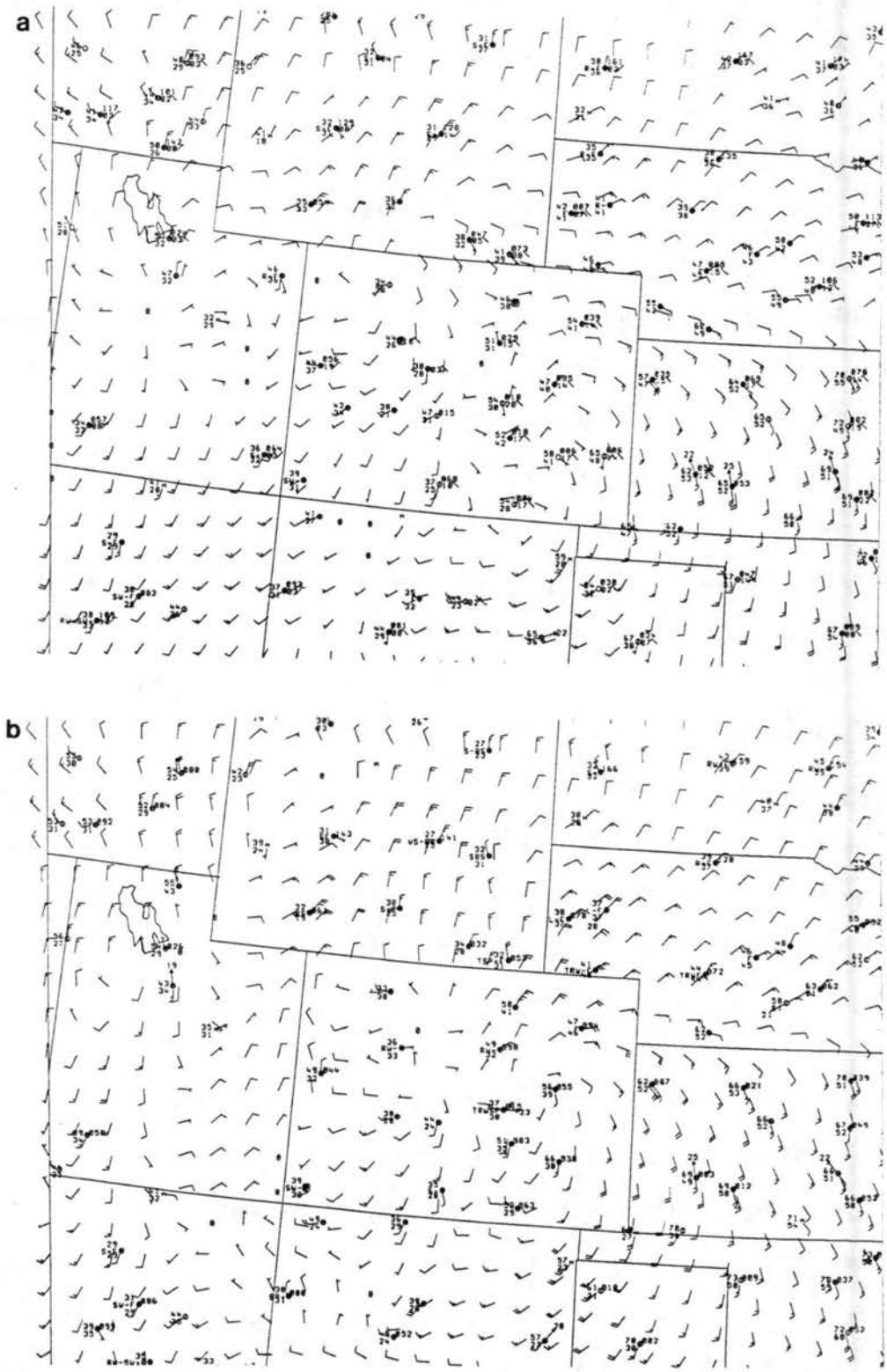

Figure 5.6: MAPS surface wind barb (knots) analyses and SAO reports from (a) 1800 UTC and (b) 2200 UTC 8 March 1992.

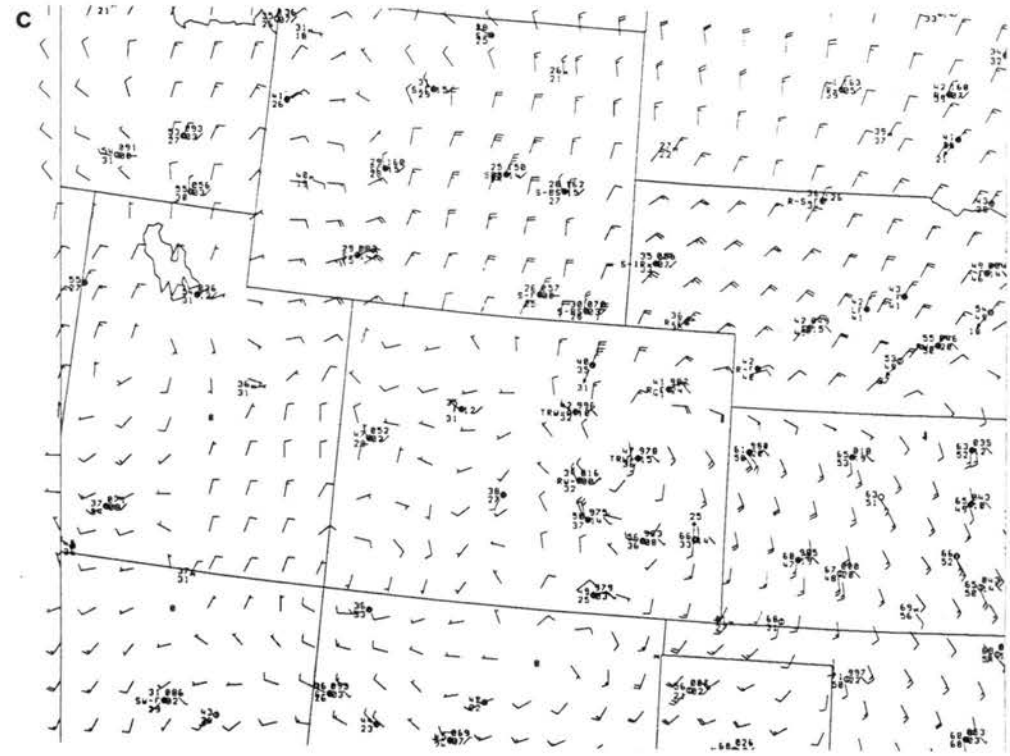

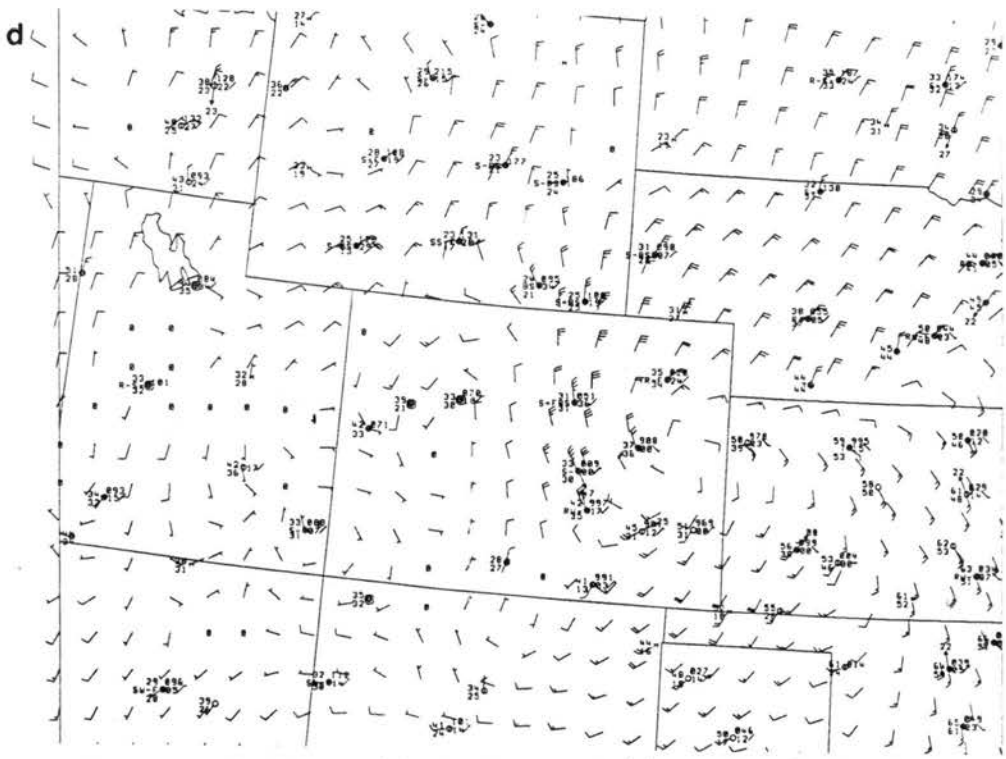

Figure 5.6: Continued: (c) 0000 UTC and (d) 0300 UTC 9 March 1992.

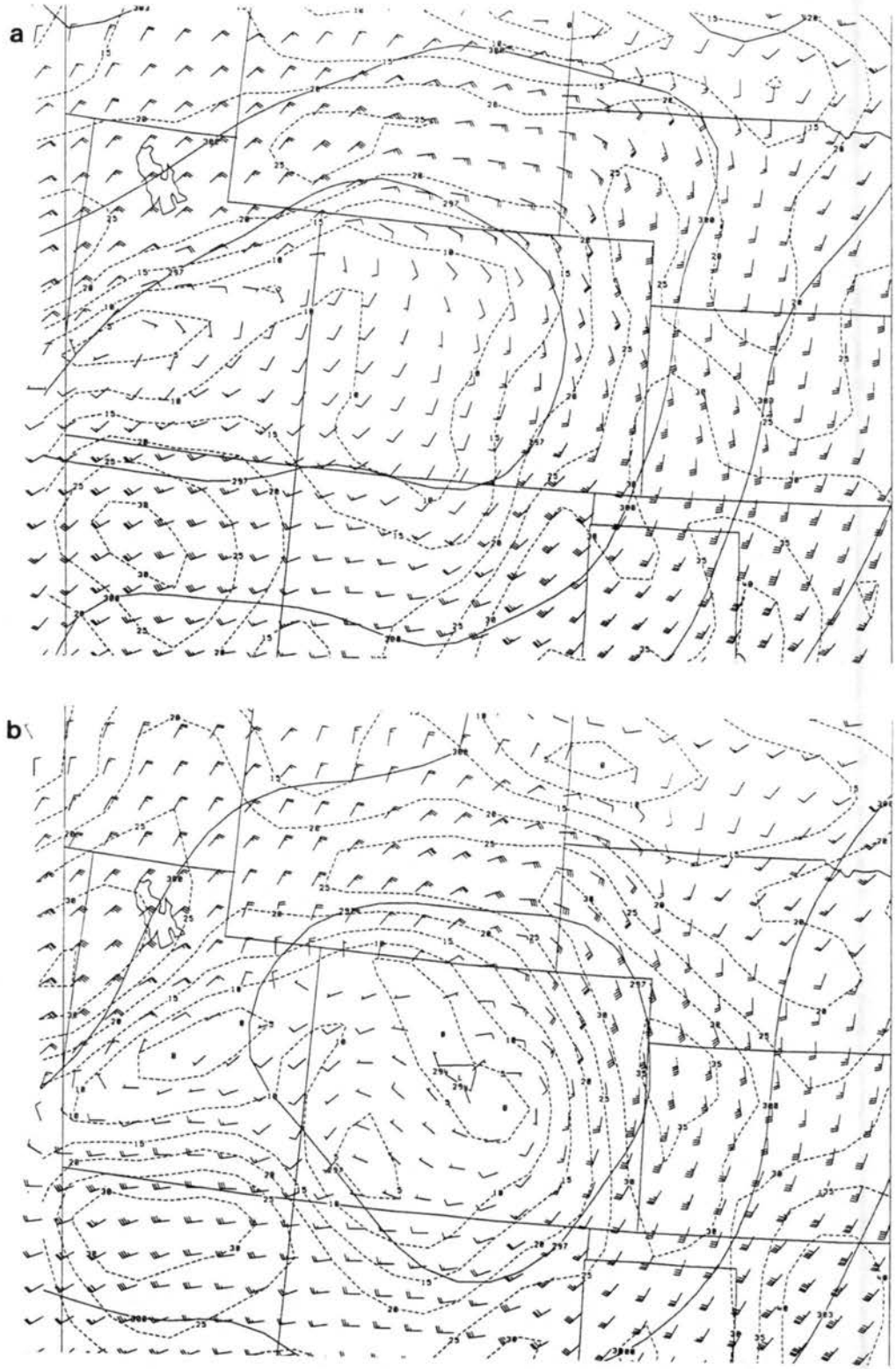

Figure 5.7: MAPS 700 mb height (dm), wind barb (knots), and isotach (knots) analyses from (a) 1800 UTC and (b) 2100 UTC 8 March 1992.

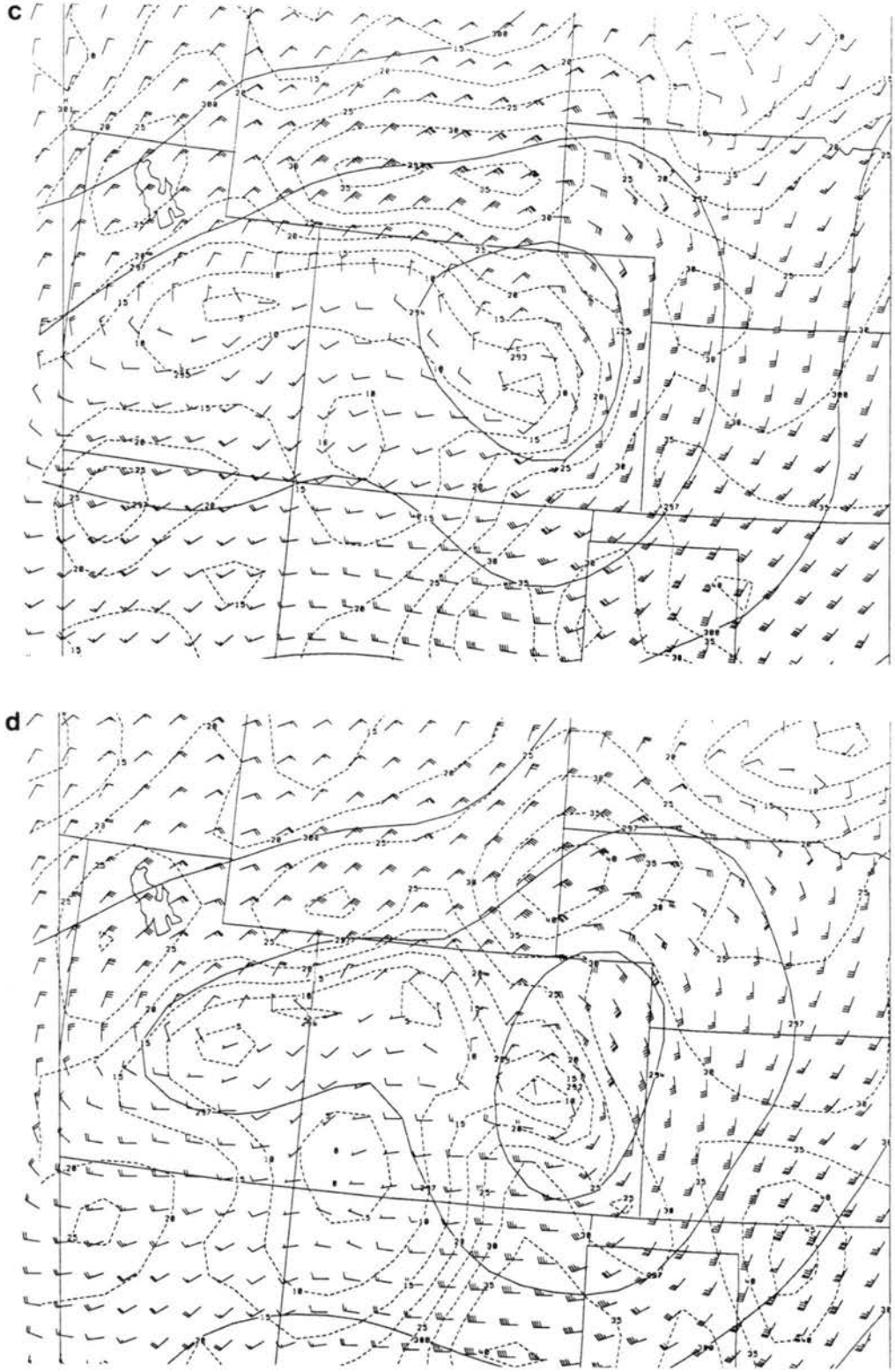

Figure 5.7: Continued: (c) 0000 UTC and (d) 0300 UTC 9 March 1992.

2100 UTC, a second cyclonic circulation is indicated over central Colorado. Apparently, the 700 mb low does not progress smoothly across the Rocky Mountain barrier but rather redevelops east of the barrier, similar to the evolution observed in the 7 January 1992 case study. Strong east-northeast flow continues over southern Wyoming in the vicinity of the surface front. The 700 mb cyclonic circulation is well defined over central Colorado at 0000 UTC with east-northeast flow strengthening to 18 m s^{-1} (35 knots) over southern Wyoming. At 0300 UTC, the 700 mb low is positioned over east-central Colorado with strong northeasterly flow exceeding 23 m s^{-1} (45 knots) over southeast Wyoming and extending southward along the northern Colorado Front Range.

The MAPS 500 mb height and wind analyses (Fig. 5.8) indicate a low and associated cyclonic circulation over southern Utah. A jet streak is evident southeast of the low with the jet axis extending across eastern New Mexico into southeast Colorado. The 500 mb low is positioned near the Four Corners at 2100 UTC with a 30 m s^{-1} (60 knot) jet streak indicated over the Texas and Oklahoma Panhandles. At 0000 UTC, the 30 m s^{-1} (60 knot) jet streak continues to be evident over the Texas and Oklahoma Panhandles. As in the 7 January 1992 case, the 500 mb low redevelops east of the mountains in the left front quadrant of the jet streak. In both cases, the low redevelops approximately 425 km northeast of the jet maxima, however, the 8-9 March jet streak and redeveloping low are located about 250 km southeast of the 7 January analyzed positions. The 500 mb low and cyclonic circulation are located over southeast Colorado at 0300 UTC, coincident with the left front quadrant of the jet streak. The region of greatest surface pressure falls (Fig. 5.5) is located beneath the left front quadrant of the jet streak, similar to the 7 January 1992 case study. A deep layer of east-northeast upslope flow is suggested over southern Wyoming and northeast Colorado.

The 1200 UTC morning rawinsonde (Fig. 5.9) from Denver indicates a seasonably unstable atmosphere with southerly winds in the boundary layer and southwesterly flow aloft. Further north at Lander, Wyoming, the atmosphere is also seasonably unstable but northeast winds are evident below 600 mb. Closer to the anticyclone, the arctic air mass is observed up to 700 mb in the Great Falls, Montana sounding with a surface temperature

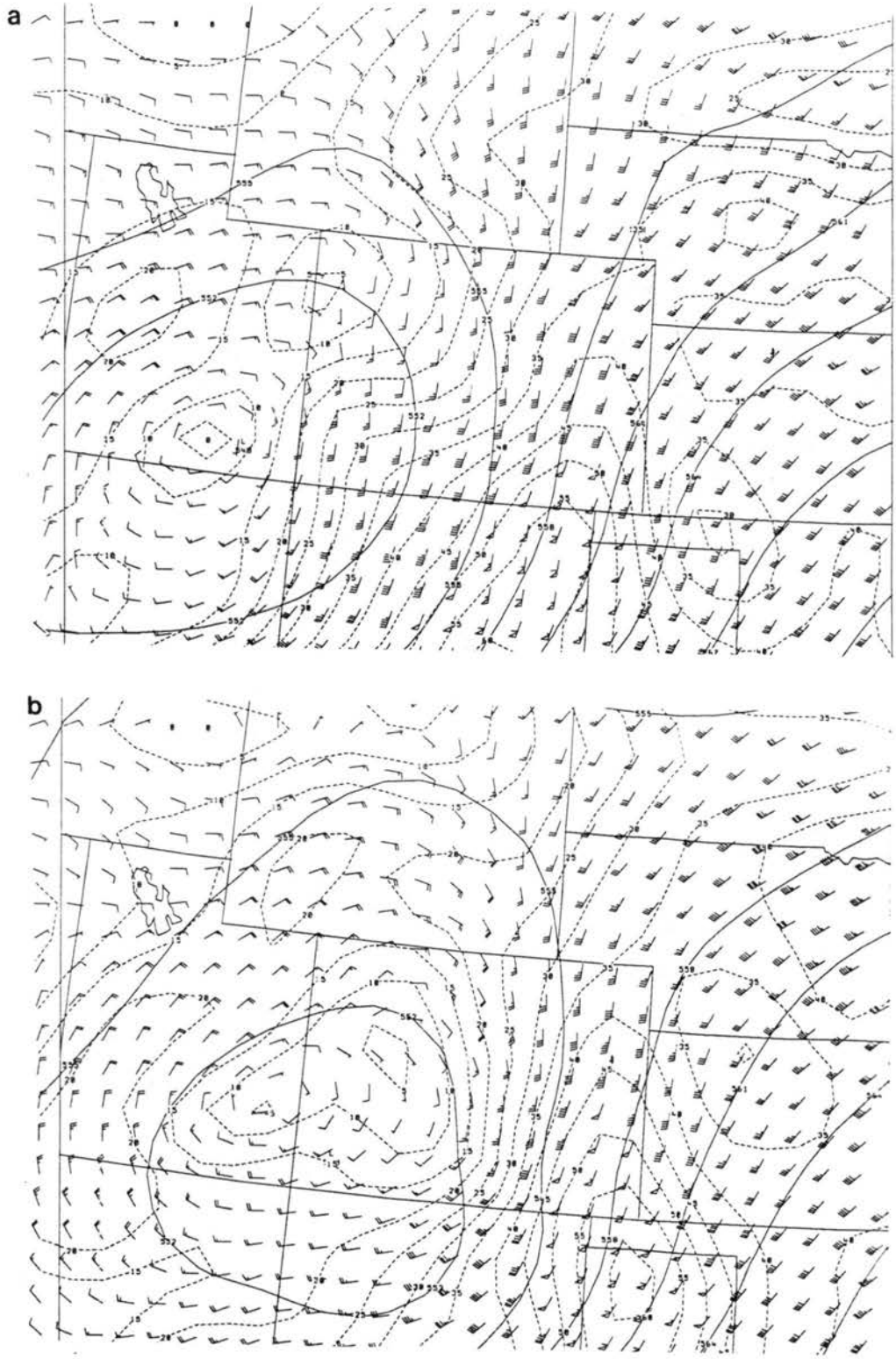

Figure 5.8: MAPS 500 mb height (dm), wind barb (knots), and isotach (knots) analyses from (a) 1800 UTC and (b) 2100 UTC 8 March 1992.

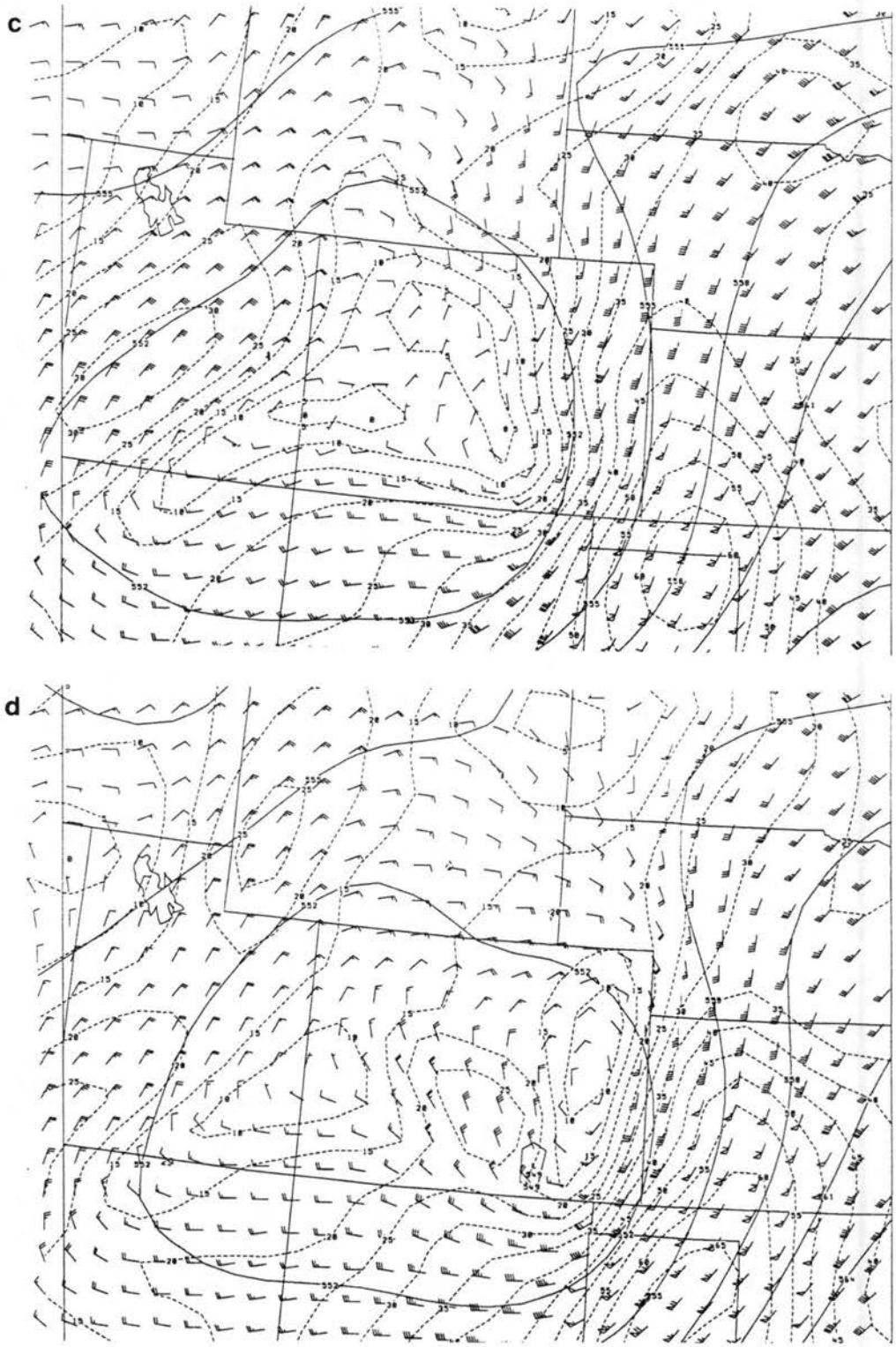

Figure 5.8: Continued: (c) 0000 UTC and (d) 0300 UTC 9 March 1992.

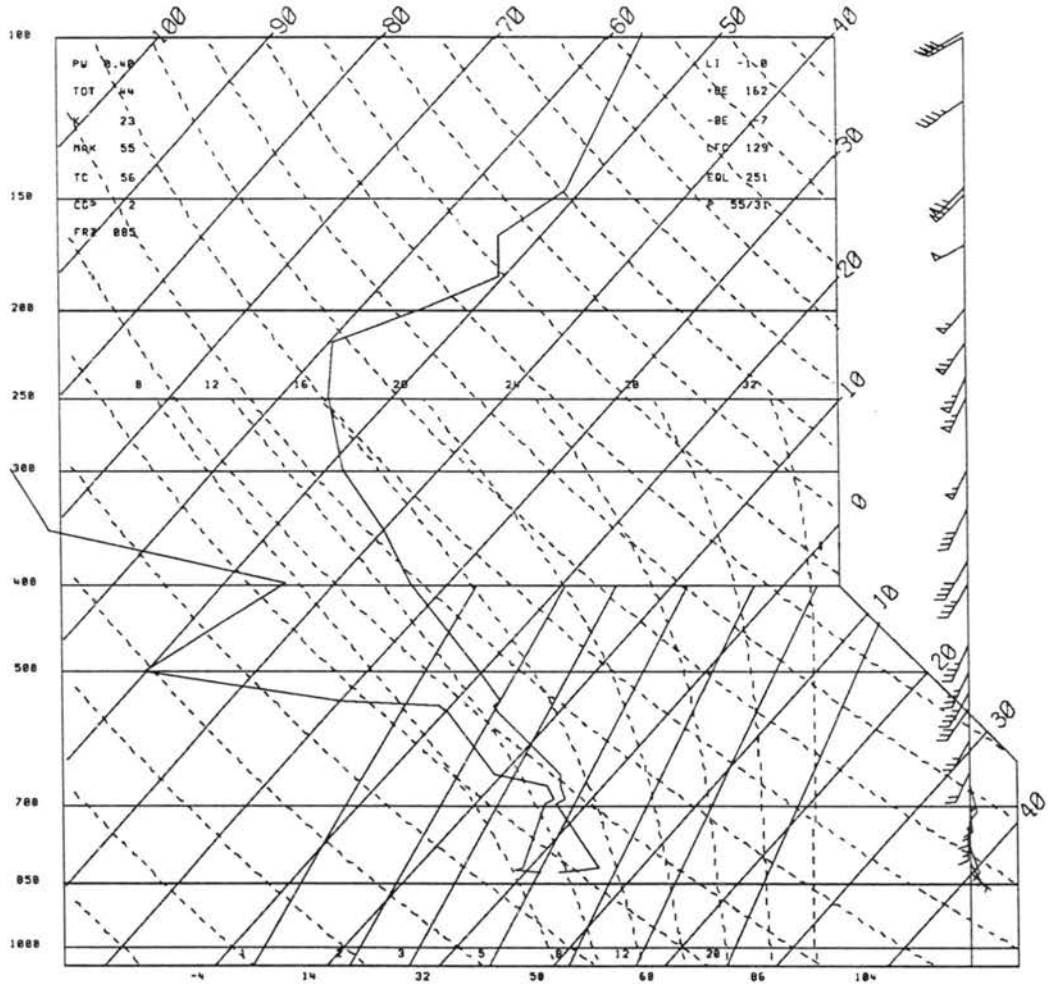

Figure 5.9: Rawinsonde observations from 1200 UTC 8 March 1992 at (a) Denver, CO.

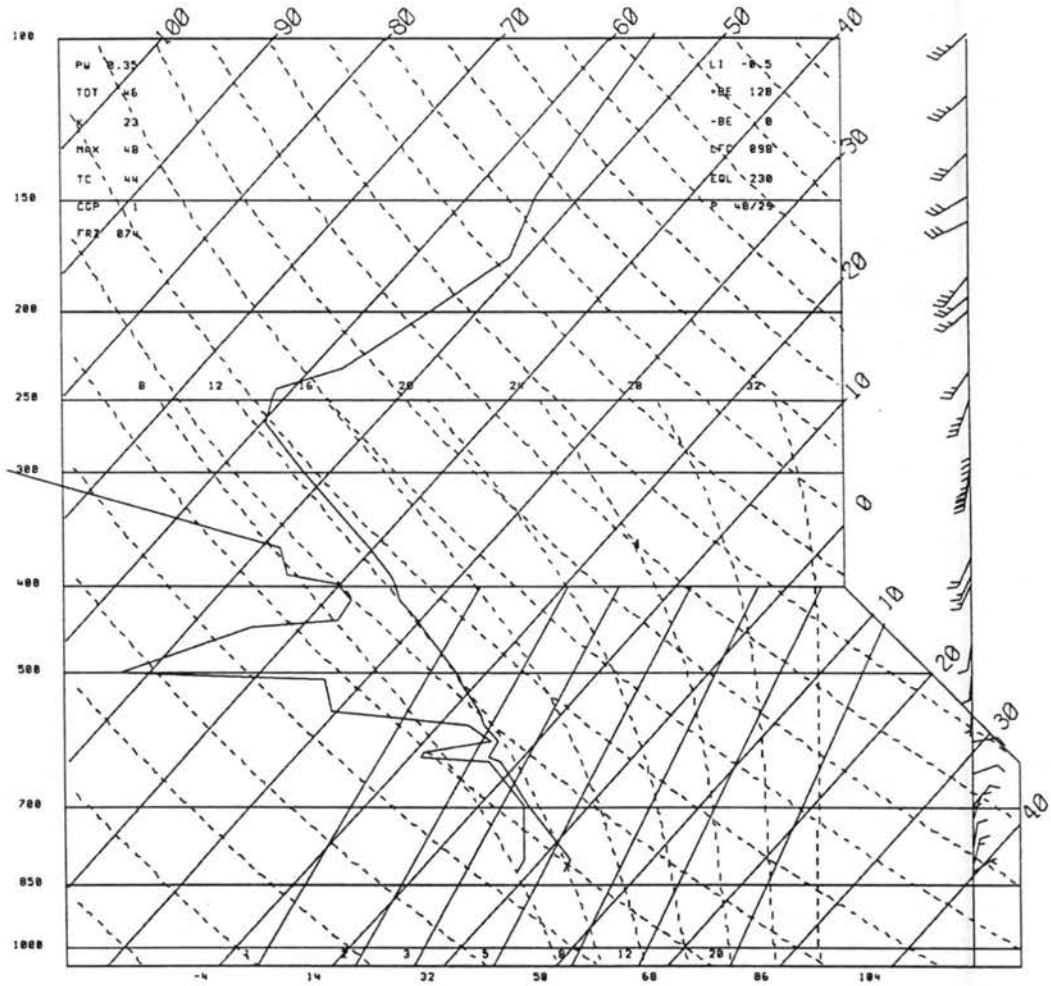

Figure 5.9: Continued: (b) Lander, WY.

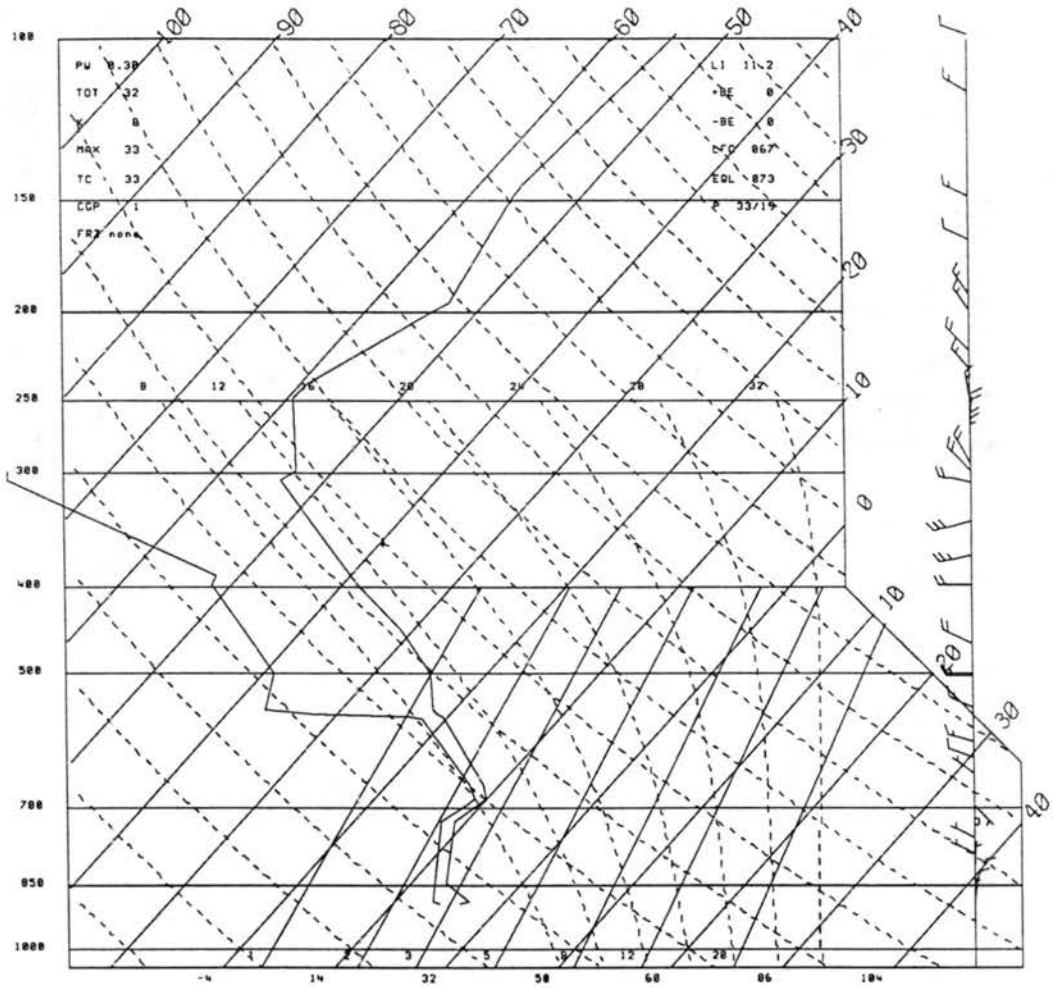

Figure 5.9: Continued: (c) Great Falls, MT.

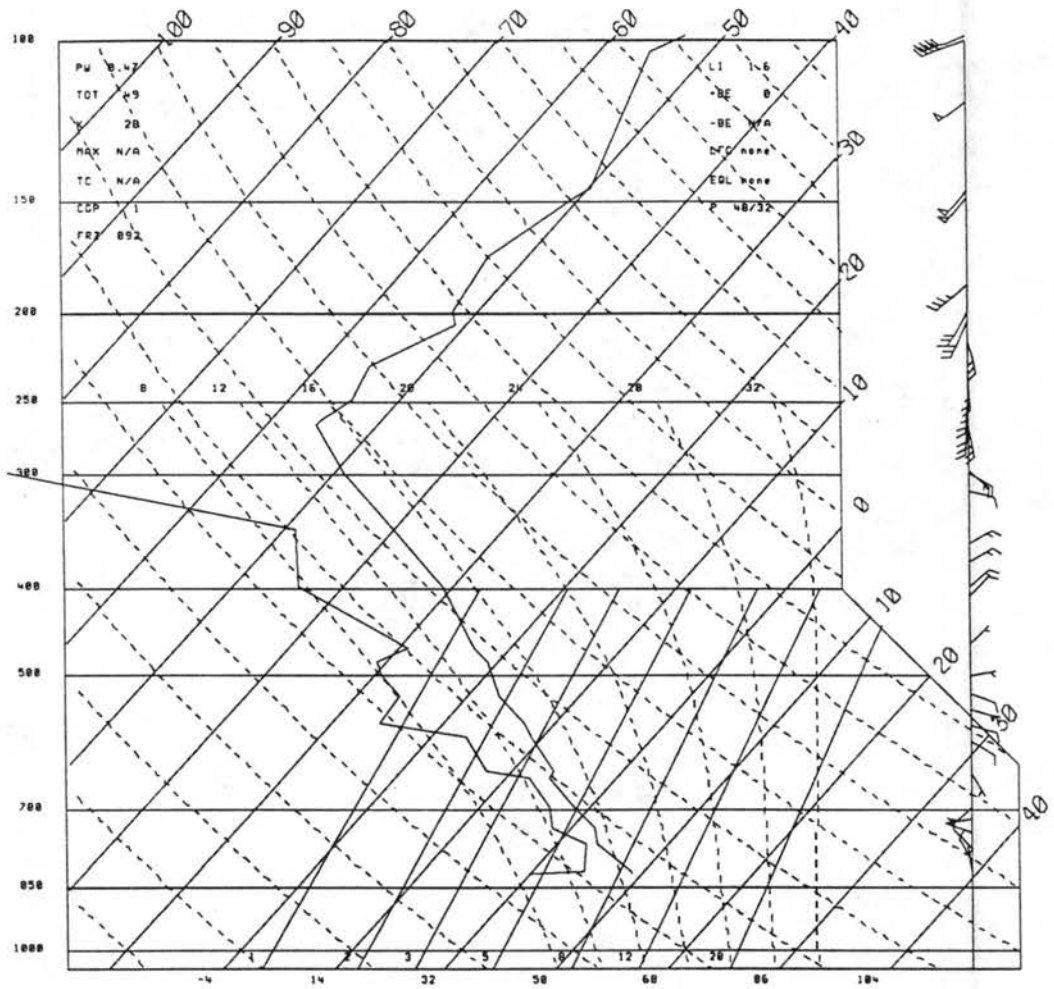

Figure 5.9: Continued: Rawinsonde observations from 0000 UTC 9 March 1992 at (d) Denver, CO.

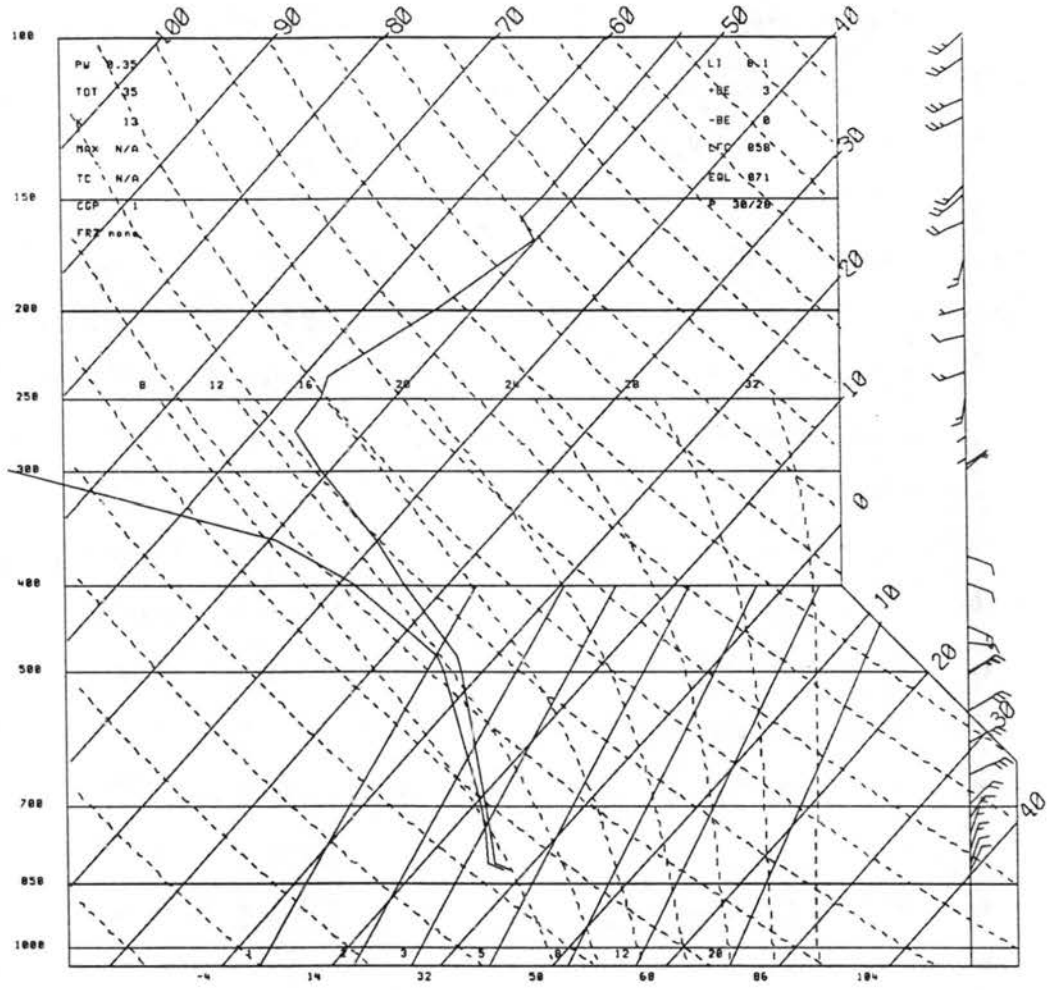

Figure 5.9: Continued: (e) Lander, WY.

around -5°C. The evening Denver sounding at 0000 UTC still shows a relatively unstable sounding but the surface flow has shifted to northerly and a layer of easterly flow is evident between 700 and 300 mb. At Lander, the air mass below 500 mb has cooled and stabilized and east-northeast flow is observed up to 300 mb.

5.1.3 Local scale observations

A close examination of the arctic front traveling through the northeast Colorado Plains and Front Range is possible using the FSL mesonet of automated surface observations and Platteville wind profiler data. The location and movement of the front is evident in a one hour time interval sequence of mesonet observations from 2200 through 0300 UTC (Fig. 5.10). The front is just entering the northeast portion of the mesonet domain at 2200 UTC as suggested by the stronger north-northeast winds at Ft. Morgan, Briggsdale, and Nunn. Weaker northeast winds at many of the other stations are typical in the afternoon with flow oriented parallel to the South Platte River drainage. The front has progressed through most of Morgan and Weld counties by 2300 UTC with northwest to northeast winds gusting to 38 knots. A 10° F drop in temperature is observed at Greeley in the one hour period. By 0000 UTC, the front has propagated into central Larimer, Boulder, Denver, and Arapahoe counties. Behind the front, wind gusts range from 18 to 37 knots. Northwest flow at Ft. Collins and northeast flow at Boulder together with a stable boundary layer suggest the development of a Longmont anticyclone regime.

The front has passed through all the mesonet locations by 0100 UTC except for the three highest mountain stations and the southernmost Elbert location. Wind gusts have increased at the northern stations with Nunn reaching 42 knots. The front passes through Elbert by 0200 UTC and is growing deeper with time as evidenced by the wind shift at Rollinsville, elevation 2749 m, and Ward, elevation 3005 m. A wind gust of 49 knots is observed at Nunn while the wind direction at Ft. Morgan has shifted from north to east. Strong winds are evident at all the non-mountain stations at 0300 UTC with gusts exceeding 50 knots at Nunn. North-northeast flow at Longmont, Boulder, and Lakewood continues to suggest a Longmont anticyclone regime and strong easterly flow has developed at Ft. Morgan. The easterly flow might suggest the development of a cold air damming

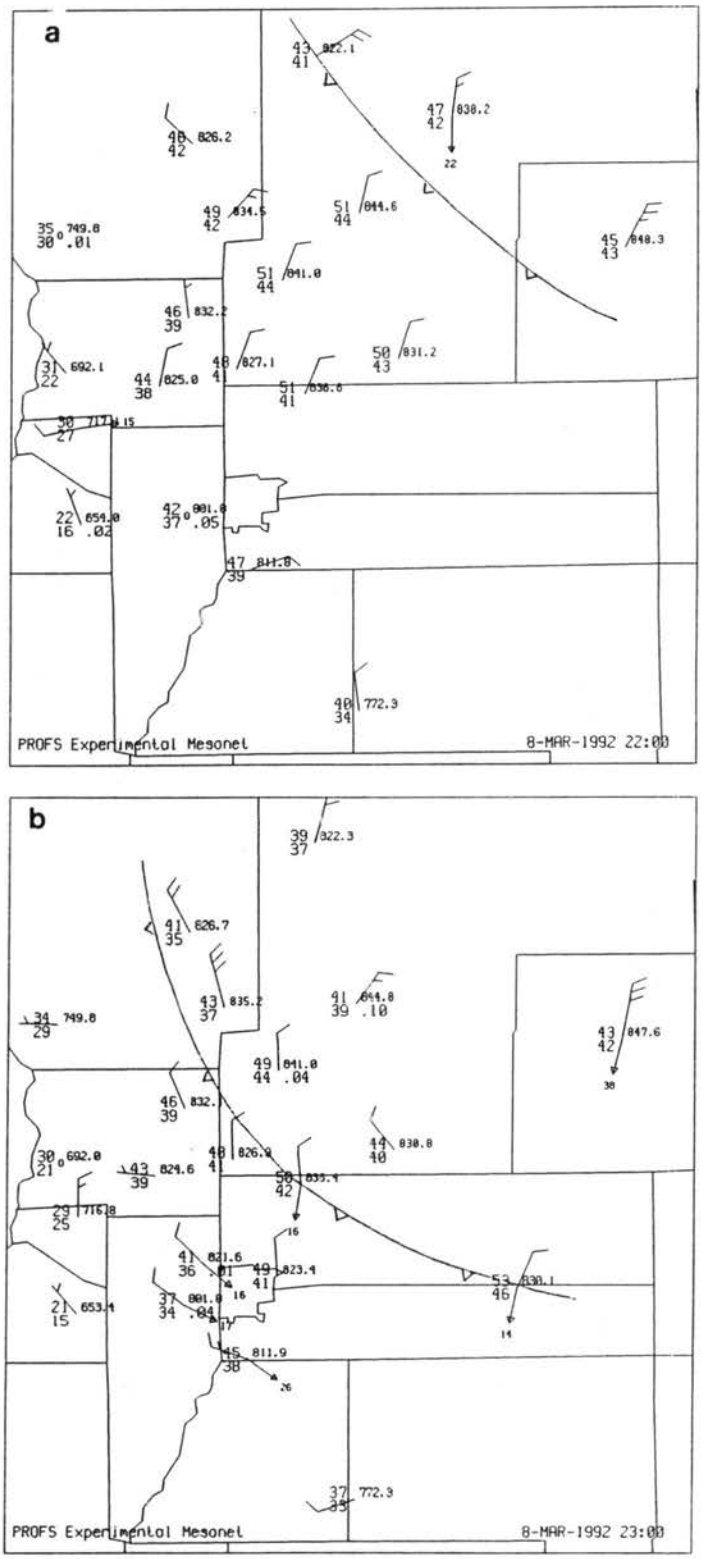

Figure 5.10: Automated surface observations from the FSL mesonet for (a) 2200 UTC and (b) 2300 UTC 8 March 1992 (winds are in knots).

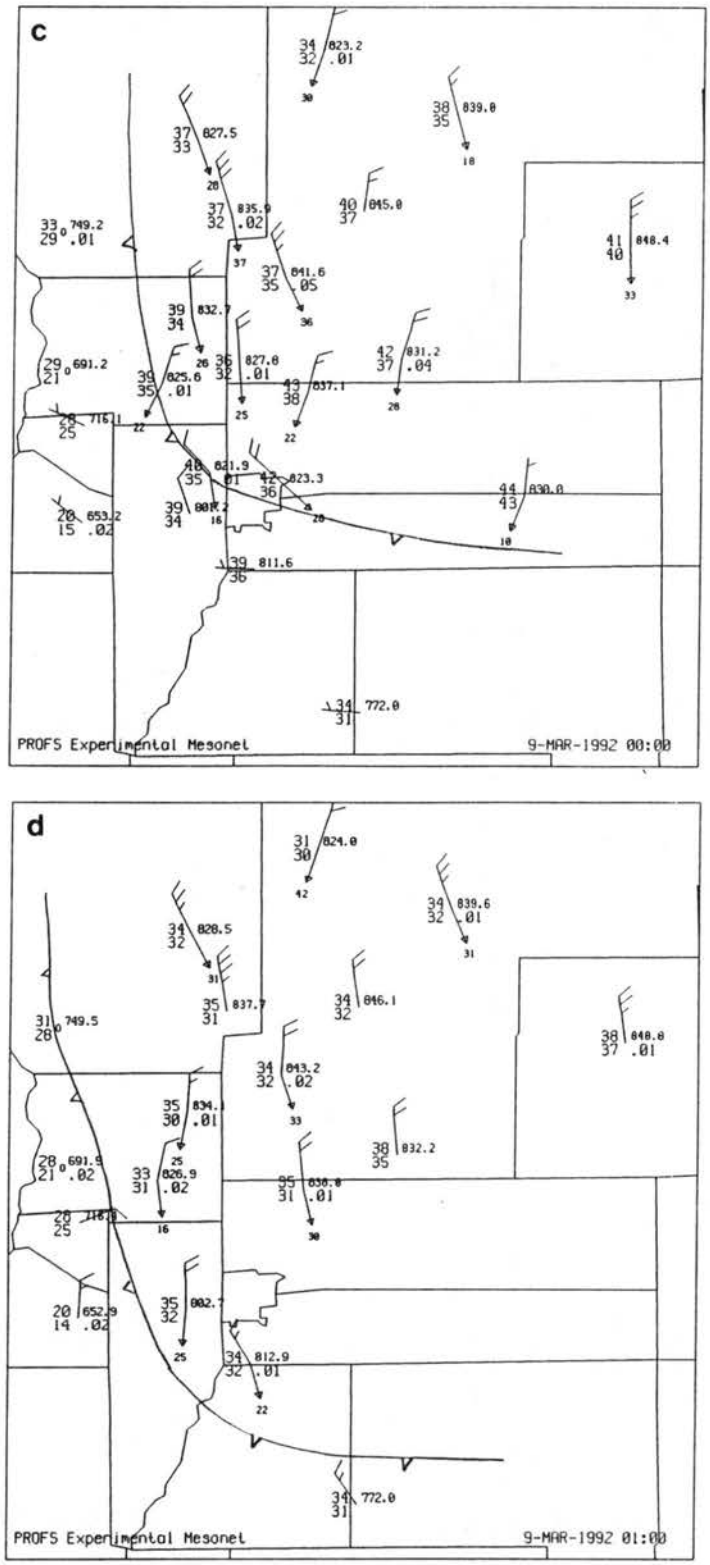

Figure 5.10: Continued: (c) 0000 UTC and (d) 0100 UTC 9 March 1992

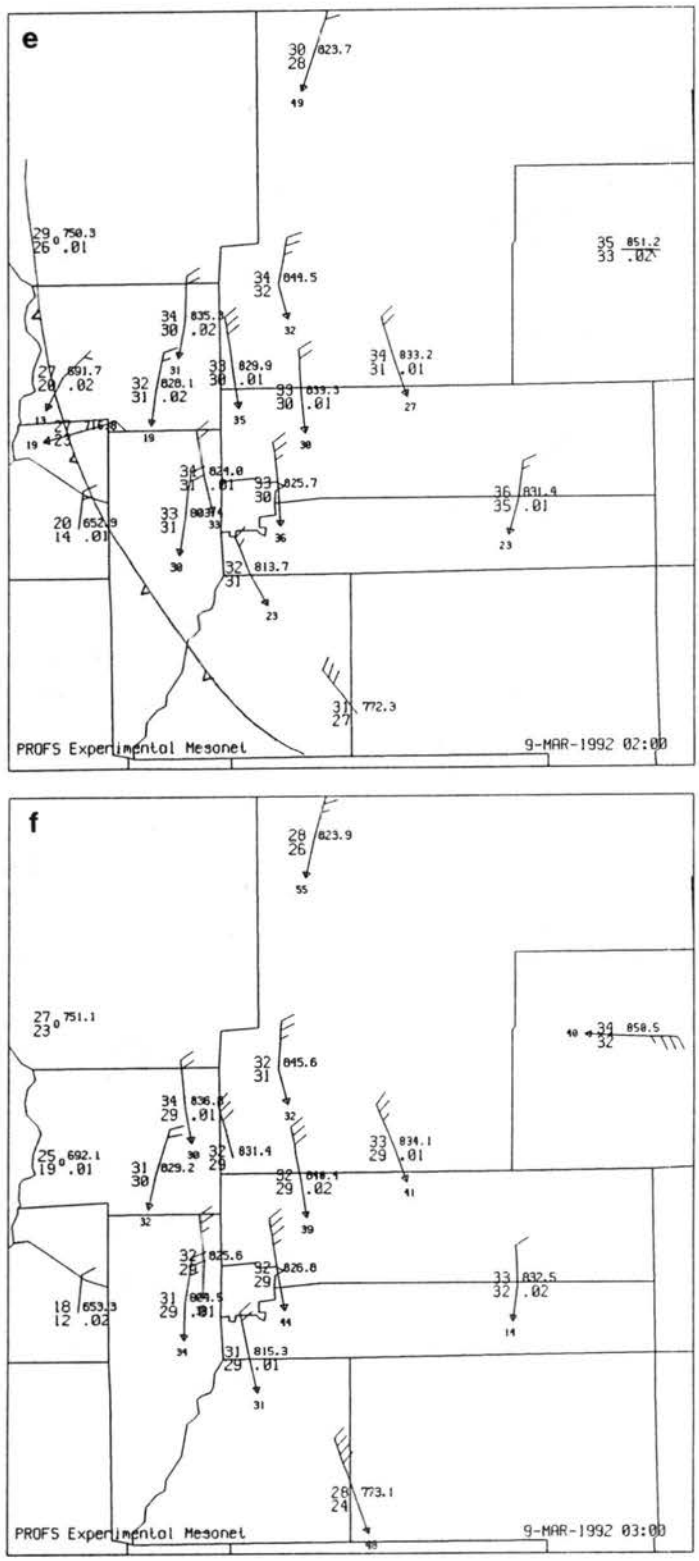

Figure 5.10: Continued: (e) 0200 UTC and (f) 0300 UTC 9 March 1992

situation (e.g. Dunn 1987), however, the lack of colder temperatures observed along the Front Range does not support the cold air damming hypothesis.

A time-height cross section of winds from the Platteville profiler (Fig. 5.11) indicates a shallow layer of easterlies beneath a tall column of southerlies at 1800 UTC. By 2200 UTC, the layer of easterlies has increased in depth to about 5 km. The mesonet observations indicate that the arctic front passes Platteville between 2200 and 2300 UTC. Evidently, post-frontal precipitation has adversely affected much of the Doppler wind profiler signal at 2300 UTC. The boundary layer winds from 0000 to 0200 UTC appear reasonable and they indicate the development of strong north-northeast winds exceeding 25 m s^{-1} up to about 3.5 km. Deep easterly flow is evident above the arctic layer up to at least 7 km.

Reflectivity data from the Doppler radar (Fig. 5.12) located about 10 km northeast of Denver suggests the development of convective showers prior to frontal passage and then the development of widespread precipitation with embedded convection following frontal passage. The development of scattered convective showers in the unstable air mass with reflectivities exceeding 35 dBZ are indicated along the Front Range and in Morgan county at 2100 UTC. The convective showers have intensified by 2300 UTC with reflectivities greater than 40 dBZ in several areas and one region exceeding 55 dBZ in southwestern Washington county. The precipitation coverage appears to spiral counter-clockwise around the mid-level cyclone located east of Denver and does not appear to be correlated to the frontal location. By 0100 UTC, widespread post-frontal precipitation is indicated with some embedded cells of higher reflectivities greater than 40 dBZ. 0300 UTC surface observations within the local radar domain report all the precipitation to be in the form of snow and a widespread area of 20 to 30 dBZ reflectivity suggests significant snowfall intensity over most of the domain except the southeast corner. The precipitation intensity appears to be more uniform over the domain with little evidence of embedded cells of higher reflectivities.

Infrared satellite data (Fig. 5.13) suggests the development of a large area of precipitation over central and northeast Colorado. At 2100 UTC, a band of cold cloud tops are observed in association with the convection that developed east of the Rocky

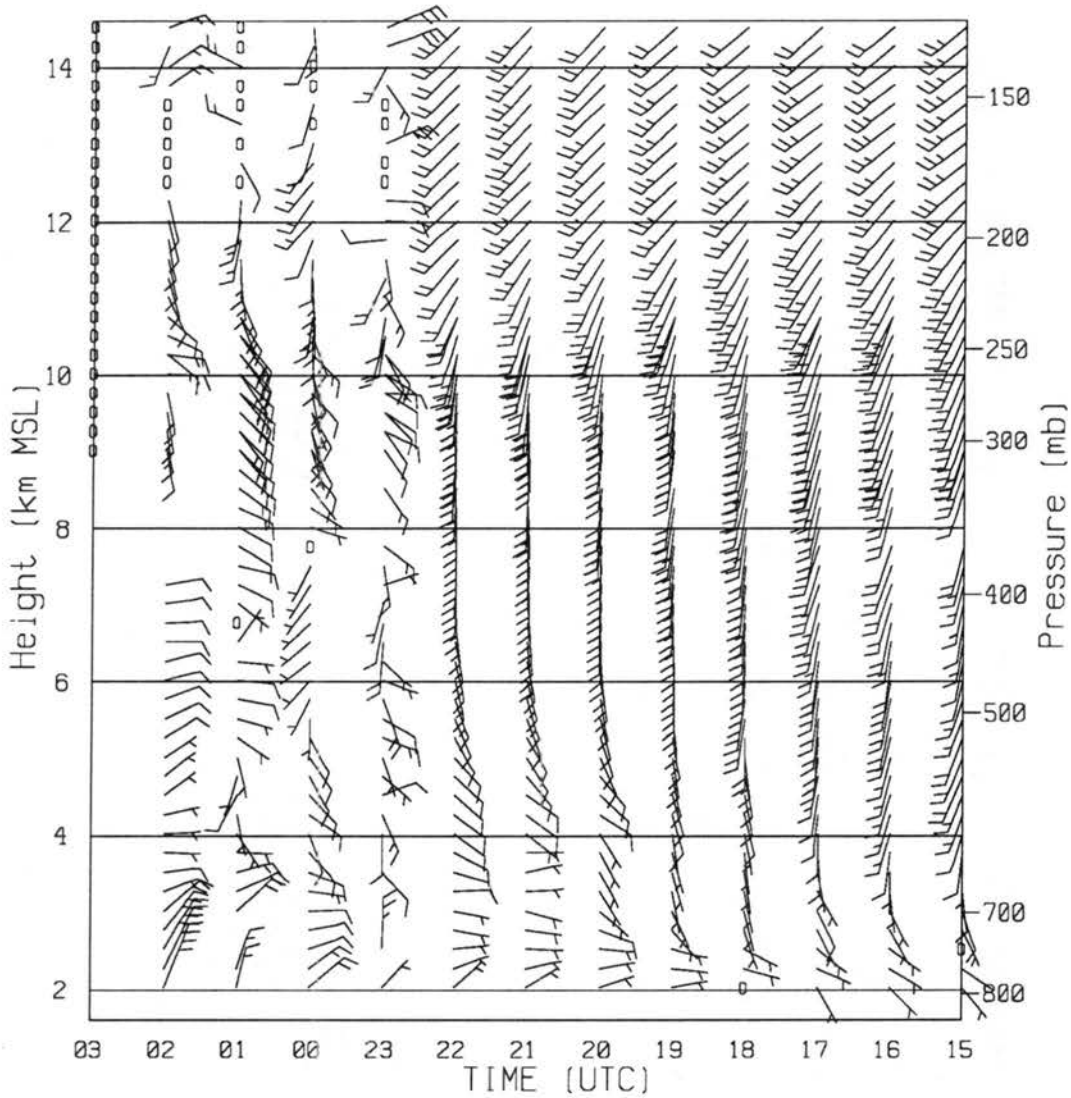

Figure 5.11: Time-height series of wind (m s^{-1}) from the Platteville, CO wind profiler from (a) 1500 8 March to 0300 UTC 9 March 1992.

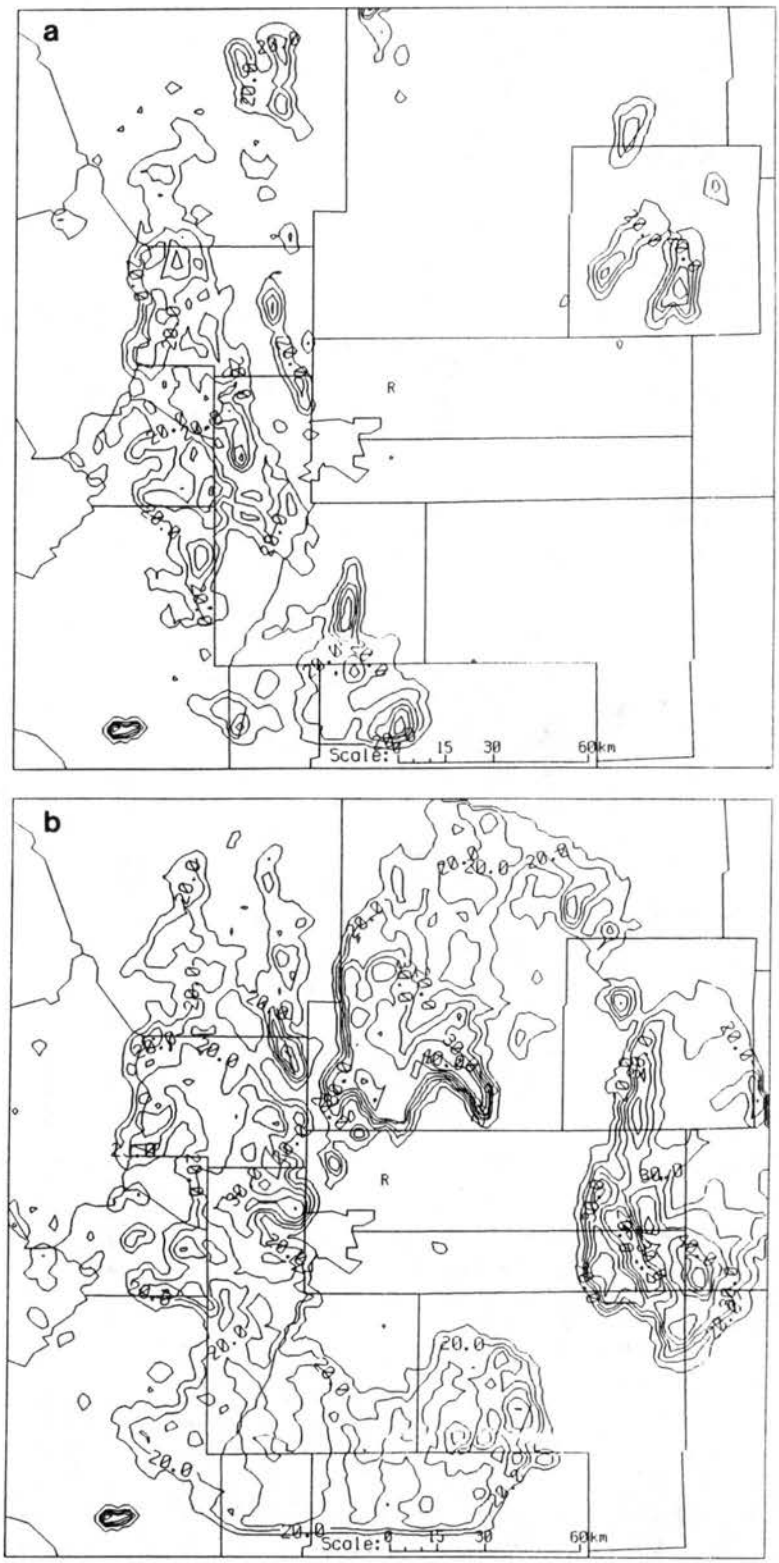

Figure 5.12: Prototype WSR-88D radar reflectivity (dBZ) from just northeast of Denver (denoted by the "R"). Ground clutter is not removed. (a) 2100 UTC and (b) 2300 UTC 8 March 1992.

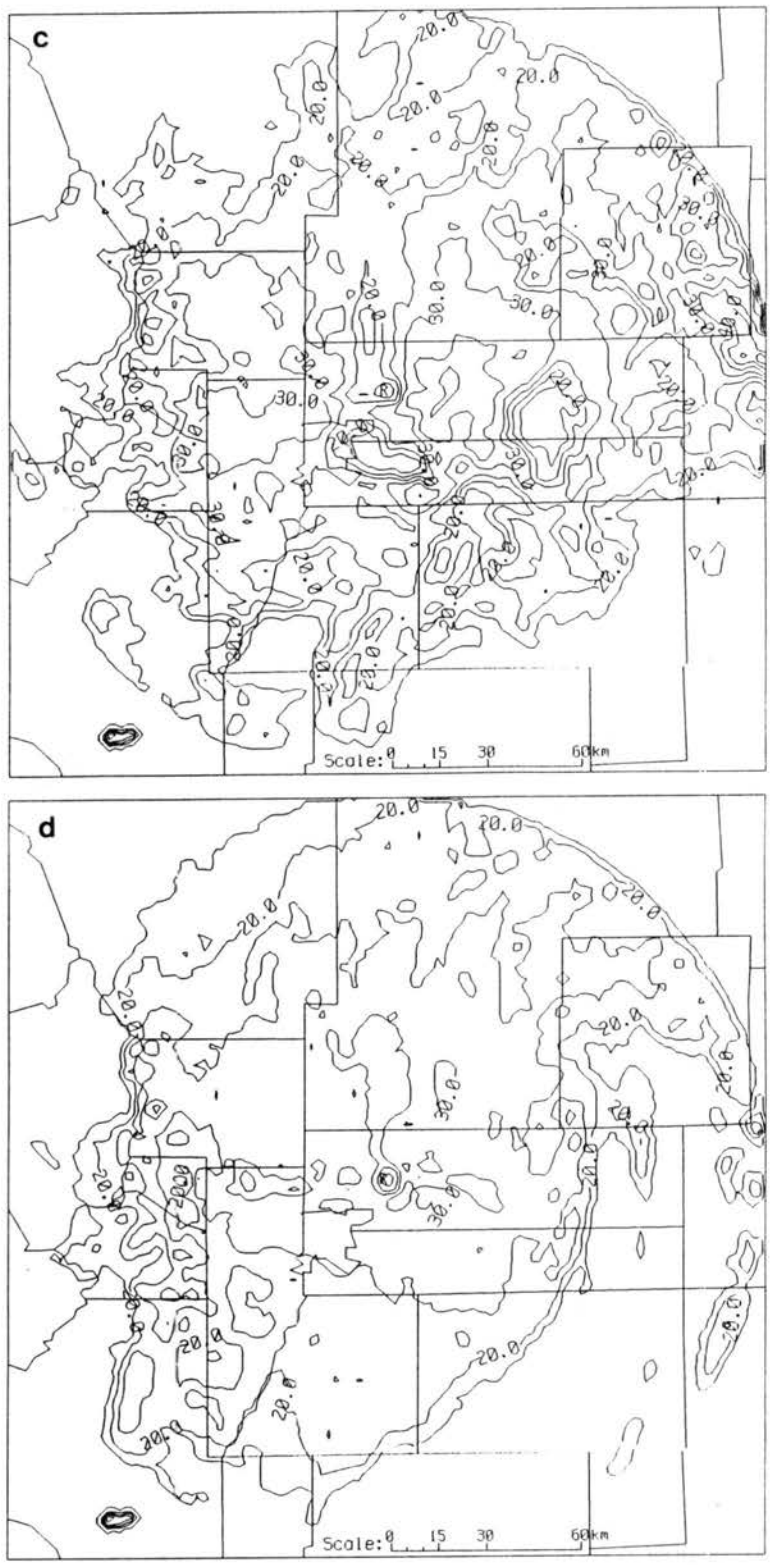

Figure 5.12: Continued: (c) 0100 UTC and (d) 0300 UTC 9 March 1992.

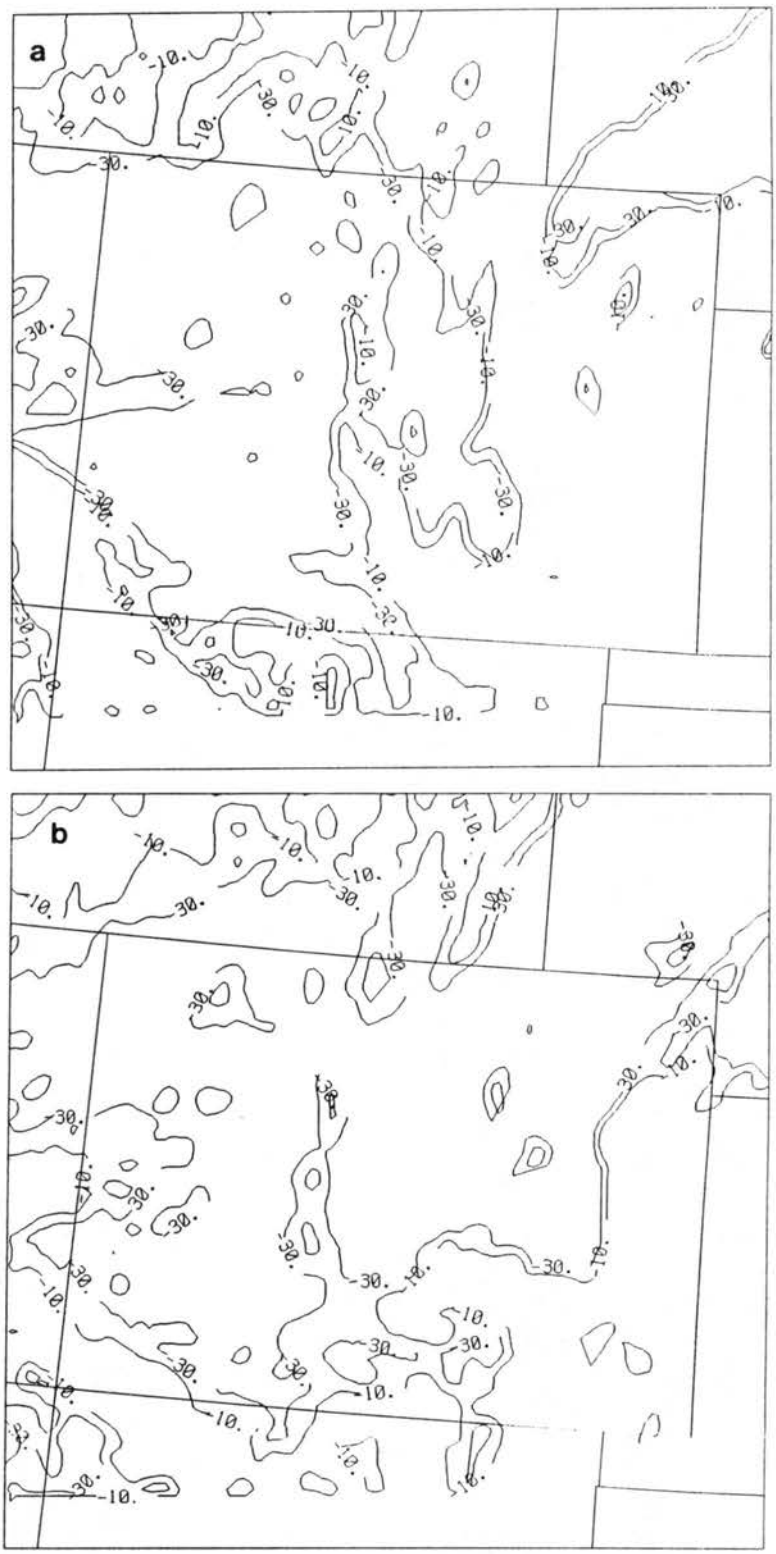

Figure 5.13: Infrared satellite data (°C) for (a) 2100 UTC and (b) 2300 UTC 8 March 1992.

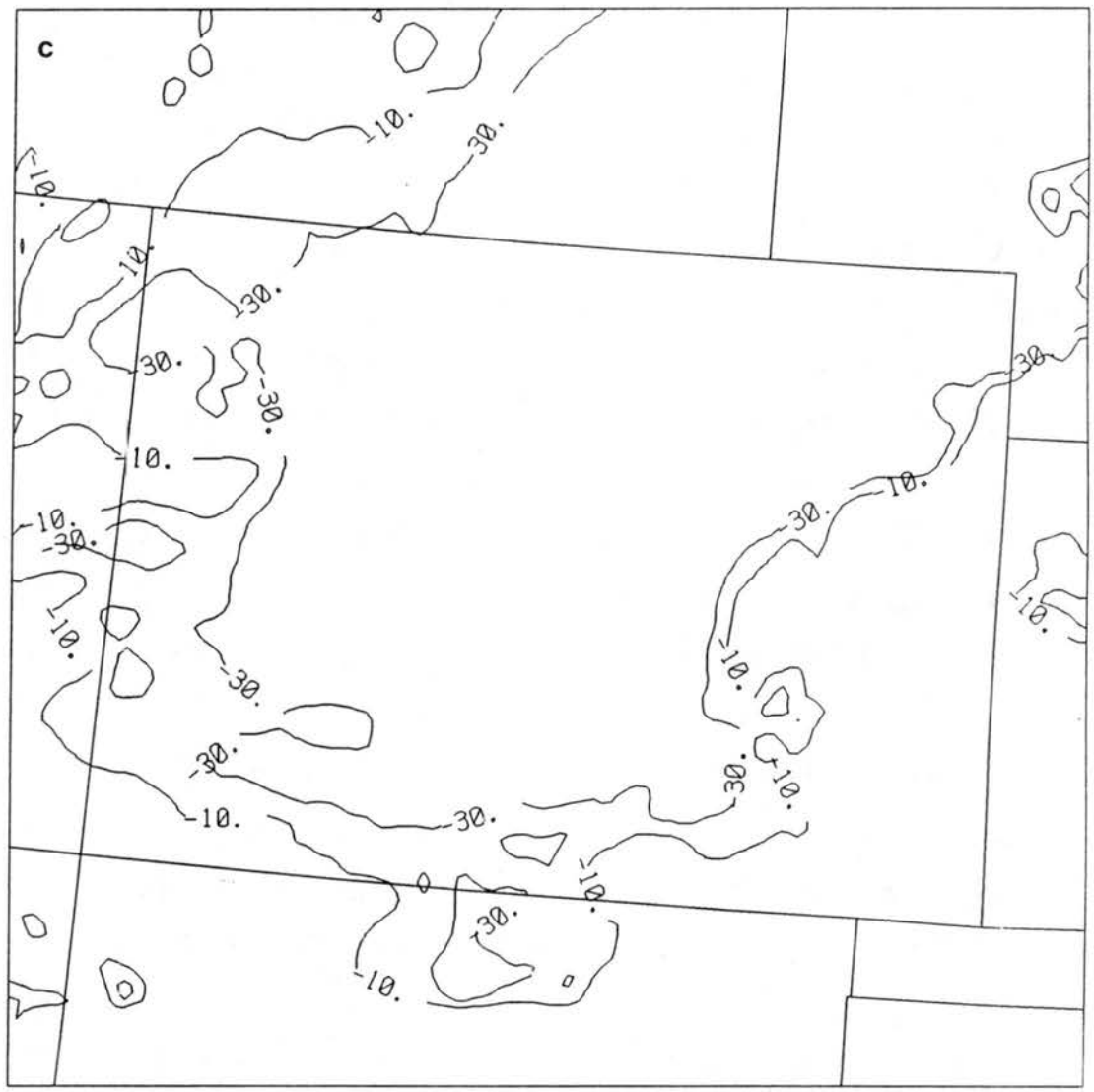

Figure 5.13: Continued: (c) 0300 UTC 9 March 1992.

Mountain barrier in the unstable air mass. Most of northeast Colorado is covered by cold cloud tops at 2300 UTC. By 0300 UTC, a large region of cold cloud tops extends from the Nebraska Panhandle and southeast Wyoming across northeast and central Colorado and appears to be wrapping around the mid-level cyclone. A dry slot is suggested over southeast Colorado.

5.1.4 Summary

The observations indicate that the 8-9 March 1992 storm can be described as a deep cyclonic system interacting with a shallow, arctic anticyclonic system to the north (Reinking and Boatman 1986). Many characteristics of the storm are typical of a Colorado spring storm (Fawcett and Saylor 1965). The interesting mesoscale features that the modeling study will focus on include: 1) the convective activity that developed over the Colorado Eastern Plains in the pre-frontal unstable air mass, 2) the evolution of a strong arctic front that progressed through northeast Colorado, and 3) the development of post-frontal heavy snow and high winds. The morning soundings indicate a seasonable unstable environment that aided in the development of afternoon convection as observed by surface reports and Doppler radar data. Upper air MAPS and NGM analyses and Platteville wind profiler data indicate the development of a deep layer of easterly, upslope flow over northeastern Colorado. At the surface, the FSL mesonet indicates the movement of the strong arctic front as it travels from Ft. Morgan at 2200 UTC, to Denver by 0000 UTC, and up the Palmer Lake Divide by 0200 UTC. The development of a Longmont anticyclone regime (Young and Johnson 1984) is suggested by the observations of strong north-northwest flow over the Cheyenne Ridge, weaker north-northeast flow at Boulder, and a stable boundary layer. Doppler radar, infrared satellite, and surface observations indicate the development of heavy snow and high winds behind the front that persisted beyond 0300 UTC.

5.2 Model Simulations

The primary mesoscale features of the 8-9 March 1992 blizzard are: 1) the pre-frontal convection, 2) the arctic cold front, 3) the post-frontal heavy snow, and 4) the post-frontal high winds. RAMS is initialized with real-time 10 km grid increment LAPS

analyses to determine if these features can be resolved by the model forecast. The seven RAMS simulations are initialized with analyses from 2100 UTC 8 March. Only 6 h forecasts are possible because of data losses at FSL resulting from power outages caused by the storm. Model physics are identical to those employed by the 7 January 1992 case study. The LSFC and LMIC simulations are presented first, followed by the four other sensitivity experiments (LAPS, LBAL, MAPS, MTOP) and then the true operational forecast (LFCS).

5.2.1 LSFC simulation - RAMS initialized with LAPS

The LSFC simulation is initialized with the 10 km grid interval LAPS mass, wind, and moisture analyses. The separate LAPS surface analysis is also blended into the model initialization. A comparison of the low-level (146 m AGL) RAMS forecast winds and potential temperature with SAO reports (Fig. 5.14), FSL mesonet observations (Fig. 5.10), and LAPS surface analyses (Fig. 5.15) indicates that the model simulation developed the arctic front and post-frontal high winds, but differences are noted especially in the area south of the front. The 3 h forecast valid at 0000 UTC 9 March indicates strong northeasterly flow across all of northeast Colorado and over the Palmer Lake Divide. In contrast, the LAPS analysis shows southerly flow in the Limon (LIC) area. Although weak northeasterly flow was occurring south of the front at the time of model initialization, the flow reversed to southerly ahead of the front and the model simulation was unsuccessful at predicting this flow reversal. The model forecast shows a relatively strong gradient of potential temperature positioned between Denver (DEN) and Colorado Springs (COS) that extends east-northeast to the Nebraska-Kansas border, suggesting the approximate location of the front. It appears that the over-forecast of northeasterly flow has pushed the front through the Denver area a little faster than observed and the lack of predicted southerly flow creates a weaker potential temperature gradient than is indicated by the LAPS analysis. The frontal location and magnitude appears to be better forecast away from the mountain barrier when compared to the LAPS analysis and the observations at Imperial (IMP), NE and Goodland (GLD), KS.

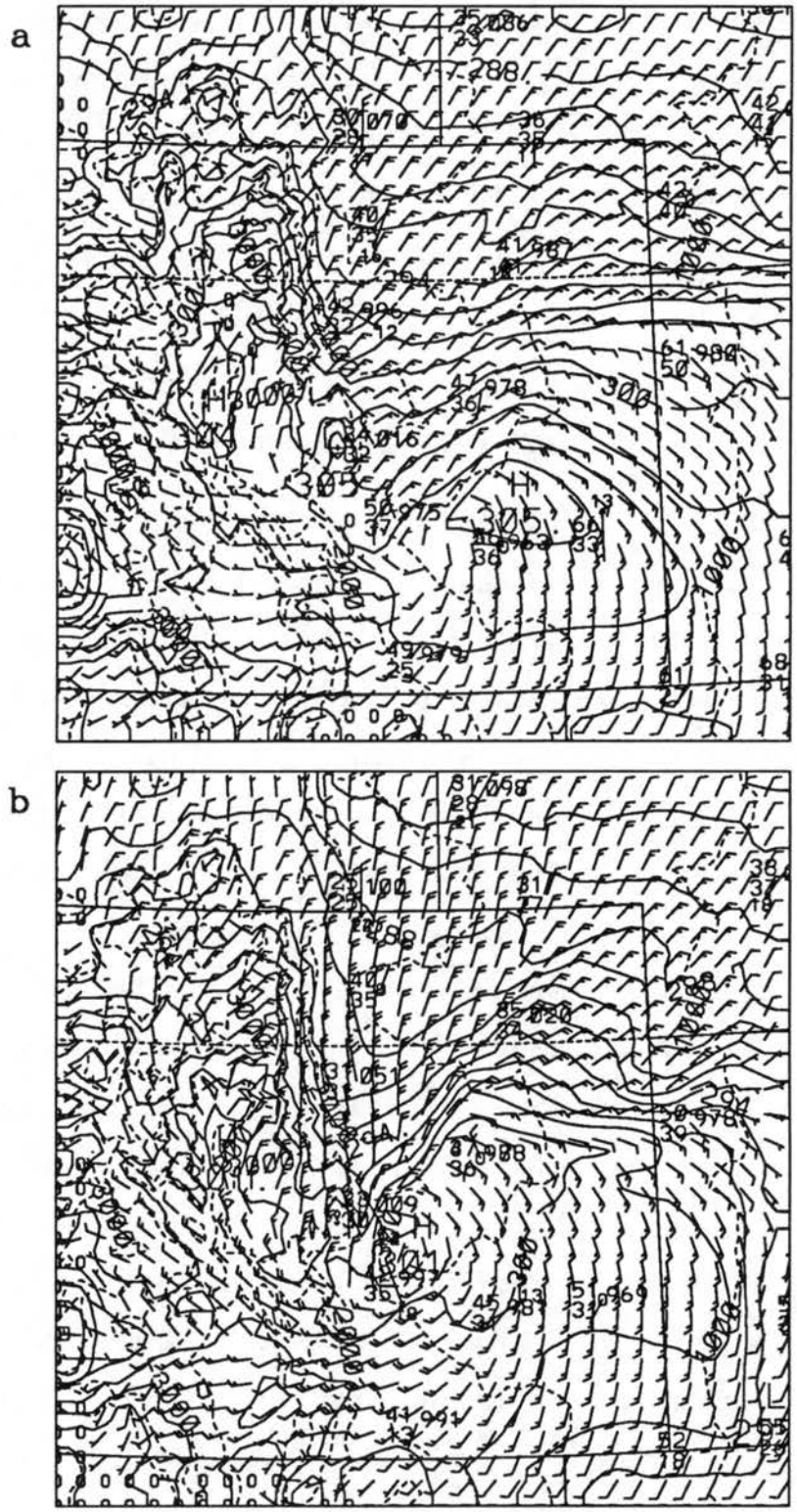

Figure 5.14: RAMS (LSFC) low-level (146 m AGL) potential temperature (K, contour interval = 1.5 K) and wind (m s^{-1}) predictions and actual SAO reports at model validation time from (a) the 3 h forecast valid at 0000 UTC and (b) the 6 h forecast valid at 0300 UTC 9 March 1992. Dashed contours represent model topography. Wind barbs are displayed at every other grid point.

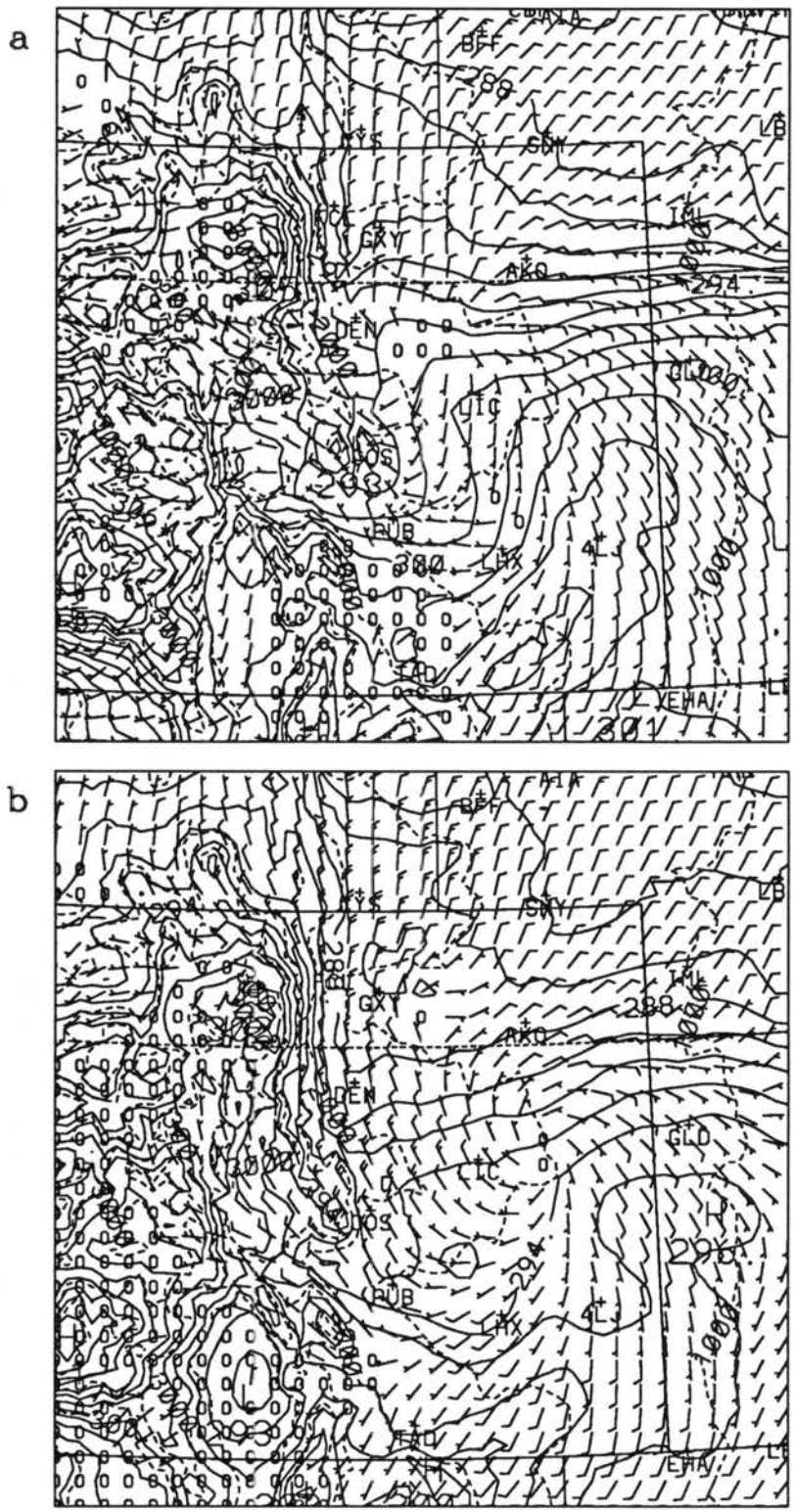

Figure 5.15: LAPS surface wind (m s^{-1}) analyses from (a) 0000 UTC and (b) 0300 UTC 9 March 1992. SAO locations east of the Continental Divide are indicated by standard 3-letter abbreviations. Wind barbs are displayed at every other model grid point.

More significant southerly flow has developed ahead of the front in the 6 h forecast valid at 0300 UTC 9 March. A surface cyclonic circulation is positioned northeast of Pueblo (PUB) about 140 km southwest of the LAPS analyzed location east of Limon. The forecast potential temperature gradient is now stronger than the LAPS analyzed gradient and the forecast suggests greater southward movement of the front along the Front Range to Colorado Springs. The forecast frontal location near the Kansas border appears reasonable based on the 11°F decrease in temperature and dew point at Goodland during the previous three hours. A large area of strong forecast winds exceeding 20 m s^{-1} exists north of the front which compares favorably with some FSL mesonet observations, but appears to be too strong when compared to the Akron (AKO) SAO wind report. A small easterly component is evident in the winds along the Front Range suggesting that the model has at least partially resolved the Longmont anticyclone regime. Qualitatively, the mesoscale features resolved by the 8-9 March surface forecasts show less agreement to observations than comparable forecasts from the 7 January 1992 case study.

RAMS forecasts of 500 mb height and wind (Fig. 5.16) show reasonably close agreement with the respective 500 mb MAPS analyses (Fig. 5.17). Both the 3 h RAMS forecast and the 0000 UTC MAPS analysis indicate an area of weak wind speeds west of Denver, Colorado Springs, and Pueblo with a surrounding region of cyclonic circulation. Predicted wind speeds are strongest (30 m s^{-1}) in the southeast portion of the domain, similar to the MAPS analysis. The shape of the 500 mb forecast height field is similar to MAPS, but the predicted magnitude is about 10 to 20 m higher than the MAPS analysis. A similar difference in magnitude was observed in the 7 January case study.

At 6 h, the RAMS forecast indicates a cyclonic circulation southwest of Pueblo that is about 140 km west-southwest of the MAPS analyzed position northeast of La Junta (LHX). Both the RAMS forecast and MAPS analysis continue to show highest wind speeds in the southeast corner of the domain. The forecast suggests relatively stronger wind speeds to the west and northeast of the low, but these are difficult to verify because of the sparsity of upper air observations. The predicted heights continue to be somewhat higher than the MAPS analyzed heights. As with the 7 January case study, the RAMS forecasts appear to

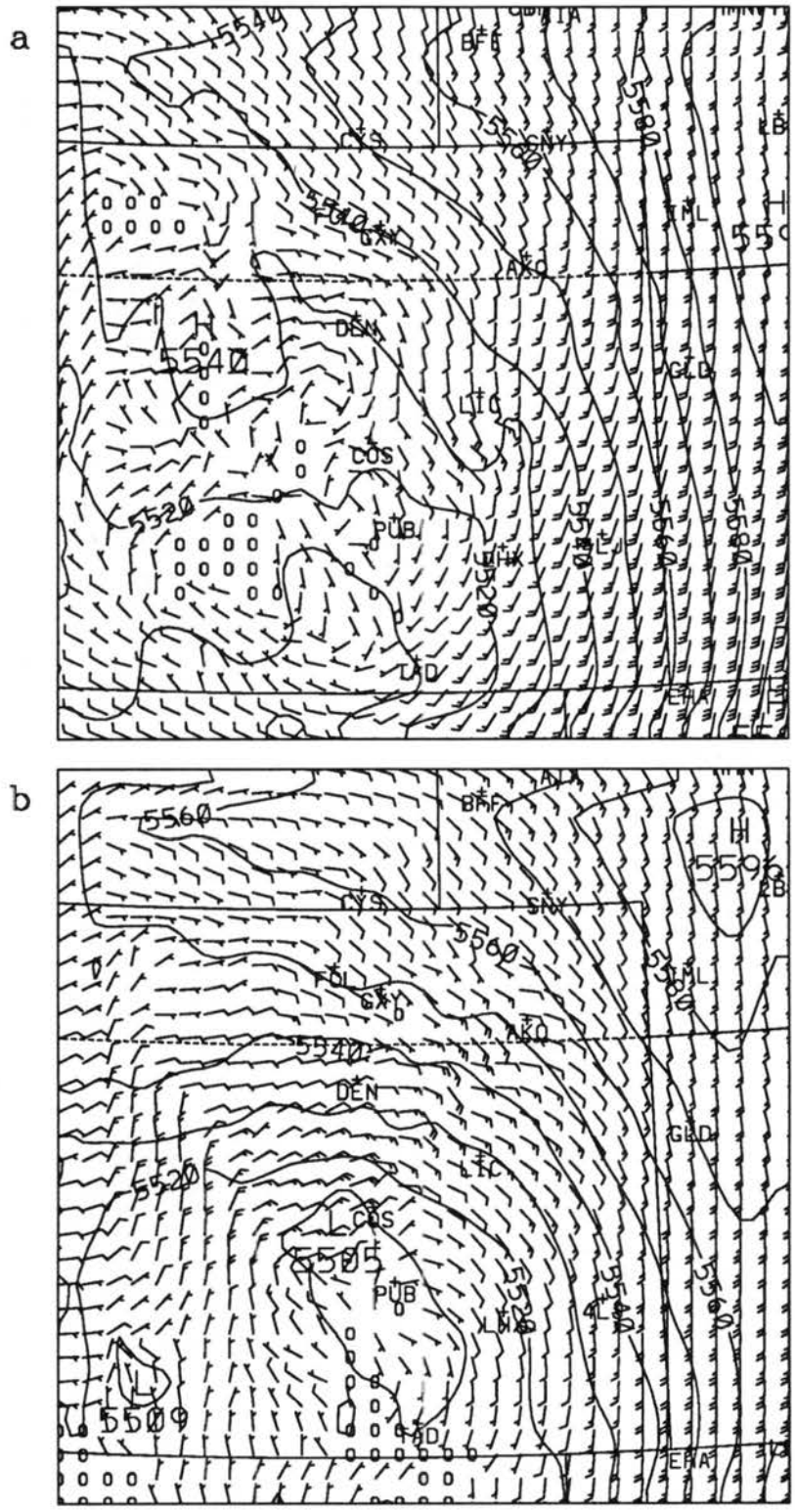

Figure 5.16: RAMS (LSFC) 500 mb height (m) and wind (m s^{-1}) predictions from (a) the 3 h forecast valid at 0000 UTC and (b) the 6 h forecast valid at 0300 UTC 9 March 1992.

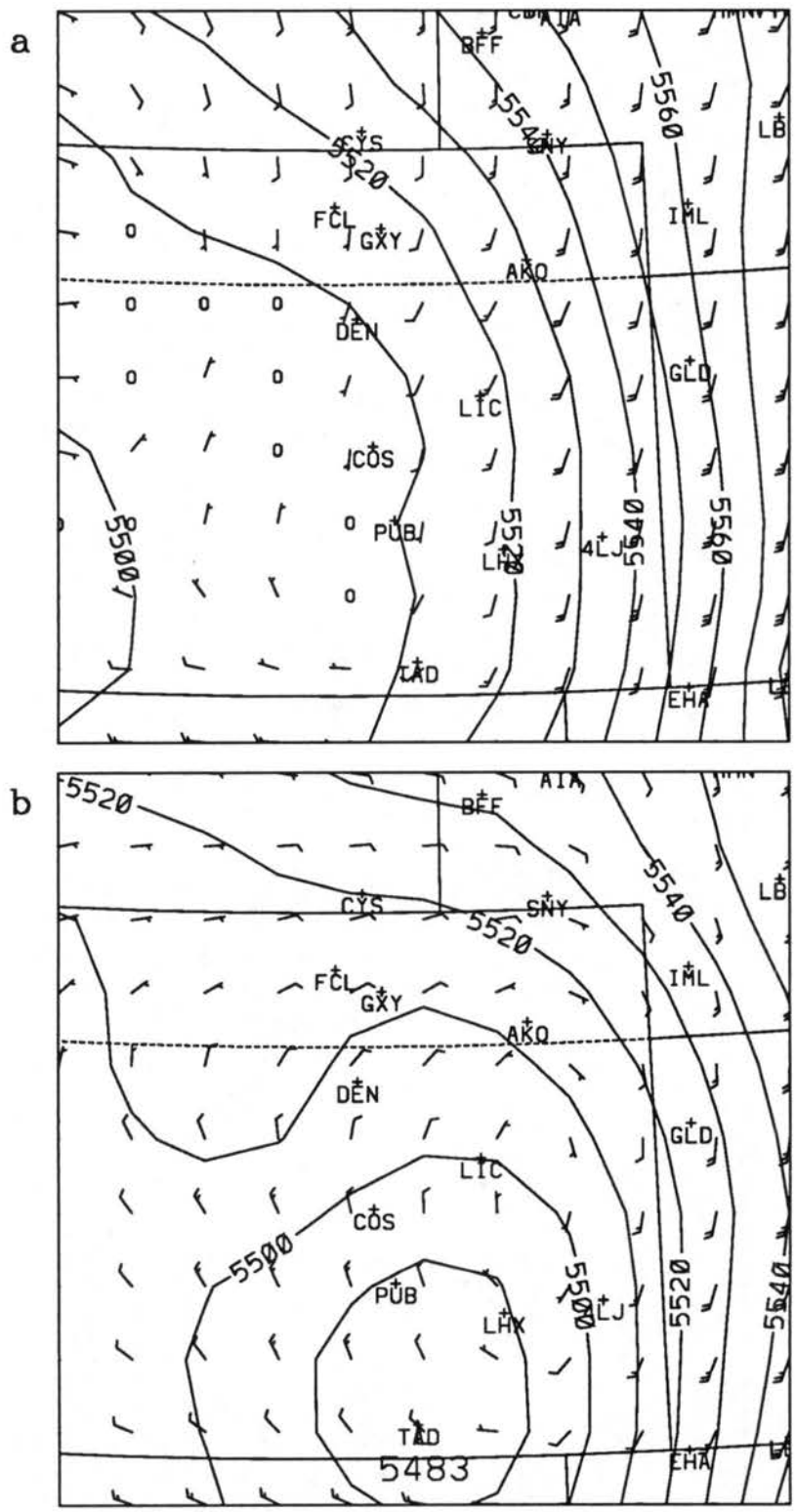

Figure 5.17: MAPS 500 mb height (m) and wind (m s^{-1}) analyses from (a) 0000 UTC and (b) 0300 UTC 9 March 1992.

have developed the general characteristics of the 500 mb flow, but it is difficult to ascertain if RAMS has correctly provided any additional mesoscale information.

Hourly wind profiler data from Platteville are the only high temporal resolution upper air observations available for comparison with the model predictions. A time series of RAMS upper air wind forecasts from near Platteville (Fig. 5.18) indicate that the primary flow regimes are resolved. Between 2100 and 2200 UTC, low-level northeasterly flow is evident up to about 5 km with mostly southerly flow aloft. Following frontal passage, north-northwest boundary layer winds strengthen to 20 m s^{-1} and the depth at 0300 UTC extends to near 3.5 km, similar to the Platteville observations (Fig. 5.11). A layer of predicted easterly flow is indicated above the arctic layer which gets deeper with time extending up to 8 km by 0300 UTC.

Several areas of significantly greater maximum upward vertical motion are predicted by RAMS for 8-9 March (Fig. 5.19) than for 7 January 1992 (Fig. 4.22). The 3 h forecast of vertical motion indicates two centers of maximum ascent, one southwest of Colorado Springs (>4 m s^{-1}) and the other south of Limon (>6 m s^{-1}), that are located over regions of low-level convergence. At 0300 UTC, maximum forecast upward vertical velocity continues to exist over regions of low-level convergence, but the magnitude has decreased since 0000 UTC. The strongest ascent is in an area extending from south of Denver northeastward to west of Akron. Another line of ascent appears to be positioned along the front west of Goodland.

A representative vertical cross section of potential temperature and vertical velocity through the region of maximum ascent south of Limon (Fig. 5.20, see Fig. 5.19a for location) indicates a tall, narrow column of upward vertical velocity. Low-level convergence and a relatively unstable lower troposphere likely contributed to the initiation of the rising motion. The prominent undulation in potential temperature that is colocated with the area of ascent suggests that a significant amount of latent heat has been released which has likely enhanced the rising motion. The magnitude of the potential temperature jump and the upward vertical velocity indicate that the model has released an unrealistically large amount of latent heat. This is corroborated by a separate simulation where cloud

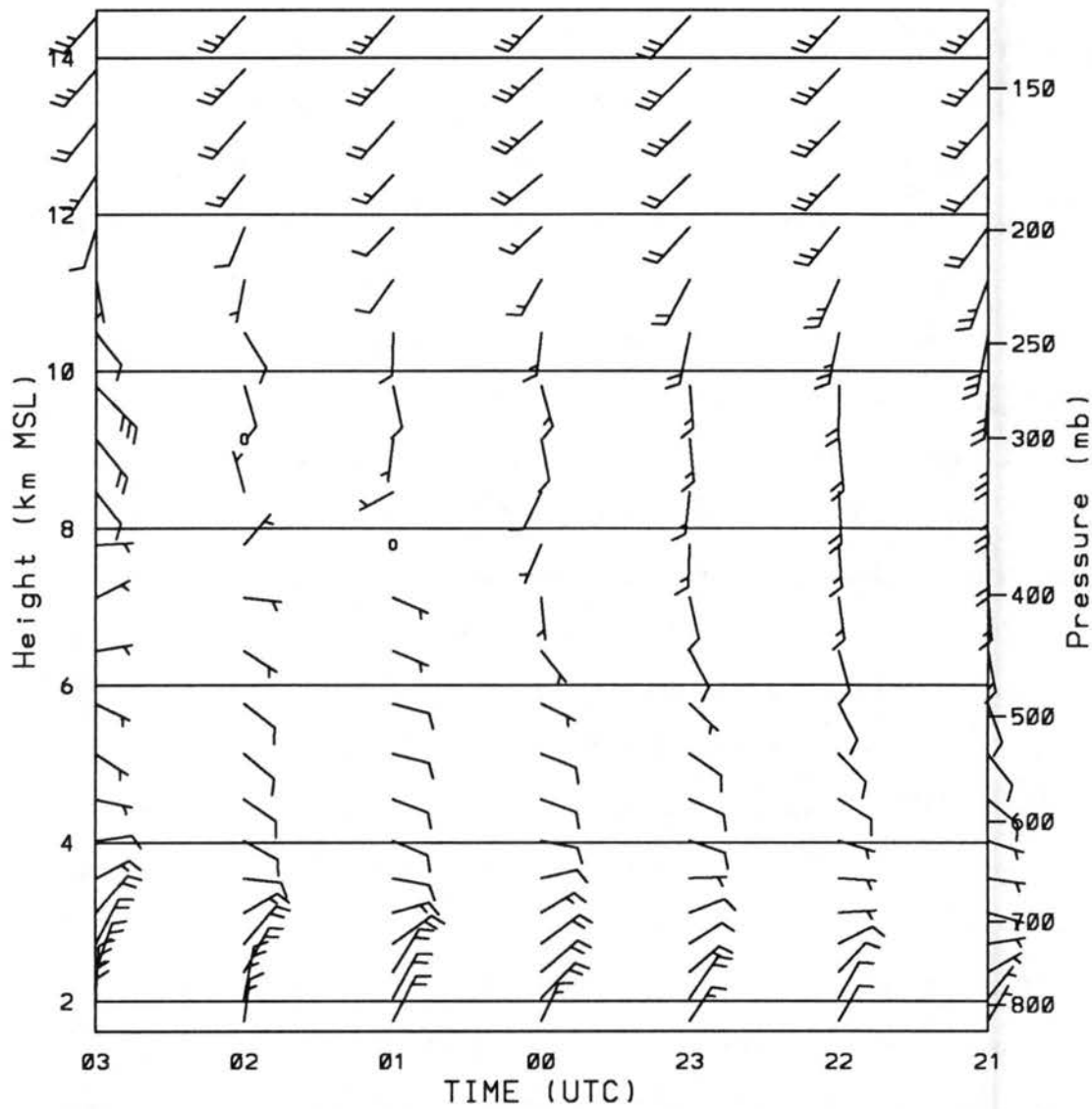

Figure 5.18: Time-height series of RAMS (LSFC) forecast wind (m s^{-1}) for the model grid point closest to Platteville, CO from the 0 to 6 h prediction valid at 2100 UTC 8 March through 0300 UTC 9 March 1992.

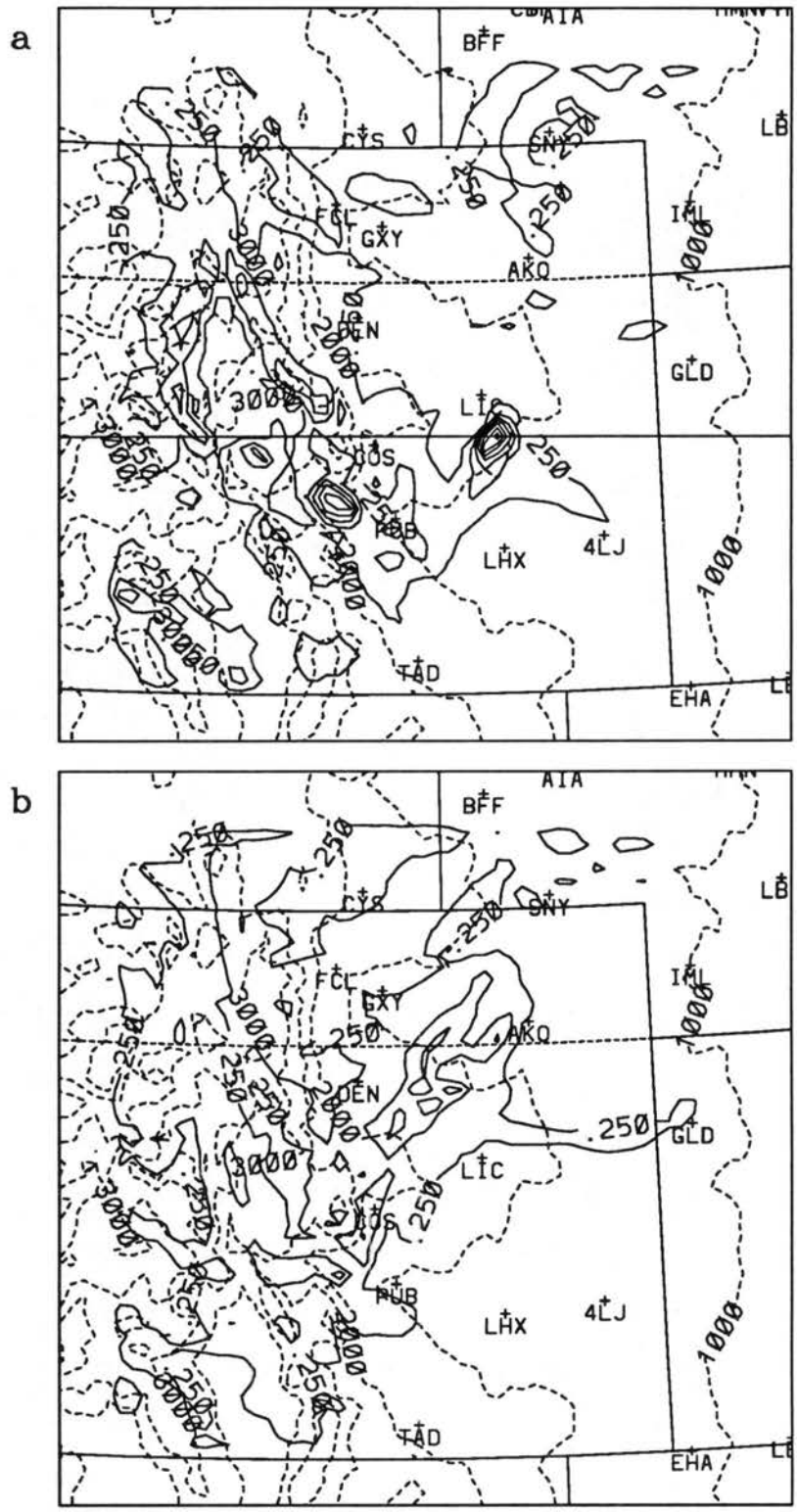

Figure 5.19: RAMS (LSFC) maximum upward vertical motion (m s^{-1}) predictions from (a) the 3 h forecast valid at 0000 UTC and (b) the 6 h forecast valid at 0300 UTC 9 March 1992. Lowest contour is 0.25 m s−1 and contour interval is 1.0 m s^{-1}.

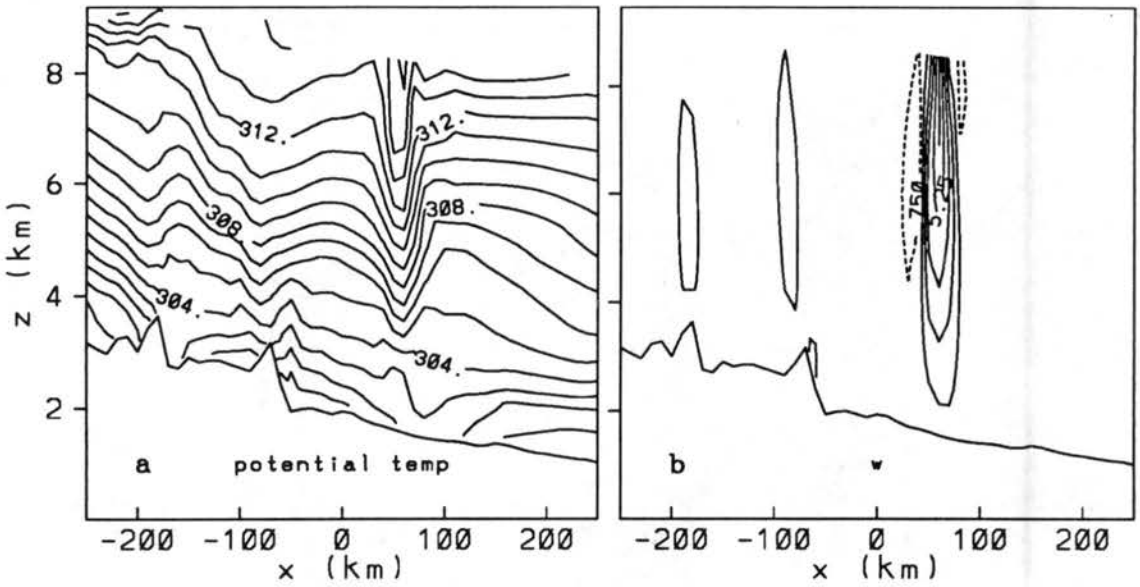

Figure 5.20: West-east vertical cross sections from RAMS (LSFC) 3 h forecast valid at 0000 UTC 9 March 1992 of (a) potential temperature (K) and (b) upward vertical motion (m s^{-1}, contour interval = 1.5 m s^{-1}). Cross section location is represented by the solid line in Fig. 5.19a.

water and latent heating are not considered. A vertical cross section for the same location (Fig. 5.21) does not indicate the potential temperature undulation and the upward vertical velocity does not exceed 1.0 m s^{-1} anywhere in the domain. The 6 h low-level wind and potential temperature forecast from this simulation (Fig. 5.22) suggests a smoother, sharper front. The predicted front has also passed Limon, consistent with the SAO, which was not forecast by the LSFC simulation. Evidently, the spatial resolution of the model is not sufficient to correctly resolve the convection that was observed with this storm. Two approaches are possible to rectify this problem: 1) increase the model grid interval or 2) introduce a cumulus parameterization scheme designed for mesoscale models. The first option requires significantly more computer resources making it presently infeasible for real-time operations at FSL. The second option has only recently been addressed by Weissbluth and Cotton (1993) with a convective parameterization scheme specifically designed for mesoscale models. All other convective parameterization schemes prior to Weissbluth and Cotton were designed for larger grid interval models and are not theoretically valid for mesoscale simulations. Both approaches are beyond the scope of this dissertation, but are recommended for future research.

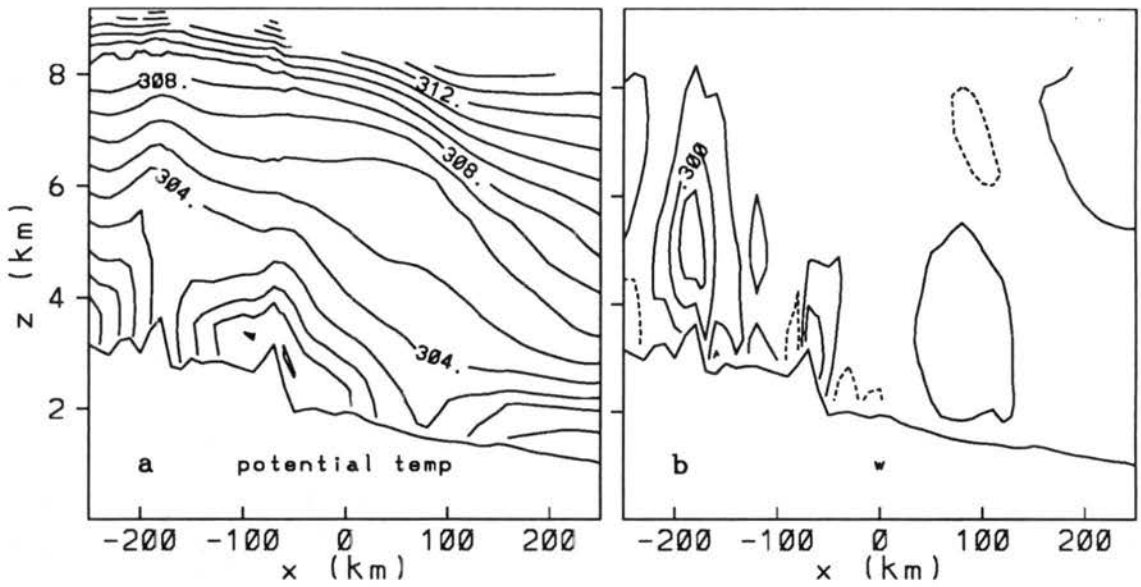

Figure 5.21: As in Fig. 5.20 except for RAMS forecast using no cloud water (upward vertical motion contour interval = 0.2 m s^{-1}).

The predictions of maximum upward vertical motion indicate an area of ascent located west of La Junta at 2200 UTC (not shown) that rotates northeastward to south of Limon by 0000 UTC (Fig. 5.19a) and then north and northwestward to an area from southeast of Denver to west of Akron (Fig. 5.19b). This area of ascent is positioned in the left front quadrant of the 500 and 700 mb jet streaks. The stronger forecast 500 mb winds to the northeast of the low (Fig. 5.16b) and the increase in easterly flow between 8 and 10 km at 0300 UTC in the forecast time series (Fig. 5.18) are likely affected by the vertical motion and excess latent heating as discussed above. The 6 h forecast also suggests a line of ascent near the frontal position from north of Limon to Goodland. Based on the Doppler radar and infrared satellite observations at 0300 UTC, the 6 h vertical motion prediction appears better than the 3 h forecast. This is likely attributed to less observed convection at 0300 UTC than at 0000 UTC.

The RAMS forecasts indicate a band of moisture extending westward from Goodland into the Front Range with a dry slot wrapping into the system from the south. Fig. 5.23 depicts RAMS predictions of the highest total (vapor and liquid) mixing ratio in the column. The forecast dry slot (<2.5 g kg^{-1}) is located south of La Junta at 2200 UTC (not shown) and moves over La Junta by 0000 UTC and wraps into Limon by 0300 UTC.

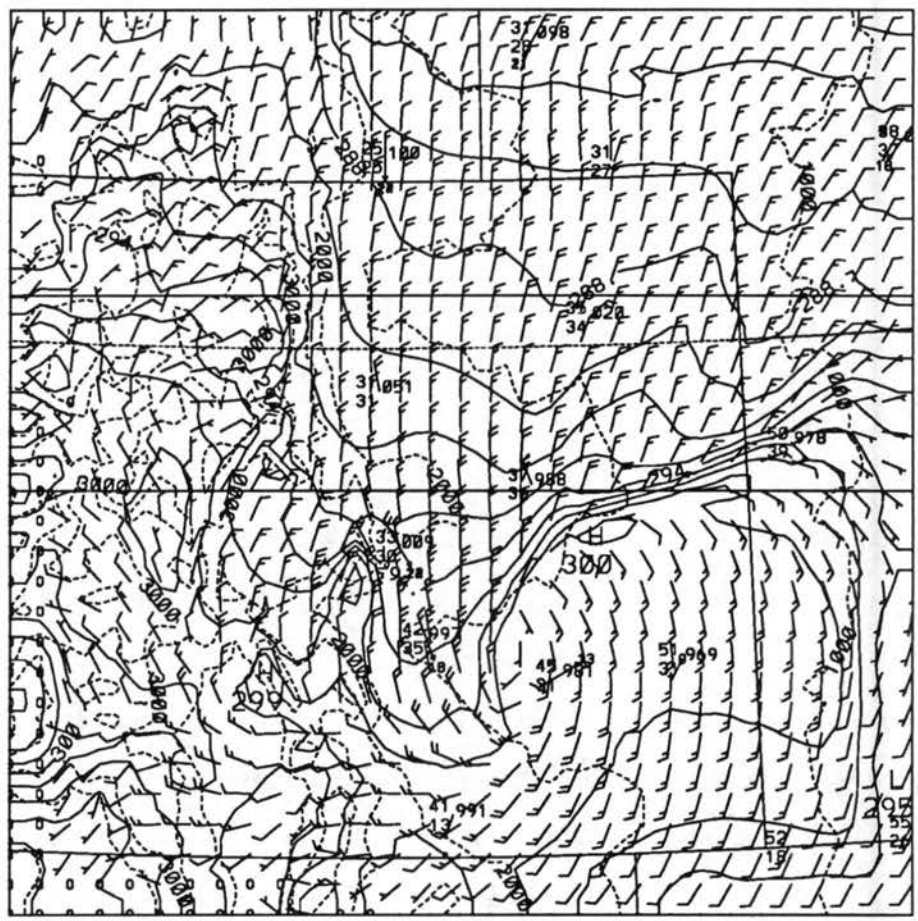

Figure 5.22: RAMS (with no cloud water) low-level (146 m AGL) potential temperature (K, contour interval = 1.5 K) and wind (m s^{-1}) predictions and actual SAO reports at model validation time from the 6 h forecast valid at 0300 UTC 9 March 1992.

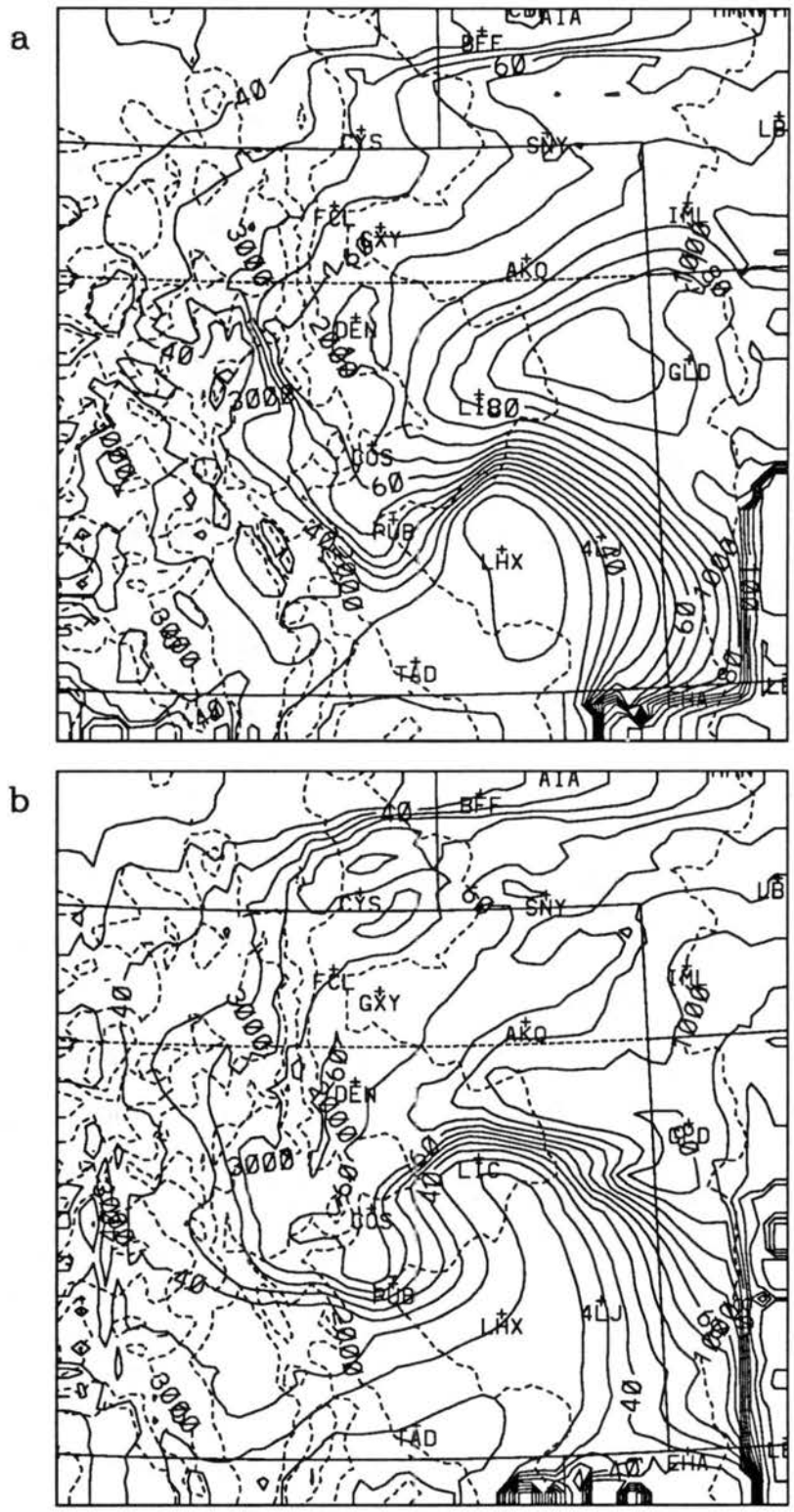

Figure 5.23: RAMS (LSFC) maximum total (vapor and liquid) mixing ratio (g kg^{-1}) predictions from (a) the 3 h forecast valid at 0000 UTC and (b) the 6 h forecast valid at 0300 UTC 9 March 1992. Contour interval is 0.5 g kg^{-1} and 10 units = 1.0 g kg^{-1}.

The band of greatest forecast moisture (>8.0 g kg^{-1}) remains nearly stationary through the period resulting in a strengthening of the moisture gradient between the dry and moist air masses. The area of maximum ascent is colocated with the region of greatest moisture gradient through 0100 UTC. After 0100 UTC, the maximum ascent area progresses over the top of the arctic air mass.

The combination of a moist and unstable air mass colocated with the jet streak's left front quadrant suggests the efficient development of a secondary circulation with rising motion and latent heat release in this area. The 6 h RAMS forecast of 600 mb wind with 700-500 mb thickness (Fig. 5.24) indicates a thickness maximum colocated with the region of maximum ascent. Latent heating associated with the ascent is a likely contributor to the thermal ridge which acts to enhance the forecast warm advection.

Other representative vertical cross sections through the frontal interface suggest the development of significant easterly component flow along the frontal boundary that likely contributed to upslope flow along the boundary and over the Front Range. Two west-east vertical cross sections of potential temperature and u-component wind from the 6-h RAMS forecast with no latent heating (Fig. 5.25, see Fig. 5.22 for locations) illustrate these features without the adverse effects of excessive latent heating and vertical motion. The southern cross section suggests that the eastern edge of the surface front is positioned about 150 km east of center and the western edge is contained by the elevated terrain near 150 km west of center. The prediction shows the front to have a significant slope with a maximum of easterly component flow along the frontal boundary. Further north, the eastern edge of the front is outside the illustrated domain and the western edge of the front has begun to spill over the Continental Divide. Easterly component flow is also indicated along the frontal boundary suggesting upslope flow forced by the boundary and the topography.

The RAMS forecasts suggest that several features combined to generate the heavy snowfall that occurred along the Front Range during the latter portion of the forecast period including: 1) a region of ascent that has developed in moist, unstable air located within the left front quadrant of a mid-level jet streak, 2) latent heat release in the ascent

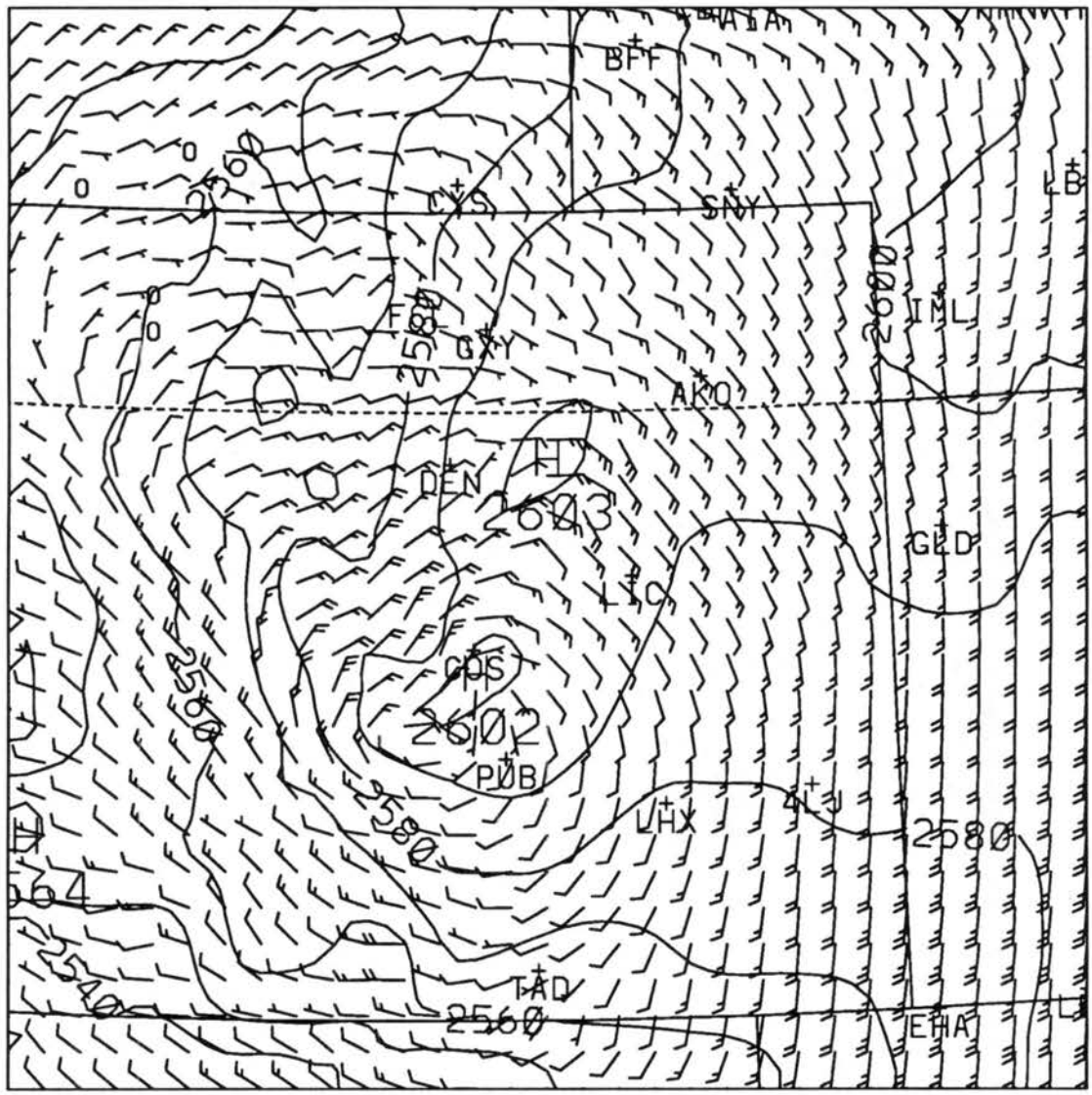

Figure 5.24: RAMS (LSFC) 600 mb wind (m s^{-1}) and 700-500 mb thickness (m) forecast from the 6 h forecast valid at 0300 UTC 9 March 1992.

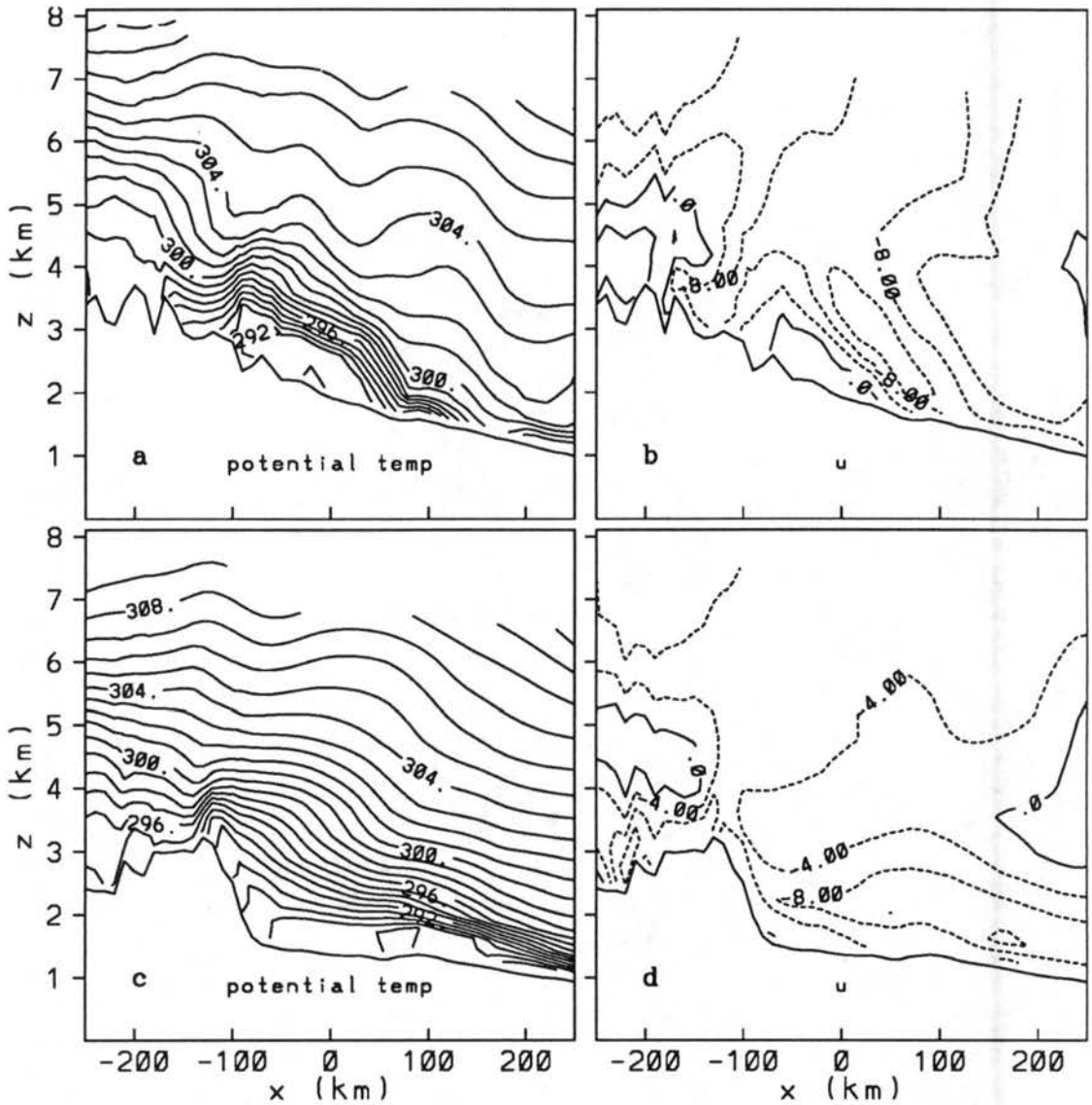

Figure 5.25: West-east vertical cross sections from RAMS (with no cloud water) 6 h forecast valid at 0300 UTC 9 March 1992. Cross section locations are represented by the two solid lines in Fig. 5.22. The northern cross section shows (a) potential temperature (K) and (b) u-component wind (m s^{-1}, contour interval = 4.0 m s^{-1}) and the southern cross section shows (c) potential temperature (K) and (d) u-component wind (m s^{-1}, contour interval = 4.0 m s^{-1}).

area that enhances warm advection immediately upstream of this region, 3) strong easterly flow that is forced upward by the arctic front and the Front Range topography, and 4) a possible seeder-feeder effect (Cotton and Anthes 1989) where precipitation is generated in the ascent area above the cold front and the precipitation intensity is enhanced as the precipitate fall through the arctic air mass.

5.2.2 LMIC simulation - a full microphysics prediction

The LMIC simulation uses the same initialization as the LSFC simulation, however, liquid and ice phase microphysics are included. Hence, precipitation processes and their effects on other processes can be investigated.

The mass and wind fields are similar for the LSFC and LMIC simulations. Low-level (146 m AGL) potential temperature and wind forecasts from the LMIC simulation (Fig. 5.26) indicate a similar structure and evolution of the arctic front. The 3 h forecast indicates strong northeasterly flow over all of northeast Colorado and the Palmer Lake Divide. As with LSFC, LMIC was unsuccessful at predicting the development of southerly winds ahead of the front in the vicinity of Limon. The position and strength of the arctic front as suggested by the potential temperature forecast is very close to the LSFC prediction.

The 6 h LMIC wind forecast continues to agree closely with the LSFC prediction. The position of the arctic front is also very close to the LSFC location, however, the potential temperature gradient is stronger suggesting that LMIC has predicted a sharper frontal boundary. Although the LAPS analysis does not indicate as sharp a front, the LMIC simulation appears to be more realistic when considering human observations that describe a rapid transition from tranquil to turbulent weather conditions in a very short time span. Post-frontal precipitation processes likely contributed to a rapid cooling of the atmosphere behind the front and the strengthening of the frontal boundary. As with LSFC, the LMIC frontal position is too far north in the Limon vicinity as suggested by the Limon SAO.

The structure of the LMIC 500 mb forecast height and wind fields are similar to the comparable LSFC predictions. The primary difference is that the magnitude of the 500 mb

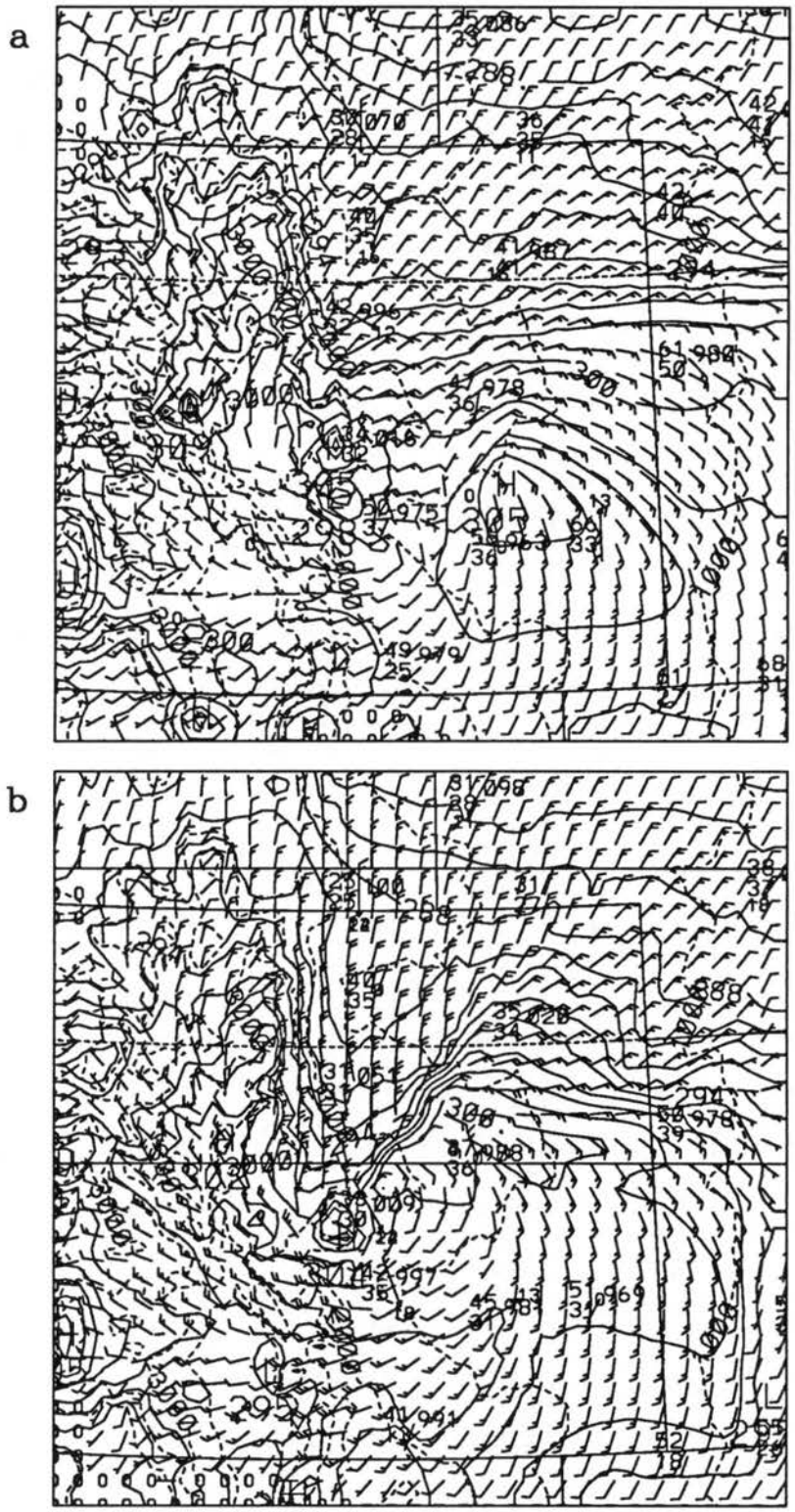

Figure 5.26: RAMS (LMIC) low-level (146 m AGL) potential temperature (K, contour interval = 1.5 K) and wind (m s^{-1}) predictions and actual SAO reports at model validation time from (a) the 3 h forecast valid at 0000 UTC and (b) the 6 h forecast valid at 0300 UTC 9 March 1992.

height is closer to the MAPS analysis in LMIC than for LSFC. For example, at 0300 UTC, the lowest heights are 5489 m for LMIC (Fig. 5.27), 5505 m for LSFC (Fig. 5.16b), and 5483 m as analyzed by MAPS (Fig. 5.17b). A time series of LMIC wind predictions from

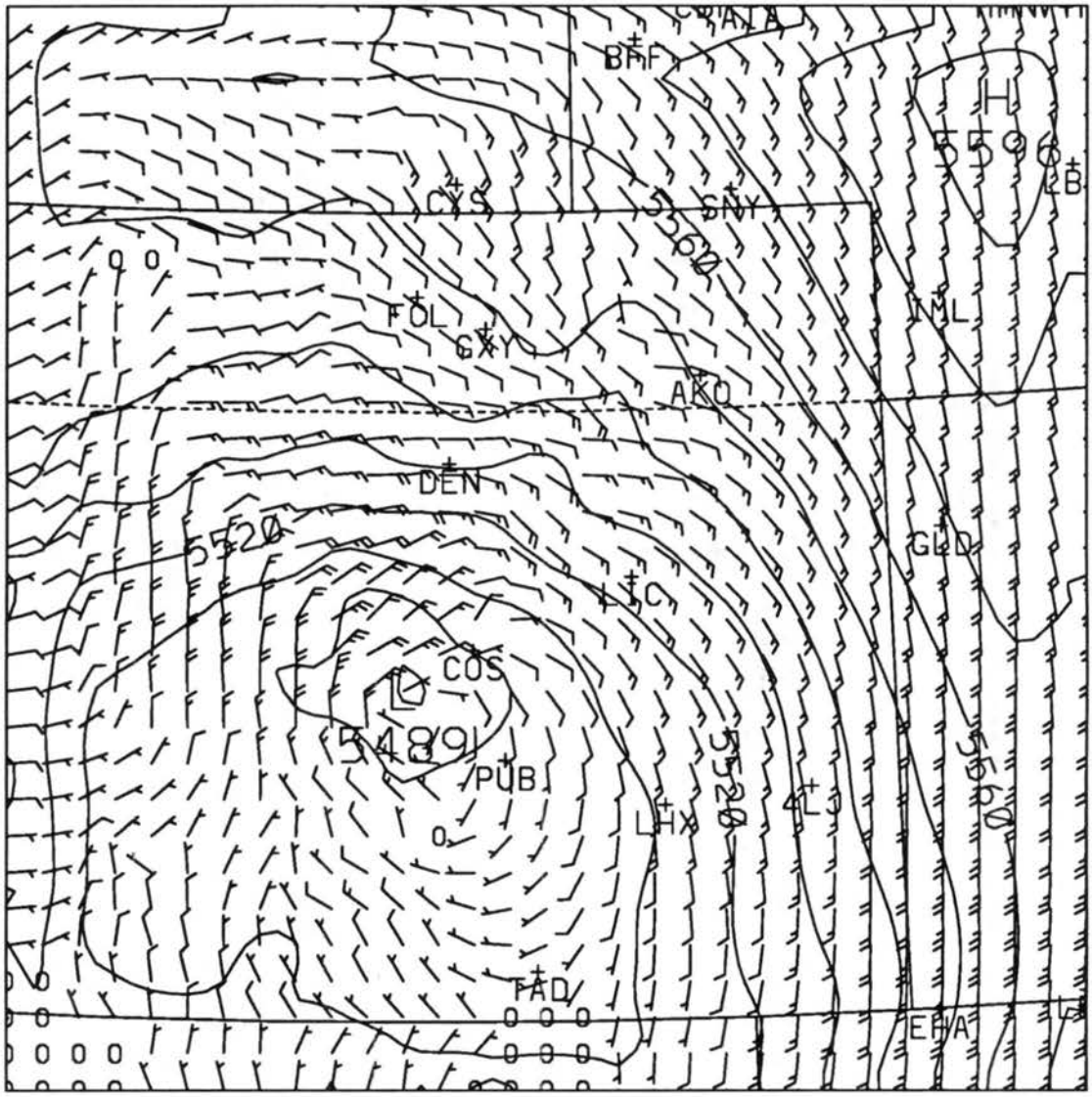

Figure 5.27: RAMS (LMIC) 500 mb height (m) and wind (m s^{-1}) predictions from the 6 h forecast valid at 0300 UTC 9 March 1992.

near Platteville (not shown) indicate a close agreement with the LSFC forecasts. Both simulations resolved the primary flow regimes as observed by the Platteville wind profiler (Fig. 5.11) including the development of strong north-northeast boundary layer winds following frontal passage and the generation of a deep layer of easterly flow above the arctic air mass.

Maximum upward vertical velocity predicted by LMIC (Fig. 5.28) is similar to the LSFC forecasts. As with the 7 January case study, the magnitude of LMIC ascent is somewhat larger than the values predicted by LSFC due to the extra latent heat release by freezing processes. This acts to accentuate the unrealistically large amounts of latent heat release in the vicinity of convection as discussed in the previous section. The 6 h forecast of maximum ascent has decreased in intensity and correlates better with the radar and satellite observations probably due to the decrease in observed convection. The forecasts of moisture (not shown) are similar for the LMIC and LSFC simulations. The LMIC moisture predictions show a band of moisture extending west-southwestward from northeast Colorado and a dry slot over southeast Colorado that wrap around the mid-level cyclone with time.

Mixing ratio forecasts of the various microphysical species at the lowest model level (Figs. 5.29 and 5.30) suggest that the LMIC simulation has resolved the areal extent of the steady precipitation and has defined the rain-snow line reasonably well, but the areal coverage of convective precipitation does not correlate as well with the observations. The 3 h mixing ratio prediction of all microphysical species indicates the heaviest precipitation to be occurring over the higher terrain of the Rocky Mountains and in two areas over the Plains near Limon and the Nebraska Panhandle. Since graupel is often associated with convective activity, the graupel forecast suggests that the areas of heavy precipitation southwest of Denver, west of Colorado Springs, and in the Nebraska Panhandle are primarily the result of convection. The area of heavy precipitation south of Limon is also likely convectively induced, but the precipitation has mostly melted to rain in the warmer air. Doppler radar data suggest convective activity is also occurring northeast of Denver, but apparently the model resolution is insufficient to depict this activity.

Snow is forecast over much of the higher terrain which is difficult to verify, but is reasonable given the synoptic conditions. A west-east band of lighter intensity precipitation is forecast from west of Cheyenne (CYS) to Sydney (SNY) that appears to have developed in the upslope flow behind the front. The predictions of snow and rain indicate snow in the Cheyenne area, changing to mixed rain and snow along the border between Colorado

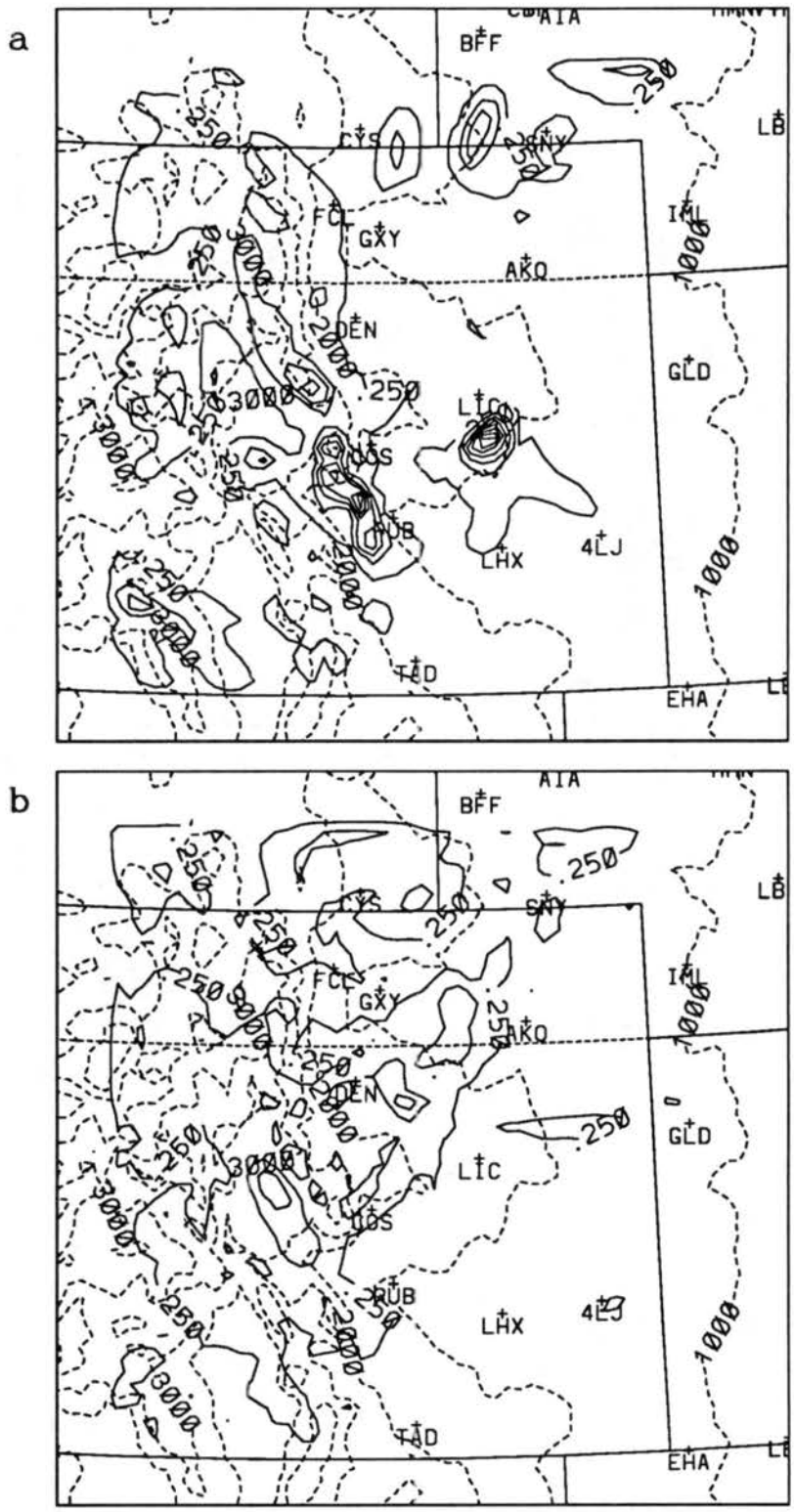

Figure 5.28: RAMS (LMIC) maximum upward vertical motion (m s^{-1}) predictions from (a) the 3 h forecast valid at 0000 UTC and (b) the 6 h forecast valid at 0300 UTC 9 March 1992. Lowest contour is 0.25 m s−1 and contour interval is 1.0 m s^{-1}.

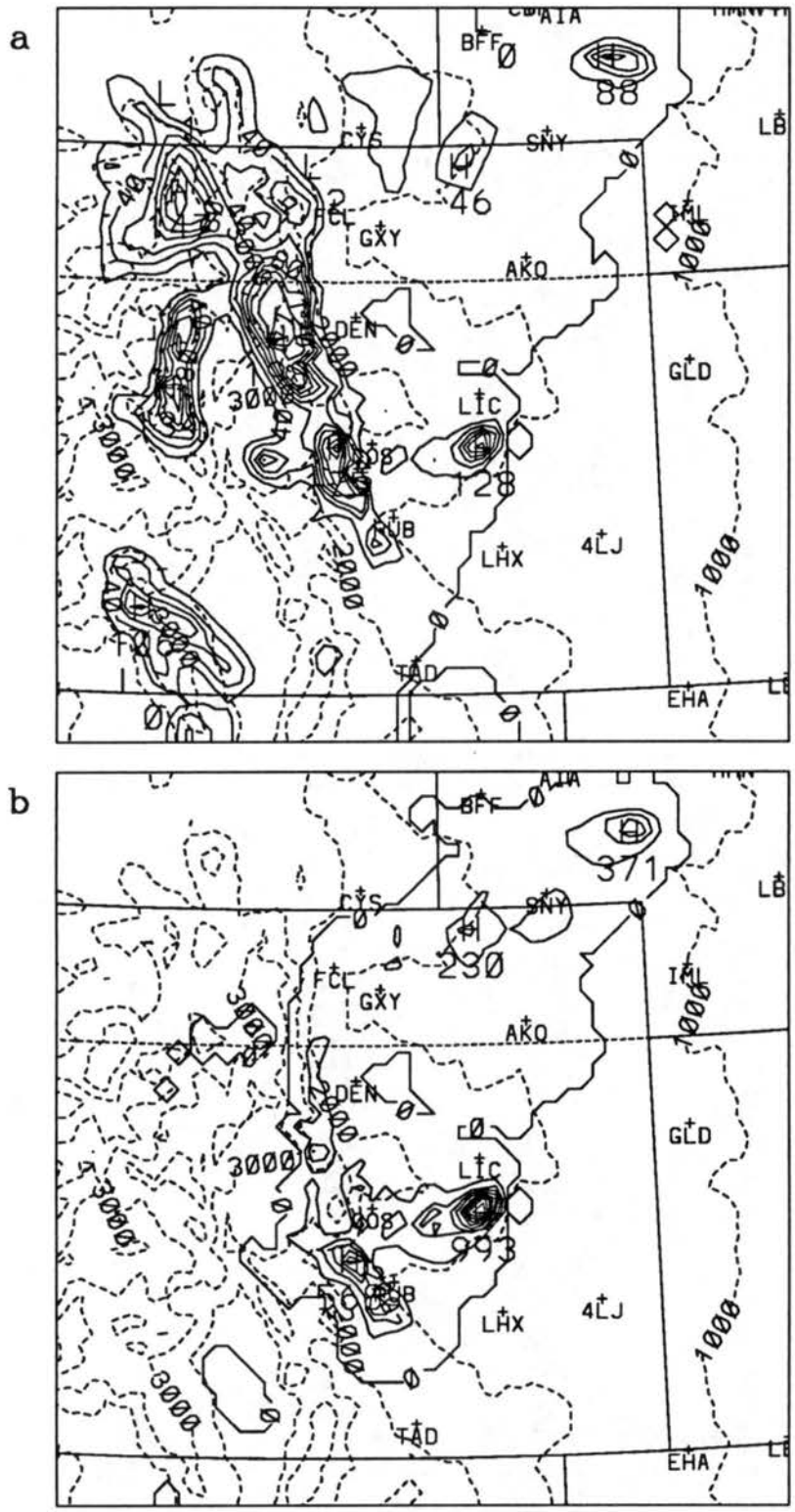

Figure 5.29: RAMS (LMIC) 3 h low-level (146 AGL) mixing ratio forecast valid at 0000 UTC 9 March 1992 of (a) total condensate (g kg^{-1}, contour interval = 0.2 g kg^{-1}, 100 units = 1.0 g kg^{-1}) and (b) rain (g kg^{-1}, contour interval = 0.1 g kg^{-1}, 100 units = 0.1 g kg^{-1}).

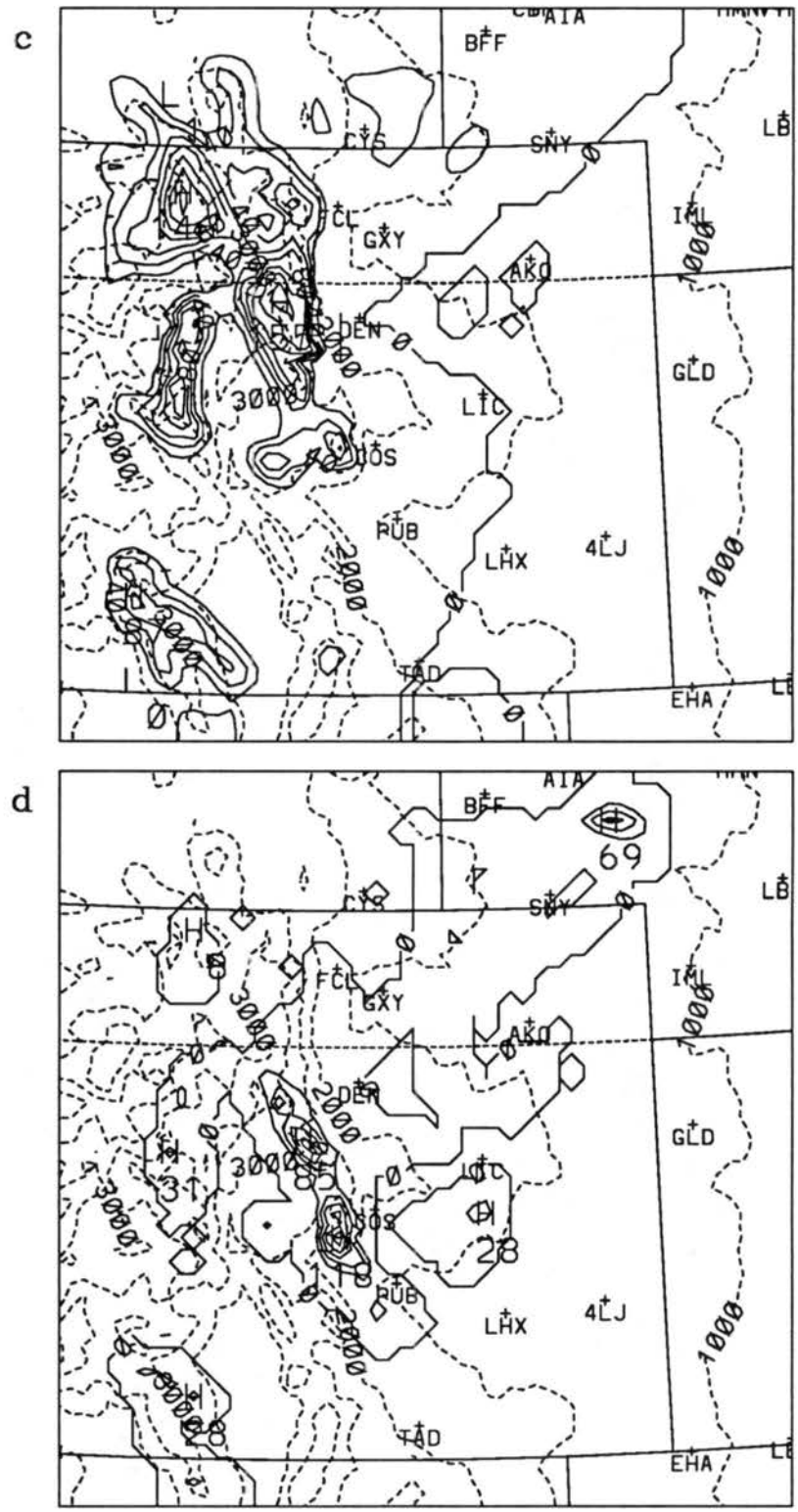

Figure 5.29: Continued: (c) snow and aggregate (g kg^{-1}, contour interval = 0.2 g kg^{-1}, 100 units = 1.0 g kg^{-1}) and (d) graupel (g kg^{-1}, contour interval = 0.2 g kg^{-1}, 100 units = 1.0 g kg^{-1}).

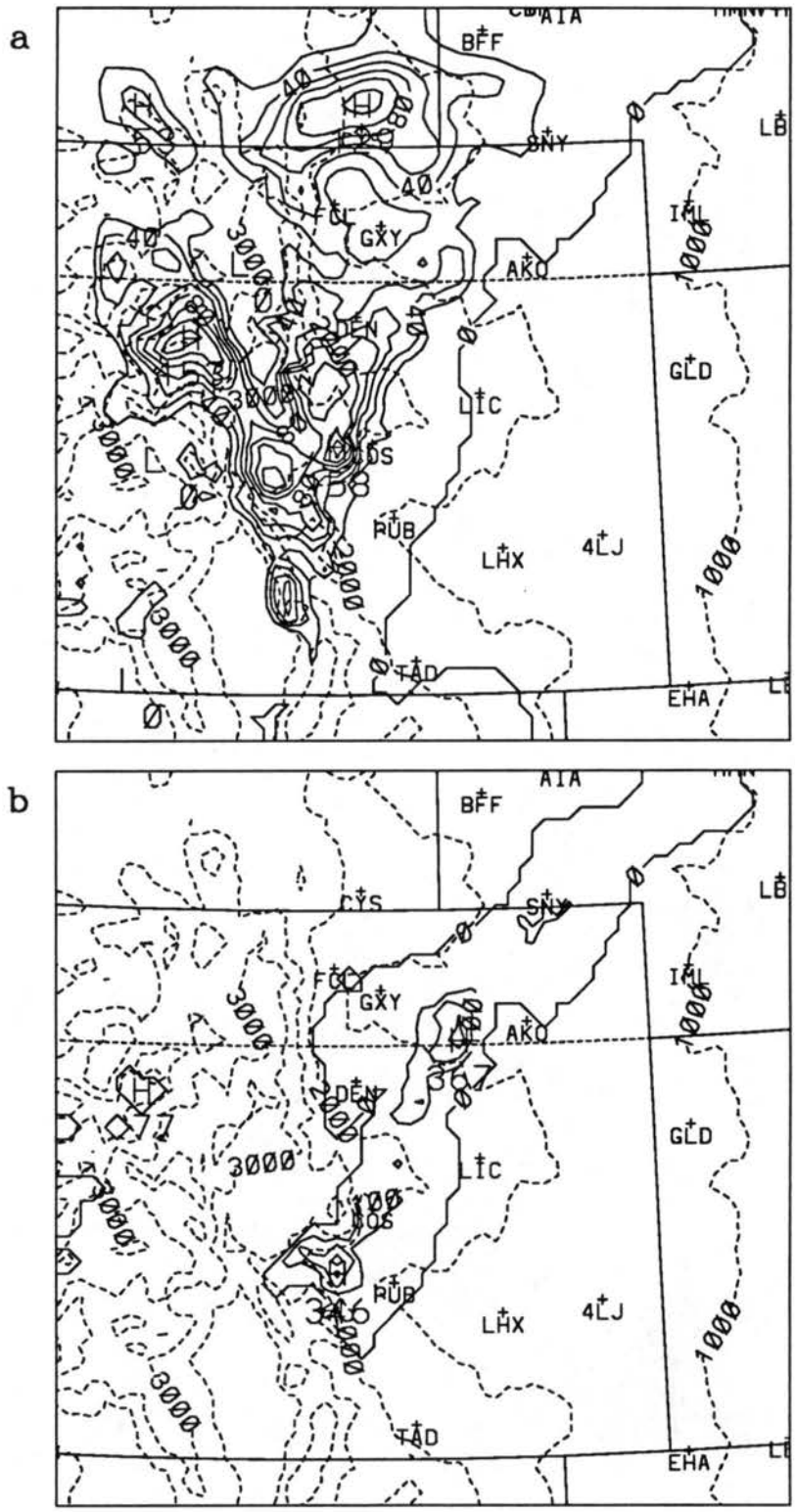

Figure 5.30: As in Fig. 5.29 except for 6 h forecast valid at 0300 UTC 9 March 1992.

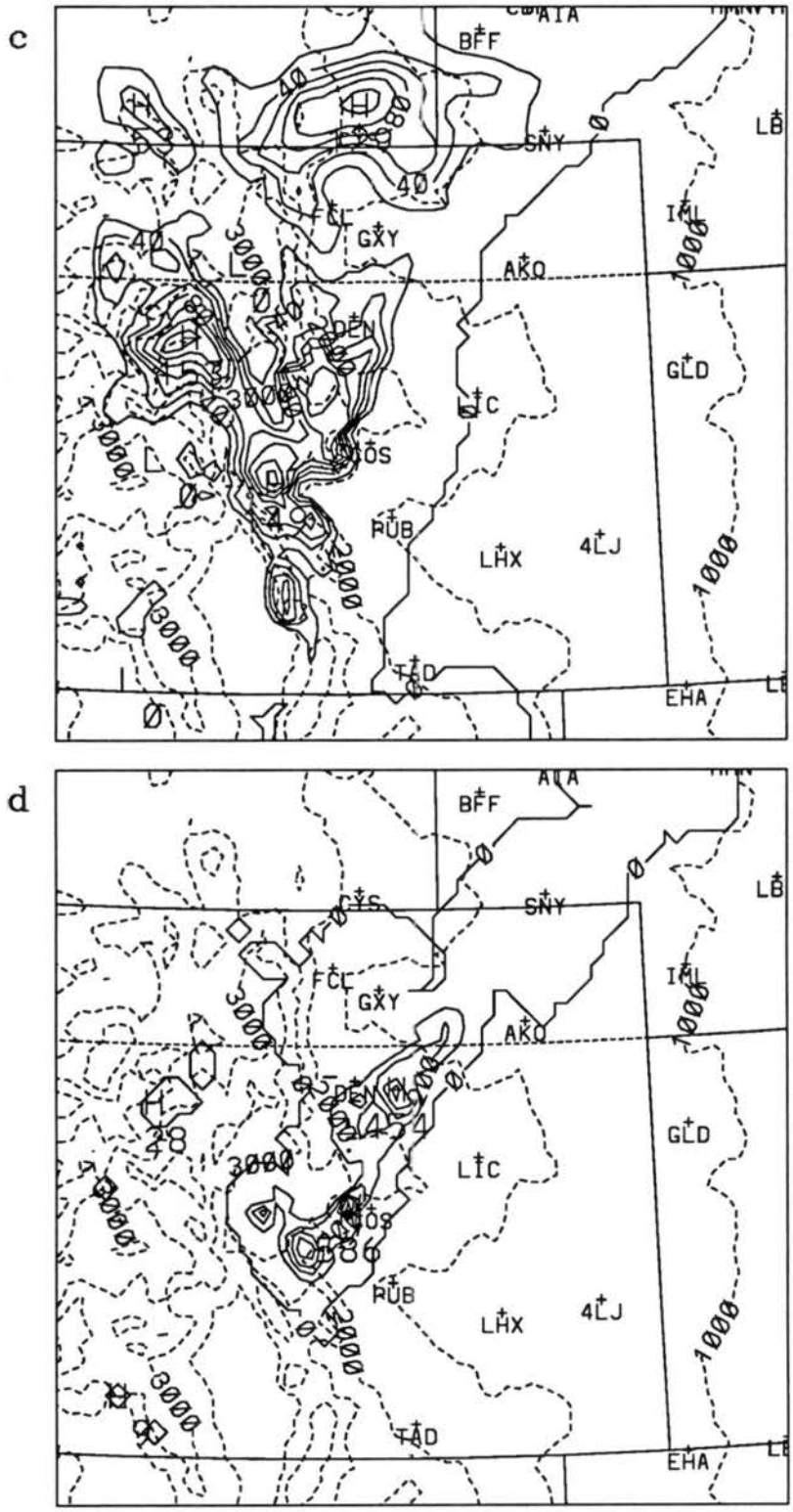

Figure 5.30: Continued:

and the extreme southwest Nebraska Panhandle, and all rain around Sydney. The forecast rain-snow line correlates well with the observations of light snow at Laramie and Cheyenne and light rain at Sydney. The areal coverage of precipitation extends west of a southwest-northeast line positioned from Trinidad (TAD) to the northeast corner of Colorado which corresponds well with the infrared satellite data from 2300 UTC (Fig. 5.13b).

The 6 h mixing ratio forecast of all microphysical species shows the heaviest precipitation to remain over the higher terrain but has decreased somewhat in intensity from 0000 UTC. The west-east band of precipitation over southeast Wyoming and the Nebraska Panhandle has increased in intensity and has spread southward along the northern Colorado Front Range. This correlates well with the Cheyenne observations that have increased from light to heavy snow between 0000 and 0300 UTC (Fig. 5.4). Another band of precipitation has developed from between Denver and Colorado Springs northeastward to west of Akron which corresponds to the forecast frontal position. Significant graupel is predicted along this band suggesting that the simulated convective activity is confined to the frontal boundary region, which is reasonable based on the surface observations (Fig. 5.6d) and the Doppler radar data (Fig. 5.12) Predicted snowfall is located mostly west of a line from Sydney to Colorado Springs and some areas of light rain exist east of this line. The predicted rain-snow line continues to correlate well with the observations of light snow at Colorado Springs and rain at Pueblo and Akron. The areal coverage of all precipitation continues to be west of the line extending from Trinidad to the northeast corner of Colorado which corresponds well with infrared satellite data (Fig. 5.13).

Representative vertical cross sections through the frontal interface provide an indication of the precipitation processes that are occurring. Two west-east vertical cross sections, one through the surface front and the other well north of the surface front (see Fig. 5.26b for locations), from the RAMS 6 h forecast are illustrated in Figs. 5.31 and 5.32. The prediction of potential temperature along the southern cross section suggests that the eastern edge of the surface front is positioned about 30 km west of the center north-south axis, about 180 km west of the frontal position in the simulation with no latent heating. Combined snow and aggregates are located mostly along the surface frontal boundary

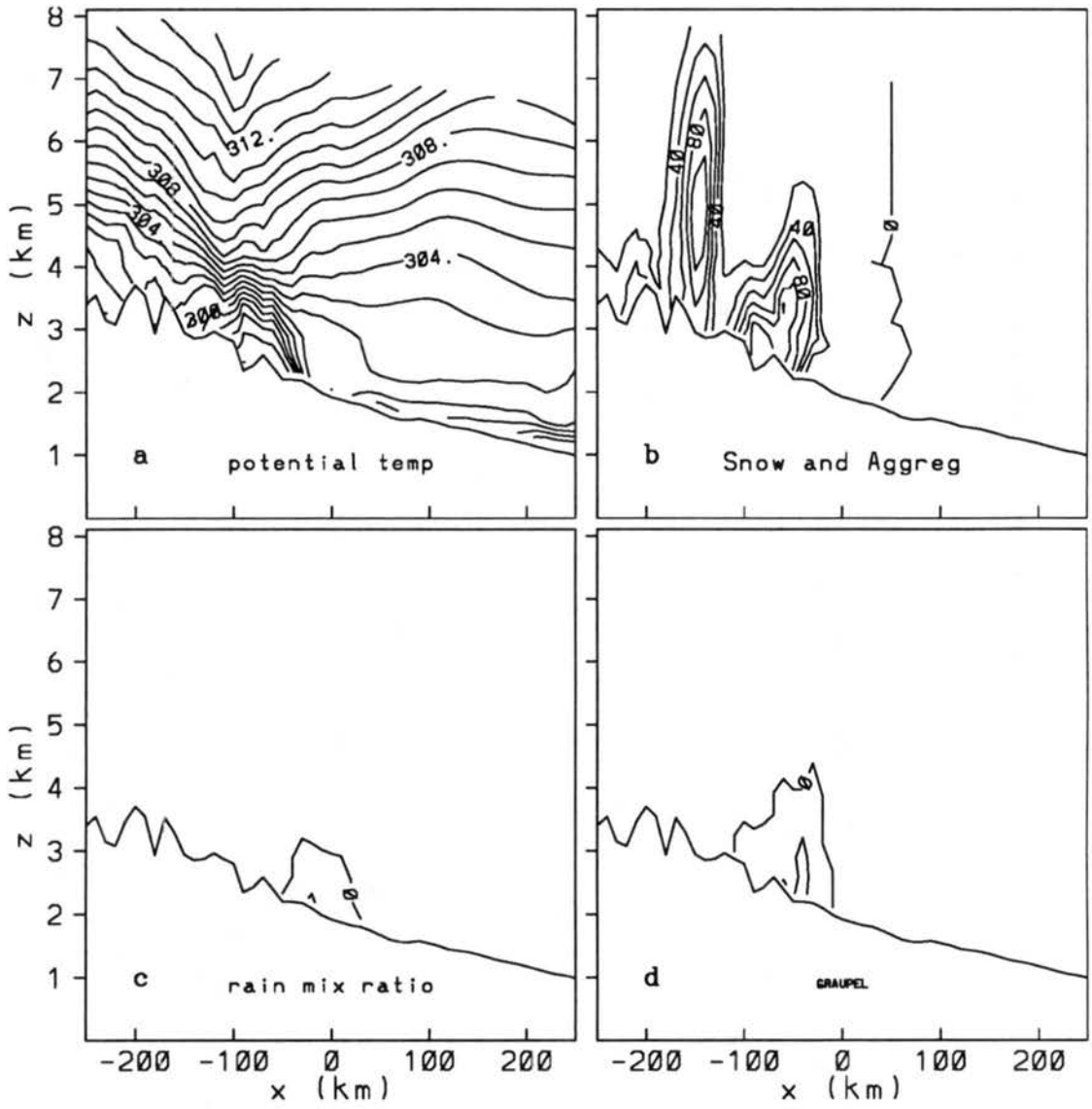

Figure 5.31: West-east vertical cross sections from RAMS (LMIC) 6 h forecast valid at 0300 UTC 9 March 1992 of (a) potential temperature (K), (b) snow and aggregate mixing ratio (g kg^{-1}, contour interval = 0.2 g kg^{-1}, 10 units = 0.1 g kg^{-1}), (c) rain mixing ratio (g kg^{-1}, contour interval = 0.1 g kg^{-1}), and (d) graupel mixing ratio (g kg^{-1}, contour interval = 0.2 g kg^{-1}). Cross section location is represented by the southern solid line in Fig. 5.26b.

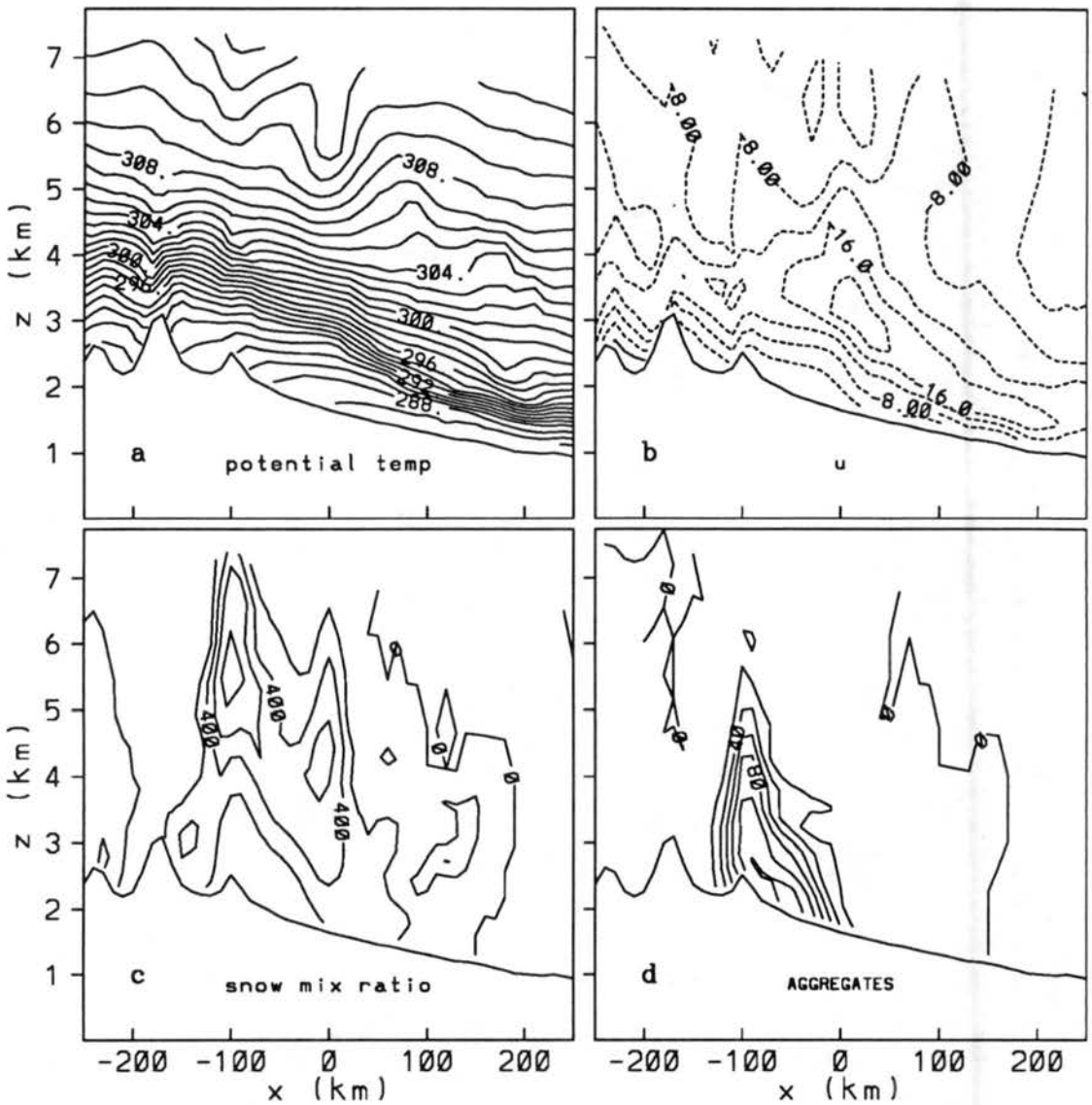

Figure 5.32: West-east vertical cross sections from RAMS (LMIC) 6 h forecast valid at 0300 UTC 9 March 1992 of (a) potential temperature (K), (b) u-component wind (m s^{-1}, contour interval = 4.0 m s^{-1}), (c) snow mixing ratio (g kg^{-1}, contour interval = 0.2 g kg^{-1}, 100 units = 0.1 g kg^{-1}), and (d) aggregate mixing ratio (g kg^{-1}, contour interval = 0.2 g kg^{-1}, 10 units = 0.1 g kg^{-1}). Cross section location is represented by the northern solid line in Fig. 5.26b.

and westward with two maximum areas, one along the surface frontal boundary and the other over the higher terrain. Both regions extend up above the arctic air mass where the upward vertical motion has been enhanced by significant amounts of latent heating. Graupel is mostly confined to near the surface and within the frontal boundary while small amounts of rain are predicted near the surface east of the surface front.

The 6 h forecast of potential temperature along the northern cross section suggests that the surface front is east of the illustrated domain. The frontal boundary aloft tilts up from east to west with a height of about 2 km at the eastern boundary and about 4 km over the mountains. Significant easterly component, upslope flow is forecast along the entire domain with maximum speeds of greater than 20 m s^{-1} illustrated along the frontal interface. A wide area of snow has developed within the upslope flow. A minimum of snow is located west of the mountain barrier where a weak mountain wave and downslope flow are indicated in the potential temperature and u-component wind fields. Aggregates are mostly confined to below the frontal boundary where strong winds are predicted and a possible seeder-feeder mechanism is occurring.

The RAMS 6 h quantitative melted precipitation forecast (Fig. 5.33) is compared to 6 h melted precipitation observations (Fig. 5.34) derived from stations that report on an hourly schedule. The RAMS forecast indicates highest precipitation amounts over the high terrain from west of Denver south to west of Colorado Springs. This area agrees well with the region of highest observed 6 h precipitation. However, the forecast amounts are significantly higher than the observed amounts. This is likely related to the problem of not fully resolving the convection as discussed previously and also due to the lack of observations over the highest terrain where heavier precipitation amounts likely fell. The two areas of heavier forecast precipitation southwest and northwest of Limon appear to be convectively induced. The radar and satellite data suggested that convection occurred in these areas, but surface stations that report hourly precipitation are not available. It is encouraging that the model predicted convective activity in the pre-frontal air mass, but it is unlikely that the model correctly resolved the convective precipitation details due to insufficient resolution and no cumulus parameterization.

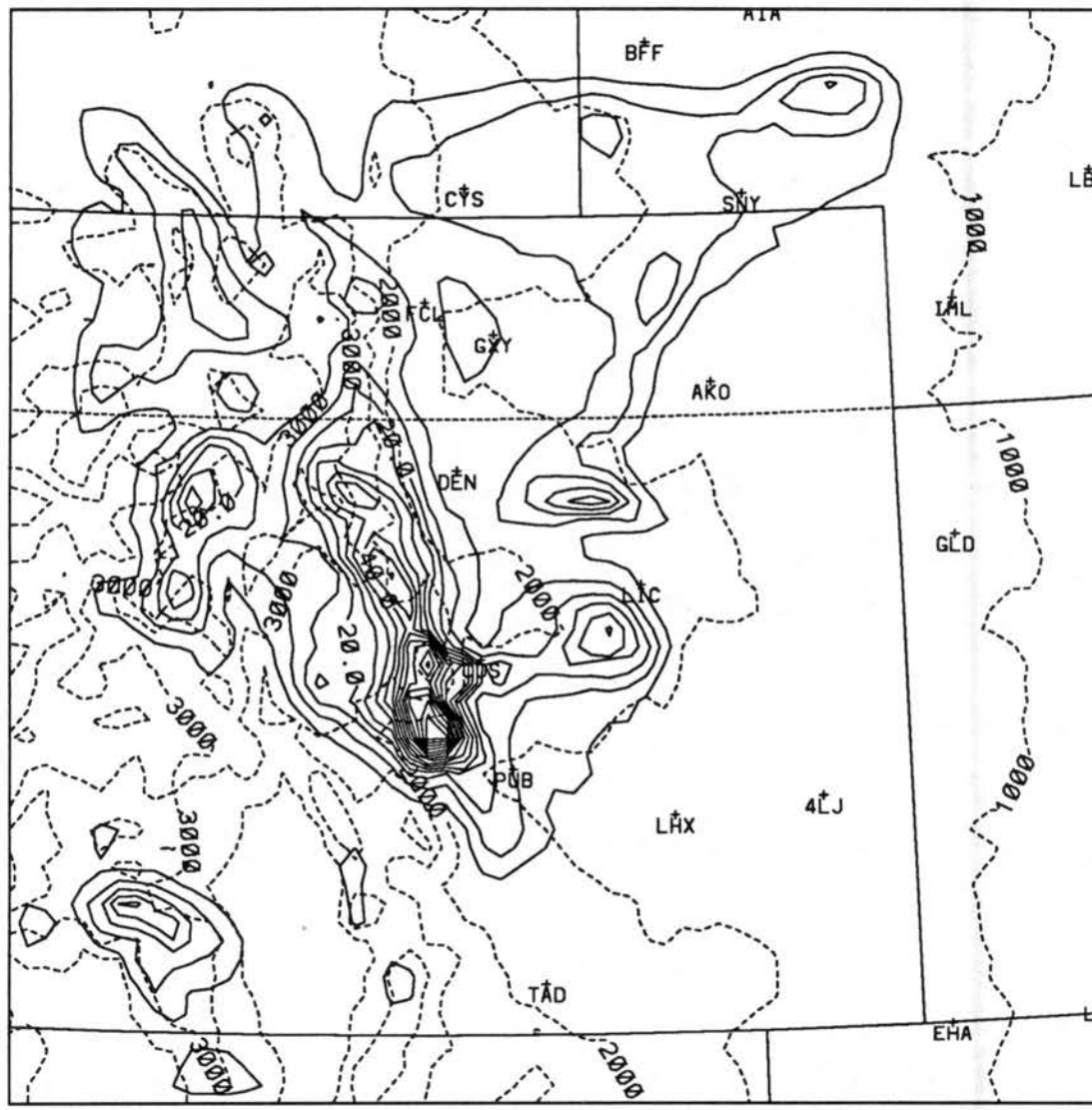

Figure 5.33: RAMS (LMIC) 12 h melted precipitation (mm) forecast. Contour interval is 5 mm.

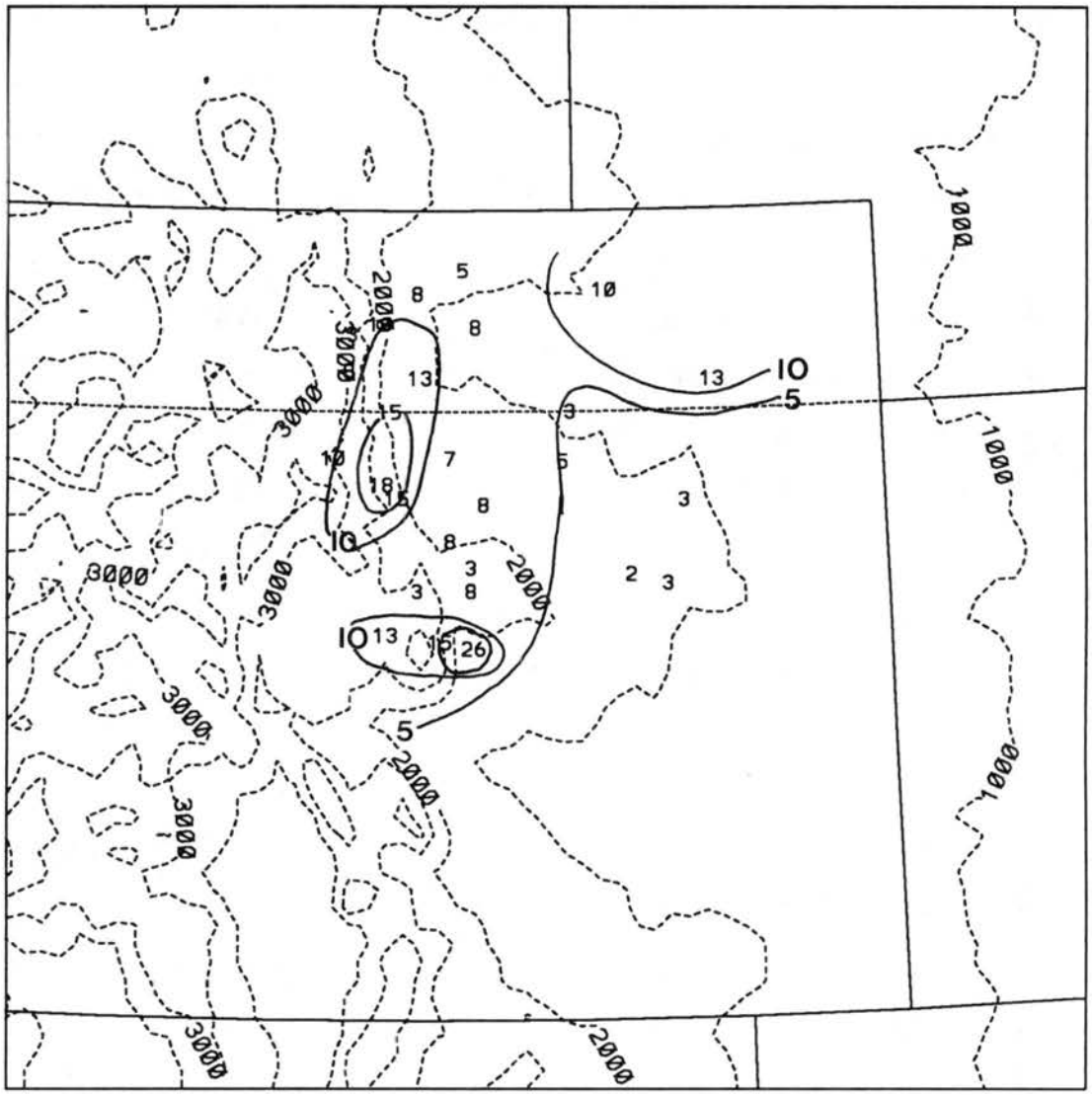

Figure 5.34: Observed 6 h melted precipitation from 2100 UTC 8 March through 0300 UTC 9 March 1992.

5.2.3 Other sensitivity simulations

Comparisons of predictions from the four sensitivity simulations (LAPS-initialized with LAPS data except separate LAPS surface analyses are not included, LBAL-initialized with the LAPS variationally adjusted mass and wind analyses, MAPS-initialized with MAPS data and LAPS topography, MTOP-initialized with MAPS data and MAPS topography) to the LSFC forecasts show more interesting differences than were observed in the 7 January 1992 case study comparisons. First, similar to the 7 January results, improvements are noted in all the predictions that used LAPS topography when compared to MTOP suggesting that better representation of the actual terrain contributes significantly to improved forecasts. Second, LSFC and LAPS generated stronger surface potential temperature gradients suggesting that the higher resolution LAPS initialization allows for a more realistic frontal prediction. Finally, the LBAL simulation is significantly better at predicting the surface flow reversal ahead of the front and the LBAL forecasts of vertical motion correlate better with the observations.

The 3 h forecasts of potential temperature and wind (Fig. 5.35) show a stronger potential temperature gradient along the northern Colorado Front Range in the three simulations using the LAPS topography (i.e. LAPS, LBAL, MAPS) resulting in a better forecast of the arctic front against the mountain barrier. The surface frontal position over the Plains is similar in all the simulations. The LBAL prediction of southeasterly flow over the southern half of the Palmer Lake Divide agrees well with the Limon SAO (Fig. 5.14a) and LAPS analysis (Fig. 5.15a) and is a significant improvement over the other simulations which failed to predict this flow reversal ahead of the front.

The same improvements in frontal structure along the more realistic LAPS topography are indicated in the 6 h forecasts of potential temperature and wind (Fig. 5.36). The position of the surface front over the Plains is similar for LSFC (Fig. 5.14b), LAPS, and MAPS except LSFC and LAPS predict a stronger potential temperature gradient suggesting a tighter frontal interface. Although all the simulations have made similar errors in the placement of the surface cyclonic circulation, the LBAL simulation indicates that the northeasterly flow is further south along the eastern side of the Palmer Lake Divide which

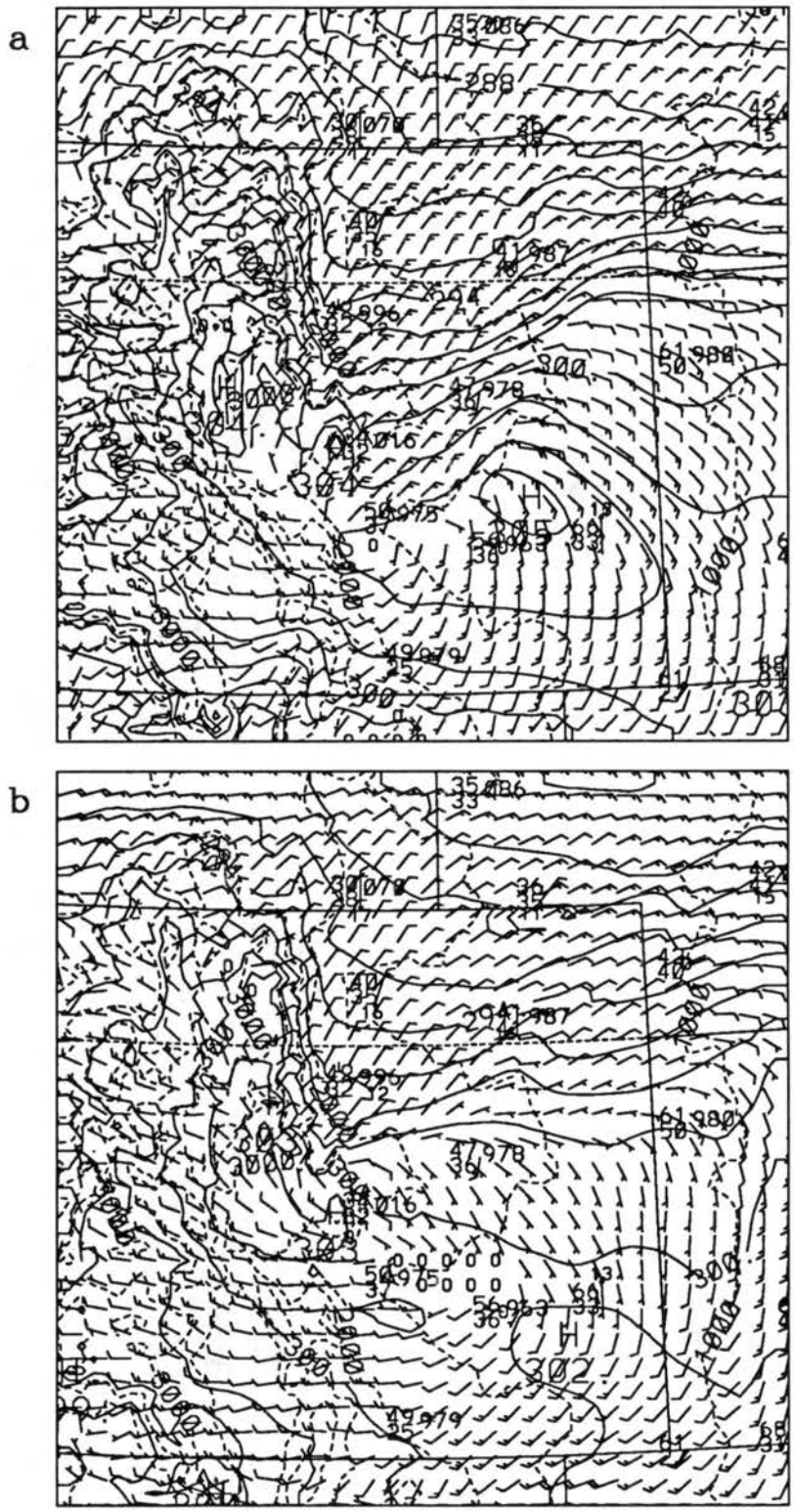

Figure 5.35: RAMS low-level (146 m AGL) potential temperature (K, contour interval 1.5 K) and wind (m s^{-1}) predictions and actual SAO reports at model validation time from 0000 UTC 9 March 1992 for (a) the LAPS simulation and (b) the LBAL simulation.

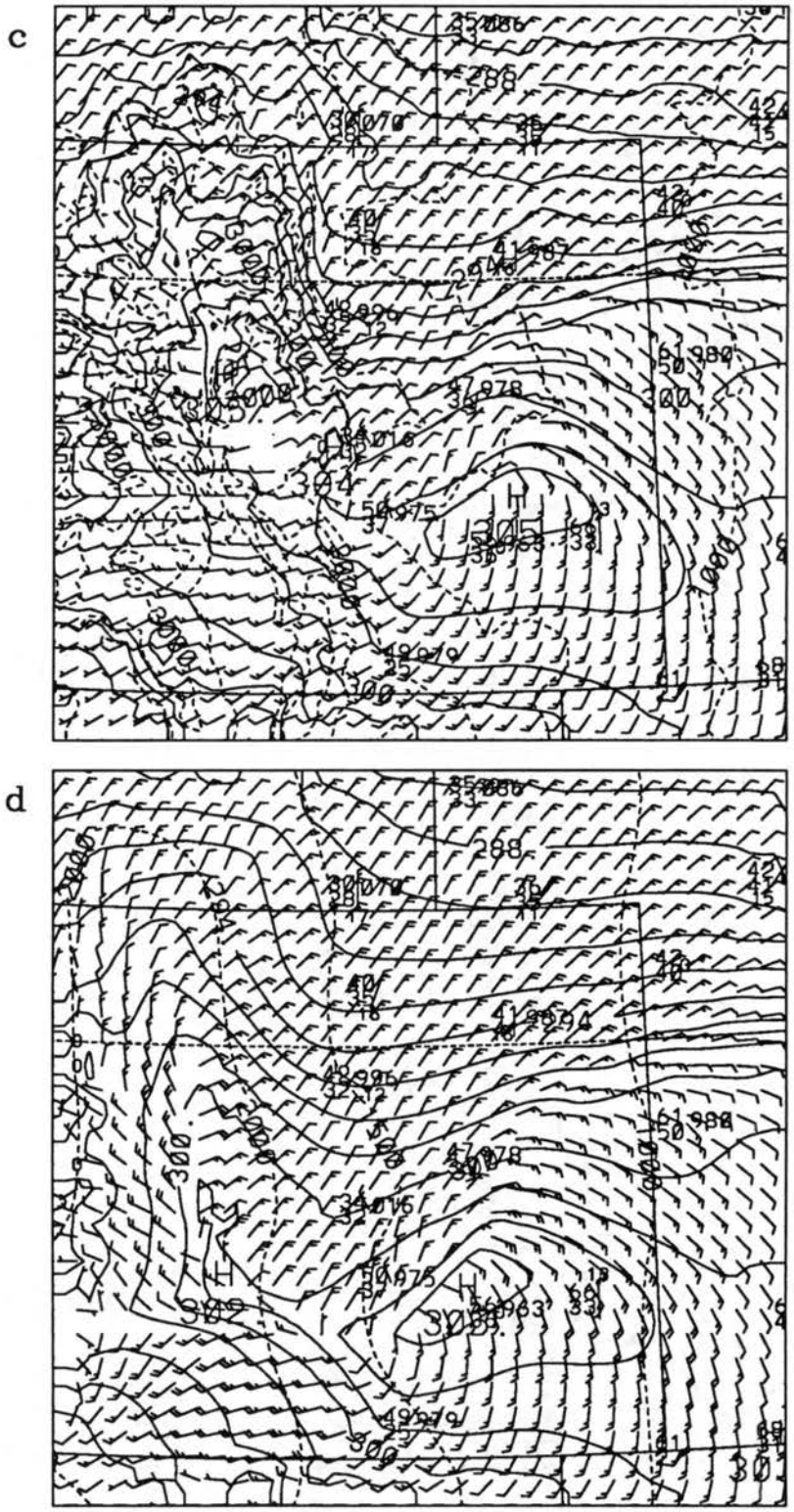

Figure 5.35: Continued: (c) the MAPS simulation and (d) the MTOP simulation.

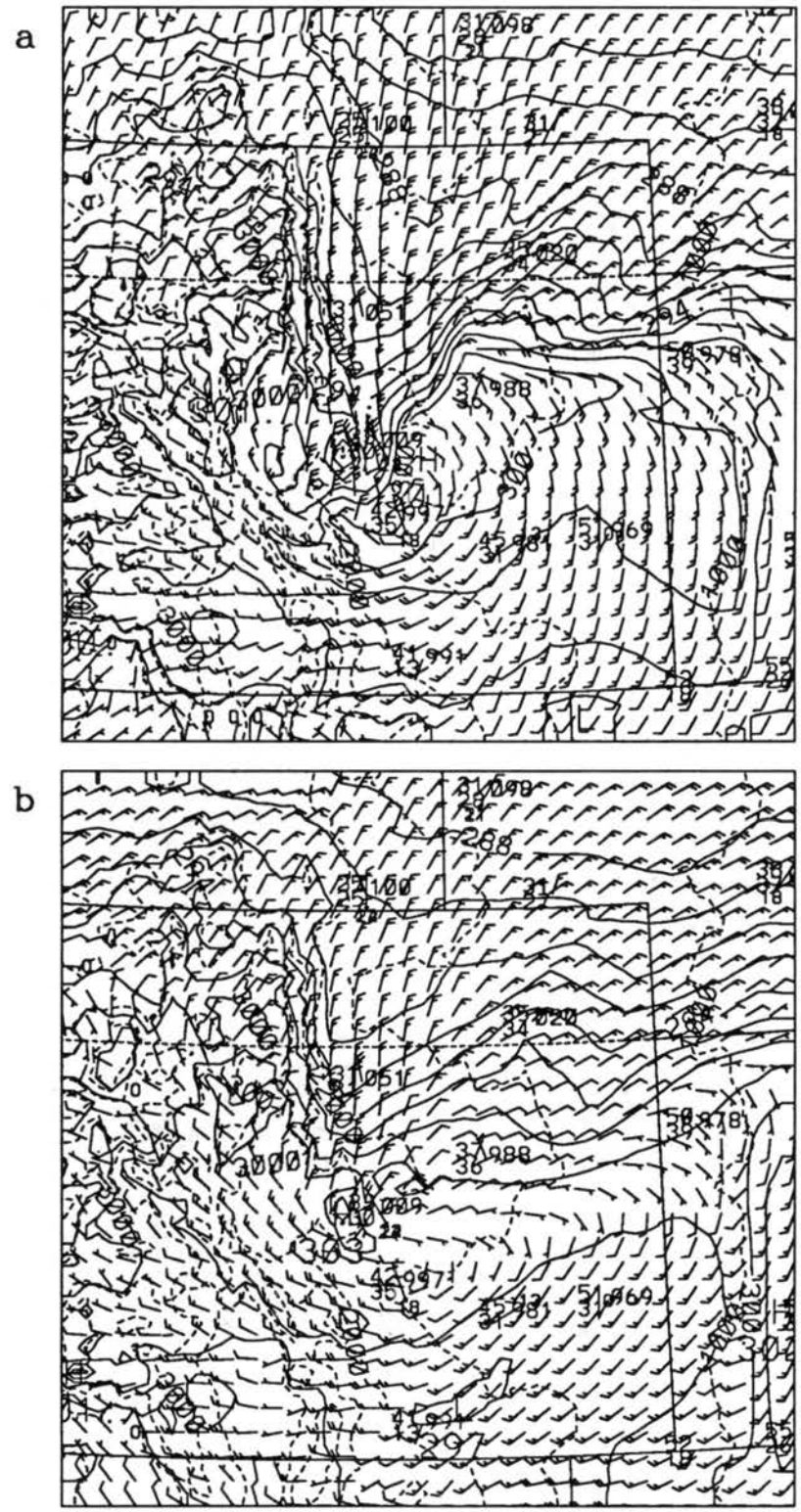

Figure 5.36: As in Fig. 5.35 except for 6 h forecast valid at 0300 UTC 9 March 1992.

c

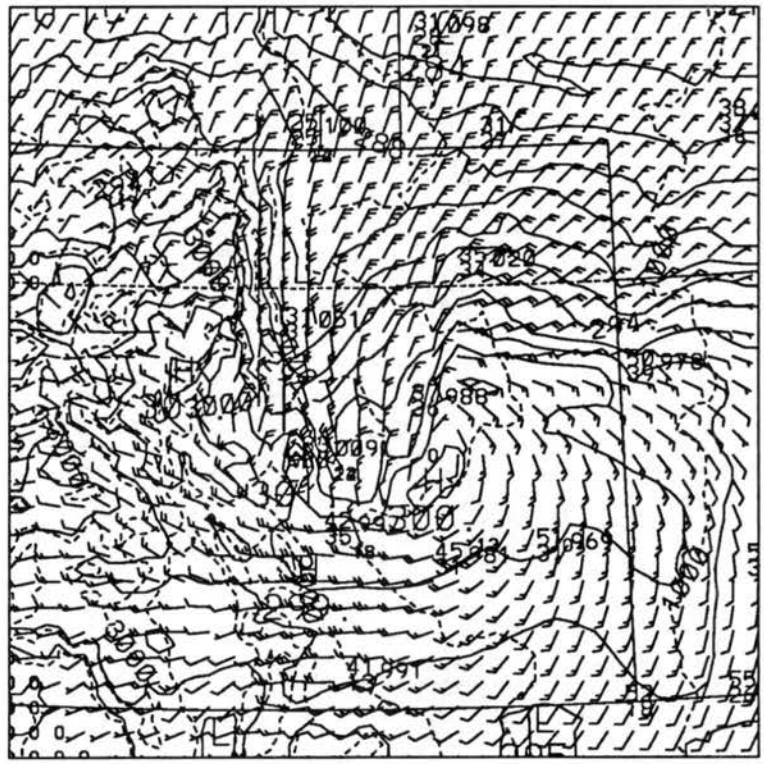

d

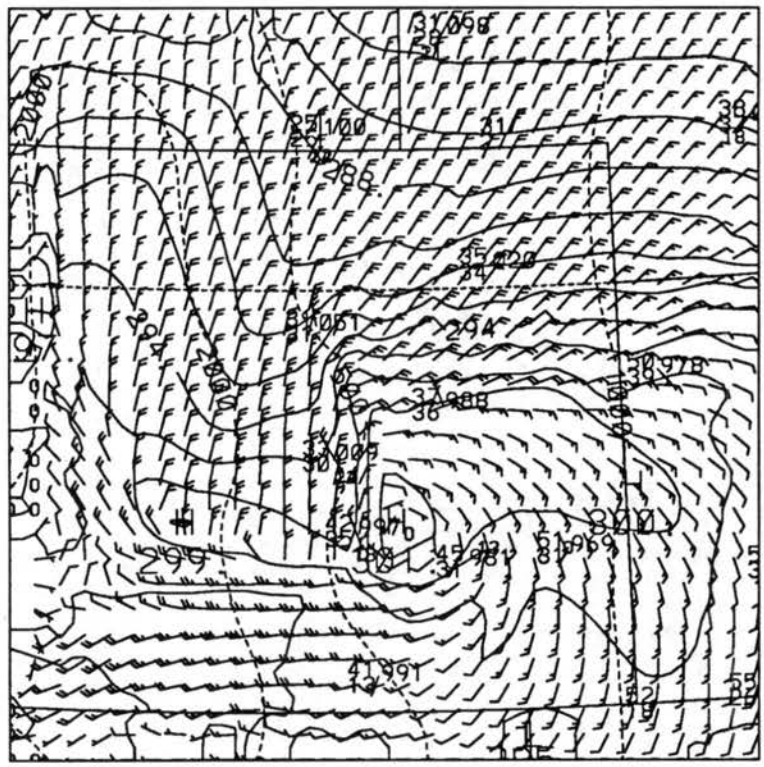

Figure 5.36: Continued:

agrees better with the Limon SAO. Curiously, LBAL does not suggest a sharp frontal interface which may be the result of the variational analysis scheme that tends to smooth the initial fields.

Upper air comparisons away from terrain-influenced regions are similar with the exception of LBAL which has less spuriously large ascent regions and hence less adverse effects due to excess latent heating. Time series of forecast winds near Platteville (not shown) indicate that all four sensitivity simulations resolved the structure and evolution of the primary flow regimes observed by the Platteville wind profiler (Fig. 5.11). The 3 h predictions of maximum vertical motion (Fig. 5.37) indicate close agreement between LAPS and LSFC. Maximum ascent predicted by LBAL is mostly confined to over the higher terrain and the magnitudes are considerably smaller. For example, the area of maximum ascent south of Limon is about an order of magnitude smaller than the LSFC and LAPS forecasts. MAPS and MTOP also show spuriously large ascent regions that are stretched out along the area of surface convergence between the northeasterlies and southerlies over southeast Colorado.

Six hour forecasts of maximum vertical motion (Fig. 5.38) continue to indicate a close agreement between LAPS and LSFC. Regions of large upward vertical motion are observed in LAPS, MAPS, and MTOP, but the maximum magnitude has decreased since the 3 h predictions probably due to less convection at this time. LBAL continues to show less areas of large ascent and the forecast correlates somewhat better to observations than the other simulations. For instance, the north-south band of maximum ascent through Ft. Collins with upward vertical motion decreasing away from the mountain barrier corresponds better to the observed upslope conditions than the other simulations which predict a relative minimum in ascent near Greeley.

Representative vertical cross sections through the frontal interface illustrate the differences in upper air structure. West-east vertical cross sections of 6 h potential temperature and vertical motion forecasts positioned south of Denver are illustrated in Figs. 5.39-5.42 (see Fig. 5.38 for location). The LAPS potential temperature prediction suggests the surface frontal boundary to be located at about the domain center with the cold air mostly

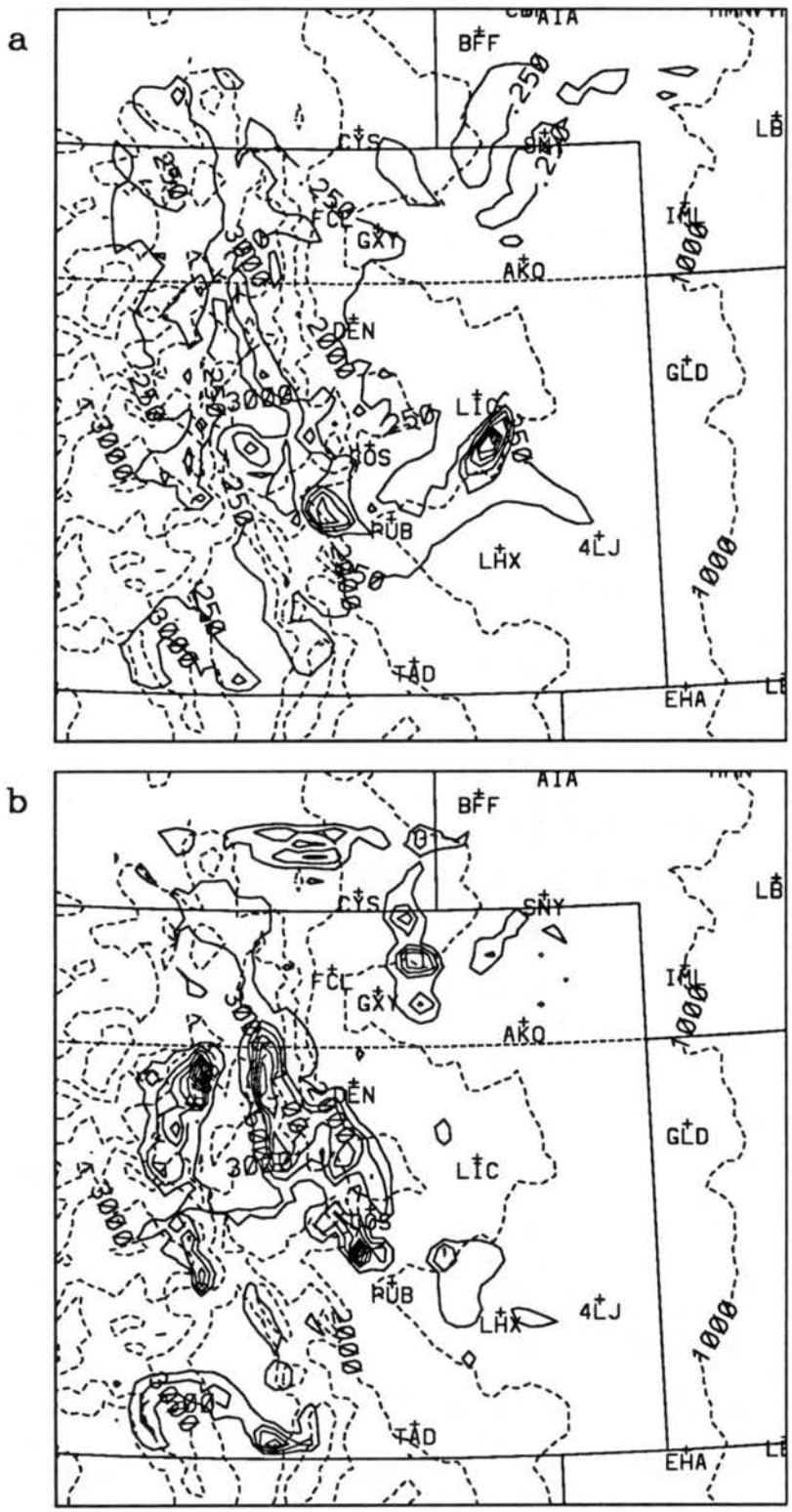

Figure 5.37: RAMS maximum upward vertical motion (m s^{-1}) predictions from the 3 h forecast valid at 0000 UTC 9 March 1992 for (a) the LAPS simulation (contour interval = 1.0 m s^{-1}) and (b) the LBAL simulation (contour interval = 0.25 m s^{-1}).

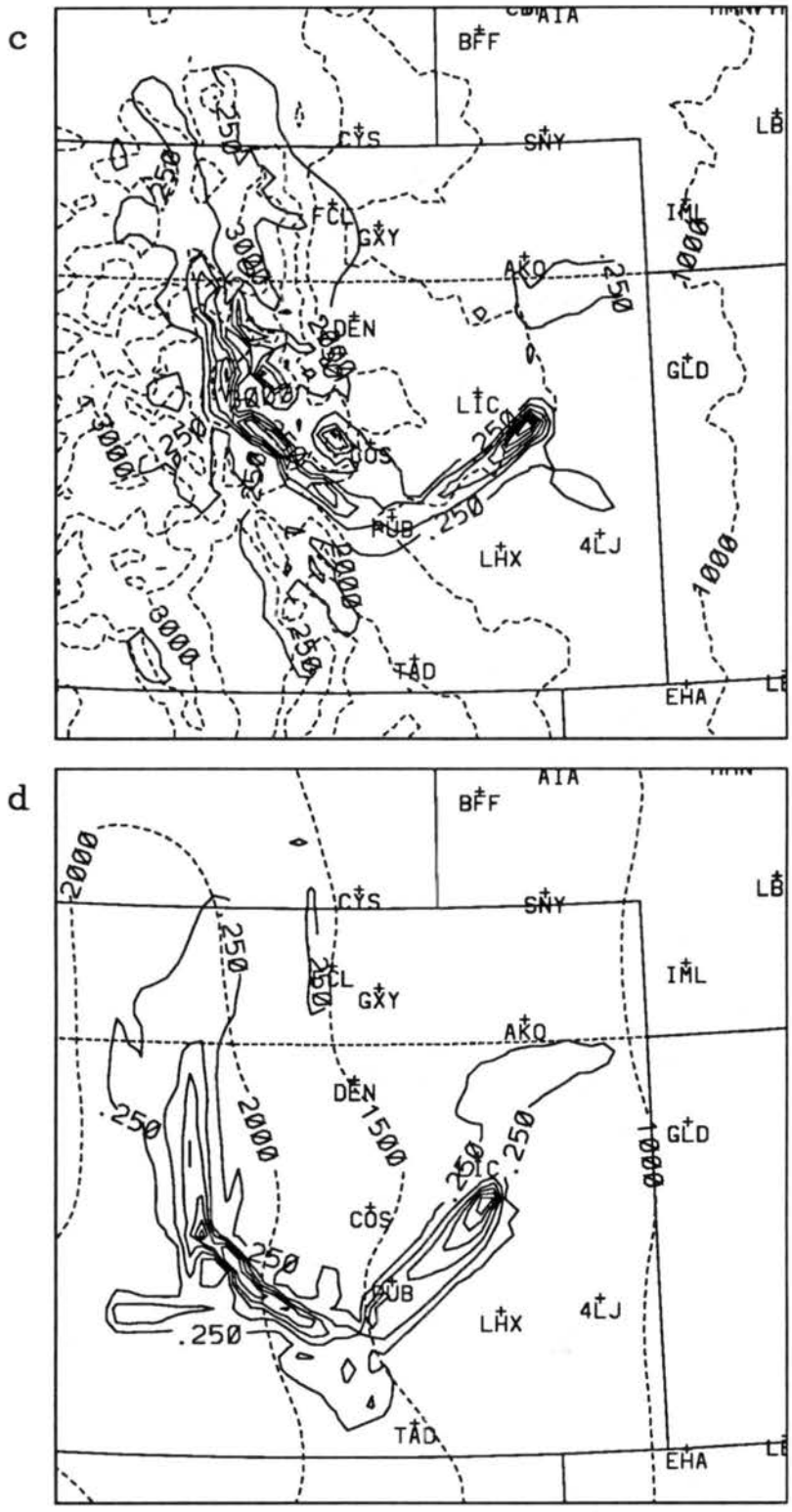

Figure 5.37: Continued: (c) the MAPS simulation (contour interval = 1.0 m s^{-1}) and (d) the MTOP simulation (contour interval = 1.0 m s^{-1}).

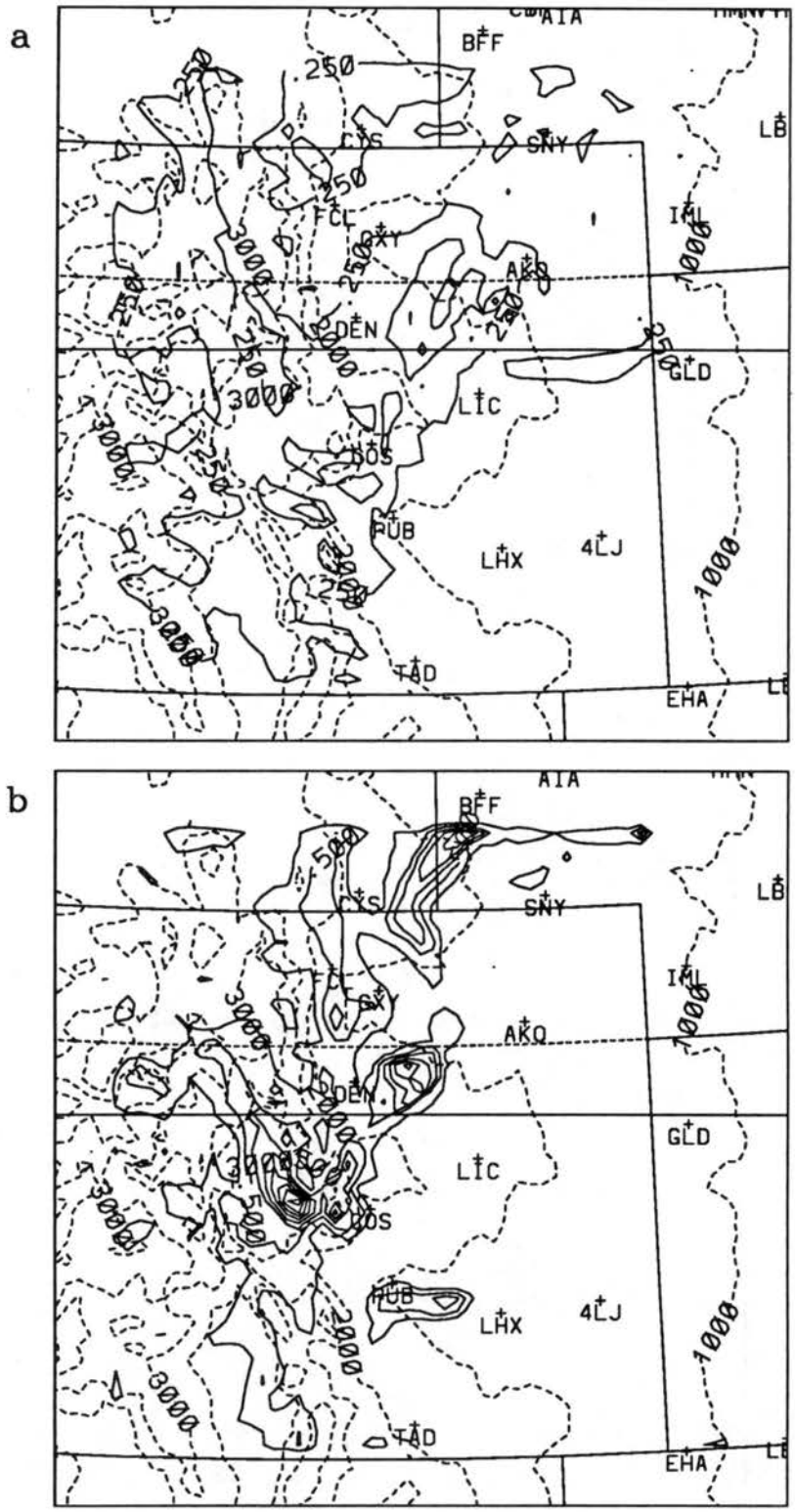

Figure 5.38: As in Fig. 5.37 except for 6 h forecast valid at 0300 UTC 9 March 1992.

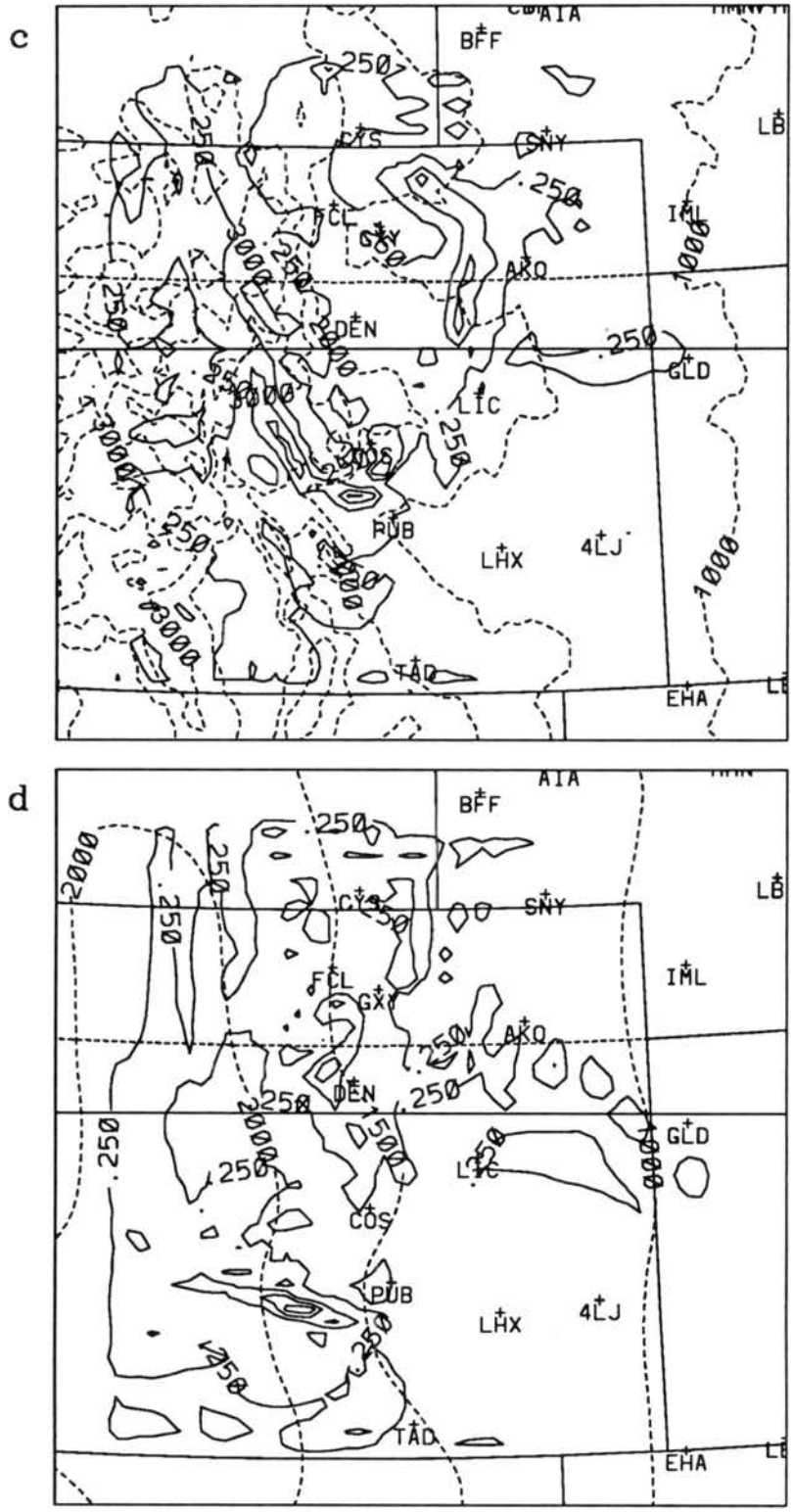

Figure 5.38: Continued:

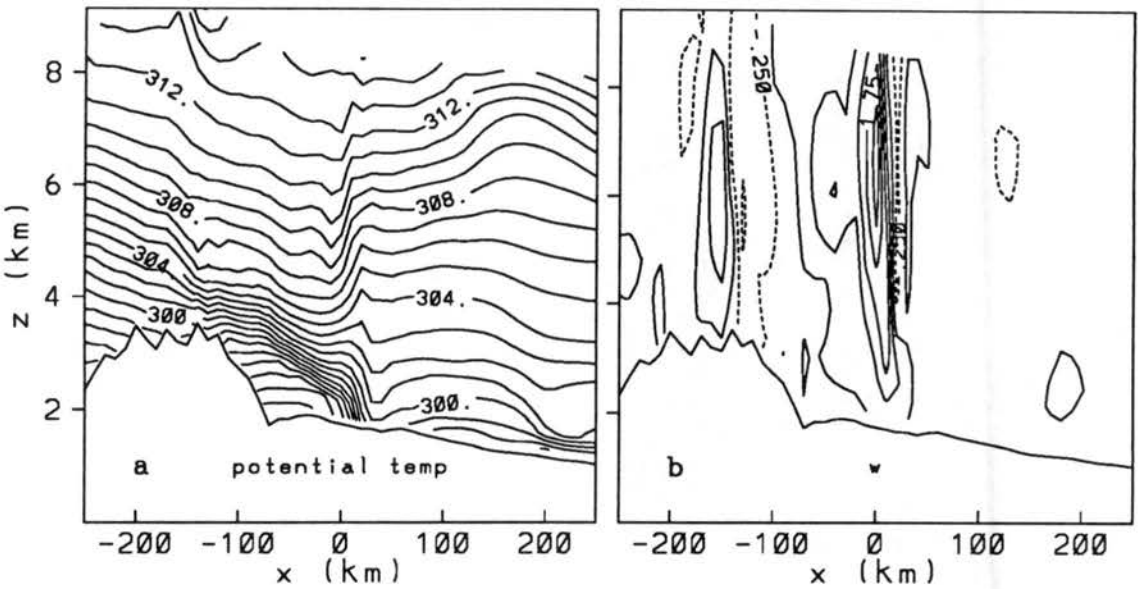

Figure 5.39: West-east vertical cross sections from RAMS (LAPS) 6 h forecast valid at 0300 UTC 9 March 1992 of (a) potential temperature (K) and (b) upward vertical motion (m s^{-1}, contour interval = 0.5 m s^{-1}). Cross section location is represented by the solid line in Fig. 5.38.

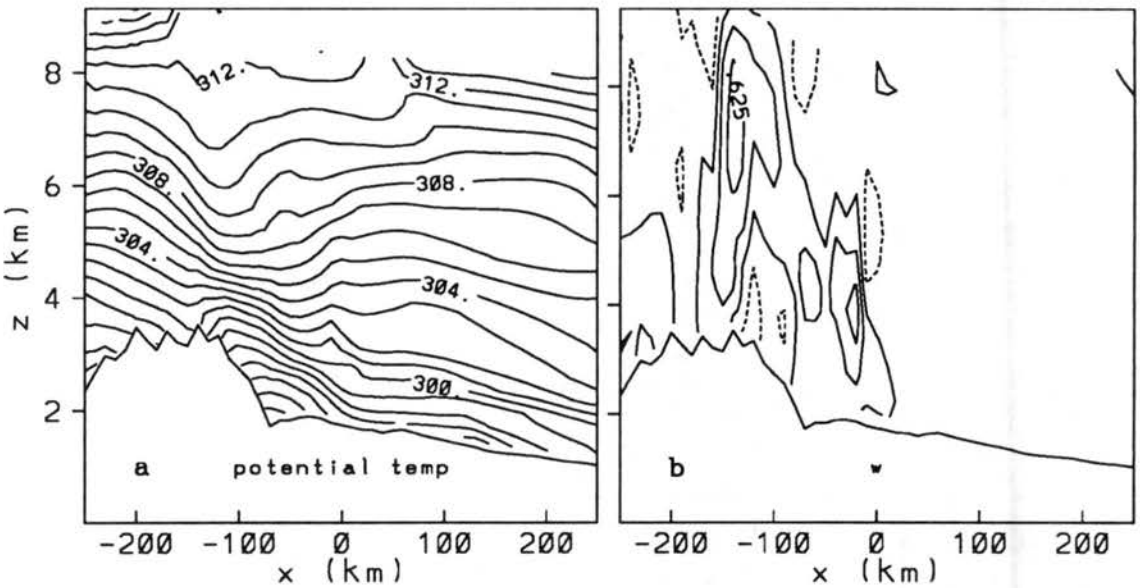

Figure 5.40: As in Fig. 4.39 except for the LBAL simulation (upward vertical motion contour interval = 0.25 m s^{-1}).

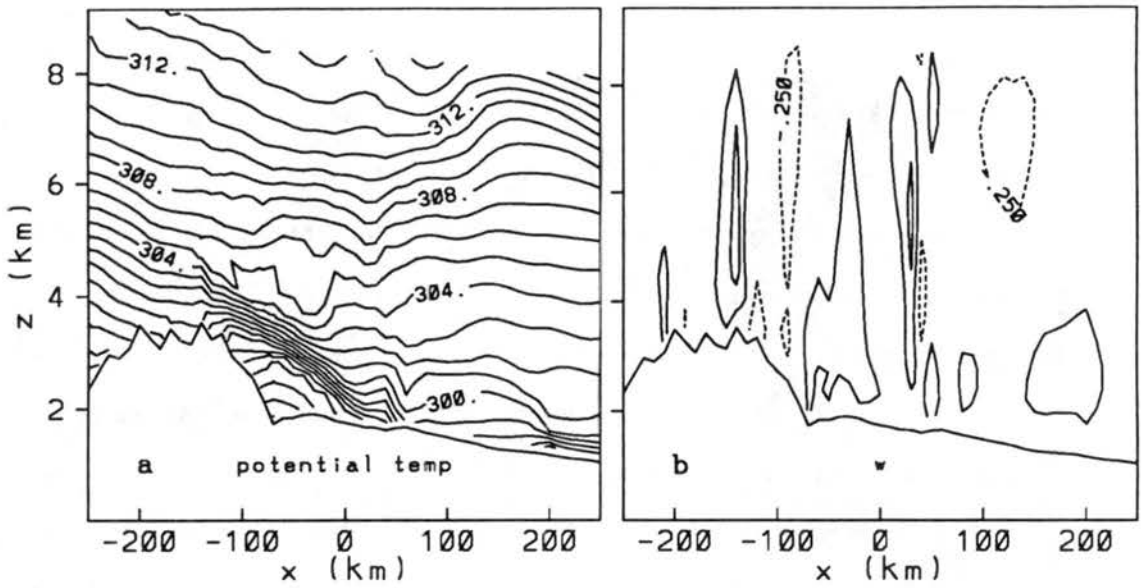

Figure 5.41: As in Fig. 4.39 except for the MAPS simulation.

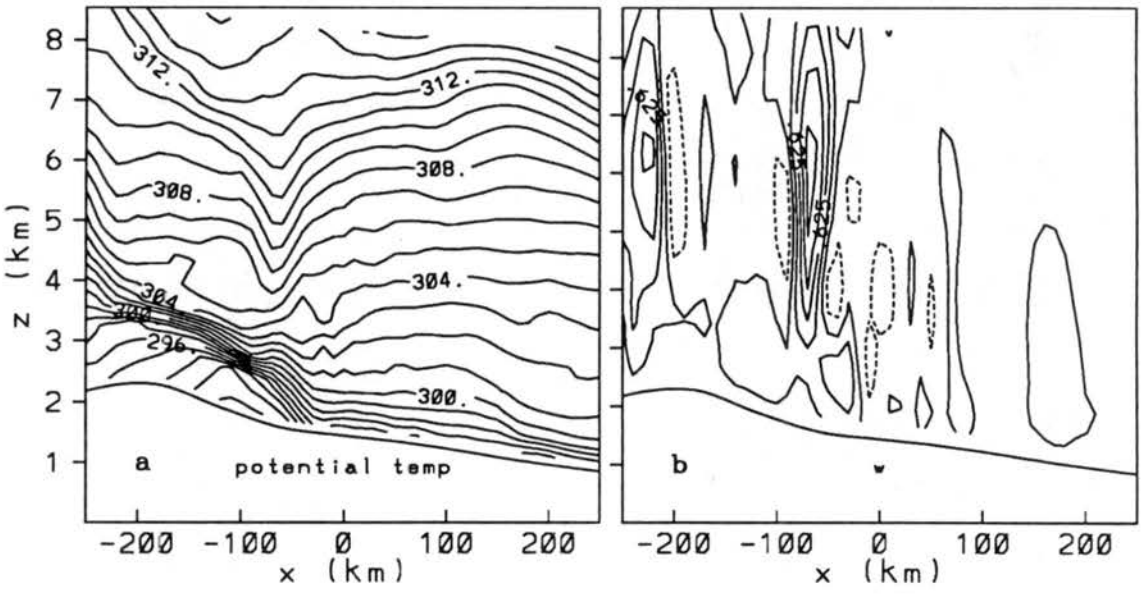

Figure 5.42: As in Fig. 4.39 except for the MTOP simulation (upward vertical motion contour interval = 0.25 m s^{-1}).

trapped east of the mountain barrier. Two columns of strong upward vertical motion are evident above the surface front and over the highest terrain. Large amounts of latent heating appear to deform the potential temperature field in these regions especially over the surface front. Compensating downward vertical motion surrounding the two columns of ascent is probably too large resulting in an area of descent over the Front Range where heavy precipitation was observed. The LBAL forecast indicates a weaker potential temperature gradient suggesting a more diffuse frontal interface. The cold air is trapped between the Continental Divide and the domain center, similar to the LAPS prediction. A broader, but weaker, area of ascent is forecast west of the surface front and only a weak, shallow area of descent is observed over the Front Range.

The MAPS forecast frontal position is similar to LAPS as suggested by the potential temperature field. Three columns of significant, but weaker than LAPS, upward vertical motion are observed over and west of the surface front. Compensating downward motion is also observed surrounding the regions of ascent. The MTOP forecast of potential temperature suggests that the surface front is located about 30 km west of the predicted frontal positions from the other three simulations (LAPS, LBAL, MAPS). With much shallower topography, the cold air is not trapped east of the mountain barrier illustrating the importance of using an accurate representation of the topography for predictions of arctic air mass propagation in mountainous terrain. As in LAPS and MAPS, significant columns of ascent appear to be forced by the surface front and the topography. Adverse effects from excessive amounts of latent heat over the surface front are suggested by the undulation in the potential temperature field.

5.2.4 LFCS simulation - an operational forecast

The LFCS experiment uses lateral boundary conditions from the larger domain MAPS prediction to simulate a true real-time, operational forecast. The primary objective of the LFCS experiment is to determine if the model prediction quality can be maintained using a real-time, operational configuration. Although the simulations attempted thus far contain spurious predictions due to excessive amounts of latent heat release, the LFCS predictions

realistically represent many of the important mesoscale features of the 8-9 March 1992 case study.

Model output from LFCS suggests that prediction quality is maintained away from the lateral boundaries, similar to the results from the 7 January 1992 case study. LFCS predictions of low-level potential temperature and winds (Fig. 5.43) indicate similar surface frontal positions at 3 and 6 h when compared to the LSFC simulation (Fig. 5.14). Both experiments were successful in developing the arctic front and the post-frontal high winds, and both were unsuccessful at predicting the observed flow reversal south of the front over the Palmer Lake Divide.

A comparison of upper air predictions from LFCS and LSFC also indicate a similar evolution of mass, wind, and moisture away from the lateral boundaries. For example, the LFCS time series of forecast upper air wind from near Platteville (Fig. 5.44) is nearly identical to the LSFC simulation (Fig. 5.18) and agrees well with the Platteville wind profiler observations (Fig. 5.11). The LFCS results from 8-9 March and 7 January 1992 suggest that the forecast lateral boundary conditions have only a minimal effect on the RAMS predictions through 6 h.

5.3 Model Validation

Quantitative RAMS model validation for the 8-9 March 1992 simulations follows the same format used for the 7 January 1992 case study. This includes the analysis of bias, RMS, and MRBP statistics generated from a comparison of LAPS analyses and model predictions for surface and upper air.

5.3.1 Surface

Hourly bias and RMS differences of temperature, mixing ratio, dew point, wind speed, and wind direction are generated for the seven RAMS simulations using all available surface observations compared to model predicted variables (Fig. 5.45). Recall that the statistical results are weighted towards the model performance in the FSL mesonet domain where about half of the observations are located. Also, since SAO surface pressures are not available, the mixing ratio results are valid for only the mesonet area.

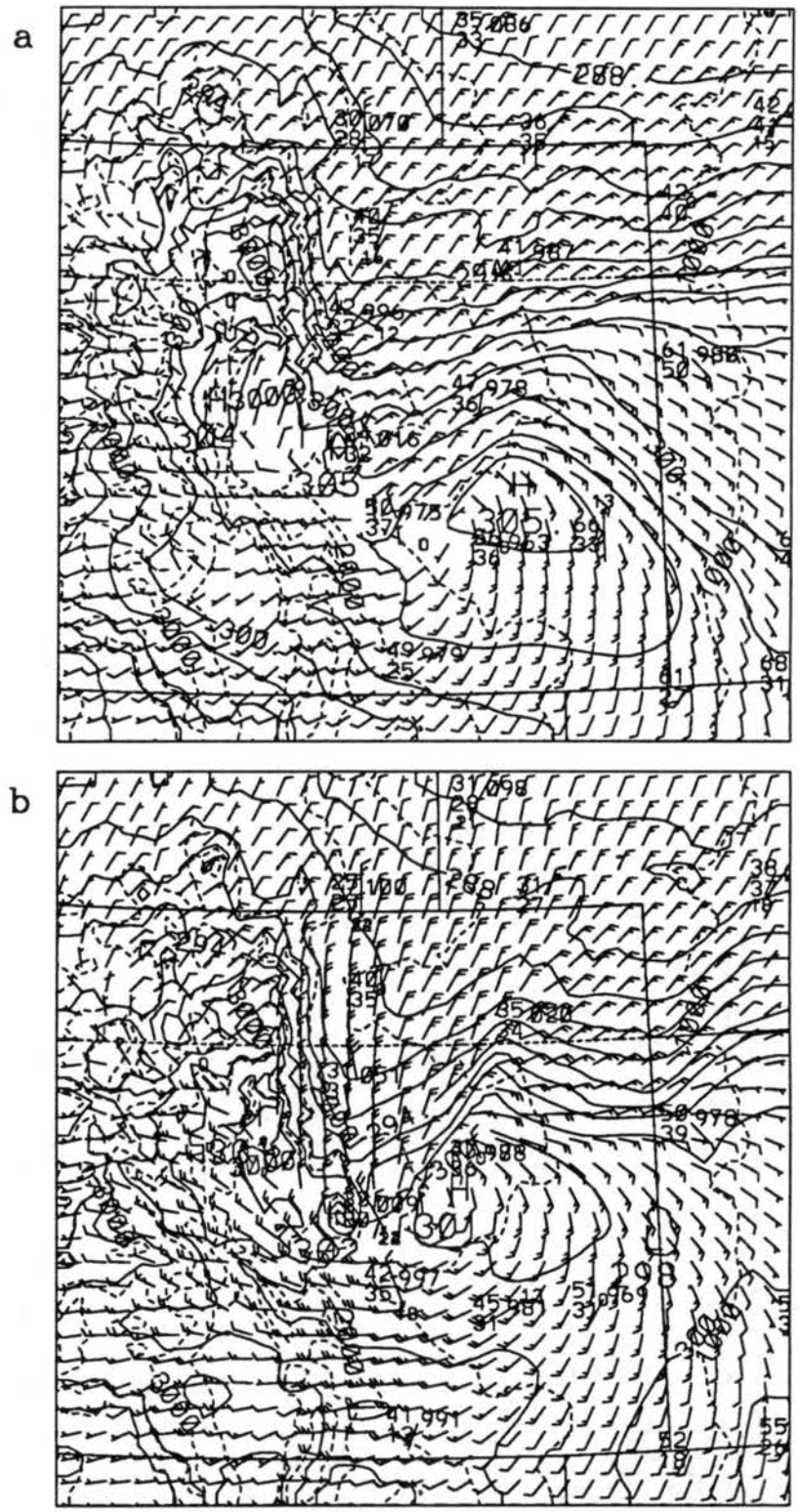

Figure 5.43: RAMS (LFCS) low-level (146 m AGL) potential temperature (K, contour interval = 1.5 K) and wind ($m\ s^{-1}$) predictions and actual SAO reports at model validation time from (a) the 3 h forecast valid at 0000 UTC and (b) the 6 h forecast valid at 0300 UTC 9 March 1992.

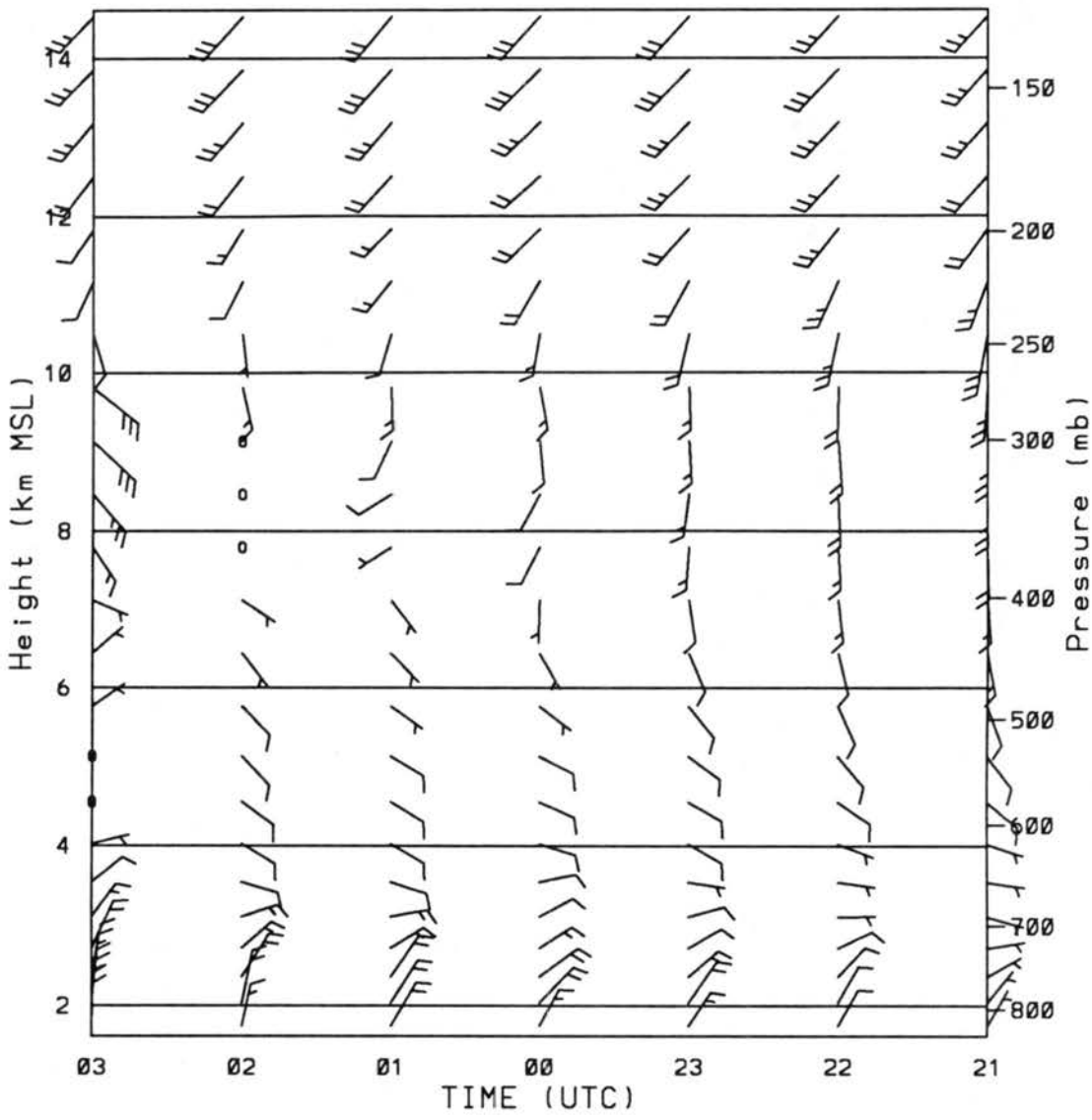

Figure 5.44: Time-height series of RAMS (LFCS) forecast wind (m s^{-1}) for the model grid point closest to Platteville, CO from the 0 to 6 h prediction valid at 2100 UTC 8 March through 0300 UTC 9 March 1992.

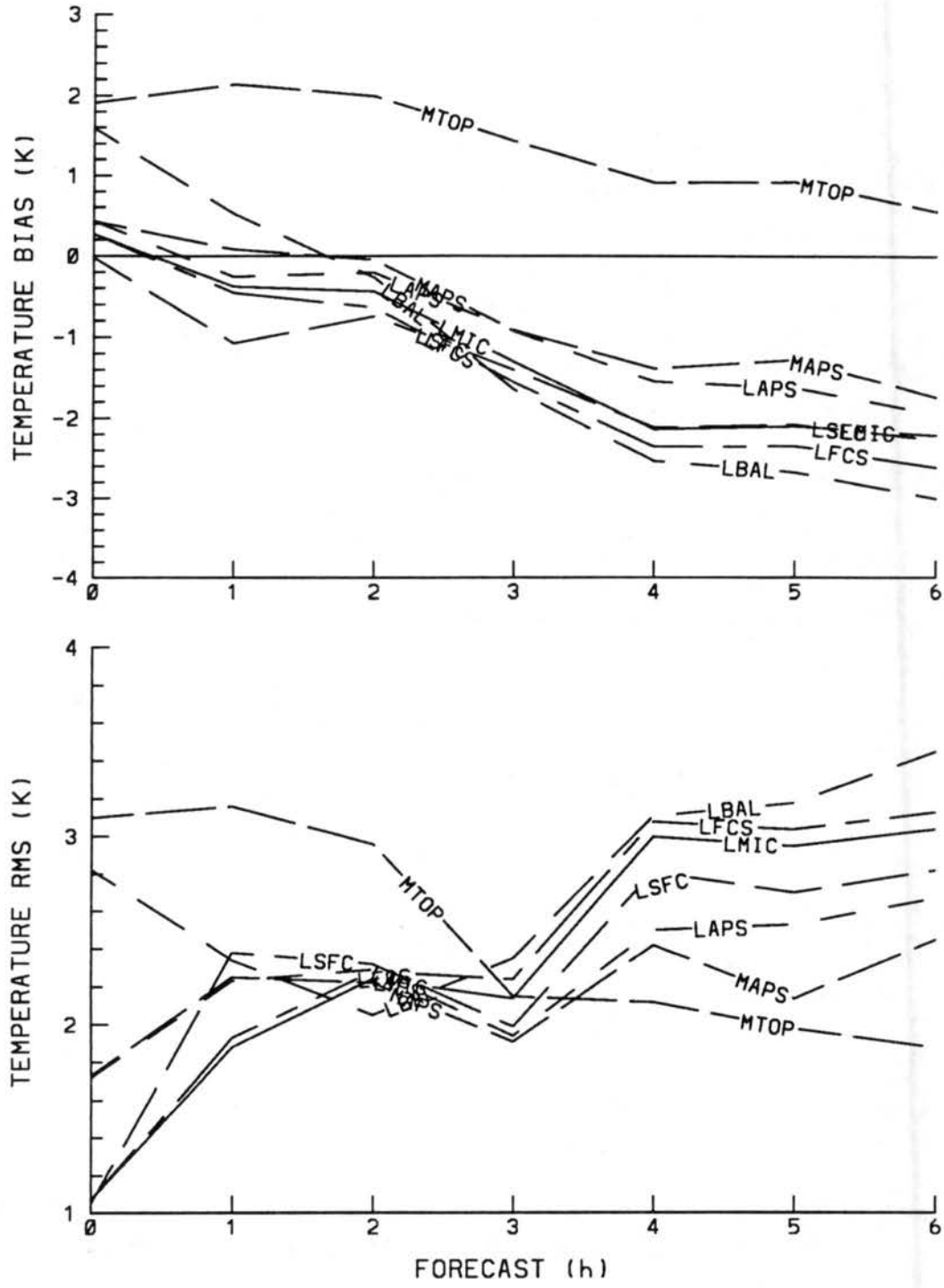

Figure 5.45: Hourly bias and RMS differences for the seven RAMS simulations compared to surface observations. Differences are computed by subtracting RAMS from the observations for (a) temperature (K).

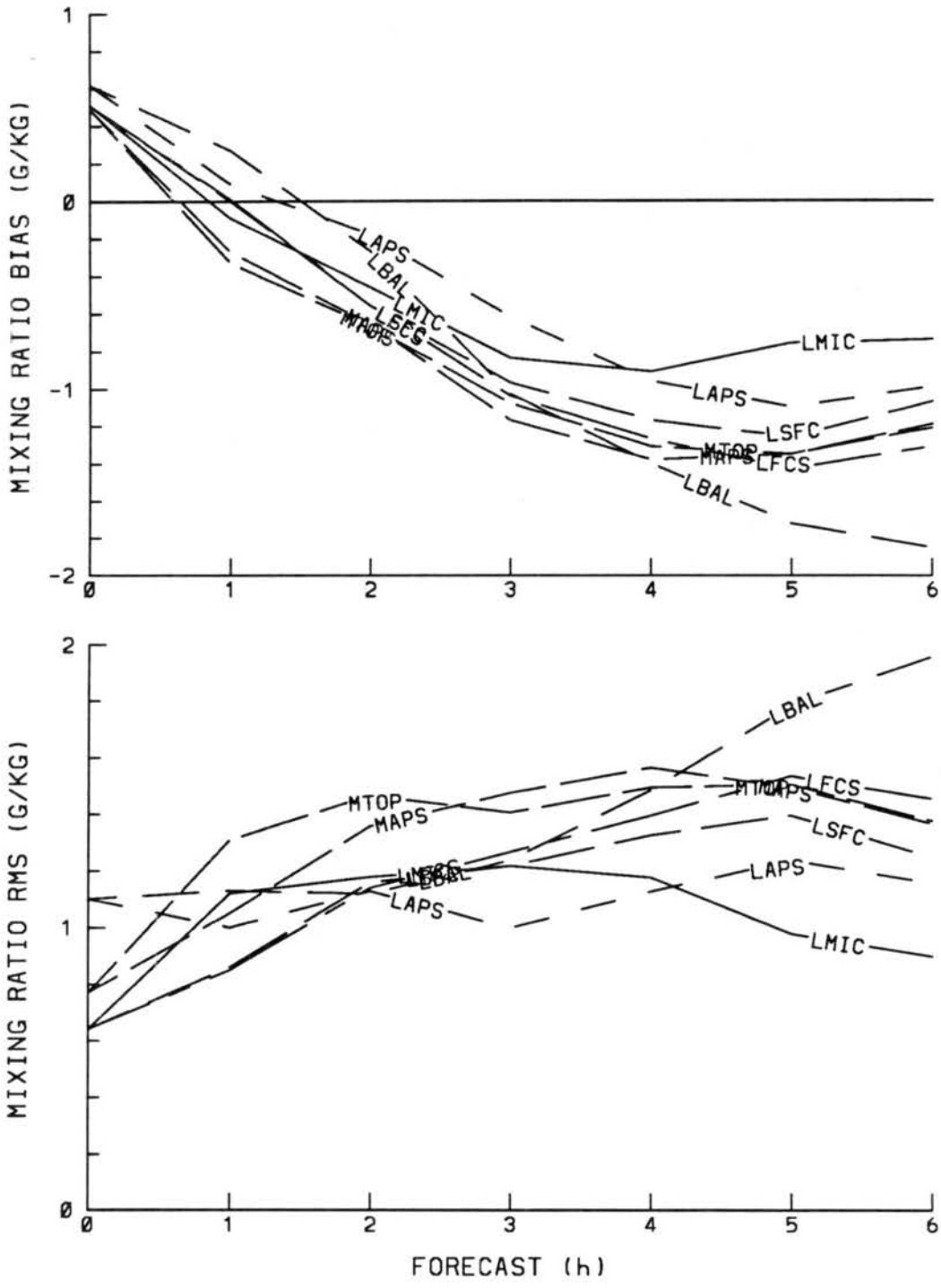

Figure 5.45: Continued: (b) mixing ratio (g kg^{-1}).

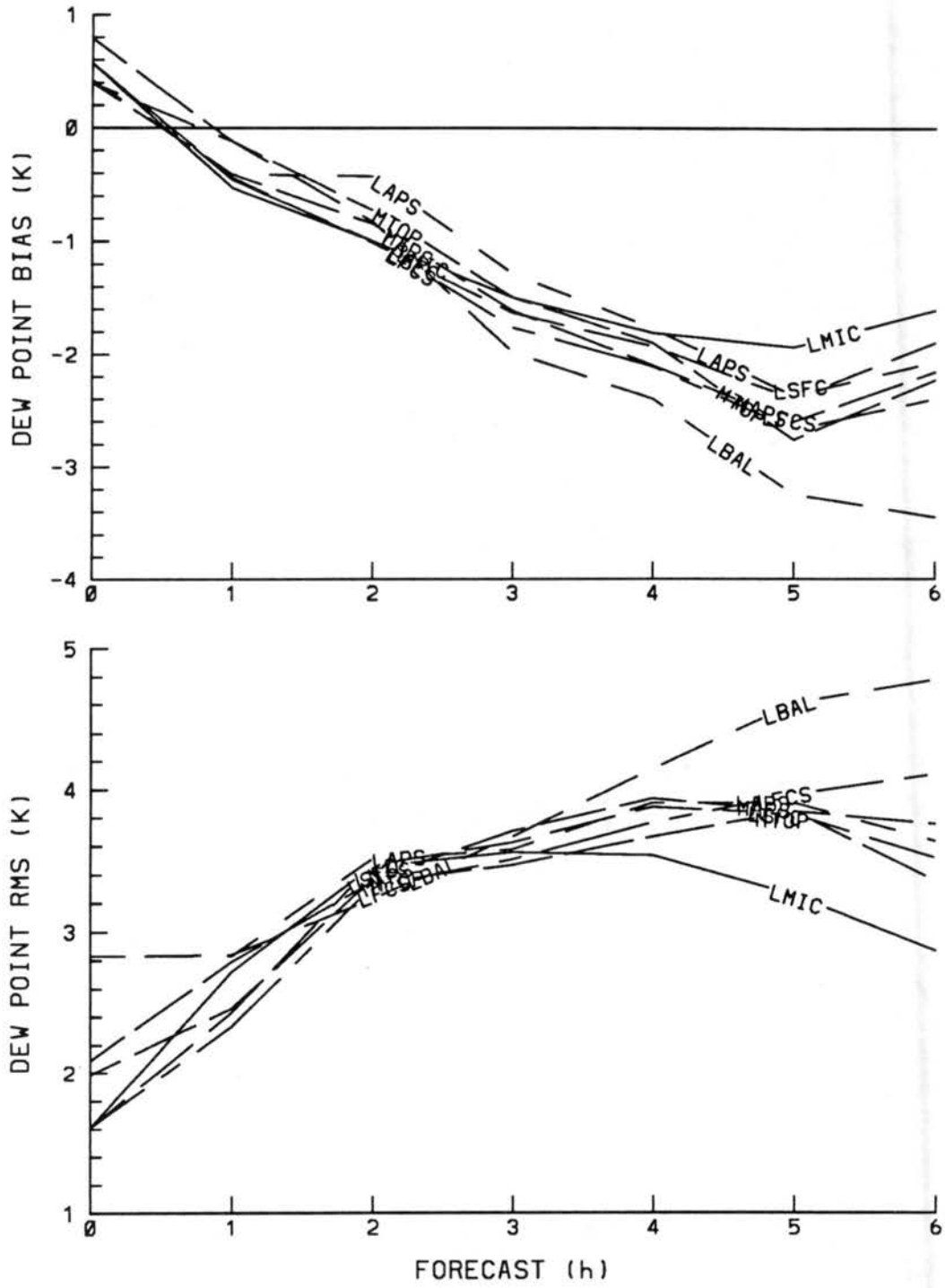

Figure 5.45: Continued: (c) dew point (K).

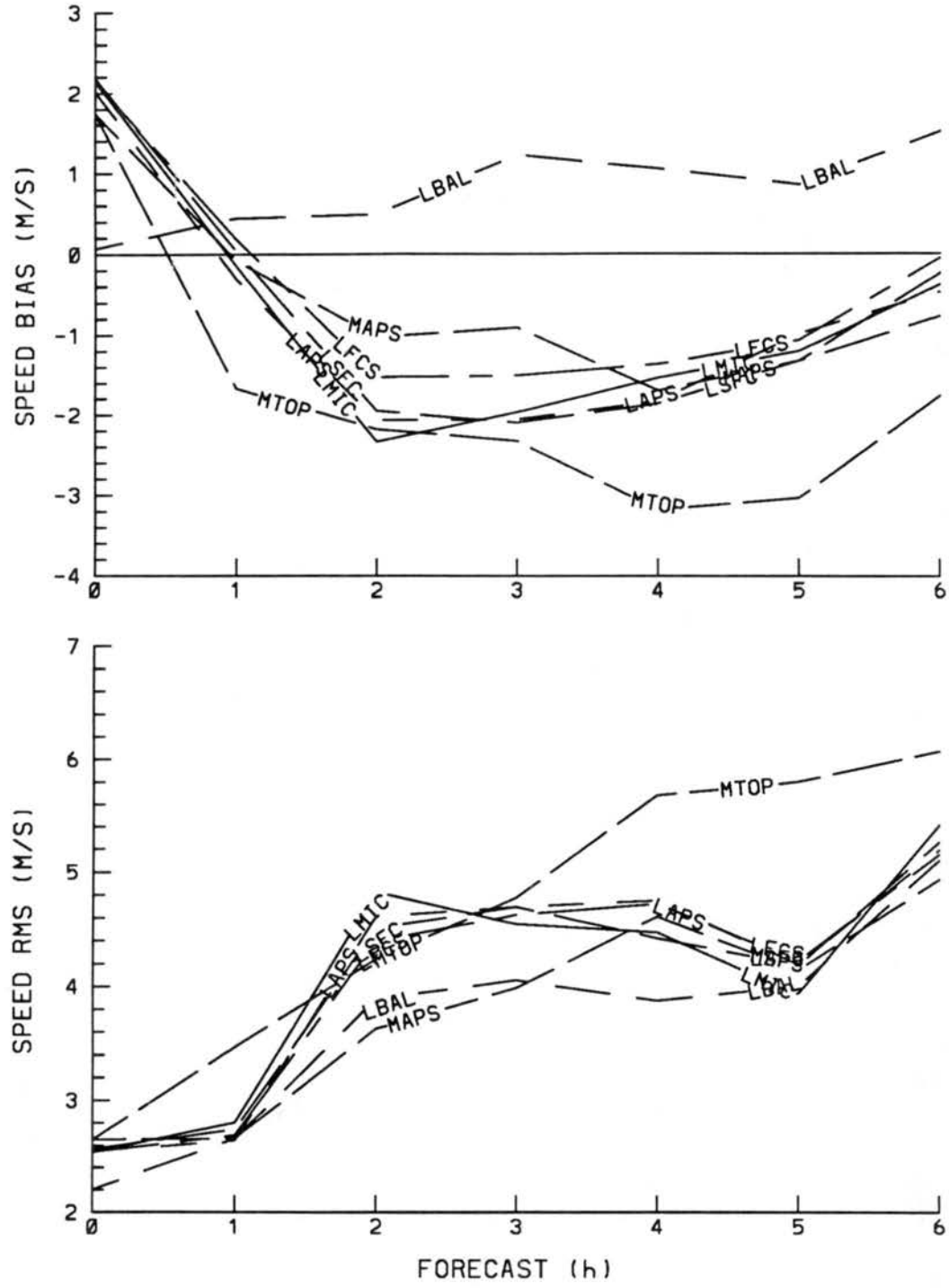

Figure 5.45: Continued: (d) wind speed (m s^{-1}).

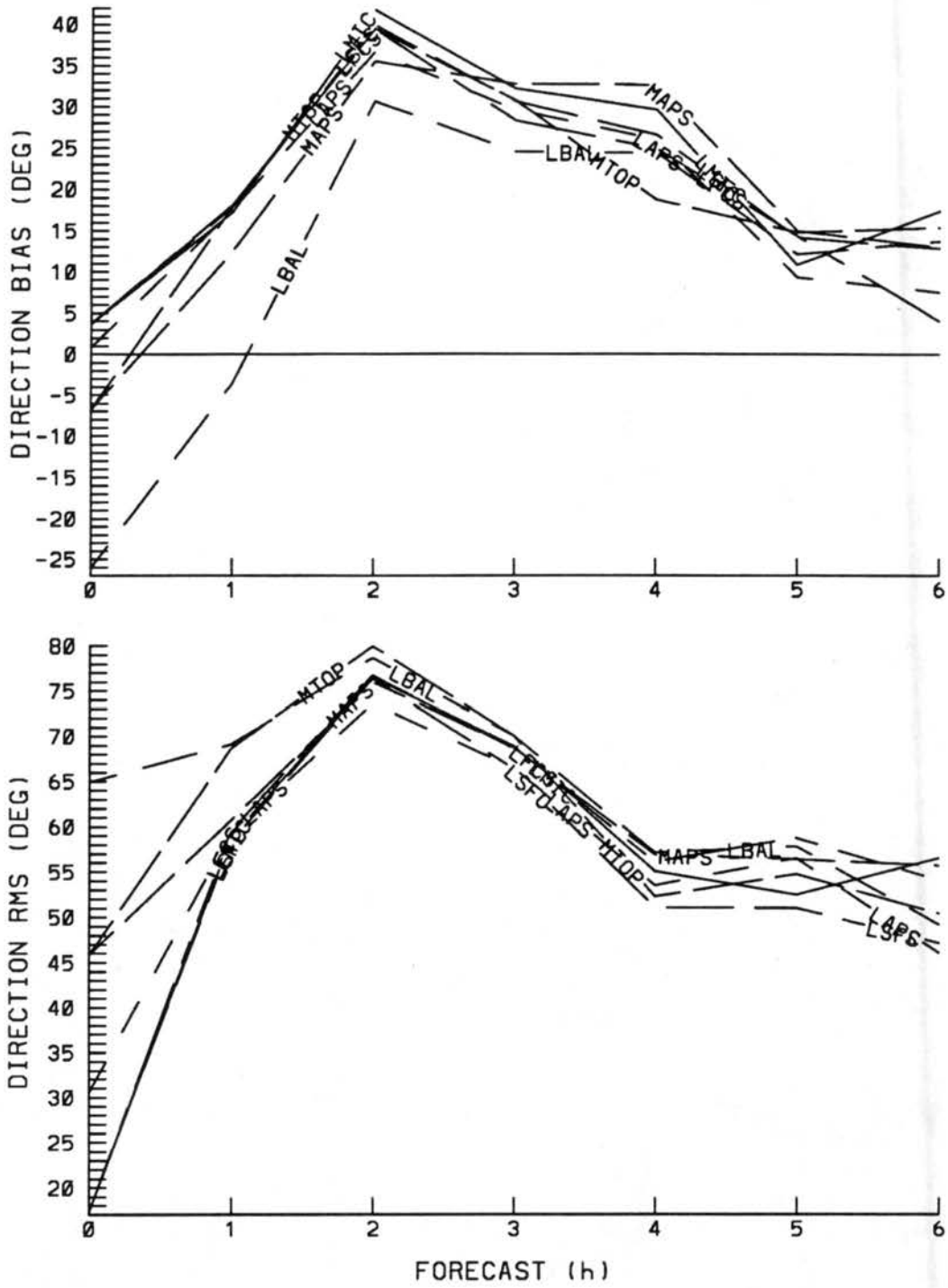

Figure 5.45: Continued: (e) wind direction (degrees).

The same diurnal trend that was observed in the temperature bias statistics for 7 January is also observed in the 8-9 March results. Since the model temperatures are adjusted using the standard lapse rate to account for the differences in elevation between the surface observation and the lowest model sigma level, cold model biases will be indicated when the boundary layer is well mixed (i.e. typical of afternoon) and warm model biases will be indicated when the boundary layer is stable (i.e. typically between sunset and sunrise). With the exception of MTOP, temperature biases are less than one degree during the first two hours and rise to 1.5 to 3 degrees by six hours, somewhat larger than the 7 January results. MAPS and especially MTOP tend to be warmer than the LAPS initialized runs (LAPS, LBAL, LSFC, LMIC, LFCS), similar to the 7 January results. Bias and RMS results suggest that the LAPS simulations improved upon the MAPS runs (MAPS and MTOP) prior to 3 h, but the MAPS runs show better performance than LAPS after 3 h.

All the simulations initially show about equal performance in mixing ratio bias and RMS. A moist bias in the model predictions is evident with time and the LMIC simulation shows closer agreement to the observations than the other runs after 4 h. Bias differences of around 1 g kg^{-1} and RMS differences greater than 1 g kg^{-1} are larger than the 7 January results which is probably influenced by the climatology of greater absolute moisture in March than in January. Similar results are indicated in the dew point statistics where a moist bias develops with time and RMS differences are mostly between 2 and 4 degrees.

Wind speed bias differences are similar for LAPS, LSFC, LMIC, LFCS, and MAPS which show a high model wind speed bias of 2 m s^{-1} to develop by 2 h which diminishes slowly with time. The MTOP simulation is similar through 3 h, but the performance degrades after that time. The LBAL results are significantly different with a low bias of mostly less than 1 m s^{-1}. Two factors likely contributed to the differences noted in the LBAL results. First, the LBAL forecasts defined the flow reversal ahead of the front better than the other runs and second, the adverse effects of excessive latent heat release are less evident in LBAL. The RMS differences indicate less agreement with the observations for MTOP than for the other simulations suggesting that better terrain representation results in significantly improved forecasts of wind speed. The wind direction bias and RMS results

are similar for all the simulations except LBAL prior to 4 h. Unlike 7 January, the direction bias is mostly positive. This is likely due to the northeasterly flow predicted ahead of the front in an area where observations were mostly southerly. Since LBAL agreed better with observations in this region, the LBAL bias is less positive through 4 h.

Hourly bias, RMS, and MRBP statistics are calculated for all seven RAMS simulations using LAPS gridded surface analyses compared to RAMS predictions of temperature, mixing ratio, wind speed, and wind direction (Fig. 5.46). Recall that the statistical results are representative of the whole domain, but the method assumes that the LAPS gridded analyses represent the actual surface conditions which may not be a good assumption in data sparse areas.

The temperature bias results show the same diurnal trend but the gridded comparisons are around 1 degree cooler than the observational comparison, similar to the 7 January results. Bias and RMS statistics indicate that all the runs agree about equally with the analyses. The temperature agreement measures are all high with values exceeding 90%. All the simulations show about equal agreement except for MTOP which is consistently lower. Bias results from the mixing ratio comparison show a moist bias developing with time, but the magnitudes of 0.1 to 0.5 g kg^{-1} are less than the observational comparison bias. RMS differences are mostly between 0.7 and 1.5 g kg^{-1}. MRBP agreement measures decrease with time but remain above 70% for the five LAPS initialized runs. At 6 h, LMIC shows best agreement with the LAPS analyses, followed by the other four LAPS runs (LAPS, LBAL, LSFC, LFCS), and then MAPS and MTOP with agreement measures of around 60%.

The gridded comparison of speed is similar to the observational comparison with a fast bias increasing with time for all the simulations except LBAL which has much smaller speed biases of less than 1 m s^{-1}. RMS results indicate better agreement with the analyses for LBAL, less agreement for MTOP, with the other simulations in between with about equal agreement. MRBP agreement measure starts high but decreases rapidly with time. Curiously, LBAL, which performed well in the other statistical categories, shows significantly less agreement through 3 h than the other simulations. The direction bias is

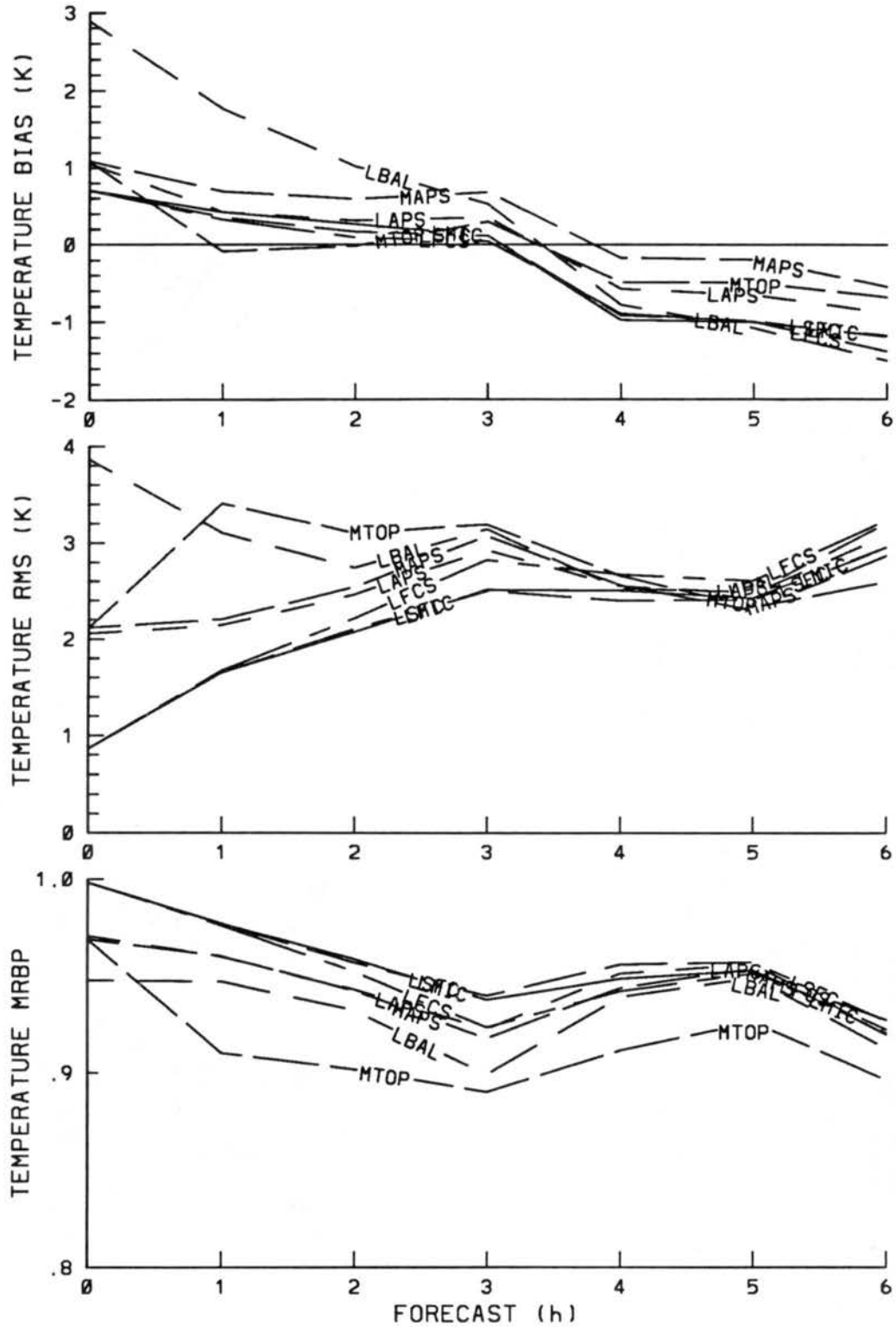

Figure 5.46: Hourly bias, RMS, and MRBP statistics for the seven RAMS simulations compared to LAPS gridded surface analyses. Differences are computed by subtracting RAMS from LAPS for (a) temperature (K).

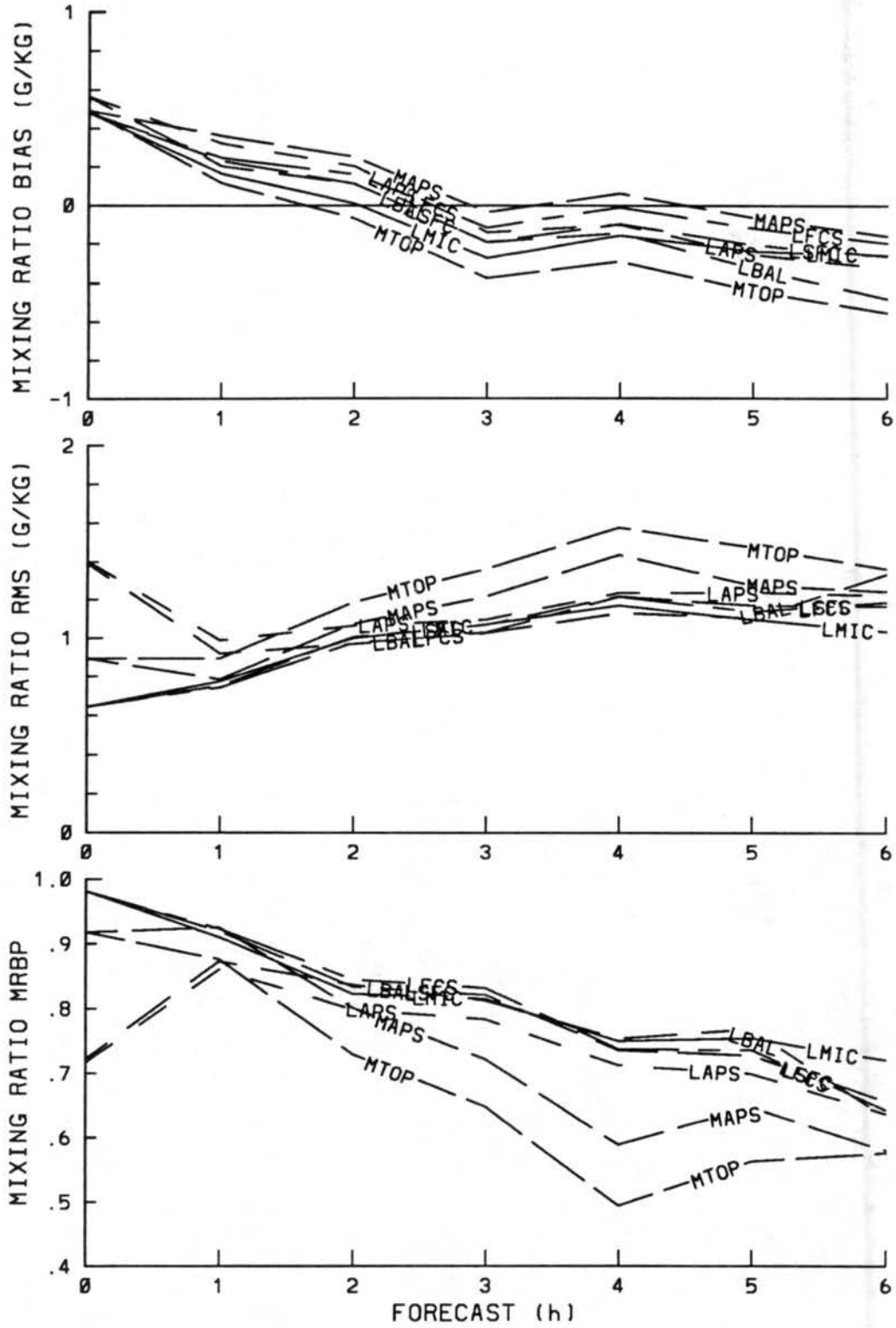

Figure 5.46: Continued: (b) mixing ratio (g kg^{-1}).

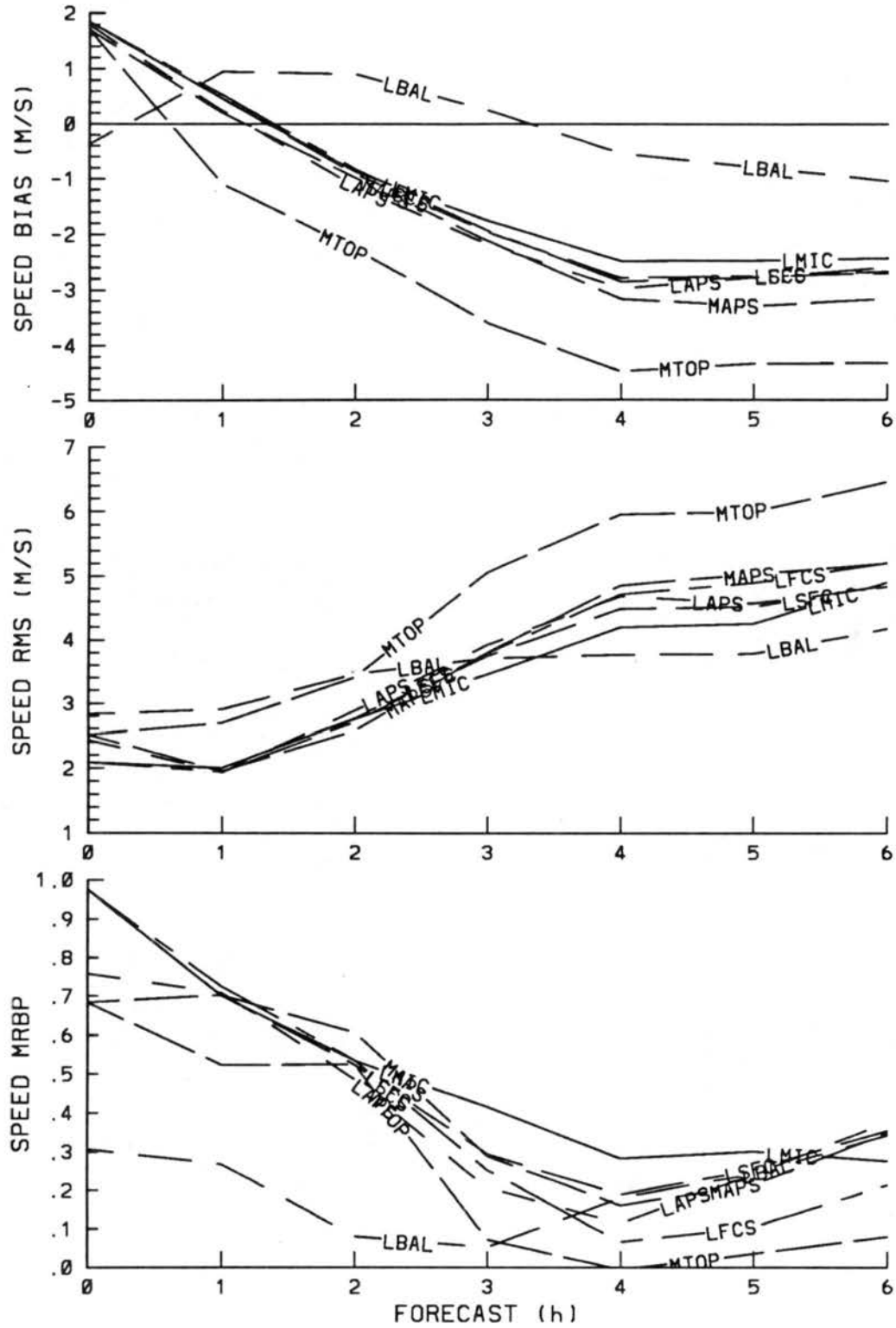

Figure 5.46: Continued: (c) wind speed (m s^{-1}).

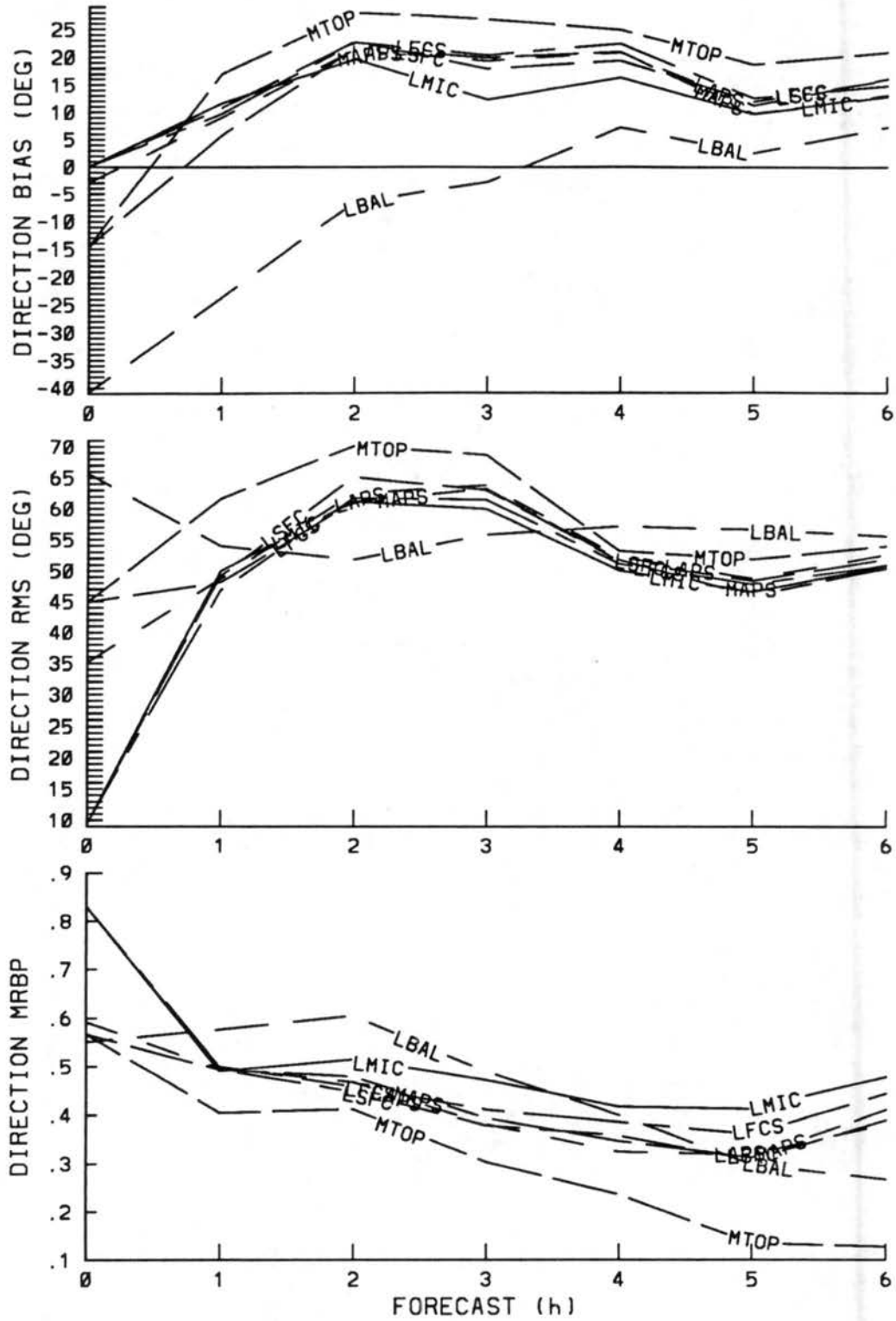

Figure 5.46: Continued: (d) wind direction (degrees).

similar to the observations comparison with a positive bias developing with time, except smaller in magnitude. Less direction bias is indicated for LBAL while MTOP shows greater bias than the other simulations. RMS results are about equal for all the simulations after 3 h with values around 55 degrees. MRBP results indicate agreement measures initially around 50 to 60% and decrease with time to around 40 to 50%. MTOP again shows significantly less agreement with the analyses than the other simulations. Although LBAL showed less agreement in wind speed, better agreement is indicated before 3 h in wind direction suggesting that the simulation improved upon the other runs by reversing the flow south of the front but did not make any improvements in the predictions of speed.

5.3.2 Upper air

Upper air model validation statistics are computed by comparing the model forecast with the corresponding LAPS three-dimensional analysis on each sigma level and at 500 mb. Recall that due to insufficient upper air data resolution, the model predictions may be unfairly penalized for generating any features with resolution greater than the observations.

MRBP agreement measure statistics of temperature, perturbation Exner function (π^*), relative humidity, u, v, and total wind speeds, and absolute vorticity are illustrated in Fig. 5.47 for the 6 h RAMS forecasts. Agreement measures are highest for the mass variables (temperature and π^*) with values mostly greater than 80%. The four LAPS simulations (LAPS, LSFC, LBAL, LMIC) show only minor variations in agreement measure.

Close agreement is indicated between the true forecast (LFCS) and the four LAPS simulations suggesting that the forecast lateral boundary conditions have had only minimal adverse effects. The MAPS simulation shows close agreement with the LAPS simulations, however, less agreement is indicated for MTOP suggesting that the majority of the improvement by LAPS over MAPS is due to better topography representation rather than improvements to the data initialization.

Relative humidity statistics indicate better than 80% agreement near the surface and the agreement decreases with height. Recall that the moisture comparison is affected the most by insufficient observations since moisture typically exhibits the greatest amount of

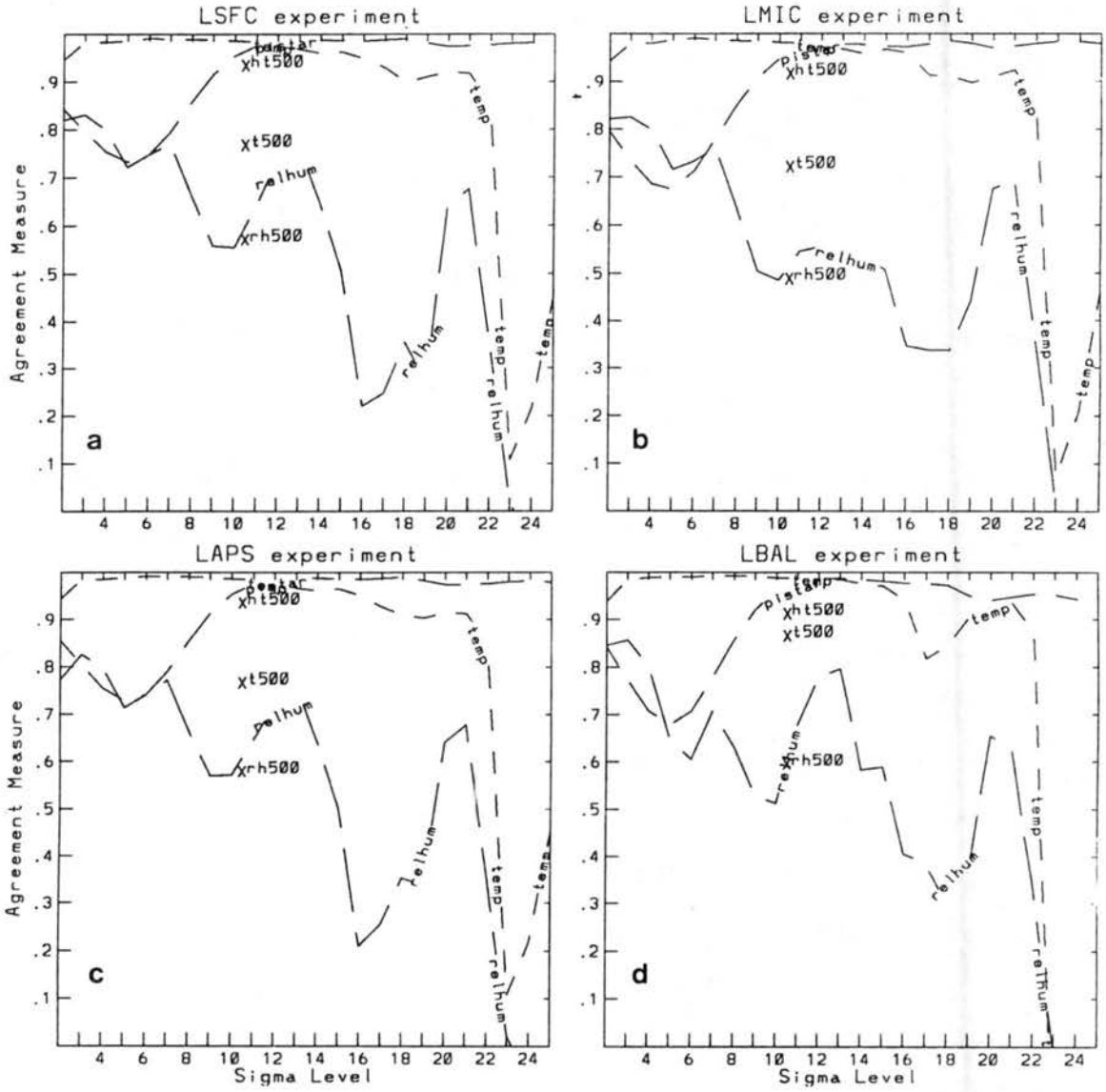

Figure 5.47: Upper air MRBP statistics for the seven RAMS simulations and the MAPS forecast compared to LAPS gridded upper air analyses. Thermodynamic variables from the 6 h forecasts valid at 0300 UTC 9 March 1992 are presented for (a) LSFC, (b) LMIC, (c) LAPS, and (d) LBAL simulations.

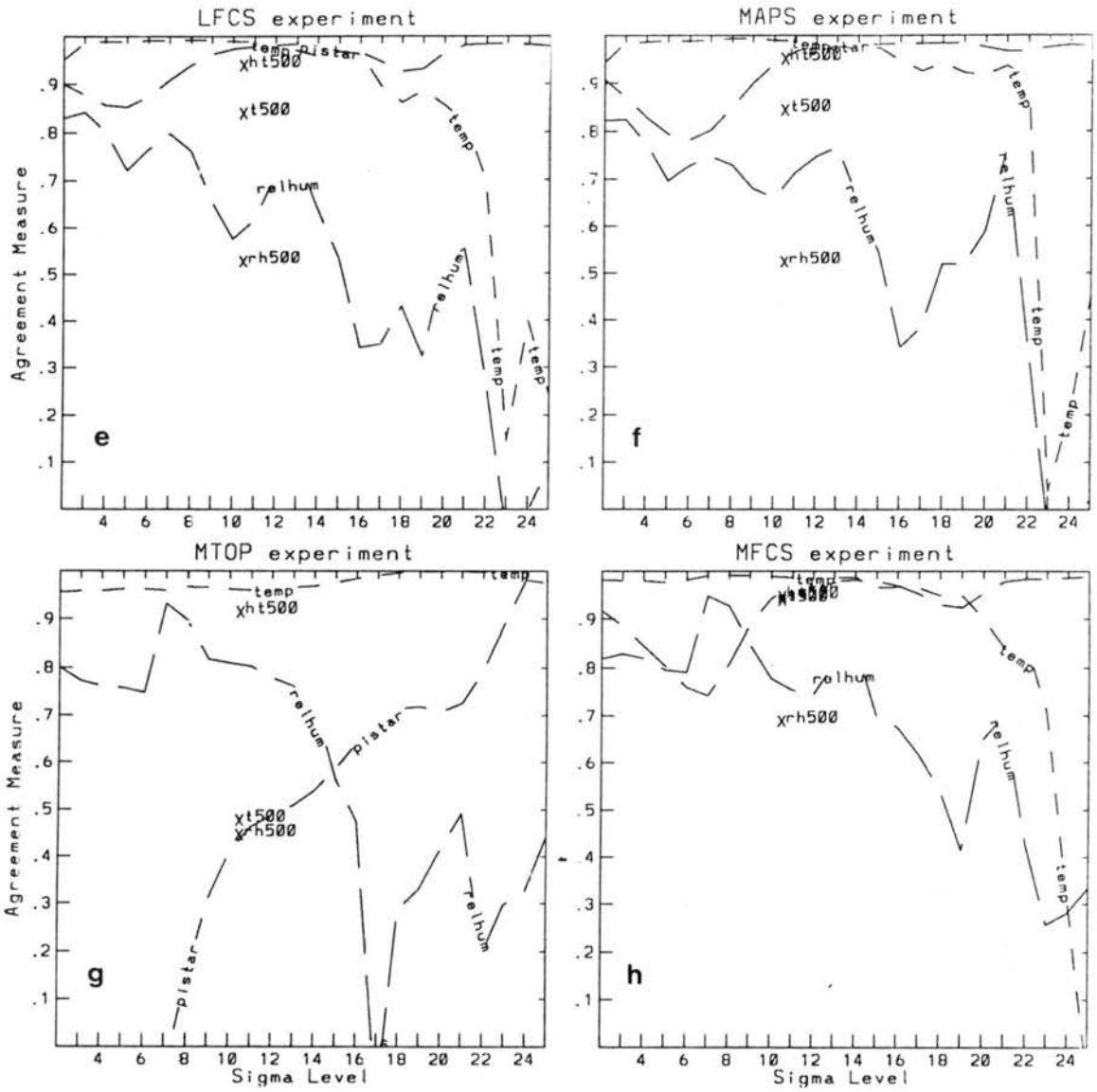

Figure 5.47: Continued: (e) LFCS, (f) MAPS, (g) MTOP, and (h) MFCS simulations.

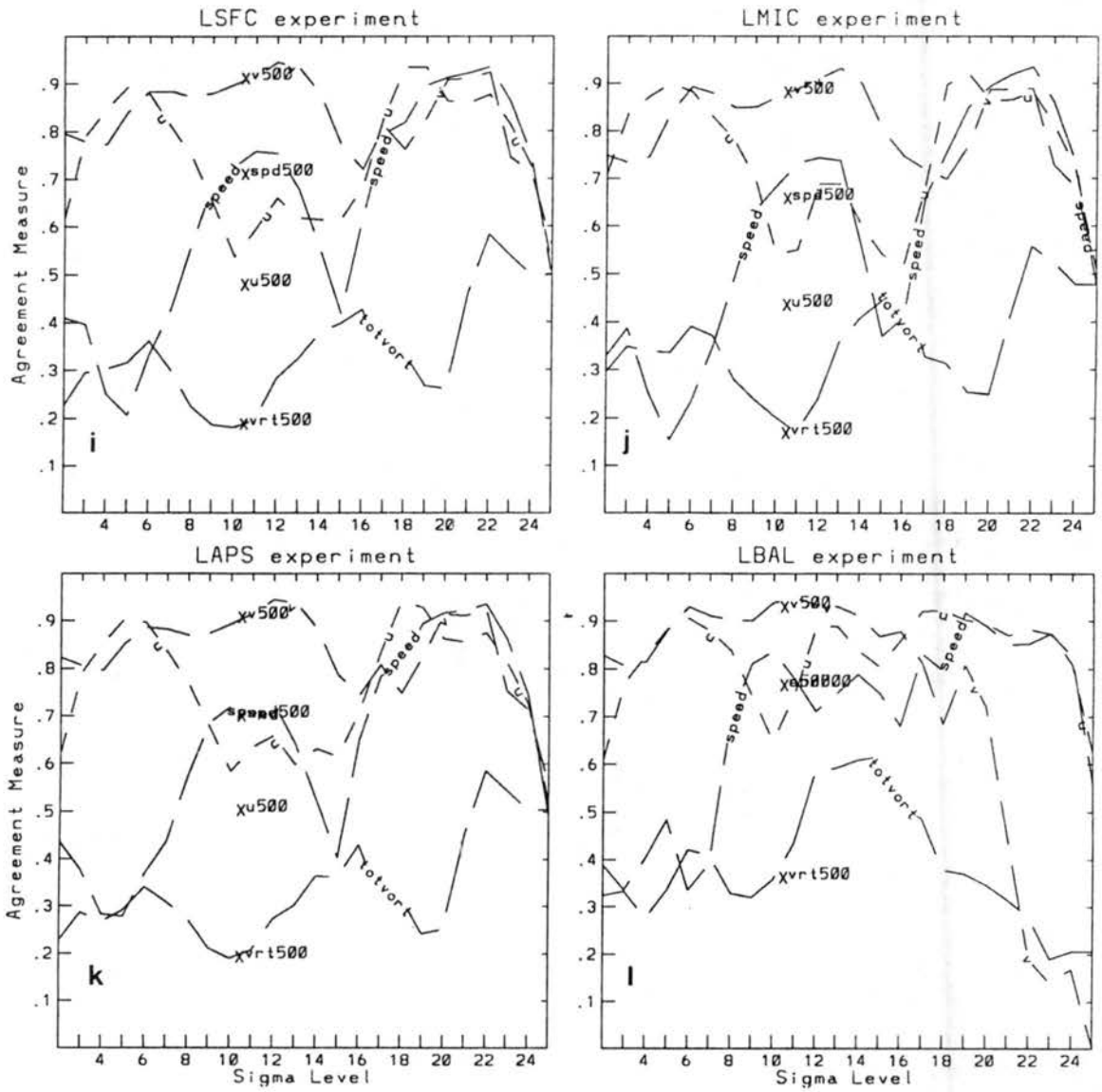

Figure 5.47: Continued: Wind variables presented for (i) LSFC, (j) LMIC, (k) LAPS, and (l) LBAL simulations.

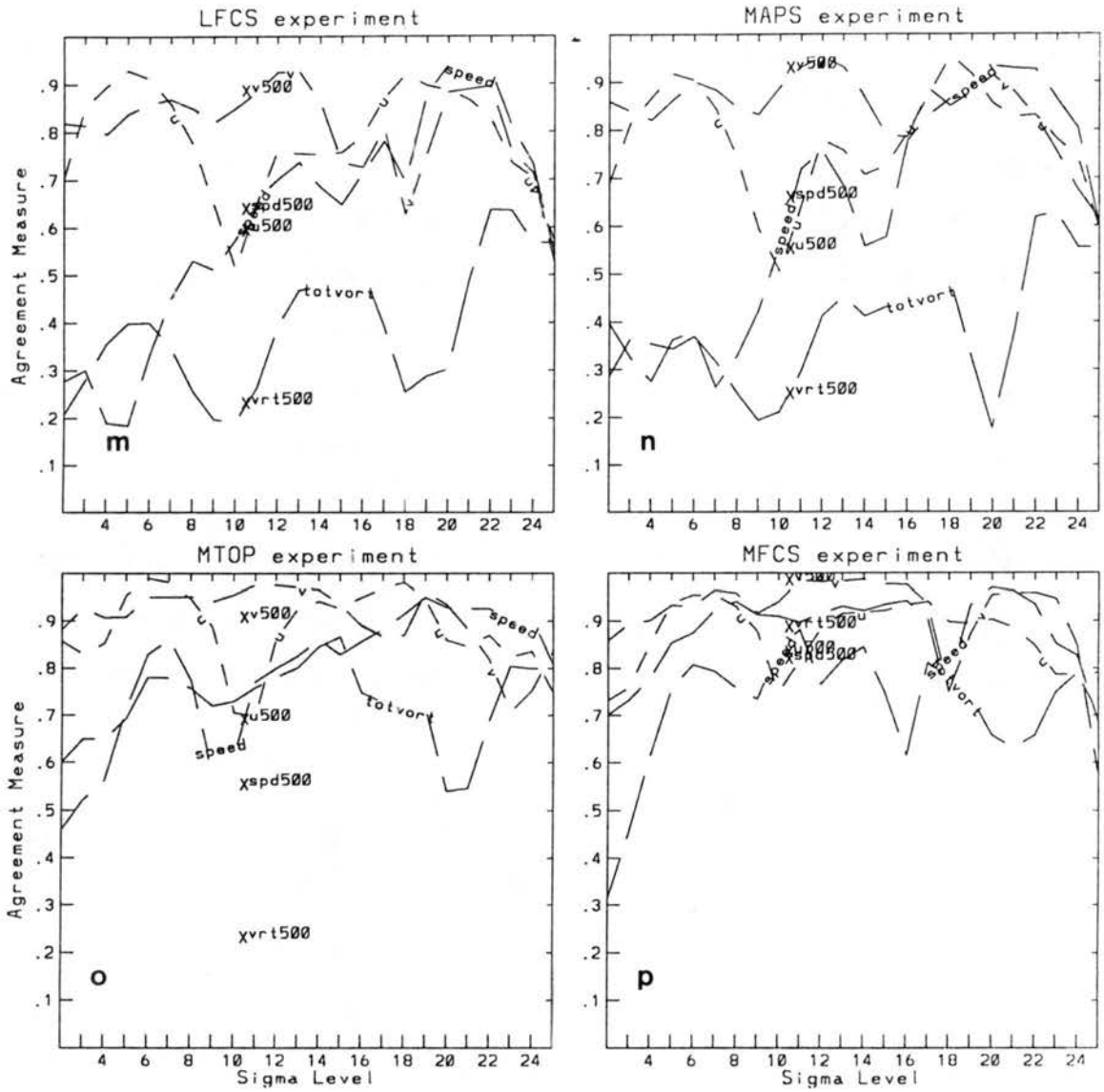

Figure 5.47: Continued: (m) LFCS, (n) MAPS, (o) MTOP, and (p) MFCS simulations.

atmospheric spatial variability. Agreement measures for u- and v-component wind speeds are mostly in the range of 60 to 90%. The 500 mb agreement measures are close to their respective values on sigma surfaces except for temperature which is consistently lower, due to interpolation error introduced during the conversion from the sigma to isobaric coordinate system.

A comparison of the operational MAPS forecast from the MAPS 60 km grid increment prediction model (MFCS) with LAPS indicates results similar to the upper air comparison results from the 7 January case study where MFCS shows higher agreement with the analyses for all parameters except near the surface. This result is probably due to insufficient upper air observations as discussed above. A comparison of the results from 8-9 March 1992 to Thompson's (1993) whole season results indicates significant improvement in all variables except upper level moisture, corroborating the 7 January 1992 results. Significant improvement is again observed near the surface in mass (from 50 to 90%) and moisture (from 30 to 80%). These results add further evidence to the suggestion that the additional mesoscale surface observations along with a more realistic terrain representation have improved the predictions of surface temperature and moisture, however, a larger comparison sample is still required to make a statistically significant conclusion.

5.4 Comparison to Operational Forecasts

An objective of the qualitative comparison between the LFCS experiment and other operational models is to determine if the RAMS predictions add value to currently available regional scale model forecasts. Results from the 7 January 1992 case study indicate that the LAPS initialized RAMS predictions did add value to the operational forecasts from NMC's NGM and FSL's MAPS models. A comparison of the 8-9 March RAMS model output with the same two operational model forecasts adds further evidence to support this conclusion.

The MAPS 3 h forecast (valid at 0000 UTC) of surface potential temperature and wind (Fig. 5.48a) indicates a wide baroclinic zone positioned across southeast Wyoming, northeast Colorado, and southern Nebraska. The frontal position as suggested by the

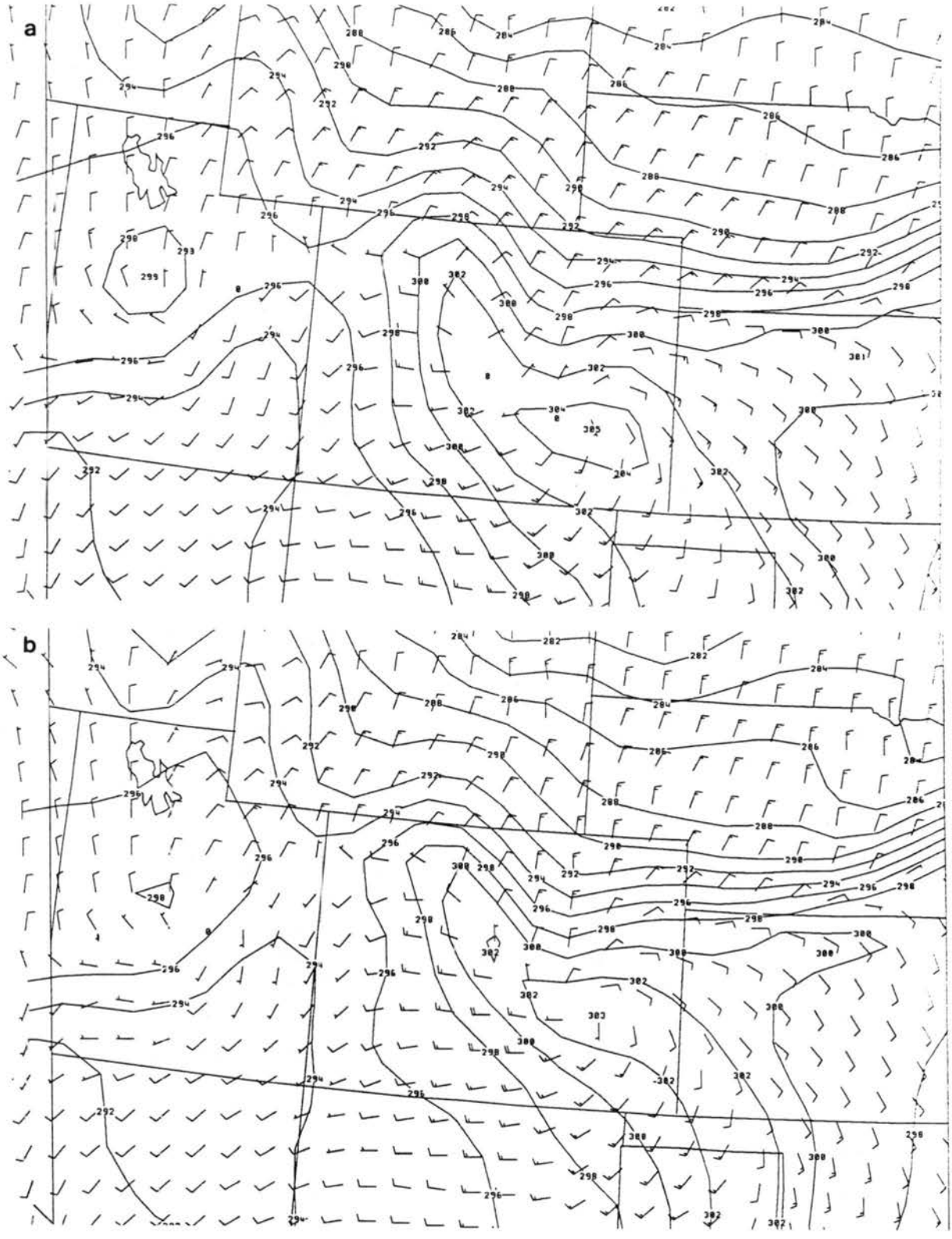

Figure 5.48: MAPS potential temperature (K) and surface wind (knots) predictions from (a) the 3 h forecast valid at 0000 UTC and (b) the 6 h forecast valid at 0300 UTC 9 March 1992.

potential temperature gradient agrees approximately with the observations. However, mesoscale details such as the trapping of cold air east of the mountain barrier are not apparent probably due to smoother topographic representation and the coarser 60 km grid increment. Similar to RAMS, MAPS was unable to predict the flow reversal ahead of the surface front and the forecast center of the cyclonic circulation was too far south. Stronger winds of 8 m s^{-1} (15 knots) are predicted behind the front but these are significantly weaker than the 15 to 20 m s^{-1} winds observed by the FSL mesonet.

The NGM forecast valid at 0000 UTC is a 12 h prediction since the NGM is run only twice a day. The ability to initialize RAMS with LAPS at any hour is an inherent advantage over the current NMC operational models. The NGM 12 h forecast of mean sea level pressure, 1000-500 mb thickness, and low-level winds (Fig. 5.49a) positions the baroclinic zone through northern Wyoming and South Dakota, well north of the observed location. Although the forecast position of the cyclonic circulation is closer to the observed location than either the MAPS or RAMS predicted locations, there is no hint of a cold front or the development of upslope flow in northeast Colorado. The under-forecast of the frontal strength and ensuing snow by the NGM is a typical model error (Junker et al. 1989) that often leads to erroneous public forecasts.

The MAPS 6 h forecast (valid at 0300 UTC) of surface temperature and winds (Fig. 5.48b) indicates a stronger potential temperature gradient across northeast Colorado suggesting strengthening of the arctic front. The position of the front over the Plains agrees well with observations, but the surge of cold air south along the Front Range into Colorado Springs is not indicated. The surface cyclone remains south of the observed position and stronger post-frontal winds are under-forecast when compared to observations. NGM forecast products are only available at 6 h increments to the operational community, hence the user must subjectively interpolate between the 12 and 18 h NGM products to obtain a forecast valid at 0300 UTC. The NGM 18 h forecast of mean sea level pressure, 1000-500 mb thickness, and low-level winds (Fig. 5.49b) suggests that the cold air and upslope flow remain north of Colorado in Wyoming and northern Nebraska. The NGM thickness forecast indicates that warmer air wrapping around the cyclone has

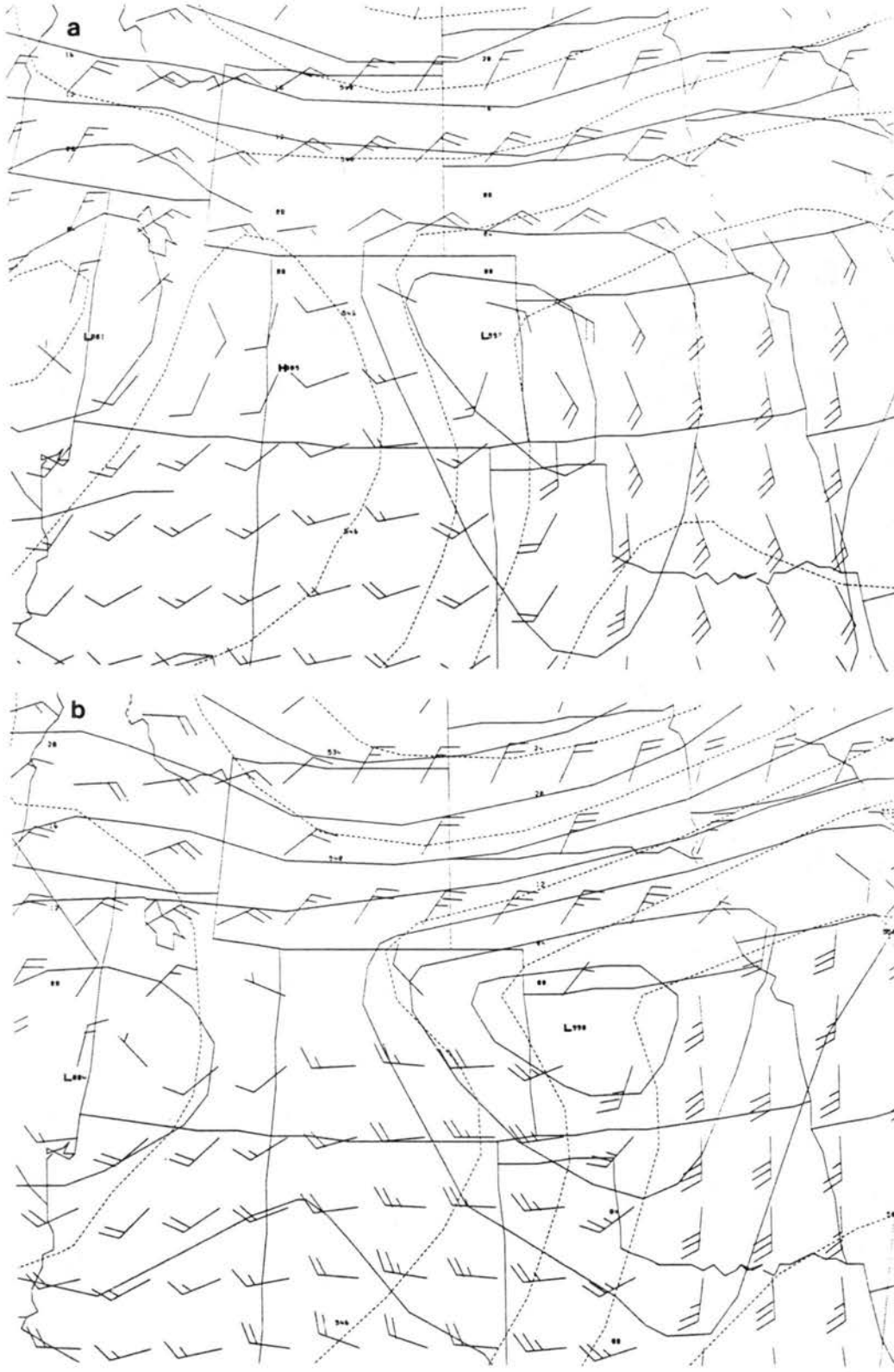

Figure 5.49: NGM mean sea-level pressure (mb), 1000-500 mb thickness (m), and surface wind (knots) predictions from (a) the 12 h forecast valid at 0000 UTC and (b) the 18 h forecast valid at 0600 UTC 9 March 1992.

entered northeast Colorado, a significantly different scenario than observed. The RAMS frontal evolution forecast is clearly superior than the NGM prediction. The MAPS and RAMS forecasts contained similar errors in cyclone position and flow ahead of the front, but RAMS appears to have a better forecast in the strength of the post-frontal winds and the position and strength of the front near the mountains. These improvements are likely due to the better topography representation in RAMS.

The NGM 12 h forecast (valid at 0000 UTC) of precipitation (Fig. 5.50) indicates an area of greater than 0.6 cm (0.25 inches) of melted precipitation over northeast Colorado. Although northeast Colorado did receive approximately this amount of precipitation by

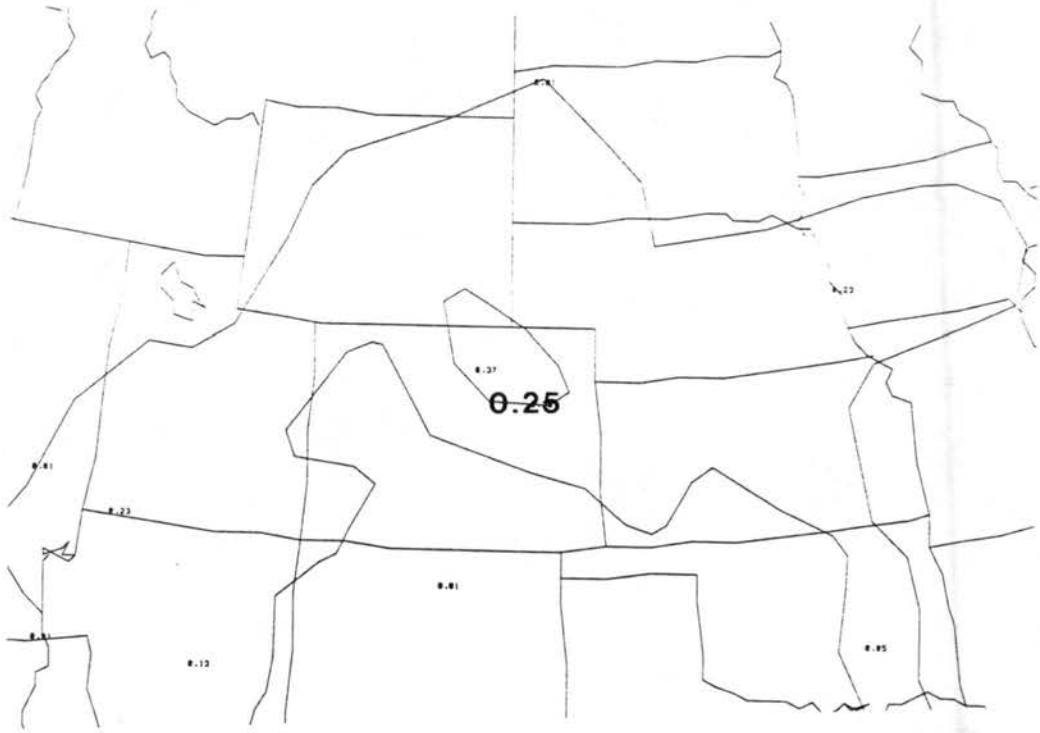

Figure 5.50: NGM 12 h melted precipitation (inches) forecast valid at 0000 UTC 9 March 1992.

0000 UTC, there are indications that the NGM did not properly forecast the whole scenario. The area of precipitation appears to be in an area of forecast warm advection and the band of predicted precipitation that extends from northeast Colorado, across Nebraska, and into Iowa is likely the result of warm front dynamics. However, the NGM completely missed the propagation of the arctic front into Colorado and its ramifications

on the precipitation. With forecast thicknesses between 5520 and 5580 m over northeast Colorado, the model precipitation is likely in the form of rain which was not observed. Unfortunately, the MAPS precipitation forecasts are not available for comparison. Although the RAMS precipitation forecast was adversely affected by excessive latent heat release, there are indications that the RAMS prediction has correctly resolved some of the mesoscale detail of the observed precipitation. This capability combined with the improved prediction of the frontal evolution, especially in the vicinity of the mountains, suggests that the RAMS forecasts are capable of adding significant value to the currently available short-range (0-12 h) operational predictions.

5.5 Discussion

The case study presentation from 8-9 March 1992 adds further evidence that a mesoscale numerical model initialized with high resolution (10 km horizontal grid interval), non-homogeneous data can successfully detect and predict mesoscale features. Observations from 8-9 March indicate several interesting mesoscale features including 1) convective activity that developed over the Colorado Eastern Plains in a pre-frontal unstable air mass, 2) a strong arctic front that progressed through northeast Colorado, and 3) post-frontal heavy snow and high winds that created blizzard conditions. RAMS model predictions initialized with LAPS analyses were able to resolve some of these mesoscale features. The true RAMS forecast (LFCS) indicates the development of an arctic front that progressed across northeast Colorado. High winds are predicted behind the front that agree well with observations. The full microphysics simulation (LMIC) indicates the development of deep upslope flow behind the surface front that aids in the generation of heavy snow. The forecast rain-snow line agrees well with observations.

Although the model predictions suggest convective activity in the unstable pre-frontal air mass, the predictions are unable to correctly resolve the convection when compared to observations. Either the model grid interval must be decreased or a cumulus parameterization scheme designed specifically for mesoscale models (e.g. Weissbluth and Cotton 1993) must be employed. The inability to correctly resolve convection creates regions of excessively high upward vertical motion and latent heating that appear to have adverse effects

on the arctic front evolution and the precipitation amounts. Despite this shortcoming, a qualitative comparison to other operational forecast models and a quantitative statistical model validation indicate that the RAMS predictions are capable of adding local scale, short-range (0-12 h) forecast value to the currently available regional scale model forecasts. These results corroborate the findings of the 7 January case study. Results from the sensitivity simulations suggest that the LAPS variationally adjusted mass and wind initialization (LBAL) may improve the low-level wind forecasts. Similar to the 7 January case study, the majority of the RAMS forecast improvements are due to improved representation of the topography rather than better initialization by LAPS compared to MAPS, except near the surface where additional local data sources add significant mesoscale detail to the LAPS analyses.

An improved scientific understanding of the case study is possible by evaluating the model output in combination with observations and other larger domain model simulations. The observations from 8-9 March suggest that this storm is typical of a Colorado deep cyclonic system interacting with a shallow, arctic anticyclonic system to the north. MAPS analyses indicate that an eastward propagating, upper level Four Corners low redeveloped east of the mountains in the left front quadrant of a jet streak, a scenario similar to 7 January except the redevelopment occurred about 250 km southeast over southeast Colorado. The Platteville profiler and MAPS analyses indicated the development of deep easterly flow over northeast Colorado, north of the upper level low. During the same time, an arctic front, originally north of Colorado, is drawn southward and slid underneath the layer of deep easterlies. Following frontal passage, the appearance of a Longmont anticyclone regime is suggested by the FSL mesonet observations.

Three-dimensional views of the RAMS simulations provide a higher resolution view of the southward propagating arctic front and its interaction with the deep layer of easterlies. As the arctic front impinges on the Colorado Front Range, an area of cold air behind the front becomes trapped east of the mountain barrier. The easterly component flow is strongest at the frontal interface and an upslope condition is forced by the frontal boundary and the topography. The model simulations suggest that several factors combined to

generate the heavy snow that was observed along the Front Range including: 1) a region of ascent that developed in moist, unstable air located within the left front quadrant of a mid-level jet streak and propagated over the arctic air mass, 2) latent heat release in the ascent area that enhances warm advection immediately upstream of this region, 3) strong upslope flow, and 4) a possible seeder-feeder effect.

Both case studies have demonstrated the strong influence of the Colorado topography on the resultant flow that can have significant repercussions on the weather. The next chapter will investigate several idealized simulations designed to isolate pertinent topographic influences on flow characteristics that relate to these and other case studies and to the general theory of flow around an obstacle.

Chapter 6

IDEALIZED SIMULATIONS

Results from the case study experiments indicate that a significant portion of the model forecast improvement was due to better representation of the topography, suggesting the importance of orography on the resulting flow field. The Longmont anticyclone flow regime, evident in both case studies, contains surface flow characteristics that are similar to some results from low Froude number flow around an isolated obstacle. A series of numerical experiments using RAMS with idealized topography and horizontally homogeneous initial conditions are conducted to investigate low Froude number flow around an obstacle. It is beyond the scope of this dissertation to provide an exhaustive numerical survey of this subject. Instead, the specific objectives are to investigate typical flow characteristics in the lee of barriers representative of Colorado topography and to compare the numerical results with actual observations. The objectives will be addressed by initializing RAMS with a range of constant low Froude number conditions. The idealized model topography is designed to approximately represent two significant orographic features that can affect the weather along the Colorado Front Range: 1) the primary north-south Rocky Mountain barrier and 2) the west-east Cheyenne Ridge located along the Colorado-Wyoming border. Results from the idealized simulations will first be compared to the findings of previous investigations including theoretical, physical model, observational, and numerical experiments. Second, the numerical predictions of wind, especially in the lee of the barriers, will be compared to the observations and numerical predictions along the Front Range from the two case studies. The results will enhance the scientific understanding of these and related case studies.

6.1 Model Design

The idealized simulations are designed to facilitate an equitable comparison with the non-homogeneous initialized numerical experiments already presented. Table 6.1 summarizes the model options of the idealized simulations.

The model grid resolution is the same as that used for the case study numerical experiments (i.e. 10 km horizontal grid interval). To reduce the lateral boundary effects in the vicinity of the topographic barrier, the idealized model domain is increased to cover an 800 x 800 km area. The vertical grid remains the same with 25 levels in a stretched sigma-z coordinate. The vertical stretch factor is 1.1 with spacing nearest the ground set to 300 m and a maximum vertical spacing of 750 m.

The model simulations are divided into two categories based on model topography. The first category uses a north-south ellipsoid shaped mountain barrier located in the center of the model domain (Fig. 6.1). Maximum barrier height is 4000 m and the surrounding terrain is level at 2000 m. Barrier height is determined by:

$$dist = 9(x_c - x)^2 + (y_c - y)^2$$

if $(dist \leq 625)$ then

$$z = cos\left(\frac{dist}{625} \times \pi\right) \times 1000 + 3000$$

else

$$z = 2000\,,$$

where x and y represent the x- and y-coordinate, subscript c indicates the model domain center coordinate, and *dist* is the relative distance from the domain center. Hence, the north-south extent is 500 km and the length to width aspect ratio is 3:1 ($\beta = \frac{L_y}{L_x} = 3$). The "cigar" shaped barrier is roughly representative of the main north-south Rocky Mountain barrier in Colorado. The second category of simulations uses an west-east half-ellipsoid shaped barrier positioned adjacent to the northeast corner of the main barrier used in the

Table 6.1: Model options for idealized simulations.

Model Category	Option
grid dimensions	81 x 81 x 25
horizontal resolution	10 km
vertical resolution	300 m stretched to 750 m
model top height	15.3 km
idealized topography	1) north-south ellipsoid 2) north-south and east-west ellipsoids
initialization	horizontally homogeneous 1) west wind at 7.07 m s^{-1} 2) northwest wind at 10.0 m s^{-1} constant Froude number (0.3–1.0)
thermodynamics	dry nonhydrostatic
radiation	none
Coriolis	1) no 2) yes
lower boundary condition	free-slip
lateral boundary condition	Klemp-Wilhelmson radiative
top boundary condition	Rigid lid with 5 point Rayleigh friction-absorbing layer
turbulence	deformation K closure
time-step	30 s

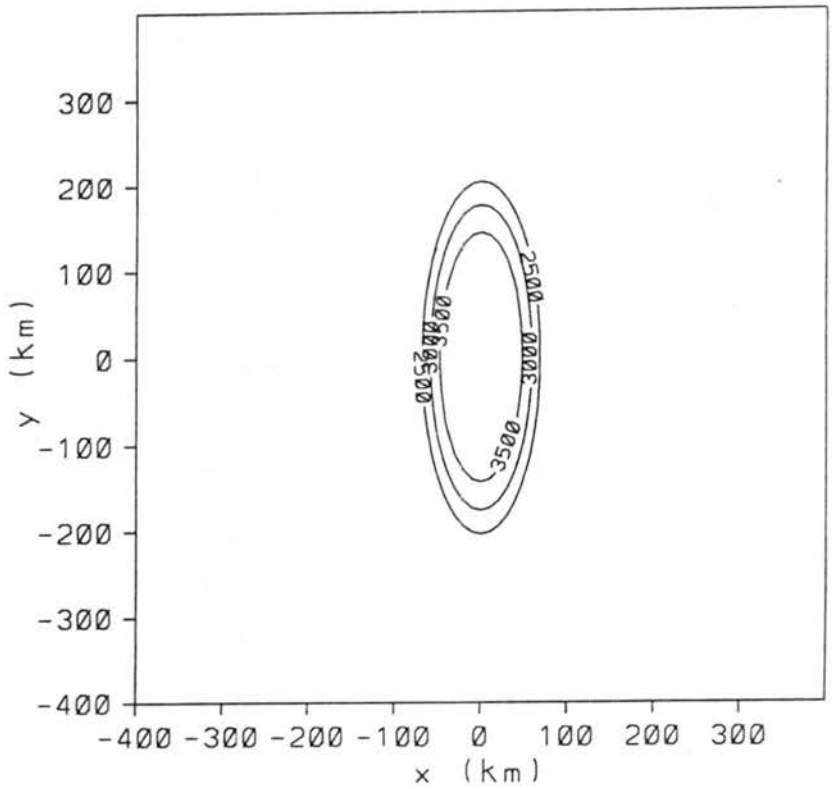

Figure 6.1: Cigar topography (m).

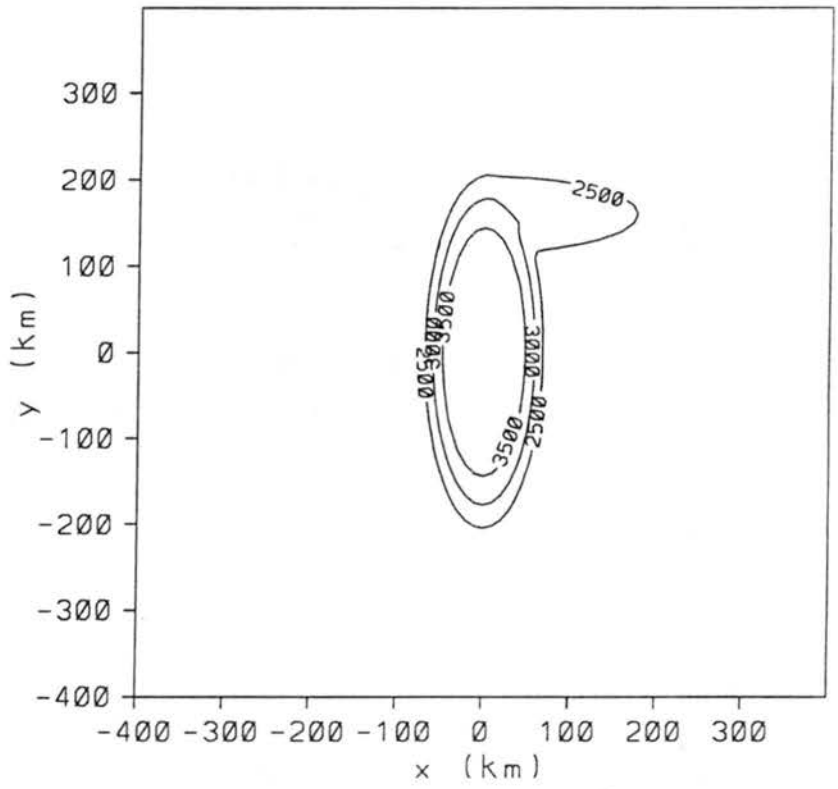

Figure 6.2: Fang topography (m).

first category (Fig. 6.2). Maximum height of the second barrier is 3000 m. Secondary barrier height is determined from:

$$dist = (x_c - x)^2 + 16\,(y_{57} - y)^2$$

$$\text{if } (x \geq 41 \text{ and } dist \leq 625) \text{ then}$$

$$z = cos\left(\frac{dist}{625} \times \pi\right) \times 500 + 2500\,,$$

where y_{57} is the grid line of the major axis. The west-east extent is 250 km and the length to width aspect ratio is 4:1 ($\beta = 4$). The "fang" shaped topography approximates the orography of the north-south Rocky Mountain barrier and the west-east extension of the Cheyenne Ridge.

RAMS model physics are selected to emulate relevant previous investigations and to complement the case study experiments. A completely dry, nonhydrostatic version of RAMS is utilized and radiational effects are not considered. A free-slip lower boundary condition is employed to facilitate comparison to previous investigations (e.g Smolarkiewicz and Rotunno 1989a). The model assumes no temperature gradient between the ground and the lowest atmospheric level. On the lateral boundaries, the Klemp and Wilhelmson (1978) radiative boundary condition is applied with a constant phase speed of 20 m s^{-1}. A rigid lid with a Rayleigh friction-absorbing layer five grid points deep is used for the top boundary condition.

A deformation K turbulence closure scheme is used to parameterize subgrid mixing. The ad hoc procedure (Pielke 1984, p. 328) allows the user to control the amount of diffusion necessary to maintain computational integrity while producing realistic results. The eddy exchange coefficient (K) is controlled by two parameters: 1) a leading coefficient that controls the relative magnitude of K and 2) a minimum K (K_{min}) value for which the computed K can not fall below. Several experiments were conducted with the leading coefficient arbitrarily varied and minimal differences were noted in the forecast of state variables. More significant differences were observed in parallel simulations with K_{min} values ranging from 0.1 to 1.0. The primary difference noted is the eventual occurrence

of breaking lee waves for lower K_{min} values while no wave breaking occurred with higher K_{min} values. However, the development of the lee side surface wind structure prior to wave breaking was consistent in all cases. Although care must be taken when comparing results from before and after wave breaking, the final outcome was similar for all cases. The simulations utilizing the lowest K_{min} value without significant numerical noise are presented in the following sections and references to the higher K_{min} results are noted only when significant differences occur.

The selection of horizontally homogeneous initializations (Table 6.2) is designed to encompass the atmospheric conditions conducive to the development of lee circulations along the Colorado Front Range.

Table 6.2: Model initialization for idealized simulations.

1) Cigar Topography
   a) West wind, no Coriolis force
      Fr = 0.3, 0.5, 0.6, 0.7, 0.8, 0.9, 1.0
   b) West wind, Coriolis force
      Fr = 0.3, 0.5, 0.7, 0.9
   c) Northwest wind, no Coriolis force
      Fr = 0.3, 0.5, 0.7, 0.9
   d) Northwest wind, Coriolis force
      Fr = 0.3, 0.5, 0.7, 0.9

2) Fang Topography
   a) West wind, no Coriolis force
      Fr = 0.3, 0.5, 0.7, 0.9
   b) West wind, Coriolis force
      Fr = 0.3, 0.5, 0.7, 0.9
   c) Northwest wind, no Coriolis force
      Fr = 0.3, 0.5, 0.7, 0.9
   d) Northwest wind, Coriolis force
      Fr = 0.3, 0.5, 0.7, 0.9

Two wind directions are considered, west and northwest. Wind speed is constant with height and is set to 10 m s^{-1} for the northwest simulations and 7.07 m s^{-1} for the west simulations. Hence, for the same thermodynamic profile, the Froude number will be

equivalent for the two wind directions. The thermodynamic profile is defined such that the Froude number is constant for the entire model depth. Simulations are conducted for constant Froude numbers varying between 0.3 and 1.0. To investigate the effects of the earth's rotation, simulations are conducted with and without the Coriolis force. All simulations are conducted using the two categories of idealized topography, "Cigar" and "Fang."

6.2 Model Simulations

6.2.1 Cigar topography

6.2.1.1 West wind, no Coriolis force

Parallel simulations were conducted using the cigar ($\beta = 3$) topography with no Coriolis force and uniform westerly flow at 7.07 m s^{-1} for Froude numbers of 0.3, 0.5, 0.6, 0.7, 0.8, 0.9, and 1.0. The value of K_{min} is 0.1. Figure 6.3 illustrates low-level streamlines at 6 h for Fr = 0.3, 0.5, 0.6, 0.7, and 0.9. Two distinct lee vortices are apparent for Fr $\leq$ 0.6. The appearance of the lee vortices is consistent with the results of previous investigations using a circular barrier (Hunt and Snyder 1980, Smolarkiewicz and Rotunno 1989a) with one significant difference. For the circular barrier, the vortices appeared for Fr $\leq \sim$0.5, somewhat less than the threshold for the $\beta = 3$ topography. This result is consistent with the analytically derived diagram (Smith 1989b) indicating that as β increases, the threshold Froude number also increases to obtain a lower boundary upwind stagnation point, possibly associated with the lee vortices. The $\beta = 3$ results also indicate that the lee vortices form closer to the lateral boundaries of the barrier for lower Froude number, but the terrain height over which they form is about constant.

Previous investigations have studied the possible correlation between the lee vortices with wave breaking and an upwind flow reversal region. Smith (1989c) and Crook et al. (1990) suggested a correspondence between the dissipative effects of breaking lee waves and the formation of the lee vortices, while Rotunno and Smolarkiewicz (1991) indicated that they were separate physical mechanisms. The $\beta = 3$ results also indicate no correlation between the two mechanisms. In the $K_{min} = 1.0$ simulations, cross sections of potential

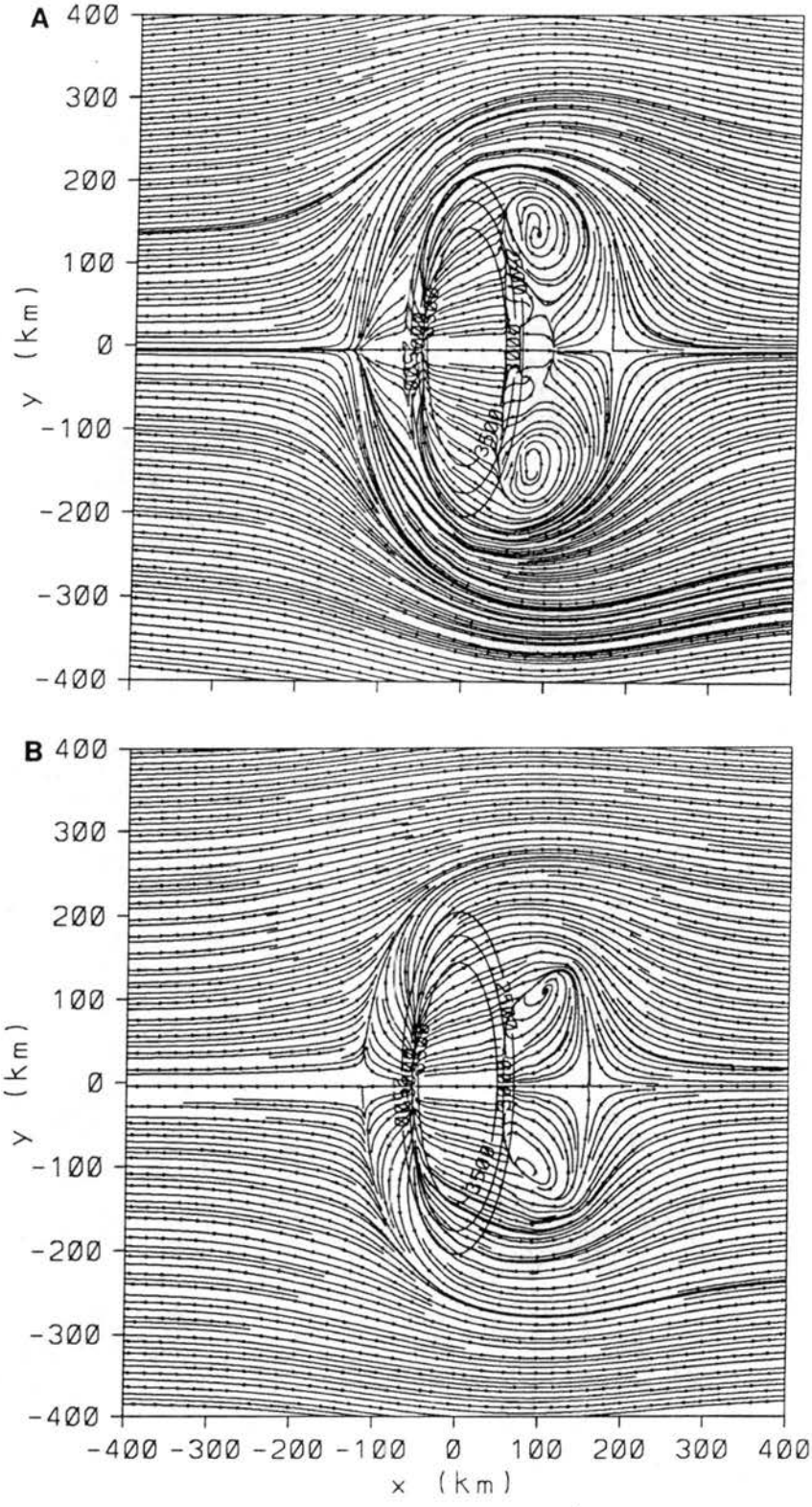

Figure 6.3: Low-level (146 AGL) streamlines at 6 h using cigar topography initialized with west wind and no Coriolis force for (a) Fr = 0.3 and (b) Fr = 0.5.

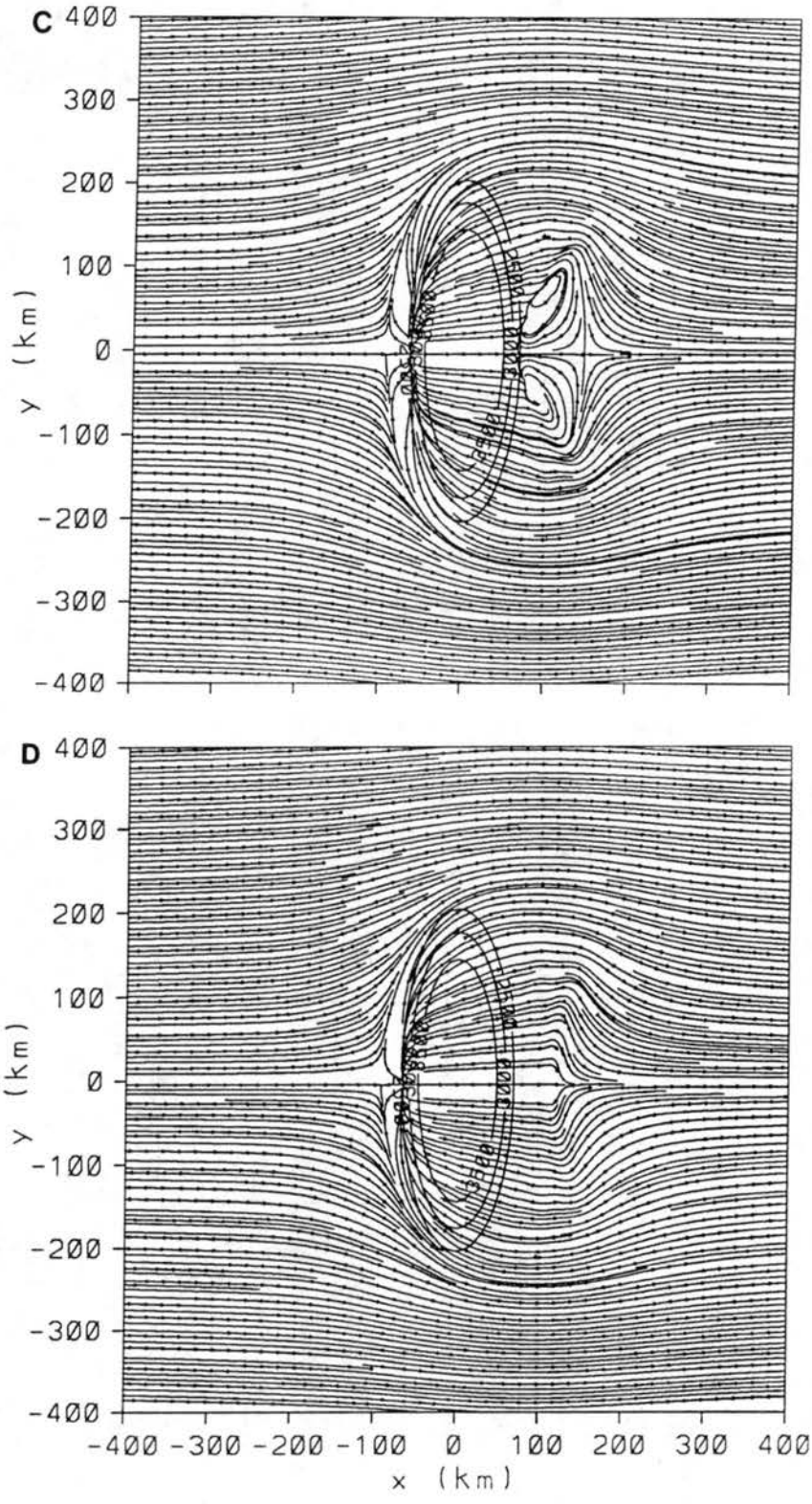

Figure 6.3: Continued: (c) Fr = 0.6 and (d) Fr = 0.7.

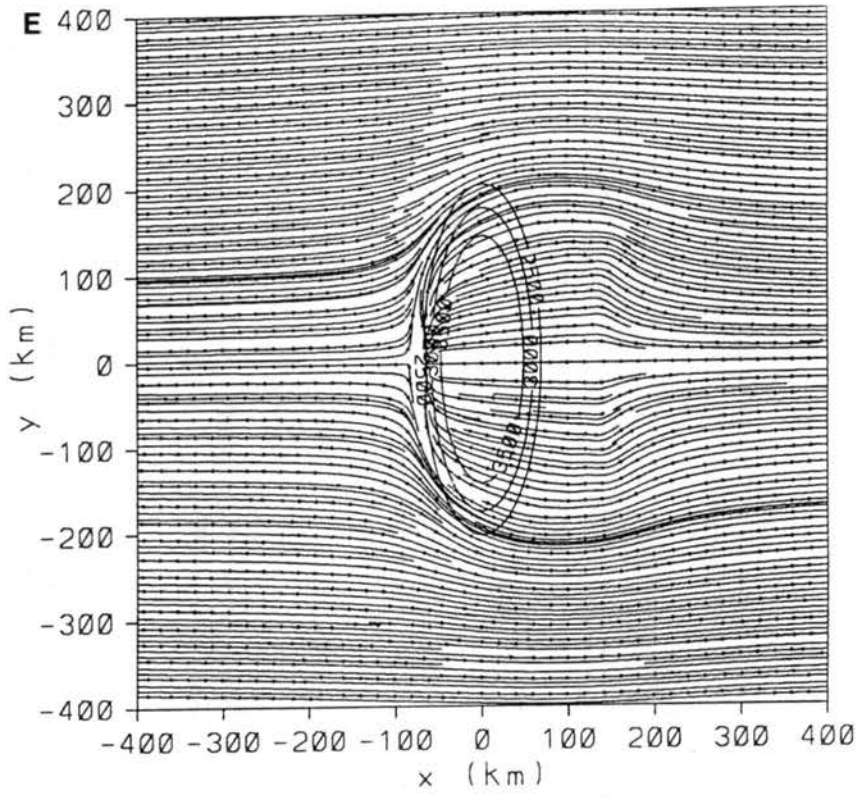

Figure 6.3: Continued: (e) Fr = 0.9.

temperature do not show any evidence of wave breaking yet the vortices still develop for Fr $\leq$ 0.7. Furthermore, no stagnation point aloft is observed, a necessary condition for wave breaking according to the linear theory (Smith 1989b). The regime diagram (Smith 1989b) for $\beta = 3$ also seems to indicate the possibility of wave breaking and flow splitting as two separate phenomena.

The linear theory predicts that the presence of an upwind flow reversal and associated lower boundary stagnation point are required for flow splitting. Flow splitting and lee vortex generation have occurred simultaneously in several experiments (Smolarkiewicz and Rotunno 1989a). However, for $\beta = 0.5$, Smolarkiewicz and Rotunno (1990) found the generation of lee vortices without upwind flow reversal indicating an independence between the two phenomena. Although, the $\beta = 3$ experiments show a close correspondence between upwind flow reversal and lee vortex development, the Fr = 0.7 simulation shows upwind flow reversal without lee vortex generation.

The $\beta = 3$ topography simulations indicate several important results. First, neither lee wave breaking nor upwind flow reversal are necessary for the generation of lee vortices.

However, both upstream blocking and lee wave development are important processes to the phenomena. Second, the development of lee vortices is *not* a bifurcation in the mountain airflow problem, as suggested by Smith (1989c), but rather a smooth transition as the Froude number decreases. Finally, the generation of vertical vorticity by the tilting of horizontal vorticity (Rotunno and Smolarkiewicz 1991) appears to be correct, however several more processes are important to complete the scenario. A comparison of results between the Fr = 0.3 and 0.9 simulations will demonstrate these conclusions.

Low-level streamlines at 1 h (Fig. 6.4) for Fr = 0.3 show that a stagnation point has already developed west of the barrier and flow splitting around the mountain is evident. For the less stable Fr = 0.9 case, all the flow is traveling over the top of the barrier and only a very minimal amount of flow splitting is suggested. The 1 h perturbation Exner function (π^*), which is proportional to perturbation pressure, analysis for Fr = 0.3 and Fr = 0.9 (Fig. 6.4) indicates the strength of the blocking generated by the flow against the barrier. As expected, π^* is greater for Fr = 0.3. The result is the generation of a *mesoscale* pressure gradient (Mayr 1993) that forces the flow splitting for Fr = 0.3. The presence of the cross-barrier pressure gradient creates increased flow over the mountain which is greater for Fr = 0.3 (Figs. 6.5a and 6.6a). Maximum wind speed on the downwind side of the barrier for Fr = 0.3 suggests that lee wave dynamics are also enhancing the cross-barrier flow.

Vertical motion analyses (Figs. 6.5b and 6.6b) indicate stronger ascent on the west side of the mountain for Fr = 0.9 which is consistent with the less stable environment. In the lee, about equal downward vertical velocity is illustrated for both cases and the areal coverage is closely correlated to the barrier shape. The low-level generation of vertical vorticity (ζ) by tilting ($\frac{\partial u}{\partial z}\frac{\partial w}{\partial y} - \frac{\partial v}{\partial z}\frac{\partial w}{\partial x}$, Figs. 6.5c and 6.6c) shows similar shape for both cases with a horseshoe region of cyclonic vorticity generation surrounding the southern portion of the barrier and a similar area of anticyclonic vorticity generation surrounding the northern portion of the barrier. The Fr = 0.3 vertical vorticity generation by tilting is a full order of magnitude larger than the generation term for Fr = 0.9. Maximum low-level vertical vorticity (Figs. 6.5d and 6.6d) is closely correlated to the regions of greatest

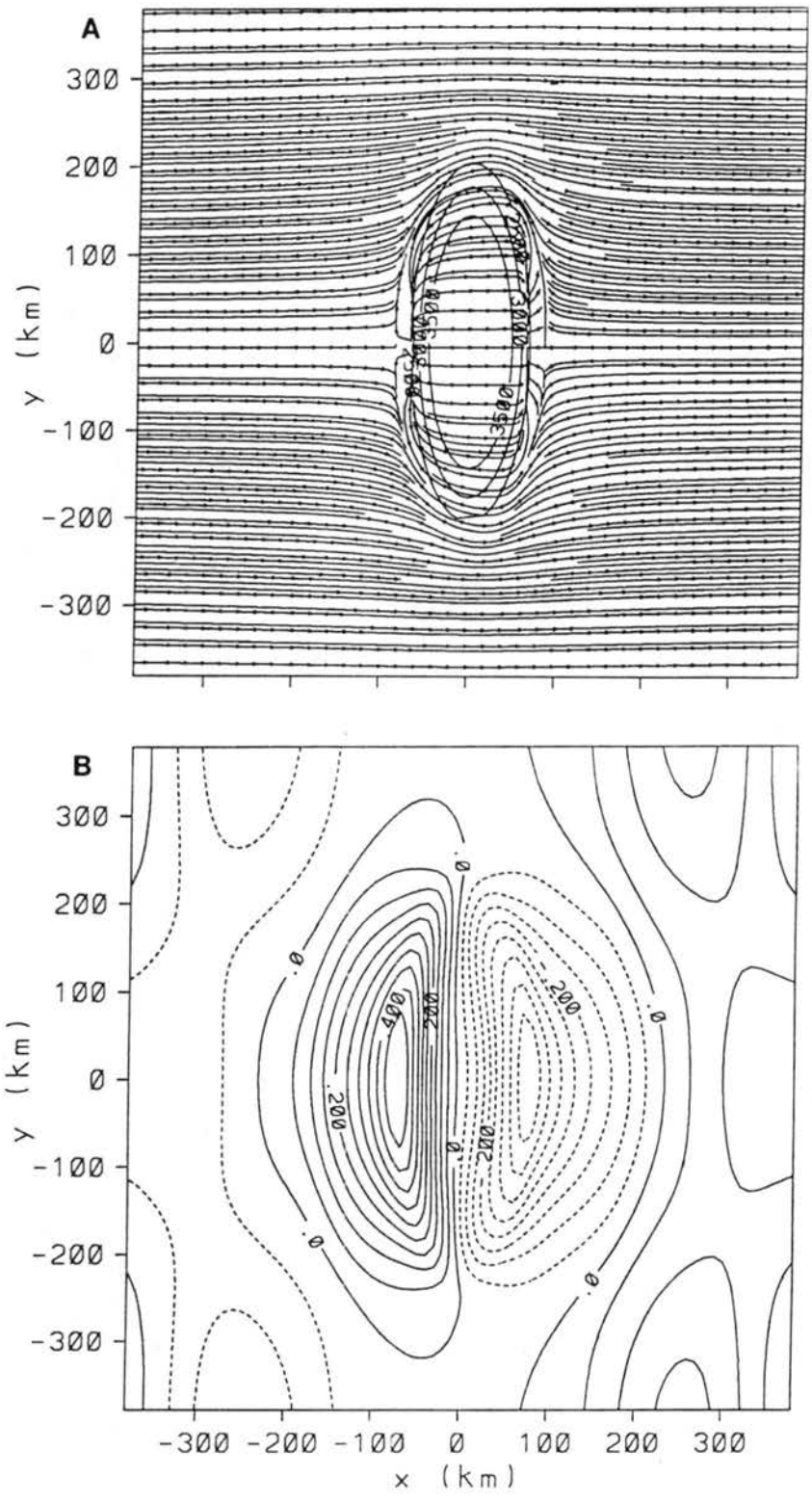

Figure 6.4: Low-level (146 AGL) 1 h forecasts of (a) streamlines and (b) perturbation Exner function (J deg^{-1} kg $^{-1}$, contour interval = 0.05 J deg^{-1} kg $^{-1}$) using cigar topography initialized with west wind and no Coriolis force for Fr = 0.3.

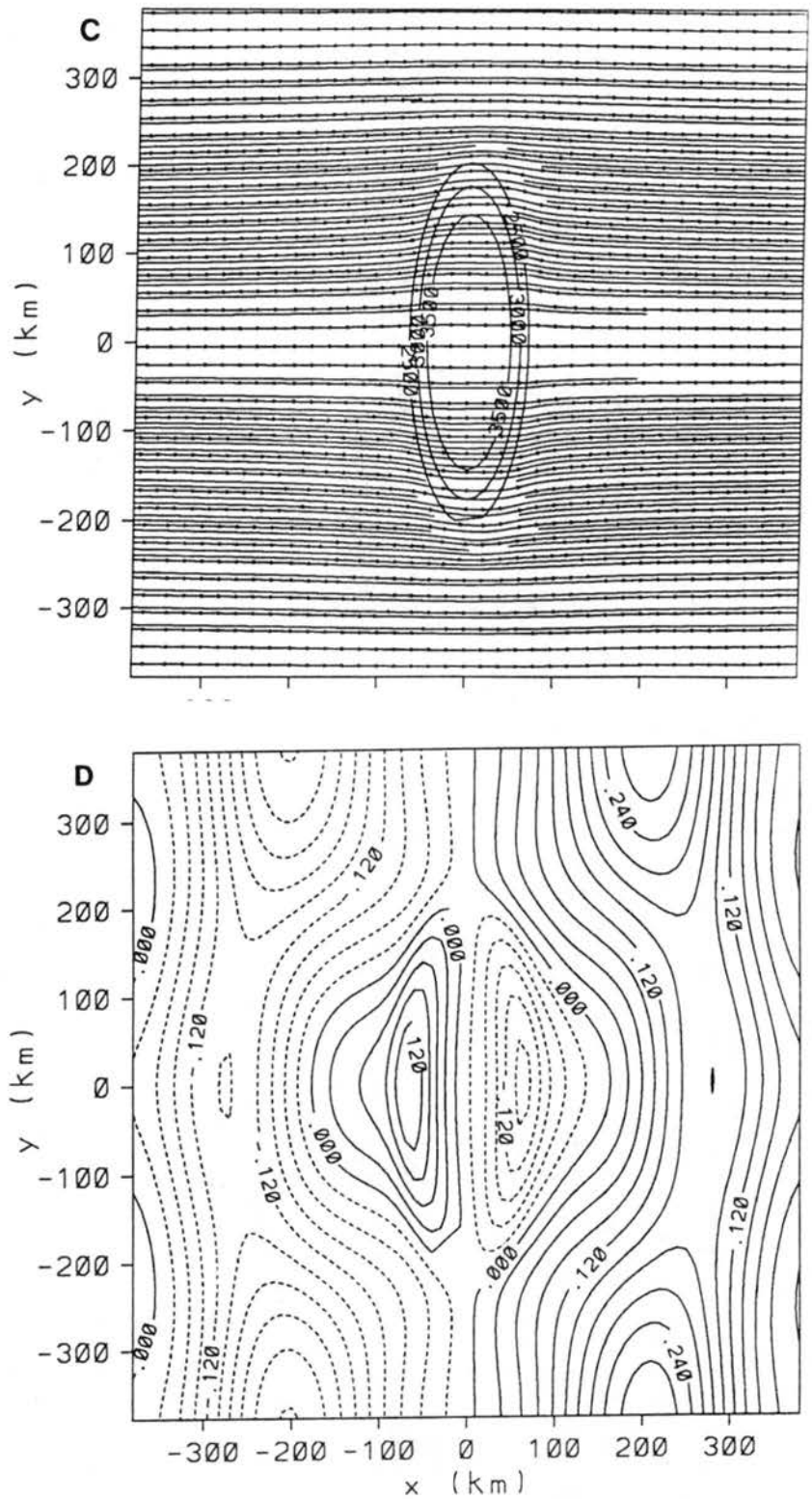

Figure 6.4: Continued: (c) streamlines and (d) perturbation Exner function (J deg^{-1} kg $^{-1}$, contour interval = 0.03 J deg^{-1} kg $^{-1}$) for Fr = 0.9.

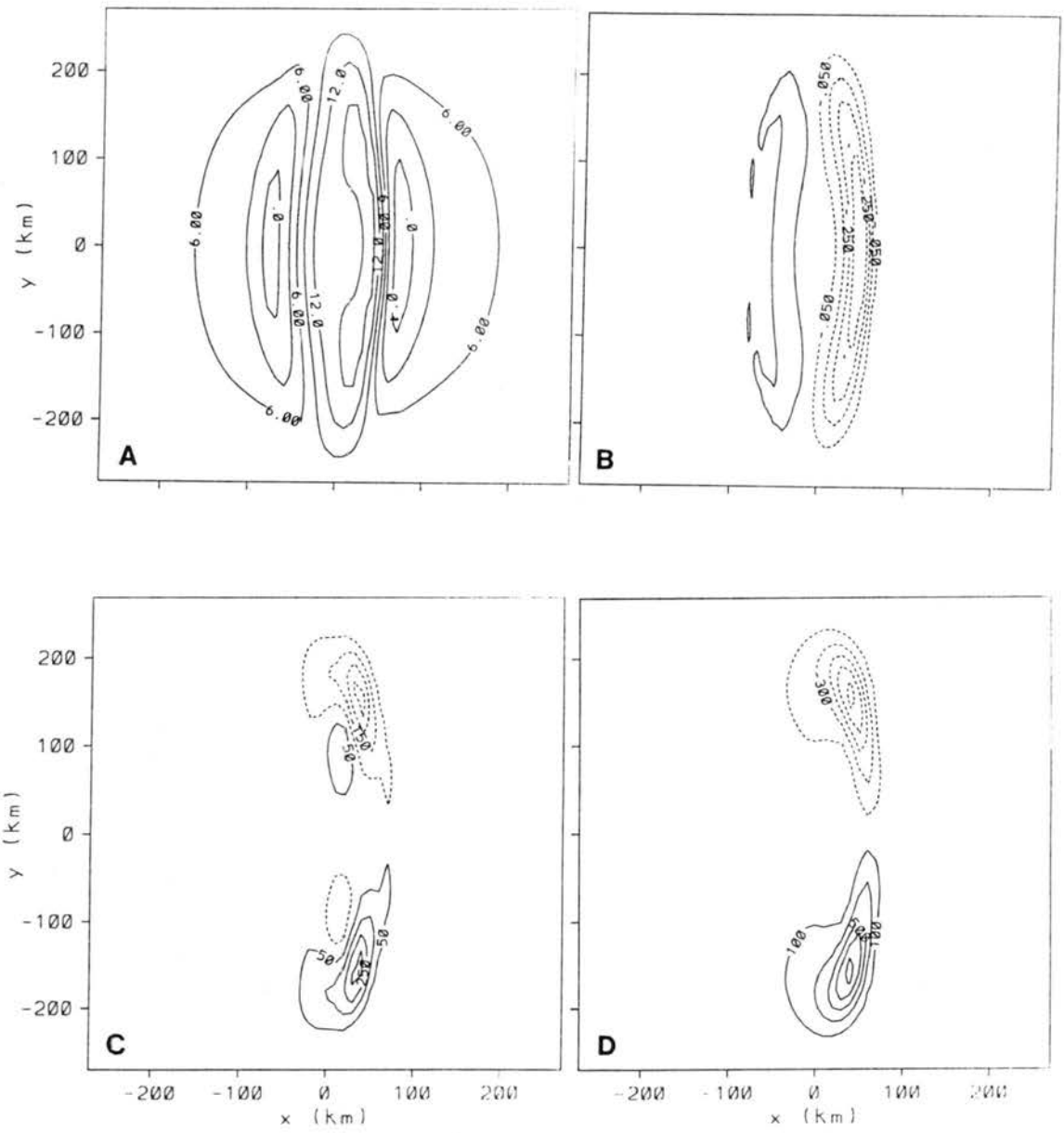

Figure 6.5: Low-level (146 AGL) 1 h forecasts of (a) u-component wind (m s^{-1}), (b) vertical motion (m s^{-1}), (c) tilting into vertical vorticity (s^{-2}, contour interval = 1.0×10^{-8} s^{-2}), and (d) vertical vorticity (s^{-1}, contour interval = 2.0×10^{-5} s^{-1}). Simulations initialized with cigar topography, west wind, no Coriolis force, and Fr = 0.3.

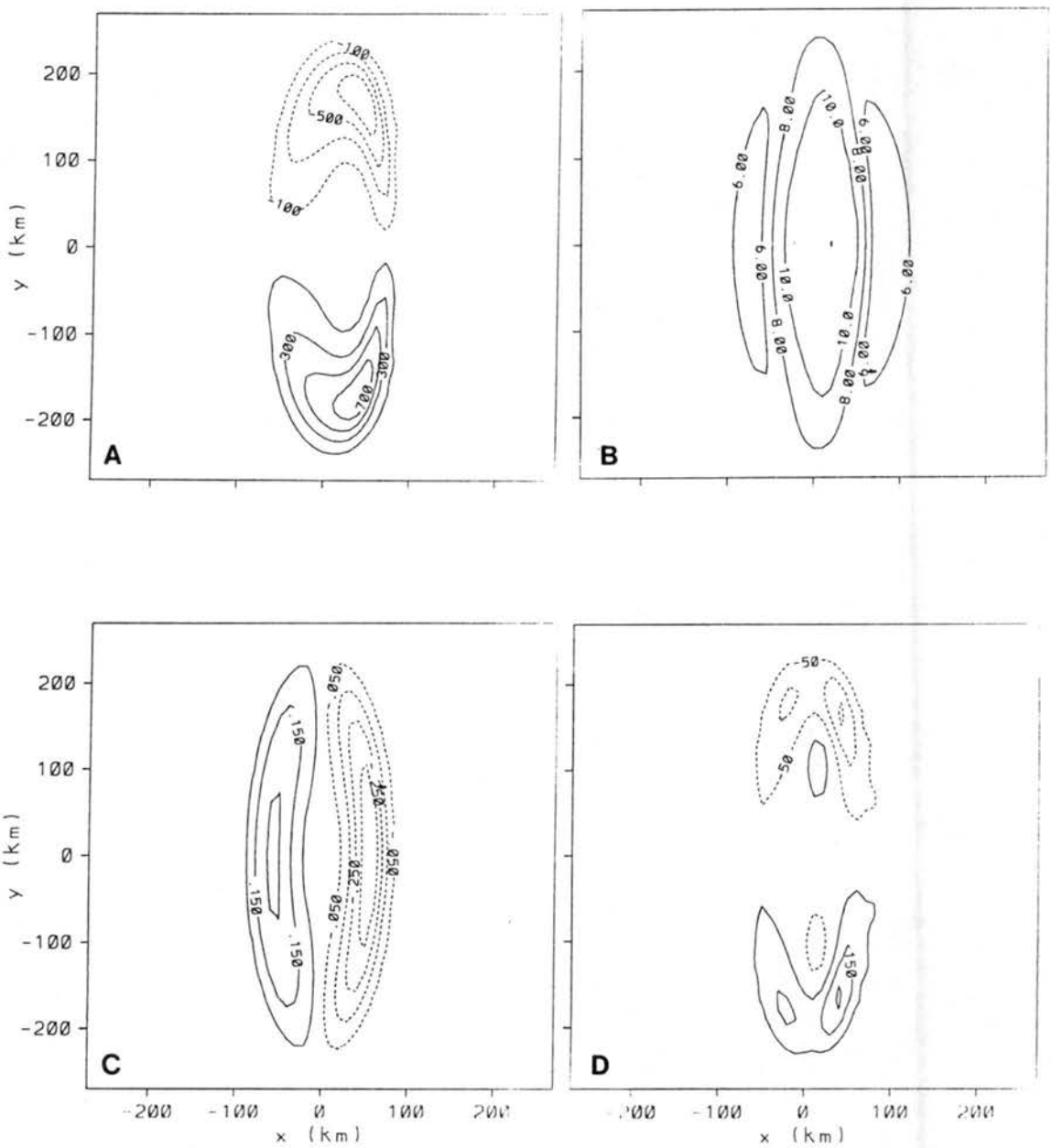

Figure 6.6: As in Fig. 6.5 except for Fr = 0.9. (Tilting term contour interval is 1.0×10^{-9} s^{-2} and vertical vorticity contour interval is = 2.0×10^{-6} s^{-1}).

tilting and the Fr = 0.3 vertical vorticity is also a full order of magnitude greater than the Fr = 0.9 vertical vorticity.

Representative vertical cross sections provide an improved understanding towards the creation of the vorticity tilting. Figures 6.7 and 6.8 depict north-south vertical cross sections for the 1 h forecast of u, w, and generation of vertical vorticity by tilting located 20 km east of the barrier crest. The u-component wind is greatest at the surface for all cases. A pair of u wind maxima are located about 120 km north and south of the domain center. The maximum magnitude increases with decreasing Froude apparently in response to a greater pressure gradient in the vertical due to the developing upstream blocking. A couplet of maximum downward vertical velocity is observed in approximately the same location for all cases. As suggested previously, the couplet location is initially correlated to the slope of the hill irregardless of the Froude number. The model predictions indicate the development of horizontal vorticity in both the $\hat{i}\,(\frac{\partial w}{\partial y} - \frac{\partial v}{\partial z})$ and $\hat{j}\,(\frac{\partial u}{\partial z} - \frac{\partial w}{\partial x})$ components. The $\hat{i}$ component of horizontal vorticity results from vertical shear in v and is greater for lower Froude number. The $\hat{j}$ component of horizontal vorticity results from the vertical distribution of westerlies and is correlated to the amount of upstream blocking. The barrier shape creates horizontal variations in w; however, in both cases, the horizontal gradient of w is small compared to the vertical gradients of u and v.

This configuration provides a positive generation of vertical vorticity by tilting located south of the southern downward vertical velocity maximum due to westerly flow decreasing with height ($\frac{\partial u}{\partial z} < 0$) and the vertical velocity increasing southward ($\frac{\partial w}{\partial y} < 0$). The second half of the tilting term ($\frac{\partial v}{\partial z}\frac{\partial w}{\partial x}$) is considerably smaller 20 km east of the barrier due to very little vertical gradient in v. However, it is more significant further east where the vertical gradient of v is greater and an eastward extension of maximum tilting is observed (Figs. 6.9 and 6.10). Similarly, negative generation of vertical vorticity by tilting is observed north and east of the northern downward vertical velocity maximum. Although, the location of maximum tilting is about the same for all Fr $\leq$ 1, the magnitude is greater for lower Froude number due to the larger vertical gradients of u and v and greater horizontal gradients of w. Hence, the strength of the tilting is controlled by the strength

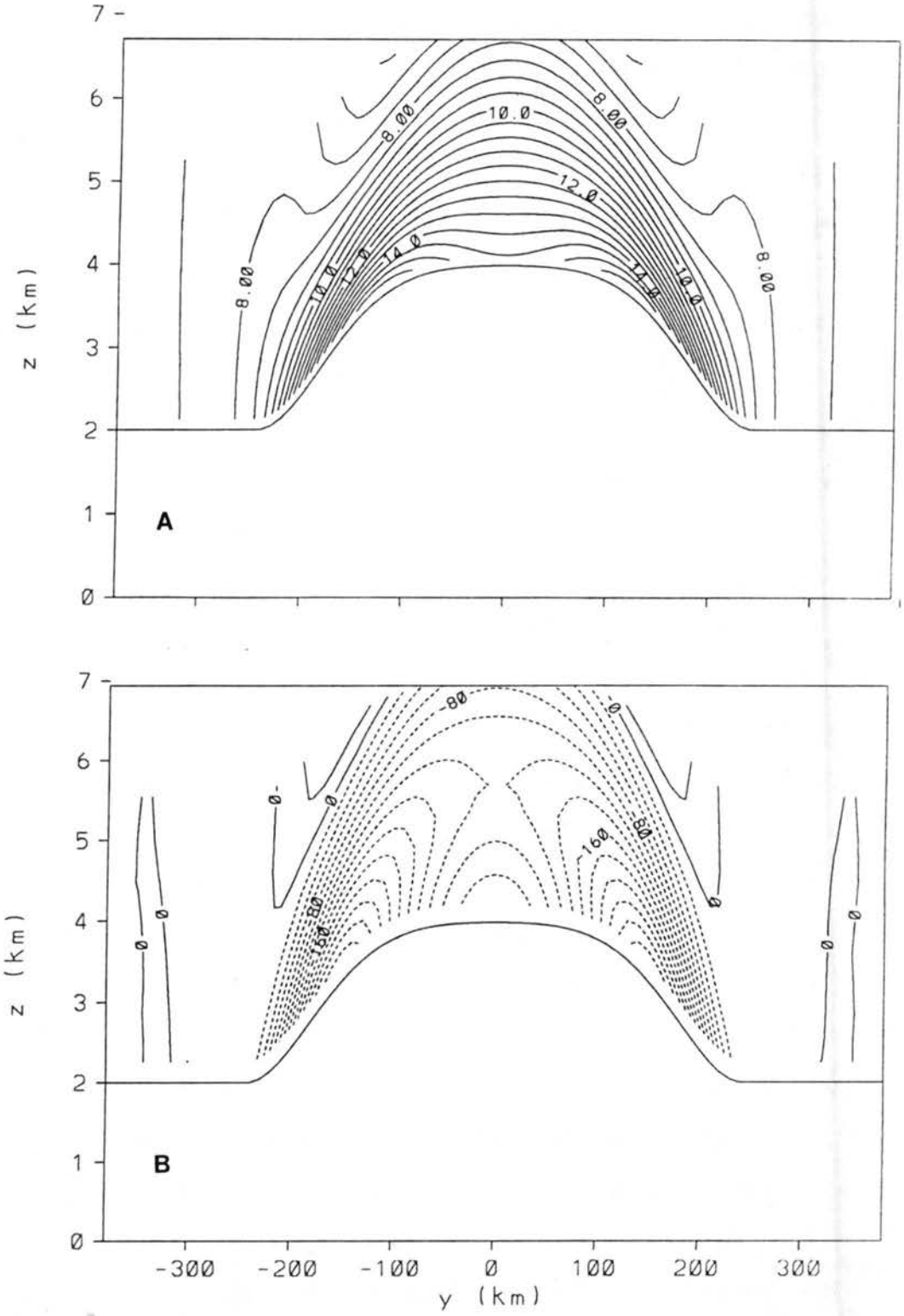

Figure 6.7: North-south vertical cross sections located 20 km east of the barrier crest for Fr = 0.3 initialized with cigar topography, west wind, and no Coriolis force. 1 h forecasts of (a) u-component wind (m s^{-1}) and (b) vertical motion (m s^{-1}), contour interval = 0.02 m s^{-1}).

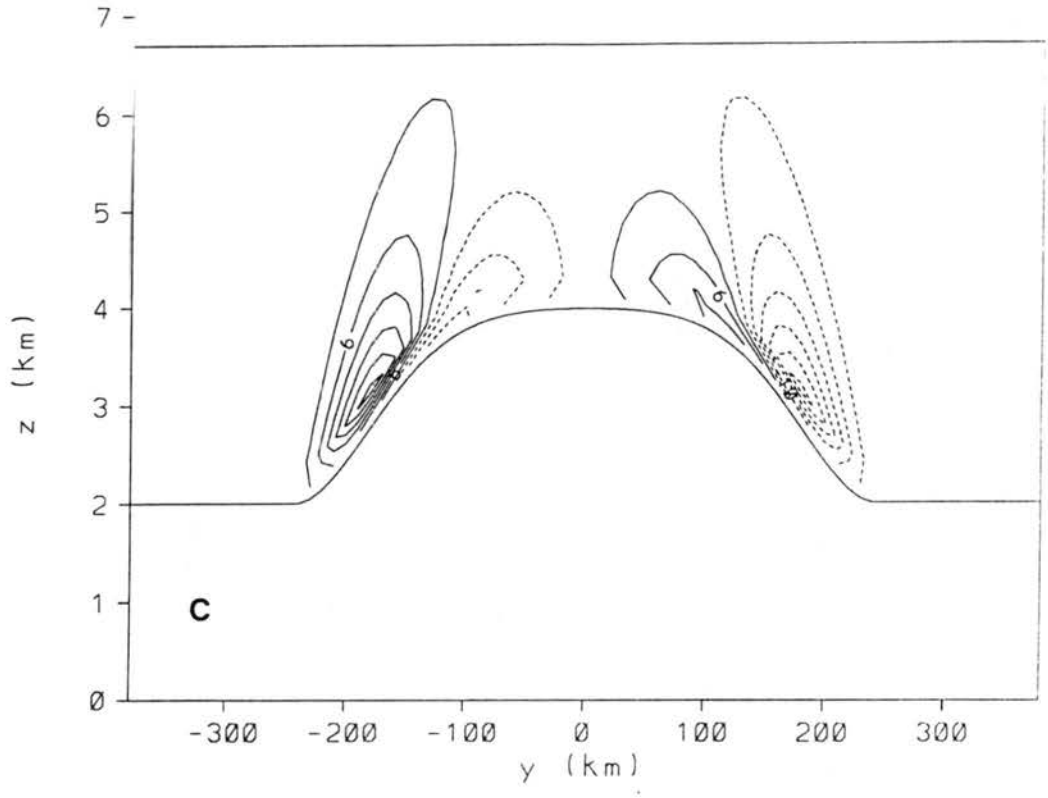

Figure 6.7: Continued: (c) tilting into vertical vorticity (s^{-2}, contour interval = 4.0×10^{-9} s^{-2}).

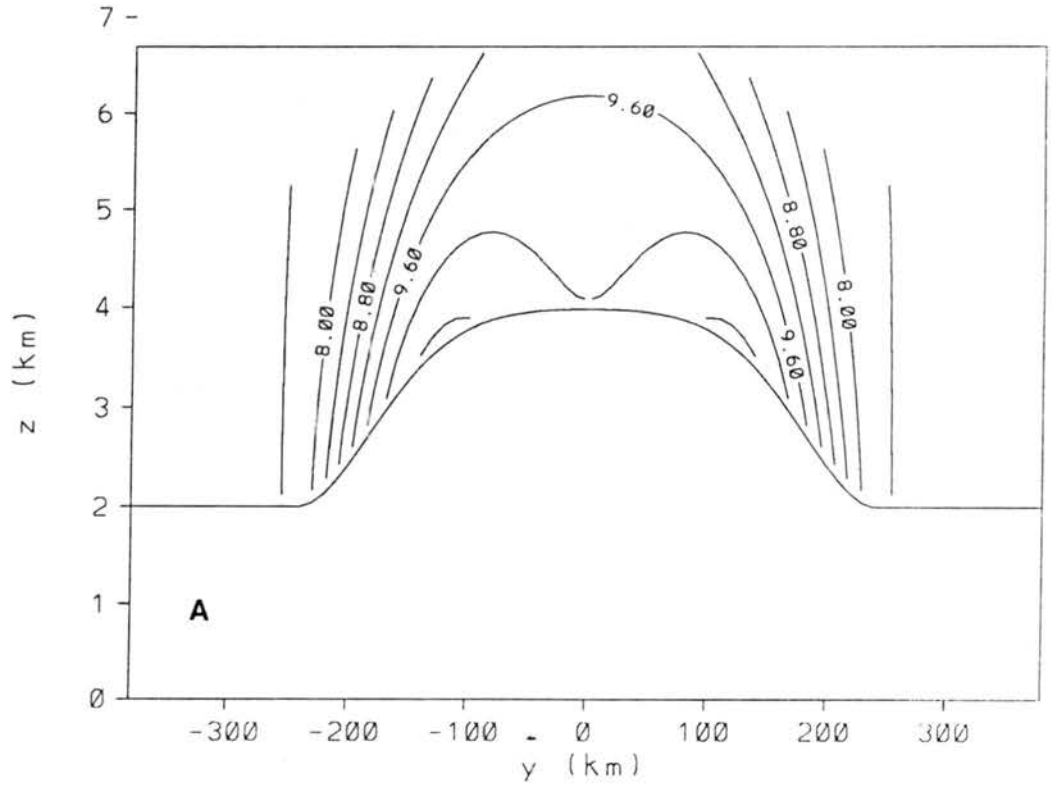

Figure 6.8: As in Fig. 6.7 except for Fr = 0.9.

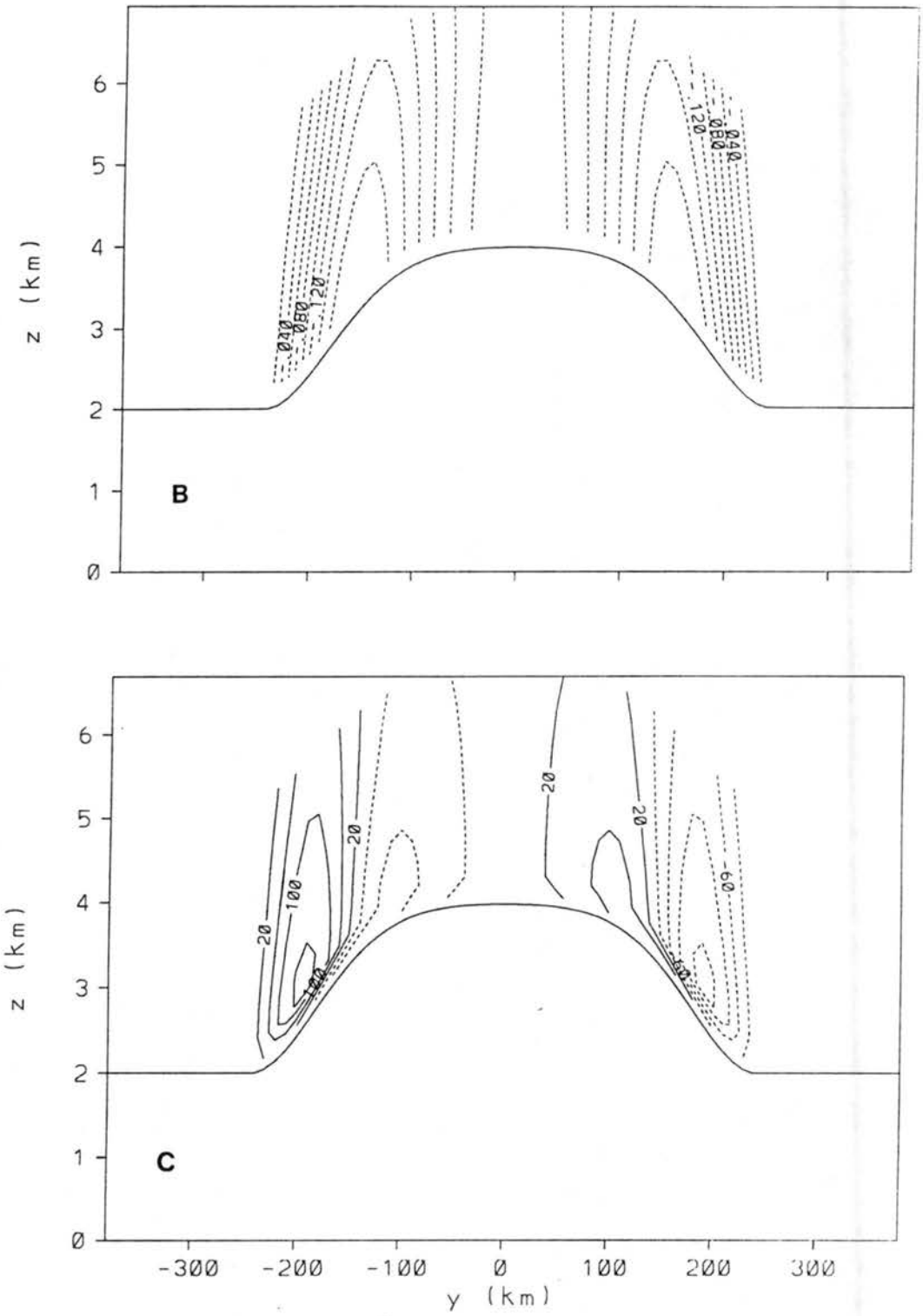

Figure 6.8: Continued: (Vertical vorticity contour interval = 4.0×10^{-10} s^{-2}).

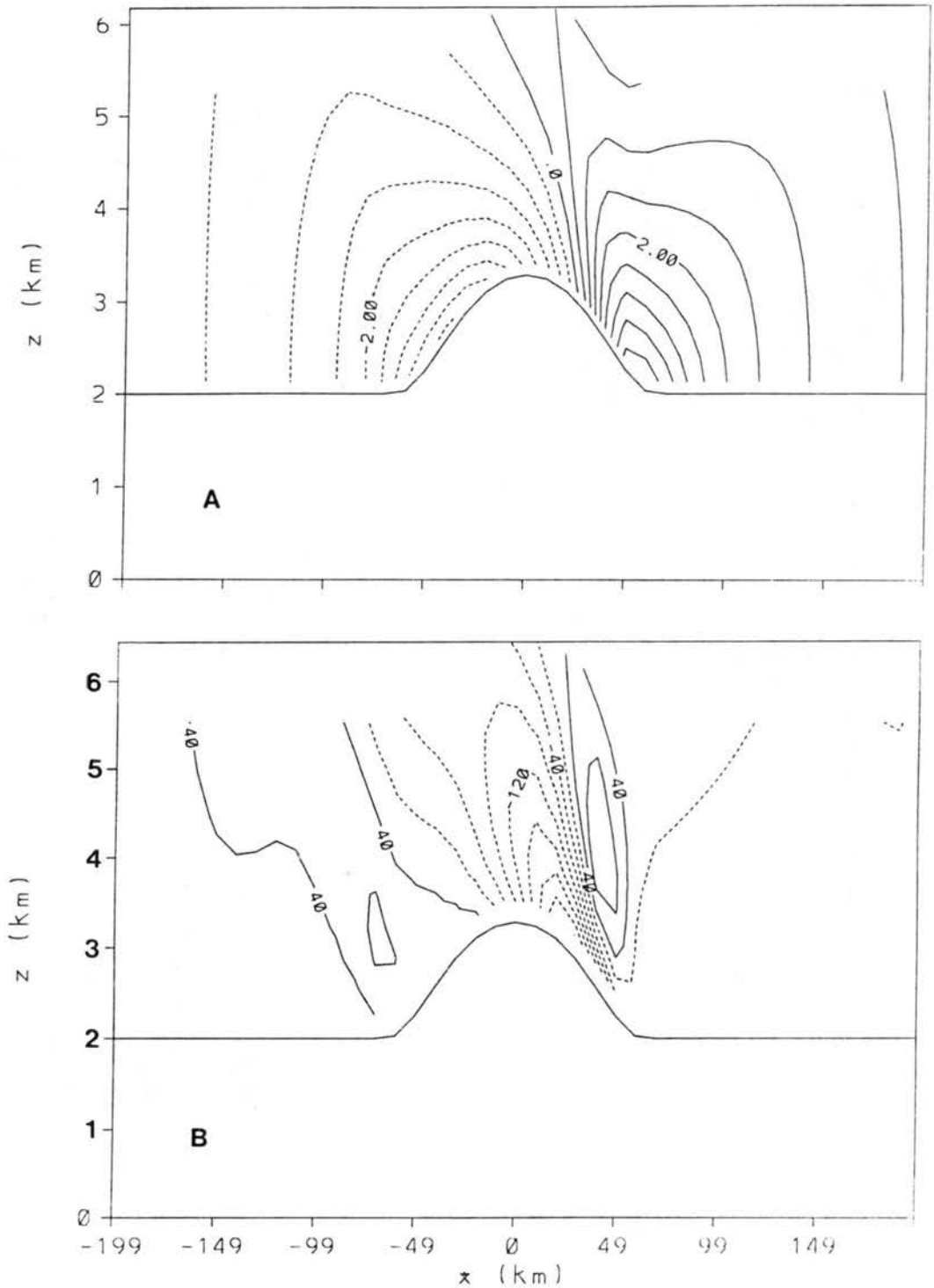

Figure 6.9: West-east vertical cross sections located 160 km south of the domain center for Fr = 0.3 initialized with cigar topography, west wind, and no Coriolis force. 1 h forecasts of (a) v-component wind (m s^{-1}) and (b) vertical motion (m s^{-1}, contour interval = 0.04 m s^{-1}).

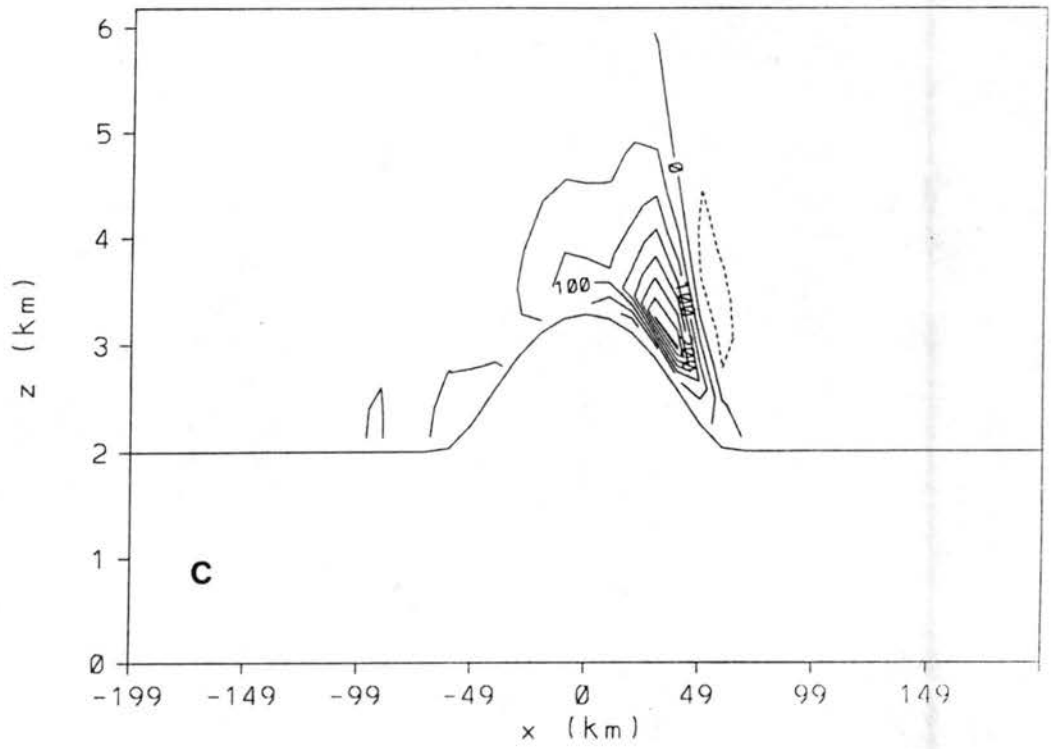

Figure 6.9: Continued: (c) vertical vorticity tilting term (s^{-2}, contour interval = 5.0×10^{-9} s^{-2}).

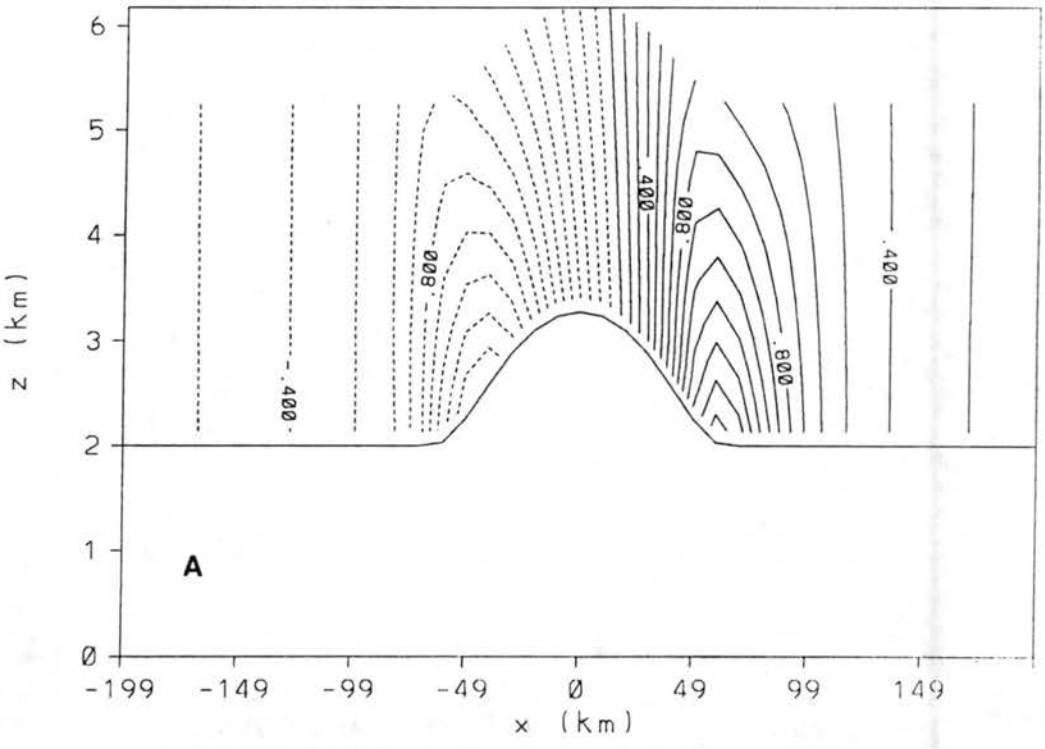

Figure 6.10: As in Fig. 6.9 except for Fr = 0.9.

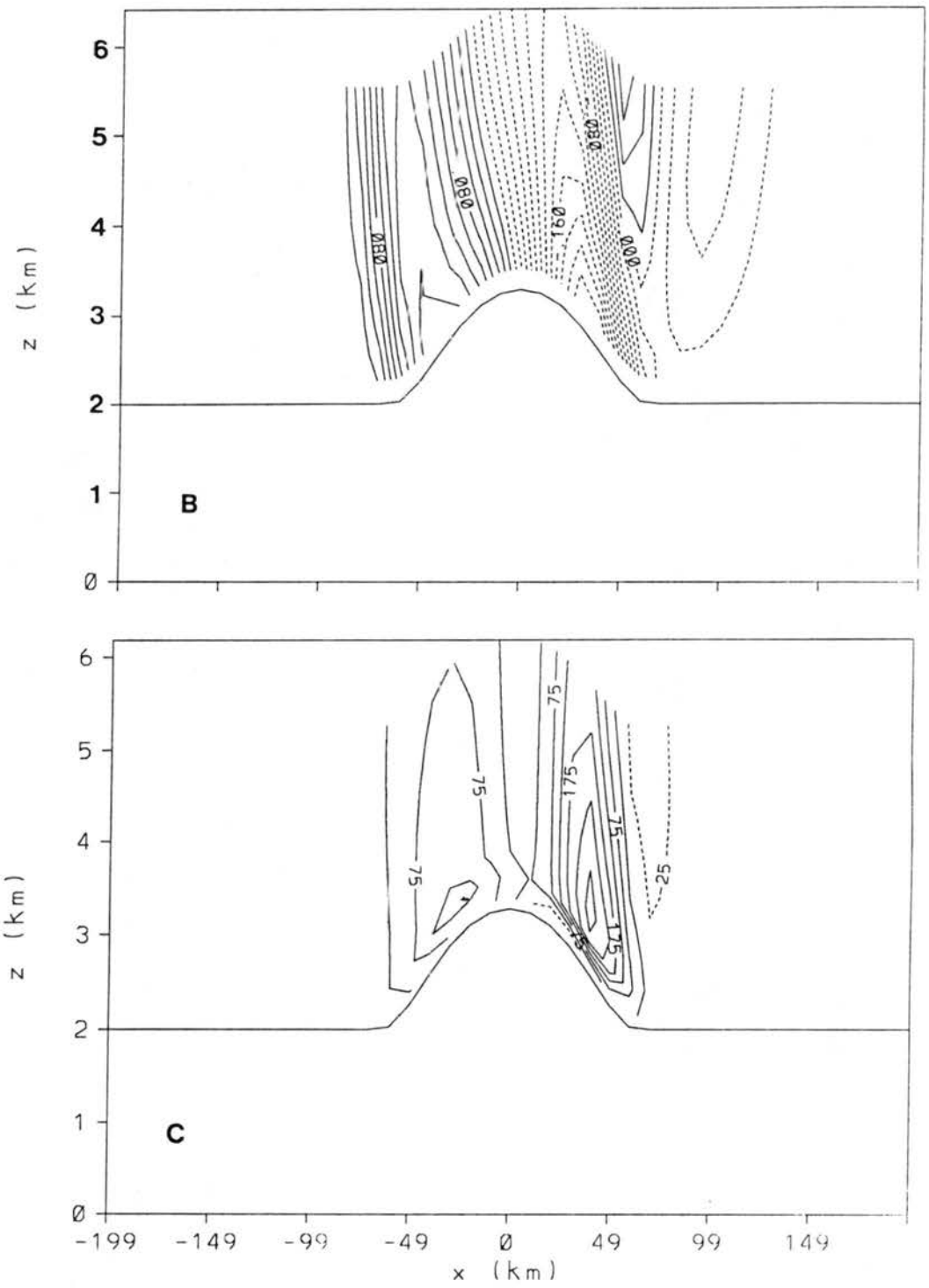

Figure 6.10: Continued: (Vertical vorticity contour interval = 5.0×10^{-10} s^{-2}).

of the blocking, while the location of greatest tilting is determined by the horizontal gradients of w which are initially controlled by the barrier shape. The two regions of maximum tilting are located about 150 to 160 km from the center east-west axis and are positioned immediately upstream from the points of maximum observed surface vertical vorticity (Figs. 6.5d and 6.6d).

West-east vertical cross sections for the 1 h forecast of vertical vorticity divergence ($-\zeta\nabla_H \cdot \vec{V}$), vertical vorticity advection ($-\vec{V} \cdot \nabla_H\zeta$), and vertical vorticity (ζ) located through the maximum tilting (160 km south of the domain center) are depicted in Figs. 6.11 and 6.12. Regions of maximum vertical vorticity convergence and positive vertical vorticity advection are colocated with the area of greatest vertical vorticity located at the surface about 40 km east of the domain center. As with the tilting, the magnitudes of all the terms increase as Froude number decreases. The relative strengths of vorticity convergence and advection are nearly equal for the Fr = 0.3 case, while vorticity advection is significantly larger than convergence for the Fr = 0.9 simulation. Apparently, as the Froude number decreases, the stronger horizontal gradients in the surface wind components associated with the development of the lee vortex creates a more significant contribution by the convergence term.

The development of the lee vortices can be summarized as follows. Horizontal vorticity results from 1) blocking which creates a vertical gradient in the westerly flow and 2) the north-south variation in the lee wave structure resulting from the barrier shape which creates a horizontal gradient in the vertical motion. Vertical vorticity is generated by tilting of the horizontal vorticity. The strength of the upstream blocking controls the strength of the vertical gradient in u and hence the amount of tilting. Thus, the tilting contribution increases as Froude number decreases due to more significant blocking. The vertical motion gradient contributes less to the tilting strength but controls the sign of the tilting. Hence, the barrier shape controls the initial location of greatest tilting implying that the initial tilting location is not correlated to Froude number.

The evolution of maximum vertical vorticity is controlled by the convergence and advection of vertical vorticity in addition to the tilting. Streamlines and π^* at 3 h (Fig. 6.13)

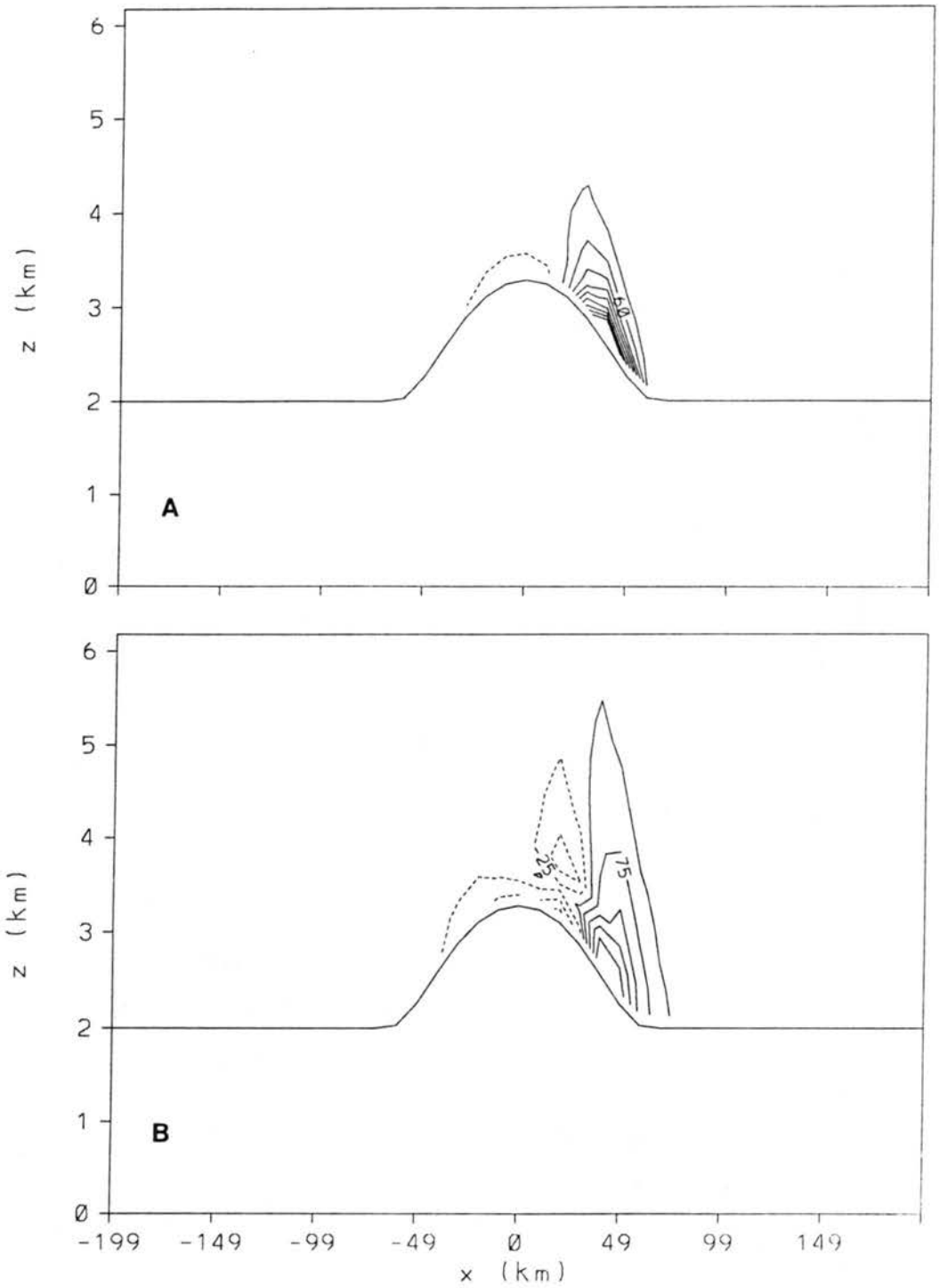

Figure 6.11: As in Fig. 6.9 except for (a) vertical vorticity divergence (s^{-2}, contour interval = 4.0×10^{-9} s^{-2}) and (b) vertical vorticity advection (s^{-2}, contour interval = 5.0×10^{-9} s^{-2}).

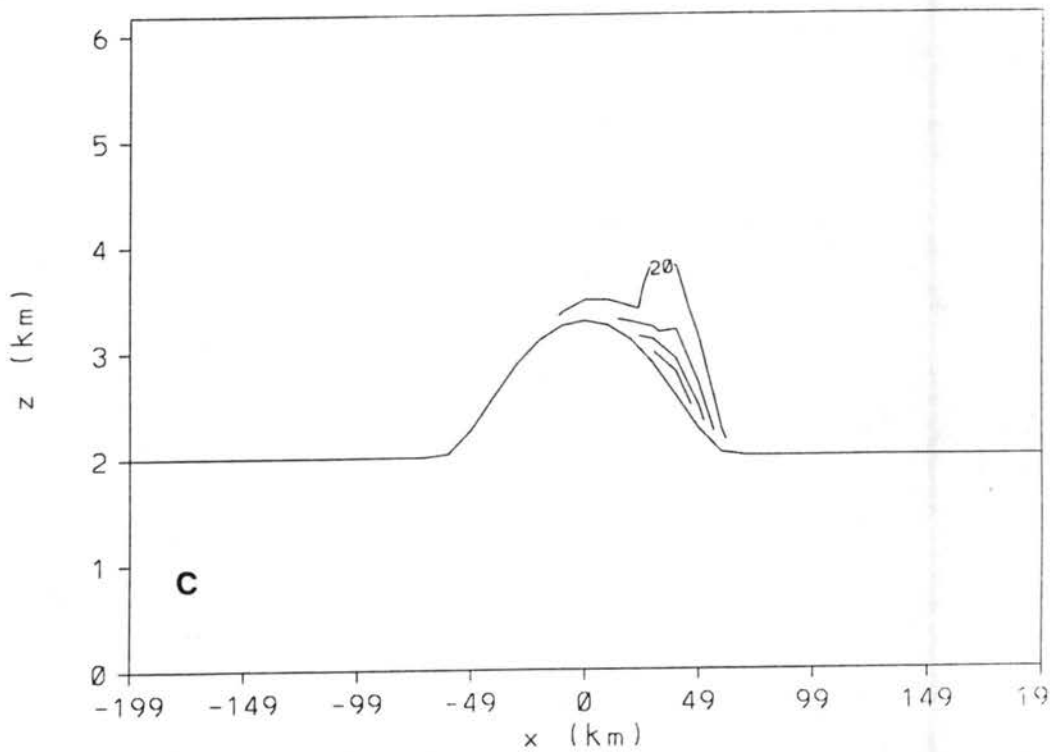

Figure 6.11: Continued: (c) vertical vorticity (s^{-1}, contour interval = 2.0×10^{-5} s^{-1}).

for Fr = 0.3 indicate a positive pressure perturbation on the windward side of the mountain suggesting continued blocking. In the lee, a couplet of negative perturbations are colocated with the lee vortices. The result is a mesoscale pressure gradient that forces cross-barrier flow towards the vortices. For Fr = 0.9, the magnitude of π^* is about one-third of the Fr = 0.3 π^* magnitude suggesting less blocking. In the lee, the negative pressure perturbation is symmetric about the east-west center axis, hence the cross-barrier flow is primarily from west to east. Figure 6.14 depicts north-south vertical cross sections of u for Fr = 0.3 and 0.9 at 3 and 5 h located 20 km east of the barrier crest. The upstream blocking and mesoscale pressure gradient determines the region of maximum u which in turn controls the region of maximum downward vertical velocity. Hence, maximum downward vertical velocity for Fr = 0.3 evolves into a nearly stationary couplet positioned about 180 km north and south of the domain center resulting in the maintenance of the north-south gradient of w with time. For Fr = 0.9, maximum downward vertical velocity evolves into a single north-south elongated region symmetric about the east-west center

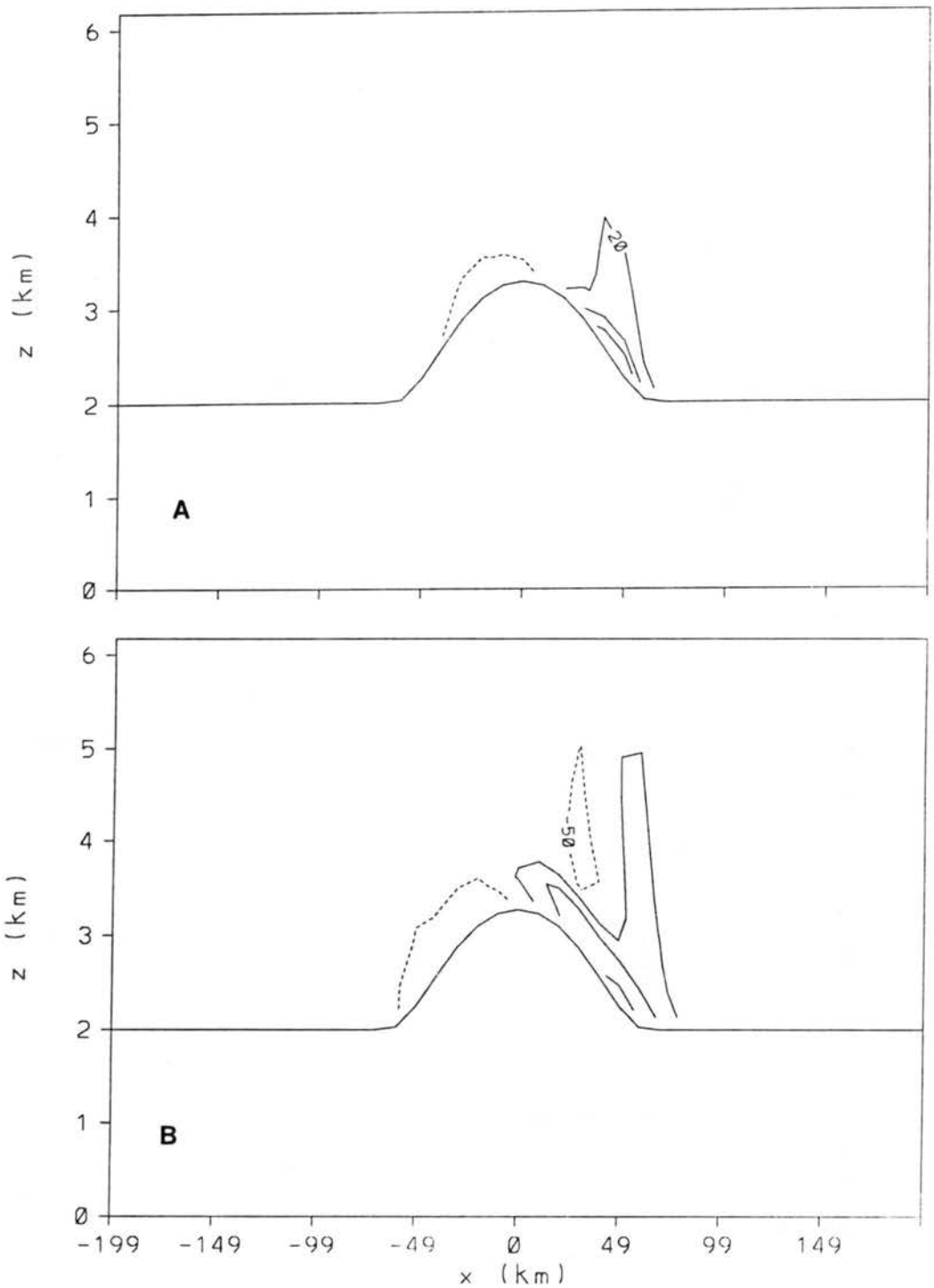

Figure 6.12: As in Fig. 6.10 except for (a) vertical vorticity divergence (s^{-2}, contour interval = 4.0×10^{-10} s^{-2}) and (b) vertical vorticity advection (s^{-2}, contour interval = 1.0×10^{-9} s^{-2}).

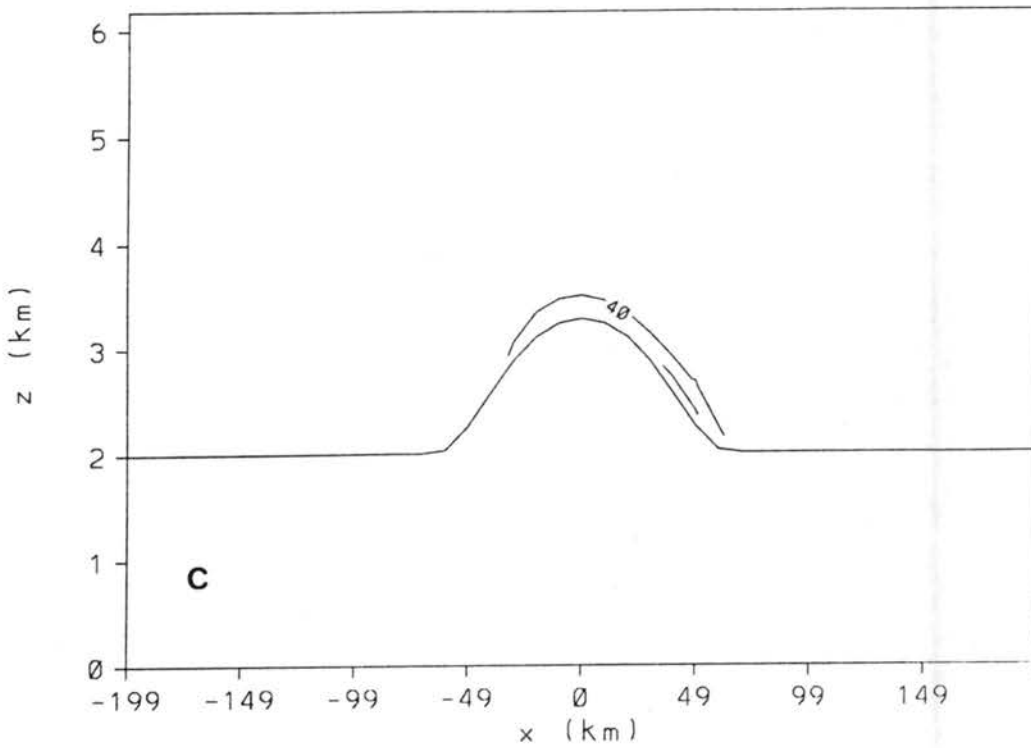

Figure 6.12: Continued: (c) vertical vorticity (s^{-1}, contour interval = 4.0×10^{-6} s^{-1}).

line. The result is a nearly constant north-south gradient of w that extends inward towards the east-west center line. Hence, for the low Froude number cases, significant tilting combined with convergence and advection create the vortices positioned due east of the maximum u. As the Froude number approaches one, the tilting becomes less significant and is not sufficient to generate a closed circulation, but a maximum of vertical vorticity is observed east of maximum u. Convergence of vorticity is not significant, but tilting and vorticity advection affect the location of the observed maximum vertical vorticity. Since the maximum wind speed moves to the center of the barrier, the two centers of maximum vorticity tend to pinch towards the east-west center line. The evolution of the vorticity centers is slower for the larger Froude number cases and their final positions are closer to the east-west center line.

Figure 6.15 also depicts the smooth increase in vertical vorticity as Froude number decreases indicating the generation of lee vortices to be a smooth transition and not a bifurcation with decreasing Froude number. Finally, Fig. 6.16 illustrates an east-west

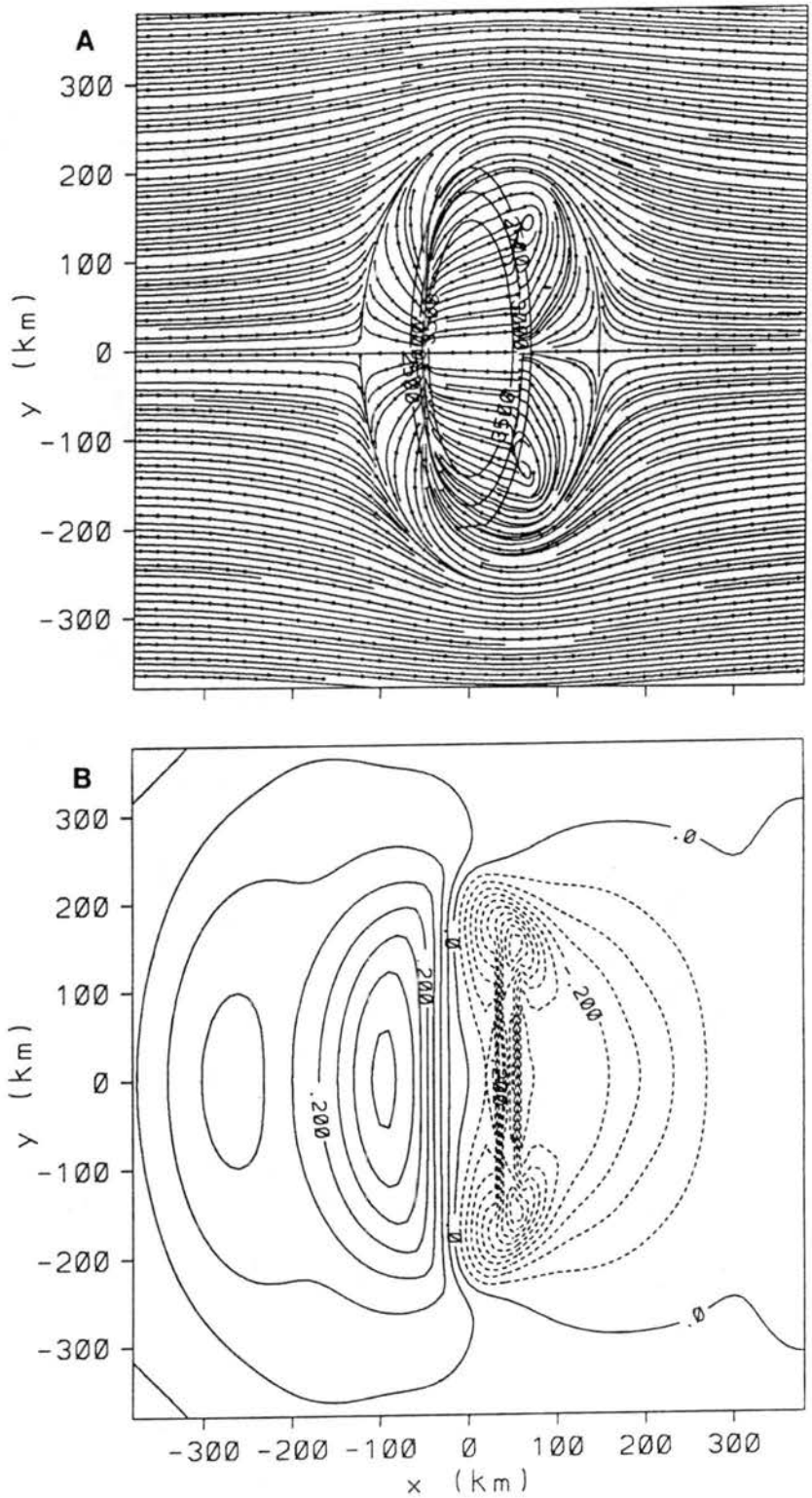

Figure 6.13: Low-level (146 AGL) 3 h forecasts of (a) streamlines and (b) perturbation Exner function (J deg^{-1} kg $^{-1}$, contour interval = 0.05 J deg^{-1} kg $^{-1}$) using cigar topography initialized with west wind and no Coriolis force for Fr = 0.3.

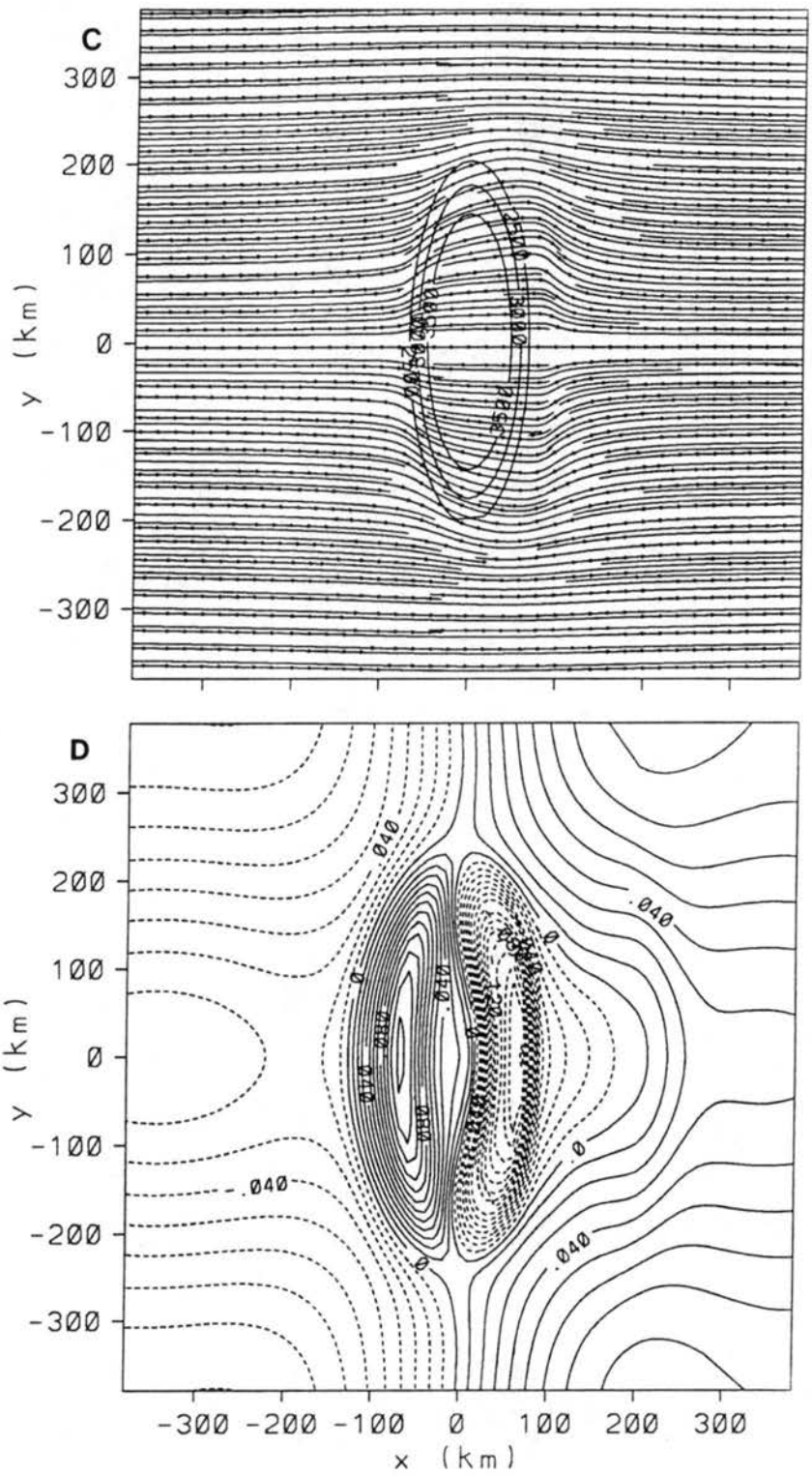

Figure 6.13: Continued: (c) streamlines and (d) perturbation Exner function (J deg^{-1} kg $^{-1}$, contour interval = 0.01 J deg^{-1} kg $^{-1}$) for Fr = 0.9.

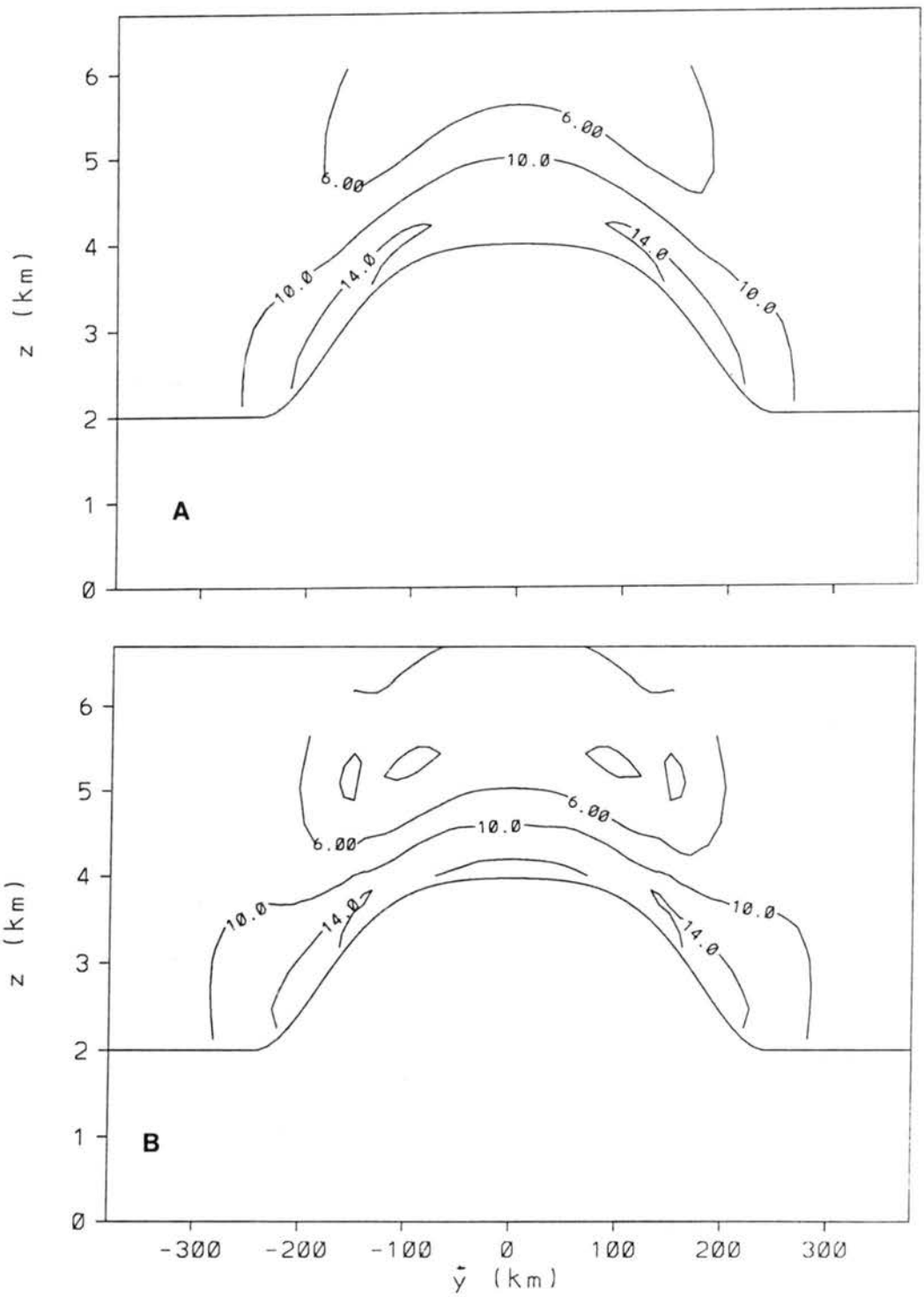

Figure 6.14: North-south vertical cross sections of u-component wind (m s $^{-1}$) positioned 20 km east of the barrier crest initialized with cigar topography, west wind, no Coriolis force, and Fr = 0.3 from the (a) 3 h and (b) 5 h forecasts.

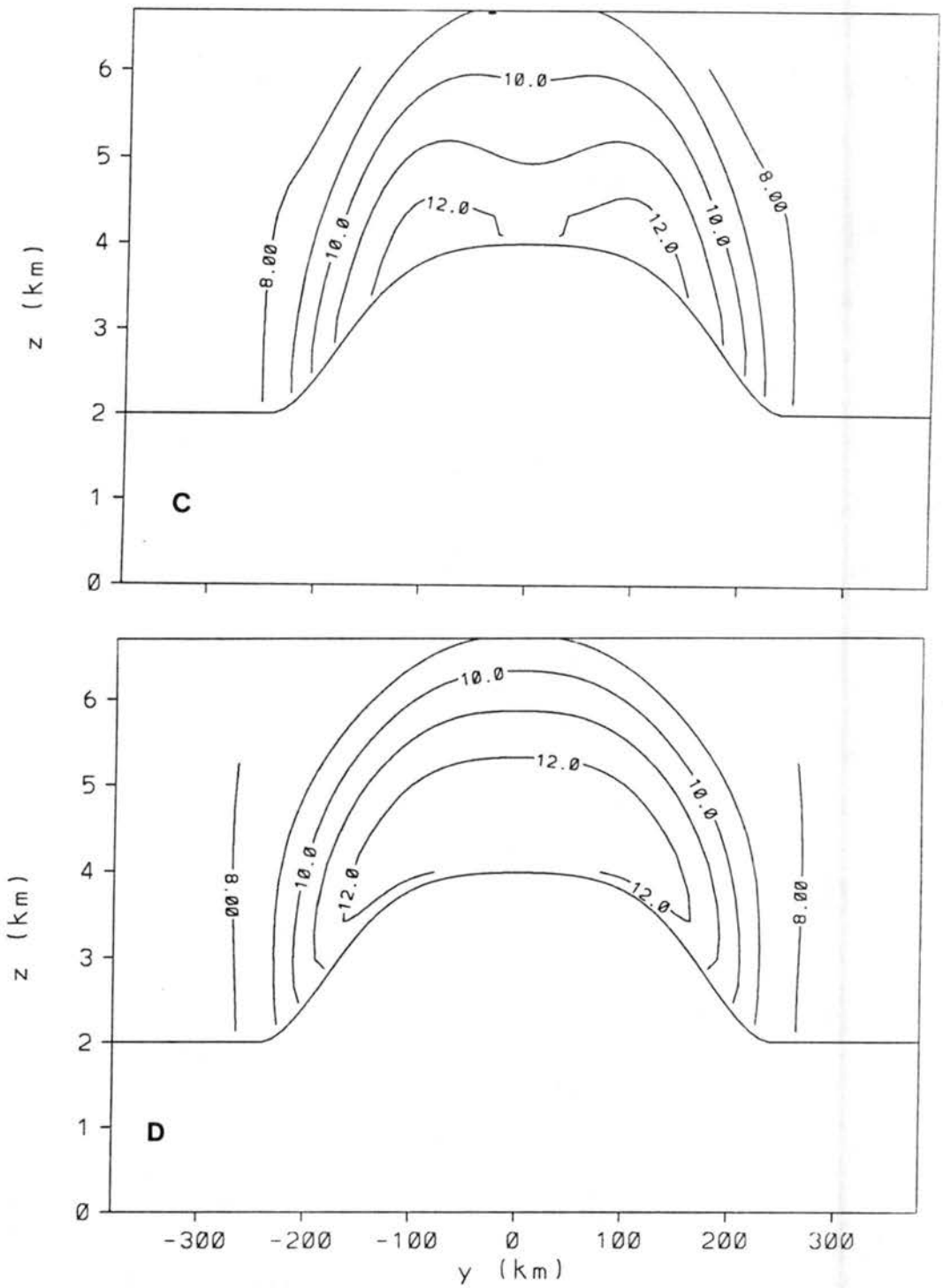

Figure 6.14: Continued: Fr = 0.9 from the (c) 3 h and (d) 5 h forecasts.

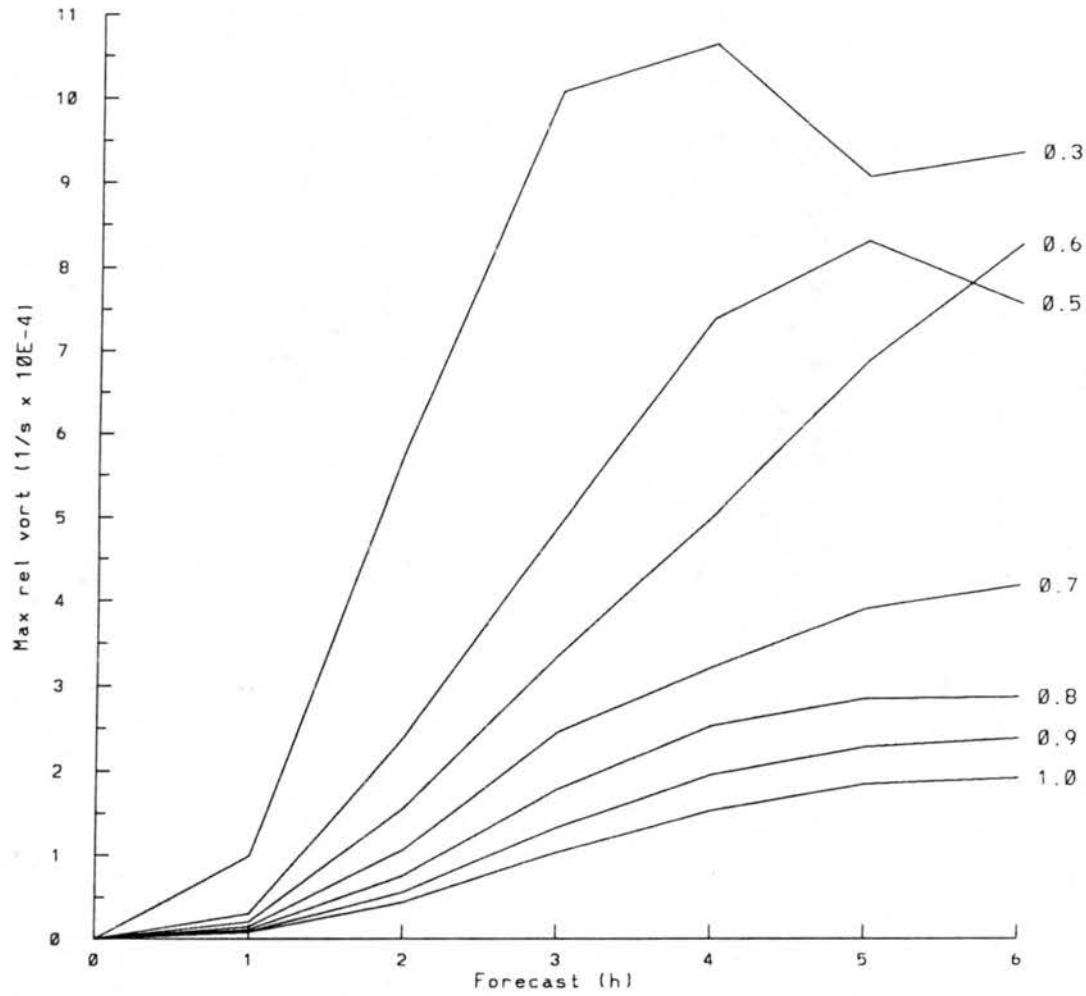

Figure 6.15: Maximum vertical vorticity ($\times 10^{-4}$ s^{-1}) for all cigar topography simulations initialized with west wind and no Coriolis force. Froude number is indicated to the right of each solid line.

vertical cross section of potential temperature for Fr = 0.3 at 1 h located approximately through the maximum vertical vorticity (same location as Figs. 6.11 and 6.12). The cross

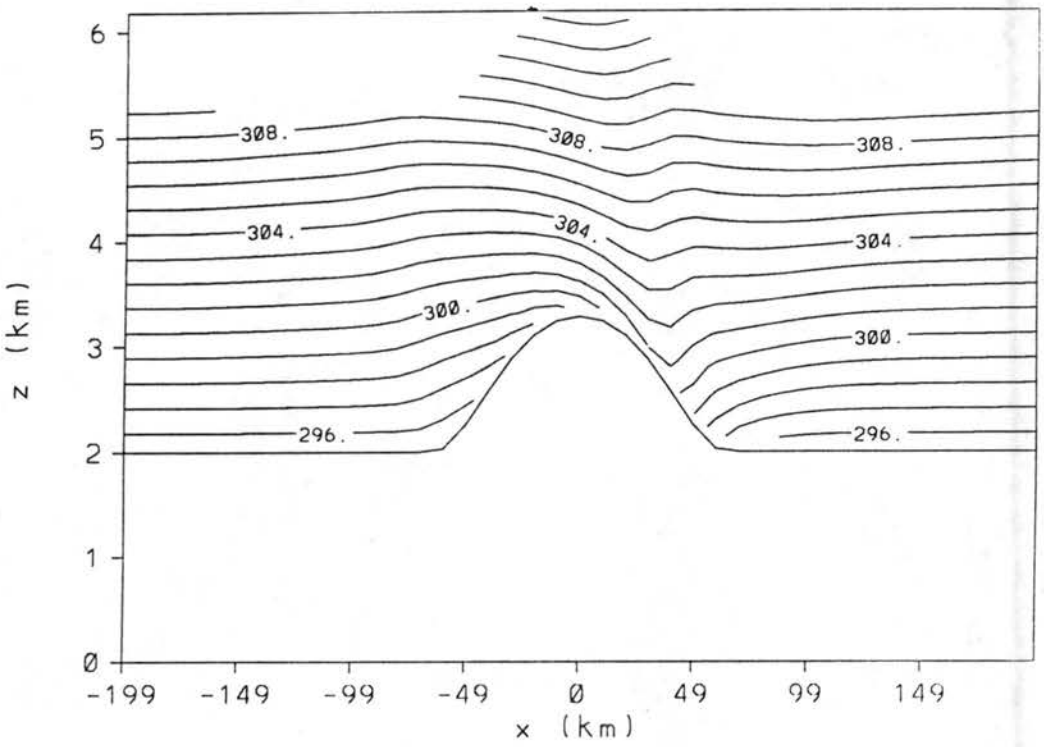

Figure 6.16: West-east vertical cross section located 160 km south of the domain center of potential temperature (K) at 1 h for Fr = 0.3 initialized with cigar topography, west wind, and no Coriolis force.

section demonstrates the importance of the lee wave in the placement of the vertical velocity profile, however wave breaking is not evident indicating that wave breaking is not required for the generation of lee vortices.

6.2.1.2 West wind, Coriolis force

The rotational effects of earth are investigated by duplicating the above simulations with the Coriolis force included for Fr = 0.3, 0.5, 0.7, and 0.9. Parallel simulations using K_{min} = 0.1 and 0.3 were completed. Although both simulations depicted similar characteristics including wave breaking, less high frequency variations were observed in the K_{min} = 0.3 results. Hence, model output shown is from the K_{min} = 0.3 simulations. Low-level streamlines at 6 h are illustrated in Fig. 6.17. Low-level flow separation is displaced approximately 120 km south and is coincident for all simulations. As the low-level flow approaches the barrier and slows, the decrease in Coriolis force creates an imbalance with the pressure gradient force resulting in a northward deflection of the flow which causes most of the flow to pass on the left side of the barrier (Pierrehumbert and Wyman 1985, Thorsteinsson 1988). An anticyclonic lee vortex is observed for the Fr = 0.3 and 0.5 cases while only the Fr = 0.3 simulation develops a cyclonic vortex. In all cases, the cyclonic vorticity is initially greater than the anticyclonic vorticity (Fig. 6.18). However, by 6 h, the anticyclonic vorticity becomes greater for the Fr = 0.3 and 0.5 cases.

Although the lee side vorticity pattern is altered, the generation mechanisms (i.e. tilting, stretching, and advection) remain the same. The effects of the Coriolis force on blocking are minimal after 1 h as evidenced by the pressure perturbation field for Fr = 0.3 (Fig. 6.19a). However, the cyclonic circulation is stronger than the anticyclonic circulation. Figures 6.20 and 6.21 show west-east vertical cross sections for the Fr = 0.3, 1 h forecast of relative vertical vorticity divergence, planetary vertical vorticity divergence, total vertical vorticity divergence, and relative vertical vorticity that transect the regions of greatest cyclonic and anticyclonic relative vertical vorticity. Positive and negative relative vertical vorticity are generated by tilting, similar to the no Coriolis force case. However, the stretching of planetary vertical vorticity tends to strengthen the cyclonic vorticity and weaken the anticyclonic vorticity. After 3 h, the Coriolis effects have had time to significantly influence the blocking as indicated by a northward deviation of the positive pressure perturbation on the west side of the barrier and a southward deviation of the negative pressure perturbation on the east side of the barrier (Fig. 6.19b). The result

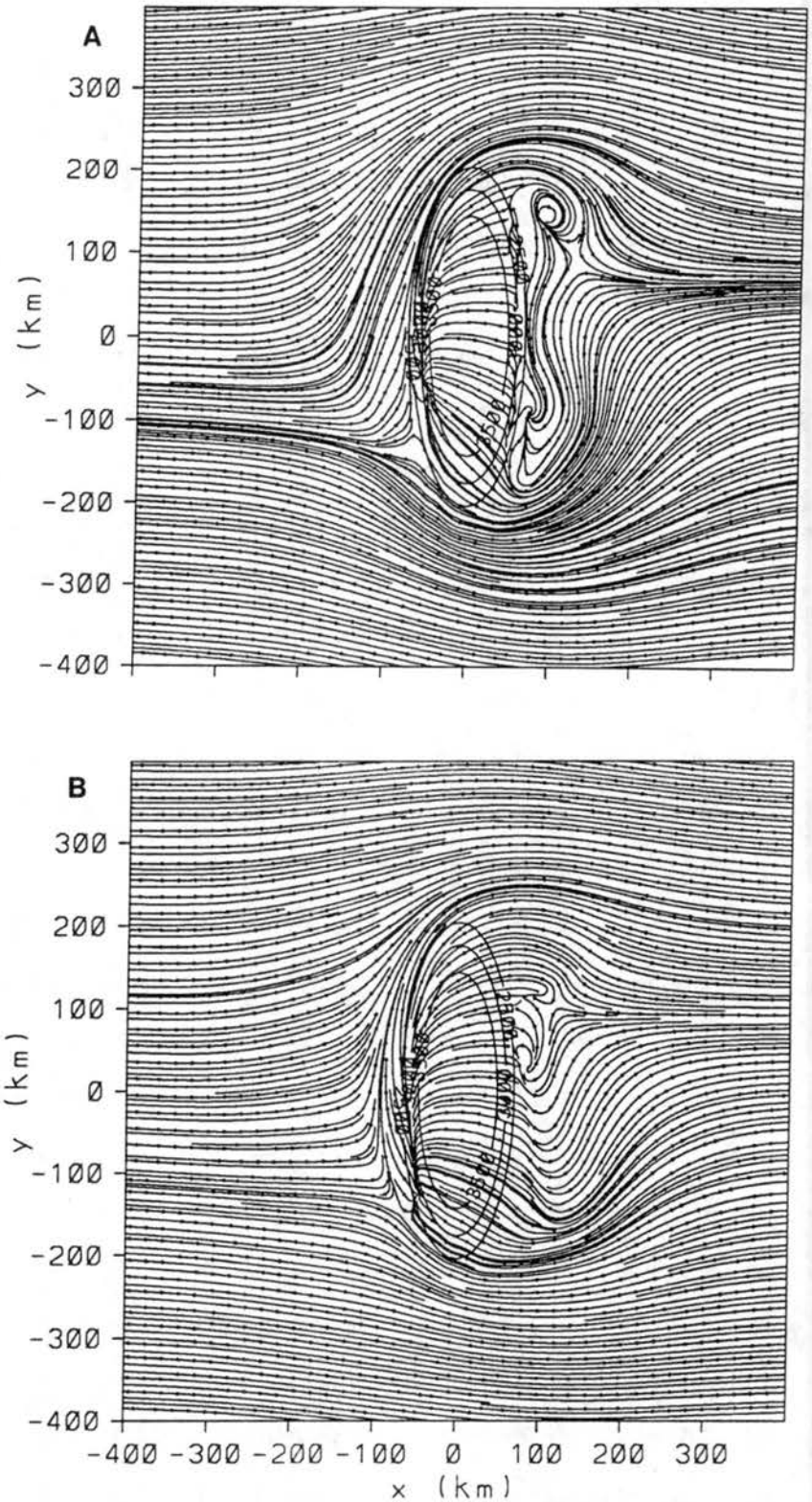

Figure 6.17: Low-level (146 AGL) streamlines at 6 h using cigar topography initialized with west wind and Coriolis force for (a) Fr = 0.3 and (b) Fr = 0.5.

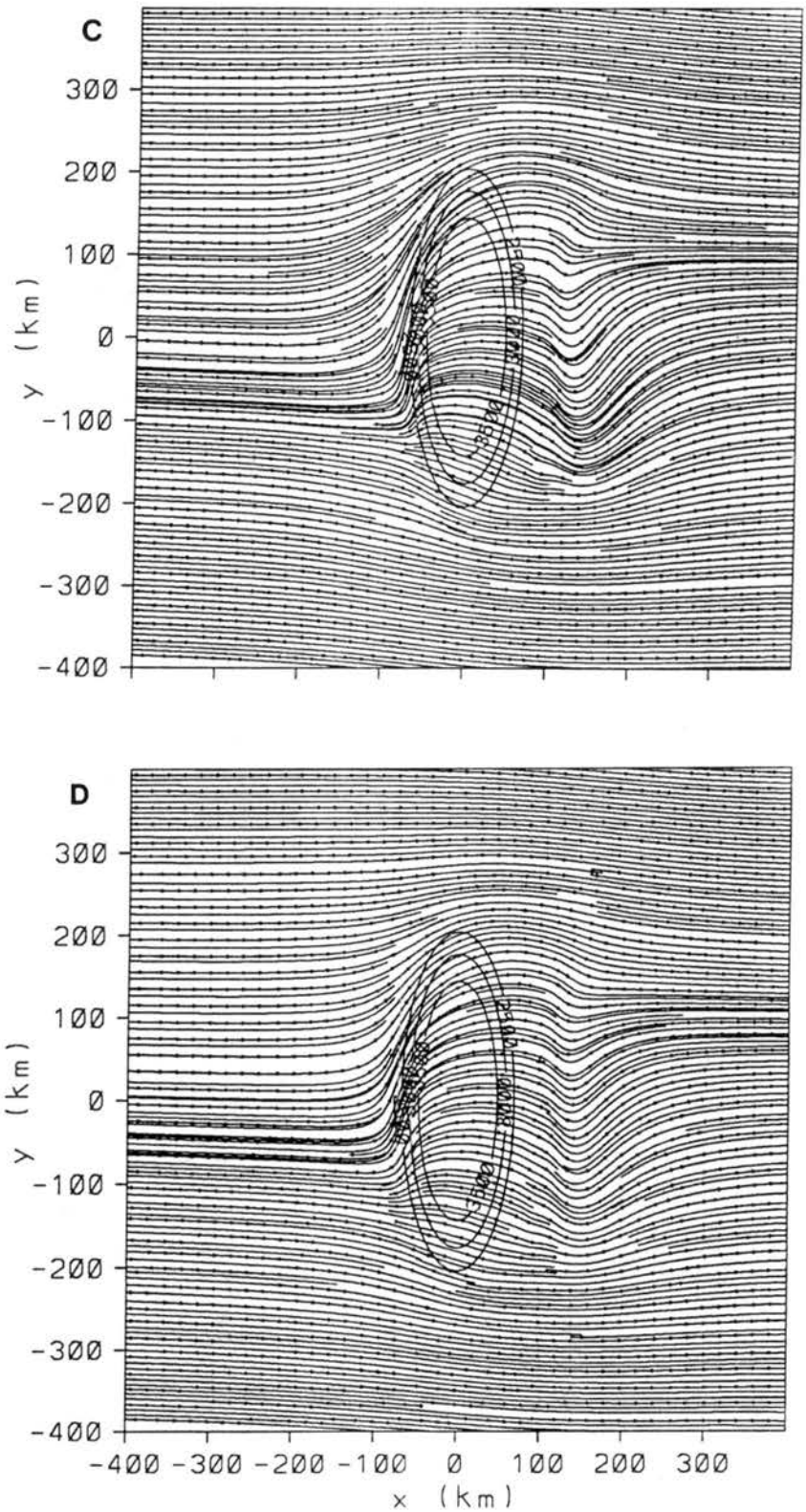

Figure 6.17: Continued: (c) Fr = 0.7 and (d) Fr = 0.9.

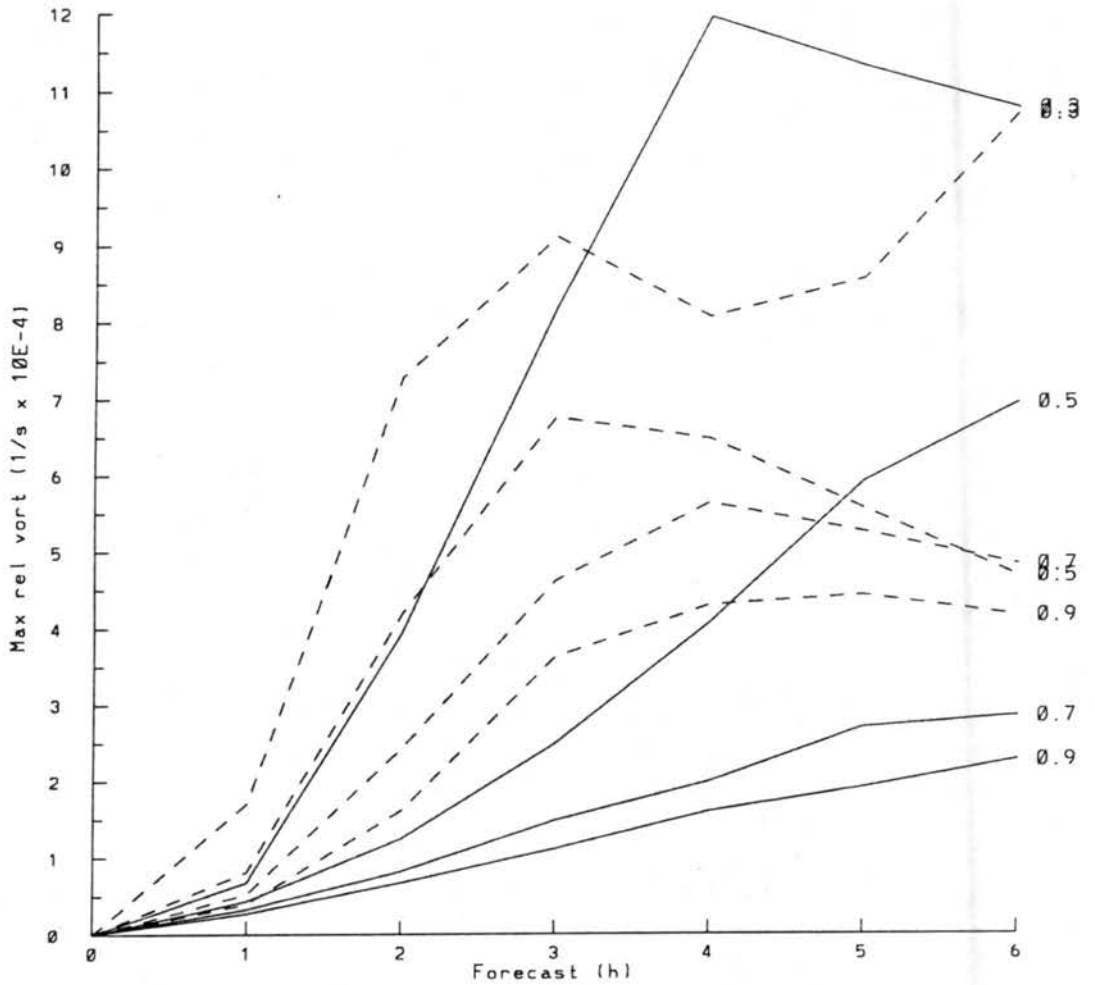

Figure 6.18: Maximum vertical vorticity ($\times 10^{-4}$ s^{-1}) for all cigar topography simulations initialized with west wind and Coriolis force. Dashed lines represent cyclonic vorticity and solid lines represent anticyclonic vorticity. Froude number is indicated to the right of each line.

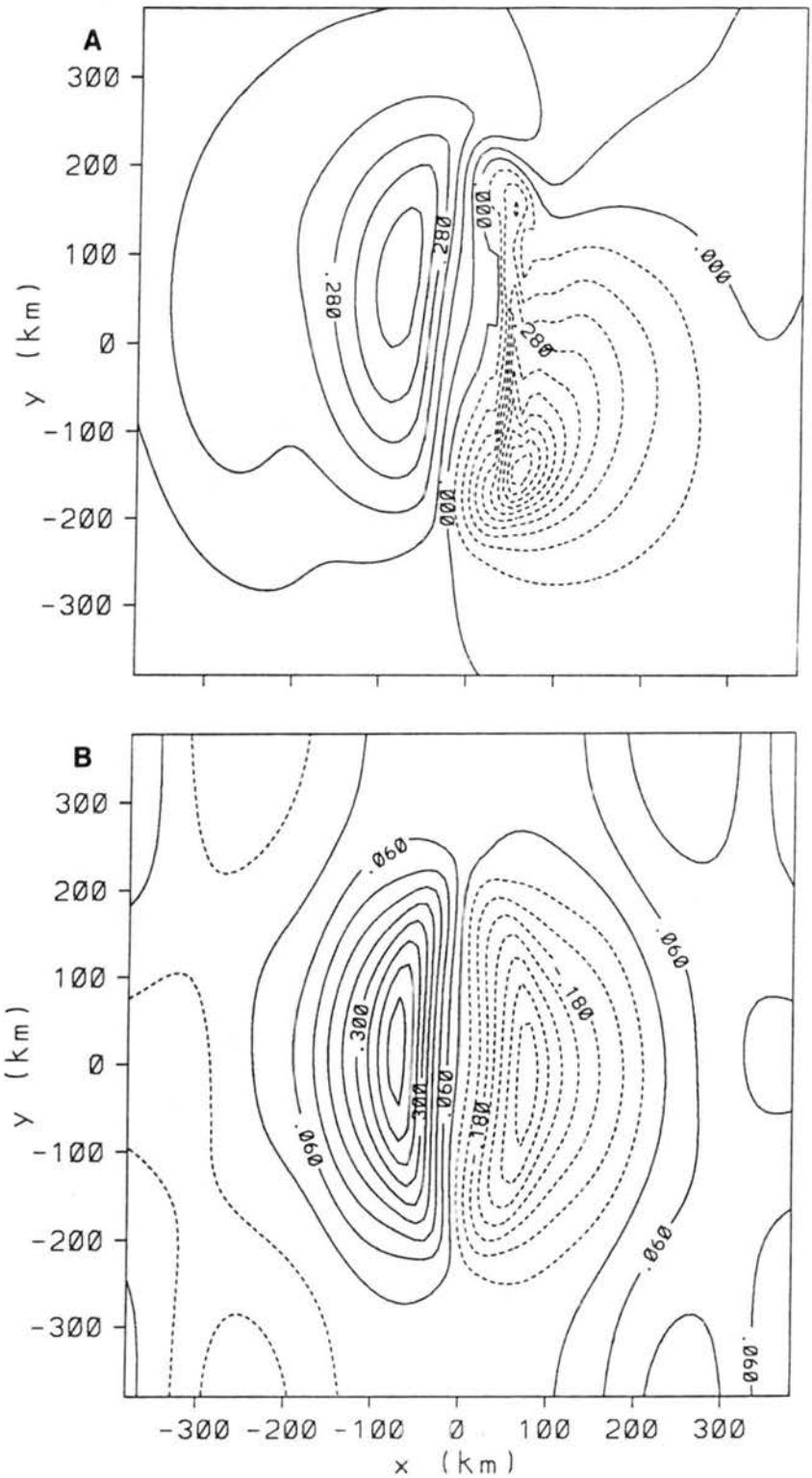

Figure 6.19: Low-level (146 AGL) perturbation Exner function (J deg^{-1} kg $^{-1}$) at (a) 1 h (contour interval = 0.06 J deg^{-1} kg $^{-1}$) and (b) 3 h (contour interval = 0.07 J deg^{-1} kg $^{-1}$) using cigar topography initialized with west wind and Coriolis force for Fr = 0.3.

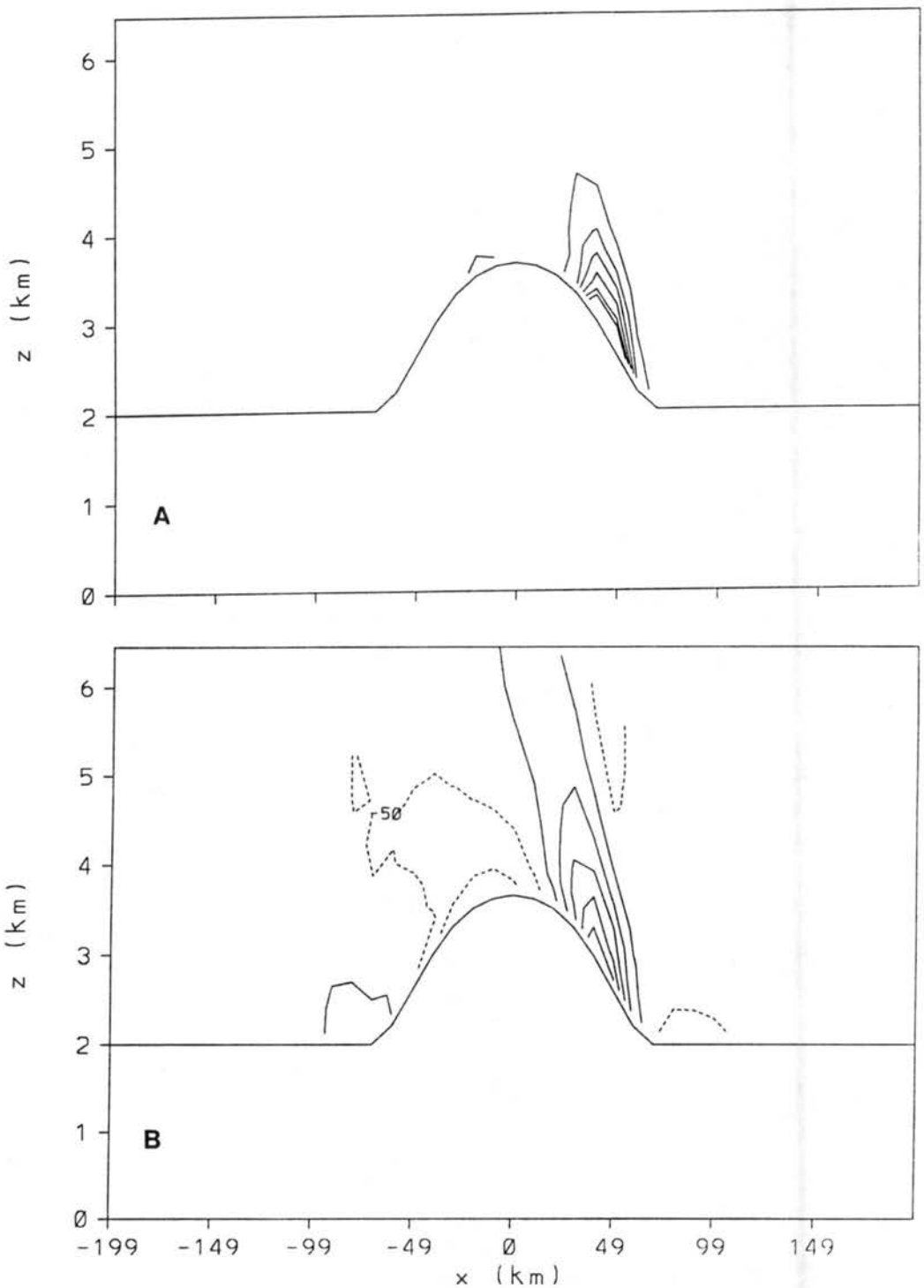

Figure 6.20: West-east vertical cross sections located 130 km south of the domain center for Fr = 0.3 initialized with cigar topography, west wind, and Coriolis force. 1 h forecasts of (a) relative vertical vorticity divergence (s^{-2}, contour interval = 1.0×10^{-8} s^{-2}) and (b) planetary vertical vorticity divergence (s^{-2}, contour interval = 1.0×10^{-8} s^{-2}).

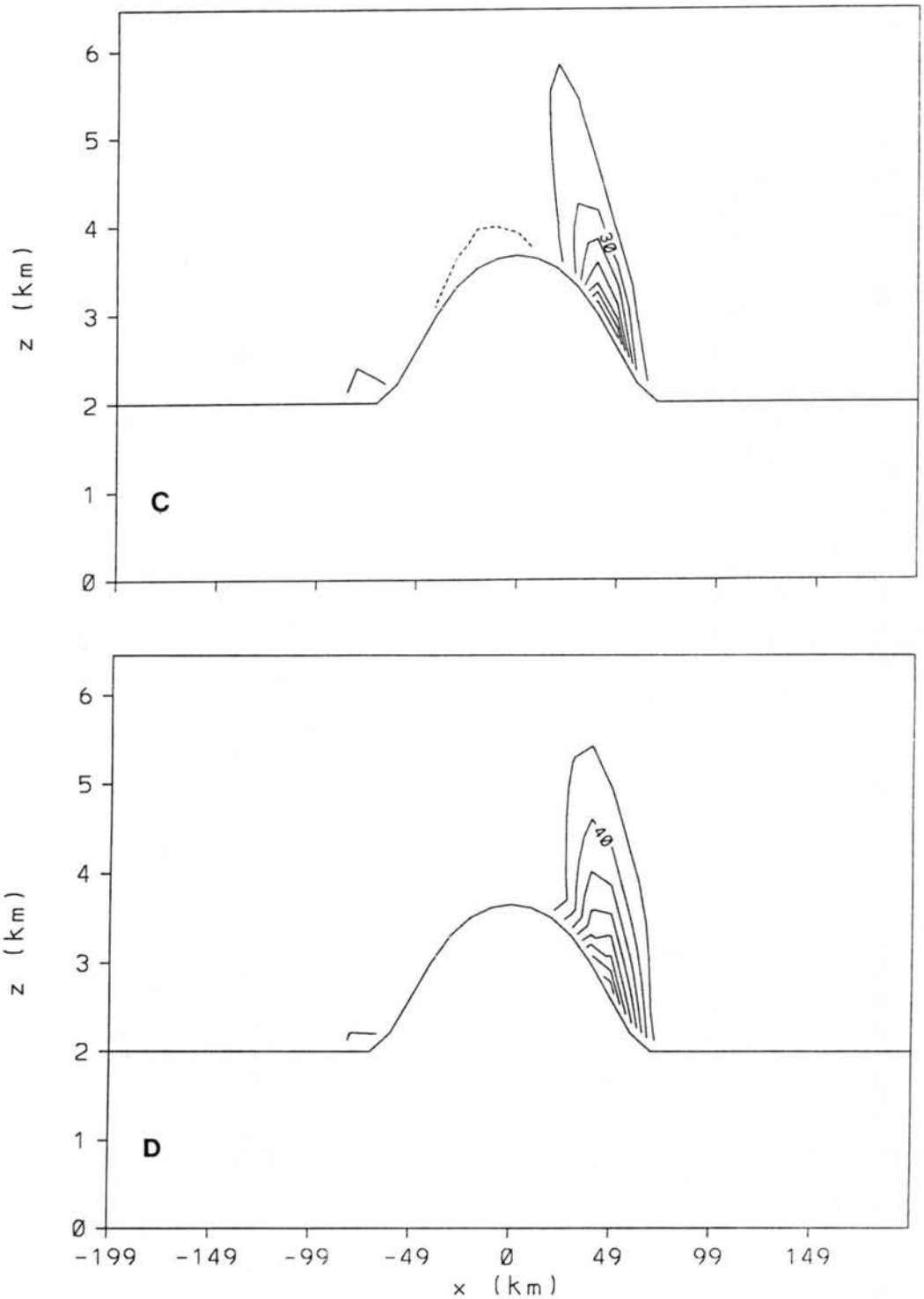

Figure 6.20: Continued: (c) total vertical vorticity divergence (s^{-2}, contour interval = 2.0×10^{-8} s^{-2}) and (d) total relative vertical vorticity (s^{-1}, contour interval = 2.0×10^{-5} s^{-1}).

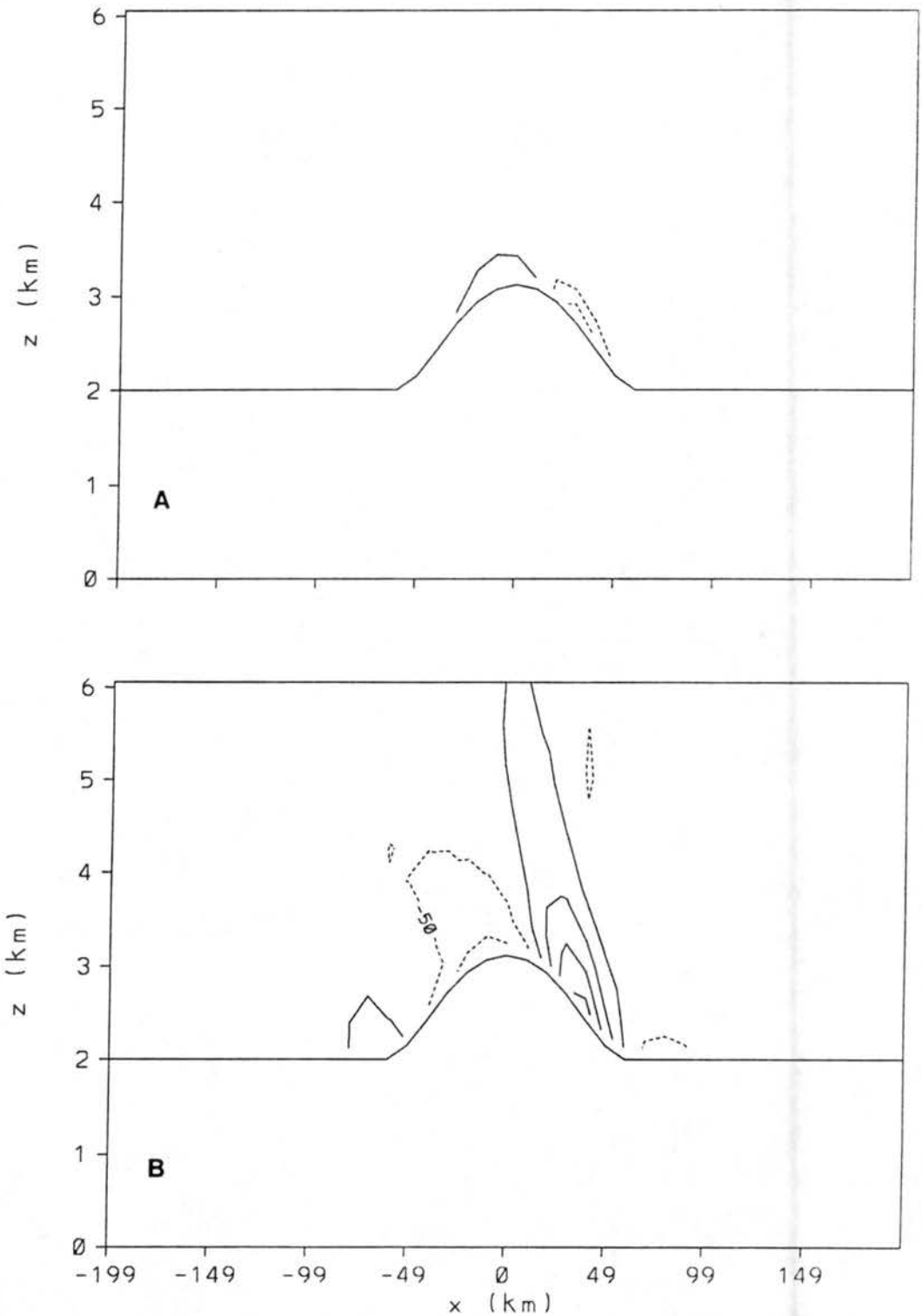

Figure 6.21: As in Fig. 6.20 except for cross sections are located 170 km north of domain center.

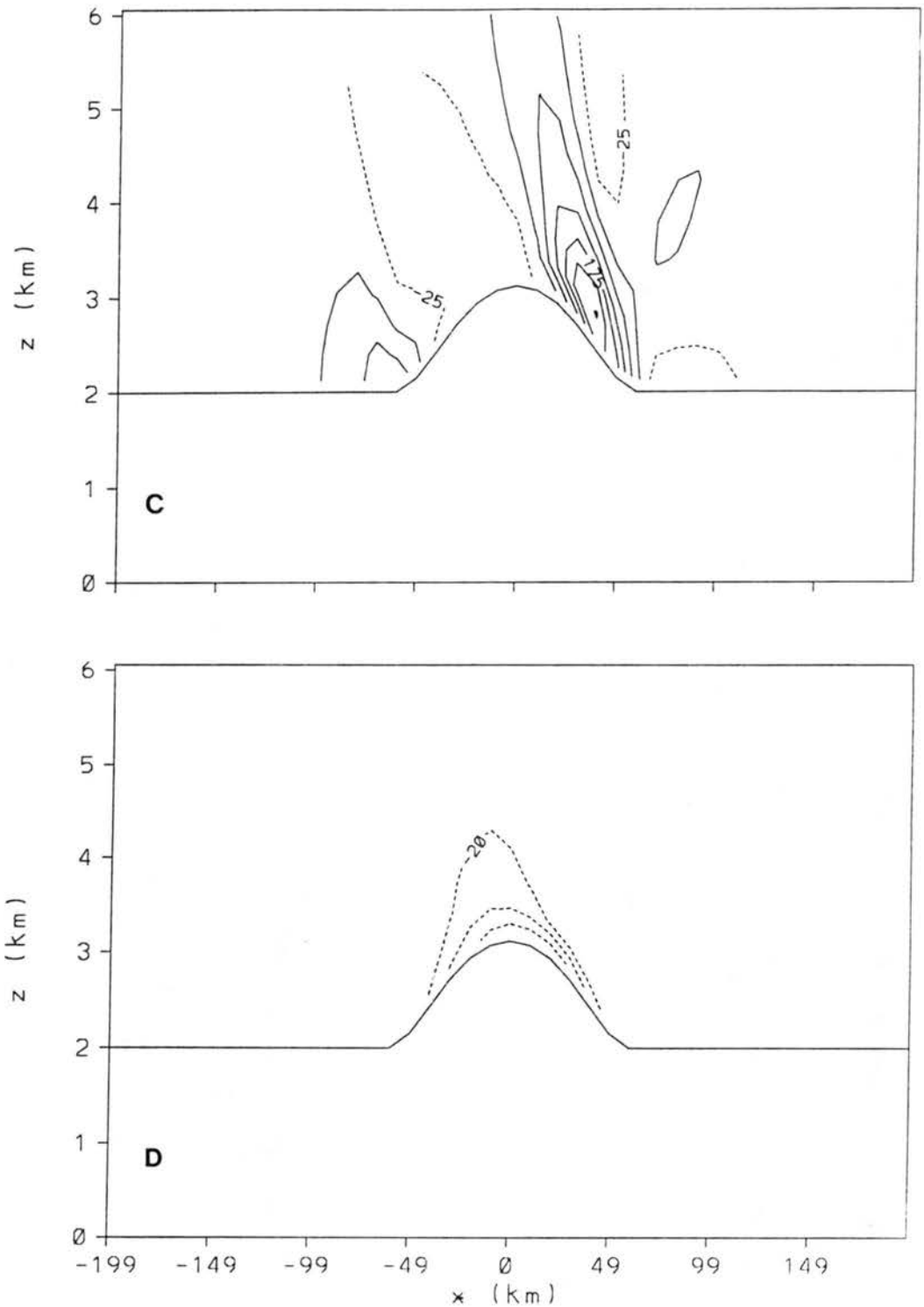

Figure 6.21: Continued: (Total vorticity divergence contour interval is 5.0×10^{-9} s^{-2}).

is a stronger westerly flow over the northern portion of the barrier (Fig. 6.22) that creates greater tilting and increased generation of anticyclonic vorticity. Also, the southerly flow

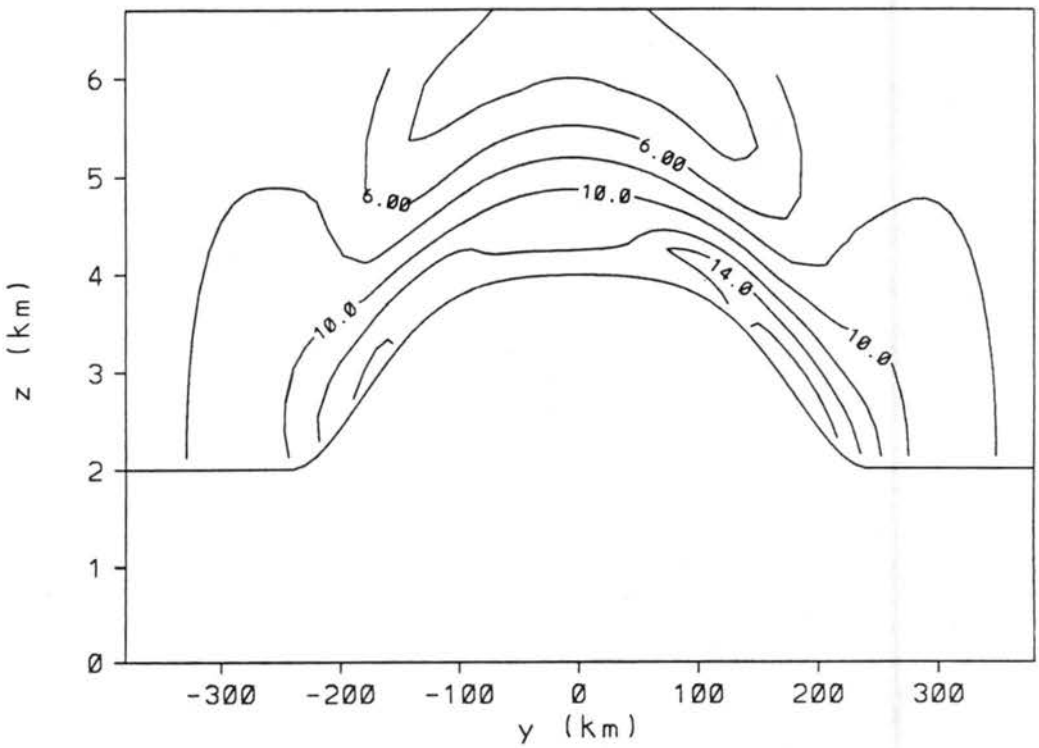

Figure 6.22: North-south vertical cross section located 20 km east of the barrier crest of u-component wind (m s^{-1}) at 3 h for Fr = 0.3 initialized with cigar topography, west wind, and Coriolis force.

that develops to the southeast of the barrier tends to advect cyclonic vorticity northward creating an elongated region of cyclonic vorticity as opposed to the concentrated region of anticyclonic vorticity located northeast of the barrier. For the larger Froude number cases (i.e. Fr =0.7 and 0.9), upstream blocking is less significant creating maximum westerly flow that is weaker and closer to the center of the barrier. The result is less generation of vertical vorticity by tilting and the cyclonic vorticity remains greater than the anticyclonic vorticity due to the influences of planetary vertical vorticity divergence.

The effects of the Coriolis force on lee vortex development can be summarized as follows. In the early stages, the Coriolis effects have not had sufficient time to significantly influence the blocking resulting in lee vortex generation processes by tilting similar to the no Coriolis force case. The primary difference is the stretching of planetary vertical

vorticity that strengthens the cyclonic vorticity while weakening the anticyclonic vorticity. With time, the Coriolis force influences the blocking evolution in the low Froude number cases such that westerly flow over the barrier is greater to the north resulting in a stronger anticyclonic vortex. For the higher Froude number cases, blocking influences are much less significant resulting in no vortex development due to less generation of horizontal vorticity by the tilting processes. The cyclonic vorticity remains larger than the anticyclonic vorticity due to planetary vertical vorticity divergence. In general, with or without the Coriolis force, the tilting of horizontal vorticity into the vertical is the generation mechanism, but the stretching and advection of vertical vorticity play an important role in defining the final lee vortex configuration.

6.2.1.3 Northwest wind, no Coriolis force

The effects of a different wind direction relative to the mountain barrier are investigated by repeating the above simulations with a northwesterly initial flow for Fr = 0.3, 0.5, 0.7, and 0.9. A northwest geostrophic wind is often observed together with a stable environment creating low Froude number conditions along the Colorado Front Range. Low-level streamlines at 3 and 6 h are illustrated in Figs. 6.23 and 6.24. Upwind flow reversal and a low-level stagnation point are only evident for the Fr = 0.3 case and they are positioned about 170 km north of the center east-west axis. Flow separation is indicated in the same location for the higher Froude number simulations. Downwind of the barrier, the Fr = 0.3 streamlines indicate a closed cyclonic vortex. No other closed circulations are evident in any of the simulations, but regions of cyclonic and anticyclonic vorticity are suggested in the flow fields. In all cases, these features appear to propagate downstream with time. Maximum cyclonic vorticity remains greater than maximum anticyclonic vorticity at all times except for Fr = 0.5 at 6 h (Fig. 6.25).

An evaluation of blocking and vorticity tilting, stretching, and advection provides an understanding of the simulated features. Streamlines and π^* at 1 h for Fr = 0.3 (Fig. 6.26) show an upwind positive pressure perturbation displaced northward and a downwind negative pressure perturbation displaced southward. Cross-barrier flow is oriented from the

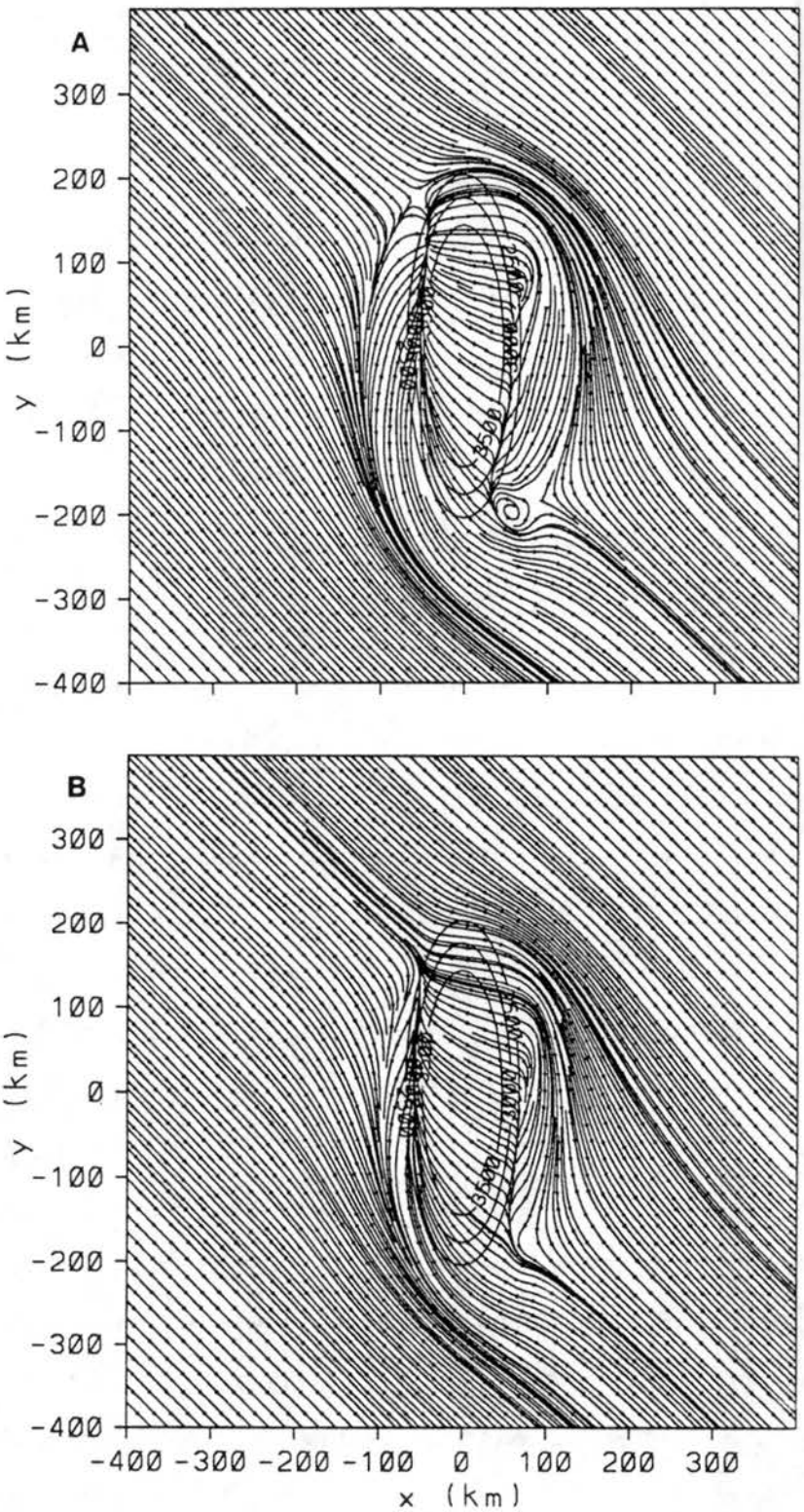

Figure 6.23: Low-level (146 AGL) streamlines at 3 h using cigar topography initialized with northwest wind and no Coriolis force for (a) Fr = 0.3 and (b) Fr = 0.5.

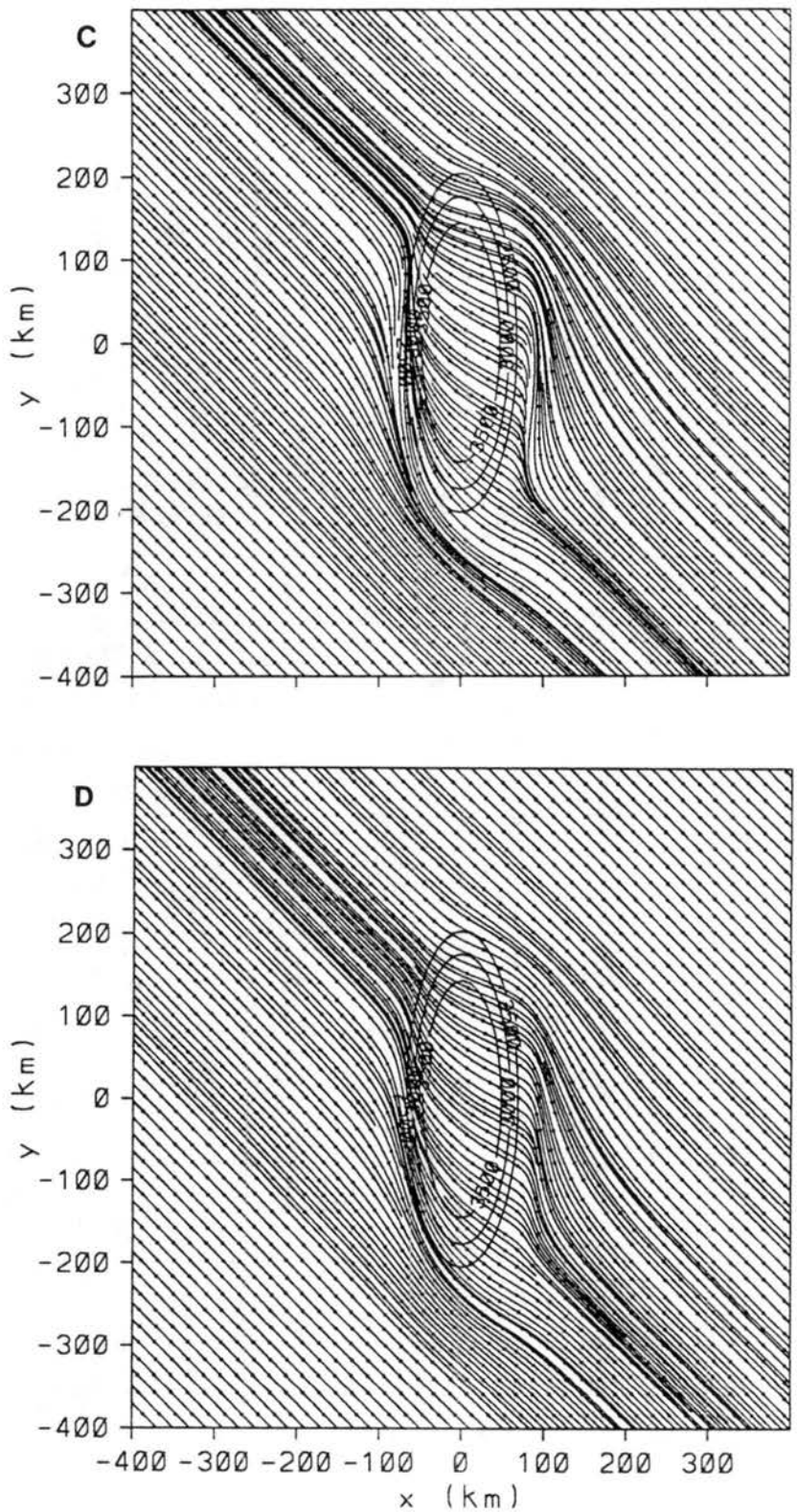

Figure 6.23: Continued: (c) Fr = 0.7 and (d) Fr = 0.9.

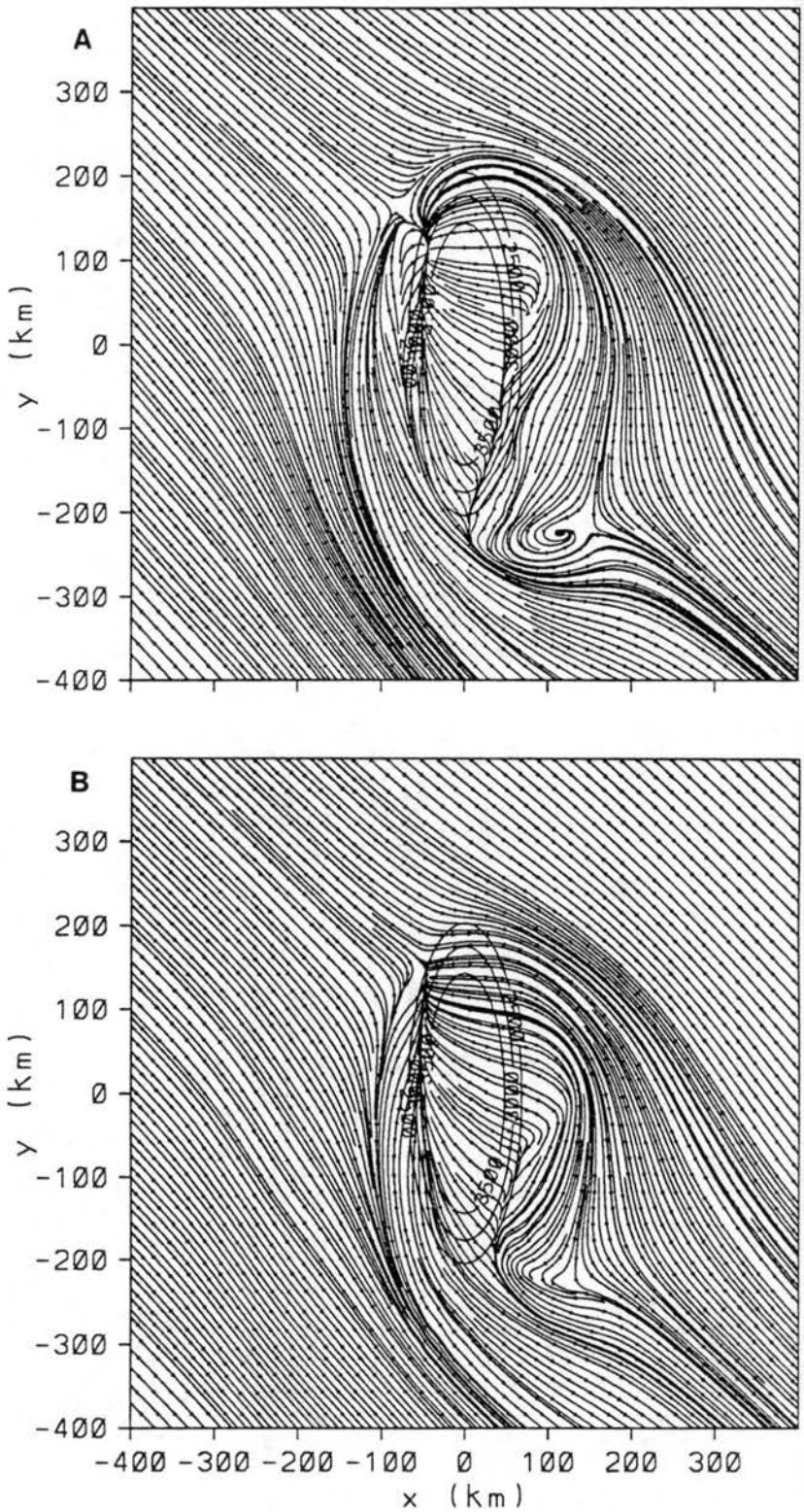

Figure 6.24: As in Fig 6.23 except for 6 h forecast.

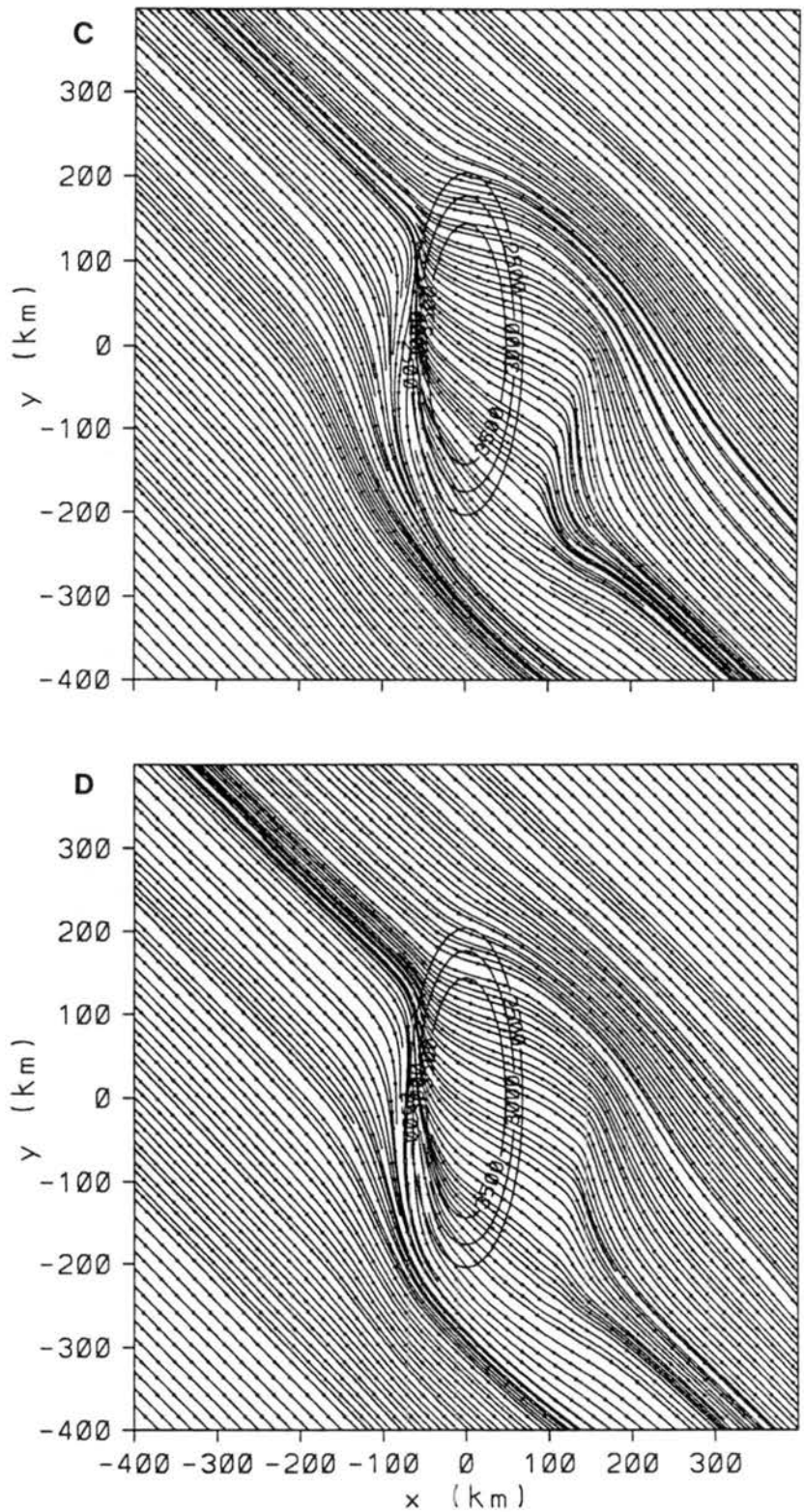

Figure 6.24: Continued:

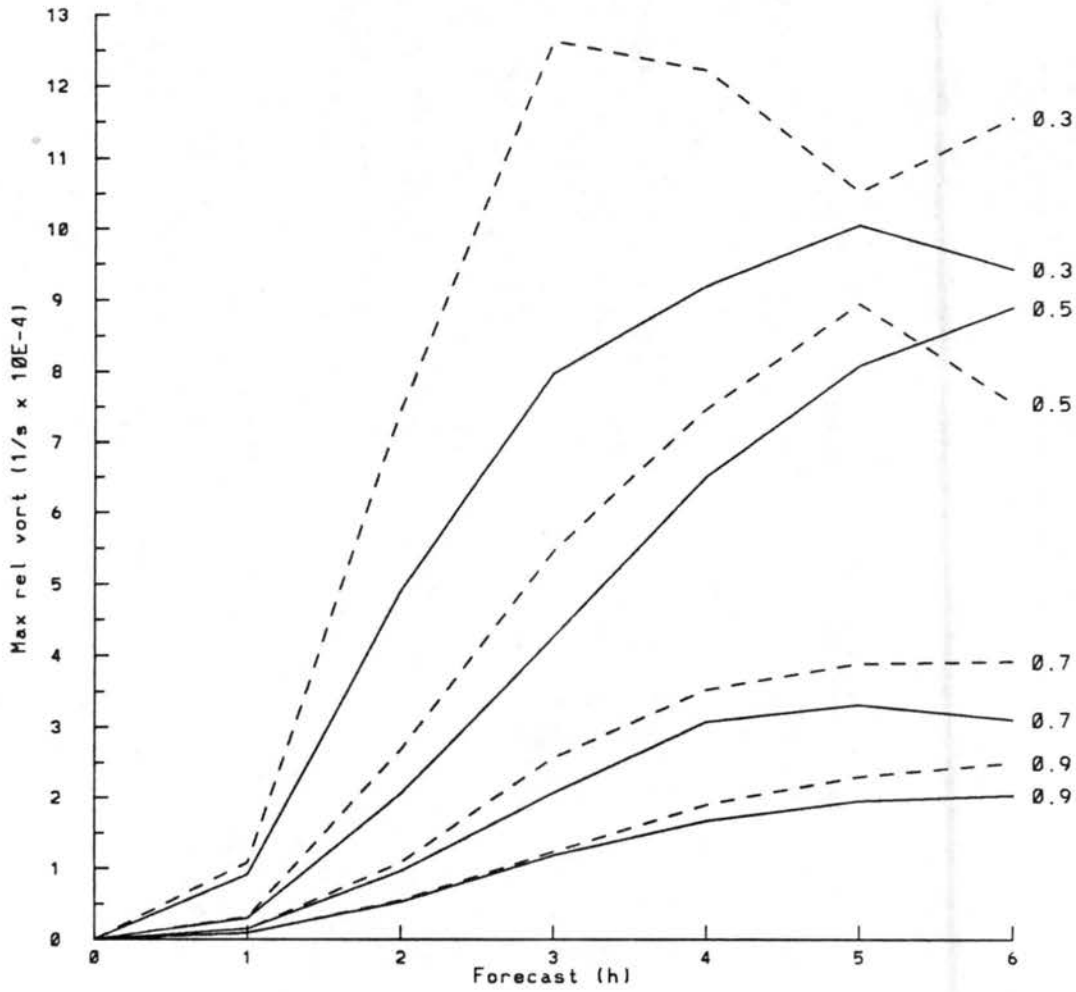

Figure 6.25: Maximum vertical vorticity ($\times 10^{-4}$ s^{-1}) for all cigar topography simulations initialized with northwest wind and no Coriolis force. Dashed lines represent cyclonic vorticity and solid lines represent anticyclonic vorticity. Froude number is indicated to the right of each line.

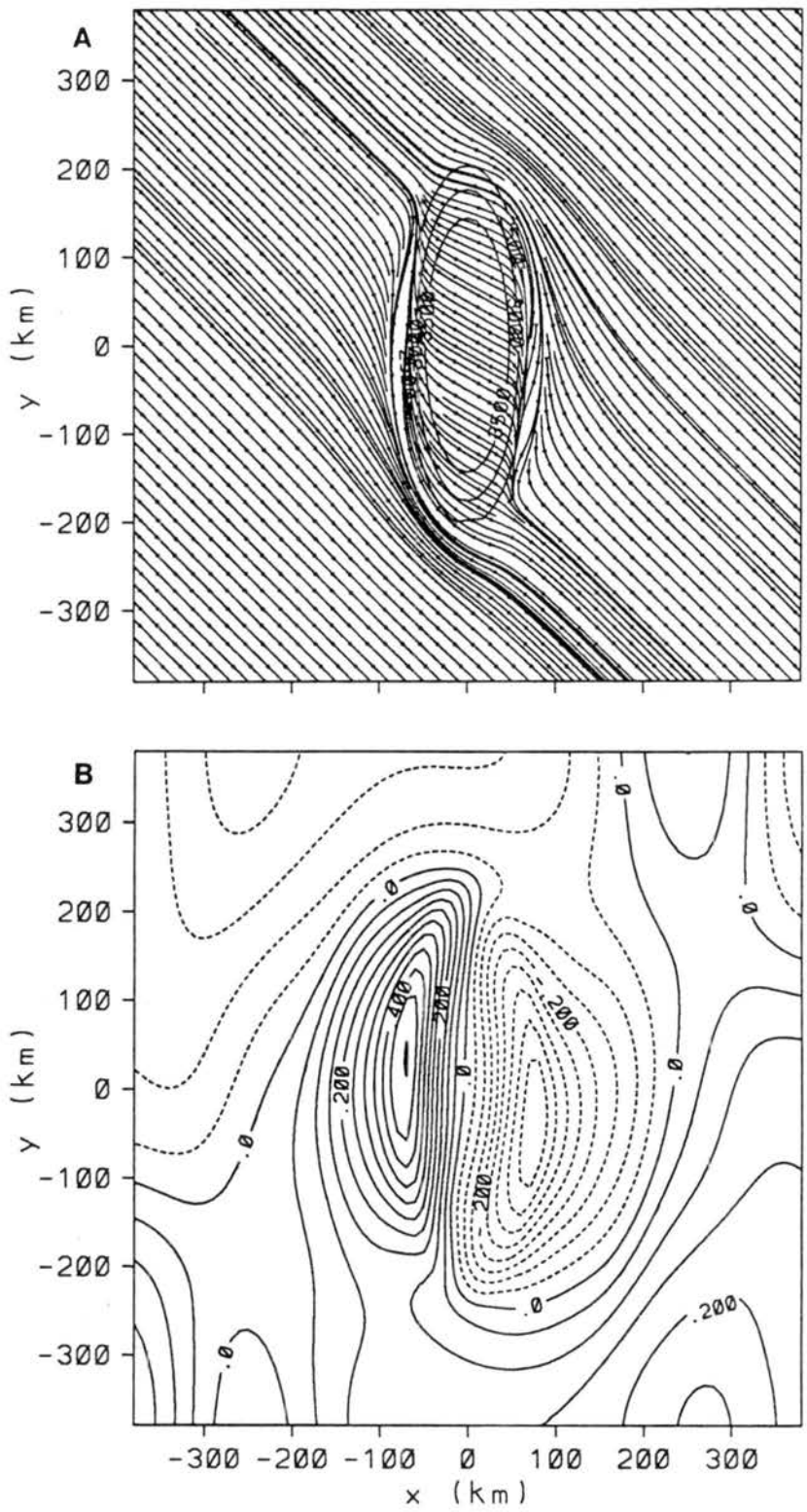

Figure 6.26: Low-level (146 AGL) 1 h forecasts of (a) streamlines and (b) perturbation Exner function (J deg^{-1} kg $^{-1}$, contour interval = 0.05 J deg^{-1} kg $^{-1}$) using cigar topography initialized with northwest wind and no Coriolis force for Fr = 0.3.

positive to the negative pressure perturbation in response to the mesoscale pressure gradient and the closed cyclonic vortex has not yet developed. Figure 6.27 illustrates the 1 h vertical motion, vorticity tilting, vertical vorticity advection, and vertical vorticity for the Fr = 0.3 simulation. Downward vertical motion is evident downstream of the cross-barrier flow and the areal coverage is closely correlated with the terrain shape. Positive generation of vertical vorticity by tilting, positioned south of the mountain, results from downward motion increasing northward ($\frac{\partial w}{\partial y} > 0$) and westerly component flow decreasing with height ($\frac{\partial u}{\partial z} < 0$), similar to the west wind simulation.

A horseshoe area of anticyclonic vorticity generation surrounds the northern portion of the barrier and extends southward along the downwind side of the barrier. In contrast to the west wind simulations, the negative vorticity generation appears to be the result of downward motion increasing eastward ($\frac{\partial w}{\partial x} > 0$) and northerly component flow decreasing with height ($\frac{\partial v}{\partial z} > 0$). In addition to vorticity tilting, the northerly along-barrier flow tends to advect the anticyclonic vorticity downstream creating an elongated convergence zone that does not evolve into a closed vortex. The downstream propagation of the wave features observed in the streamline fields (Figs. 6.23 and 6.24) also appears to be the result of vertical vorticity advection. For example, the northerly along-barrier flow in the Fr = 0.3 simulation advects the cyclonic vortex southward into the stronger northwesterly flow travelling around the southern end of the mountain which then advects the vortex southeastward.

6.2.1.4 Northwest wind, Coriolis force

Parallel simulations are conducted with the addition of the Coriolis force for Fr = 0.3, 0.5, 0.7, and 0.9 to investigate the rotational effects of earth. Figures 6.28 and 6.29 illustrate low-level streamlines at 3 and 6 h. For Fr = 0.3, the development of an upwind low-level stagnation point is indicated and the stagnation point moves south with time, similar to the evolution observed in the west wind case. A closed cyclonic vortex is evident at 3 and 6 h, and in contrast to the no Coriolis simulation, a closed anticyclonic vortex develops by 6 h. The development of a closed cyclonic vortex is evident at 3 h for Fr = 0.5, but the vortex disappears by 6 h. Interestingly, upwind flow reversal develops

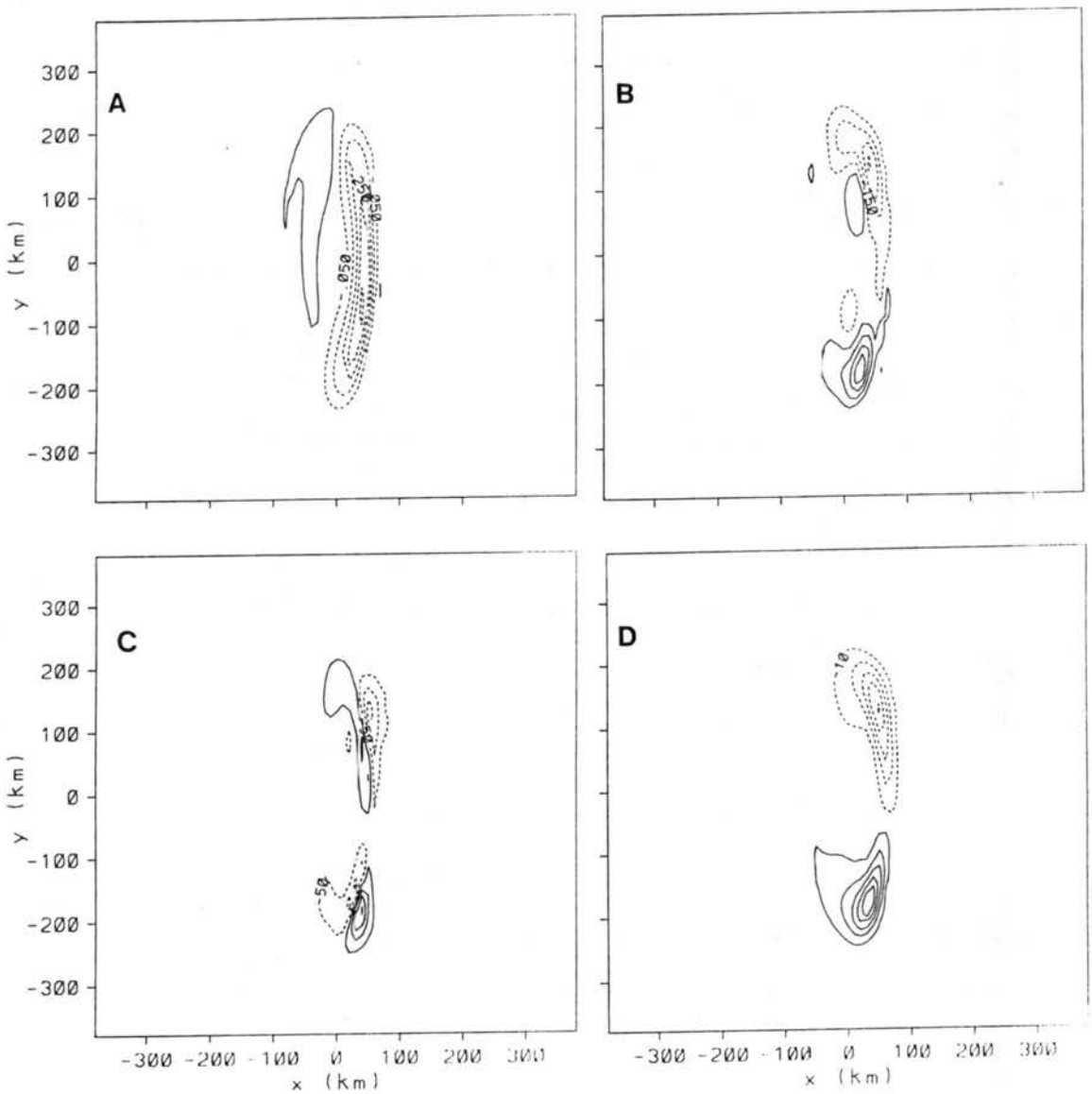

Figure 6.27: Low-level (146 AGL) 1 h forecasts of (a) vertical motion (m s^{-1}), (b) tilting into vertical vorticity (s^{-2}, contour interval = 1.0×10^{-8} s^{-2}), (c) vertical vorticity advection (s^{-2}, contour interval = 1.0×10^{-8} s^{-2}), and vertical vorticity (s^{-1}, contour interval = 2.0×10^{-5} s^{-1}). Simulations initialized with cigar topography, northwest wind, no Coriolis force, and Fr = 0.3.

by 6 h while the closed cyclonic vortex disappears suggesting again that the generation of lee vortices are not dependent on the development of an upwind low-level stagnation point. The Fr = 0.7 and 0.9 flow patterns appear similar for the Coriolis and no Coriolis simulations. The propagation of downwind features away from the barrier is again evident, however the propagation speed appears slower for the Coriolis simulations. Similar to the west wind simulations, the maximum cyclonic vorticity is initially greater than maximum anticyclonic vorticity for all cases (Fig. 6.30). However, by 6 h, the anticyclonic vorticity becomes greater for the Fr = 0.3 and 0.5 cases.

The effects of the Coriolis force are minimal during the early stages of lee vortex development, hence the downwind characteristics at 3 h are similar to the no Coriolis experiment. The primary differences are the stronger cyclonic vortices for Fr = 0.3 and 0.5. As with the west wind case, the tilting, stretching, and advection of planetary vertical vorticity tends to strengthen the cyclonic vortices. With time, the Coriolis effects force the flow separation southward and the cross-barrier mesoscale pressure gradient strengthens across the northern portion of the mountain. The result is increased anticyclonic vorticity and the development of a closed anticyclonic vortex for Fr = 0.3. Over the southern portion of the mountain, the cross-barrier mesoscale pressure gradient is weakening, hence maximum cyclonic vorticity decreases and the closed cyclonic vortex disappears for Fr = 0.5.

6.2.2 Fang topography

6.2.2.1 West wind, no Coriolis force

Parallel simulations are performed using the fang topography with no Coriolis force and a K_{min} value of 0.1 initialized with a uniform 7.07 m s^{-1} west wind for Froude numbers of 0.3, 0.5, 0.7, and 0.9. Low-level streamlines at 6 h are illustrated in Fig. 6.31. Flow separation is indicated on the windward side of the barrier for all cases. A pair of lee vortices develop for the Fr = 0.3 and 0.5 simulations, similar to the cigar topography cases. The development and magnitude of the cyclonic vortices are quite similar for the two topography experiments (Fig. 6.32). However, the anticyclonic vortex develops further south and east, along the southern boundary of the east-west barrier extension, and is a little stronger in magnitude.

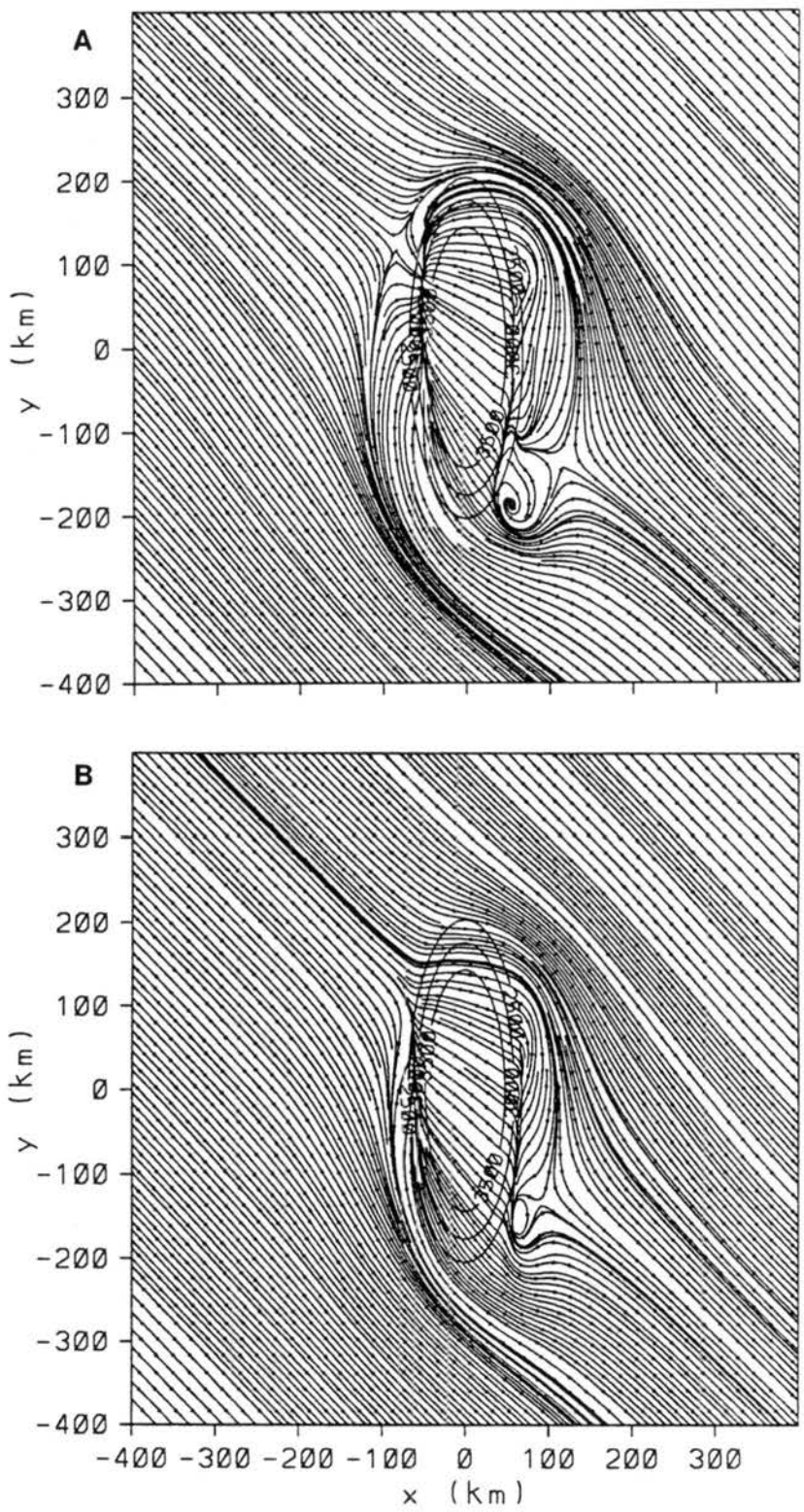

Figure 6.28: Low-level (146 AGL) streamlines at 3 h using cigar topography initialized with northwest wind and Coriolis force for (a) Fr = 0.3 and (b) Fr = 0.5.

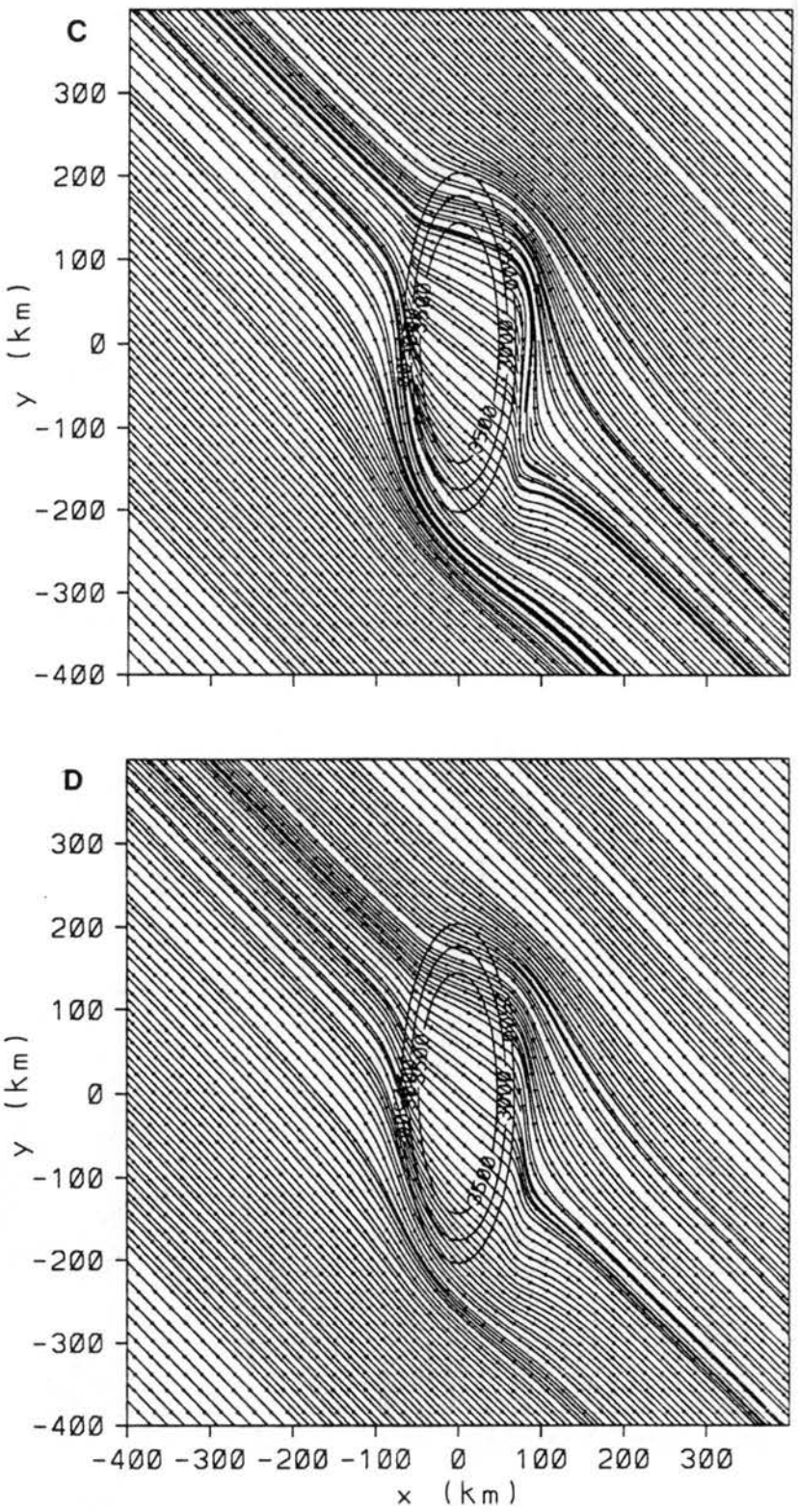

Figure 6.28: Continued: (c) Fr = 0.7 and (d) Fr = 0.9.

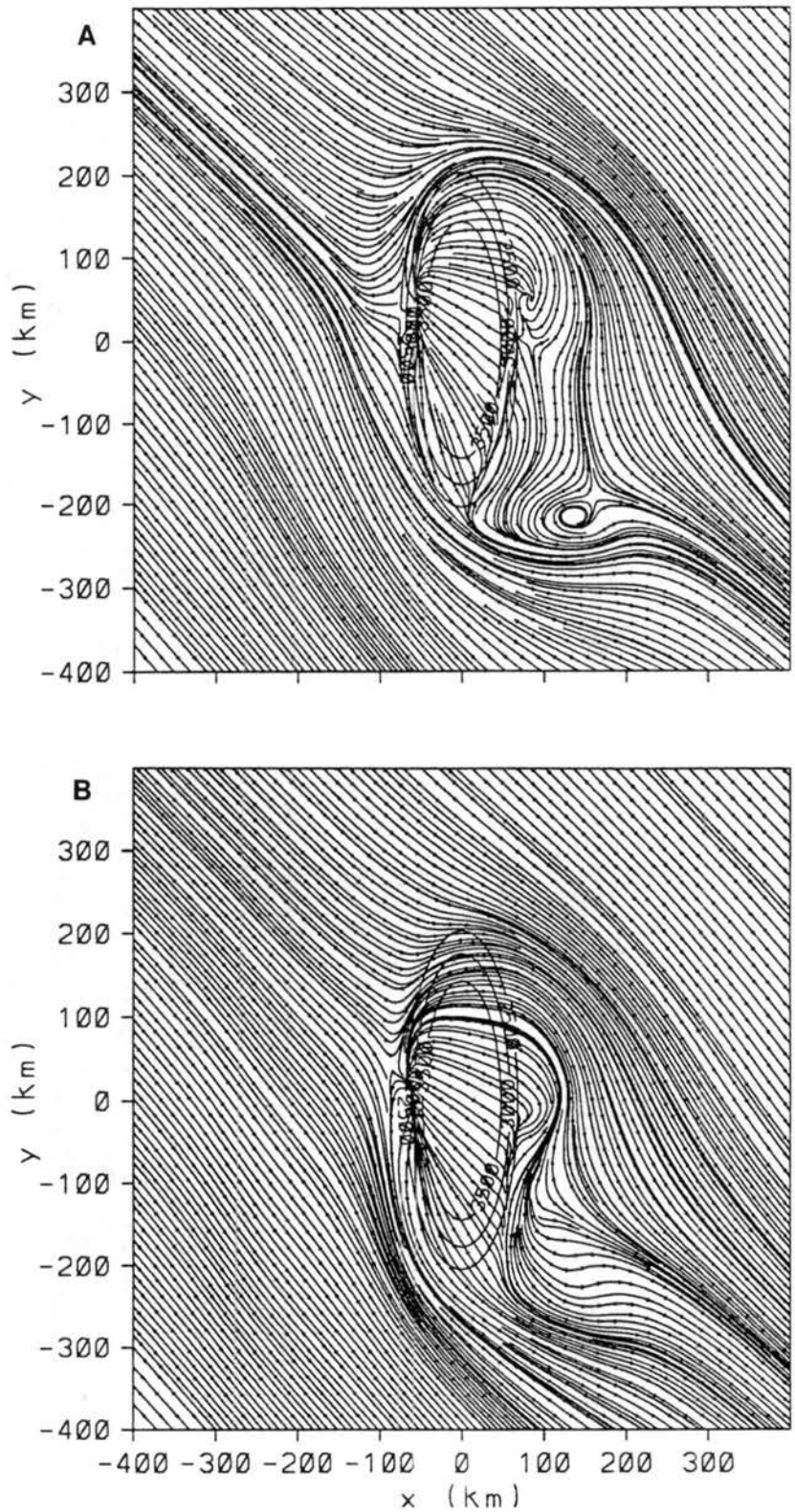

Figure 6.29: As in Fig 6.28 except for 6 h forecast.

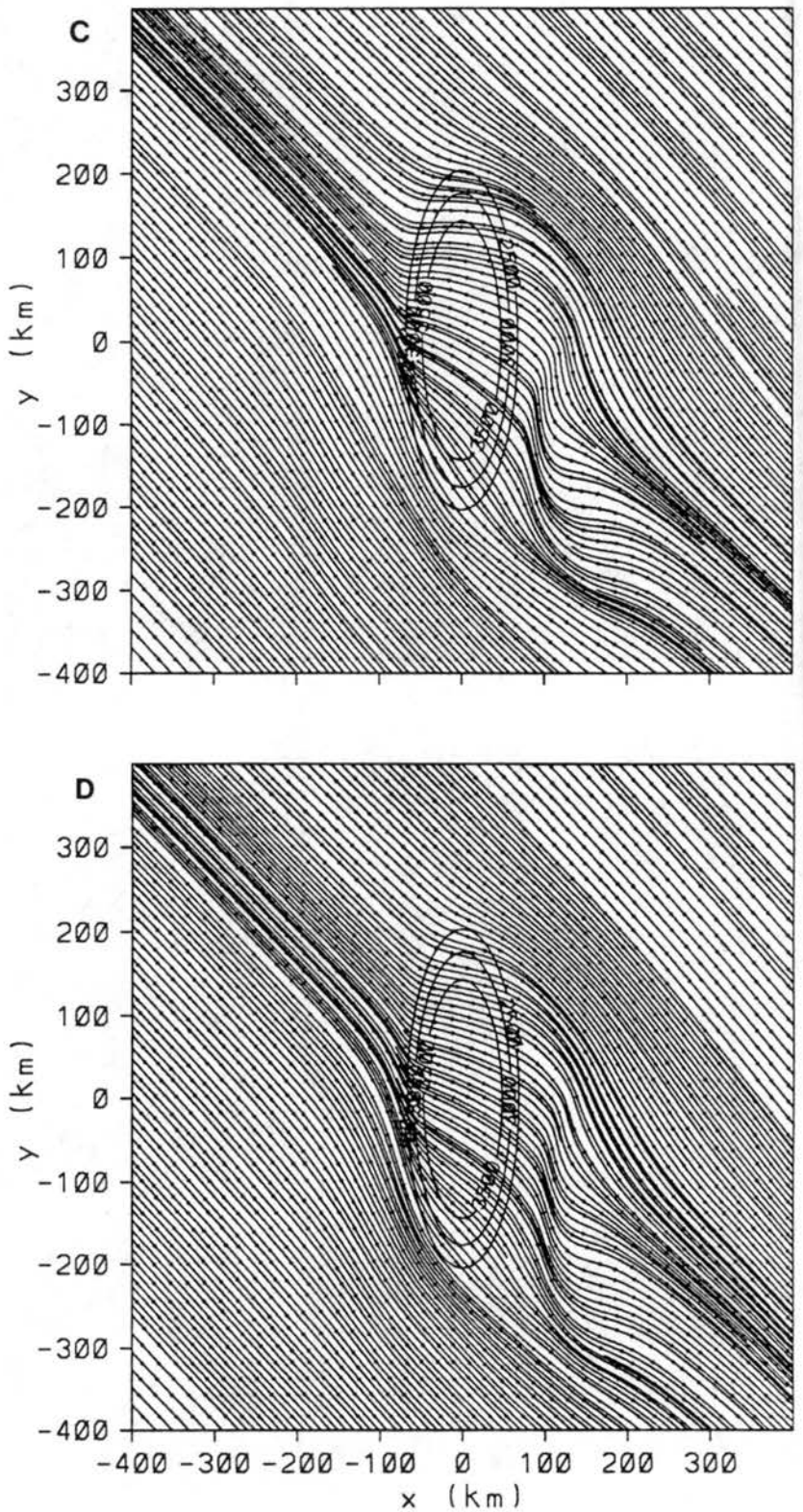

Figure 6.29: Continued:

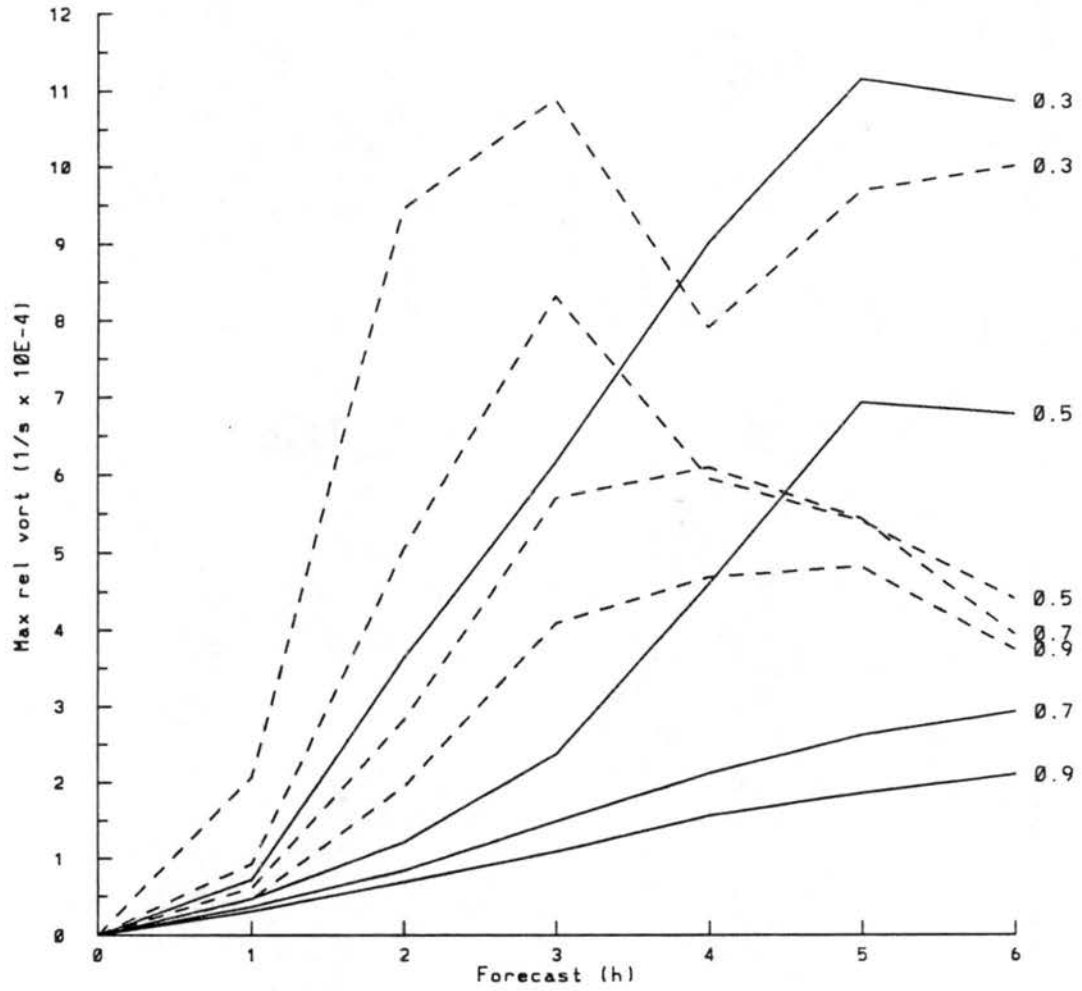

Figure 6.30: Maximum vertical vorticity ($\times 10^{-4}$ s^{-1}) for all cigar topography simulations initialized with northwest wind and Coriolis force. Dashed lines represent cyclonic vorticity and solid lines represent anticyclonic vorticity. Froude number is indicated to the right of each line.

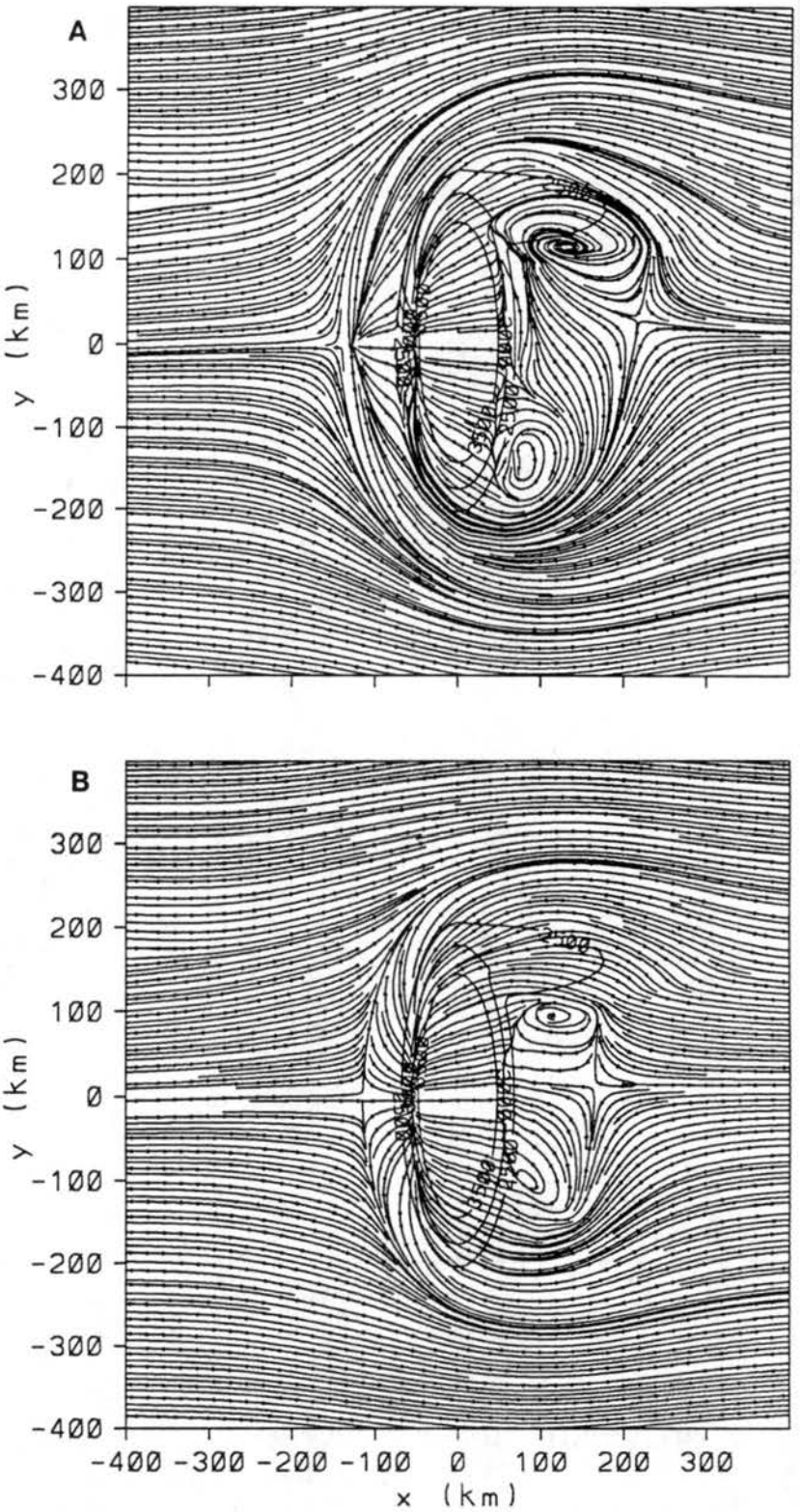

Figure 6.31: Low-level (146 AGL) streamlines at 6 h using fang topography initialized with west wind and no Coriolis force for (a) Fr = 0.3 and (b) Fr = 0.5.

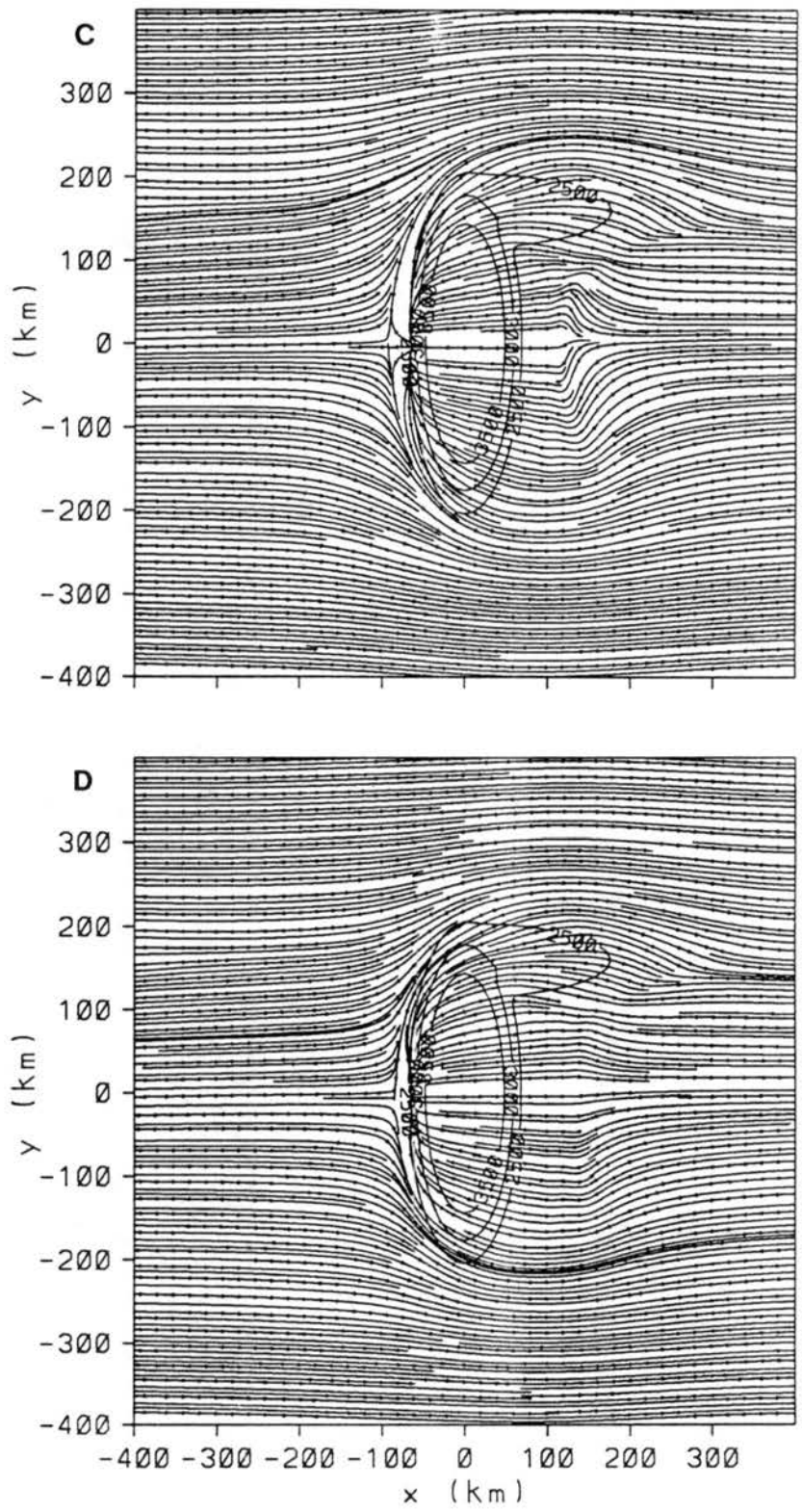

Figure 6.31: Continued: (c) Fr = 0.7 and (d) Fr = 0.9.

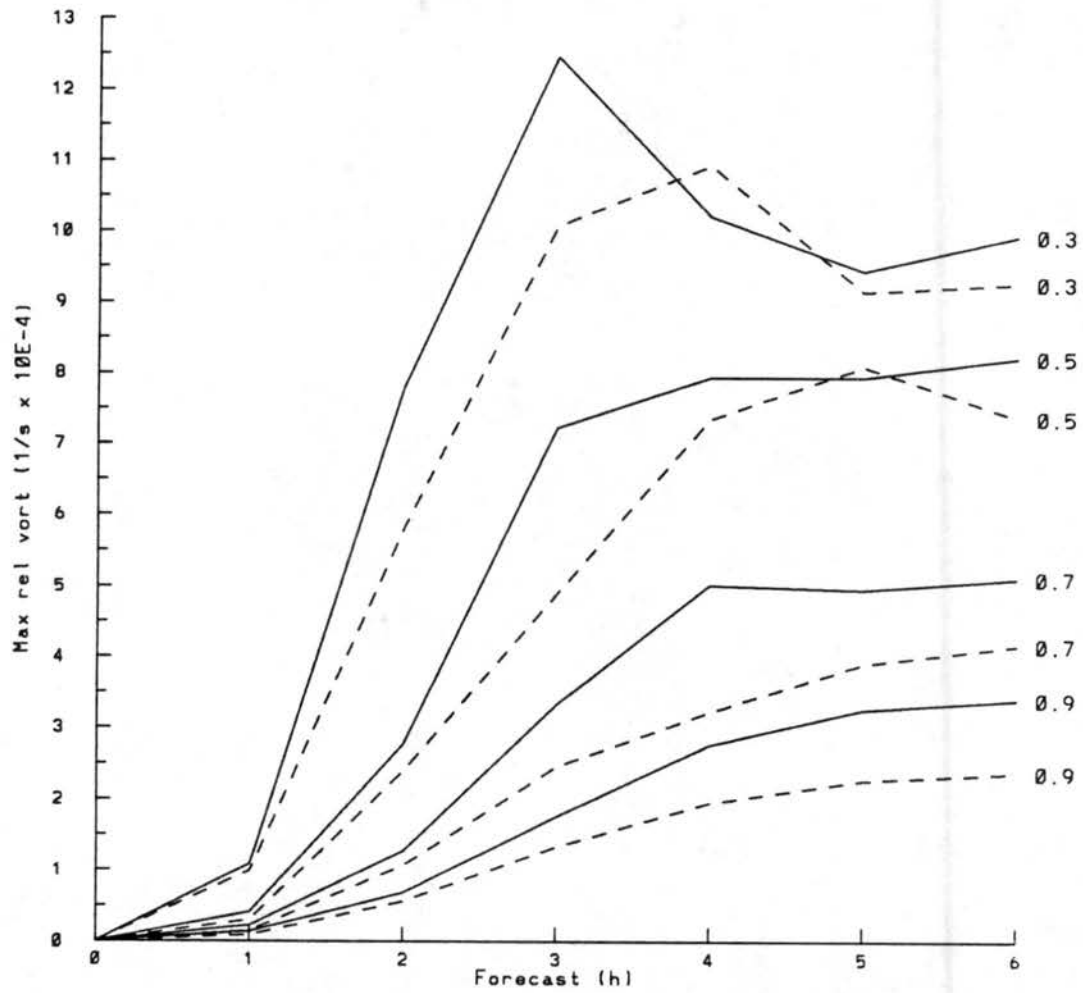

Figure 6.32: Maximum vertical vorticity ($\times 10^{-4}$ s^{-1}) for all fang topography simulations initialized with west wind and no Coriolis force. Dashed lines represent cyclonic vorticity and solid lines represent anticyclonic vorticity. Froude number is indicated to the right of each line.

A comparison of the Fr = 0.3 u, w, vorticity tilting, and vertical vorticity for the two topography experiments (Figs. 6.5 and 6.33) indicates the differences that create the southeastward displacement of the anticyclonic circulation. The east-west barrier extension causes less development in the lee wave structure resulting in weaker downward vertical motion that extends further east. This configuration forces the southeastward displacement in the positions of the vorticity tilting and the resultant vertical vorticity.

6.2.2.2 West wind, Coriolis force

Parallel simulations are conducted with the addition of the Coriolis force for Fr = 0.3, 0.5, 0.7, and 0.9 to investigate the earth rotational effects. The development and location of the flow separation point is similar to the cigar topography experiment with a southward displacement of 120 km indicated after 6 h (Fig. 6.34). The generation of the southern cyclonic vorticity area in the lee of the barrier is similar to the cyclonic vorticity development in the cigar topography case, however differences are noted in the development of the northern anticyclonic vorticity region. With the fang topography, the formation of a closed cyclonic vortex is evident for Fr = 0.3 and 0.5, but closed anticyclonic vortices do not develop for any Froude number. Similar to the cigar topography cases, the maximum cyclonic vorticity is initially greater than the anticyclonic vorticity, but the maximum anticyclonic vorticity becomes larger than the cyclonic vorticity with time for Fr = 0.3 and 0.5 (Fig. 6.35). Although maximum anticyclonic vorticity for the fang simulations is equal to or greater than the anticyclonic vorticity for the cigar topography cases (Fig. 6.18), a closed anticyclonic vortex is unable to develop. Since the westerly flow remains stronger over the east-west barrier extension, the resulting maximum anticyclonic vorticity region located to the south is comprised of stronger shear vorticity and weaker rotational vorticity.

6.2.2.3 Northwest wind, no Coriolis force

The previous simulations are repeated with a northwest initial flow for Fr = 0.3, 0.5, 0.7, and 0.9 to investigate the effects of a different wind direction relative to the mountain barrier. Low-level streamlines at 6 h are illustrated in Fig. 6.36. Upwind

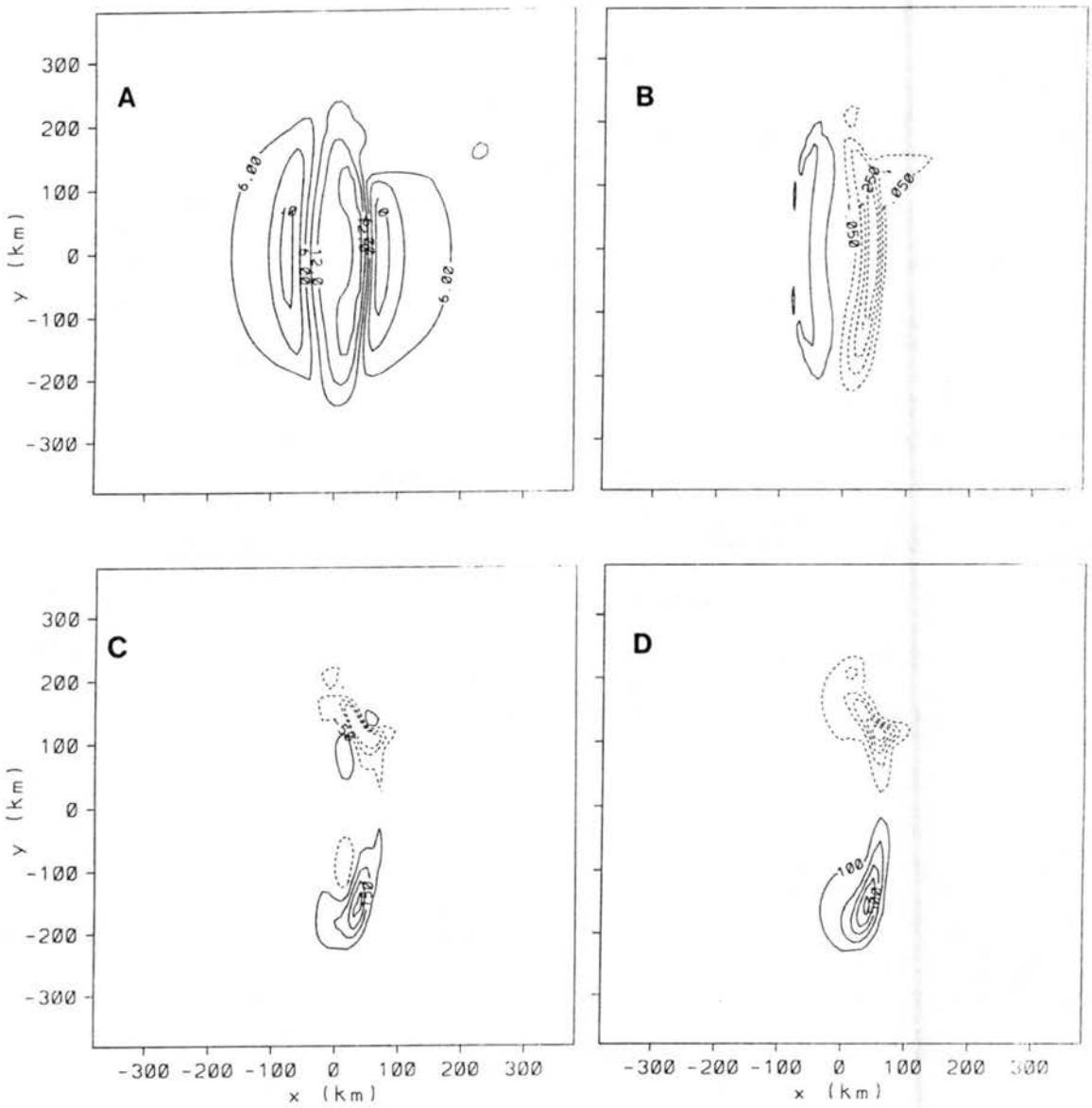

Figure 6.33: Low-level (146 AGL) 1 h forecasts of (a) u-component wind (m s^{-1}), (b) vertical motion (m s^{-1}), (c) tilting into vertical vorticity (s^{-2}, contour interval = 1.0 $\times$ 10^{-8} s^{-2}), and (d) vertical vorticity (s^{-1}, contour interval = 2.0 $\times$ 10^{-5} s^{-1}). Simulations initialized with fang topography, west wind, no Coriolis force, and Fr = 0.3.

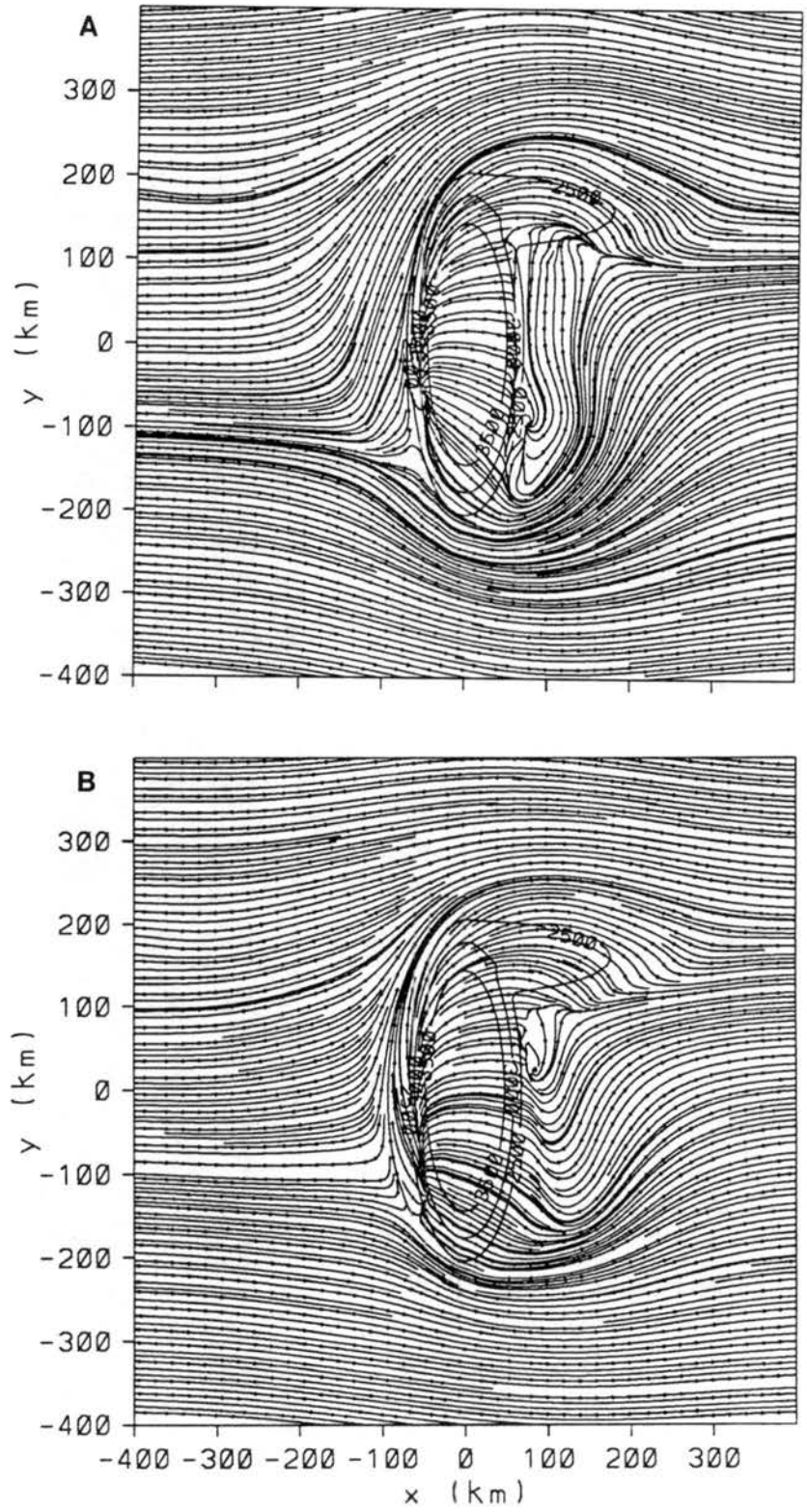

Figure 6.34: Low-level (146 AGL) streamlines at 6 h using fang topography initialized with west wind and Coriolis force for (a) Fr = 0.3 and (b) Fr = 0.5.

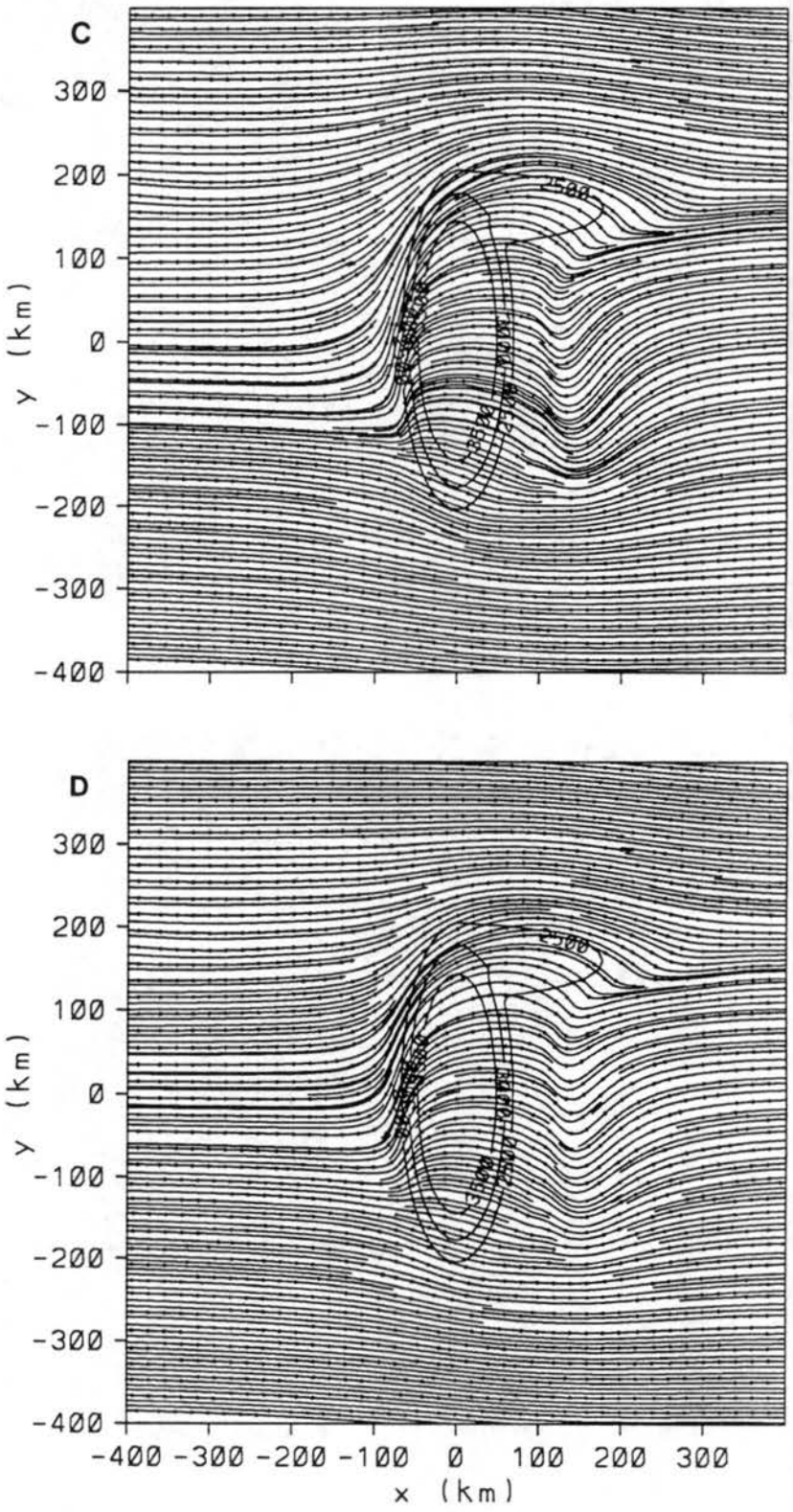

Figure 6.34: Continued: (c) Fr = 0.7 and (d) Fr = 0.9.

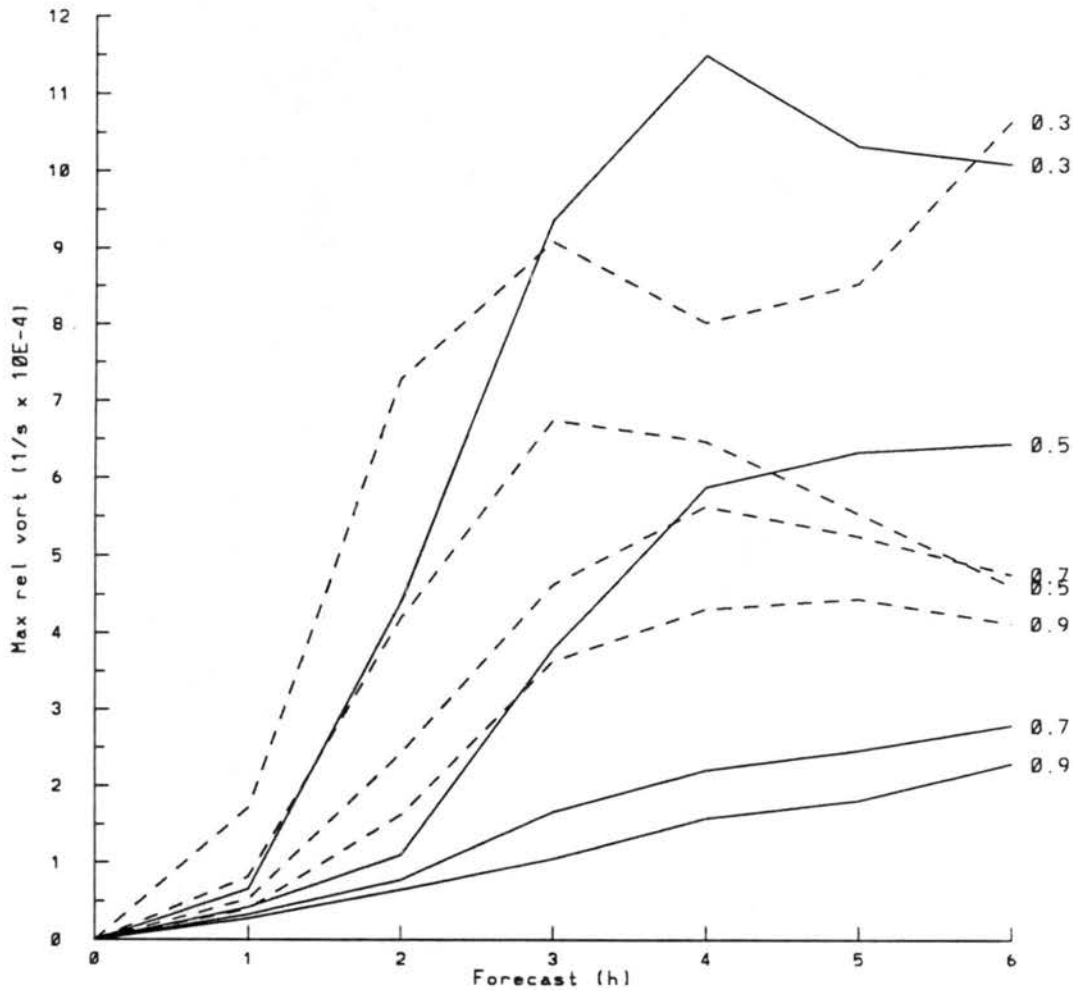

Figure 6.35: Maximum vertical vorticity ($\times$ 10 $^{-4}$ s^{-1}) for all fang topography simulations initialized with west wind and Coriolis force. Dashed lines represent cyclonic vorticity and solid lines represent anticyclonic vorticity. Froude number is indicated to the right of each line.

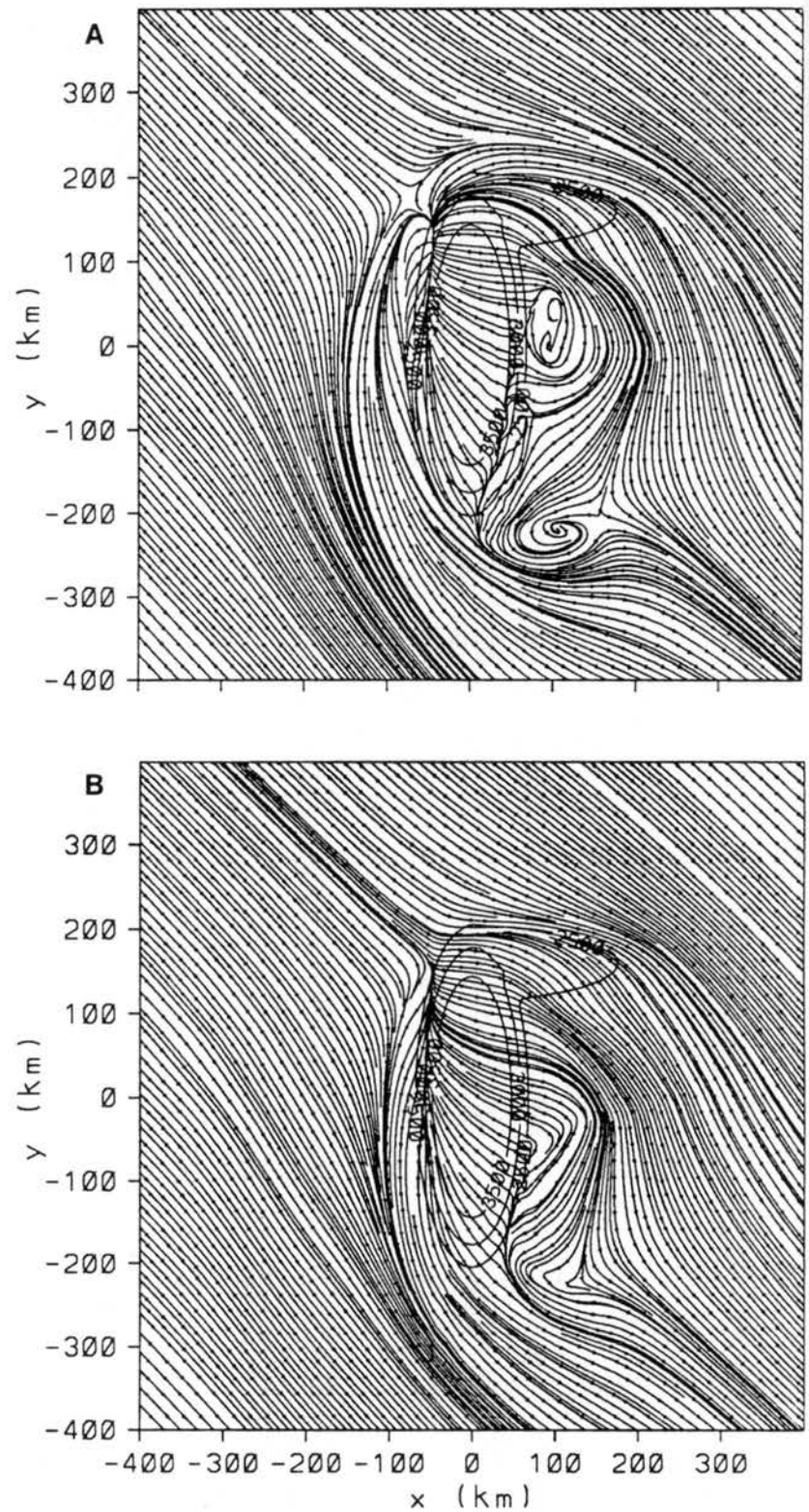

Figure 6.36: Low-level (146 AGL) streamlines at 6 h using fang topography initialized with northwest wind and no Coriolis force for (a) Fr = 0.3 and (b) Fr = 0.5.

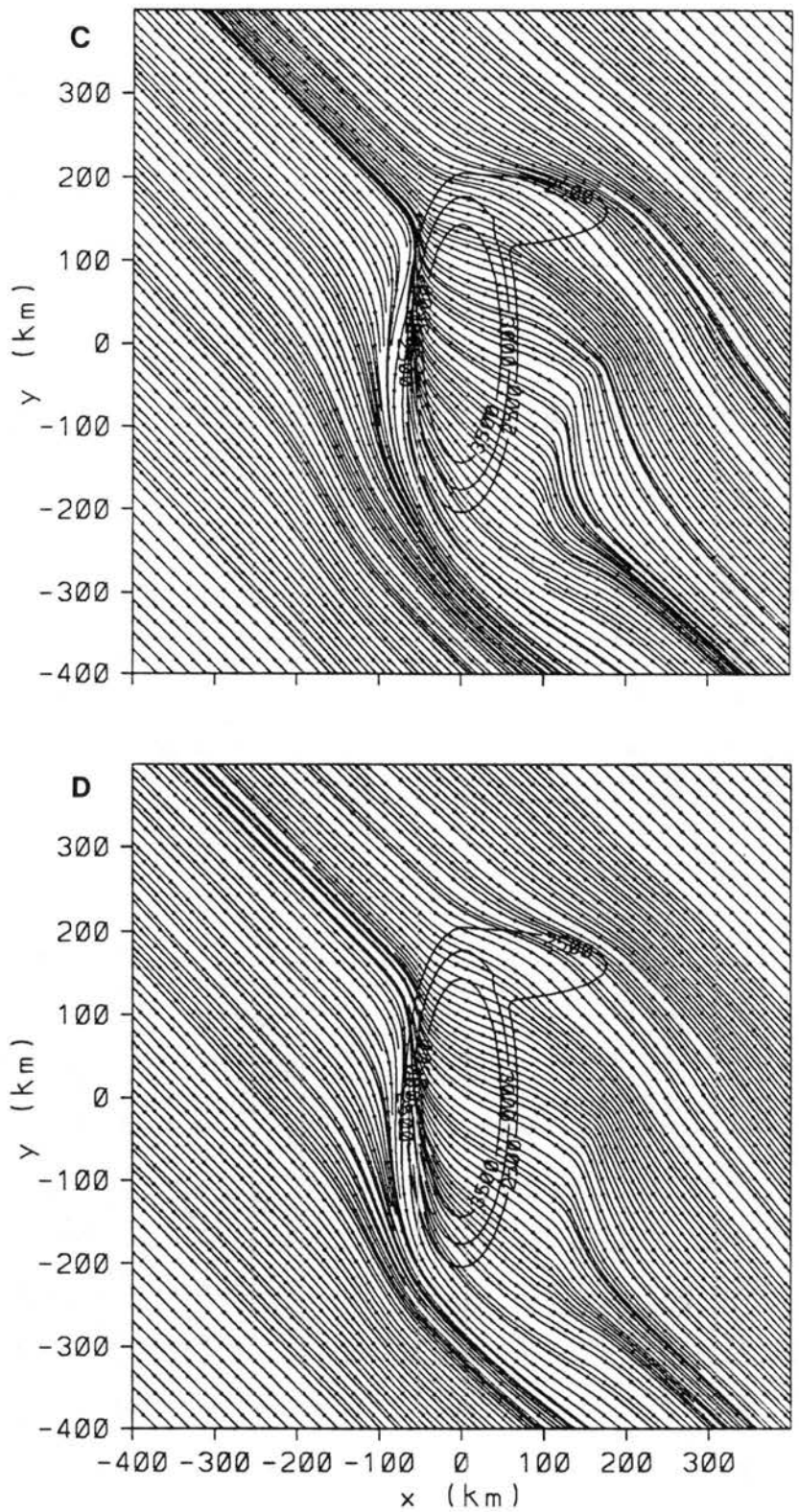

Figure 6.36: Continued: (c) Fr = 0.7 and (d) Fr = 0.9.

flow reversal and a low-level stagnation point for Fr = 0.3 and flow separation for the other simulations are indicated about 170 km north of the center east-west axis, similar to the cigar topography experiments. The development of a closed anticyclonic vortex for Fr = 0.3 with fang topography is the most significant difference when compared to the cigar topography cases. Recall that the formation of northerly along-barrier flow in the lee of the cigar topography tends to advect anticyclonic vorticity downstream creating an elongated convergence zone that does not evolve into a closed vortex. The east-west extension of the fang topography forces the low-level flow around the barrier that prevents the northerly along-barrier flow from forming. The result is a closed anticyclonic vortex for Fr = 0.3. As with the west wind experiments, a comparison of maximum vorticity between the two topography cases (Figs. 6.25 and 6.37) shows that the maximum cyclonic vorticity is nearly identical while the maximum anticyclonic vorticity vorticity for the fang topography is equal to or greater than the maximum anticyclonic vorticity for the cigar topography.

6.2.2.4 Northwest wind, Coriolis force

Parallel simulations are performed with the addition of the Coriolis force for Fr = 0.3, 0.5, 0.7, 0.9 to investigate the rotational effects of earth. Low-level streamlines at 6 h are illustrated in Fig. 6.38. Upwind flow characteristics are similar for the two topography experiments with the development of flow separation northwest of the barrier and the location moves south with time. Downwind flow characteristics are also quite similar for the two topography experiments suggesting that the Cheyenne Ridge has only a minimal effect on the lee surface wind direction for northwest wind situations. However, the Cheyenne Ridge likely provides a significant contribution to increased wind speeds south of the barrier due to lee wave effects. Upwind flow reversal and closed anticyclonic and cyclonic lee vortices are indicated for Fr = 0.3. Maximum cyclonic vorticity is about equal for the two topography cases. As with the cigar topography simulations, the maximum anticyclonic vorticity becomes greater than the maximum cyclonic vorticity after 4 h for Fr = 0.3 and 0.5, but the maximum anticyclonic values are a little larger for the fang topography cases (Fig. 6.39).

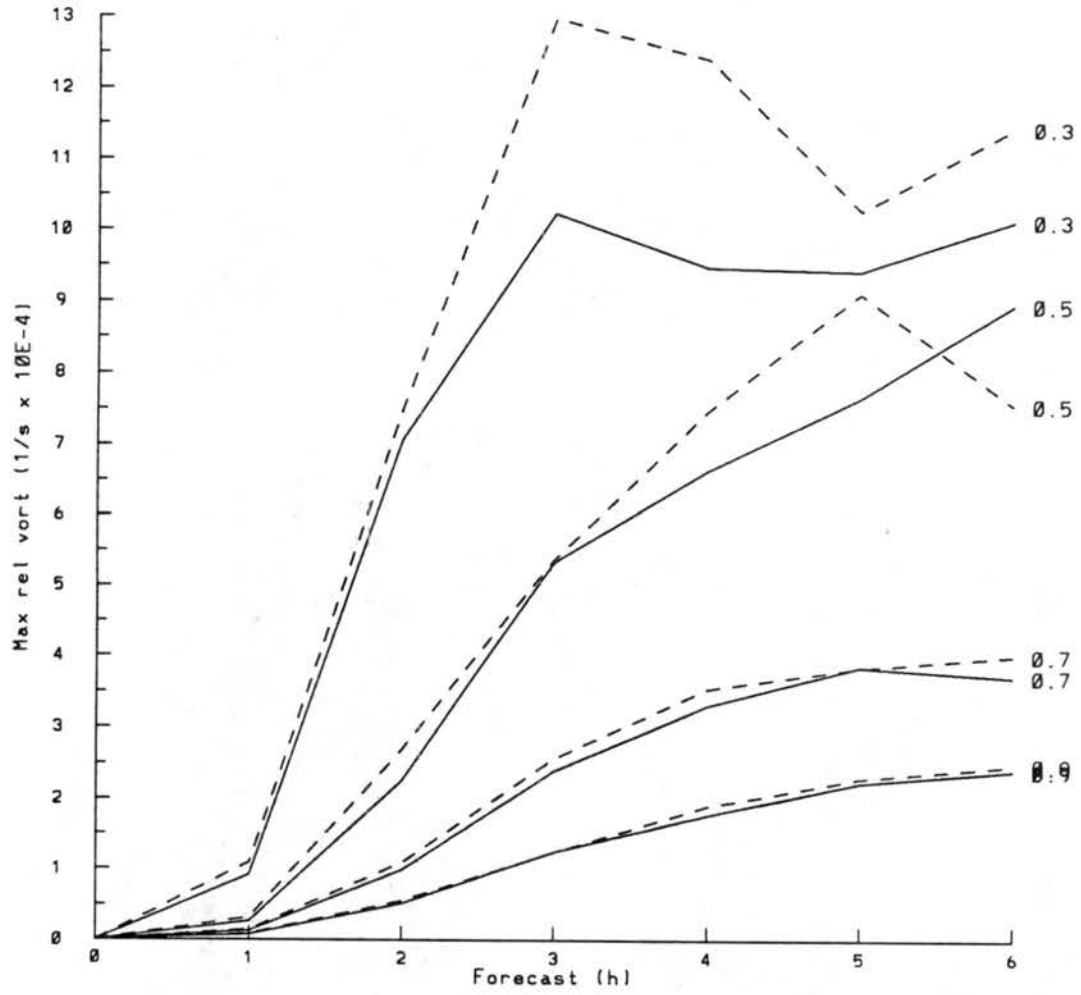

Figure 6.37: Maximum vertical vorticity ($\times 10^{-4}$ s^{-1}) for all fang topography simulations initialized with northwest wind and no Coriolis force. Dashed lines represent cyclonic vorticity and solid lines represent anticyclonic vorticity. Froude number is indicated to the right of each line.

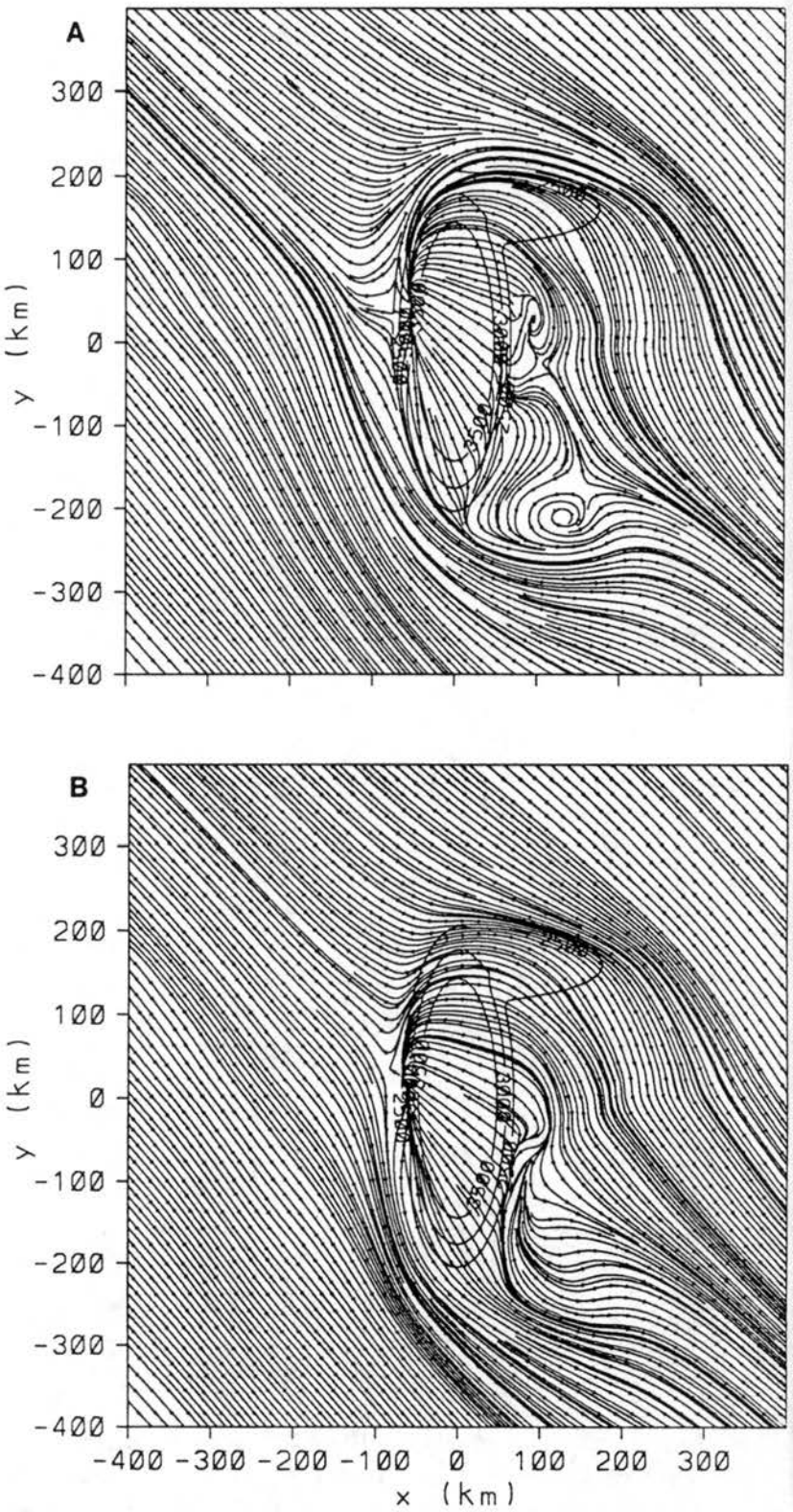

Figure 6.38: Low-level (146 AGL) streamlines at 6 h using fang topography initialized with northwest wind and Coriolis force for (a) Fr = 0.3 and (b) Fr = 0.5.

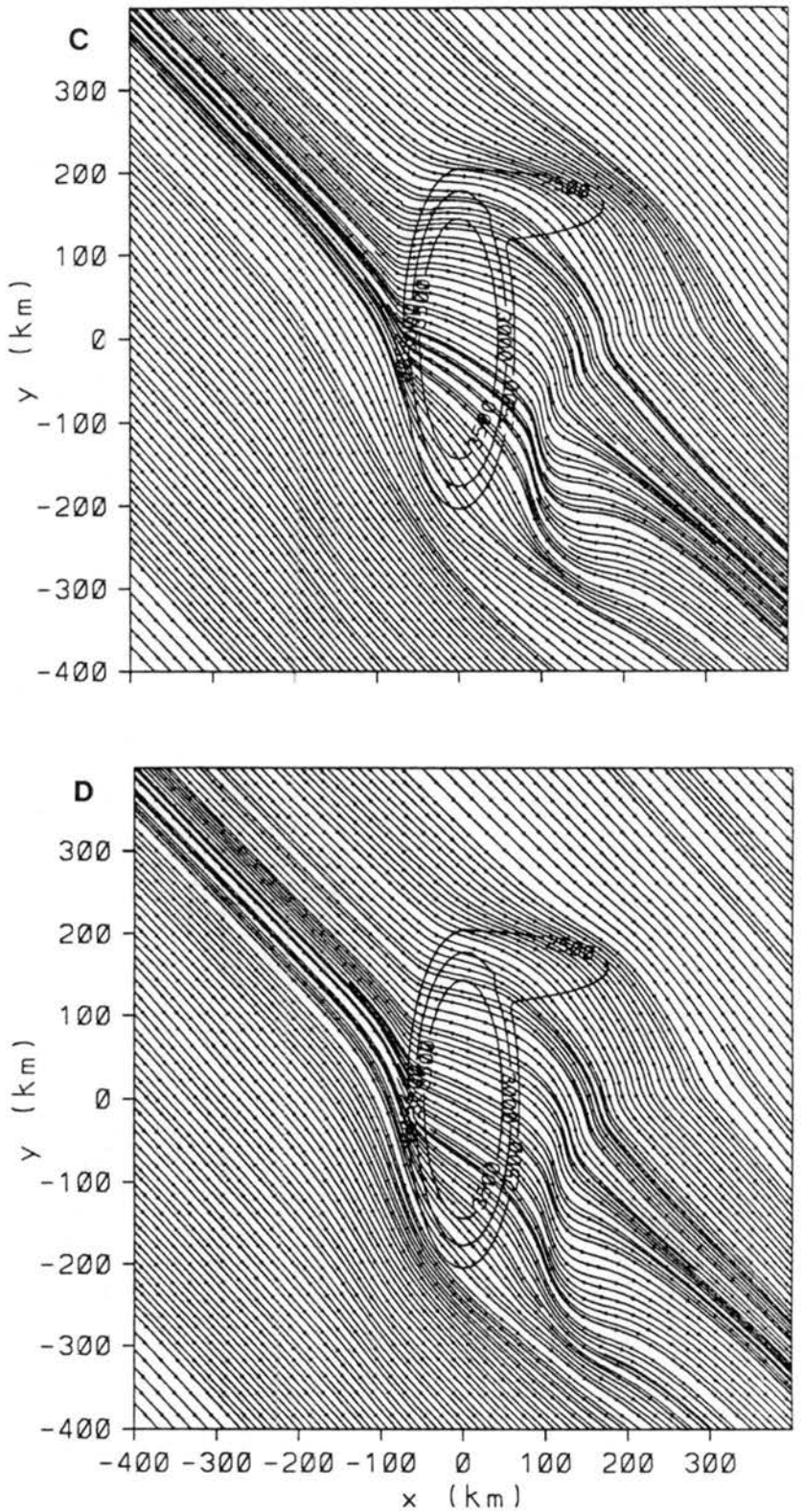

Figure 6.38: Continued: (c) Fr = 0.7 and (d) Fr = 0.9.

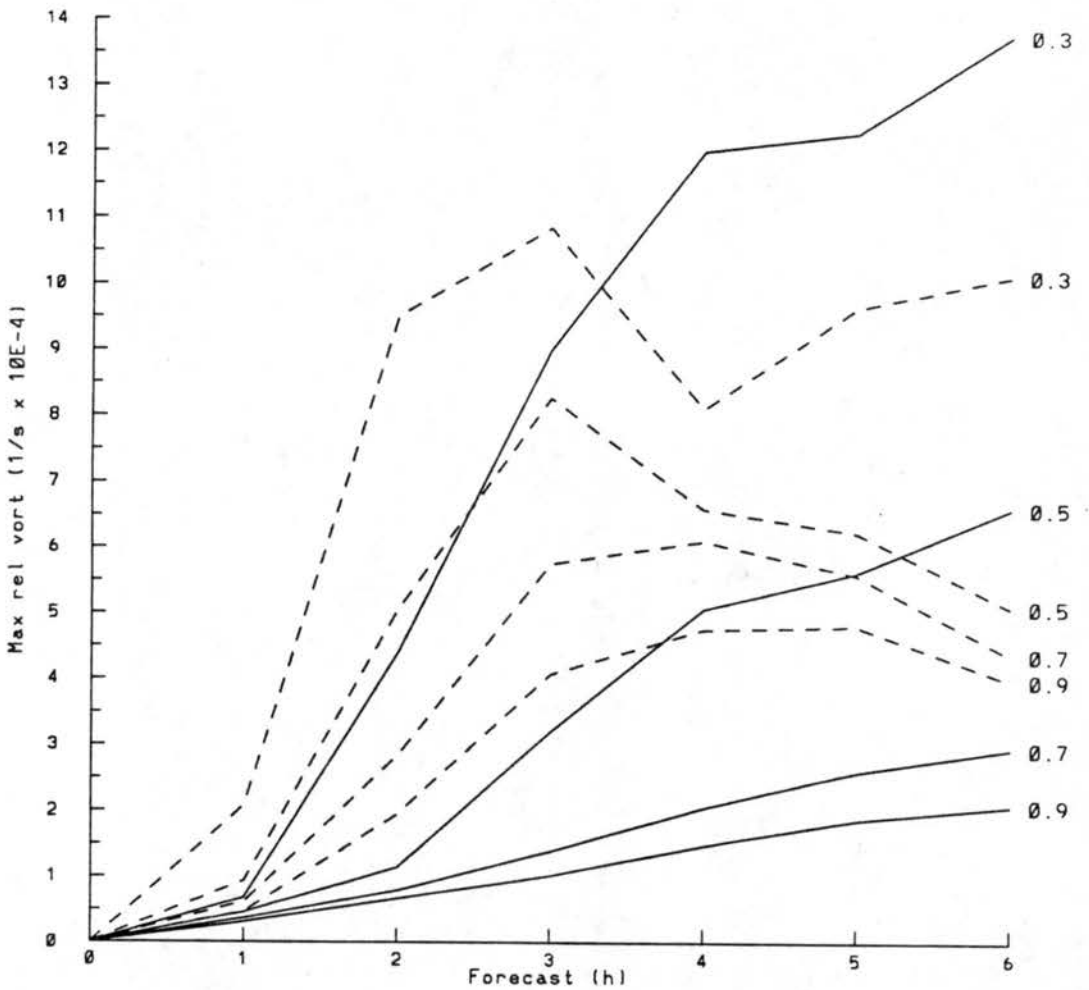

Figure 6.39: Maximum vertical vorticity ($\times$ 10 $^{-4}$ s^{-1}) for all fang topography simulations initialized with northwest wind and Coriolis force. Dashed lines represent cyclonic vorticity and solid lines represent anticyclonic vorticity. Froude number is indicated to the right of each line.

6.2.3 Summary

Results from the idealized simulations indicate that lee vortices develop with low Froude number flow past an isolated barrier using a free-slip lower boundary condition, consistent with the results of Smolarkiewicz and Rotunno (1989a). For westerly flow past the cigar topography ($\beta = 3$), lee vortex generation occurs for $\mathrm{Fr} \leq 0.6$ suggesting that the Froude number threshold for lee vortex generation increases as the barrier length to width aspect ratio (β) increases. The results indicate that neither upwind stagnation points nor wave breaking are necessary conditions for lee vortex development, despite their frequent coexistence. As the Froude number decreases, the generation of lee vortices is a smooth transition rather than a bifurcation as suggested by Smith (1989c).

The processes that are important to the development and evolution of the lee vortices are 1) the generation of horizontal vorticity by baroclinic processes, as proposed by Rotunno and Smolarkiewicz (1991), 2) the tilting of horizontal vorticity into vertical vorticity, and 3) the stretching and advection of vertical vorticity. In addition, the stretching and advection of planetary vertical vorticity must be included when considering the rotational effects of earth. Two factors which influence the location and strength of the vorticity tilting are upstream blocking and lee wave structure. Upstream blocking creates a vertical gradient in the horizontal flow and horizontal variations in the lee wave structure create a horizontal gradient in the vertical motion. The result is generation of horizontal vorticity which tilts into vertical vorticity. The strength of the upstream blocking controls the strength of the vertical gradient in the horizontal flow and hence the amount of tilting. The horizontal gradient of vertical motion contributes significantly less to the tilting strength but controls the sign of the tilting. Thus, the Froude number controls the magnitude of vertical vorticity generation, but the barrier shape controls the location of vertical vorticity generation. Finally, the stretching and advection of vertical vorticity control the evolution of the lee flow characteristics.

6.3 Comparison to Case Study Simulations

A comparison of the idealized topography model simulations with observations from the two case studies shows some interesting similarities. FSL mesonet wind observations

from 1800 UTC 7 January to 0000 UTC 8 January 1992 (Fig. 4.14) indicate strong westerly flow over the barrier, weak northeasterly flow adjacent to the barrier, and strong north-northwesterly flow over the Eastern Plains. These flow characteristics are similar to the features predicted by the idealized simulations using cigar and fang topography initialized with a northwest wind and Fr = 0.3 and 0.5 at 3 h (Fig. 6.28) and Fr = 0.5 at 6 h (Figs. 6.29, 6.38, and 6.40). Although difficult to assess an actual Froude number from the available observations, an estimate from the 1200 UTC Denver rawinsonde (Fig. 4.11a) is possible. Using the potential temperature gradient of 6 K from the layer between 800 and 700 mb, a barrier perpendicular wind speed of 7 m s^{-1}, and a barrier height of 2000 m, the observed Froude number is estimated at 0.23. It is likely that the Froude number increased during the day in response to increasing wind speeds as observed by the Platteville wind profiler (Fig. 4.13). A doubling of the observed wind speed between 1200 and 1800 UTC raises the estimated Froude number to near 0.5 suggesting that the comparison between the 7 January observations with the Fr = 0.5 idealized simulations is credible. The comparison indicates that much of the mesoscale variation observed in the 7 January 1992 surface flow is orographically-influenced and that the north-south Rocky Mountain barrier is the primary contributor to the altered wind directions. However, the Cheyenne Ridge likely contributed to the increased wind speeds observed south of the west-east barrier.

The post-frontal synoptic flow observed during the 8-9 March 1992 blizzard is more northerly in direction, hence the comparison of observations with the idealized simulations is less favorable. The FSL mesonet wind observations (Fig. 5.10) show strong north-northwest winds over the the Eastern Plains with strong north-northeast winds adjacent to the Front Range. This scenario is similar to the idealized flow characteristics east of the barrier for northwest initial flow with Fr = 0.7 at 3 h for the cigar (Fig. 6.28) and fang (not shown) topographies. An observed Froude number of 0.60 is estimated from the 0000 UTC Denver rawinsonde using a potential temperature gradient of 8.5 K from the layer between the surface and 700 mb, a wind speed of 20 m s^{-1} from the Platteville wind profiler, and a barrier height of 2000 m. The comparison suggests that the mesoscale variation in wind

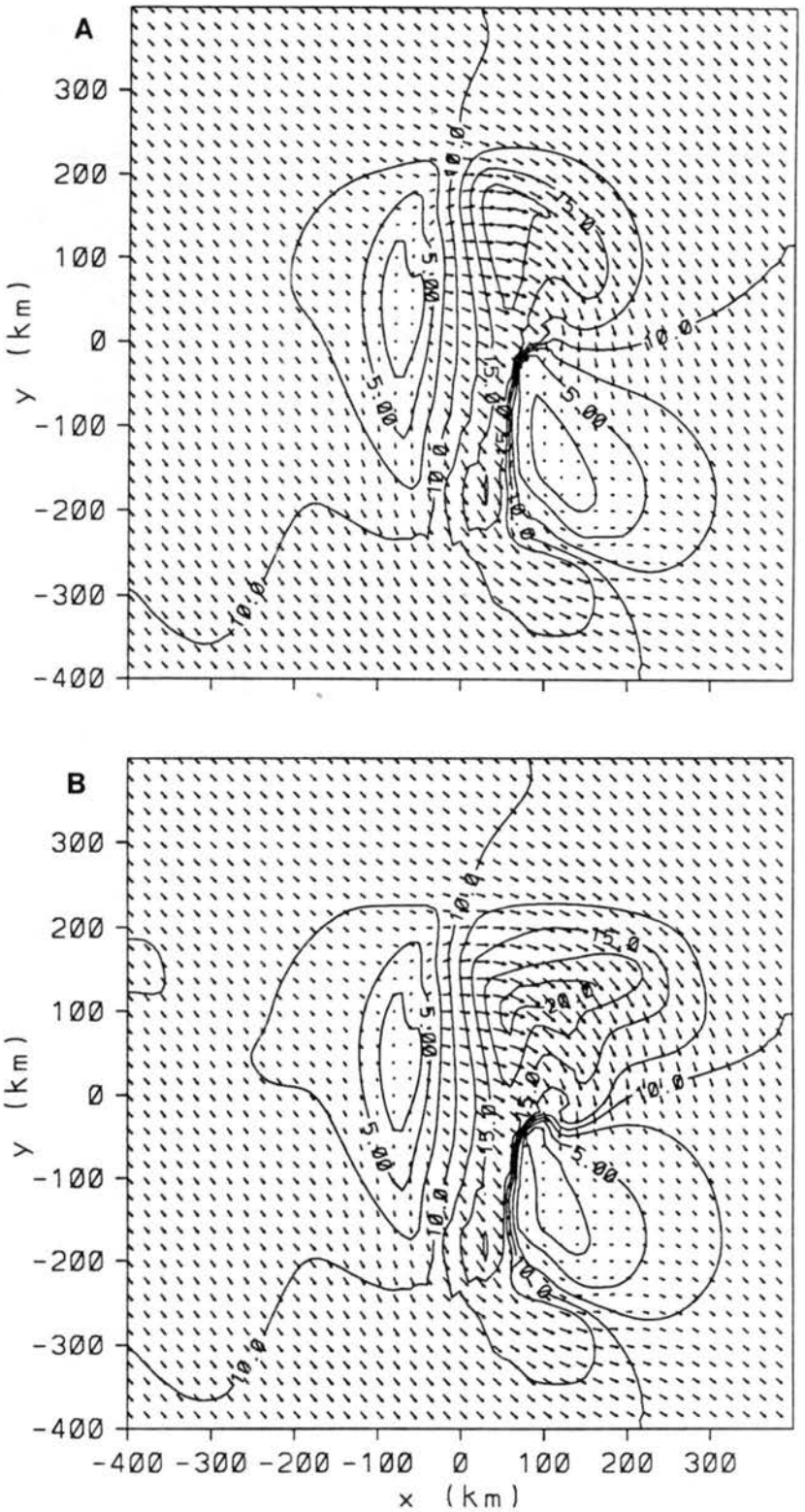

Figure 6.40: Low-level (146 AGL) wind vectors and isotachs (m s^{-1}) from the 6 h forecasts initialized with Fr = 0.5, northwest wind, and Coriolis force using (a) cigar topography (maximum vector is 19.8 m s^{-1}) and (b) fang topography (maximum vector is 20.9 m s^{-1}).

direction is topographically induced. The results demonstrate the significant impact that the orography can have on the surface flow in the vicinity of the Colorado Front Range and also demonstrates the capability of the model to resolve these important features that can contribute to improved operational forecasts.

Chapter 7

SUMMARY

The dissertation results are summarized in this chapter. The discussion includes results from the two case studies and from the idealized simulations. Finally, suggested topics for future research are proposed.

7.1 Case Study Results

Two objectives of this dissertation are to evaluate the accuracy of forecasts from a mesoscale numerical model initialized with high-resolution, non-homogeneous data and to determine if the model forecasts can resolve mesoscale features and thus add value to currently available national domain model predictions. The RAMS numerical model was initialized with high-resolution (10 km horizontal grid interval) operational LAPS analyses for two significant Colorado Front Range snowstorms, 7 January and 8-9 March 1992. Both storms are ideal for this investigation since observations contained strong winds, heavy snowfall, and significant mesoscale precipitation variation.

An unusual aspect of the 7 January snowstorm was the observed band of heavy snow (20-40 cm) that fell along a north-south line approximately 40 km east of the Front Range mountain barrier, while the barrier itself received less than 5 cm of snowfall. Significant mesoscale variation was also observed in the surface winds with strong, westerly downslope flow over the Front Range, weak northeasterly flow adjacent to the Front Range, and strong north-northwest flow over the Eastern Plains that generated blizzard conditions for most of the day. The combination of a stable boundary layer, strong geostrophic northwesterly flow over the Cheyenne Ridge, and weak northeasterly flow adjacent to the Front Range suggests the development of a Longmont anticyclone regime (Young and Johnson 1984). Although the associated convergence zone between the westerlies and northeasterlies has

been correlated with bands of enhanced snowfall in other storms, the heavy snow band with this system fell further east in the region of strong north-northwesterly flow.

A variety of interesting severe weather was associated with the 8-9 March snowstorm. The predominant mesoscale feature was a strong, fast moving arctic front that pushed southward across eastern Colorado. The national domain operational forecast models underestimated the severity of the front which caught many weekend travelers by surprise. Ahead of the front, strong thunderstorms developed in relatively warm, unstable air where numerous hail reports and two tornadoes were observed. Heavy snow and strong northerly winds produced blizzard conditions following frontal passage. As with the 7 January case, suggestions of a Longmont anticyclone regime were evident in the local scale observations.

The RAMS model simulations were successful in resolving most of the pertinent mesoscale features observed in both cases. In general, the surface flow characteristics were well predicted. The 7 January simulations resolved the three major surface wind regimes including 1) the persistent strong downslope flow east of the mountain barrier crest, 2) the development of weak northeasterlies adjacent to the Front Range, and 3) the generation of strong northwesterlies at the surface and low-levels over the Eastern Plains. The 8-9 March simulations were successful at predicting the development of the arctic front and the strong post-frontal high winds. Although difficult to verify, the model predictions appeared to resolve the upper air mesoscale flow features. Time series comparisons of upper level model forecast winds with wind profiler observations showed excellent agreement. Precipitation forecasts from the full microphysics simulations were capable of accurately resolving mesoscale features. The simulations were successful at predicting the eastward displacement of greatest snowfall away from the mountain barrier for 7 January and the development of post-frontal heavy snowfall for 8-9 March. The 8-9 March forecast rain-snow line also agreed well with observations.

The most noticeable forecast errors appeared to be related to the inability of the model to correctly resolve the 8-9 March pre-frontal convection. Although the model was successful at indicating the occurrence of convection in this environment, unrealistically large amounts of latent heat release created adverse effects on several fields including

concentrated regions of excessively large upward vertical velocities and precipitation. To rectify this problem, either the model grid interval must be decreased or a cumulus parameterization scheme designed specifically for mesoscale models must be employed. Despite this shortcoming, a qualitative comparison to other operational forecast models and a quantitative statistical model validation indicate that the RAMS predictions are capable of adding local scale, short-range (0-12 h) forecast value to the currently available regional scale model forecasts. Parallel simulations suggest that the addition of the separate LAPS surface analyses to the model initialization provides minor forecast improvement near the surface. The majority of the forecast improvement is due to the improved representation of the topography rather than a better initialization by LAPS compared to a MAPS initialization.

Another objective of this dissertation is to demonstrate the ability to utilize the model output to provide an improved scientific understanding of mesoscale weather events. An evaluation of the model simulations in combination with previous investigations, actual observations, and other larger domain model simulations was useful in formulating conceptual models of the two case study systems (Figs. 7.1 and 7.2). Three-dimensional views of the 7 January RAMS simulations provided insight into why the heavy snow fell east of the mountain barrier and east of the Longmont anticyclone convergence zone. A primary difference between this and other typical Front Range heavy snow storms was the development of a trapped lee wave that created a region of dry downslope flow with little or no precipitation over the Front Range. The heavy snow band appears to be the result of two features: 1) a low-level area of ascent that developed within the eastern half of the trapped lee wave and 2) moist mid-level easterly component flow that ascended over the mountain wave. The two regions of ascent were coincident about 40 km east of the mountain barrier and the model predicted a north-south band of heavy snow along this region. As the model predicted easterly flow backed to northerly, the forecast snowfall decreased which agreed with the surface observations of decreasing snowfall intensity.

Three-dimensional views of the 8-9 March RAMS simulations indicate precipitation processes that are typical of a Colorado cyclonic upslope event interacting with a shallow,

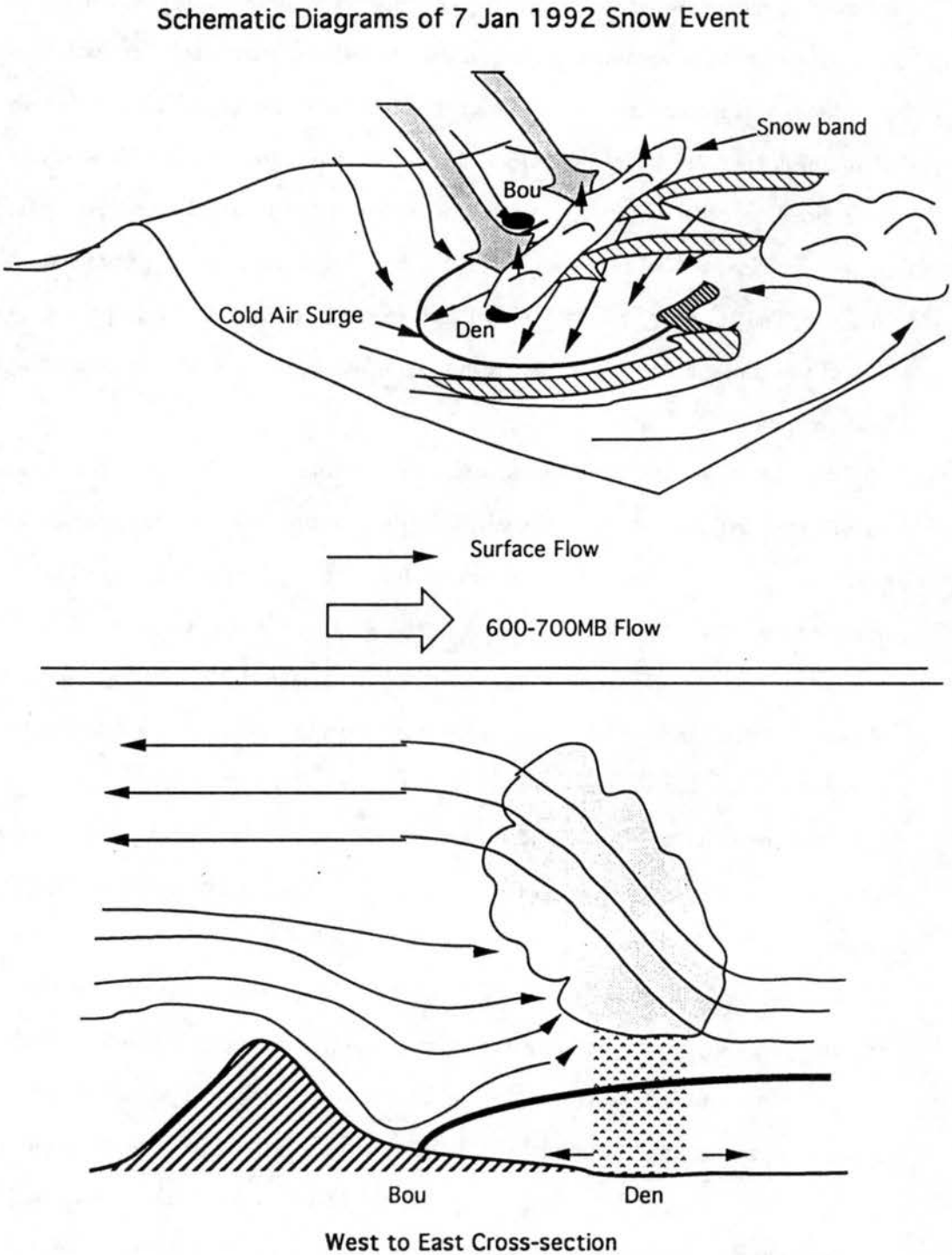

Figure 7.1: Conceptual model of 7 January 1992 snow storm.

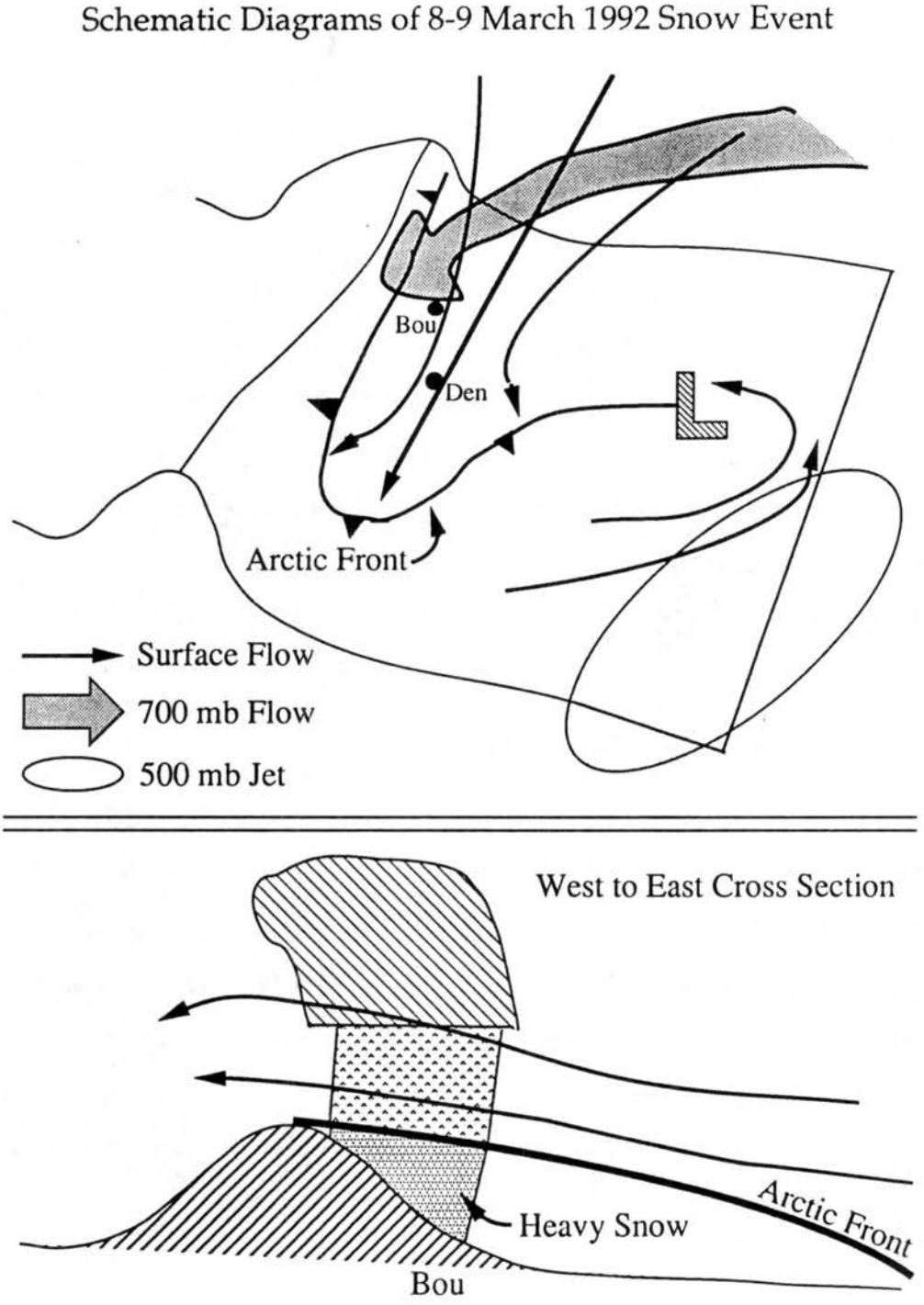

Figure 7.2: Conceptual model of 8-9 March 1992 snow storm.

southward moving arctic front. Easterly component flow developed north of the cyclone. The flow was strongest along the arctic frontal interface which created an upslope condition forced by the frontal boundary and the topography. In addition to the strong upslope flow, the model simulations suggest several other factors that contributed to the generation of heavy snow including a region of ascent that developed in moist, unstable air located within the left front quadrant of a mid-level jet streak and propagated over the arctic air mass, latent heat release in the ascent area that enhanced warm advection immediately upstream of this region, and a possible seeder-feeder effect.

The case study simulations were designed to emulate a real-time operational forecast using relatively inexpensive computer equipment that is currently available. The results of this investigation portend the ability to run regional domain operational mesoscale numerical models in the local weather forecast office. The mesoscale forecasts can add significant value to the currently available national domain model forecasts and they can help the operational forecaster formulate conceptual models of the atmosphere that can be applied towards an improved understanding of current and future meteorological events.

7.2 Idealized Simulations Results

The case study simulation results suggest that flow past the Colorado Rocky Mountain barrier creates a significant amount of the observed mesoscale variation in the lee flow configuration. A series of RAMS numerical experiments using idealized topography and horizontally homogeneous initial conditions were designed to investigate low Froude number flow around an isolated obstacle. The idealized model topography was specified to approximately represent two significant orographic features that can affect the weather along the Colorado Front Range: 1) the primary north-south Rocky Mountain barrier and 2) the west-east Cheyenne Ridge.

A comparison of the results to previous investigations corroborates and suggests several interesting conclusions. The idealized simulations indicate that lee vortices develop with low Froude number flow past an isolated barrier using a free-slip lower boundary condition, consistent with the results of Smolarkiewicz and Rotunno (1989a). The generation of lee vortices is a smooth transition as the Froude number decreases and is not a

bifurcation dependent on the development of upwind stagnation points nor wave breaking as suggested by linear theory (Smith 1989c).

The two factors that influence the strength and location of lee vortex generation are upstream blocking and lee wave structure. The resulting processes include 1) the generation of horizontal vorticity by baroclinic processes, as proposed by Rotunno and Smolarkiewicz (1991), 2) the tilting of horizontal vorticity into vertical vorticity that may create closed lee vortices, and 3) the stretching and advection of vertical vorticity that affects the evolving configuration of the lee flow. In addition, the stretching and advection of planetary vorticity must be included in order to represent the rotational effects of earth. The results indicate that the Froude number controls the strength of the lee vertical vorticity centers, the barrier shape controls the initial location of vertical vorticity generation, and vorticity stretching and advection control the evolution of the vorticity centers.

A comparison of the idealized simulations to the case study analyses reveals similar flow characteristics for the Fr = 0.5 and the 7 January 1992 experiments. The results suggest that much of the mesoscale variation observed in the 7 January surface flow is orographically influenced and that the north-south Rocky Mountain barrier is the primary contributor to the variation in wind direction, while the Cheyenne Ridge likely contributed to increased wind speeds observed over the Eastern Plains. Comparing the idealized simulations to the 8-9 March 1992 experiments indicates similar results that further demonstrate the significant impact that orography can have on the surface flow over northeast Colorado and also demonstrate the capability of a mesoscale model to resolve these important features that can contribute to improved operational forecasts.

7.3 Future Research Topics

The investigation results show that an operational mesoscale numerical model can add significant value to currently available national domain operational model predictions. However, the mesoscale forecasts have only been evaluated for two meteorological events and improvements to the model configuration may produce better predictions.

With further case study and real-time simulations, a statistically significant validation can be established for the current model configuration. Then, improvements to the model configuration can be tested and compared to the original configuration. Specific relevant topics are discussed below.

• The development of a real-time environment where RAMS is initialized with LAPS on a routine basis. Thompson (1993) completed a similar investigation initializing RAMS with MAPS. The objectives are two-fold. First, real-time forecasts would be available for critical objective review in a quasi-operational setting, such as a daily weather briefing. Second, the daily model output would be available to complete a statistically significant quantitative evaluation. A statistical baseline for this RAMS configuration should be established for comparison to other operational models and to possible improvements of the current RAMS configuration.

• The development of a full four-dimensional data assimilation (4DDA) system is possible with the LAPS analysis package and the RAMS forecast model. Using the current RAMS initialized with LAPS configuration, the 1 h RAMS forecast can be used as a background field for the next hours LAPS analysis, which in turn would initialize a new RAMS forecast, which in turn would provide a new LAPS background field, and so forth. The results from this investigation have demonstrated the capability of accurately forecasting mesoscale variation. In theory, these forecasts would introduce mesoscale variation into the LAPS analyses in data sparse regions. RAMS initialized with the improved LAPS analyses would generate better forecasts that are incorporated into future LAPS analyses, etc.

• The development of a non-homogeneous initialized soil model. Several investigations have described the importance of mesoscale variations in soil temperature and moisture to the resulting weather (e.g. Lanicci et al. 1987, Pielke and Avissar 1990, Pielke et al. 1991, Papineau 1992). Using high resolution data sources such as Doppler radar and digital satellite imagery, a non-homogeneous analysis of soil temperature and moisture is possible. A non-homogeneous initialization of the RAMS soil model would likely be a significant improvement over the current initialization scheme which uses surface air temperature and moisture data. If successful, the 4DDA scheme described above could be extended to the soil model.

• The design of a model configuration that better represents convection. Adverse effects due to incorrectly resolving the convection were noted in the 8-9 March case study. Increasing the grid resolution may solve these problems, but possibly at the expense of losing the capability to operate in real-time. An alternative is to incorporate a cumulus parameterization scheme designed specifically for mesoscale resolution models, such as the scheme developed by Weissbluth and Cotton (1993).

• The reduction of adverse effects by the lateral boundaries. Although the Davies lateral boundary nudging scheme did not introduce deleterious influences on the case study forecasts, the scheme does require an accurate larger domain forecast to be available which requires waiting for the completion of that particular model simulation. Alternatives to this configuration would be to increase the local domain size such that an alternative lateral boundary condition could be used or to use the RAMS nested grid system. A proposed nested grid system is initializing a national domain grid with MAPS analysis data and initializing a higher resolution, regional domain grid with LAPS analysis data. The simultaneous initialization of more than one grid with separate initializations has not yet been attempted with RAMS.

• The utilization of three-dimensional (3-D) visualization. The high resolution, full physics numerical model generates an enormous amount of output data. Using the standard two-dimensional techniques to view the model output would require an extensive effort to peruse the data. Although not discussed in this investigation, the utilization of 3-D visualization was invaluable in evaluating the enormous amount of model output. Three-dimensional visualization aids in rapidly determining the areas of interest, at which time the two-dimensional techniques can be applied to a specific region. The process of formulating conceptual models is greatly enhanced by having the capability to view the model data in three dimensions.

In addition to research applications, 3-D visualization has important operational applications that are currently undeveloped. If the operational forecaster is to utilize the mesoscale model forecasts in a timely manner, one must have the capability to rapidly peruse the model predictions. Developing efficient 3-D visualization techniques will be an

important part of implementing an operational mesoscale prediction model in the local weather office. Some 3-D visualization techniques have been developed for research applications, but more development is still required. Transforming these techniques to function efficiently in an operational environment is also required if one is to take full advantage of the value added by an operational mesoscale forecast model.

Results from the idealized simulations demonstrate that the mesoscale model can be utilized to gain an improved scientific understanding of mesoscale weather events. The experiments conducted in this investigation were designed to investigate a particular flow regime, i.e. low Froude number flow characteristics often observed in northeast Colorado. Several extensions to these experiments are possible. The investigation of other wind directions is warranted. The relationship between surface friction and lee vortex generation can be investigated by changing the lower boundary condition in the model. Finally, parallel experiments that consider other topography features, such as the Palmer Lake Divide or real topography, would provide a more complete understanding of the flow characteristics in the vicinity of the Colorado Front Range.

REFERENCES

Abbs, D. J., and R. A. Pielke, 1987: Numerical simulations of orographic effects on NE Colorado snowstorms. *Meteor. Atmos. Phys.*, **37**, 1–10.

Abe, M., 1932: The formation of cloud by the obstruction of Mount Fuji. *Geophys. Mag.*, **6**, 1–13.

Albers, S. C., 1989: A severe weather forecast scheme incorporating mesoscale analyses. *Preprints, 12th Conference on Weather Analysis and Forecasting*, 2-6 October 1989, Monterey, CA, AMS, Boston, 242-246.

Baines, P. G., 1979: Observations of stratified flow past three-dimensional barriers. *J. Geophys. Res.*, **84**, 7834–7838.

Benjamin, S. G., K. A. Brewster, R. Brümmer, B. F. Jewett, T. W. Schlatter, T. L. Smith, and P. A. Stamus, 1991: An isentropic three-hourly data assimilation system using ACARS aircraft data. *Mon. Wea. Rev.*, **119**, 888–906.

Bennetts, D. A., and B. J. Hoskins, 1979: Conditional symmetric instability–A possible explanation for frontal rainbands. *Quart. J. Roy. Meteor. Soc.*, **105**, 945–962.

Birkenheuer, D., 1991: An algorithm for operational water vapor analyses integrating GOES and dual–channel microwave radiometer data on the local scale. *J. Appl. Meteor.*, **30**, 834–843.

Black, T. L., and F. Mesinger, 1991: Small scale circulations in NMC's 30 km eta model. *Preprints, Ninth Conference on Numerical Weather Prediction*, 14–18 October 1991, Denver, AMS, Boston, 229–230.

Boatman, J. F., and R. F. Reinking, 1984: Synoptic and mesoscale circulations and precipitation mechanisms in shallow upslope storms over the western high plains. *Mon. Wea. Rev.*, **112**, 1725–1744.

Bosart, L. F., 1975: New England coastal frontogenesis. *Quart. J. Roy. Meteor. Soc.*, **101**, 957-978.

Brighton, P. W. M., 1978: Strongly stratified flow past three-dimensional obstacles. *Quart. J. Roy. Meteor. Soc.*, **104**, 289–307.

Castro, I. P., 1987: A note on lee wave structures in stratified flow over three-dimensional obstacles. *Tellus*, **39A**, 72–81.

Castro, I. P., W. H. Snyder, and G. L. Marsh, 1983: Stratified flow over three-dimensional ridges. *J. Fluid Mech.*, **135**, 261–282.

Chen, C., and W. R. Cotton, 1983: A one-dimensional simulation of the stratocumulus-capped mixed layer. *Boundary Layer Meteor.*, **25**, 289–321.

Clark, T. L., and W. R. Peltier, 1977: On the evolution and stability of finite-amplitude mountain waves. *J. Atmos. Sci.*, **34**, 1715–1730.

Colman, B. R., 1989: Mesoscale analysis of an upslope snowstorm in Colorado. *Preprints, 12th Conference on Weather Analysis and Forecasting*, 2–6 October 1989, Monterey, Calif., AMS, Boston, 372–377.

Corby, G. A., 1954: The airflow over mountains: A review of the state of current knowledge. *Quart. J. Roy. Meteor. Soc.*, **80**, 491–521.

Cotton, W. R., and R. A. Anthes, 1989: *Storm and Cloud Dynamics.* Academic Press, 883 pp.

Cotton, W. R., G. Thompson, and P. W. Mielke, Jr., 1993: Realtime mesoscale prediction on workstations. Accepted *Bull. Am. Meteor. Soc.*

Cram, J. M., 1990: Numerical simulation and analysis of the propagation of a prefrontal squall line. Ph.D. Thesis, Colorado State University, Department of Atmospheric Science, 332 pp.

Crook, N. A., T. L. Clark, and M. W. Moncrieff, 1990: The Denver cyclone. Part I: Generation in low Froude number flow. *J. Atmos. Sci.*, **47**, 2725–2742.

Davies, H. C., 1976: A lateral boundary formulation for multi-level prediction models. *Quart. J. Roy. Meteor. Soc.*, **102**, 405–418.

Drazin, P. G., 1961: On the steady flow of a fluid of variable density past an obstacle. *Tellus*, **23**, 239–251.

Dudhia, J., 1993: A nonhydrostatic version of the Penn State-NCAR mesoscale model: Validation tests and simulation of an Atlantic cyclone and cold front. *Mon. Wea. Rev.*, **121**, 1493–1513.

Dunn, L. B., 1987: Cold-air damming by the Front Range of the Colorado Rockies and its relationship to locally heavy snows. *Wea. Forecasting*, **2**, 177–189.

Dunn, L. B., 1988: Vertical motion evaluation of a Colorado snowstorm from a synoptician's perspective. *Wea. Forecasting*, **3**, 261–272.

Dunn, L. B., 1992: Evidence of ascent in a sloped barrier jet and an associated heavy-snow band. *Mon. Wea. Rev.*, **120**, 914–924.

Durran, D. R., 1990: Mountain waves and downslope winds. In *Atmospheric Processes over Complex Terrain*, Ed., W. Blumen, AMS, Boston, MA, Chapter 4, 59–81.

Fawcett, E. B., and H. K. Saylor, 1965: A study of the distribution of weather accompanying Colorado cyclogenesis. *Mon. Wea. Rev.*, **93**, 359–367.

Flatau, P. J., G. J. Tripoli, J. Verlinde, and W. R. Cotton, 1989: The CSU-RAMS cloud microphysical module: General theory and code documentation. Dept. of Atmospheric Science Paper No. 451, Colorado State University, 88 pp.

Gerrity, J. G., 1977: The LFM model–1976: A documentation. NOAA Tech. Memo. No. 60, NWS, NMC, 68 pp.

Hoke, J. E., N. A. Phillips, G. J. DiMego, J. J. Tuccillo, and J. G. Sela, 1989: The regional analysis and forecast system in the national meteorological center. *Wea. Forecasting*, **4**, 323–334.

Horsley, T., 1945: New light on the standing wave. *Aeronautics*, **11**, 38–41.

Howard, K. W., and E. I. Tollerud, 1988: The structure and evolution of heavy-snow-producing Colorado cyclones. *Preprints, Palmen Symposium on Extratropical Cyclones and Their Role in the General Circulation*, 29 August–2 September 1988, Helsinki, Finland, 168–171.

Hunt, J. C. R., and W. H. Snyder, 1980: Experiments on stably and neutrally stratified flow over a model three-dimensional hill. *J. Fluid Mech.*, **96**, 671–704.

Junker, N. W., J. E. Hoke, and R. H. Grumm, 1989: Performance of NMC's regional models. *Wea. Forecasting*, **4**, 368–390.

Klemp, J. B., and D. K. Lilly, 1978: Numerical simulation of hydrostatic mountain waves. *J. Atmos. Sci.*, **35**, 78–107.

Lanicci, J. M., T. N. Carlson, and T. T. Warner, 1987: Sensitivity of the Great Plains severe-storm environment to soil-moisture distribution. *Mon. Wea. Rev.*, **115**, 2660–2673.

Lee, T. J., 1992: The impact of vegetation on the atmospheric boundary layer and convective storms. Ph.D. Thesis, Colorado State University, Department of Atmospheric Science, 137 pp.

Lee, T. J., R. A. Pielke, R. C. Kessler, and J. Weaver, 1989: Influence of cold pools downstream of mountain barriers on downslope winds and flushing. *Mon. Wea. Rev.*, **117**, 2041–2058.

Lilly, D. K., 1981: Doppler radar observations of upslope snowstorms. *Preprints, Second Conference on Mountain Meteorology*, November 1981, Steamboat Springs, CO, AMS, Boston, 346–353.

Louis, J. F., 1979: A parametric model of vertical eddy fluxes in the atmosphere. *Boundary Layer Meteor.*, **17**, 187–202.

Mayr, G. J., 1993: Evolution of orogenic blocking. Ph.D. Thesis, Colorado State University, Department of Atmospheric Science, 113 pp.

McGinley, J. A., 1987: A variational analysis scheme for analysis of the ALPEX data set. *Meteor. Atmos. Phys.*, **36**, 5–23.

McGinley, J. A., 1989: The local analysis and prediction system. *Preprints, 12th Conference on Weather Analysis and Forecasting*, 2–6 October 1989, Monterey, Calif., AMS, Boston, 15–20.

McGinley, J. A., S. C. Albers, and P. A. Stamus, 1991: Validation of a composite convective index as defined by a real-time local analysis system. *Wea. Forecasting*, **6**, 337–356.

Meroney, R. N., 1990: Fluid dynamics of flow over hills/mountains–Insights obtained through physical modeling. In *Atmospheric Processes over Complex Terrain*, Ed., W. Blumen, AMS, Boston, MA, Chapter 7, 145–171.

Mesinger, F., Z. I. Janjić, S. Ničković, D. Gavrilov, and D. G. Deaven, 1988: The step-mountain coordinate: Model description and performance for cases of alpine lee cyclogenesis and for a case of an Appalachian redevelopment. *Mon. Wea. Rev.*, **116**, 1493–1518.

Mielke, P. W., 1984: Meteorological applications of permutation techniques based on distance functions. In *Handbook of Statistics, Vol. 4*, Eds., P. R. Krishnaiah and P. K. Sen, North-Holland, Amsterdam, 813–830.

Mielke, P. W., 1986: Non-metric statistical analysis: Some metric alternatives. *J. Stat. Plann. Inference*, **13**, 377–387.

Mielke, P. W., 1991: The application of multivariate permutation methods based on distance functions in the earth sciences. *Earth–Science Rev.*, *31*, 55-71.

Nicholls, 1993: Applications of the RAMS numerical model to dispersion over urban areas. *NATO Advanced Study Institute: Wind Climate in Cities*, Karlsruhe, Germany.

Papineau, J. M. 1992: A performance evaluation of the NGM and RAMS models for the 29-30 March 1991 Front Range storm. M.S. Thesis, Colorado State University, Department of Atmospheric Science, pp. 73.

Parish, T. R., 1982: Barrier winds along the Sierra Nevada mountains. *J. Appl. Meteor.*, **21**, 925–930.

Peltier, W. R., and T. L. Clark, 1979: The evolution and stability of finite-amplitude mountain waves. Part II: Surface wave drag abd severe downslope windstorms. *J. Atmos. Sci.*, **36**, 1498–1529.

Phillips, D. S., 1984: Analytical surface pressure and drag for linear hydrostatic flow over three-dimensional elliptical mountains. *J. Atmos. Sci.*, **41**, 1073–1084.

Pielke, R. A., 1984: *Mesoscale Meteorological Modeling.* Academic Press, 612 pp.

Pielke, R. A., and R. Avissar, 1990: Influence of landscape structure on local and regional climate. *Landscape Ecol.*, **4**, 133–155.

Pielke, R. A., W. R. Cotton, R. L. Walko, C. J. Tremback, W. A. Lyons, L. D. Grasso, M. E. Nicholls, M. D. Moran, D. A. Wesley, T. J. Lee, and J. H. Copeland, 1992: A comprehensive meteorological modeling system - RAMS. *Meteor. Atmos. Phys.*, **49**, 69–91.

Pielke, R. A., G. A. Dalu, J. S. Snook, T. J. Lee, and T. G. F. Kittel, 1991: Nonlinear influence of mesoscale land use on weather and climate. *J. Climate*, **4**, 1053–1069.

Pierrehumbert, R. T., 1984: Linear results on the barrier effects of mesoscale mountains. *J. Atmos. Sci.*, **41**, 1356–1367.

Pierrehumbert, R. T., and B. Wyman, 1985: Upstream effects of mesoscale mountains. *J. Atmos. Sci.*, **42**, 977–1003.

Queney, P., 1948: The problem of air flow over a mountain: A summary of theoretical studies. *Bull. Am. Meteor. Soc.*, **29**, 16–26.

Rasmussen, R., M. Politovich, J. Marwitz, W. Sand, J. McGinley, J. Smart, R. Pielke, S. Rutledge, D. Wesley, G. Stossmeister, B. Bernstein, K. Elmore, N. Powell, E. Westwater, B. B. Stankov, and D. Burrows, 1992: Winter Icing and Storms Project (WISP). *Bull. Am. Meteor. Soc.*, **73**, 951–974.

Reinking, R. F., and J. F. Boatman, 1986: Upslope precipitation events. In *Mesoscale Meteorology and Forecasting*, Ed., P. S. Ray, AMS, Boston, MA, Chapter 19, 437–471.

Ross, B. B., 1986: An overview of numerical weather prediction. In *Mesoscale Meteorology and Forecasting*, Ed., P. S. Ray, AMS, Boston, MA, Chapter 30, 720–751.

Rotunno, R., and P. K. Smolarkiewicz, 1991: Further results on lee-vortices in low-froude-number flow. *J. Atmos. Sci.*, **48**, 2204–2211.

Schlatter, T. W., D. V. Baker, and J. F. Henz, 1983: Profiling Colorado's Christmas Eve blizzard. *Weatherwise*, **36**, 60–66.

Schmidt, J. M., and J. S. Snook, 1992: A numerical and observational investigation of the 7 January 1992 Denver, Colorado, blizzard: A regional-scale perspective. *Preprints, Sixth Conference on Mountain Meteorology*, 29 September–2 October 1992, Portland, OR, AMS, Boston, 161–165.

Scorer, R. S., 1949: Theory of waves in the lee of mountains. *Quart. J Roy. Meteor. Soc.*, **75**, 41–56.

Sheppard, P. A., 1956: Airflow over mountains. *Quart. J. Roy. Meteor. Soc.*, **82**, 528–529.

Smagorinsky, J., 1963: General circulation experiments with the primitive equations. I: The basic experiment. *Mon. Wea. Rev.*, **91**, 99-164.

Smith, R. B., 1980: Linear theory of stratified hydrostatic flow past an isolated mountain. *Tellus*, **32**, 348–364.

Smith, R. B., 1982: Synoptic observations and theory of orographically disturbed wind and pressure. *J. Atmos. Sci.*, **39**, 60–70.

Smith, R. B., 1988: Linear theory of stratified flow past an isolated mountain in isoteric coordinates. *J. Atmos. Sci.*, **45**, 3889–3896.

Smith, R. B., 1989a: Mountain-induced stagnation points in hydrostatic flow. *Tellus*, **41A**, 270–274.

Smith, R. B., 1989b: Hydrostatic airflow over mountains. *Adv. Geophys.*, **31**, 1–41.

Smith, R. B., 1989c: Comment on "Low froude number flow past three-dimensional obstacles. Part I: Baroclinically generated lee vortices." *J. Atmos. Sci.*, **46**, 3611–3613.

Smith, R. B., 1990: Why can't stably stratified air rise over high ground? In *Atmospheric Processes over Complex Terrain*, Ed., W. Blumen, AMS, Boston, MA, Appendix to Chapter 5, 105–107.

Smith, T. L., and S. G. Benjamin, 1993: Impact of network wind profiler data on a 3-h data assimilation system. *Bull. Am. Meteor. Soc.*, **74**, 801–807.

Smolarkiewicz, P. K., R. Rasmussen, and T. L. Clark, 1988: On the dynamics of Hawaiian cloud bands: Island forcing. *J. Atmos. Sci.*, **45**, 1872–1905.

Smolarkiewicz, P. K., and R. Rotunno, 1989a: Low Froude number flow past three-dimensional obstacles. Part I: Baroclinically generated lee vortices. *J. Atmos. Sci.*, **46**, 1154–1164.

Smolarkiewicz, P. K., and R. Rotunno, 1989b: Reply (to comment by R. B. Smith). *J. Atmos. Sci.*, **46**, 3614–3617.

Smolarkiewicz, P. K., and R. Rotunno, 1990: Low Froude number flow past three-dimensional obstacles. Part II: Upwind flow reversal zone. *J. Atmos. Sci.*, **47**, 1498–1511.

Snook, J. S., 1992: Current techniques for real-time evaluation of conditional symmetric instability. *Wea. Forecasting*, **7**, 430–439.

Snook, J. S., and J. A. McGinley, 1990: Integration of GOES-VAS sounding data in a local scale analysis. *Preprints, Fifth Conference on Satellite Meteorology and Oceanography*, 3–7 September 1990, London, England, AMS, Boston, 349–353.

Snook, J. S., and J. M. Schmidt, 1992: A numerical and observational investigation of the 7 January 1992 Denver, Colorado, blizzard: Local-scale perspective. *Preprints, Sixth Conference on Mountain Meteorology*, 29 September–2 October 1992, Portland, OR, AMS, Boston, 101–105.

Snyder, W. H., R. S. Thompson, R. E. Eskridge, R. E. Lawson, I. P. Castro, J. T. Lee, J. C. R. Hunt, and Y. Ogawa, 1985: The structure of strongly stratified flow over hills: dividing-streamline concept. *J. Fluid Mech.*, **152**, 249–288.

Somieski, F., 1981: Linear theory of three-dimensional flow over mesoscale mountains. *Beitr. Phys. Atmos.*, **54**, 315–334.

Spangler, T. C., 1987: Comparison of actual dividing-streamline heights to height predictions using the Froude number. *J. Clim. Appl. Meteor.*, **26**, 204–207.

Stein, J., 1992: Investigation of the regime diagram of hydrostatic flow over a mountain with a primitive equation model. Part I: Two-dimensional flows. *Mon. Wea. Rev.*, **120**, 2962–2976.

Storm Data, 1992: National Climatic Data Center, 34.

Thompson, G., 1993: Prototype real-time mesoscale prediction during the 1991-1992 winter season and statistical verification of model data. M.S. Thesis, Colorado State University, Department of Atmospheric Science, 105 pp.

Thorsteinsson, S., 1988: Finite amplitude stratified air flow past isolated mountains on an f-plane. *Tellus*, **40A**, 220–236.

Tollerud, E. I., K. W. Howard, X.-P. Zhong, 1991: Jet streaks and their relationship to heavy precipitation in Colorado Front Range winter storms. *Preprints, First International Symposium on Winter Storms*, 14–18 January 1991, New Orleans, LA, AMS, Boston, 97–100.

Tremback, C. J., 1990: Numerical simulation of a mesoscale convective complex: Model development and numerical results. Ph.D. Thesis, Colorado State University, Department of Atmospheric Science, 247 pp.

Tremback, C. J., and R. Kessler, 1985: A surface temperature and moisture parameterization for use in mesoscale numerical models. *Seventh Conference on Numerical Weather Prediction*, Montreal, Canada, AMS, Boston, 355–358.

Tritton, D. J., 1977: *Physical Fluid Dynamics.* Van Nostrand Reinhold Company Ltd., 362 pp.

Tucker, D. F., P. W. Mielke, and E. R. Reiter, 1989: The verification of numerical models with multivariate randomized block permutation procedures. *Meteor. Atmos. Phys.*, **40**, 181–188.

Warner, T. T., R. A. Anthes, and A. L. McNab, 1978: Numerical simulations with a three-dimensional mesoscale model. *Mon. Wea. Rev.*, **106**, 1079–1099.

Warner, T. L., and N. L. Seaman, 1990: A real-time, mesoscale numerical weather-prediction system used for research, teaching, and public service at the Pennsylvania State University. *Bull. Am. Meteor. Soc.*, **71**, 792–805.

Weissbluth, M. J., and W. R. Cotton, 1993: The representation of convection in mesoscale models. Part I: Scheme fabrication and calibration. Accepted *J. Atmos. Sci.*

Wesley, D. A., 1991: An investigation of the effects of topography on Colorado Front Range winter storms. Ph.D. Thesis, Colorado State University, Department of Atmospheric Science, 197 pp.

Wesley, D. A., and R. A. Pielke, 1990: Observations of blocking-induced convergence zones and effects on precipitation in complex terrain. *Atmos. Res.*, **25**, 235–276.

Wesley, D. A., J. F. Weaver, R. A. Pielke, 1990: Heavy snowfall during an arctic outbreak along the Colorado Front Range. *Nat. Wea. Digest*, **15**, 2–19.

Wurtele, M., 1957: The three-dimensional lee wave. *Beitr. Phys. Atmos.*, **29**, 242–252.

Young, G. S., and R. H. Johnson, 1984: Meso- and microscale features of a Colorado cold front. *J. Clim. Appl. Meteor.*, **23**, 1315–1325.